26th IMEKO TC4 International Symposium
24th International Workshop on ADC/DAC Modelling&Testing
Pordenone, 20/21 September 2023

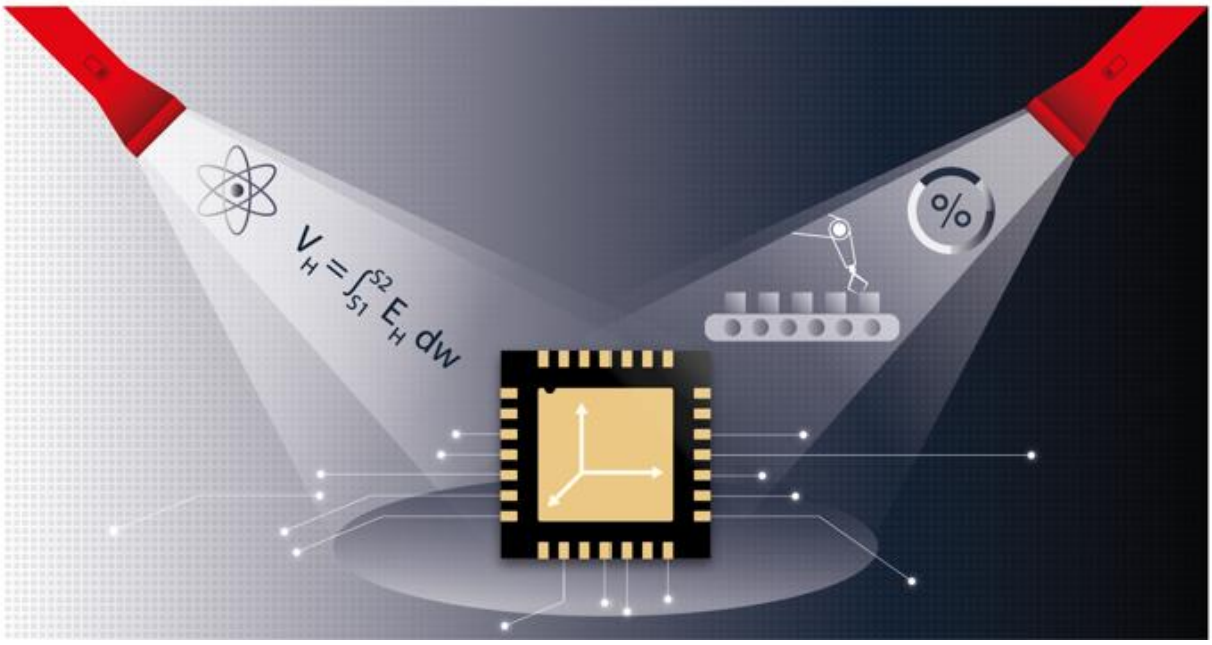

ACADEMIA meets INDUSTRY

IMEKO TC-4 International Symposium

PROCEEDINGS

ISBN: 978-3-033-09885-5

SENIS magnetic & current measurement

IMEKO

Coiltech

WMC

26th IMEKO TC4 International Symposium

24th International Workshop on ADC and DAC Modelling and Testing (IWADC)

IMEKO TC-4 2023

PROCEEDINGS

September 20-21, 2023

Pordenone, Italy

© 2023 IMEKO

ISBN: 978-3-033-09885-5

All rights reserved. No part of this publication may be reproduced in any form, nor may it be stored in a retrieval system or transmitted in any form, without written permission from the copyright holders.

Welcome Message from the Organizing Committee

On behalf of the Organizing Committee, we extend a warm welcome to you for the 26th IMEKO TC4 International Symposium and 24th International Workshop on ADC and DAC Modelling and Testing (IWADC).

The conference commences with an elegant evening of networking at the IMEKO-TC4 Gala Dinner, held at the renowned Villa Gozzi on September 19th, 2023. Villa Gozzi holds a distinguished reputation as one of the most notable Venetian residences in the Pordenone area, and it is particularly associated with the Gozzi brothers, Gasparo and Carlo, who were prominent 18th-century Venetian writers. Originally built in the 17th century by the Gozzi family, who were esteemed merchants in the silk trade from Venice, the Villa served as their family residence and the headquarters of their agricultural business. Moreover, it became a vibrant center for cultural exchanges and gatherings. Gasparo and Carlo Gozzi, sons of Jacopo Antonio and Angiola Tiepolo, who belonged to ancient Venetian nobility, were renowned for hosting literary salons and delightful strolls, warmly welcoming guests from Venice and beyond.

Following this exquisite evening, the Scientific Conference IMEKO-TC4 takes place on September 20th and 21st at the Exhibition Center in Pordenone, Italy. Notably, this prestigious International Symposium IMEKO-TC4 is organized concurrently with the industry-driven World Magnetic Conference at the international trade show COILTECH Italy for the very first time.

The main objective of the IMEKO-TC4 symposium is to foster collaboration between academic researchers and industry engineers, with a specific focus on promoting innovation. This event aims to bring together experts and researchers from diverse communities engaged in measurements, sensors, and related fields, creating an environment that facilitates the exchange of scientific knowledge and ideas.

IMEKO-TC4's primary interest lies in the theoretical and practical aspects of measuring electrical quantities through electronic instruments. The organization provides a forum for the dissemination of ideas about electrical and electronic measuring techniques, as well as the principles of implementing information and communication technology for measurement and accuracy enhancement.

We would like to take this opportunity to express our gratitude to all the members of the Technical Program Committee, the Special Session Organizers, and the anonymous Reviewers, whose contributions have made this outstanding program possible. We also extend our appreciation to the Authors for submitting their papers and sharing their scientific findings with the IMEKO TC-4 community. The symposium received and peer-reviewed 59 papers from all over the world, and 48 of them have been accepted for either oral or poster presentation.

Special thanks are due to all the local Organizing Committee members, whose significant efforts were devoted to the successful organization of this event. In particular, we extend our heartfelt appreciation to our main sponsor, COILTECH, for their generous support, which made this event possible.

The Organizing Committee:

Symposium Chair – Dr. Dragana Popovic Renella, SENIS Switzerland
Scientific Chair – Prof. Alexandru Salceanu, IMEKO officer
Deputy Chairs – Sebastian Küster, COILTECH and Prof. Marco Villani, WMC

Technical Program Overview

The technical program of the 26th IMEKO TC4 International Symposium and 24th International Workshop on ADC and DAC Modelling and Testing (IWADC) evolves over two days and includes five keynote speeches, eleven oral sessions and a poster session.

The keynote speeches are:

- Academia meets Industry - and boosts Innovation and Entrepreneurship by Dr. Dragana Popovic Renella, SENIS Group, Switzerland
- The AMPWISE project by Mr. Damien Piguet, CSEM Switzerland, Prof. Eric M. Yeatman, Imperial College London, England and Mr. Sasa Spasic, SENIS, Switzerland
- Nano-scale traceable magnetic field measurements by Prof. Hans Werner Schumacher, Physikalisch-Technische Bundesanstalt (PTB), Germany
- Contactless electric current sensors by Prof. Pavel Ripka, Czech Technical University, Czeck Republic
- EMF Monitoring: from the general public requirements to the industrial needs by Prof. Nikola Djuric, University of Novi Sad, Serbia

The sessions cover the whole spectrum of electrical measurements, from primary metrology to topics shared with other disciplines.

The oral sessions titles are:

- Metrology, Calibration, Standards and Electrical Quantities Measurements
- Quantum Electrical Metrology
- Biomedical Measurements
- Measurement Systems and ADC&DAC Modelling and Testing
- Signal and Image Processing
- Waveform Analysis and Measurements
- E-Mobility and Sensor Networks
- Special Session: New Trends and Applications of Magnetic Field and Electric Current Measurement in Industry and Science
- Special Session: Magnetic Sensor Systems
- Special Session: Metrology in Industry 4.0: The Bridge of Uncertainty
- Special Session: Innovations in Measurements for Electrical Machines Condition Monitoring

As Technical Program Chairs, we would like to thank all the members of the Technical Program Committee and the Reviewers, who allowed to improve the level of the contributions.

The Technical Program Chairs:

Dr. Jakub Svatos, Czech Technical University, Czech Republic
Prof. Platon Sovilj, University of Novi Sad, Serbia

The Committee

IMEKO TC4 CHAIR

Prof. Jan Saliga, *Technical University of Kosice, Slovakia*

GENERAL SYMPOSIUM CHAIR

Dr. Dragana Popovic Renella, *SENIS AG, Switzerland*

SCIENTIFIC CHAIR

Prof. Alexandru Salceanu, *Technical University of Iasi, Romania and International Measurement Confederation Officer*

DEPUTY CO-CHAIRS

Mr. Sebastian Küster, *COILTECH, Italy*

Prof. Marco Villani, *World Magnetic Conference, Italy*

TECHNICAL PROGRAM CO-CHAIRS

Prof. Platon Sovilj, *University of Novi Sad, Serbia*

Dr. Jakub Svatos, Czech Technical University, *Czech Republic*

SPECIAL SESSIONS CHAIR

Prof. Luca De Vito, *University of Sannio, Italy*

INTERNATIONAL PROGRAM COMMITTEE

IMEKO TC4 members: https://www.imeko.org/index.php/tc4-homepage/tc4-members

TC-4 Chair Jan Saliga, Technical University of Košice, Slovakia
TC-4 Vice-Chair Dragana Popovic Renella, SENIS Group, Switzerland
TC-4 Vice-Chair Luca Callegaro, Istituto Nazionale di Ricerca Metrologica, Italy
TC-4 Scientific Secretary Platon Sovilj, University of Novi Sad, Serbia
TC-4 Scientific Secretary Jakub Svatos, Czech Technical University, Czech Republic
TC-4 Honorary Chair Mario Savino, Politecnico di Bari, Italy
TC-4 Past Chairs:
Linus Michaeli, Technical University of Kosice, Slovakia
Pasquale Daponte, University of Sannio, Italy
Antonio Manuel da Cruz Serra, University of Lisbon, Portugal
Janusz Mindykowski, Uniwersytet Morski w Gdyni, Poland
Dominique Dallet, University of Bordeaux, France
Alexandru Salceanu, Technical University of IAŞI, Romania

Raul Land, Estonia
Dušan Agrež, Slovenia
Pedro M. Ramos, Portugal
Joaquin Del Rio Fernández, Spain
Gelson Rocha, Brazil
George Milushev, Bulgaria
Yurij Tesyk, Ukraine
Olfa Kanoun, Germany
Victor I. Didenko, Russia
Izzet Kale, United Kingdom
Laurent Francis, Belgium
Leo van Biesen, Belgium
Mihai Cretu, Romania
Luca De Vito, Italy
Christian Eugène, Belgium
Vladimir Haasz, Czech Republic
Cristian Fosalau, Romania
Damir Ilic, Croatia
Oleh Velychko, Ukraine
Voicu Groza, Canada
Elefterios Kayafas, Greece
He Qing, China
Michael M. Surdu, Ukraine
Vilmos Pálfi, Hungary
Theodore Laopoulos, Greece

Program IMEKO-TC4 2023

September 19th

19.30-23	Gala Dinner at Villa Gozzi

September 20th

	IMEKO Hall 9-1	*COILTECH Halls*	*IMEKO Hall 9-2*
9:00	Registration		
9:30-10	Opening Ceremony – Welcome Addresses		
10-10:45	1st Key Note		
10:45-11		Coffee Break	
11-12	2nd Key Note		
12-12:30	Session B (#8, #15)		Session A (#37, #39)
12:30-13	Session B (#16, #26)		Session C (#48, #49)
13-14		Lunch	
14-14:30	Special Session 3 (#33, #38)		Special Session 4 (#44, #45)
14:30-15	Special Session 3 (#52,#55)		Session E (#11. #35)
15-15:30	Session D (#12, #42)		Session F (#7, #21)
15-16	Session		
16-16:20		Coffee Break	
16:20-17:30	Poster Session		
17:30-21		Apéro Party	

September 21st

	IMEKO Hall 9-1	*COILTECH Halls*	*IMEKO Hall 9-2*
9:00-9:45	3rd Key Note		
9:45-10:30	4th Key Note		
10:30-11		Coffee Break	
11-11:45	5th Key Note		
11:45-13	TC4 Board Meeting	Company booths visiting at COILTECH	
13-14		Lunch	
14-14:30	Special Session 5 (#27, #29)		Session G (#9, #30)
14:30-15:15	Session Session 5 (#32, #34, #36)		Special Session 7 (#23, #57, #58)
15:30-16:15	Closing and Award Ceremony		

- **Key note 1:**

Chairs: Prof. Jan Saliga, Technical University of Kosice, Slovakia and Prof. Luca De Vito, University of Sannio, Italy

Academia meets Industry - and boosts Innovation and Entrepreneurship by Dr. Dragana Popovic Renella, SENIS Group, Switzerland

Related papers to this key note:

#25 Novel 3D Hall sensor and its application in inspection robots
Dragana Popovic Renella, Thomas Kaltenbacher, Sasa Spasic, SENIS Group, Switzerland
Andrea Cavelti, Giorgio Valsecchi, Lennart Nachtigall, Marco Hutter, RSL ETH Zurich, Switzerland

#40 Introducing the SENIS SENCS1Dx: A Novel Current Sensor IC with Ultra-High Bandwidth and Exceptional Magnetic Resolution
Radivoje S. Popovic, Dragana Popovic Renella, Sasa Dimitrijevic, Bojan Milenkovic, Sasa Spasic, SENIS Group, Switzerland

- **Key note 2:**

Chairs: Dr. Dragana Popovic Renella, SENIS Group, Switzerland and Prof. Pavel Ripka, Czech Technical University, Czech Republic

The AMPWISE project by Mr. Damien Piguet, CSEM Switzerland, Prof. Eric M. Yeatman, Imperial College London, England and Mr. Sasa Spasic, SENIS, Switzerland

Related papers to this key note:

#50 The AMPWISE Project
M. Blagojevic [1] , A. Dieudonne[2] , L. Kamecki[3] , M. E. Kiziroglou[4] , K. Krastev[2] , D. Marty[3] , D. Piguet[5] , S. Spasic[1] , S. W. Wright[4] and E. M. Yeatman[4]

[1] Senis AG, Baar, Switzerland
[2] Safran Electrical & Power, Blagnac, France
[3] Serma Ingenierie, Cornebarrieu, France
[4] Imperial College London, U.K
[5] CSEM, Neuchatel, Switzerland

- **Key note 3:**

Chairs: Dr. Alexander Stuck, SENIS Group Switzerland and Prof. Luca Callegaro, Istituto Nazionale di Ricerca Metrologica, Italy

Nano-scale traceable magnetic field measurements by Prof. Hans Werner Schumacher, Physikalisch-Technische Bundesanstalt (PTB), Germany

- **Key note 4:**

Chairs: Prof. Platon Sovilj, University of Novi Sad, Serbia and Prof. Daniel Belega, Politehnica University Timisoara, Romania

Contactless electric current sensors by Prof. Pavel Ripka, Czech Technical University, Czech Republic

- **Key note 5:**

Chair: Dr. Jakub Svatos, Czech Technical University, Czech Republic and Prof. Theodore Laopoulos, Aristotle University of Thessaloniki, Greece

EMF Monitoring: from the general public requirements to the industrial needs by Prof. Nikola Djuric, University of Novi Sad, Serbia

---

- **Session A - Metrology, Calibration, Standards and Electrical Quantities Measurements**

Chairs: Prof. Luca De Vito, University of Sannio, Italy and Prof. Platon Sovilj, University of Novi Sad, Serbia

#37 A 10 V PJVS-based DC voltage realization at INRiM
Paolo Durandetto, Bruno Trinchera, Danilo Serazio, Emanuele Enrico, INRiM - Istituto Nazionale di Ricerca Metrologica, Torino, Italy

#39 Power System Frequency and ROCOF Measurement by Means of Electronic Instruments
Daniel Belega, Gabriel Găspăresc, Department of Measurements and Optical Electronics, University Politehnica Timisoara, Timisoara, Romania

- **Session B - Quantum Electrical Metrology**

Chairs: Prof. Luca Callegaro, Istituto Nazionale di Ricerca Metrologica, Italy and Dr. Jakub Svatos, Czech Technical University, Czech Republic

#8 The development and tests of a preamplifier for the spectrum analyzer adopted for noise measurements in quantum Hall standard
Marcin Wojciechowski, Kateryna Hovorova, GUM (Central Office of Measures), Warsaw, Poland

#15 A calibration procedure for dc resistance ratio bridges
Martina Marzano, Cristina Cassiago, Vincenzo D'Elia, Enrico Gasparotto, Luca Callegaro, INRIM - Istituto Nazionale di Ricerca Metrologica, Torino

#16 A simple and accurate resistance comparator with a long-scale ratiometric digital multimeter
Martina Marzano, Vincenzo D'Elia, Luca Callegaro, INRIM Istituto Nazionale di Ricerca Metrologica, Torino, Italy
Massimo Ortolano, Politecnico di Torino, Torino, Italy

#26 Atomic density calibration at high-temperature
Erxat Arkin, Jia Kong, Department of physics, Hangzhou Dianzi University, China
Jiqing Fu, Qing He, Magnetic quality laboratory, National Institute of Metrology, Beijing, China

#31 Quantum sampling modular setup for practical power measurements based on a programmable binary Josephson voltage standard
Bruno Trinchera, Paolo Durandetto, Danilo Serazio, INRiM-Istituto Nazionale di Ricerca Metrologica, Strade delle Cacce 91, 10135-Torino, Italy

- **Session C - Biomedical Measurements**

Chair: Prof. Jan Sobotka, CTU, Prague and Prof. Platon Sovilj, University of Novi Sad, Serbia

#48 Novel quality assessment protocol based on Kiviat diagram for pulsed wave Doppler diagnostic systems: first results
Giorgia Fiori, Gabriele Bocchetta, Maurizio Schmid, Silvia Conforto, Salvatore Andrea Sciuto, Andrea Scorza, Dep. of Industrial, Electronic and Mechanical Engineering, Roma TRE University, Rome, Italy

#49 First experimental results of a novel arterial simulator with PWV adjustment
Federico Filippi, Giorgia Fiori, Gabriele Bocchetta, Salvatore Andrea Sciuto, Andrea Scorza, Dep. of Industrial, Electronic and Mechanical Engineering, Roma TRE University, Rome, Italy

- **Session D - Measurement Systems and ADC&DAC Modelling and Testing**

Chair: Prof. Theodore Laopoulos, Aristotle University of Thessaloniki, Greece and Prof. Jan Saliga, Technical University of Kosice, Slovakia

#12 ADC Input Currents Measurement
Jakub Svatos, Jan Fischer, Jan Holub, Czech Technical University in Prague, Faculty of Electrical Engineering, Department of Measurement, Prague, Czechia

#42 Case study of NI G Web technology application for remote educational laboratory
Jozef Kromka, Levente Fekete, Jan Saliga, Technical University of Kosice, Kosice, Slovakia

- **Session E - Signal and Image Processing**

Chair: Prof. Daniel Belega, Politehnica University Timisoara, Romania and Prof. Jan Saliga, Technical University of Kosice, Slovakia

#11 Lossless real-time signal encoding for two-channel signals: A case study on ECG
Jozef Kromka, Ondrej Kovac, Jan Saliga, Technical University of Kosice, Kosice, Slovakia

#35 Custom Synthesizable VHDL Processor for Embedded Capacitive Angle Sensor Data Processing
Milos Drutarovsky[1], Ondrej Benedik[2], Miroslav Sokol[1], Pavol Galajda[1], Jan Saliga[1], Jan Ligus[2], Cristian D Stratyinski[2]

[1] Technical University of Kosice, Kosice, Slovakia
[2] CTRL Ltd., Kosice, Slovakia

- **Session F - Waveform Analysis and Measurements**

Chair: Prof. Jan Holub, CTU, Prague and Dr. Ondrej Kovac from TUKE, Kosice, Slovakia

#7 Accurate Frequency and Damping Factor Estimation by Means of an Improved Three-point Interpolated DFT Algorithm

Daniel Belega, Department of Measurements and Optical Electronics, University Politehnica Timisoara, Timisoara, Romania
Dario Petri, Department of Industrial Engineering, University of Trento, Trento, Italy
Dominique Dallet, IMS Laboratory, Bordeaux INP, University of Bordeaux, Talence Cedex, France

#21 Characterization of an accurate phase measurement system using transmission lines

Luca De Vito, Francesco Picariello, Sergio Rapuano, Ioan Tudosa, Department of Engineering, University of Sannio, Benevento, Italy

- **Session G - E-Mobility and Sensor Networks**

Chair: Dr. Jakub Svatos, Czech Technical University, Czech Republic and Prof. Platon Sovilj, University of Novi Sad, Serbia

#9 The Wireless EMF Monitoring in Sensitive Areas around Kindergartens and Schools

Nikola Djuric, Dragan Kljajic, Tamara Skoric, Faculty of Technical Sciences, University of Novi Sad, Novi Sad, Serbia
Nicola Pasquino, Dept. of Electrical Engineering and Information Technologies, University of Naples Federico II, Naples, Italy

#30 Rapid Prototyping of Vehicle Software Defined Functions

Jan Sobotka, Jirí Novák , Jirí Pinkava, Czech Technical University in Prague, Prague, Czech Republic

- **Special Session 3: New Trends and Applications of Magnetic Field and Electric Current Measurement in Industry and Science**

Chairs: Dr. Alexander Stuck, SENIS Group Switzerland and Prof. Pavel Ripka, Czech Technical University, Czech Republic

#33 Crosstalk in Gapped-core Contactless Current Sensor

Noby George, Pavel Ripka, Václav Grim, Department of Measurement, FEL, Czech Technical University in Prague, Prague

#38 Quantum magnetometry with OPM: Novel applications in non-destructive testing?

Andreas Blug[1] , Kerstin Thiemann[1] , Simon Philipp[2] , Thomas Straub[2] , Alexander Bertz[1]
[1] Fraunhofer Institute for Physical Measurement Techniques IPM, Freiburg, Germany
[2] Fraunhofer Institute for Mechanics of Materials IWM, Freiburg, Germany

#52 Teamwork of Simulations and Hall Sensor Measurements for the Design of Magnetic Sensor Systems

Thomas Schliesch, Thomas Lindner, Max Baermann GmbH, Germany,

#55 First results on torque estimation by FEA and experimental analysis in a novel CSFH-based microgripper

Gabriele Bocchetta[1] , Giorgia Fiori[1] , Federico Filippi[1] , Pietro Ursi[2] , Salvatore Andrea Sciuto[1] , Andrea Scorza[1]
[1] Dep. of Industrial, Electronic and Mechanical Engineering, Roma TRE University, Rome, Italy
[2] Dep. of General Surgery and Surgical Specialties “Paride Stefanini”, Sapienza University of Rome, Rome, Italy

- **Special Session 5: Magnetic Sensor Systems**

Chair: Dr. Jürgen Gerber, INNOMAG e.V., Germany and Prof. Luca De Vito, University of Sannio, Italy

#27 DIN SPEC 91411: A standardized representation of magnetic scales

Jürgen Gerber, INNOMAG e.V., Kaiserslautern, Germany
Rolf Slatter, ITK Dr. Kassen GmbH, Lahnau, Germany

#29 Pole positioning for precise magnetic measurement systems

Sebastian Rivera, Rolf Slatter, ITK Dr. Kassen GmbH, Lahnau- Germany

#32 Analytical Models and Magnetic Position Systems

Michael Ortner[1], Alexandre Boisselet[2], Luiz G. Enger[1], Florian Slanovc[1], Peter Leitner[1], Daniel Markó[1]
[1] Silicon Austria Labs, Villach, Austria
[2] Infineon Technologies Austria, Villach, Austria

#34 Rapid Prototyping of Automotive Magnetic Positioning Systems

Luiz G. Enger, Aleš Travnik, Peter Leitner, Florian Slanovc, Daniel Markó, Michael Ortner, Silicon Austria Labs, Villach, Austria

#36 Practical limitations of accurate magnetic measurements in industrial applications

A.Stuck, M. Mijalkovic, M.Vidojevic, D. Popovic, Senis Group, Switzerland

- **Special Session 4: Metrology in Industry 4.0: The Bridge of Uncertainty**

Chairs: Prof. Platon Sovilj, University of Novi Sad, Serbia and Prof. Marjan Urekar, University of Novi Sad, Serbia

#44 Metrology and Capacity Building in Higher Education: Project Knowledge Triangle for a Low Carbon Economy (KALCEA)

Platon Sovilj, Sanja Mandić, Dragan Pejić, Đorđe Novaković, Marjan Urekar, University of Novi Sad, Faculty of Technical Sciences, Serbia

#45 Digital Stochastic Measurement and Industry 4.0

Platon Sovilj, Dragan Pejić, Marjan Urekar, Sanja Mandić, University of Novi Sad, Faculty of Technical Sciences, Serbia

- **Special Session 7: Innovations in Measurements for Electrical Machines Condition Monitoring**

Chairs: Dr. Andrea Credo, University of l'Aquila, Italy and Dr. Jakub Svatos, Czech Technical University, Czech Republic

#23 Towards new IEC standards for the electrical characterization of graphene
Alessandro Cultrera[1,2], Luca Callegaro[1] , Danilo Serazio[1] , Norbert Fabricius[2,3]
[1] INRIM – Istituto Nazionale di Ricerca Metrologica, strada delle Cacce 91, 10135 Turin, Italy
[2] ISC –International Standards Consulting GmbH & Co. KG, Gehrden, Deutschland
[3] IEC – International Electrotechnical Commission, Technical Committee 113 "Nanotechnology for electrotechnical products and systems"

#57 Magnetic stray field analysis over large areas using Hall- and magneto-optical sensors
Benjamin Wenzel, Matthias Schmidt, Matesy GmbH, Jena, Germany

#58 Current Measurements for Fault Diagnosis in Induction Motors
Simone Mari, Andrea Credo, Giovanni Bucci, Fabrizio Ciancetta, Edoardo Fiorucci, Andrea Fioravanti, University of L'Aquila, Dept. of Industrial and Information Engineering and Economics, L'Aquila (AQ), Italy

---

- **Poster Session**

#6 Evaluation of the long-term drift of measuring instruments and standards using time series
Oleh Velychko, Tetyana Gordiyenko, State Enterprise "All-Ukrainian state research and production center for standardization, metrology, certification and consumers' rights protection" (SE "Ukrmetrteststandard"), Kyiv, Ukraine

#10 Evaluation of Long-Term Stability of HighPrecision Standard for Low-Frequency Voltage Measurement
Oleh Velychko, Valentyn Isaiev, State Enterprise "All-Ukrainian state research and production center for standardization, metrology, certification and consumers' rights protection" (SE "Ukrmetrteststandard"), Kyiv, Ukraine

#17 Traceability routes for magnetic measurements
Marco Coïsson, INRIM, Torino (TO), Italy
Javier Diaz De Aguilar Rois, Yolanda Alvarez Sanmamed, Sergio Molto González, CEM, Tres Cantos (Madrid), Spain, Oliver Power, Robert Walsh, Orrie Larmour NSAI, Dublin, Ireland

#19 A new type of rack for the clamp ammeter
Hongrui Yan, Xinyan Wang, Xiao Liu, Jianbo Liu, Qian Chen, Bin Deng, Shandong Engineering Research Center of Reliability Evaluationfor Electric Energy Metering Devices, Shandong Institute of Metrology, Jinan, China

#22 Study on Calibration Method for Emergency Lighting and Evacuation Indicating System
Bin Deng, Ze-Xin Guan, Xue-Feng Ma, Ru Jia, Hong-Rui Yan, Shandong Engineering Research Center of Reliability Evaluation for Electric Energy Metering Devices, Shandong Institute of Metrology ,Jinan, Shandong, China
Dong-Sheng Zhao, Hai-Long Xu, Guang-Kun Dong, Fan-Li Kong, Shandong Institute of Metrology and Science, Jinan,Shandong, China

#24 Verification of thermal converters by means of a pulsed Josephson standard

Krzysztof Kubiczek[2] , Paolo Durandetto[1] , Pier Paolo Capra[1] , Claudio Francese[1] , Marco Lanzillotti[1] , Luca Roncaglione[1] , Marian Kampik[2] , Andrea Sosso[1]
[1] INRiM - Istituto Nazionale di Ricerca Metrologica, Turin, Italy
[2] Department of Measurement Science, Electronics and Control, Faculty of Electrical Engineering, Silesian University of Technology, Gliwice, Poland

#41 The Design of Vehicle Surround View Monitor

Antonia Juskova and Ondrej Kovac, Technical University of Kosice, Kosice, Slovakia

#43 Phase measurement methods based on timer modules

Sanja Mandić, Dragan Pejić, Đorđe Novaković, Marjan Urekar, Platon Sovilj, University of Novi Sad, Faculty of Technical Sciences, Serbia

#46 Decoding Cognitive Processes in Arithmetic Tasks: An EEG-Based Convolutional Neural Network Model

Nikola Petrović[1] , Lemana Spahić[2] , Sanja Mandić[1] , Platon Sovilj[1]
[1] University of Novi Sad, Faculty of Technical Sciences, Serbia
[2] Verlab Research Institute for Biomedical Engineering, Medical Devices and Artificial Intelligence, Sarajevo, Bosnia and Herzegovina

#47 Demonstration stand for non-destructive conductive material defect inspection by eddy current

Jan Saliga[1] , Pavol Kababik[2] , Ondrej Kovac[1] , Alena Pietrikova[1]
[1] Technical University of Kosice, Letna 9, 042 00 Kosice, Slovakia
[2] Magna Electronics Slovakia s.r.o. 044 58 Kechnec 265, Slovakia

#56 A Preliminary Comparison of Three Methods for the Assessment of Pulse Wave Transit Time in an Arterial Simulator

Federico Filippi, Giorgia Fiori, Gabriele Bocchetta, Salvatore Andrea Sciuto, Andrea Scorza, Dep. of Industrial, Electronic and Mechanical Engineering, Roma TRE University, Rome, Italy

#59 Phase Noise Measurement of ASIC Voltage Controlled Oscillator and PLL Circuit ADF4002

Patrik Jurík, Miroslav Sokol, Pavol Galajda, Department of Electronics and Multimedia Telecommunications, Technical University of Kosice, Kosice, Slovakia

CONTENT

# of paper	Title	Page number
6	Evaluation of the long-term drift of measuring instruments and standards using time series	1
7	Accurate Frequency and Damping Factor Estimation by Means of an Improved Three-point Interpolated DFT Algorithm	6
8	The development and tests of a preamplifier for the spectrum analyzer adopted for noise measurements in quantum Hall standard	11
9	The Wireless EMF Monitoring in Sensitive Areas around Kindergartens and Schools	16
10	Evaluation of Long-Term Stability of High-Precision Standard for Low-Frequency Voltage Measurement	22
11	Lossless real-time signal encoding for two-channel signals: A case study on ECG	26
12	ADC Input Currents Measurement	30
15	A calibration procedure for dc resistance ratio bridges	35
16	A simple and accurate resistance comparator with a long-scale ratiometric digital multimeter	39
17	Traceability routes for magnetic measurements	43
19	A new type of rack for the clamp ammeter	48
21	Characterization of an accurate phase measurement system using transmission lines	53
22	Study on Calibration Method for Emergency Lighting and Evacuation Indicating System	59
23	Towards new IEC standards for the electrical characterization of graphene	64
24	Verification of thermal converters by means of a pulsed Josephson standard	69
25	Novel 3D Hall sensor and its application in inspection robots	72
26	Atomic density calibration at high-temperature	76
27	DIN SPEC 91411: A standardized representation of magnetic scales	79
29	Pole positioning for precise magnetic measurement systems	84
30	Rapid Prototyping of Vehicle Software Defined Functions	88
31	Quantum sampling modular setup for practical power measurements based on a programmable binary Josephson voltage standard	92
32	Analytical Models and Magnetic Position Systems	97
33	Crosstalk in Gapped-core Contactless Current Sensor	101
34	Rapid Prototyping of Automotive Magnetic Positioning Systems	105
35	Custom Synthesizable VHDL Processor for Embedded Capacitive Angle Sensor Data Processing	109
36	Practical limitations of accurate magnetic measurements in industrial applications	114
37	A 10 V PJVS-based DC voltage realization at INRiM	117
38	Quantum magnetometry with OPM: Novel applications in non-destructive testing?	122
39	Power System Frequency and ROCOF Measurement by Means of Electronic Instrument	126

40	Introducing the SENIS SENCS1Dx: A Novel Current Sensor IC with Ultra-High Bandwidth and Exceptional Magnetic Resolution	131
41	The Design of Vehicle Surround View Monitor	135
42	Case study of NI G Web technology application for remote educational laboratory	140
43	Phase measurement methods based on timer modules	144
44	Metrology and Capacity Building in Higher Education: Project Knowledge triangle for a low carbon economy (KALCEA)	148
45	Digital Stochastic Measurement and Industry 4.0	151
46	Decoding Cognitive Processes in Arithmetic Tasks: An EEG-Based Convolutional Neural Network Model	154
47	Demonstration stand for non-destructive conductive material defect inspection by eddy current	160
48	Novel quality assessment protocol based on Kiviat diagram for pulsed wave Doppler diagnostic systems: first results	165
49	First experimental results of a novel arterial simulator with PWV adjustment	170
50	The AMPWISE Project	174
52	Teamwork of Simulations and Hall Sensor Measurements for the Design of Magnetic Sensor Systems	178
55	First results on torque estimation by FEA and experimental analysis in a novel CSFH-based microgripper	182
56	A Preliminary Comparison of Three Methods for the Assessment of Pulse Wave Transit Time in an Arterial Simulator	186
57	Magnetic stray field analysis over large areas using Hall- and magneto-optical sensors	190
58	Current Measurements for Fault Diagnosis in Induction Motors	194
59	Phase Noise Measurement of ASIC Voltage Controlled Oscillator and PLL Circuit ADF4002	198

26th IMEKO TC4 International Symposium
24th International Workshop on ADC and DAC Modelling and Testing
IMEKO TC-4 2023
Pordenone, Italy / September 20-21, 2023

Evaluation of the long-term drift of measuring instruments and standards using time series

Oleh Velychko[1,2], Tetyana Gordiyenko[1,3]

[1] *State Enterprise "All-Ukrainian state research and production center for standardization, metrology, certification and consumers' rights protection" (SE "Ukrmetrteststandard"), Metrologichna Str., 4, 03143, Kyiv, Ukraine*
[2]*velychko@ukrcsm.kiev.ua*, [3]*t_gord@hotmail.com*

***Abstract* – Drift is an undesirable property of all measuring instruments and standards during their life cycle. The analysis of instrumental drift of measuring instruments and standards is important in metrology. Reliable accounting for drift plays an important role in maintaining measurement accuracy. For resistance, capacitance and inductance standards long-term drift is predictable. The analysis of drift types and the main methods of its evaluation for measuring instruments between its calibrations has been carried out. The results of evaluation of the long-term drift of inductance and capacitance standards for high-precision calibration of measuring instruments using a polynomial regression and an Exponentially Weighted Moving Average charts are presented.**

I. INTRODUCTION

Drift is an undesirable property of all measuring instruments and standards during their life cycle. It can be caused by many factors: the environment, mechanical vibrations, temperature changes, electric and magnetic fields, and so on.

Reliable accounting for drift plays an important role in maintaining measurement accuracy. Unaccounted for drift can lead to significant measurement errors. The drift uncertainty can be estimated from its history of successive calibrations. In the absence of such a history, an estimate of the order of magnitude of the calibration uncertainty can be made.

The calibrated values of many measuring instruments and standards have a predictable drift over time. To provide a statement about the measurement uncertainty, when calibrating a measuring instrument for the entire calibration interval, time drift must be taken into account. For many electrical standards times drift is predictable.

II.THE LONG-TIME DRIFT OF MEASURING INSTRUMENTS

Instrumental drift of measuring instrument (VIM, 4.21) [1] is continuous or incremental change over time in indication, due to changes in metrological properties of a measuring instrument. This drift is related neither to a change in a quantity being measured nor to a change of any recognized influence quantity. It is applicable to both the measuring instrument and the measurement standard.

Depending on the time interval used, short-term and long-term drifts are distinguished. It is rather difficult to try to accurately determine the degree of short-term drift by means of a calibration study. Long-term drift can be evaluated without any problems by successive calibrations of the measuring instrument or standard.

Calibration drift refers to the change in instrument readings over a specified period of time during normal, continuous operation. This drift is estimated by a value obtained by subtracting a known reference value from the current measured value. Time drift since the last calibration of a measuring instrument is a major contributor to the overall measurement uncertainty [2, 3].

The drift is of several main types: zero drift; span drift or sensitivity drift; zonal drift, nonlinear, power [4]. Evaluation of long-term drift is mandatory for establishing calibration intervals [5].

III.EVALUATION METHODS OF THE DRIFT OF MEASURING INSTRUMENTS

A drift (trend) is the main tendency of a certain process to change over time or a time series, which is described by various equations: linear, logarithmic, power, etc. The actual drift type is established on the basis of selection of its functional model by statistical methods or smoothing of the original time series. Data time series are used to predict a certain process or phenomenon. A drift line is a line along which the points representing data from a certain data series are located on a chart.

Drift rarely continues at the same speed and in the same direction for a long period of time. To determine the degree and nature of any drift, the measurement results are plotted on a specific time scale (days, months, years). Such an experiment captures the maximum change that can occur within a set period of time, and allows you to make the necessary correction to the measurement result. Uncorrected drift can be considered as a type A component in measurement uncertainty analysis.

The ordinary least squares (OLS) method can be used to research drift, which is one of the basic methods of regression analysis for estimating unknown parameters of regression models based on sample data. It is based on the minimization of the sum of squared deviations of the selected function from the studied data. The theoretical values are determined using a mathematical function that best represents the underlying drift of the time series. This function is called an adequate function, which is calculated by the OLS method.

The coefficient of determination is used to assess the accuracy of such a drift model

$$R^2 = \sigma_{\hat{y}}^2 / \sigma_y^2, \quad (1)$$

where $\sigma_{\hat{y}}$ and σ_y are dispersions of theoretical data obtained according to the drift model and empirical data, respectively.

The most reliable drift line is if its approximation probability value (R^2) is equal to or close to 1. The drift model is adequate for the process under study and reflects the tendency of its development over time with R^2 values close to 1.

IV.EVALUATION OF THE DRIFT OF MEASURING INSTRUMENTS BETWEEN CALIBRATIONS

In [6], instrumental drift of measuring standards or measuring instruments is distinguished. This distinguishes between systematic drift, in which the model that describes the relationship between the measured value and the "true" value changes over time, and random drift or residual biases, which appear as deviations between the model and the values obtained during calibration.

Common practice is to establish the relationship between $y(t)$ and $x(t)$, termed the calibration model, which often takes the form of a polynomial of suitable degree n (usually 1, 2 or 3):

$$y(t) = a_0 + a_1 x(t) + a_2 x^2(t) + ... + a_n x^n(t). \quad (2)$$

The OLS method is not suitable for the vast majority of calibrations, since it only makes sense if the following conditions are met [6]: there is no uncertainty associated with x (during calibration are always measurement uncertainties); the measurement uncertainty is constant across the full range of measurements (this is rarely met on calibration); there is no covariance between either the $x_i(t)$ and $y_i(t)$ (these variances are frequent on calibration). At the same time, the OLS method can be used in a number of cases to estimate the calibration intervals.

In [6], to evaluate the drift of the measuring instrument, it is proposed to calculate the deviations between two established corrections at certain points and calculate the average value and standard deviation of the resulting corrections. These characteristics represent the contribution of the instrument drift to the measurement uncertainty.

Document [7] proposes general method for optimizing and justifying the calibration intervals of measuring instruments. It takes into account the recommendations of international standards ISO 10012 [8] and ISO/IEC 17025 [3]. To optimize and justify the calibration intervals of measuring instruments, it is important to take into account the evolution of one (or more) characteristics of working standards in the laboratory, as well as the contribution of standards to the assessment of the uncertainty of measurements made under actual conditions of use. The OLS method is used for modeling of maximum instrumental drift of a calibrated measuring instrument for certain period (for example 6 years).

In [9] describes the drift algorithm for random behavior of the metrological characteristics of measuring instruments. This paper also provides useful an overview of various methods for accounting for the drift of measuring instruments. The method for calculating the drift estimate As-Found Versus As-Left is considered in more detail. It is based on the collection of appropriate samples of calibration data of the measuring instrument, their analysis to assess the statistical characteristics of the drift error. These characteristics are used to predict the drift of the measuring instrument and demonstrate the possibility of making the necessary corrections.

The method of correlation estimation of the deviation drift in time is considered in [10]. It is based on the analysis of the sample and the calculation of the standard deviation to obtain the corresponding unbiased maximum mean. If the deviation drift is greater than the unbiased maximum mean, then it is considered to have a strong time correlation. In another case, the deviation drift is considered to have no time correlation, so part of the deviation drift can be ignored when calculating the amount of drift.

A cumulative sum (CUSUM) charts to identify process disorder caused by the influence of a non-random variable is show in [11]. These charts are more sensitive to small shifts in the level of process adjustment, unlike Shewhart charts. This makes it possible detect long-term drift of metrological characteristics of measuring instruments. The peculiarity of CUSUM charts is that the decision regarding the compliance of the metrological characteristics of measuring instruments with the established requirements is made taking into account information about all the obtained results (from the first to the last inclusive). Paper does not show the consideration of measurement uncertainty during calibration when using CUSUM charts.

The issue of long-term stability of standards is covered in [12]. This issue is also mentioned in the standard IEC/ISO 17025 [5] and the guideline JCGM 100 [2]. Control charts are presented and validated with simulations and real data sets. They are tools for evaluating the statistical control of the measurement process. Autocorrelation of measurement data obtained over a long period of time has been found to limit the relevance of

control charts. At the same time, time series analysis seems more acceptable than conventional control charts.

A method for accounting of time drift based on the guidance in JCGM 100 [2] is proposed in [13]. An additional measurement uncertainty component is calculated using a linear regression of measurement data. In this article, much attention is paid to estimating the measurement uncertainty of drift after calibration, and appropriate options are proposed. Three methods are proposed for reducing the full expression of measurement uncertainty to a single value of uncertainty valid over the calibration interval.

In general, the contribution of time drift to measurement error cannot be averaged over a series of measurements. This drift is usually not stable enough for precision calibrations. In [14] describes a fairly general method for effectively suppressing parasitic effects caused by slow drifts. The effectiveness of the method is illustrated by applying the obtained optimal strategies for some precision measurements.

A standardized approach to uncertainty evaluation provides the basis for fulfilling measurement requirements. An approach for estimating the uncertainty of calibration and measurement processes is shown in [15]. Assessing trueness and precision in many ways limits the ability to compare observations and evaluate changes in measurement uncertainties over time. It is important to adjust the drift estimate and specify the assumptions for users of the measurement uncertainty estimate.

V.EVALUATION OF THE DRIFT OF ELECTRICAL STANDARD FOR CALIBRATIONS

The general scheme of global metrological traceability at different measurement levels is presented in [16]. At the middle level of metrological traceability are calibration laboratories, one of the main tasks of whose is the calibration of working standards and measuring instruments [17]. Calibration laboratories of national metrological institutes carry out the most precise calibrations of working standards.

The analysis of international standards and guides on statistical methods estimation of the measurement results recommendations for those applications in laboratories is described in [18] and the use of statistical methods for evaluating measurement results is shown in [19]. The analysis of the long-term drift of standards will be limited to examples of standards of resistance, capacitance and inductance.

The methodologies for the evaluation of historical data of electrical resistance standards of 10 Ω and of 100 Ω presents in [20] to ensure precision calibration of measuring instruments. These methodologies using for improvement their metrological characteristic in relation to manufacturer's specification and measurement uncertainty. Linear regression was applied to the obtained calibration data for a time period of 60 months (5 years) for both 10 Ω and 100 Ω resistors. The uncertainty of fitting the data to a straight line was estimated by the regression method. Estimated uncertainties of the one-year predicted resistance value are 6.4 ppm for 10 Ω and 0.0012 % for 100 Ω.

In SE "Ukrmetrteststandard" (Kyiv, Ukraine), national standards of inductance and capacitance units have been created and used for precision calibrations. These standards took part in comparisons of standards within the framework of from 2006 to 2018. Continuous measurements showed high stability of these standards over a rather long time period. Time series of measurement data for the inductance standard from 2009 to 2022, and for the capacitance standard from 2011 to 2022.

The thermostatically adjustable inductance measures P5109 (No. 424) of 10 mH and P5113 (No. 1003) of 100 mH of the inductance standard contain a built-in precision thermostat with two temperature sensors. Their instability is 10 ppm/year. The results of evaluating the long-term drift of measures of 10 mH and 100 mH of the inductance standard at 1 kHz using 3rd-order polynomial regression are show on Figs 1 and 2. In the figures, the green solid line shows the mean value for the drift, and the red dashed line shows the corresponding polynomial approximation of the drift. The specified approximations of the drift lines of the inductance measures have the probability values of R^2 equal to 0.66 and 0.78, respectively, that is, they confirm their adequacy (less than 1.00).

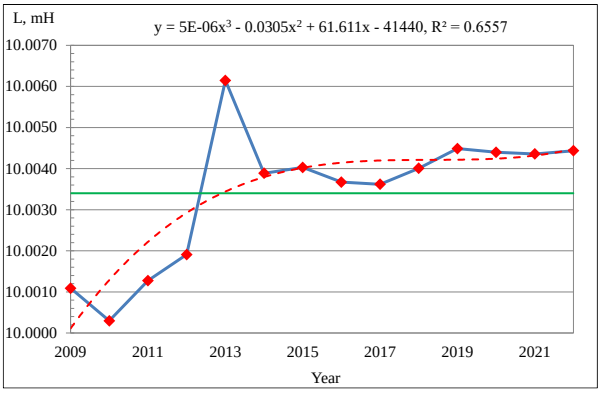

Fig. 1. Drift for 10 mH with polynomial regression.

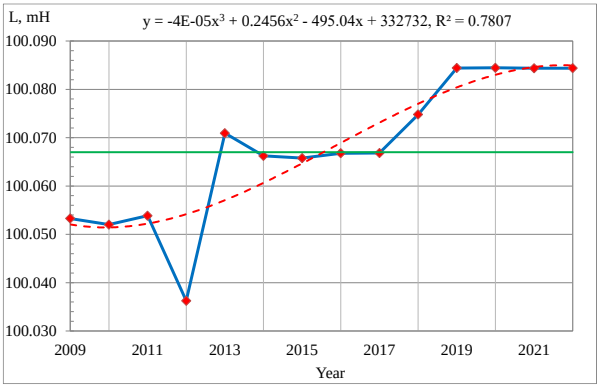

Fig. 2. Drift for 100 mH with polynomial regression

The average value of 10 mH measure from 2009 to 2022 is 10.0034, and 100 mH measure is 100.0067. The difference between the maximum and minimum values of 10 mH measure for the same time period is 0.0058, and 100 mH is 0.048. The difference between the last and first values of 10 mH measure for the same time period is 0.0033, and 10 mH measure is 0.031. The standard deviation of 100 mH measure from 2009 to 2022 is 0.0016, and 100 mH measure is 0.015.

The capacitance measures Andeen-Hagerling model AH11A of 10 pF and 100 pF are fused silica dielectric capacitors in hermetically sealed dry nitrogen filled metal containers. Their instability stability is better than 0.3 ppm/year. The results of evaluating the long-term drift of those measures using 2nd-order polynomial regression are show on Figs 3 and 4. The designations in these figures are the same as in the previous figures. The specified approximations of the drift lines of the capacitance measures have the probability values of R^2 equal to 0.13 and 0.70, respectively, that is, they confirm their adequacy (less than 1.00).

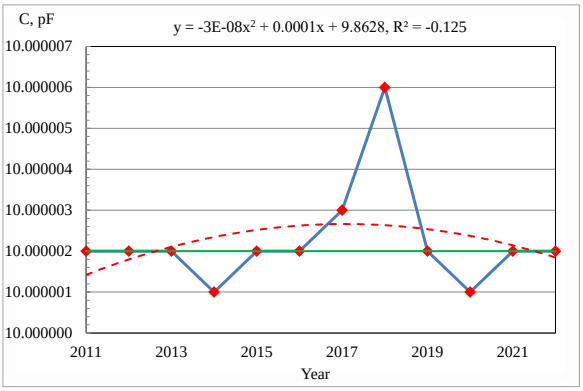

Fig. 3. Drift for 10 pF with polynomial regression

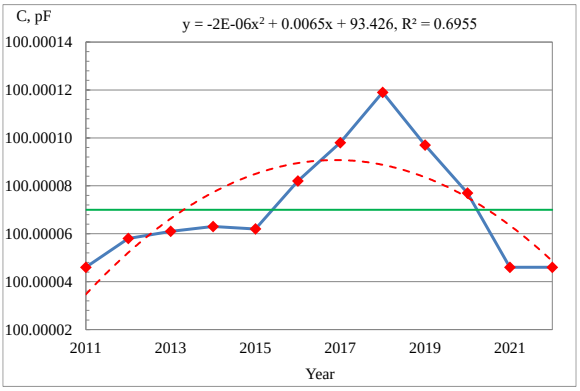

Fig. 4. Drift for 100 pF with polynomial regression.

The average value of 10 pF measure from 2011 to 2022 is 10.000005, and 100 pF measure is 100.0067. The difference between the maximum and minimum values of 10 pF measure for the same time period is 0.5 ppm, and 100 pF is 0.5 ppm. The difference between the last and first values of 10 pF measure for the same time period is 0, and 100 pF measure is 0. The standard deviation of 10 pF measure from 2011 to 2022 is 0.13 ppm, and 100 pF measure is 0.24 ppm.

Since CUSUM chart cannot be applied to data with a large number of digits after the decimal point, a Exponentially Weighted Moving Average (EWMA) chart was chosen also to analyze the long-term drift of inductance and capacitance standards. In addition, EWMA charts are applied to absolute data, not only to relative data, as applied in CUSUM charts. This is quite convenient precisely for evaluating the values of the measures under consideration.

EWMA refers to the average value of data obtained over time. The weight of the EWMA decreases exponentially for each period further into the past. Since the EWMA contains a previously calculated average, the result of the exponentially weighted moving average will be cumulative. Therefore, all received data contribute to the result, but the contribution factor is reduced when calculating the next period of EWMA. EWMA is a good tool for detecting smaller shifts in time averages bounded by a process. This allows for the analysis of long-term drift of inductance and capacitance measures.

The results of the evaluation of the long-term drift of standard inductance measurements of 10 mH and 100 mH at 1 kHz using EWMA are shown in Fig. 5 and 6. In the figures, the green solid line shows the average value of the drift (CL), and the red dashed line shows both the upper (UCL) and the lower (LCL) control limits.

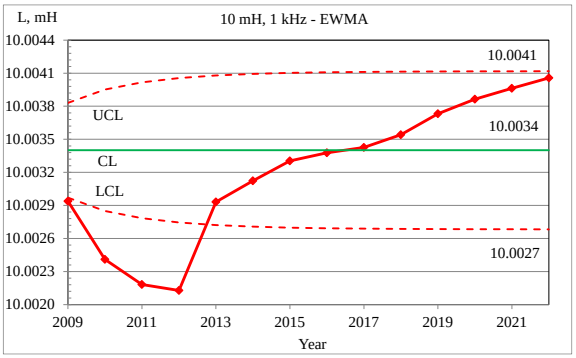

Fig. 5. Drift for 10 mH with EWMA.

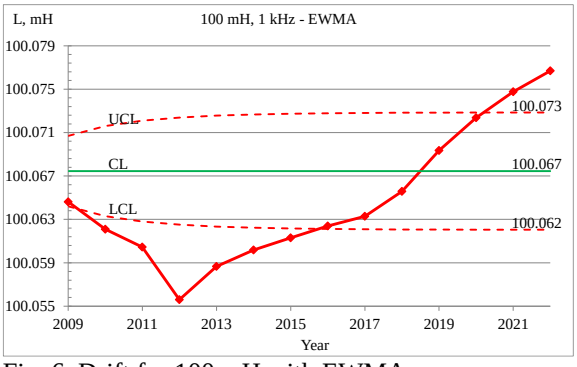

Fig. 6. Drift for 100 mH with EWMA.

The results of the evaluation of the long-term drift of standard inductance measurements of 10 pF and 100 pF using EWMA are shown in Fig. 7 and 8. The designations in these figures are the same as in the previous figures.

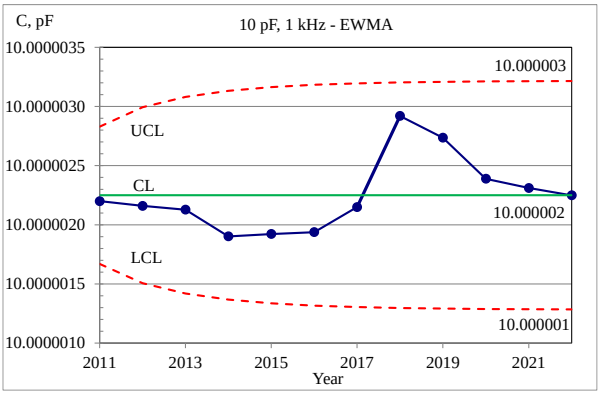

Fig. 7. Drift for 10 pF with EWMA.

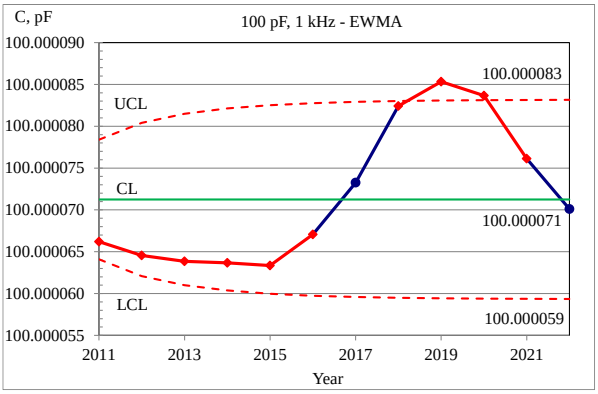

Fig. 8. Drift for 100 pF with EWMA.

VI. CONCLUSION

An analysis of the main drift assessment methods allows you to select methods for estimating the long-term drift of measuring instruments between their calibrations. To assess the drift of electrical standards for the calibration of measuring instruments, regression analysis methods are most often used. 3rd degree polynomials were sufficient to approximate the drift of the inductance standards, and 2nd degree polynomials were sufficient for the capacitance standards.

Since CUSUM chart cannot be applied to data with a large number of digits after the decimal point, a EWMA chart was chosen also to analyze the very small long-term drift of high-precision inductance and capacitance standards. Evaluation of the drift of these standards for high-precision calibration at frequency of 1 kHz using polynomial regression and EWMA charts was applied. Consistent results have been obtained.

REFERENCES

[1] JCGM 200, International vocabulary of metrology, Basic and general concepts and associated terms (VIM), 3-rd edition, 2012, 105 p.

[2] JCGM 100, Uncertainty of measurement, Part 3: Guide to the expression of uncertainty in measurement (GUM), 2008, 134 p.

[3] EA-04/02 M, “Evaluation of the Uncertainty of Measurement in Calibration,” EA, 2013.

[4] NIST/SEMATECH, “e-Handbook of Statistical Methods”, 2006.

[5] ISO/IEC 17025, “General requirements for the competence of testing and calibration laboratories,” ISO/IEC, 2017.

[6] J-M Pou and L Leblond, “Evaluate and quantify the drift of a measuring instrument,” Proc. of 19th Intern. Congress of Metrology, 2019, 12004, 13 p.

[7] FD X 07-014, “Metrology – Optimization of metrological confirmation intervals for measuring equipment”, AFNOR, 2006.

[8] ISO 10012, “Measurement management systems – Requirements for measurement processes and measuring equipment,” ISO, 2003.

[9] G Luo, and al., “Analysis and Research Based on Instrument Drift Data,” IEEE Access, 2021, 9, 56918.

[10] S. Sikström and F. Jönsson, “A model for stochastic drift in memory strength to account for judgments of learning,” Psychol. Rev., 112, 2005, 4, 932.

[11] E T Volodarsky and I O Pototskiy, “Theoretical substantiation and application of CUSUM-charts,” Proc. of 2019 IEEE 8th Intern. Conf. on Advanced Optoelectr. and Lasers (CAOL), 2019, pp. 636–639.

[12] C Romain, “Evaluation of the Long-Term Stability of Metrology Instruments,” In Applied Aspects of Modern Metrology, London: IntechOpen, 2021.

[13] C J. Delker, and al., “Calculating interval uncertainties for calibration standards that drift with time,” SAND2020-3749J, 2020.

[14] V V Yashchuk, “Optimal measurement strategies for effective suppression of drift errors,” Rev Sci Instrum. 2009, 80(11), 115101.

[15] J Csavina, and al., “Traceable measurements and calibration: a primer on uncertainty analysis,” Ecosphere, 2017, 8(2), 01683.

[16] O Velychko and T Gordiyenko, “Metrological Traceability at Different Measurement Levels”, In Standards, Methods and Solutions of Metrology, London: IntechOpen, 2019.

[17] O N Velichko, “Traceability of measurement results at different levels of metrological work,” Measurement Techniques, 52, 2009, 11, 1242–1248.

[18] O Velychko and T Gordiyenko, “The implementation of general guides and standards on regional level in the field of metrology”, Journal of Physics: Conf. Series, 238, 2010, 012044, 6.

[19] O Velychko and T Gordiyenko, “The estimation of the measurement results with using statistical methods,” Journal of Physics: Conf. Series, 2015, 588, 012017.

[20] M M Costa and A. L C França, “Using historical data to improve electrical resistance standards measurement uncertainty,” Proc. of 25th IMEKO TC4 Intern. Symposium, 2022, 125–129.

26th IMEKO TC4 International Symposium
24th International Workshop on ADC and DAC Modelling and Testing
IMEKO TC-4 2023
Pordenone, Italy / September 20-21, 2023

Accurate Frequency and Damping Factor Estimation by Means of an Improved Three-point Interpolated DFT Algorithm

Daniel Belega[1], Dario Petri[2], Dominique Dallet[3]

[1]*Department of Measurements and Optical Electronics, University Politehnica Timisoara, Bv. V. Parvan, Nr. 2, 300223, Timisoara, Romania, email: daniel.belega@upt.ro*
[2]*Department of Industrial Engineering, University of Trento, Via Sommarive, 9, 38123, Trento, Italy, email: dario.petri@unitn.it*
[3]*IMS Laboratory, Bordeaux INP, University of Bordeaux, CNRS UMR5218, 351 Cours de la Libération, Bâtiment A31, 33405, Talence Cedex, France, email: dominique.dallet@ims-bordeaux.fr*

***Abstract* – In this paper an algorithm for frequency and damping factor estimation of a real-valued noisy damped sinusoid is proposed. It is an extension of the three-point Interpolated Discrete Fourier Transform (3p-IpDFT) undamped sinusoid frequency estimator based on Maximum Sidelobe Decay (MSD) windows. Analytical expressions for the frequency and the damping factor estimators are provided and the related estimation errors due to the contribution of the spectral image component are derived and compensated. The accuracies of the proposed algorithm and other state-of-the-art frequency-domain based algorithms are compared to each other through computer simulations.**

I. INTRODUCTION

Damped sinusoids have a relevant role in many application areas such as radar, nuclear magnetic resonance, optics, and mechanics [1]-[4]. Quite often the signal parameters need to be estimated accurately and in real-time. To that aim the so-called Interpolated Discrete-Time Fourier Transform (IpDTFT) algorithms are often employed [3]-[9]. These algorithms allow to reduce the picket-fence effect on the estimated signal parameters due to the finite number of samples used in the time-frequency transformation. Specifically, the IpDTFT algorithms estimate the signal frequency and the damping factor by interpolating two or more relevant DTFT samples of the analyzed signal [3]-[9]. Moreover, to reduce the detrimental effect of the spectral interference from other spectral tones, including the image components, the acquired signal is multiplied by a suitable window [10]. The Maximum Sidelobe Decay (MSD) cosine windows [11] are often used since they ensure both high spectral leakage suppression and allow to estimate the unknown parameters using simple analytical expressions [9]. When a few sinusoids cycles are analyzed, more than two interpolation points are used in order to compensate the effect of spectral leakage from the fundamental image component. A three-point Interpolated Discrete Fourier Transform (3p-IpDFT) algorithm based on the rectangular window has been proposed in [12] for undamped sinusoid frequency estimation. Its analytical expression has been derived in [13] and then it has been extended to signals weighted by cosine windows in [14]. In this paper that algorithm is further extended to real-valued noisy damped sinusoids weighted by MSD windows. The expressions for both 3p-IpDFT frequency and damping factor estimators are firstly derived. Then the contribution of the spectral image component to the derived estimators is analyzed and the obtained expressions are used to improve estimation accuracy. The proposed procedure is called the improved 3p-IpDFT (3p-IpDFTi) algorithm, and its accuracy is compared with that of other state-of-the-art frequency domain-based algorithms.

II. THE PROPOSED 3P-IPDTFTI ALGORITHM

The analyzed discrete-time noisy damped sinusoid is modelled as:

$$y(m) = Ae^{-\frac{2\pi}{M}\alpha m}\cos\left(2\pi\frac{\vartheta}{M}m+\phi\right)+e(m)$$
$$= x(m)+e(m),\quad m=0,1,2,\ldots,M-1, \qquad (1)$$

where $x(\cdot)$ is the noise free damped sinusoid of amplitude A, normalized frequency ϑ, phase ϕ, and normalized damping factor α, while $e(\cdot)$ is an additive white Gaussian noise with zero mean and variance σ_n^2. M is the acquisition length.

The normalized damping factor α has been selected as signal parameter for symmetry with the definition of the normalized frequency ν, which also represents the number of analyzed signal cycles and it is expressed as:

$$\vartheta = l+\delta, \qquad (2)$$

where l is the rounded value of ϑ, and δ ($-0.5 \le \delta < 0.5$) is the rounding error, which corresponds to the inter-bin frequency location. $\delta = 0$ if coherent sampling occurs.

To reduce the spectral leakage contribution on the frequency and the damping factor estimates, the acquired signal is multiplied by the H-term MSD window and the analyzed signal becomes $y_w(m) = y(m) \cdot w(m)$.

The DTFT of the noise free weighted damped sinusoid $x_w(m)$ is given by:

$$X_w(\lambda) = \tilde{X}_w(\lambda) + \tilde{X}_{iw}(\lambda), \tag{3}$$

where $\tilde{X}_w(\lambda)$ and $\tilde{X}_{iw}(\lambda)$ are the transforms of the fundamental component and the spectral image of the weighted damped sinusoid $x_w(m) = x(m) \cdot w(m)$, respectively. The related expressions are [9]:

$$\tilde{X}_w(\lambda) \cong \frac{(2H-2)!}{2^{2H}} \frac{AM}{\pi} \frac{\left(1-e^{-2\pi(\alpha+j(\lambda-\vartheta))}\right)e^{j\phi}}{(\alpha+j(\lambda-\vartheta))\prod_{h=1}^{H-1}\left[(\alpha+j(\lambda-\vartheta))^2+h^2\right]}, \tag{4a}$$

and

$$\tilde{X}_{iw}(\lambda) \cong \frac{(2H-2)!}{2^{2H}} \frac{AM}{\pi} \frac{\left(1-e^{-2\pi(\alpha+j(\lambda+\vartheta))}\right)e^{-j\phi}}{(\alpha+j(\lambda+\vartheta))\prod_{h=1}^{H-1}\left[(\alpha+j(\lambda+\vartheta))^2+h^2\right]}. \tag{4b}$$

The 3p-IpDFT algorithm exploits the following interpolation function [14]:

$$h = H \frac{Y_w(l+1)-Y_w(l-1)}{Y_w(l-1)-2Y_w(l)+Y_w(l+1)}. \tag{5}$$

Since both the spectral image component and wideband noise often provides minor contributions (5) can be written as:

$$h \cong H \frac{\tilde{X}_w(l+1)-\tilde{X}_w(l-1)}{\tilde{X}_w(l-1)-2\tilde{X}_w(l)+\tilde{X}_w(l+1)}. \tag{6}$$

By using (4a), after some algebra the following relationships are derived:

$$\begin{aligned} \tilde{X}_w(l-1) &\cong \frac{\alpha-j\delta+j(H-1)}{\alpha-j\delta-jH}\tilde{X}_w(l), \\ \tilde{X}_w(l+1) &\cong \frac{\alpha-j\delta-j(H-1)}{\alpha-j\delta+jH}\tilde{X}_w(l). \end{aligned} \tag{7}$$

By replacing (7) into (6), after some manipulations we obtain:

$$h \cong \delta + j\alpha. \tag{8}$$

which shows that the 3p-IpDFT inter-bin frequency location and damping factor estimators can be obtained as:

$$\hat{\delta} = Re\{h\} \text{ and } \hat{\alpha} = Im\{h\}, \tag{9}$$

where $Re\{\cdot\}$ and $Im\{\cdot\}$ are the real- and imaginary-part operators.

The following Proposition provides the contribution to (9) of the spectral image component.

Proposition:

The contribution of the spectral image component on the estimators of the inter-bin frequency location δ and the damping factor α returned by the 3p-IpDFT algorithm based on the H-term MSD window is given by:

$$\begin{aligned} \Delta\delta + j\Delta\alpha \cong -2(l+\delta)\frac{\alpha-j\delta}{\alpha+j\delta+j2l} \cdot \frac{1-e^{-2\pi(\alpha+j\delta)}}{1-e^{-2\pi(\alpha-j\delta)}} \\ \times \frac{\prod_{h=1}^{H}[(\alpha-j\delta)^2+h^2]}{\prod_{h=1}^{H}[(\alpha+j\delta+j2l)^2+h^2]} \cdot e^{-j2\phi}, \end{aligned} \tag{10}$$

where $\Delta\delta = \hat{\delta} - \delta$ and $\Delta\alpha = \hat{\alpha} - \alpha$. The proof of this Proposition is given in the Appendix.

Expression (10) allows to infer the following remarks:

- if the signal phase changes while the other parameters are kept constant, as it often occurs in practice due to noncoherent sampling, the estimation errors $\Delta\delta$ and $\Delta\alpha$ exhibit two in quadrature sinewave like behaviors;
- the estimation errors $\Delta\delta$ and $\Delta\alpha$ decreases as ϑ increases.

Fig. 1 shows the inter-bin frequency location (Fig. 1(a)) and the damping factor (Fig. 1(b)) estimation errors returned by simulations and by (10) as a function of the signal phase ϕ, which varies in the range [0, 2π) rad with a step of $\pi/20$ rad. A noise free damped sinusoid with A = 1 p.u., ϑ = 3.3 cycles, α = 1, and M = 512 samples is considered and the rectangular or the two-term MSD (or Hann) window are applied.

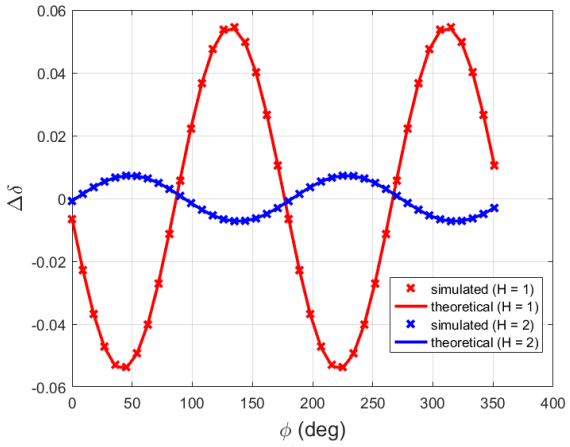

(a)

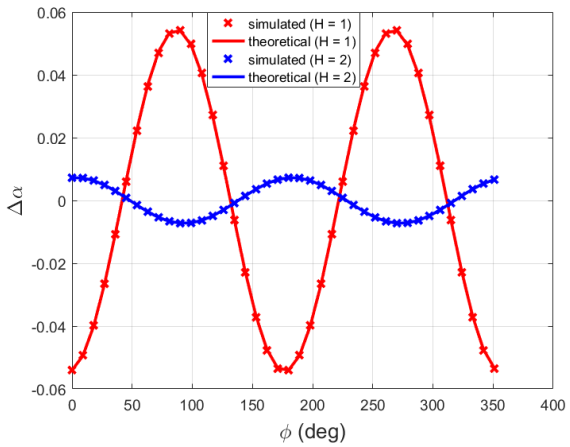

(b)

Fig. 1. Real-valued noise-free damped sinusoid: simulation and theoretical results (10) for the contribution of the spectral image component to the estimated frequency $\Delta\delta$ (a) and damping factor $\Delta\alpha$ (b) versus the signal phase ϕ. Sinusoid parameters A = 1 p.u., ϑ = 3.3 cycles, α = 1, and M = 512 samples. Rectangular (H = 1) or Hann (H = 2) windows.

As we can see, the agreement between the theory and the simulations is very good. For the contribution $\Delta\delta$, the maximum differences between the theoretical and simulated results are $6.3\cdot10^{-4}$ and $3.3\cdot10^{-5}$ when H = 1 and H = 2, respectively. Similarly, the contribution $\Delta\alpha$ exhibits maximum differences equal to $5.8\cdot10^{-4}$ and $3.0\cdot10^{-5}$ when H = 1 and H = 2, respectively.

Expression (10) enables the improvement of the algorithm accuracy. The derived procedure – called the 3p-IpDFTi algorithm – requires to perform the following steps:

Step 1: acquire M samples of the signal $y(m)$ to be analyzed
Step 2: compute the DFT of the weighted signal $y_w(m)$
Step 3: determine the integer part of the acquired signal cycles l
Step 4: apply the 3p-IpDFT algorithm and compute the estimators $\hat{\delta}$ and $\hat{\alpha}$ using (9)
Step 5: compute $\hat{\phi} = angle\{\gamma\}$, where:

$$\gamma = \frac{(\hat{\alpha}-j\hat{\delta})\prod_{h=1}^{H-1}\left[(\hat{\alpha}-j\hat{\delta})^2+h^2\right]}{1-e^{-2\pi(\hat{\alpha}-j\hat{\delta})}}Y_w(l),$$

Step 6: compute the estimation errors $\Delta\delta$ and $\Delta\alpha$ using (10) applied to the estimated values $\hat{\delta}$, $\hat{\alpha}$, and $\hat{\phi}$
Step7: compute the compensated estimates $\hat{\delta}_c = \hat{\delta} - \Delta\delta$ and $\hat{\alpha}_c = \hat{\alpha} - \Delta\alpha$.

III. ACCURACY ASSESSMENT AND COMPARISON

In this Section the Root Mean Squares (*RMSE*s) of the proposed 3p-IpDFTi algorithm, the classical 2p-IpDFT algorithm [8], the Aboutanios algorithm [4], the 3p-IpDFT algorithm, and the 3p-RVCI-(*H*-1) algorithm [3] are compared to each other. Both the rectangular and the Hann windows are considered for signal weighting.

Undistorted or harmonically distorted noisy damped sinusoids with amplitude A = 1 p.u. and normalized damping factor α = 1 are analyzed. A white Gaussian noise with zero mean and variance corresponding to *SNR* = 40 dB is added to the signal and 10,000 runs of M = 512 samples each with the signal phase ϕ randomly chosen in the range [0, 2π) rad are performed for each considered value of the number of analyzed cycles ϑ. The obtained *RMSE*s are reported in Figs. 2 and 3 as a function of ϑ, which varies in the range [1.5, 8] cycles with a step of 0.1 cycles.

Fig. 2 shows the *RMSE*s for the inter-bin frequency location (Fig. 2(a)) and the damping factor (Fig. 2(b)) estimates obtained when a noisy undistorted damped sinusoid is analyzed, and the rectangular window is used. Thanks to the compensation of the contribution from the spectral image component, the proposed 3p-IpDFTi algorithm well outperforms the others.

Fig. 3 shows the *RMSE*s for the inter-bin frequency location (Fig. 3(a)) and the damping factor (Fig. 3(b)) estimates as a function of *SNR* when ϑ = 3.3 cycles and α = 1. *SNR* varies in the range [0, 60] dB with a step of 5 dB. When *SNR* is smaller than about 10 dB the 3p-RVCI-0 algorithm is not able to provides accurate *RMSE*s estimates.

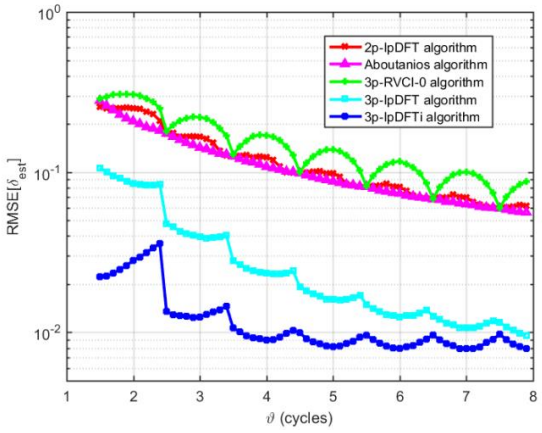

(a)

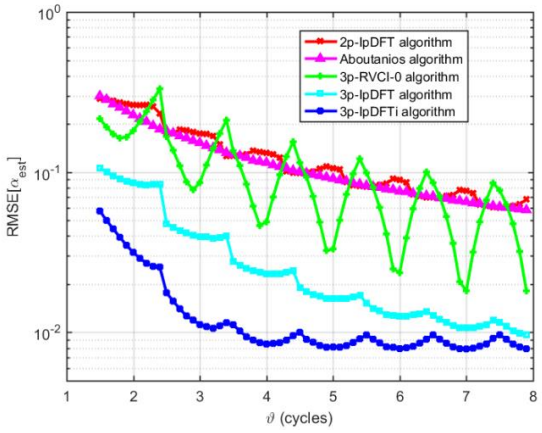

(b)

Fig. 2. Real-valued noisy damped sinusoids: *RMSE*s of the frequency δ (a) and the damping factor α (b) estimates returned by the considered algorithms versus the number of analyzed cycles ϑ. Damping factor α = 1, *SNR* = 40 dB, phase at random, and M = 512 samples. Rectangular window.

The square root of the Cramér-Rao Lower Bound (CRLB) is also shown in the figure to enable a visual assessment of the algorithm efficiency [15].

In Fig. 3 it can be observed that when *SNR* is greater than about 10 dB the proposed 3p-IpDFTi algorithm outperforms the others since it compensates the contribution of the spectral image component. However, when *SNR* is greater than about 40 dB the residual contribution prevails on the effect of wideband noise. The other considered algorithms exhibit a similar behavior, but at lower *SNR* thresholds. When *SNR* is smaller than about 10 dB outliers due to noise occur [16].

Fig. 4 shows the *RMSE*s for the inter-bin frequency location (Fig. 4(a)) and the damping factor (Fig. 4(b) estimates obtained when a noisy harmonically distorted damped sinusoid is analyzed, and the Hann window is used. The signal is affected by a 2nd and a 3rd damped harmonics with amplitudes equal to 0.1 p.u. and 0.05 p.u., respectively, and damping factors equal to 1.2 and 1.5, respectively.

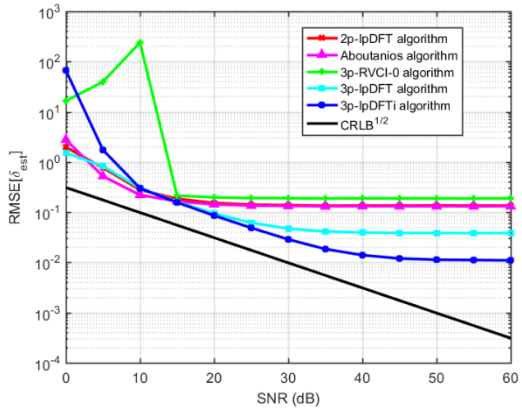

(a)

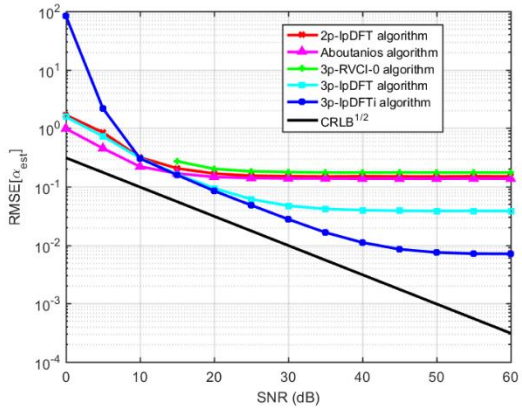

(b)

Fig. 3. Real-valued noisy damped sinusoids: *RMSE*s of the frequency δ (a) and the damping factor α (b) estimates returned by the considered algorithms versus *SNR* when the number of analyzed cycles $\vartheta = 3.3$ cycles, the damping factor $\alpha = 1$, phase at random, and $M = 512$ samples. Rectangular window. The $\sqrt{CRLB}$ is also shown.

As we can see, the proposed 3p-IpDFTi algorithm outperforms the others when less than about 3.5 cycles are analyzed. For greater values of ϑ the 3p-RVCI-1 algorithm provides a slightly better inter-bin frequency location. Conversely, the 2p-IpDFT and the Aboutanios algorithms return a bit more accurate damping factor estimates, while the 3p-RVCI-1 algorithm exhibits poor accuracy.

III. CONCLUSIONS

In this paper the 3p-IpDFTi algorithm based on the MSD windows has been proposed for frequency and damping factor estimation of a real-valued noisy damped sinusoid. The algorithm compensates the contribution of the spectral image component on the returned estimates, so assuring a better accuracy than the classical 2p-IpDFT [8], the Aboutanios [4], and the 3p-RVCI-(*H*-1) [3] algorithms when only few signal cycles are analyzed. Due to its implementation simplicity, the 3p-IpDFTi algorithm is suitable for real-time, fast-response damped sinusoid parameter estimation.

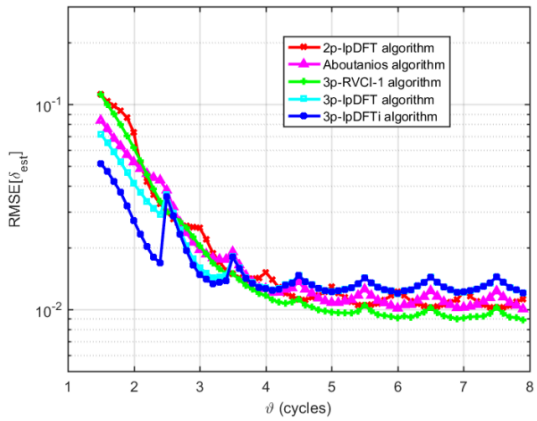

(a)

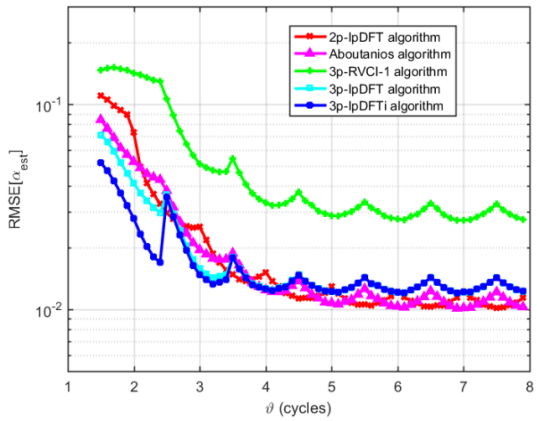

(b)

Fig. 4. Real-valued noisy harmonically distorted damped sinusoids: *RMSE*s of the frequency δ(a) and the damping factor α (b) estimates returned by the considered algorithms versus the number of analyzed cycles ϑ. Damping factor $\alpha = 1$, *SNR* = 40 dB, phase at random, and $M = 512$ samples. 2nd and 3rd harmonics with damping factors equal to 1.2 and 1.5 and amplitudes equal to 10% and 5% of the fundamental. Hann window.

APPENDIX

PROOF OF THE PROPOSITION

For a noise free signal, by using (3), the interpolation function (5) becomes:

$$h = H\frac{\tilde{X}_w(l+1)+\tilde{X}_{iw}(l+1)-\tilde{X}_w(l-1)-\tilde{X}_{iw}(l-1)}{\tilde{X}_w(l-1)+\tilde{X}_{iw}(l-1)-2\tilde{X}_w(l)-2\tilde{X}_{iw}(l)+\tilde{X}_w(l+1)+\tilde{X}_{iw}(l+1)} = H\frac{\tilde{X}_w(l+1)-\tilde{X}_w(l-1)}{\tilde{X}_w(l-1)-2\tilde{X}_w(l)+\tilde{X}_w(l+1)}\frac{1+\frac{\tilde{X}_{iw}(l+1)-\tilde{X}_{iw}(l-1)}{\tilde{X}_w(l+1)-\tilde{X}_w(l-1)}}{1+\frac{\tilde{X}_{iw}(l-1)-2\tilde{X}_{iw}(l)+\tilde{X}_{iw}(l+1)}{\tilde{X}_w(l-1)-2\tilde{X}_w(l)+\tilde{X}_w(l+1)}}. \quad \text{(A.1)}$$

If enough sinusoid cycles are observed, the contribution of the spectral image on the DFT samples is small, and so we have:

$\left|\frac{\tilde{X}_{iw}(l-1)-2\tilde{X}_{iw}(l)+\tilde{X}_{iw}(l+1)}{\tilde{X}_w(l-1)-2\tilde{X}_w(l)+\tilde{X}_w(l+1)}\right| \ll 1$. By using the approximation $(1+x)^{-1} \cong 1-x$, when $|x| << 1$, and neglecting the product of spectral image components, (A.1) becomes:

$$h \cong H\frac{\tilde{X}_w(l+1)-\tilde{X}_w(l-1)}{\tilde{X}_w(l-1)-2\tilde{X}_w(l)+\tilde{X}_w(l+1)}(1+\varepsilon), \qquad \text{(A.2)}$$

where:

$$\varepsilon \cong 1+\frac{\tilde{X}_{iw}(l+1)-\tilde{X}_{iw}(l-1)}{\tilde{X}_w(l+1)-\tilde{X}_w(l-1)}-\frac{\tilde{X}_{iw}(l-1)-2\tilde{X}_{iw}(l)+\tilde{X}_{iw}(l+1)}{\tilde{X}_w(l-1)-2\tilde{X}_w(l)+\tilde{X}_w(l+1)}$$

From (A.2) and (8) we obtain:

$$\hat{h} = \hat{\delta} + j\hat{\alpha} = (\delta + j\alpha)(1+\varepsilon). \qquad \text{(A.3)}$$

From which it results:

$$\Delta\delta + j\Delta\alpha = (\delta + j\alpha)\varepsilon. \qquad \text{(A.4)}$$

From (4a) we achieve:

$$\tilde{X}_{iw}(l-1) \cong \frac{\alpha+j(\delta+2l)+j(H-1)}{\alpha+j(\delta+2l)-jH}\tilde{X}_{iw}(l),$$
$$\tilde{X}_{iw}(l+1) \cong \frac{\alpha+j(\delta+2l)-j(H-1)}{\alpha+j(\delta+2l)+jH}\tilde{X}_{iw}(l). \qquad \text{(A.5)}$$

From (7) and (A.5), after some algebra the expression of ε becomes:

$$\varepsilon \cong 2\frac{j(l+\delta)}{\alpha-j\delta}\frac{(\alpha-j\delta+jH)(\alpha-j\delta-jH)}{(\alpha+j(\delta+2l)+jH)(\alpha+j(\delta+2l)-jH)}\frac{\tilde{X}_{iw}(l)}{\tilde{X}_w(l)}. \qquad \text{(A.6)}$$

From (4a) and (4b) it follows:

$$\frac{\tilde{X}_{iw}(l)}{\tilde{X}_w(l)} = \frac{1-e^{-2\pi(\alpha+j\delta)}}{1-e^{-2\pi(\alpha-j\delta)}}\frac{\alpha-j\delta}{\alpha+j(\delta+2l)}\frac{\prod_{h=1}^{H}[(\alpha-j\delta)^2+h^2]}{\prod_{h=1}^{H}[(\alpha+j\delta+j2l)^2+h^2]}e^{-j2\phi} \qquad \text{(A.7)}$$

Finally, by replacing (A.6) and (A.7) into (A.4), (10) can be achieved.

REFERENCES

[1] H. Günther, "NMR spectroscopy: basic principles, concepts and applications in chemistry", John Wiley & Sons, 2013.

[2] J.C. Visschers, E. Wilson, T. Connelly, A. Mudrov, L. Bougasi, "Rapid parameter determination of discrete damped sinusoidal oscillations", Optics Express, vol. 29, no. 5, 2021, pp. 6863-6878.

[3] K. Duda, T. P. Zielinski, L. B. Magalas, M. Majewski, "DFT based estimation of damped oscillation's parameters in low frequency mechanical spectroscopy", IEEE Trans. Instrum. Meas., vol. 60, no. 11, Nov. 2011, pp. 3608–3618.

[4] E. Aboutanios, "Estimation of the frequency and decay factor of a decaying exponential in noise", IEEE Trans. Signal Process., vol. 58, no. 2, Feb. 2010, pp. 501–509.

[5] M. Bertocco, C. Offeli, D. Petri, "Analysis of damped sinusoidal signals via a frequency-domain interpolation algorithm", IEEE Trans. Instrum. Meas. vol. 43, no. 2, Apr. 1994, pp. 245–250.

[6] K. Wang, H. Wen, L. Xu, L.Wang, "Two Points Interpolated DFT Algorithm for Accurate Estimation of Damping Factor and Frequency", IEEE Signal Process. Letter, vol. 28, 2021, pp. 499-502.

[7] R. Diao, Q. Meng, "An interpolation algorithm for discrete Fourier transforms of weighted damped sinusoidal signals", IEEE Trans. Instrum. Meas., vol. 63, no. 6, June 2014, pp. 1505–1523.

[8] R. Diao, Q. Meng, H. Fan, "Interpolation algorithms based on Rife-Vincent window for discrete Fourier transforms of damped signals (in Chinese)", Journal of Mechanical Engineering, vol. 51, no. 4, Feb. 2015.

[9] D. Belega, D. Petri, "Fast interpolated DTFT estimators of frequency and damping factor of real-valued damped sinusoids", Measurement, vol. 217, Aug. 2023.

[10] F.J. Harris, "On the use of windows for harmonic analysis with the discrete Fourier transform", Proceedings of the IEEE, vol. 66, no. 1, Jan. 1978, pp. 51–83.

[11] A.H. Nuttall, "Some windows with very good sidelobe behavior", IEEE Trans. Acoust. Speech Signal Process., vol. ASSP-29, no. 1, Feb. 1981, pp. 84–91.

[12] E. Jacobsen, P. Kootsookos," Fast, accurate frequency estimators", IEEE Signal Process. Mag., vol. 24, May 2007, pp. 123-125.

[13] C. Candan, "A method for fine resolution frequency estimation from three DFT samples", IEEE Signal Process. Lett., vol. 18, no. 6, June 2011, pp. 351-354.

[14] D. Belega, D. Petri," Frequency estimation by two- or three-point interpolated Fourier algorithms based on cosine windows", Signal Process., vol. 114, 2015, pp. 115-125.

[15] Y. Yao, S.M. Pandit, "Cramér-Rao lower bounds for a damped sinusoidal process", IEEE Trans. Signal Process., vol. 43, no. 4, Apr. 1995, pp. 878–885.

[16] E. Aboutanios, "Estimating the parameters of sinusoids and decaying sinusoids in noise", IEEE Instrum. Meas. Mag., vol. 14, no. 2, Apr. 2011, pp. 8–14.

26th IMEKO TC4 International Symposium
24th International Workshop on ADC and DAC Modelling and Testing
IMEKO TC-4 2023
Pordenone, Italy / September 20-21, 2023

The development and tests of a preamplifier for the spectrum analyzer adopted for noise measurements in quantum Hall standard

Marcin Wojciechowski[1], Kateryna Hovorova[1]

[1]*GUM (Central Office of Measures), Elektoralna 2 Str., 00-139 Warsaw, Poland,*
marcin.wojciechowski@gum.gov.pl, kateryna.hovorova@gum.gov.pl

***Abstract* – This paper describes setups for measuring noise in the frequency range from 10 kHz to 100 MHz of semiconductor structures made of new Dirac-materials - 2D-COF/MOF intended for the construction of QHRS quantum standards. The main emphasis was placed on the preamplifiers. The first design gives solution with equivalent input noise value of about 1 nV/$\sqrt{Hz}$ at 100 kHz and 400 V/V amplification, second - improves the spectrum analyzer's noise figure (NF) from 7 dB to 0.64 dB.**

I. INTRODUCTION

Revolutionary changes in the International System of Units, the recognition of classical standards as too inaccurate, and the transition to standard physical constants force scientists to work on increasing the number of significant figures of these constants. Promising this direction is the development of quantum standards characterized by excellent repeatability with atomic accuracy. An important path here is the development of semiconductor materials from the Dirac-materials family [1].

After tests with graphene for the implementation of the quantum Hall resistance standard (QHRS), the time has come for even more chemically and physically attractive structures of two-dimensional covalent-metalorganic frameworks (2D-COF/MOF) [2,3]. Models made of new materials will be subjected to various tests. The measurement of electrical noise is quite important here because, in the case of too much noise, it will not be possible to measure a given quantity with sufficient precision to be able to determine as many significant figures of a given constant as possible after conversion.

In the international EURAMET EMPIR 20FUN03 COMET project called "Two dimensional lattices of covalent- and metal-organic frameworks for the Quantum Hall resistance standard", one of the tasks is to adapt the equipment to measure the noise of model semiconductor structures with the greatest possible precision. The model of the new semiconductor structure designed to build the standard of the measurement unit should be characterized by low noise. It is difficult to estimate its value for a hitherto unknown structure intended for a specific application here. Measuring its total value in a wide frequency band can also be difficult due to the frequency limitations of individual methods and measuring instruments. For the selection of the measurement method and the design of the target measuring apparatus using a given semiconductor structure model, it is important to determine the corner frequency (f_c). This is a frequency on a broadband noise characteristic for which pink noise 1/f is equal to thermal white noise. Different semiconductor structures have different fc frequencies, the value of which can range from a few kilohertz to hundreds of megahertz. In the project, work on the study of electrical noise characteristics of the new semiconductor structure is carried out in two ways. Noise in the low-frequency range, where the highest noise power values occur, mainly associated with pink 1/f noise, is studied, and correlation methods are used to eliminate noise inside the instruments [4]. Work is also underway to prepare a set of measuring equipment for broadband noise testing of a semiconductor structure model, including the purpose of determining its f_c frequency. In Fig.1. exemplary characteristics of the noise spectral density for models made of two different materials with quite different f_c frequencies, for graphene [4] and a semiconductor material of MOSFET transistors with a channel length and width of 5/8 µm [5], were presented.

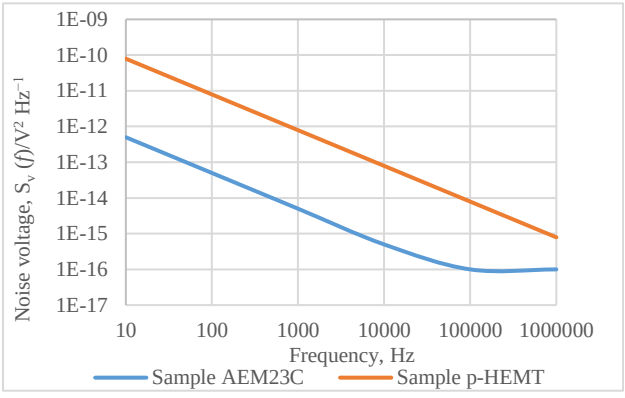

Fig. 1. Characteristics of noise spectral density for two models made of different semiconductor materials, showing differences in the occurrence of corner frequencies.

The article will describe the components of the measurement system for testing the broadband noise of the

model of the new semiconductor structure in the frequency range from 10 kHz to 100 MHz, which will also make it possible to find the f_c frequency.

II. DESCRIPTION OF THE CONSTRUCTION OF THE MEASURING SETUP

The measuring setup consists of two basic elements: a spectrum analyzer and a preamplifier.

A. Spectrum analyzer

The ESCI 3 measuring radio frequency receiver with a built-in spectrum analyzer function was used as a spectrum analyzer. The precision of this measuring device is evidenced by the fact that it allows the measurement of antenna signals at the level of several microvolts.

The spectrum analyzer measures the magnitude of the electrical power of the input signal over the full frequency range, which is from 9 kHz to 3 GHz. Since the 3 GHz frequency reaches the microwave band, it is important to match the input and output impedances of other devices connected to it to avoid signal reflections. There are two impedance-matching systems for high-frequency ranges. Television systems use 75 Ω and microwave measuring systems use 50 Ω. The measurement setup is operated in a 50 Ω impedance matching system in this task.

It is possible to set the spectrum analyzer to a different reading unit instead of power, e.g. voltage, but the instrument will convert this voltage from the measured power on 50 Ω input impedance. If a voltage source with an impedance other than 50 Ω is connected to the input, the indicated voltage value will not correspond to the actual voltage connected to the input. Although we are operating at lower frequencies, the 50 Ω impedance matching rule still applies, so preamplifiers should also have a 50 Ω output impedance.

The spectrum analyzer measures the power of variable signals dissipated into its input resistance. The noise power spectral density of this resistance expressed as the root mean square (RMS) of the noise voltage per 1 Hz of the band, is given by [6]:

$$\overline{v_n^2} = 4k_BTR \tag{1}$$

where k_B is the Boltzmann constant in joules per Kelvin (J/K), T is the absolute resistor temperature in Kelvin (K), and R is the analyzer input resistance in ohms (Ω).

The RMS of the noise voltage for a given bandwidth Δf in Hertz (Hz) measured with the input resistor is:

$$v_n = \sqrt{\overline{v_n^2}}\sqrt{\Delta f} = \sqrt{4k_BTR\Delta f} \tag{2}$$

and the noise power dissipated by this resistor is [6]:

$$P = v_n^2/R = 4k_BT\Delta f \tag{3}$$

The noise arising on the output resistor of devices connected to the analyzer is transferred to its input. The maximum noise power transfer occurs when the equivalent resistance of the input circuit is equal to the noise-producing resistance. In this case, there are two 50 Ω resistors. The noise power dissipated in the resistors is divided equally between each of them. Because only half of the source noise voltage is deposited across each of these resistors, the outcome noise power is given by :

$$P = k_BT\Delta f \tag{4}$$

where P is the thermal noise power in watts (W) and is independent of the noise-generating resistance [7]. The noise value visible on the spectrum analyzer in the absence of active devices connected to the input depends only on the temperature.

This power, expressed in dBm at room temperature assumed to be 300 K for a given band Δf, is expressed by the formula:

$$P(\text{dBm}) = -174\ \text{dBm} + 10\log(\Delta f) \tag{5}$$

therefore, for the assumed frequency range, it gives a noise power value of -94 dBm, which corresponds to about -13 dBμV, and the RMS value of the noise voltage for the assumed 50 Ω system of 4.5 μV (about 13 $\mu V_{p\text{-}p}$).

B. Preamplifier

The preamplifier for the spectrum analyzer in the noise measurement setup usually consists of several amplification stages, and when using sensitive analyzers it can have a total amplification of only a few hundred times. It is a trans-impedance electronic component. Its task is to match the impedance of the tested element to the input impedance of the analyzer; hence its output impedance must be 50 Ω, and the input impedance should be matched to the impedance of the tested noise source.

The second task of the preamplifier is to reduce the noise figure (NF) of the measurement setup with the spectrum analyzer. In this case, the NF of the ESCI analyzer is 7 dB.

The NF and the noise factor (F) are values that indicate the deterioration of the signal-to-noise ratio (SNR) caused by components in the signal chain. These values are used to evaluate the performance of an amplifier or radio receiver, with lower values indicating better performance.

In order to organize the entire theoretical part of the task, the known formulas describing the relationships between SNR, F and NF will be presented below, where the i index refers to the input and the o index to the output of individual amplification stages or the entire measurement system, and the dB index means that the value is presented in decibels. In the Friis formula, the k index at F and power gain G denotes the number of the amplifying stage [8]:

$$F = \frac{SNR_i}{SNR_0} \tag{6}$$

$$NF = 10\log_{10}(F) = 10\log_{10}\left(\frac{SNR_i}{SNR_0}\right) = \\ = SNR_{i,\ dB} - SNR_{0,\ dB} \tag{7}$$

$$F_{total} = F_1 + \frac{F_2 - 1}{G_1} + \frac{F_3 - 1}{G_1 G_2} + \frac{F_4 - 1}{G_1 G_2 G_3} \tag{8}$$

$$F_{setup} = F_{LNA} + \frac{F_{SA} - 1}{G_{LNA}} \tag{9}$$

where F_{setup}, F_{LNA} and F_{SA} are the noise factors of the whole measuring setup, the low-noise preamplifier (LNA), and the spectrum analyzer itself, respectively, and G_{LNA} is the gain of the LNA.

It is important to choose the right components for the construction of the first amplifying stage of the preamplifier, especially the active element, i.e., the transistor. This project decided to choose a transistor with a noise level below 1 nV/$\sqrt{Hz}$ operating at least in the frequency range of up to 100 MHz. Typically, transistors with such a low noise factor also have a low crossover frequency of pink noise with white noise. MOSFETs can have a remarkably high f_c frequency of up to several GHz. JFETs and BJTs have a very lower f_c even below the kHz range, but JFETs typically exhibit more flicker noise at low frequencies than BJTs and can have f_c as high as several kHz in JFETs not selected for flicker noise. The 1/f noise characteristics of JFET transistors are more linear than other transistors. [9,10]

The spectral density of the *1/f* noise voltage in the CMOS fabrication process as a function of the frequency *f* is often modelled as:

$$V_n^2 = \frac{K}{C_{ox}^2 WLf} \tag{10}$$

where K is a process-dependent constant, K equal to 5 x 10^{-9} fC^2/μm^2 for NMOS devices and 2 x 10^{-10} fC^2/μm^2 for hidden channel PMOS devices. C_{ox} is the oxide capacitance and W and L are the width and length of the channel, respectively. [11]

In graphene, the fc can be on the order of 100 Hz, but in MOSFETs and millimeter-wave structures it can be several GHz, hence the f_c frequency of a new and untested semiconductor structure may be in this range.

Due to the non-linearity of the noise characteristics and the low input impedance of the BJT transistors and the too-high f_c frequency of the MOSFET transistors, it was decided to use a JFET transistor. Finally, the BF 862 N-FET transistor with the following parameters was selected: equivalent noise input voltage at 100 kHz typical value of 0.8 nV/$\sqrt{Hz}$, and typical transition frequency of 715 MHz, both parameters meet assumptions.

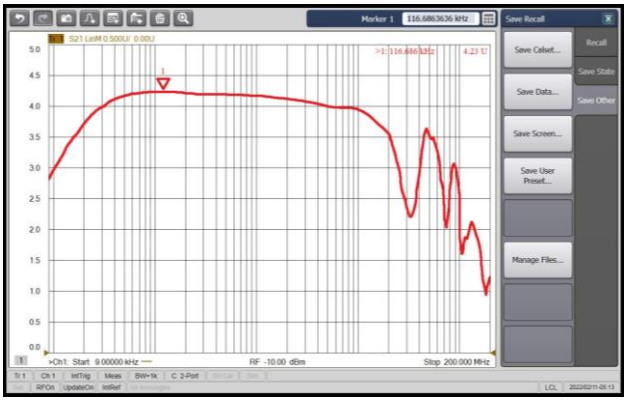

Fig. 2. The frequency response of the first-stage preamplifier based on the BF862 transistor.

The first stage of the preamplifier with an input impedance of about 100 kΩ was made. Fig. 2 shows the frequency response of the first stage of the preamplifier, from which its gain can be estimated at about 4 V/V in the range from about 10 kHz to about 30 MHz. The LMH6629 operational amplifier was used in the second and third stages. These stages have a gain of 10 V/V in the 900 MHz range and an input noise voltage equivalent of 0.69 nV/$\sqrt{Hz}$. The preamplifier made in this way has an input noise equivalent of 1 nV/$\sqrt{Hz}$ and a gain of about 400 V/V, which gives the RMS noise at the output of the entire preamplifier, including the band up to 30 MHz, at the level of 5.5 μV. Although the first stage of the preamplifier with the BF 862 transistor can work up to 100 MHz, its characteristics above 30 MHz do not indicate the possibility of making precise measurements, for these reasons, for operation in the higher frequency range, it was decided to use in the first stages a wideband FET transistor with the symbol CE3512K2, with the best catalog value NF = 0.30 dB, which means that to obtain the output noise value, the input noise must be multiplied by the gain and multiplied by 1.035. Finally, the second version of the preamplifier was made of two CE3512K2 transistors and an LMH6629 circuit. Due to the battery power supply, the transistor drain current is limited to 3 mA. This allowed us to obtain NF at the level of 0.5 dB and gain of the stage at the level of 12.5 dB. The first two preamplifier stages, made identically, allowed to obtain NF of 0.53 at 25 dB gain. The third stage has NF = 8 dB and a gain of 20 dB.

After substituting all components of the noise factors and power gains of the individual amplification stages of the preamplifier into the formula (8), the resulting value F_{LNA} = 1.15, which allows the calculation of NF_{LNA} = 0.59 dB. After substituting the above-calculated F_{LNA} value and the gain value of the entire preamplifier and the noise factor of the spectrum analyzer F_{SA} = 5.01 into the formula (9), a slight change in noise factor was obtained (F_{setup} = 1.16), and as a result of the noise figure of the entire measurement setup at the level of 0.64 dB. This means that thanks to the use of the preamplifier made here, an improvement in

noise figure was obtained from 7 dB for the spectrum analyzer alone to 0.64 dB for the entire measurement setup.

The second variant of the preamplifier has a voltage gain of about 178 V/V. An additional LMH6629 stage can be added to increase the amplification. It is also possible to connect a commercial amplifier HVA-200-40-F to the first two stages of the preamplifier, the connection of which will slightly reduce the quality of the noise parameters of the system, but will enable operation with the overall amplification of the extended version of the preamplifier up to 65 dB and extend the f_c frequency search range to 200 MHz.

III. TESTING THE BROADBAND ELECTRICAL NOISE MEASUREMENT SETUP

There are three elements in the measurement process here: the measured sample, which is the source of noise, the preamplifier matching the impedance of the sample to the impedance of the spectrum analyzer, amplifying the signal from the sample and improving the input noise parameters of the spectrum analyzer, and as the third element, the spectrum analyzer itself. To check the operation of one of the mentioned elements, the other two are reference devices with known parameters and characteristics.

An exemplary system for checking the parameters of the elements listed above is seen in Fig. 3. The noise source is the analyzer's 50 Ω terminator, which is connected to the inputs of an amplifier with known parameters. The terminator shorts the high 1 MΩ impedance of the HVA-200M-40-F amplifier, hence the input noise is at the level of 1 nV/$\sqrt{Hz}$, and the prominent noise is the noise of the electronic circuits related to the inputs, which in the midpoint of the 100 MHz band is 5.5 nV/$\sqrt{Hz}$ with 10 V/V gain set. So the total noise related to the input being the square root from the sum of the squares of both noises is 5.6 nV/$\sqrt{Hz}$ (the input current noise is omitted due to the low input resistance). The last numerical value, after taking into account the above gain and bandwidth values, gives the RMS voltage value of the broadband noise occurring at the output of the amplifier at the level of 560 µV, which corresponds to 55 dBµV. Due to the impedance matching of the amplifier output with the spectrum analyzer input, the power of -52 dBm (6.3 nW) is transferred to the analyzer.

On the monitor screen of the spectrum analyzer shown in Fig.3, there is a graph of the measurement of the noise mentioned above and the amplifier shown in the same photo. The average noise value in the design-relevant range, i.e. from 10 kHz to 100 MHz, is almost constant at -102.7 dBm. Above 100 MHz, the noise decreases slightly with increasing frequency, so towards the end of the visible 200 MHz range it is a few dBm less. During the measurement in the non-essential frequency range, the amplifier was disconnected to show in one picture the displayed floor noise level, the average value of which is almost constant and amounts to -123.9 dBm. The given value exceeds the value calculated from the theoretical formula (5). First of all, the formula does not take into account the NF of the analyzer itself and the components present in the analyzer, such as attenuators, filters, and conversion factors vary for different settings, which affect the final value of the input noise of the analyzer.

Fig. 3. An essential setup for checking the parameters of components included in the measurement system, consisting of a spectrum analyzer, an amplifier with known parameters, including equivalent voltage and current of input noise and frequency characteristics, and a source of white noise.

There are two more important pieces of information on the spectrum analyzer screen: RBW 100 Hz and AQT 160 s. This means that the IF (intermediate frequency) filter with 100 Hz band resolution (RBW) has been applied according to the setting. The second abbreviation means acquisition time (AQT) and is equal to 160 s, but it also means that the video bandwidth (VBW) filter, which is used to smooth the waveforms on the screen, has been abandoned in favour of the FFT (fast Fourier transformation) filter, which allows for greater precision of measurement data processing and accelerates the frequency sweep on the screen. When using the FFT filter, it must be considered about the RWB bandwidth conversion factor of 1.056 when converting RMS noise to noise spectral density.

IV. CONCLUSION

This work aims to present the classical method of measuring electrical noise using a spectrum analyzer as a modern tool in the search for f_c frequency at the crossover of pink 1/*f* noise and white noise frequency characteristics, thanks to a special approach to the construction of the device connected at the input of the analyzer. This device is an ultra-low noise preamplifier in which special

attention has been paid to the selection of the first amplification stage. The selection of subsequent stages was to lead to the optimal reduction of the noise figure of the whole setup and impedance matching to the 50 Ω input of the analyzer. Although the use of the correlation method of noise elimination from the theoretical point of view gives better possibilities of eliminating the noise of the measuring device, the set of apparatus presented here gives better possibilities for the broadband measurement of the amount of electrical noise and detection of the f_c frequency of the tested semiconductor structures, including 2D-COF/MOF structures used for building models of the quantum Hall resistance standard, while using popular spectrum analyzers and minimizing expenditure on additional measuring equipment. The proposed electrical noise measurement setup meets the assumptions for operation in the frequency range from 10 kHz to 100 MHz.

V. ACKNOWLEDGEMENTS

This project 20FUN03 COMET "Two dimensional lattices of covalent- and metal-organic frameworks for the Quantum Hall resistance standard" has received funding from the EMPIR programme co-financed by the Participating States and from the European Union's Horizon 2020 research and innovation programme.

Funder ID: 10.13039/100014132

REFERENCES

[1] T. O. Wehling, A. V. Balatsky, "Dirac materials", Advances in Physics, vol.63, No.1, July 2014, pp.1- 76.

[2] Ed.: S. K. Ghosh, "Metal-organic frameworks (MOFs) for environmental applications", Elsevier Science, 2019, p. 451.

[3] M. Wang, M. Wang, H.-H. Lin, M. Ballabio, H. Zhong, M. Bonn, S. Zhou, T. Heine, E. Cánovas, R. Dong, "High-Mobility Semiconducting Two-Dimensional Conjugated Covalent Organic Frameworks with p-Type Doping", Journal of the American Chemical Society, vol.142, No.52, December 2020, pp.21622-21627.

[4] M. Marzano, A. Cultrera, M. Ortolano, L. Callegaro, „A correlation noise spectrometer for flicker noise measurement in graphene samples", Measurement Science and Technology, vol. 30, No.3, February 2019, p.9

[5] C. Toro, Jr., "Improved 1/f Noise Measurements for Microwave Transistors" (2004). USF Tampa Graduate Theses and Dissertations.

[6] J. B. Johnson, "Electronic noise: The first two decades," IEEE Spectr., vol. 8, pp. 42–46, Feb. 1971.

[7] M. J. Buckingham. Noise in Electronic Devices and Systems. Ellis Horwood Limited, Chichester, England, 1983.

[8] H. T. Friis Papers, Manuscript Division, Library of Congress, Washington, D.C., 2014.

[9] W.M. Leach Jr.," Fundamentals of Low-Noise Electronic Analysis and Design", Georgia Institute of Technology, Atlanta, Georgia 30332-0250 USA, 2000-2001.

[10] R. F. Voss, "Linearity of 1/f Noise Mechanisms". Physical Review Letters. 40 (14): 913–916, doi/10.1103/physrevlett.40.913, 1978.

[11] K. H. Lundberg, "Noise sources in bulk CMOS", Massachusetts Institute of Technology, 77 Massachusetts Avenue, Cambridge, 2002.

26th IMEKO TC4 International Symposium
24th International Workshop on ADC and DAC Modelling and Testing
IMEKO TC-4 2023
Pordenone, Italy / September 20-21, 2023

The Wireless EMF Monitoring in Sensitive Areas around Kindergartens and Schools

Nikola Djuric[1], Dragan Kljajic[1], Tamara Skoric[1] and Nicola Pasquino[2]

[1]*Faculty of Technical Sciences, University of Novi Sad, Novi Sad, Serbia*
[2]*Dept. of Electrical Engineering and Information Technologies, University of Naples Federico II, Naples, Italy*

***Abstract* – The appearance of modern electromagnetic field (EMF) monitoring networks, such as the Serbian EMF RATEL network, has enabled wireless observation of EMF level in various surroundings, particularly in areas where people experience increased sensitivity to EMF exposure. Such areas are residential locations, where persons can reside many hours per day, kindergartens, schools, hospitals and children's playgrounds. They demand daily, comprehensive EMF monitoring, compliance checking with prescribed reference levels, as well as transparent dissemination of acquired results. This paper presents an analysis of EMF monitoring in sensitive areas on a case study of two kindergartens and an elementary school in the Serbian city of Novi Sad.**

I. INTRODUCTION

Mobile radio networks are present worldwide, providing various services and benefits to increase the quality of modern person's life [1]. However, their base stations are well known sources of electromagnetic fields (EMF), causing a strong debate due to their alleged adverse effects on health [2].

Consequently, researchers have dedicated a great effort to measure and monitor human exposure to EMF, in order to disclose physical mechanisms of interaction between EMF and human tissues, as well as any undesirable exposure endings on health [2], along with beneficial ones [3].

In line with those activities, the International Commission on Non-Ionizing Radiation Protection (ICNIRP) [4] has published the "Guidelines for limiting exposure to electromagnetic fields (100 kHz to 300 GHz)" – ICNIRP 2020 [5], summarizing available scientifically-based guidelines for health protection against EMF exposure.

Although the ICNIRP 2020 Guidelines are not mandatory, they have been considered by many international and national bodies as a reference for EMF legislation, which will act as safeguard for population against EMF exposure.

Regarding the significance of the EMF exposure threats, innovative monitoring methods and strong experimental evidence are persistently expected and required [6]. Thus, as a contribution to this subject, the Serbian EMF RATEL network [7] offers the approach of continuous and wireless broadband EMF monitoring [8].

The paper is organized as follows. Section II will briefly report essentials on the EMF RATEL network and its monitoring approach, while Section III will present a case study of monitoring in areas close to two kindergartens and an elementary school. Section IV will show the results of the analysis of acquired EMF data, while Section V concludes this paper.

II. THE EMF RATEL MONITORING NETWORK

The Serbian EMF RATEL monitoring system is based on autonomous EMF monitoring sensors, located over the area of relevance, as illustrated in Fig. 1.

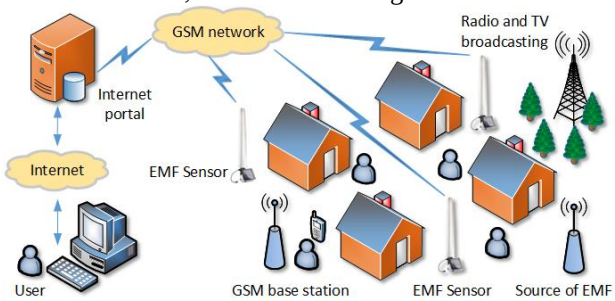

Fig. 1. The EMF RATEL concept.

Sensors run long-term monitoring of EMF level, on predetermined and permanent sites, storing acquired measurement results in their internal memory, periodically transferring data to EMF RATEL database [8], over the GSM network.

After processing, measurements data are disseminated through an open Internet portal [7], with the aim to timely inform community on EMF levels in their surroundings.

The EMF RATEL network has been designed to use EMF monitoring sensors displayed in Fig. 2 [9]-[11].

Fig. 2. Sensors in EMF RATEL system.

Sensors monitor the contribution of neighboring EMF sources, in a wide range of frequencies (i.e., they perform wideband monitoring), regardless of the EMF source position relative to sensor (isotropic measurement). Sensors are compliant with the ITU-T K.83 standard [12] and ready for 5G [9]-[11], [13].

Regarding a case study of monitoring in sensitive areas of two kindergartens and an elementary school, in the Serbian city of Novi Sad, the wideband EMF monitoring was performed using: AMB 8059 sensor with EP-1B-03 electric field probe [9], covering the frequency range from 100 kHz to 7 GHz, and MonitEM sensor with WPF8 electric field probe [10], covering the range 100 kHz to 8 GHz.

Both probes provide cumulative level of the electric field strength, i.e., the overall field strength on location, which originates from all neighboring EMF sources.

III. A CASE STUDY OF EMF MONITORING

The EMF RATEL system is designed for the observation of EMF in urban areas, employing sensors in major cities of the Republic of Serbia, whose number is associated with the number of the city population. Sensors mostly cover areas of special interest in the cities, providing daily EMF monitoring to the local community.

Regarding the city of Novi Sad, six sensors are currently installed in the areas of special interest, marked with blue circles in Fig. 3. However, for this case study, only three of them were considered, marked with additional red circle line. The intention is to present continuous monitoring and comprehensive analysis of measurement data, which could be valuable for residential community and their concerns on EMF exposure, mainly when considering precaution on the sensitive part of the population.

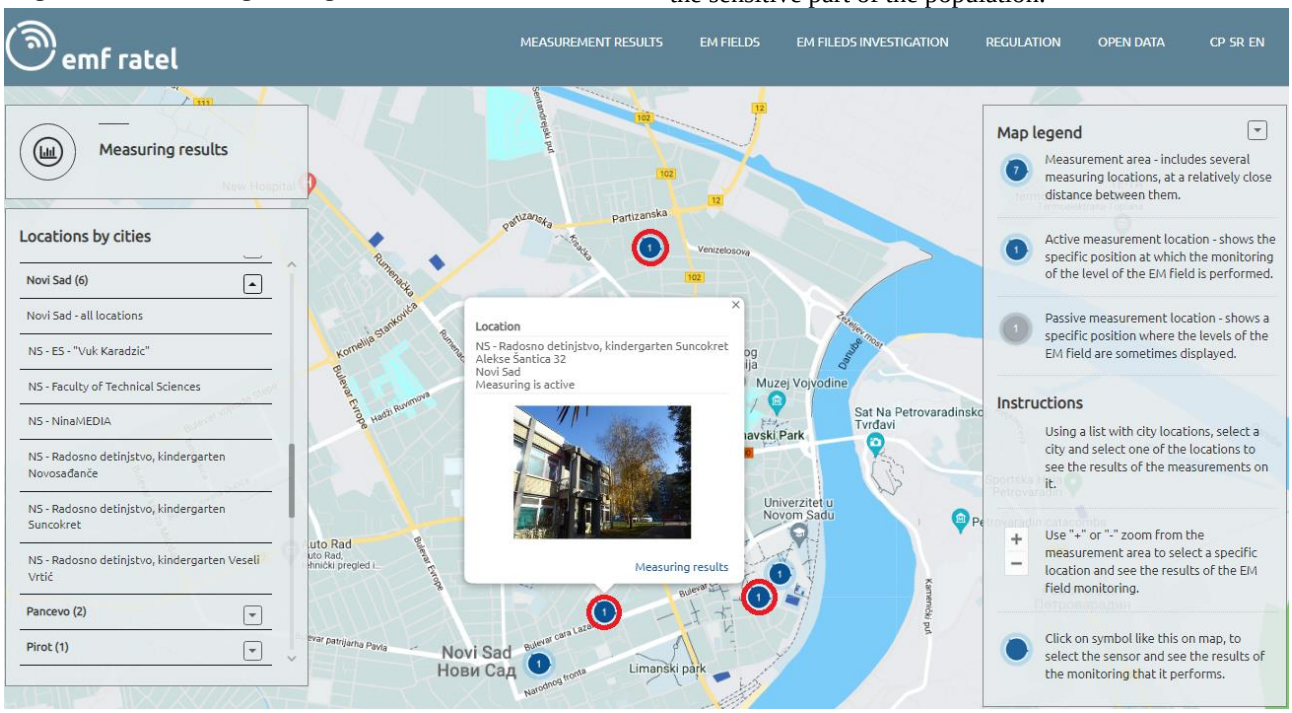

Fig. 3. The EMF RATEL sensors in the city of Novi Sad (three of them used for a case study) [7].

The chosen locations are the kindergartens "Suncokret" and "Veseli vrtic", both located in the southern part of the city and the elementary school "Vuk Karadzic", which is in the northern part of the city, as shown in Fig. 3.

Those locations have been carefully chosen as typical representatives of sensitive places in Novi Sad city, with high, medium and low density of residential population.

A. Basic overview of monitoring locations

The kindergarten "Suncokret", highlighted with red rectangle in Fig. 4, is situated in a highly populated part of the city. It is surrounded by the elementary school "Sonja Marinkovic" on north-west, several twelve-floor residential buildings on south-east, and a few individual households on the south-west.

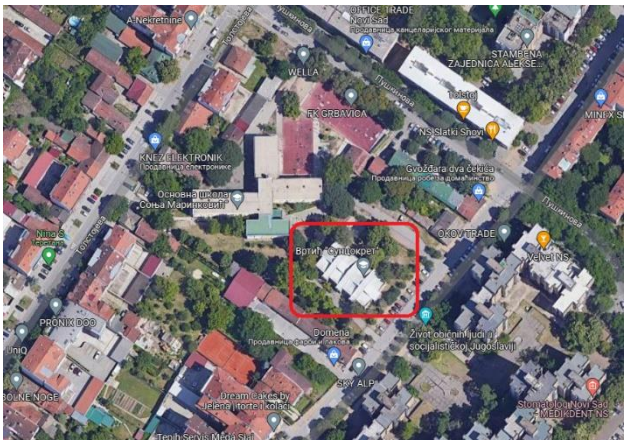

Fig. 4. Location of the kindergarten "Suncokret".

Kindergarten “Veseli vrtic”, marked with red rectangle line in Fig. 5, is situated in a medium-populated residential area, within the campus of the University of Novi Sad. The location is encircled by facilities of student’s dormitory “Slobodan Bajic” and the building of Science-Technological Park, on the north-west, elementary school “Jovan Popovic” on the south, as well as several eight-floor buildings on south-west side.

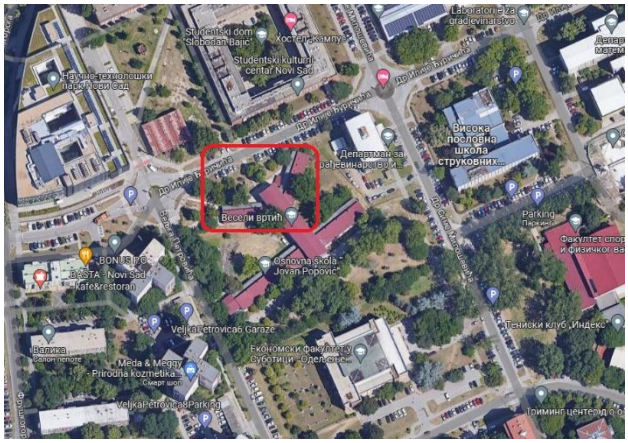

Fig. 5. Location of kindergarten “Veseli vrtic”.

The elementary school “Vuk Karadzic”, which is highlighted with red rectangle line in Fig. 6, is situated in a low-populated residential area of the city. It is surrounded by individual households in a very quiet street and with low intensity of traffic. Also, the location is bounded by the railway on the south side, additionally preventing circulation of the population and decreasing needs for an extensive coverage by the radio networks signal.

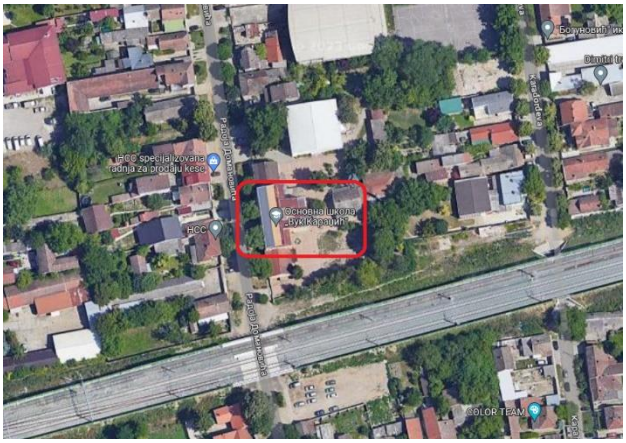

Fig. 6. Location of elementary school “Vuk Karadzic”.

B. Dissemination of acquired EMF results

At all considered locations, the AMB 8059 EMF sensors are installed, equipped with EP-1B-03 electric field probe. Regarding the kindergarten “Suncokret”, the sensor is positioned on the roof of the building, as partially shown in Fig. 7. It is located on the south-east corner of the building, close to the residential buildings, while details for other locations can be found on EMF RATEL Internet portal [7].

The sensors perform permanent measurements of the electric field strength, applying six-minute averaging, as required by standard EN 50413:2020 [14], which regulates the high-frequency field measurements and assessment of the human EMF exposure.

The acquired measurement results are published over the EMF RATEL Internet portal [7], as it is displayed in Fig. 7, for the case of the kindergarten “Suncokret”.

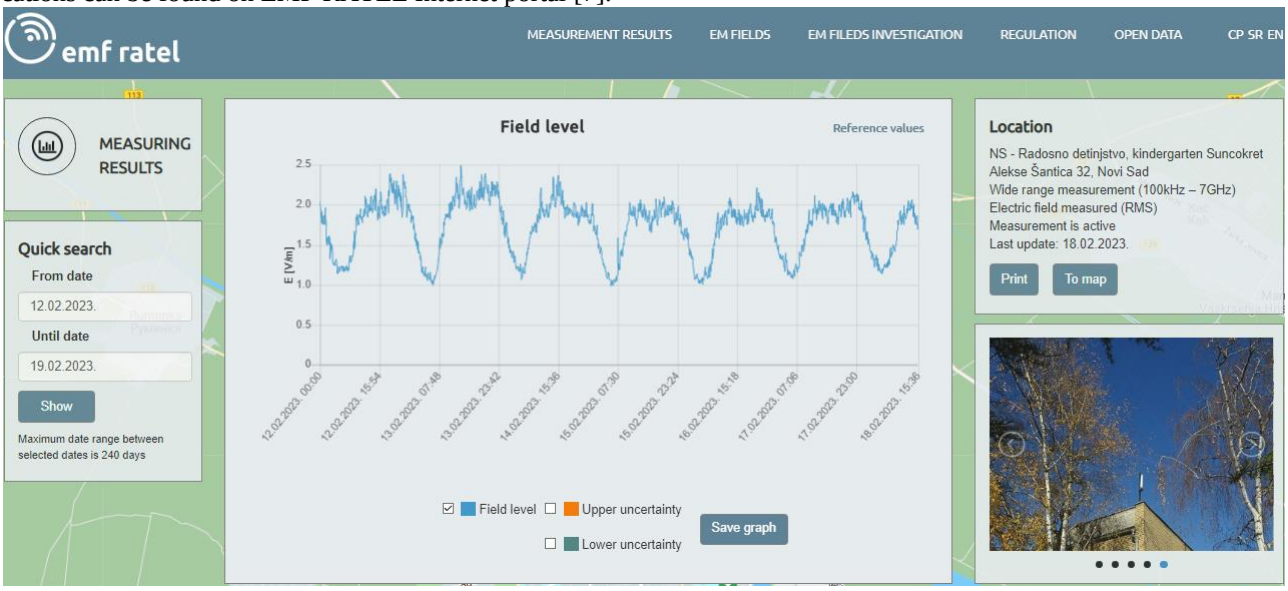

Fig. 7. Dissemination of EMF measurement results for the location of the kindergarten “Suncokret” [7].

The EMF RATEL Internet portal has numerous handy features, among which is the search option that allows the selection of a particular time interval [7].

The portal timeline graph shows daily field fluctuation, providing valuable information for the community about the existing EMF levels and happenings in the past.

IV. ANALYSIS OF EMF MEASUREMENTS

The EMF RATEL network, as one of the five most important EMF monitoring networks worldwide [15], can provide long-term monitoring, which is essential for the comprehensive field analysis.

Besides the time-line analysis, which is oriented only to one direction, additional investigation can be done, revealing hidden knowledge on EMF for considered location.

A. The weekly EMF behavior over locations

The sensors at kindergartens "Suncokret" and "Veseli vrtic" have been performing EMF monitoring since 2017, while the sensor on "Vuk Karadzic" since 2021. Sensors provide 240 field measurements (samples) per day, due to six-minute averaging [14], creating extensive data sets.

Regarding population's daily activities in urban areas, it is valuable to analyze changes of EMF during the whole week, to get deep understanding of field behavior and its balance with local environment.

By performing averaging over time on the field samples, on each day and over monitoring years, the EMF behavior on "Suncokret" location is gained and presented in Fig. 8.

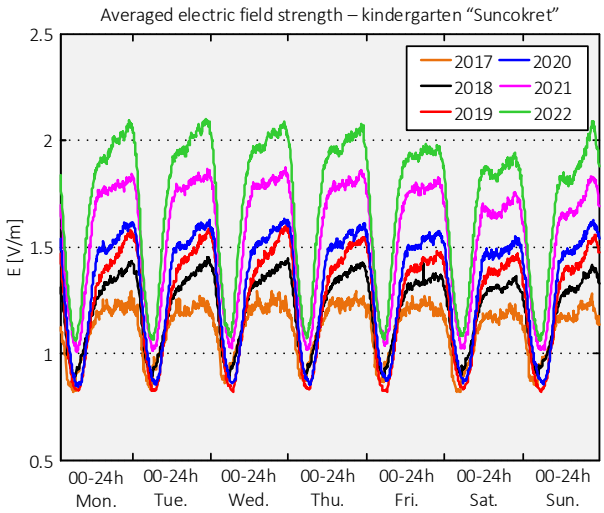

Fig. 8. EMF analysis for the kindergarten "Suncokret".

Similar analysis can be accomplished for two other locations, as shown in Fig. 9 and 10. However, for the location of "Vuk Karadzic" school only two full years and part of 2023 are presented, since monitoring started much later.

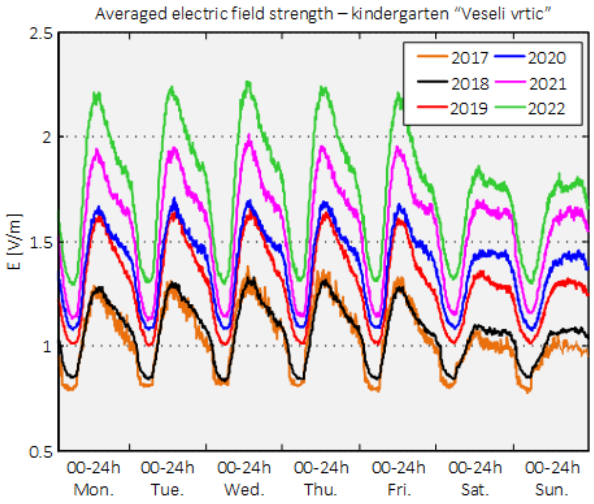

Fig. 9. EMF analysis for the kindergarten "Veseli vrtic".

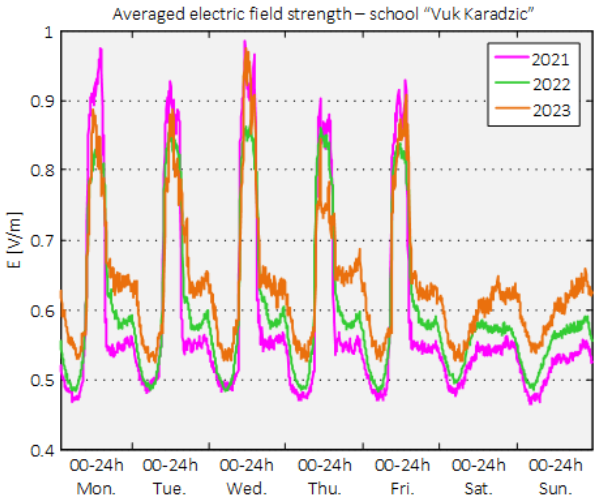

Fig. 10. EMF analysis for the school "Vuk Karadzic".

Many important details can be noticed from the presented graphs, among which is the periodicity of the field change, over working day, suggesting that similar levels of the electric field strength and its fluctuation exist almost every working day at all locations.

Also, the population density at each location has resulted in specific patterns of the field levels during working days and weekend.

Regarding location "Suncokret", the field levels are very similar over the whole week, while on "Veseli vrtic" and "Vuk Karadzic" locations, the clear difference between working days and weekend can be noticed.

This effect is particularly evident at the "Vuk Karadzic" location, where additional strong decrease of the field strength during night hours, can be observed.

However, the increase in the field levels occurring, from year to year, at all three locations, is what catches the eyes mainly. Although all acquired measurement results are far below the ICNIRP [5] and Serbian prescribed reference field levels (allowed electric field strength in Serbia are 2.5 times lower than ICNIRP levels, while the lowest allowed level is 11 V/m at 400 MHz) [16], the yearly increase of the field level should be carefully considered.

B. The field strength comparison among locations

Beside individual analysis of field strength at each location, the important comparison of field strength among locations can be completed, as depicted in Fig. 11, revealing additional hidden facts of field behavior.

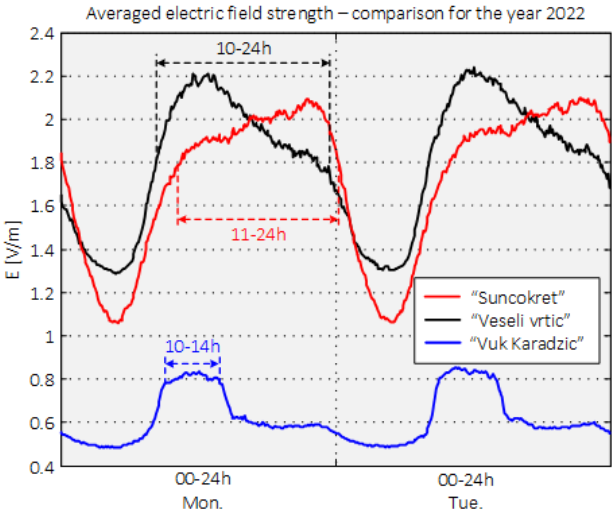

Fig. 11. Field strength per location.

To provide appropriate comparison, only year 2022 was selected. As a main outcome, the difference in field levels is evident at "Vuk Karazdic", the location with the lowest density of residential population, in comparison with the "Veseli vrtic", with medium density, and "Suncokret" with high density. The ration between the maximum measured field strengths is almost 2.5.

Also, the residential population density and activities in the area have their reflection on the time of the day with highest field strength and high levels duration, as noted in Fig. 11. For "Vuk Karazdic" school this period is relatively short, matching the time when most pupils leave/come to the school between noon and afternoon shift.

On the other hand, at "Suncokret" location, this period is extended almost to the midnight, with a slight increase in the field levels at night hours, while at the location of "Veseli vrtic", positioned between residential area and campus of the University of Novi Sad, this period is even one hour longer, with the rapid decrease of the field strength values in the afternoon and evening hours.

V. CONCLUSION

Because of population density, the city zones are regularly covered by appropriate radio network infrastructure, whose elements have influence on the levels of EMF and corresponding EMF exposure in the surroundings.

Using the continuous EMF monitoring of EMF RATEL network, the analysis of measurement data can reveal some important and hidden knowledge on EMF behavior in sensitive zones, as it is shown in a case study of two kindergartens and an elementary school of the city of Novi Sad.

ACKNOWLEDGMENT

The work has been supported by PSSTD APV, through the project grant 142-451-3156/2022-01/02 and MSTDI of the Republic of Serbia, through the project grant 451-03-47/2023-01/200156.

REFERENCES

[1] J. Nawrocki, D. Mischa, and A. Hamid Aghvami, "Modern approaches to radio network modelling and planning" – Understanding UMTS Radio Network Modelling, Planning and Automated Optimisation", Theory and Practice, John Wiley & Sons, 2006.

[2] Scientific Committee on Emerging and Newly Identified Health Risks – SCENIRH, "Final opinion on potential health effects of exposure to electromagnetic fields (EMF)", http://ec.europa.eu/health/scientific_committees/emerging/docs/scenihr_o_041.pdf, 2015.

[3] The COST BM1309 – European network for innovative uses of EMFs in biomedical applications (EMF-MED), http://cost-emf-med.eu.

[4] The International Commission for Non-Ionizing Radiation Protection (ICNIRP), https://www.icnirp.org.

[5] ICNIRP – "Guidelines for Limiting Exposure to Electromagnetic Fields (100 kHz to 300 GHz)", Health Physics, 118(5): 483–524; 2020, DOI: 10.1097/HP.0000000000001210.

[6] T. Onishi, K. Niskala, A. Christ and J. Roman, "Exposure assessment methods with respect to the 5G mobile communication systems", International Symposium on Electromagnetic Compatibility – EMC EUROPE 2020, September 23-25, 2020, Rome, Italy, pp. 1-4, DOI: 10.11-09/EMCEUROPE48519.2020.9245661.

[7] EMF RATEL Internet portal, http://emf.ratel.rs.

[8] N. Djuric, D. Kljajic, T. Gavrilov, V. Otasevic and S. Djuric, "The EMF exposure monitoring in cellular networks by Serbian EMF RATEL system", 2022 IEEE International Symposium on Measurements & Networking (M&N), Padua, Italy, 2022, pp. 1-6, DOI: 10.11-09/MN55117.2022.9887716.

[9] Narda AMB-8059 EMF Area Monitor User's Manual, 2017.

[10] Wavecontrol MonitEM User's Manual, 2016.

[11] Narda AMB-8061 Area Monitor Selective User's Manual, 2015.

[12] International Telecommunication Union ITU-T: K.83 – "Monitoring of electromagnetic field levels" (01/22), https://www.itu.int/rec/T-REC-K.83202201-P/en.

[13] S. Adda, L. Anglesio, F. Bogo, N. Pasquino, S. Trinchero, "How 5G NR signals impact on the response of broadband electric field probes", IEEE Transactions on Instrumentation and Measurement, vol. 72, 2023, DOI: 10.1109/TIM.2022.3227979.

[14] EN 50413:2020 – "Basic standard on measurement and calculation procedures for human exposure to electric, magnetic and electromagnetic fields (0 Hz – 300 GHz)".

[15] S. Iakovidis, C. Apostolidis, A. Manassas and T. Samaras "Electromagnetic fields exposure assessment in Europe utilizing publicly available data", Sensors, November 2022, pp. 8481. https://doi.org/10.3390/s22218481.

[16] "Rulebook on non-ionizing radiation exposure limits", Official gazette of the Republic of Serbia, no. 104/09, http://www.sepa.gov.rs/download/strano/pravilnik5.pdf.

26th IMEKO TC4 International Symposium
24th International Workshop on ADC and DAC Modelling and Testing
IMEKO TC-4 2023
Pordenone, Italy / September 20-21, 2023

Evaluation of Long-Term Stability of High-Precision Standard for Low-Frequency Voltage Measurement

Oleh Velychko[1,2], Valentyn Isaiev[1,3]

[1] *State Enterprise "All-Ukrainian state research and production center for standardization, metrology, certification and consumers' rights protection" (SE "Ukrmetrteststandard"), Metrologichna Str., 4, 03143, Kyiv, Ukraine*
[2]*velychko@ukrcsm.kiev.ua*, [3]*black2001w@gmail.com*

***Abstract* – The National measuring standards ensure the quality of measurements in different areas of science and technology. The actual errors of standards are not the only necessary characteristics to be determined. The long-term stability of the corrections also should be evaluated to guarantee the uncertainty of measurement is within the specified margin and, as a consequence, the metrological traceability is established. This paper mainly concerns the stability evaluation of the top-level standard for metrology service in low-frequency voltage measurement. The AC-DC transfer difference of high-precision voltage converter has been determined for almost 20 years. The measurements performed gave an opportunity to compare the deviations detected with the relevant combined uncertainties. The long-term stability estimate was within 20 μV/V for the frequency of 1 MHz.**

I. INTRODUCTION

There are four secondary standards of the voltage of alternating current (AC) with 33 precision thermal converters in Ukraine that require calibration on the National standard of AC voltage. More than 700 other precision measuring instruments (MIs) for AC voltage also are operated. These are thermal converters of different types, calibration units for voltmeters, precision digital multimeters, etc. Such MIs are used in electricity, industrial technology for civil and military purposes, and other fields of science and technology. The metrological traceability of those standards and MIs is provided by the National standard of AC voltage.

Ukraine is a member of the World Trade Organization. The strategic goal of the state is to integrate into global world structures in various spheres of life. The state continues to implement a system of mutual recognition in the results of measurements of calibration and testing laboratories. A necessary condition for the recognition of measurement results is the compliance of the calibration laboratory with the criteria of the ISO/IEC 17025 standard [1], one of the requirements of which is to ensure measurement traceability in the calibration chain.

II. BASIS FOR AC VOLTAGE MEASUREMENT

Two important factors should be kept in mind when analyzing the calibration chain to establish metrological traceability in the area of AC voltage measurements (Fig. 1). Firstly, the derived unit of voltage (V) of the redefined International System of Units is connected with two quantum constants through the Josephson constant $K_J=(2e)/h$, where e is an elementary charge, h is a Planck's constant [2]. Secondly, the Josephson standard [3] reproduces the unit of the voltage of direct current (DC). The AC/DC transfer standards are the high-precision standards for the difference between the root mean square (RMS) voltage and the equivalent DC voltage. Those standards are widely used to link AC and DC voltages [4-7].

It is necessary to compare two values of AC and DC voltages to determine the unit of AC voltage. The AC/DC transfer standard and DC voltage reference standard must be used for the high-precision reproduction of the AC

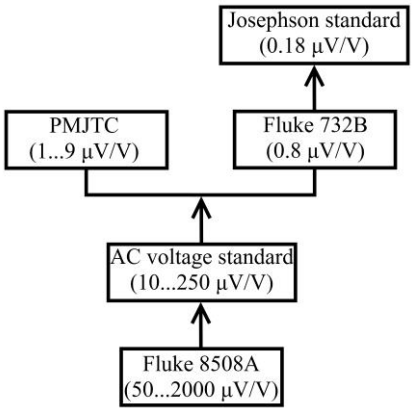

Fig. 1. Metrological traceability of the AC voltage measurements.

voltage unit. The metrological traceability will be branched to two primary standards (see Fig.1). The first one is Josephson voltage standard and the second one is planar multi-junction thermal converter (PMJTC).

The route of measurement traceability for AC voltage up to 1 MHz with corresponding measurement uncertainties from working standard (e.g., Fluke 8508A multimeter) to Josephson voltage standard is shown on Fig. 1. The Fluke 732B DC voltage reference instrument often is used as transportable for calibration with a primary standard.

The more stable each reproducible quantity in the chain is in the long term, the more reliable is ensuring the uncertainty of measurements matches the declared level.

III. MAIN MATERIAL

A. Procedure for stability determination

The focus of the current paper is the National standard of AC voltage, more precisely the AC-DC transfer standard Fluke 792A. The AC voltage standard is a complex set of MIs (voltmeters, sources, converters). It is presented in Fig. 2. For its stable operation, periodic calibration of the AC-DC voltage converter Fluke 792A [8] and DC voltage standards are carried out. The standards must have determined and confirmed characteristics (AC-DC transfer difference for Fluke 792A) with low uncertainty according to ISO/IEC 17025 standard.

The long-term stability of standards should not exceed specified values for a year. The minimum expanded uncertainty is 4 μV/V for a voltage of about 1 V and a frequency of 1 kHz following the Fluke 792A calibration certificate. The technical documentation of the National standard of AC voltage defines the interval of permissible values (from 2 to 36 μV/V) for the stability of AC-DC transfer difference.

The AC-DC voltage transfer difference is determined by sequentially applied voltage to the input of the thermal converter (an AC voltage of the required frequency, then a DC voltage of positive polarity, a DC voltage of negative polarity, and, finally, an AC voltage again). It is necessary to monitor the output voltage of the Fluke 792A reference converter.

The AC-DC voltage transfer difference $\delta_{AC\text{-}DC}$ is calculated by formula [9]:

$$\delta_{AC\text{-}DC} = \left.\frac{U_{AC} - U_{DC}}{U_{DC}}\right|_{E_{AC}=E_{DC}}, \quad (1)$$

where U_{AC} and U_{DC} are the input AC voltage and averaged DC voltage of a thermal converter respectively; E_{AC} and E_{DC} are the output thermal electromotive force (EMF) of the thermal converter, respectively, when an AC voltage or DC voltage is at the input.

PMJTC thermal converter (Germany) was used for determining the stability of the Fluke 792A instrument.

Fig. 2. General view of the AC voltage standard.

The calibration at 1.5 V of the PMJTC converter is approved by a PTB (Germany) calibration certificate. This voltage converter has very high long-term stability [10]. The results of the AC-DC difference comparison of the two voltage converters are the input data for the stability evaluation through the annual procedure.

The Fluke 792A instrument corrections given from the calibration certificate must be taken into account during the processing. A comparison of AC-DC voltage difference has been performed yearly since 2004 when the National standard of AC voltage was created in SE "Ukrmetrteststandard".

B. Results

The results of the comparison of the AC-DC difference of the PMJTC thermal converter and the Fluke 792A standard from 2004 till 2022 are presented in Table 1.

Table 1. Comparison results at 1.5 V of AC-DC voltage difference of PMJTC and Fluke 792A from 2004 till 2022

Year	AC-DC difference (μV/V) depending on frequancy (kHz)					
	0.01	0.045	1	10	100	1000
2004	0	-2.2	2.0	1.5	-5.0	16.0
2005	5.2	5.4	0	2.0	-6.5	14.2
2006	3.0	10.3	2.9	0.2	-7.7	12.7
2007	4.0	9.3	2.6	5.4	-7.0	14.0
2008	8.0	14.6	2.7	3.7	-5.0	9.0
2009	5.0	8.8	1.1	2.5	-6.2	6.0
2010	2.0	1.6	0	0.9	-2.4	8.6
2011	2.5	1.6	0	1.0	-2.0	9.0
2012	2.9	2.1	0.5	1.9	-2.9	10.0
2013	6.8	14.0	2.7	2.7	-5.5	9.1
2014	8.8	13.6	2.1	3.0	-5.7	10.9
2015	0.2	1.9	2.8	2.8	-5.0	5.0
2016	2.0	-2.8	1.7	3.0	-7.0	-4.6
2017	7.9	6.3	0.5	1.3	-2.2	3.8
2018	3.0	9.7	0.9	4.5	-3.4	21.5
2019	6.1	6.8	2.4	2.6	-6.1	9.7
2020	1.9	11.5	1.8	3.5	-7.3	1.1
2021	0.4	7.4	0.4	0.8	-4.6	12.6
2022	4.3	3.9	1.3	2.9	-3.4	4.6
Mean	3.9	6.5	1.5	2.4	-5.0	9.1

Table 1 shows that the largest AC-DC difference from 2004 to 2022 was: 8.8 μV/V in 2014 at a frequency of 0.01 kHz; 14.6 μV/V in 2008 at 0.045 kHz; 2.9 μV/V at 1 kHz in 2006; 5.4 μV/V in 2007 at 10 kHz; -7.7 μV/V in 2007 at 100 kHz; 21.5 μV/V in 2018 at 1000 kHz. Comparing two adjacent values, one can calculate that the highest instability of National standard of AC voltage has a double margin related to the maximum permissible value (36 μV/V) by National standard of AC voltage specification.

The data in Table 1 indicate a significant dissimilarity of the distribution from the normal shape for frequencies from 0.01 to 100 kHz. But, the AC-DC difference distribution has a form similar to the normal one at a frequency of 1000 kHz.

The long-term stability associated with a high-precision voltage measurement standard of 1.5 V at frequencies of 10 Hz, 1 kHz and 1 MHz are shown in Figs 3-5.

The presented long-term instability has a chaotic character. This can be explained by the different grounding configuration of the components of the investigated National standard, dissimilar temperature of the surrounding air, probable use of different connecting conductors, non-identical operating duration of MIs.

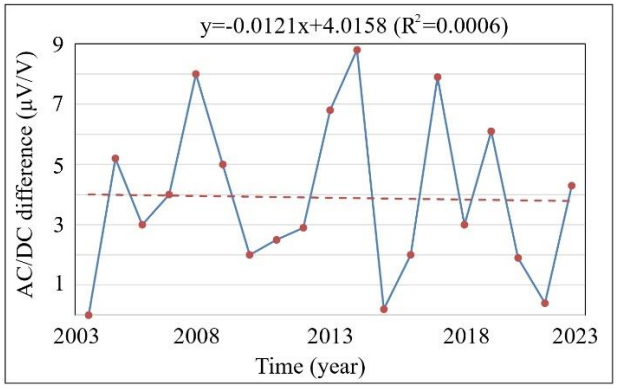

Fig. 3. The long-term stability with corresponding drift of AC/DC transfer standard at frequency of 10 Hz.

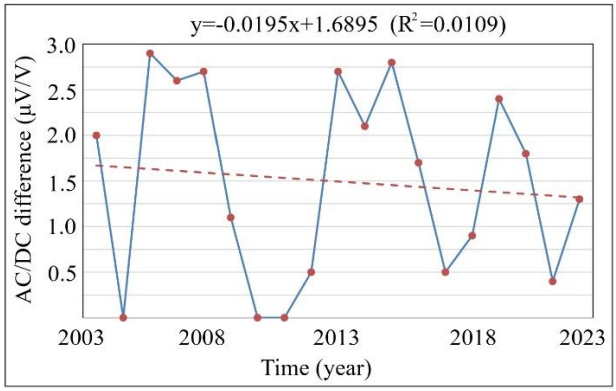

Fig. 4. The long-term stability with corresponding drift of AC/DC transfer standard at frequency of 1 kHz.

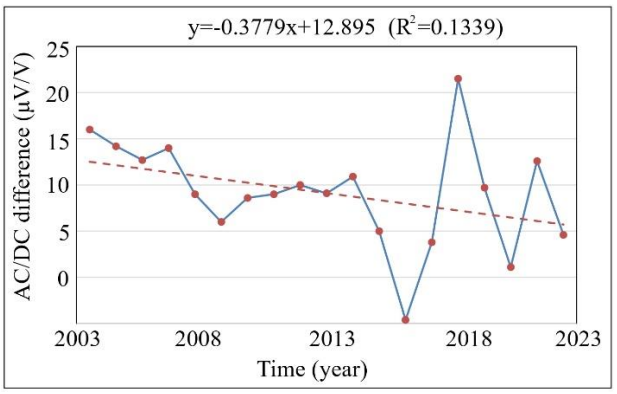

Fig. 5. The long-term stability with corresponding drift of AC/DC transfer standard at frequency of 1 MHz.

The accidental repair of some instruments and uncertain law of change of the AC-DC difference of both a PMJTC thermal converter and a reference Fluke 792A converter could be the reason as well.

C. Evaluation of measurement uncertainty

It is possible to calculate the expanded uncertainty of the AC-DC difference measurements according to Table 1, assuming the invariance of the AC-DC voltage transfer difference of the PMJTC thermal converter during the period of a study.

According to a developed methodology, the measurement model for a single value of AC-DC difference δ_{ST} has the form

$$\delta_{ST}=\delta_{DIF}-\delta_{792A}-\delta_{NS}, \quad (2)$$

where δ_{DIF} is the value determined directly from measurements; δ_{792A} is a AC-DC transfer difference of a reference Fluke 792A standard by the calibration certificate; δ_{NS} is a combined parameter associated with short-term instability of a reference Fluke 792A instrument, voltmeters of the converter output signals, and sources of direct and alternating voltage which are parts of National standard of AC voltage. The short uncertainty budget, related to a measurement model, is compiled in Table 2.

Evaluating the long-term stability of National standard of AC voltage is a main task of the work. So, comparing the combined standard uncertainty, calculated by the original methodology, with the uncertainty contribution of the long-term scattering is of interest.

The general distribution of the random variable, combined basing on several normally distributed random variables, also tends to the normal according to the central limit theorem of probability theory. The resulting distribution can often be approximated to normal even when the component distribution deviates from normal. Type A standard uncertainty (a standard deviation) of AC-DC difference measurement can be calculated by the guide for expressing uncertainty of measurement [11].

Table 2. Measurement uncertainty of AC-DC voltage difference measurements from 2004 to 2022

Characteristic	Estimate (μV/V) at frequency (kHz)					
	0.01	0.045	1	10	100	1000
Standard deviation for long-term stability S_{DIF}	0.6	1.2	0.2	0.3	0.4	1.3
Combined uncertainty for AC-DC transfer standard u_{792A}	5.5	3.0	2.0	2.0	4.0	19.0
Standard uncertainty of short-time instability u_{NS}	5.2	3.0	2.0	2.0	4.0	19.0
Standard uncertainty in assuming the rectangular distribution u_{DIF}	2.5	5.0	0.8	1.5	1.6	7.5
Combined uncertainty (normal distribution)	7.6	4.4	2.8	2.8	5.7	26.9
Combined uncertainty (rectangular distribution)	8.0	6.6	2.9	3.2	5.9	27.9

Assuming a normal law of probability distribution, standard deviation is:

$$S_{DIF} = \sqrt{\frac{\sum_{i=1}^{n}\left(\delta_i - \overline{\delta}_{DIF}\right)^2}{n(n-1)}}, \quad (3)$$

where n is a number of measurement results of AC-DC transfer difference ($n = 19$).

The standard uncertainty of AC-DC difference u_{DIF} can be calculated, if we assume a rectangular distribution low, by the formula [10]:

$$u_{DIF} = \left(\delta_{\max} - \delta_{\min}\right)/2\sqrt{3} \quad (4)$$

where $\delta_{\max}$ and $\delta_{\min}$ are the highest and the lowest values of AC-DC transfer difference depending on a frequency by Table 1.

The main contributions to a combined uncertainty are the expanded uncertainty for AC-DC transfer standard and the standard uncertainty of short-time instability as one can see in Table 2. These contributions of base components are made at each stage of the stability investigation. The last two components have been arising for the years.

Analyzing Table 2, one can see that the additional uncertainty contribution from instability adds a small percentage gain (at most 7 % for the worst measurement at 45 Hz) in assuming a normal distribution. A slightly different representation is in assuming a rectangular distribution law. This overestimation could lead to an increase in the combined uncertainty by more than half for 45 Hz and by one-fourth for 10 kHz.

IV. CONCLUSION

The long-term stability of National standard of AC voltage was investigated for 1.5 V at frequencies of 10, 45 Hz, 1, 10, 100 kHz, and 1 MHz for 19 years at SE "Ukrmetrteststandard". It is likely that the recorded standard deviation of the observations reached its highest value at a frequency of 45 Hz due to the proximity to a power frequency of 50 Hz. A large difference in standard uncertainty in estimating scatter from normal and rectangular distributions has been noticed. Therefore, further careful consideration should be given to the possibility of applying a normal or other distribution law at this frequency. For other frequencies, an overestimation by a rectangular distribution law has no significant effect on the resulting combined uncertainty.

REFERENCES

[1] ISO IEC 17025, "General requirements for the competence of testing and calibration laboratories", 2017.

[2] "The International System of Units (SI)", 9th edition, BIPM, 2019.

[3] C. J. Burroughs, and al., "NIST 10 V programmable Josephson voltage standard system", IEEE Transactions on Instrumentation and Measurement, 60, 7, 2011, 2482–2488.

[4] M. Klonz, "CCEM-K6.a: Key comparison of ac-dc voltage transfer standards at the lowest attainable level of uncertainty", Metrologia, 39(1), 2002, 01002.

[5] O. Velychko, and V. Isaiev, "A comparative analysis of ac/dc transfer standards for comparison of national standards", Eastern-European Journal of Enterprise Technologies, 6, 5(96), 2018, 14–24.

[6] O. Velychko, Yu. Darmenko, "Final Report on COOMET key comparison of AC/DC voltage transfer references (COOMET.EM-K6.a)", Metrologia, 53 (1), 2016, 01011.

[7] M. Halawa, and N. Al-Rashid, "Performance of Single Junction Thermal Voltage Converter (SJTVC) at 1 MHz via Equivalent Electrical Circuit Simulation", Proc. of 12th International Conference on Computer Modelling and Simulation, 2010, Cambridge, United Kingdom.

[8] "792A AC/DC Transfer standard. Instruction Manual", Fluke Corporation, 2006.

[9] J. R. Kinard, and T. X. Cai, "Determination of ac-dc difference in the 0.1-100 MHz frequency range", IEEE Transactions on Instrumentation and Measurement, 38, 2, 1989, 360–367.

[10] Klonz, H. Laiz, E. Kessler, "Development of thin-film multijunction thermal converters at PTB/IPHT", IEEE Transactions on Instrumentation and Measurement, 50, 6, 2001, 1490–1498.

[11] JCGM 100:2008 (GUM 1995 with minor corrections), "Evaluation of measurement data—guide to the expression of uncertainty in measurement", 2008.

26th IMEKO TC4 International Symposium
24th International Workshop on ADC and DAC Modelling and Testing
IMEKO TC-4 2023
Pordenone, Italy / September 20-21, 2023

Lossless real-time signal encoding for two-channel signals: A case study on ECG

Jozef Kromka, Ondrej Kovac, Jan Saliga

Technical University of Kosice, Letna 9, 04200 Kosice, Slovakia
e-mail addresses: {jozef.kromka, ondrej.kovac, jan.saliga}@tuke.sk

***Abstract* – This paper introduces a new encoding algorithm for the lossless, fast, and memory-efficient compression of two-channel signals. The proposed algorithm was evaluated using Electrocardiogram (ECG) signals. The results indicate that it can effectively compress ECG signals with a favorable compression ratio (CR), without relying on complex predictors, dictionaries, detectors, or additional encoding methods. By employing this method, an average CR of 1.98 was achieved, with a minimum CR of 1.54 and a maximum CR of 2.36. Moreover, it is assumed that the algorithm has the potential to enhance the achieved compression in Compressed Sensing (CS) systems.**

I. INTRODUCTION

Lossless encoding algorithms are a type of compression techniques that allows for the reduction of data size without losing any of the original information. This property makes them particularly useful for applications, where keeping the original quality of data is very important [1]. One of the fields where this property is vital is medicine, where doctors often need accurate data to precisely diagnose patients [2]. In modern medicine one of the most commonly studied signals is ECG. These signals are critical in the diagnosis and monitoring of heart conditions, and it is important to ensure that the data remains intact during the compression process. In addition to the medical field, CS systems [3], [4] could also benefit from the use of lossless encoding algorithms. The use of such algorithms in CS systems can aid in reducing the data size while maintaining the original CS information intact. This, in turn, leads to more efficient and effective compression and transmission of data, resulting in improved CS system performance.

In recent years, numerous lossless encoding algorithms have been proposed and tested on ECG signals. In one study [5], an adaptive linear prediction and two-stage Huffman coding approach was used to compress ECG signals. Another study [6] used an adaptive region prediction and variable length coding method. A peak detection and backward difference Huffman coding approach was presented in [7]. Lastly, two algorithms [8] and [9] utilizing adaptive linear prediction and Golomb-Rice coding were proposed. While these algorithms can achieve a CR greater than 2, they have the disadvantage of requiring some form of complex prediction algorithm or a dictionary, or they have a complex implementation. Hence, the encoding algorithms mentioned earlier may not be suitable for use in CS systems. CS systems are often required to compress data while maintaining low power consumption. The additional complexity introduced by these algorithms would increase the power consumption of such systems, rendering them impractical for CS applications.

This article presents a preliminary case study of the proposed lossless real-time encoding algorithm for ECG signals. The choice of ECG signals is based on the assumption that the proposed algorithm can be effectively applied to these signals. The main benefits of the proposed encoding algorithm include its memory efficiency, ease of implementation, lack of reliance on complex predictors, dictionaries, detectors, or additional encoding methods. The proposed method's advantages are intended to be utilized in real-time systems, including CS applications. However, at present, the proposed method has only been evaluated on full signals and has not been tested on signals sampled by CS systems.

The article is organized as follows: In Section II, the overall system design for the proposed encoding algorithm together with a flowchart is presented. The experimental results obtained by simulation are reported in III. The main conclusion and possible future work regarding the method are outlined in Section IV.

II. THE PROPOSED ENCODING ALGORITHM

In this paper, we propose an encoding algorithm inspired by the "quite OK image format" (QOI) which is a lossless image encoding algorithm presented by Dominic Szablewski in [10]. The algorithm has been formally verified by [11]. QOI is characterized by its ease of implementation and fast processing and incorporates commonly used techniques such as run-length encoding and dictionary-based compression.

The proposed algorithm uses some of the techniques that are used in QOI, but also some techniques that have been optimized for two-channel signals. The flowchart of the proposed encoding algorithm is shown in Fig. 1. The encoding method employs three variables in its process. The first variable, denoted by s, stores the current two-

channel sample, while the second variable, l, holds the previous two-channel sample. The third variable, run, is utilized for storing run-length data. These variables are initialized to zero at the onset of the encoding process. Subsequently, the first two-channel sample is loaded, and encoding begins.

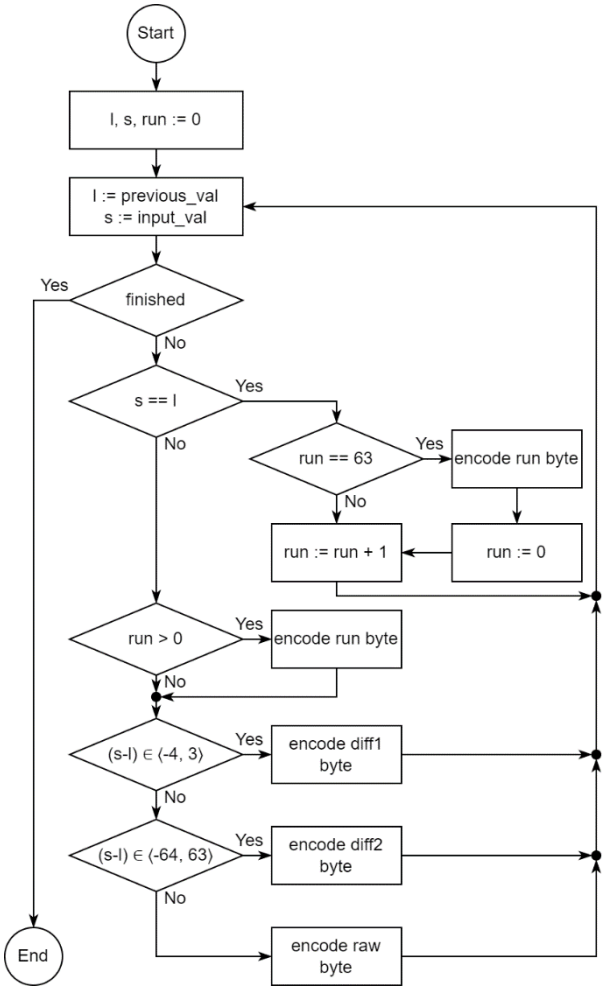

Fig. 1. The proposed encoding algorithm

The encoding process involves the comparison of the two-channel sample to the previous sample, and this comparison can yield four possible outcomes. Specifically, the sample may have the same value as the previous sample or the difference between the two may fall within the interval of $\langle -4, 3 \rangle$. Alternatively, the difference between the two samples may lie within the interval of $\langle -64, 63 \rangle$, or none of these cases. Each of these cases will be discussed in detail in the subsequent text.

In the initial case, where the value of the sample is the same as that of the previous sample, the run variable is incremented. Additionally, the algorithm verifies whether the run variable has surpassed the threshold of 63. If this threshold is exceeded, the run byte is encoded the run variable is set to zero. Moreover, the run byte is encoded if the run variable possesses a value greater than zero and the algorithm has not entered the initial case. It should be noted that the encoding of the run byte occurs prior to the execution of any other cases. The run byte is encoded and stored as illustrated in Fig. 2.

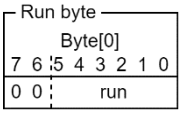

Fig. 2. Run byte encoding

The first two bits in the run byte represent the ID of the run byte, and the remaining 6 bits store the run variable.

When the difference between the current and previous samples falls within the interval of $\langle -4, 3 \rangle$, the difference for both channels is calculated. This difference is then converted into a 3-bit number, encoded, and stored according to Fig. 3. The difference for the first channel is denoted as $d1$, while the difference for the second channel is denoted as $d2$.

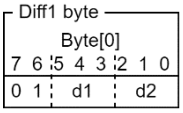

Fig. 3. Diff1 byte encoding

In the third case, when the difference between the two samples lies within the interval of $\langle -64, 63 \rangle$ the encoding is similar to the previous case. The only difference is that two bytes are utilized, and the difference values are stored as 7-bit numbers as displayed in Fig. 4.

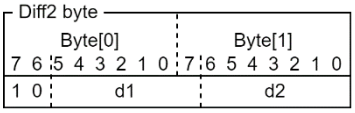

Fig. 4. Diff2 byte encoding

If none of the previously mentioned cases apply, a raw value of the two-channel sample is encoded. To encode raw values, three bytes are required. The raw values of the two-channel sample, denoted as $raw1$ and $raw2$, are stored as 11-bit values. This length was chosen because the database used for the case study contained data with this length. The encoding of raw values is depicted in Fig. 5.

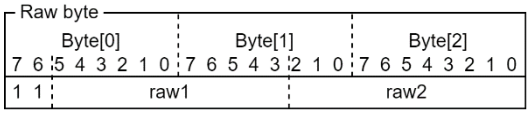

Fig. 5. Raw byte encoding

Each byte is encoded using a unique ID, which is employed in the decoding process to enable the decoding algorithm to determine how to decode the byte. The decoding process is a straightforward procedure. The decoding algorithm maintains a record of the preceding two-channel sample and reads the encoded bytes. Depending on the mask, the algorithm reads either one,

two, or three bytes. If a run byte is encountered, the algorithm produces run samples of the previous value. If the diff1 or diff2 byte is read, the algorithm outputs the value of the previous sample plus the difference. In the final scenario, when the raw byte is read, the algorithm outputs only the raw data contained within that byte.

III. PRELIMINARY RESULTS AND DISCUSSION

The proposed method was evaluated using the MIT-BIH arrhythmia database [12]. This database contains a set of 48 ECG records sampled at 360 Hz with 11-bit resolution. The evaluation was based on two metrics: CR and the time required for encoding and decoding. The CR was calculated using (1)

$$\mathrm{CR} = \frac{n_i}{n_o}, \tag{1}$$

where n_i represents the number of bits used in the original data and n_o represents the number of bits after compression.

Table 1 displays the average result obtained by the proposed method. The results from the previously mentioned methods are provided for comparison as well.

Table 1. Performance comparison of the proposed method with other methods in the MIT-BIH database

Encoding technique	Average CR
Adaptive linear prediction + two stage Huffman coding [5]	2.53
Adaptive region prediction + variable length coding [6]	2.67
Peak detection + backward difference Huffman coding [7]	2.64
Adaptive linear prediction + content adaptive Golomb-Rice coding [8]	2.77
Adaptive linear prediction + Golomb-Rice coding [9]	2.89
The proposed method	1.98

Based on the obtained results, it can be concluded that the proposed method produced an average CR that was approximately 25-45% lower than that of the other recent methods. As part of our analysis, we also report the minimum and maximum CR. The minimum CR of 1.54 was achieved for record 112 and the maximum CR of 2.36 was obtained for record 205.

In addition to evaluating the method's CR, an assessment was conducted to analyze its encoding and decoding speed, algorithm size, and the average number of instructions per sample. The preliminary evaluation was carried out on a personal computer equipped with an Intel Core i7-10700 processor, operating at a frequency of 2.9 GHz, and 16 GB of RAM. The proposed method was implemented in the C programming language and compiled on an Ubuntu operating system running under the Windows Subsystem for Linux. The algorithm was executed 1,000 times for each record resulting in average encode and decode times of 6.46 ms and 5.29 ms, respectively. With 650,000 samples per record, the average encode and decode times per sample were 9.93 ns and 8.14 ns. Notably, the simulation's performance may have been constrained by the operating system's multitasking, limiting access to full hardware resources. The algorithm's compiled size was around 5 kilobytes, though it can vary across systems. For 32-bit or 8-bit microcontrollers, the algorithm size could be significantly smaller. The final evaluation focused on assessing the average execution of instructions per sample. This assessment revealed that the system achieved an average execution of approximately 66 instructions, providing a quantitative measure of its computational performance. However, it's important to consider that this number would variate across different systems. Optimizing the algorithm's implementation could potentially reduce the instructions per sample, leading to improved performance.

While the proposed method achieves a lower CR than other recent methods, its primary advantage lies in the algorithm's simplicity of implementation and memory efficiency. In contrast to other methods, it does not require complex predictors, dictionaries, detectors, or additional encoding methods. The proposed method on the low level utilizes only subtraction and bit-shifting operations. Consequently, the proposed method is well-suited for use in systems that require real-time encoding or have limited memory or computing power resources. This feature of the proposed method could be utilized in CS systems to improve their efficiency as well. The proposed method would not significantly influence the energy consumption nor system resources and could potentially increase CR achieved by these systems.

It is worth noting that the current implementation of the method was designed such that all encoding bytes are multiples of 8 bits, which allows for byte alignment. This design feature makes it easier to implement the method on both microcontrollers and computers. We assume that it is possible to achieve a higher CR value by using encoding bytes with different lengths other than 8 bits. This approach may be well-suited for an FPGA device. The algorithm that inspired the proposed method [10] already has an FPGA implementation, which suggests that the proposed method could also be easily implemented for an FPGA device.

IV. CONCLUSION

This article introduced a novel encoding algorithm that is well-suited for the lossless, real-time, and memory-efficient encoding of two-channel signals. The proposed algorithm was tested on ECG signals, and the preliminary results demonstrated that it achieved an average CR of 1.98. Although this CR was 25-45% lower than that achieved by other recent methods, it was noted that the

proposed method does not require the use of complex predictors, dictionaries, detectors, or additional encoding methods. These design features make the proposed algorithm a promising candidate for use in systems with limited memory or computing power resources, as well as in real-time applications.

Future work is directed to: (i) evaluating the efficiency of the proposed encoding algorithm for ECG signals from the PTB Diagnostic ECG dataset [13], [14], (ii) examining the efficiency of the method when applied to signals sampled by CS systems, (iii) performing a hardware implementation of the proposed method using a microcontroller and FPGA device, in order to thoroughly assess the algorithm's speed and memory efficiency.

ACKNOWLEDGMENT

The work is a part of the project supported by the Science Grant Agency of the Slovak Republic (No. 1/0413/22).

REFERENCES

[1] K. Sayood, *Lossless Compression Handbook*. Elsevier, 2002.

[2] J. F. Burnum, "The Misinformation Era: The Fall of the Medical Record", *Ann. Intern. Med.*, roč. 110, č. 6, s. 482–484, mar. 1989, doi: 10.7326/0003-4819-110-6-482.

[3] L. De Vito, E. Picariello, F. Picariello, S. Rapuano, a I. Tudosa, "A dictionary optimization method for reconstruction of ECG signals after compressed sensing", *Sensors*, roč. 21, č. 16, 2021, doi: 10.3390/s21165282.

[4] J. Kromka, O. Kováč, J. Šaliga, a L. Michaeli, "Multiwavelet-based ECG compressed sensing with samples difference thresholding", v *25th IMEKO TC-4 INTERNATIONAL SYMPOSIUM ON MEASUREMENT OF ELECTRICAL QUANTITIES*, Brescia, Italy, sep. 2022, s. 215–220.

[5] G.-A. Luo, S.-L. Chen, a T.-L. Lin, "VLSI implementation of a lossless ECG encoder design with fuzzy decision and two-stage Huffman coding for wireless body sensor network", v *2013 9th International Conference on Information, Communications & Signal Processing*, dec. 2013, s. 1–4. doi: 10.1109/ICICS.2013.6782955.

[6] K. Li, Y. Pan, F. Chen, K.-T. Cheng, a R. Huan, "Real-time lossless ECG compression for low-power wearable medical devices based on adaptive region prediction", *Electron. Lett.*, roč. 50, č. 25, s. 1904–1906, 2014, doi: 10.1049/el.2014.3058.

[7] S.-C. Lai, P.-C. Tail, M.-K. Lee, S.-F. Lei, a C.-H. Luo, "Prototype System Design of ECG Signal Acquisition with Lossless Data Compression Algorithm Applied for Smart Devices", v *2018 IEEE International Conference on Consumer Electronics-Taiwan (ICCE-TW)*, máj. 2018, s. 1–2. doi: 10.1109/ICCE-China.2018.8448842.

[8] T.-H. Tsai a W.-T. Kuo, "An Efficient ECG Lossless Compression System for Embedded Platforms With Telemedicine Applications", *IEEE Access*, roč. 6, s. 42207–42215, 2018, doi: 10.1109/ACCESS.2018.2858857.

[9] T.-H. Tsai a F.-L. Tsai, "Efficient lossless compression scheme for multi-channel ECG signal processing", *Biomed. Signal Process. Control*, roč. 59, s. 101879, máj. 2020, doi: 10.1016/j.bspc.2020.101879.

[10] "QOI — The Quite OK Image Format". https://qoiformat.org/ (cit 03. február 2023).

[11] M. Bucev a V. Kunčak, Ed., "Formally Verified Quite OK Image Format", *Proc. 22nd Conf. Form. Methods Comput.-Aided Des. – FMCAD 2022*, 2022, doi: 10.34727/2022/isbn.978-3-85448-053-2_41.

[12] G. B. Moody a R. G. Mark, "The impact of the MIT-BIH Arrhythmia Database", *IEEE Eng. Med. Biol. Mag.*, roč. 20, č. 3, s. 45–50, máj. 2001, doi: 10.1109/51.932724.

[13] G. Al *et al.*, "PhysioBank, PhysioToolkit, and PhysioNet: components of a new research resource for complex physiologic signals", *Circulation*, roč. 101, č. 23, jún. 2000, doi: 10.1161/01.cir.101.23.e215.

[14] R.-D. Bousseljot, D. Kreiseler, a A. Schnabel, "The PTB Diagnostic ECG Database". physionet.org, 2004. doi: 10.13026/C28C71.

26th IMEKO TC4 International Symposium
24th International Workshop on ADC and DAC Modelling and Testing
IMEKO TC-4 2023
Pordenone, Italy / September 20-21, 2023

ADC Input Currents Measurement

Jakub Svatos[1], Jan Fischer[1], Jan Holub[1]

[1] *Czech Technical University in Prague, Faculty of Electrical Engineering, Department of Measurement, Technicka 2, 166 27, Prague 6, Czechia, svatoja1@fel.cvut.cz*

***Abstract* – The contribution introduces the possible issue of internal CMOS Successive Approximation Register microcontroller's Analog-to-Digital Converters input currents. If the microcontroller also contains a multiplexer, it can lead to consequences caused by the sample-and-hold block that is part of a charge redistribution Analog-to-Digital Converter. The article presents its nature, the possibility of its measurement, and a simplified model of such an MCU analog inputs behavior. The simplified model and derived formulas can help the unacquainted user in a data acquisition system with the MCU design when measuring signal sources with non-negligible internal resistance. The introduced parameters, which cannot be found in datasheets, can be essential for users.**

I. INTRODUCTION

Current microcontrollers (MCU) very often contain one or more CMOS Analog-to-Digital Converters (ADC) working on the Successive Approximation Register (SAR) principle with a typical resolution of 12 bits [1]. These MCUs are usually also equipped with a multiplexer. By the nature of the CMOS ADC principle, it inherently contains a sample-and-hold (S/H) block [2]. However, this S/H block is not independent, but it is part of the charge redistribution ADC, which results in differences from the classic S/H and, therefore, consequences that unacquainted users may not expect. The fundamental difference lies in the fact that the charge on the sampling capacitor in the CMOS ADC changes during the process of SAR operation. Each time a new sample is acquired, the measured circuit is loaded with a current pulse. This is a typical feature of CMOS SAR ADC used in MCU, which, with some exceptions (ATmega328), usually does not contain an analog buffer. In the case of specialized ADCs [3], an auxiliary block, "precharge," is used, which reduces the load by precharging the sampling capacitor to a charge corresponding to the previous sample [4]. However, this is not the case with the ADC used in MCUs. Therefore, in this type of ADC, it is necessary to take into account the current pulses in the sampling processor. These parameters are not presented in the datasheets of the manufacturers [5] and [6].

II. S/H BLOCK IN CMOS SAR ADC

The task of a classic S/H block based on bipolar technology is to maintain a constant voltage at its output during the entire conversion process of the ADC. The situation is shown in Fig. 1. The sampling capacitor is followed by a buffer with a large input impedance driving an input of the ADC [7].

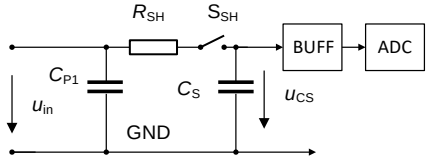

Fig. 1. Classic S/H block use with an ADC.

The input voltage u_{in} is applied to the passive S/H circuit, which takes a new sample $u_{in}(n)$. During the sampling, a transient response occurs when the voltage on the sampling capacitor C_S according to Fig. 1, must change from the previous value of $u_{in}(n\text{-}1)$ to the new value of $u_{in}(n)$. When simplifying and neglecting the capacitive charge feedthrough from the control circuit, a charge ΔQ_S flows through the S/H switch, proportional to the voltage change between the two samples.

$$\Delta Q_S = (u_{\mathrm{in}}(n) - u_{\mathrm{in}}(n-1))C_s \qquad (1)$$

If a constant input voltage u_{in} is sampled, the voltage u_{CS} on the hold capacitor practically does not change. Therefore, the capacitor does not need to be charged or discharged again, and no current flows through the input. This is entirely different from a conventional CMOS SAR ADC. During the charge redistribution process that takes place in the CMOS ADC, the voltage on the capacitor C_S, which is part of the ADC, changes. With each new sampling, even from a source of constant voltage, C_S must always be recharged to a value corresponding to the measured input voltage u_{in}. In this process, a charge ΔQ_S flows through the input. The size of this charge depends on the state of C_S after the charge redistribution process, on the value of the input voltage and on the multiplexer. The principle with a single ADC is shown in Fig. 2.

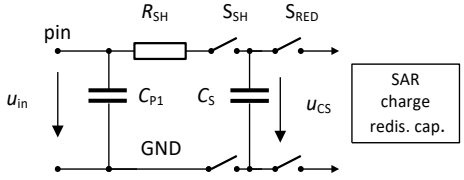

Fig. 2. Input circuit with ADC CMOS SAR.

The ADC measures a constant voltage on a single input without multiplexing. The sampling capacitor C_S is part of the charge redistribution block in the CMOS ADC, which is connected via the SRED switches.

For simplification, it can be assumed, after the charge redistribution process, a voltage remaining on the C_S, will be residual voltage U_{RES}. Very often, this voltage is equal to ½ U_{REF}, but can have a value close to zero.

In the simplified model, according to Fig. 2, the input parasitic capacitances C_{P1} at a constant value of u_{in} have a constant charge. Only C_S must be charged or discharged to the value of u_{in} again from another sample of U_{RES}. Then, with each sample acquired, charge ΔQ_s of a size according to (2) will pass through the input.

$$\Delta Q_S = (u_{\text{in}} - U_{\text{RES}})C_s \qquad (2)$$

If a constant input voltage u_{in} were measured with the sampling frequency f_{SAMP}, then according to (3), it would represent a current with an average value of I_S.

$$I_S = \Delta Q_S \cdot f_{SAMP} = (u_{\text{in}} - U_{\text{RES}})C_s \cdot f_{SAMP} \qquad (3)$$

From (2) follows, the greater the difference between input voltage and residual voltage is, the greater the charge will flow through the input at each sampling. At $u_{in} = U_{RES}$, is $\Delta Q_s = 0$, and no charge would pass through the input. This can be used for a simple experiment to determine the value of the U_{RES}, according to Fig. 3.

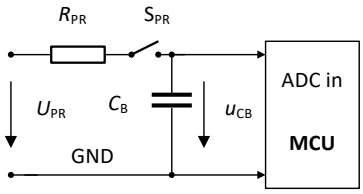

Fig. 3. Connection to determine the value of U_{RES}.

C_B with a capacity in the order of units to hundreds of nF serves as a source of a measured voltage. The smaller the capacity of the C_B is used, the more is necessary to ensure its connection to the analog input with a very short wire in order to reduce interference from the 50 Hz resp. 60 Hz. In the case of C_B = 1 nF, even the wire with a length of 10 cm will introduce a non-negligible superimposed interfering AC signal, which increases the uncertainty of the U_{RES} determination. With the S_{PR} switch opened, the MCU starts conversions of the tested ADC. After several hundred measurements, the u_{CB} voltage settles at U_{RES} value. The settling time increases with the C_B/C_S ratio. The U_{RES} value is determined by the microcontroller itself based on the data from the internal ADC.

In the MCU, the input of the CMOS SAR ADC is connected to the input pins via a multiplexer. Information about the specific solution of such a multiplexer in the MCU and its other properties and operation are usually missing from the manufacturer datasheet. Only information on the value of the C_S capacity can be found, e.g., C_{ADC} [8]. C_{ADC} expresses only the capacity of the sampling capacitor value. However, due to the multiplexor with dynamic control, according to our experiments, a non-negligible value of the capacity of other capacitors, which, due to various capacitance crosstalk from the control, must be added to this capacity as well as and also must be charged or discharged again with each sample acquired. All these capacities and the sampling capacitor C_S will be included in the simplified MCU analog input behavior model in the equivalent sampling capacity C_{SEQ}.

Based on experiments with a series of MCUs containing SAR ADCs, it was found that the behavior of ADC inputs varies by MCU design series. In some cases, with a single ADC with a simple multiplexer, the additional effect of the multiplexer is relatively small. The size of the capacity of C_{SEQ} compared to C_S can be larger in the order of units up to tens of percent. In the case of an MCU with a complex multiplexer, with, for example, a cascading principle, the difference in the size of the capacities of C_{SEQ} compared to C_S is noticeably larger. In addition, there can be even different behavior of different analog inputs connected to a different MCU input pins with a single ADC.

As already mentioned, in a multiplexer, the various capacities and crosstalk effects must be considered. For their quantification and the design of the overall analog inputs MCU model behavior in terms of input currents, experiment many sets of measurements of the charge ΔQ_S value, depending on the input voltage u_{in} value, have been performed. A measuring system with a charge amplifier was used. This allows determining the total charge passed through the selected MCU analog input at a defined input voltage u_{in} and a selected number of samples (e.g., 10 000 samples).

The results of the experiment [9] showed that for some MCUs, the input behavior can be modeled according to (2) with a small deviation.

According to the measurements of ΔQ_s, the C_S capacitance has been changed to the equivalent sampling capacity C_{SEQ}, which affects the effect of various crosstalk in the multiplex system.

$$\Delta Q_S = (u_{\text{in}} - U_{\text{RES}})C_{SEQ} \qquad (4)$$

For some MCUs, the value of C_{SEQ} was practically constant in the range of measured input voltages. For other MCUs, the size of C_{SEQ} varies with the value of u_{in} in the order of tens, sometimes even hundreds of percent, and thus showed a strong nonlinearity [7]. This concerns the ADC structure in a particular MCU, which is entirely unknown to the standard user. Therefore, measurement of the internal ADCs properties to create a simple model of the behavior of the analog inputs has been done. For example, a model described according to (4) showing the equivalent sampling capacity C_{SEQ} and its dependence on the input voltage. The aim is to roughly estimate ADC input behavior limits when working with signal sources with non-negligible internal resistance. With a constant

input voltage sampling, an RC transient occurs. The time constant is determined by the total resistance between the source u_{in} and the sample and hold circuit, expressed by the equivalent capacity of C_{SEQ}. Suppose the maximum value of C_{SEQ} is used in the calculation for a given internal resistance of the measured signal source. In that case, the correct function is ensured over the entire range of input voltages. If only the C_S given by the datasheet is used in the design, which is usually smaller than the C_{SEQ} due to not including the multiplexer properties, non-negligible measurement errors could occur in some cases. It can lead to insufficient sampling time due to the settling time of the transient during sampling or problems with the load of the measured circuit with a greater current, according to (3).

The previous text considered only a single input ADC voltage measurement. However, multiplexing and multi-channel measurement are very often used. Based on the experiments, the logical assumption that the size of ΔQ_s, or U_{RES}, due to parasitic capacitances in the multiplexer also changes with the magnitude of the voltage on the channel, which was measured in the previous multiplexer cycle. In general, a greater previously measured voltage increases the value of the U_{RES} voltage for measurements in the current channel. It also applies in the opposite direction, with a smaller voltage reducing the value of the U_{RES}.

A standard MCU user interested in the behavior of their analog inputs is not expected to be concerned with such detailed measurements with specialized charge amplifier measurement equipment. Therefore, simplified methods that are available without the need for specialized equipment, only by using the appropriate code in the MCU, have been taken into account. The validation of these simple methods of determining the C_{SEQ} was with using measurements by specialized equipment with a charge amplifier. It has been shown that even simple methods can provide information for assessing the behavior of ADC inputs in terms of input currents during the measurement. An experiment will again use the arrangement according to Fig. 3.

To verify the fact, the ADC input behaves according to the model in Fig. 2 and (4), an experiment with the discharge of an external capacitance can be used. By the S_{PR} temporarily switched on, the C_B capacitor is charged to the U_{PR} voltage. The U_{PR} voltage is chosen to the upper range of the ADC value. Subsequently, ADC conversions take place. Due to the action of the input, the charge according to (4) is sampled at each measurement. The situation from the experiment with the ADC input on pin #4 in the STM32G031F6P6 MCU, where C_B = 2200 pF, U_{PR} = 3.2 V is shown in Fig.4.

The voltage u_{CBn} after taking n samples by the ADC input with behavior corresponding to (4) will be defined by (5).

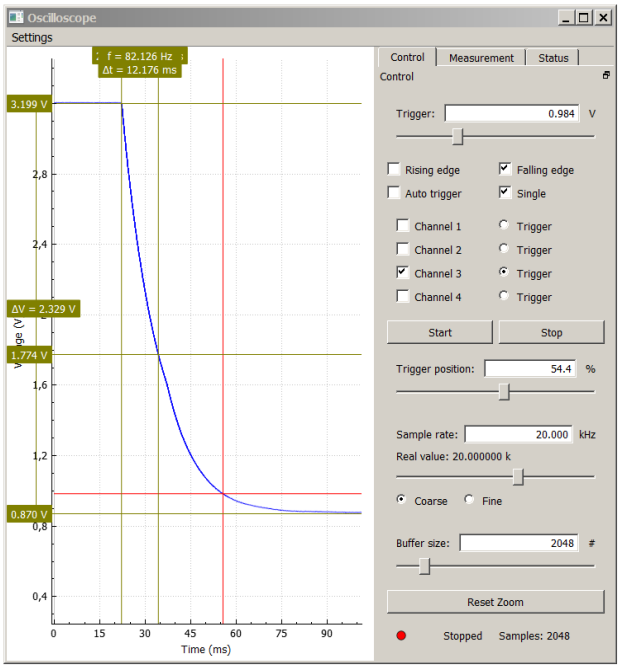

Fig. 4. Voltage at the ADC input when discharging external capacitor.

$$u_{CBn} = U_{PR} + (U_{RES} - U_{PR})\left(1 - \left(\frac{1}{1+\frac{1}{k_C}}\right)^n\right) \quad (5)$$

If the coefficient $k_C >> 1$, where $k_C = C_B/C_{SEQ}$, then the shape of the voltage u_{CBn} on C_B will approach an exponential shape, at a constant value of C_{SEQ}, at the discrete instants given by the sampling times.

The well-known relation (6) applies, similar to the value of $1/e$, where e is Euler's number, for the exponential in the time τ, here for $k_C >> 1$, corresponds to where $n = k_C$.

$$\lim_{n\to\infty}\left(\frac{1}{1+\frac{1}{n}}\right)^n = \frac{1}{e} \quad (6)$$

Thus, the number of n_{KC} samples until the voltage reaches $U_{PR} + \Delta U_{ST}/e$ to the steady value, U_{RES} determines the ratio $C_B/C_{SEQ} = n_{KC}$.

$$\Delta U_{ST} = U_{RES} - U_{PR} \quad (7)$$

In the case of a constant value of C_{SEQ}, it is sufficient to record the discretized equivalent of the transient and determine n_{KC} from it. Then to calculate C_{SEQ} from the values of C_B and k_C.

If the value of C_{SEQ} changes with the voltage, this will also affect the distortion of the exponential waveform, similar to what is seen in the record in Fig. 4.

C_B = 2200 pF was used in the experiment, the residual voltage U_{RES} = 0.87 V, and the value n_{KC} = 243. This corresponded to the capacity C_{SEQ} = 9 pF. In the datasheet, the capacity is $C_S = C_{ADC}$ = 5 pF, giving a difference of 80%. From the part below the voltage level of 1.77 V, it is clear that the size of C_{SEQ} increases even above the value

of 9 pF, which is reflected in an accelerated decrease.

A similar experiment can be performed for U_{PR} = 0 V, charging the C_B with the ADC input current. Here, C_{SEQ} reached a value of up to 12 pF. When measuring other inputs, even larger values were found.

In the experiment, according to Fig. 4, a relatively small value of capacity C_B = 2200 pF is used, which enabled the oscilloscope to record the entire waveform. Another experiment used a rather large value of capacity C_B = 100 nF, where the voltage drop was considerably slower. However, this makes it possible to determine the size of the ΔQ_s at a given input voltage. From that to, determine the value of C_{SEQ} at this selected voltage and thus replace the measurement circuits with a charge amplifier.

The experiment shows the simplified methods how to measure the size of the ΔQ_s. The correct and precise measurement method includes a charge amplifier.

To measure the total charge passed through the ADC input at N_M measurements, a setup with a charge amplifier was used. The simplified circuit diagram is in Fig. 5.

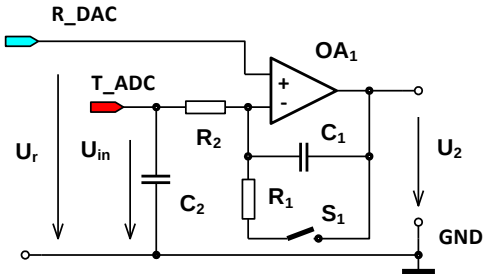

Fig. 5. Simplified circuit diagram with charge amplifier .

The control of the experiment is done using the Nucleo STM303RE kit with MCU STM32F303RE, where the DAC is used to set the voltage U_r at the input of R_DAC and the ADC to measures the voltage U_2 at the output of the charge amplifier. The used operational amplifier OA_1, MCP6002, has a negligible input current of less than 1 pA, which does not affect short-term measurements. The conversion constant of the charge amplifier is determined by the value of the capacitance C_1 = 220 nF. A quality polyester dielectric capacitor with negligible leakage current has been used. Its function is to equalize the current pulses flowing through the input of the tested ADC, to which the buffer in the output of the DAC would not be able to respond. Resistor R_2 = 4k7 has a protection function. It limits the amount of current when the voltage U_r changes and the switch S_1 is closed. The measurement process is as follows.

It the beginning, the measured ADC, whose input is connected to T_ADCA, is not sampling. A reference voltage U_r is set at the R_DAC input, at which the input charge Q_{in} will be determined. Switching the S_1 realized by the multiplexer 74HCT4053 discharges C_1. R_1 = 470 Ω limits the size of the discharge current and, at the same time, affects the time required for discharge. After opening S_1, voltage $U_2 = U_r$, neglecting the offset. The voltage U_{in} on C_2, which serves as the source of the measured voltage, then has the same value as U_r, i.e., $U_{in} = U_r$. Subsequently, the measurement of the U_{in} voltage is performed by the input of the tested ADC on the N_M samples. From the nature of the charge amplifier, the equality of the voltages $U_{in} = U_r$ results (neglecting the offset of the OA_1 and the very small voltage drop on R_2). That is, the entire measurement takes place at the defined input voltage. Due to the action of the charge passing through the input of the ADC under the test, the voltage U_2 changes

$$\Delta Q_{in} = -C_1 \cdot \Delta U_2 \qquad (8)$$

, where $\Delta U_2 = U_{2STOP} - U_{2START}$, ΔQ_{in} is the size of the total charge passed through the input of the tested ADC in the measurement process, U_{2START} is the voltage at the beginning of the measurement, and U_{2STOP} is the voltage at the end of the measurement.

The size of the charge ΔQ_s equal to one sample is determined according to (9).

$$\Delta Q_S = \frac{\Delta Q_{in}}{N_M} \qquad (9)$$

This also corresponds to the results in Fig. 6 measured using circuits with a charge amplifier, where the value of the ΔQ_s is shown as a function of the input voltage [9].

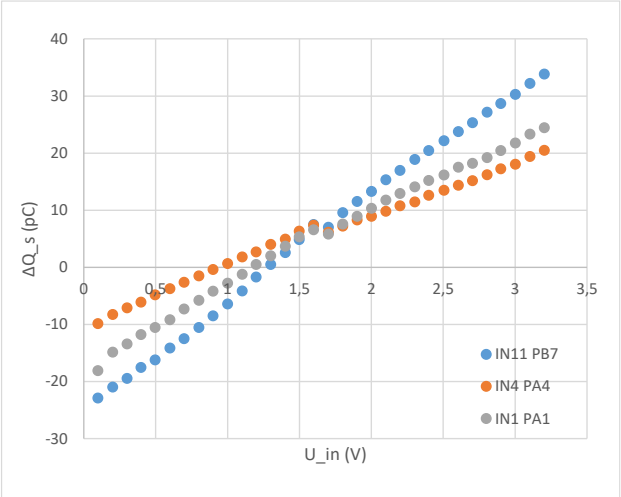

Fig. 6. STM32G031K8 ADC converter input characteristics comparison.

In the CMOS SAR ADC manufacturers' datasheets, only the value of the capacitance C_S is given, but it does not describe the complex behavior of the ADC input during the sampling. The value of the residual voltage U_{RES} is not given, and the behavior of the input during a periodic sampling, which can be roughly described by (3), is not even mentioned. Only the maximum "input leakage current" or "analog input current" value is stated. This could be, according to our experiments with a number of internal ADCs in the MCU, the size of the U_{RES} can also vary for the ADC according to the selected input of the MCU multiplexer, which can also be caused by the

cascaded multiplex system. For some MCUs, the size of ΔQ_s can change even with a deviation from the linearity given by the model according to formula (2). Thus, the sampling circuit's size of the equivalent capacitance C_{SEQ} does not have to be constant but changes with the input voltage. E.g., in the case of ADCs in STM32 series MCUs, the change in C_{SEQ} with the input voltage was from units of a percent to the increase of up to 100% in the STM32F446. However, this is still not a problem since the actual size of the input current at low sampling rates is significantly less than the manufacturer's nominal input current values.

This could be a problem when charging the sampling capacitor from a voltage source with a larger internal resistance. The smaller the sampling time is used, the smaller the internal resistance of the signal source must be. The manufacturers state this, including tables with the specific values. The problem can be when measuring the quasi-static voltage (with very slow change) on the circuit corresponding to the resistance divider according to Fig. 7, where the internal resistance of the source's measured voltage R_{TH} is greater than the value ensuring reliable charging of the sampling capacitor during the sampling.

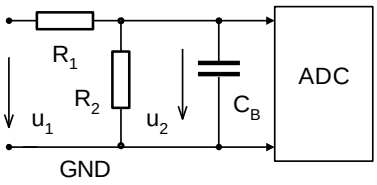

Fig. 7. Quas-static voltage measurement on the resistance divider.

Some of the online IDEs, e.g. "mbed" or "Keil studio" use a fixed setting of the sampling time, which the user cannot change for the measurement. In such a case, the solution with an auxiliary blocking capacitor C_B with a value of $C_B > 2 \cdot 2^N \cdot C_{SEQ}$, where N is the number of ADC bits, is used. In this case, C_B ensures reliable charging of the sampling capacitor. However, with periodic sampling, the size of the voltage drop on the R_{SH} due to the current I_S, see (3), must be taken into account when choosing the sampling frequency. The typical mean value of the I_S when sampling at $f_s = 100$ Hz can be in the order of nA. However, at 100 kHz, it will be in the order of µA. This value is already in the range of input currents according to the manufacturer's datasheets. Therefore, with regard to (3), it is advisable not to use the maximum sampling frequency when working with high-impedance voltage sources with the blocking capacitor C_B, as shown in Fig. 7.

III. CONCLUSION

The article presents the problems of internal CMOS SAR microcontrollers ADCs input currents, its nature and the possibility of its measurement. Based on measurements and experiments, a simplified model of the MCU analog inputs behavior was designed and verified.

This will help in the design of a data acquisition system with the MCU when measuring on signal sources with non-negligible internal resistance. Based on the mentioned procedures, it is possible to obtain data and information about the behavior of the MCU ADC, which the manufacturers do not provide in the datasheet. Mainly the value of the residual voltage, equivalent sampling capacity C_{SEQ} and its dependence on the input voltage are the parameters, which can be very important for users.

REFERENCES

[1] K. Y. Leung, K. Leung and D. R. Holberg, "A Dual Low Power 1/2 LSB NL 16b/1Msample/s SAR A/D Converter with on-chip Microcontroller," 2006 IEEE Asian Solid-State Circuits Conference, 2006, pp. 51-54, doi: 10.1109/ASSCC.2006.35784

[2] N. Gray, "ABCs of ADCs Analog-to-Digital Converter Basics", National Semiconductor Corporation, 2006.

[3] J. Steensgaard, R. Reay, et all, "A 24b 2MS/s SAR ADC with 0.03ppm INL and 106.3dB DR in 180nm CMOS", The International Solid-State Circuits Conference, 2022, pp.168-170.

[4] K. Nicholas, "Understanding the benefits of pre-charge buffers in ADCs", Planet Analog online, 2021.

[5] J. Wu, "Input Currents for High-Resolution ADCs", Texas Instruments, Application Report, 2003.

[6] M. Usach, "How to Calculate Offset Errors and Input Impedance in ADC Converters with Chopped Amplifiers", Analog Devices, Application Note, 2016.

[7] D. Hummerston, P. Hurrell, "An 18-bit 2MS/s pipelined SAR ADC utilizing a sampling distortion cancellation circuit with -107dB THD at 100kHz", Symposium on VLSI Circuits Digest of Technical Papers, Analog Devices, Newbury, U.K., 2017.

[8] STMicroelectronic, "STM32G030x6/x8", Datasheet DS12991 Rev 4, 2022.

[9] Z. Humplova, "Analysis of ADC Converter Input Behavior in STM32 Microcontrollers," Bachelor thesis, CTU FEE, 2022.

26th IMEKO TC4 International Symposium
24rd International Workshop on ADC and DAC Modelling and Testing
IMEKO TC-4 2023
Pordenone, Italy / September 20-21, 2023

A calibration procedure for dc resistance ratio bridges

Martina Marzano[1], Cristina Cassiago[1], Vincenzo D'Elia[1], Enrico Gasparotto[1], Luca Callegaro[1]

[1]*INRIM - Istituto Nazionale di Ricerca Metrologica, Torino, m.marzano@inrim.it*

***Abstract* – Current comparator bridges are nowadays widespread for the realisation of the resistance unit with the quantum Hall effect and of a midrange resistance scale in most national metrology institutes. Future quantum resistance standards, e.g. those based on novel device materials and tabletop dry cryostats, make the more achievable DC currrent comparator bridges (DCCs) the most viable alternative with respect to the more accurate but more expensive cryogenic current comparator bridges (CCCs). A calibration of the individual DCC ratios of interest by comparison with a reference CCC is a straightforward way to improve the DCC performances. The paper reports a calibration exercise on the ratio $12.9064\,\mathrm{k\Omega} : 1\,\mathrm{k\Omega}$, chosen as a benchmark since $12.9064\,\mathrm{k\Omega}$ is close to the quantized resistance value. A more complete dataset involving also decadal resistance ratios will be presented at the Conference, together with a full evaluation of the calibration uncertainty.**

I. INTRODUCTION

Primary dc resistance metrology is based on the realisation of the resistance unit with the quantum Hall effect and of a resistance scale with dc resistance ratio bridges. For this purpose, in the midrange resistance scale (say, from $1\,\Omega$ to $100\,\mathrm{k\Omega}$) modern metrology laboratories employ current comparator resistance bridges.

In a current comparator [1] the currents I_1 and I_2 flow through windings having N_1 and N_2 turns, and generate two magnetomotive forces $N_1 I_1$ and $N_2 I_2$ in opposite directions. A null flux condition gives the measurement equation $N_1 I_1 = N_2 I_2$. In a resistance bridge, the currents I_1 and I_2 flow through the two resistors R_1 and R_2 under comparison with a voltage drop[1] $V = R_1 I_1 = R_2 I_2$.

Two major classes of current comparator bridges are available:

DCC bridges, DC current comprator resistance bridges. In these bridges the magnetic flux generated by the windings follows a path determined by a high-permeability ferromagnetic core and shields. The magnetic balance condition is sensed with a fluxgate technique [2]. DCC bridges can be operated at room temperature. Fully-automated commercial versions are available; the bridge ratios available do not typically extend much beyond the 0. to 10 range. The specified accuracy is of parts in 10^7 to 10^8.

CCC bridges, Cryogenic current comparator resistance bridges. [3]. The flux path is determined by the Meissner effect in superconducting shields; the magnetic balance is sensed by a superconducting quantum-interference device (SQUID) magnetometer. CCC bridges are typically semi-automated; commercial versions are available. They are more expensive than DCCs and the operating costs are boosted by the need of liquid helium supply to achieve the cryogenic temperatures, and well-trained operators. The base accuracy reaches a few parts in 10^9.

Traditional QHE experiments, performed with GaAs devices, require large cryomagnets with magnetic fields, e.g. in the order of $10\,\mathrm{T}$, and temperatures around $1\,\mathrm{K}$, operated with large amounts of liquid helium. The financial and technical expenditures related to the operation of a CCC are considered minor with respect to the operation of the QHE resistance standard itself.

In the last few years, however, QHE metrology research focused on graphene devices, which can operate at higher temperatures and lower magnetic fields [4]; high-accuracy QHE experiments in tabletop dry cryostats have been performed [5]. Very recently, measurements of the quantum anomalous Hall effect [6] in topological insulators show that an accurate quantum resistance standard can be achieved [7] with a small permanent magnet. Such developments forecast future low-cost, easy-to-operate quantum resistance standards in compact dry cryostat, available also to smaller national metrology institutes, calibration centers and industry. In this new framework, operating a CCC might become a major bottleneck. DCCs represent thus the most viable alternative.

DCCs are less performant in terms of accuracy than CCCs. A calibration of the DCC bridge ratio readings using the more accurate CCC as a reference ratio standard is the most straightforward way to improve the DCC performances.

This paper reports a calibration exercise of two widespread models of a commercial DCC bridge by comparison with a reference CCC bridge. The calibration

[1] Actual bridges working conditions can be *close* to equilibrium; the small deviations are taken into account in the measurement model.

method proceeds by measuring the value of the resistance ratio between two thermostated resistors with the DCC and with the CCC, with the same measurement currents, and in short temporal sequence. The method has been considered in literature [5, 8]; it is here analyzed in detail.

The calibration determines the DCC bridge ratio error with an uncertainty in the order of 1×10^{-8}. The known error value can be employed to correct the DCC readings when employed for the realisation of the resistance scale or for calibration for customers, improving the measurement reliability and uncertainty with respect to the case when the sole DCC bridge specifications are employed. The results here reported focus on the specific ratio $12.9064\,\mathrm{k\Omega} : 1\,\mathrm{k\Omega}$, which has been chosen as a benchmark[2]: since $12.9064\,\mathrm{k\Omega}$ is approximately the value of the quantized Hall resistance in GaAs or graphene devices, the ratio is the first step in the realisation of a resistance scale.

The measurement exercise is ongoing at the present time. A more complete dataset involving also decadal resistance ratios will be presented at the Conference.

II. INSTRUMENTS AND STANDARDS

A. *CCC bridge*

The CCC bridge employed is manufactured by Magnicon GmbH on design of the Physikalisch-Technische Bundesanstalt (PTB). The windings turn numbers are selected by manually composing them by connecting in series individual windings having turn numbers in an (approximate) binary sequence; up to about 4646 turns can be achieved. Fractional turn numbers are simulated by a compensation network. After this initial manual setup, the measurement process is automated. The base ratio accuracy is in the 10^{-9} range.

B. *DCC bridge*

Two DCC bridges, a Measurement International MI6010B purchased in 2006 and MI6010D purchased in 2021, have been employed in the calibration exercise. These models are widespread in calibration laboratories[3]. The specified measurement range of the MI6010B is $1\,\mathrm{m\Omega}$ to $13\,\mathrm{k\Omega}$ with a base accuracy of 5×10^{-8}. The specified measurement range of the MI6010D is $1\,\mathrm{m\Omega}$ to $100\,\mathrm{k\Omega}$ with a base accuracy of 3×10^{-8}.

C. *Resistance standards*

The standard resistors employed were:

- STR1, a tailored resistor with a nominal value of $12.9064\,\mathrm{k\Omega}$, constructed from an Electro Scientific Industries (ESI), now IET Labs, model ESI SP5120.

[2]Because of the turn numbers available in the specific DCCs selected for the exercise, the ratio $12.9064\,\mathrm{k\Omega} : 10\,\mathrm{k\Omega}$ has a larger uncertainty.

[3]A higher-accuracy model, MI6010Q, is available from the same manufacturer

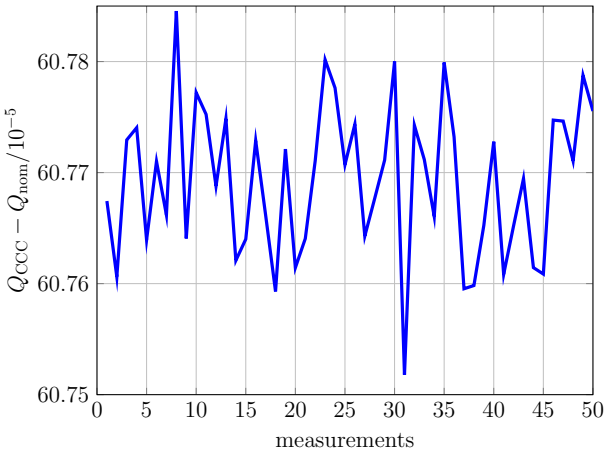

(a) CCC

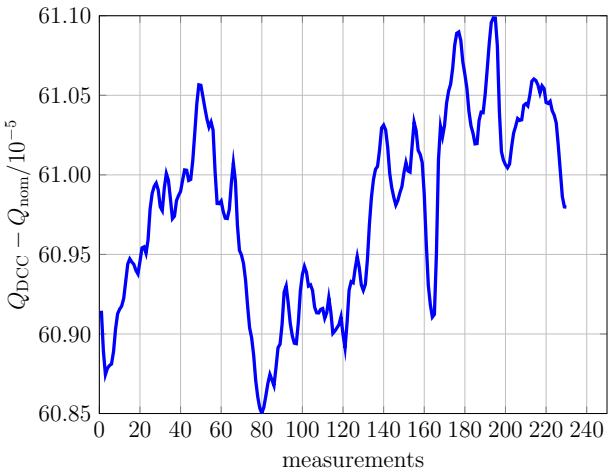

(b) MI6010D

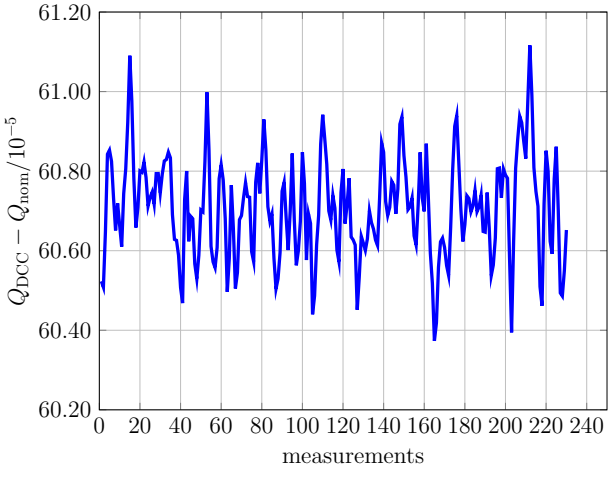

(c) MI6010B

Fig. 1. Time series of the readings given by the three instruments involved in the calibration exercise.

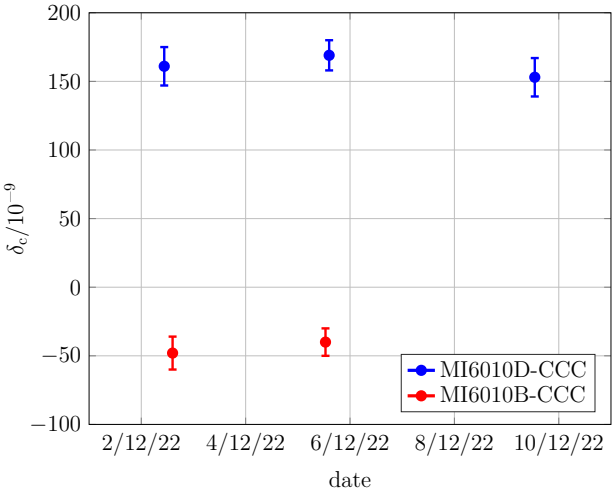

Fig. 2. Outcome of the calibration. δ_c is the relative difference between the DCC and the CCC measurement, versus the measurement date. The uncertainty bars display the standard uncertainty ($k = 1$), see also Table 1.

The resistor is enclosed in a thermostatic air bath with a nominal temperature of 27 °C with a stability within a few mK.

- STD VH01, a custom-made resistor with a nominal value of 1 kΩ, made from the parallel of 10 Vishay VHA 512T 10 kΩ components (tolerance ±0.005%) thermostated at about 27 °C.

III. EXPERIMENTAL

The calibration is performed by measuring in short temporal sequence the resistance ratio with the DCCs and with the CCC, which acts as reference ratio standard. The calibration value δ_c is the deviation

$$\delta_c = \frac{Q_{DCC} - Q_{CCC}}{Q_{nom}} \quad (1)$$

of Q_{DCC}, the ratio reading from the DCC bridge, from Q_{CCC}, the corresponding reading from the CCC bridge, relative to the nominal ratio Q_{nom}.

IV. UNCERTAINTY

The contributions to the calibration uncertainty are the uncertainty reference ratio measurement provided by the CCC, the statistical uncertainty of the readings of the DCC in the course of the calibration event, and the uncertainty associated to the stability and definability of the resistors employed as transfer standards.

A. *CCC uncertainty*

The uncertainty of the CCC is under evaluation. Provisionally, an uncertainty of 2×10^{-9} has been assigned to the measurements.

B. *DCC Type A uncertainty*

The uncertainty of the comparison is dominated by the Type A uncertainty of the DCC bridge. Since the readings time series shows a significant degree of autocorrelation, the approach proposed in [9] has been followed. Details are given in [10].

C. *Resistance standards*

The stability of the resistors during the comparison (for which a duration $\Delta t = 6$ h is considered) is a source of measurement uncertainty. In particular, the effects to be considered are the temperature, the pressure and time stability. The resistance standards involved in the reported measurements are stable in the Δt considered, as reported in Section ii.C, and this uncertainty component is thus negligible.

V. RESULTS

Figure 1 gives the time series of measurements performed with the three instruments involved in the comparison.

Figure 2 shows the measured deviations δ_c for repeated measurements.

Table 1 gives a preliminary uncertainty budget for δ_c, see Sec. iv.

VI. CONCLUSIONS AND OUTLOOK

The calibration exercise shows that it is possible to calibrate the ratio error of commercial DCC bridges by comparison with a CCC. That the measured errors have a good reproducibility over the measurement period, which encourages the possibility to performing in-use corrections to the DCC readings on the basis of the calibrated values. The calibration exercise is being extended to more values, in particular to those required to use the DCCs in the realisation of a primary resistance scale, covering ratios between decadic resistance values (10 kΩ, 1 kΩ, 100 Ω, 10 ohm and 1 Ω). These results, together with a full evaluation of the CCC measurement uncertainty, will be shown and discussed at the Conference.

VII. ACKNOWLEDGMENT

This work has been supported by the project CAPSTAN Quantum electrical Italian national capacitance standard funded by the MIUR Progetti di Ricerca di Rilevante Interesse Nazionale (PRIN) Bando 2020, grant 2020A2M33J.

VIII. *

References

[1] W. J. M. Moore and P. N. Miljanic, *The current comparator*, ser. IEE electrical measurement series. London, UK: Peter Peregrinus Ltd, 1988, vol. 4,

	CCC		DCC	
$\delta_c\,/10^{-9}$	Type A $/10^{-9}$	Comb $/10^{-9}$	Type A $/10^{-9}$	$u(\delta_c)\,/10^{-9}$
MI6010D				
161	0.8	1.3	14.2	14
169	0.7	1.4	11	11
153	0.6	1.3	14	14
MI6010B				
-48	0.8	1.3	12.3	12
-40	0.7	1.4	9.8	10

Table 1. Uncertainty budget for the calibrated value δ_c reported in Fig. 2.

iSBN 0863411126.

[2] M. P. MacMartin and N. L. Kusters, "A direct-current-comparator ratio bridge for four-terminal resistance measurements," *IEEE Trans. Instr. Meas.*, vol. 15, no. 4, pp. 212–220, 1966.

[3] J. Williams, "Cryogenic current comparators and their application to electrical metrology," *IET Science, Measurement & Technology*, vol. 5, pp. 211–224, Nov. 2011.

[4] R. Ribeiro-Palau, F. Lafont, J. Brun-Picard, D. Kazazis, A. Michon, F. Cheynis, O. Couturaud, C. Consejo, B. Jouault, W. Poirier, and F. Schopfer, "Quantum Hall resistance standard in graphene devices under relaxed experimental conditions," *Nature Nanotech.*, vol. 10, pp. 965–971, 2015.

[5] A. F. Rigosi, A. R. Panna, S. U. Payagala, M. Kruskopf, M. E. Kraft, G. R. Jones, B.-Y. Wu, H.-Y. Lee, Y. Yang, J. Hu, D. G. Jarrett, D. B. Newell, and R. E. Elmquist, "Graphene devices for tabletop and high-current quantized Hall resistance standards," *IEEE Trans. Instr. Meas.*, vol. 68, no. 6, pp. 1870–1878, 2019.

[6] H. Chi and J. S. Moodera, "Progress and prospects in the quantum anomalous Hall effect," *APL Materials*, vol. 10, no. 9, p. 090903, 2022.

[7] Y. Okazaki, T. Oe, M. Kawamura, R. Yoshimi, S. Nakamura, S. Takada, M. Mogi, K. S. Takahashi, A. Tsukazaki, M. Kawasaki, Y. Tokura, and N.-H. Kaneko, "Quantum anomalous Hall effect with a permanent magnet defines a quantum resistance standard," *Nature Phys.*, vol. 18, no. 1, pp. 25–29, Jan 2022.

[8] A. R. Panna, M. E. Kraft, A. F. Rigosi, G. R. Jones, S. U. Payagala, M. Kruskopf, D. G. Jarrett, and R. E. Elmquist, "Uncertainty of the ohm using cryogenic and non-cryogenic bridges," in *2018 Conference on Precision Electromagnetic Measurements (CPEM 2018)*, 2018, pp. 1–2.

[9] N. F. Zhang, "Calculation of the uncertainty of the mean of autocorrelated measurements," *Metrologia*, vol. 43, no. 4, pp. S276–S281, aug 2006.

[10] M. Marzano, P. P. Capra, C. Cassiago, V. D'Elia, E. Gasparotto, and L. Callegaro, "Metrological assessment of DC current comparator resistance bridges," *Measurement*, vol. 215, p. 112858, 2023.

26th IMEKO TC4 International Symposium
24rd International Workshop on ADC and DAC Modelling and Testing
IMEKO TC-4 2023
Pordenone, Italy / September 20-21, 2023

A simple and accurate resistance comparator with a long-scale ratiometric digital multimeter

Martina Marzano[1], Vincenzo D'Elia[1], Massimo Ortolano[2], Luca Callegaro[1]

[1]*INRIM Istituto Nazionale di Ricerca Metrologica, Torino, Italy, m.marzano@inrim.it*
[2]*Politecnico di Torino, Torino, Italy*

***Abstract* – This paper describes a resistance comparator, based on a long-scale digital multimeter, suitable for primary resistance metrology. The comparator measures the resistance ratio between two four-terminal standards from the readings of the multimeter, when operating in the voltage ratio mode. The quasi-simultaneous measurement of the resistors voltages strongly relaxes the stability requirements of the driving current source with respect to other published comparators, which are based on a shuttling voltage reading. Measurements between resistors of nominal value $12\,906\,\Omega$ (the quantized Hall resistance) agree with a reference value, given by a dc current comparator bridge, within a few parts in 10^8.**

I. INTRODUCTION

Accurate resistance comparators operating with resistances of a few kiloohms are key instruments for the realization of the ohm from the quantum Hall effect (QHE) in dc, and for its dissemination from National Metrology Institutes (NMIs) to calibration laboratories.

Resistance comparators based on the potentiometric method [1,2] were developed soon after the discovery of the QHE. In this type of instrument, the voltages across the two series-connected resistors under comparison are measured by difference against a fixed compensation voltage, and the resistance ratio is determined from the voltage ratio. If the difference between the two voltages across the resistors and the compensation voltage is small, the difference voltmeter loading on the potentiometer circuit is negligible and its accuracy need not to be tight. Although simple in principle, the implementation of the potentiometric method requires high-isolation switches and stable sources of voltage and current. In fact, the compensation voltage source and the current source should be stable over the time scale of the two readings, which can be of several minutes.

In subsequent years, for primary resistance metrology applications, many NMIs replaced potentiometric resistance comparators with current comparator bridges, operating either at room or at cryogenic temperature. Current comparator bridges, now commercially available, are state-of the-art instruments delivering the best accuracy to date. However, the emergence in recent years of quantum Hall resistance standards based on novel materials, such as graphene, operating in less demanding conditions than their gallium arsenide counterparts, has revived the interest in simpler and less expensive instruments which can possibly be used routinely in diverse metrological applications.

The potentiometric approach was simplified in the 1990s with the use of long-scale digital multimeters (DMMs) performing direct measurements of the two voltages across the resistances under comparison [3-7]. Stable compensation sources are no longer necessary, but stable current sources and high-isolation reversal switches are still needed.

In [8] we presented a preliminary version of a comparator based on a ratiometric DMM operating at $1:1$ resistance ratios which further simplifies the approach of [3-7]. Since a ratiometric DMM determines the ratio of the voltage at the input terminals to that at the sense terminals by internally switching in quick succession between these two pairs of terminals, the stability requirements for the current source are less demanding and the imperfect isolation of the switches is possibly compensated by the autozero feature of the DMM. Furthermore, the measurement process can be semiautomated with a minimum of external components. Here we describe an improved version of the comparator which can operate from $1:1$ to about $10:1$ resistance ratios and which is equipped with a programmable current source for more flexibility. One or both the resistors under comparison can be quantum Hall resistance standards.

II. RESISTANCE COMPARATOR SETUP

The schematic diagram of the proposed resistance comparator setup is shown in Fig. 1.

The core of the measuring system is a long-scale ratiometric DMM. We used a Keysight 3458A, but other models capable of ratiometric operation should work as well.

The two resistors under comparison are R_1 and R_2, both defined as four-terminal standards and connected in series at the low current terminals IL1 and IL2. A current source with floating output drives the two resistors with a current I at the high current terminals IH1 and IH2. We tested two different sources: a low-noise battery-operated fixed current bespoke source (described in [8] and here adapted to operate at different resistance ratios), and a commercial programmable current source (Adret Electronique 103A),

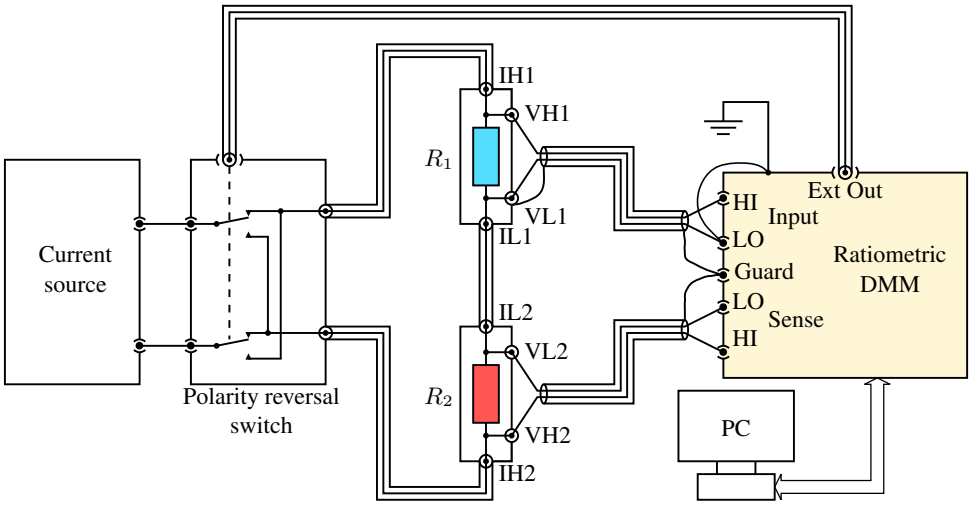

Fig. 1. Schematic diagram of the comparator. The resistors R_1 and R_2 are connected in the forward *configuration.*

which adds flexibility to the setup. To cancel the DMM gain error, the resistors R_1 and R_2 are successively connected to the DMM in two mirroring configurations, labelled *forward* and *reverse* in the following. In the forward configuration, as shown in Fig. 1, the voltage terminals VH1 and VL1 of R_1 are connected to the DMM input HI and LO terminals, respectively, and the voltage terminals VH2 and VL2 of R_2 are connected to the DMM sense HI and LO terminals, respectively. In the reverse configuration, R_1 is connected to the sense terminals and R_2 to the input terminals. The system is grounded at the DMM LO terminals to avoid any error from the common-mode input resistance[1].

To cancel the errors caused by offsets, thermoelectric voltages and bias currents, the polarity reversal switch periodically reverses the direction of I. The operation of this switch is controlled, through a driver, by the Ext Out signal generated by the DMM.

The computer PC controls the DMM and the polarity reversal switch via an IEEE-488 communication interface.

III. OPERATION AND MEASUREMENT MODEL

The operation of the resistance comparator is as follows. The system is first set in the forward configuration, and $2M \times N$ voltage ratio readings $Q^{\mathrm{F}+}_{k,j}$ and $Q^{\mathrm{F}-}_{k,j}$, $j = 1, \ldots, M$ and $k = 1, \ldots, N$, are taken by periodically reversing the current I every M readings; then the comparator is manually set in the reverse configuration, and other $2M \times N$ voltage ratio readings $Q^{\mathrm{R}+}_{k,j}$ and $Q^{\mathrm{R}-}_{k,j}$ are taken. Owing to the operation of the DMM, this measurement sequence is different from the one commonly used in other works [2, 4, 7], where the current is reversed at each voltage measurement. Once the measurement is completed, each group of M readings is averaged to yield the following sequence of average ratios[2] (with $\mathrm{X} = \mathrm{F}, \mathrm{R}$): $Q^{\mathrm{X}\pm}_k = M^{-1} \sum_{j=1}^{M} Q^{\mathrm{X}\pm}_{k,j}$; $Q^{\mathrm{X}}_k = (Q^{\mathrm{X}+}_k + Q^{\mathrm{X}-}_k)/2$; and $Q^{\mathrm{X}} = N^{-1} \sum_{k=1}^{N} Q^{\mathrm{X}}_k$. From Q^{F} and Q^{R}, the comparator reading can be obtained as

$$Q = \sqrt{\frac{Q^{\mathrm{F}}}{Q^{\mathrm{R}}}}. \tag{1}$$

Taking into account the sources of uncertainty described in the comprehensive analysis of [4], and assuming that the input and sense ranges do not change between the forward and reverse configurations[3], the measurement model can be approximated as

$$Q = \frac{R_1}{R_2}\left[1 + \epsilon + \frac{1}{2}(R_2 - R_1)(G_{\mathrm{I}} + G_{\mathrm{S}})\right], \tag{2}$$

where ϵ is the relative error due to the DMM's differential nonlinearity and transfer uncertainty between the forward and reverse configurations, and G_{I} and G_{S} are the leakage conductances at the DMM's input and sense terminals, respectively, averaged across the measurement steps and including the leakage conductances of the current source and the switch. When $R_1 \approx R_2$, the correction terms are minimized. We expect the effect of the feed-through

[1] According to the Keysight 3458A's specifications [9], for a proper operation, the voltage between the input and sense LO terminals should not exceed 0.25 V. This limitation should not cause any issue in most practical cases.

[2] It is indeed possible to compute Q^{F} and Q^{R} directly, without computing intermediate averages first, but the sequence described above allows one to analyze the stability of the measurements as reported in Sec. IV.

[3] It turns out [9] that even if it's possible to disable the input autoranging function of the Keysight 3458A, the sense autoranging function cannot be disabled. Therefore, keeping the same ranges between the forward and reverse configurations requires some caution, and might limit the range of ratios that can be measured with the best accuracy.

of the DMM's internal switches to be cancelled by its autozero mechanism, but further investigation may be needed to confirm this hypothesis.

IV. EXPERIMENTAL RESULTS

The comparator has been mainly tested at $1:1$ ratios with two $12\,906\,\Omega$ resistors: R_1 is a Vishay HZ series resistor thermally insulated in a polystyrene box; R_2 is a Vishay H series VHA resistor equipped with a standalone thermostat at $29\,^\circ\mathrm{C}$. The difference between the two resistances is about $0.3\,\Omega$. The results from the comparator were validated against reference measurements obtained by a direct current comparator bridge (DCC bridge, Measurement International AccuBridge 6010D). The DCC bridge measured in succession the ratios R_1/R_{pivot} and R_2/R_{pivot}, where R_{pivot} is a $1\,\mathrm{k}\Omega$ thermostatted resistance standard, and these two ratios were then combined to obtain a reference ratio Q^{ref}. Tests at different resistance ratios are being made, but the analysis of the results has not been completed yet.

Fig. 2 shows two example measurements at $1:1$ ratio. The first five ratio measurements after each polarity reversal are discarded and not reported in the figure. The measurement reported in Fig. 2(a), for which $M = 25$ and $N = 20$, was performed with the battery-operated bespoke current source [8] set to $I = 30\,\mu\mathrm{A}$; the measurement reported in Fig. 2(b), for which $M = 25$ and $N = 15$, was instead performed with the programmable current source set to $I = 50\,\mu\mathrm{A}$. The DMM integration time was set to $2\,\mathrm{s}$ (100 power line cycles) and the duration of each ratio measurement was about $8\,\mathrm{s}$, that is, $4\,\mathrm{s}$ for each voltage. Fig. 3 reports the Allan deviation of the measurements of Fig. 2 as a function of the integration time τ, separately for the forward and reverse configurations. It can be argued that the noise level of the programmable current source is on the average slightly higher than that of the battery-operated source, but not in a significant way.

Tab. 1 reports the uncertainty budgets for the measurements of Fig. 2. The type A uncertainty components were evaluated from the extrapolated Allan deviation at the actual measurement time. The input and sense resistances were determined by adapting the method described in [10] to the ratiometric operation of the DMM, yielding $R_{\mathrm{I}} \approx 540\,\mathrm{G}\Omega$ and $R_{\mathrm{S}} \approx 2\,\mathrm{T}\Omega$. This values do not include the leakage conductances of the current source, and further characterizations need to be performed for resistance ratios different from $1:1$. The error term ϵ which appears in (2) has been considered negligible for a $1:1$ ratio, but also in this case further characterizations are needed to confirm this hypothesis.

Tab. 2 reports the comparison between the results obtained from the measurements of Fig. 2 and those obtained from the DCC. The reported uncertainty for the DCC is the type A uncertainty component evaluated from the Al-

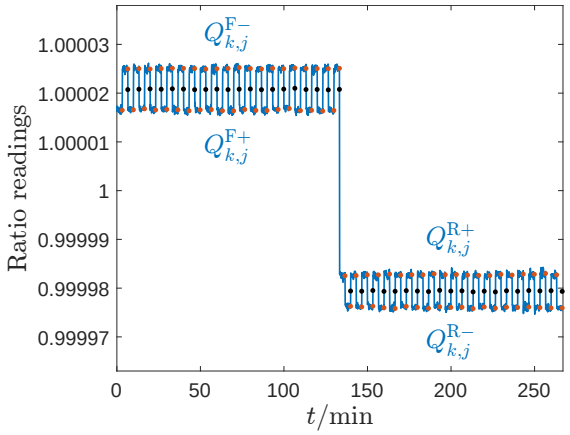

(a)

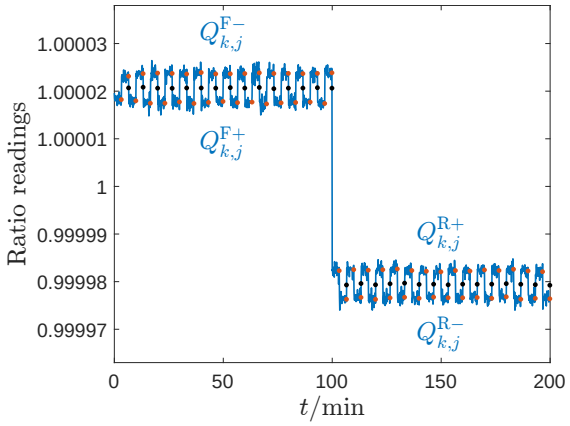

(b)

Fig. 2. Time series of the comparator readings when measuring two $12\,906\,\Omega$ resistors: (a) measurement with the bespoke current source with $I = 30\,\mu\mathrm{A}$, $M = 25$ and $N = 20$; (b) measurement with the programmable current source with $I = 50\,\mu\mathrm{A}$, $M = 25$ and $N = 15$. The blue lines (—) represent the individual ratio readings $Q^{\mathrm{F}+}_{k,j}$, $Q^{\mathrm{F}-}_{k,j}$, $Q^{\mathrm{R}+}_{k,j}$ and $Q^{\mathrm{R}-}_{k,j}$; the red bullets (•) represent the averages over M points $Q^{\mathrm{F}+}_{k}$, $Q^{\mathrm{F}-}_{k}$, $Q^{\mathrm{R}+}_{k}$ and $Q^{\mathrm{R}-}_{k}$; and the black bullets (•) represent the forward and reverse averages Q^{F}_{k} and Q^{R}_{k}. The periodic oscillations correspond to current reversal events; the large step in the middle is the switching from the forward to the reverse configuration.

Table 1. Uncertainty budgets for the measurements of Fig. 2.

i	Quantity	Type	$u_i(Q)/(\mathrm{n}\Omega\,\Omega^{-1})$ Fig. 2(a)	Fig. 2(b)
1	Q^{F}	A	8.1	11
2	Q^{R}	A	10.9	12
3	G_{I}	B	< 0.1	< 0.1
4	G_{S}	B	< 0.1	< 0.1
	Q	RSS	14	16

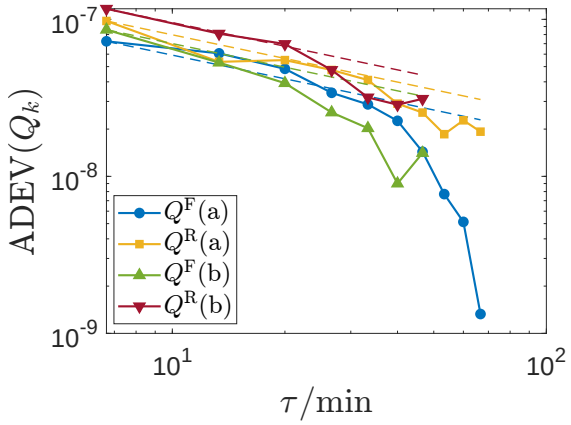

Fig. 3. Allan deviations of the measurements of Fig. 2 vs. the integration time τ: the blue line with circle markers represents the Allan deviation of the Q_k^{F}'s of Fig. 2(a); the yellow line with square markers represents the Allan deviation of the Q_k^{R}'s of Fig. 2(b); the green line with upward-pointing triangle markers represents the Allan deviation of the Q_k^{F}'s of Fig. 2(b); and the red line with downward-pointing triangle markers represents the Allan deviation of the Q_k^{R}'s of Fig. 2(b). The dashed lines represent the Allan deviation extrapolated for white noise time series.

Table 2. Comparison between the measurements of Fig. 2 and the reference measurements determined by the DCC.

Meas.	$\frac{Q-1}{\mu\Omega\,\Omega^{-1}}$	$\frac{Q^{\mathrm{DCC}}-1}{\mu\Omega\,\Omega^{-1}}$	$\frac{Q-Q^{\mathrm{DCC}}}{\mathrm{n}\Omega\,\Omega^{-1}}$
(a)	20.697(14)	20.692(21)	5(25)
(b)	20.609(19)	20.632(25)	−22(31)

lan deviation of the measurements. As can be seen from Tab. 2, the results are compatible within the standard uncertainty.

V. CONCLUSIONS AND PERSPECTIVES

The resistance comparator herewith presented allows one to measure the resistance ratio between two four-terminal resistors in a simple and automated way. The multimeter employed is available in any metrology laboratory, and the additional components required (current source, switch) are not critical. The measurements reported show that the comparator, when performing $1:1$ ratio measurements at the quantized Hall resistance level, match those of a top-of-the-line current comparator bridge, with comparable uncertainty. The comparator is now being characterised for measurements with other resistance ratio values, for which the linearity of the DMM can play a significant role. We will report about the characterisation outcome at the Conference.

VI. ACKNOWLEDGMENT

This work has been supported by the project CAPSTAN *Quantum electrical Italian national capacitance standard* funded by the MIUR *Progetti di Ricerca di Rilevante Interesse Nazionale* (PRIN) Bando 2020, grant 2020A2M33J.

REFERENCES

[1] L. Bliek, E. Braun, F. Melchert, P. Warnecke, W. Schlapp, G. Weimann, K. Ploog, G. Ebert, and G. E. Dorda, "High precision measurements of the quantized Hall resistance at the PTB," *IEE Proc. Sci. Meas. Tech.*, vol. IM-34, no. 2, pp. 304–305, 1985.

[2] G. Marullo Reedtz and M. E. Cage, "An automated potentiometric system for precision measurement of the quantized Hall resistance," *J. Res. Natl. Bur. Std*, vol. 92, no. 5, pp. 303–310, 1987.

[3] M. E. Cage, D. Yu, B. M. Jeckelmann, R. L. Steiner, and R. V. Duncan, "Investigating the use of multimeters to measure quantized Hall resistance standards," *IEEE Trans. Instr. Meas.*, vol. 40, no. 2, pp. 262–266, 1991.

[4] K. C. Lee, M. E. Cage, and P. S. Rowe, "Sources of uncertainty in a DVM-based measurement system for a quantized Hall resistance standard," *J. Res. Natl. Inst. Stand. Technol.*, vol. 99, no. 3, pp. 227–240, May-June 1994.

[5] G. Rietveld and F. P. Jans, "A DVM-based accurate measurement setup for QHE resistance measurements," in *1998 Conference on Precision Electromagnetic Measurements Digest*, Washington DC, USA, 1998, pp. 416–417.

[6] C. Rietveld and C. J. Van Mullem, "Uncertainty analysis of a DVM-based quantum Hall measurement set-up," in *Conference on Precision Electromagnetic Measurements Digest CPEM 2000*, Sydney, NSW, Australia, 2000, pp. 90–91.

[7] P. Svoboda, P. Chrobok, and P. Vašek, "A simple DMM-based measuring system for QHE resistance measurements," in *2000 Conference on Precision Electromagnetic Measurements (CPEM 2000)*, Sydney, NSW, Australia, 2000, pp. 566–567.

[8] M. Marzano, V. D'Elia, M. Ortolano, and L. Callegaro, "A resistance comparator based on a long-scale digital voltmeter," in *2022 Conference on Precision Electromagnetic Measurements (CPEM 2022)*, Wellington, New Zealand, 2022, pp. 1–2.

[9] Keysight, "3458A multimeter data sheet," Oct. 2021.

[10] G. Rietveld, "Accurate determination of the input impedance of digital voltmeters," *IEE Proc. Sci. Meas. Tech.*, vol. 151, no. 5, pp. 381–383, 2004.

26th IMEKO TC4 International Symposium
24rd International Workshop on ADC and DAC Modelling and Testing
IMEKO TC-4 2023
Pordenone, Italy / September 20-21, 2023

Traceability routes for magnetic measurements

Marco Coïsson[1], Javier Diaz De Aguilar Rois[2], Yolanda Alvarez Sanmamed[2], Sergio Molto González[2], Oliver Power[3], Robert Walsh[3], Orrie Larmour[3]

[1]*INRIM, strada delle Cacce 91, 10135 Torino (TO), Italy, m.coisson@inrim.it*
[2]*CEM, calle Alfar, 2, 28760 Tres Cantos (Madrid), Spain*
[3]*NSAI, 1 Swift Square, Northwood, Santry, Dublin 9, Ireland D09 A0E4*

***Abstract* – Magnetic measurements are vital to support European challenges in areas such as electric vehicles; health; power transformation and harvesting; clean, affordable and secure energy; information and sensor technology. However, only very few European NMIs have the capabilities to perform traceable measurements of all of the most important magnetic quantities. Consequently, the adoption of novel technologies and materials is hindered by the lack of local metrological expertise that research and development activities in academia and industry could exploit. A European project (TRaMM, 21SCP02), in the framework of the Small Collaborative Projects (SCP) call 2021, is transferring the expertise of INRIM (Italy) in the field of magnetic calibration and measurements to CEM (Spain) and NSAI (Ireland), and to interested stakeholders. An update on the training material is given, and new stakeholders are actively sought.**

I. INTRODUCTION

Magnetic measurements are relatively common in academia and in industrial research and development, as they are widely employed for the measurement of magnetic fields and for the characterisation of the magnetic cores in sensors or electronics. In addition, they are used in applications such as earth observation [1, 2], biomedicine [3, 4, 5] and health and safety requirements regarding exposure to electromagnetic fields [6, 7, 8] (The Electromagnetic Fields Directive 2013/35/EU). However, so far, the industrial and scientific communities have been unable to fully benefit from traceable and reliable measurement results because of limited access to suitable calibration facilities. With the global magnetic materials market continuously increasing at an annual growth rate of about 9.6 % [9], it is crucial to develop sustainable magnetic measurement capabilities that will support these end-users.

Even though the calibration of teslameters and coils, or the measurement of the magnetic properties of steel sheets for power applications (electrical motors, transformers) are already standardised, only a few European NMIs are capable of providing a comprehensive set of measurement and calibration services in these areas. This requires very specific instruments and techniques. In addition, new research activities and industrial products, in the fields of biomedicine [10], theragnostics [11], water remediation [12, 13], and security [14, 15] are expanding the need for traceable magnetic measurements for e.g. the characterisation of magnetic nanoparticles, rings, ribbons or bulk materials, or for sensing devices involving magnetoelectric phenomena [16, 17, 18, 19, 20].

Other fields requiring traceable and reliable magnetic measurements are all those where magnetic materials are exploited for energy conversion, harvesting and storage, such as automotive and powertrains, aerospace, and smart grids [21, 22, 23]. All these applications attract both scientific research and industry while offering development and market opportunities, especially for SMEs that wish to be dynamic and innovative, enabling them to offer breakthrough technologies and solutions to new potential customers and markets. In spite of this exciting innovation and development, easy access to the measurement and calibration capabilities for magnetic field and magnetic material characterisations are still mostly lacking, leaving industry and academia with the unaddressed need to properly validate their technological solutions through traceable magnetic measurements.

To partially fill the disparity between the existing expertise at the European level, and the market and stakeholders needs, the TRaMM project (Traceability routes for magnetic measurements), within the Small Collaborative Projects call 2021 [24], is developing training material to transfer the expertise of the Italian NMI (INRIM) in this field to two partners, CEM and NSAI, respectively the NMIs of Spain and Ireland, and to interested stakeholders. At the European scale, the project aims at strengthening the collaboration among NMIs and at offering a set of measurement and calibration services to academia and industry that better address their current needs. Figure 1 shows the PERT diagram of the project.

II. FEEDBACK FROM STAKEHOLDERS

The TRaMM project is now in full development. Several stakeholders, belonging to academia and public research institutions, industries and companies have been asked to participate in an anonymous online survey to identify their primary interests and needs in the field of magnetic mea-

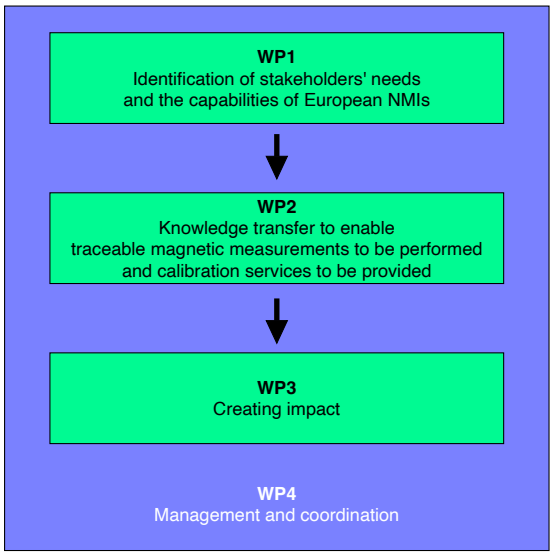

Fig. 1. PERT diagram of the TRaMM project.

surements and calibrations. Figure 2 summarises the geographical distribution of the stakeholders that have decided to participate in the survey, updated at May 2023, whereas Figure 3 summarises the received responses in terms of applications of interest for the stakeholders. All the most important areas are significanlty represented: research and development (34%), calibration and testing (45%), and manufacturing and in-field applications (20%).

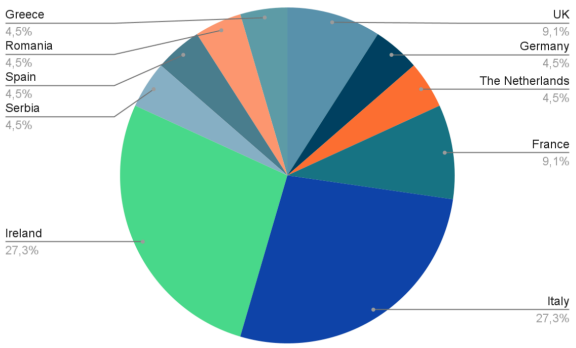

Fig. 2. Geographical distribution of the stakeholders.

Figure 4 reports the stakeholders' needs in terms of magnetic field measurements. More than half of the interested stakeholders declare their need to measure (or to calibrate probes capable of measuring) both DC and AC magnetic fields, whereas only a small percentage of them require only AC measurements. The low to intermediate field ranges are the most representative, leaving only 22% of the answers for the relatively high field range above 50 mT.

For those stakeholders aiming at characterising magnetic materials, there is a widespread interest in powders and nanoparticles, that may find applications in pigments

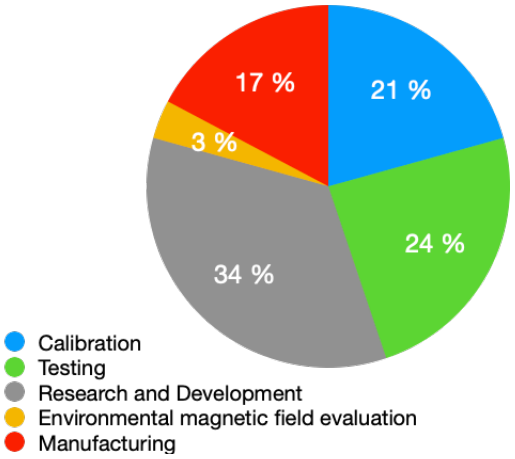

Fig. 3. Distribution of applications of interest for the stakeholders.

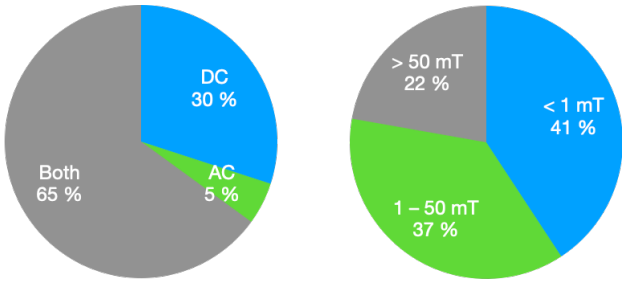

Fig. 4. Distribution of magnetic field regimes (AC, DC, or both, left) and intensity (right) according to the stakeholders' needs.

[31], loading of polymers for multifunctional materials [32], environment applications [33] and cancer treatment [34]. 'Traditional' materials such as steel sheets and ferrite rings are no longer the only materials taken into consideration, as thin films, ribbons, wires and nanostructures, which may find application in sensors and ICT [35], play a role of comparable importance in the stakeholders' interest. Figure 5 summarises the received responses. Overall, almost two thirds of the materials the stakeholders work with what can be labelled as soft magnetic materials.

Interestingly, while 63% of the received responses point to the need for characterising the intrinsic properties of a material, there is already a significant request (37%) for methods to characterise finished products or components. At present, there are neither recognised laboratory methods nor international standards available for such configurations. This suggests that possible future research line could attempt to address these needs.

Finally, the stakeholders are clearly aware that international standards are still missing for many of the magnetic measurement and calibration activities that they are relying

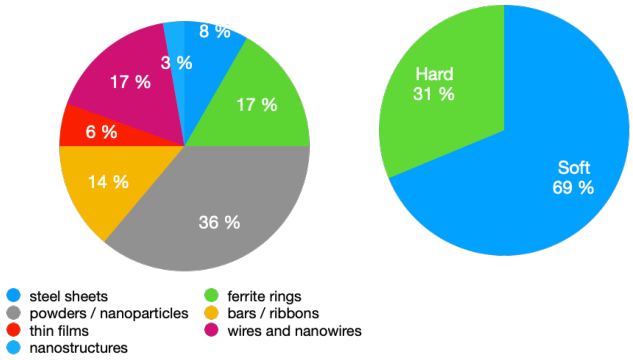

Fig. 5. Distribution of the stakeholders' interests in the characterisation of magnetic materials (left), and their classification as either magnetically soft or hard (right).

upon, as summarised in Figure 6. Interestingly, all of them declare they would benefit from the existence of an international standard, even though a few of them admit that its absence is not an impedance for their activities.

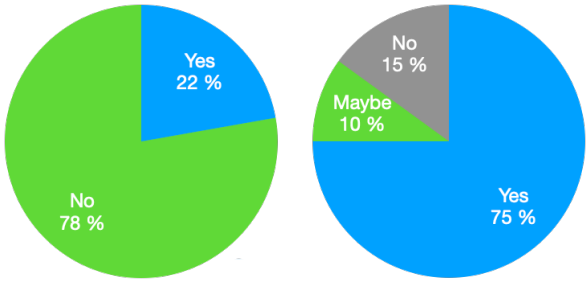

Fig. 6. Existence of international standards (left) and perceived need of them (right) for the magnetic measurement and calibration activities performed by the stakeholders.

III. TRAINING FOR THE PROJECT PARTNERS AND FOR THE STAKEHOLDERS

The TRaMM project is delivering training on magnetic measurements and calibrations to CEM and NSAI (as project partners), but also to interested stakeholders, through online training material made of commented slides and videos that are available through the project website [36] and on the dedicated YouTube channel [37]. All the training material is publicly and freely available. Any academic group or company that would like to be involved as a stakeholder is invited to contact the project coordinator. Besides online training, specific events open to the project partners only have been and will be organised in INRIM laboratories. These offer hands-on sessions focussed on utilising equipment for calibration of magnetic probes and for the characterisation of magnetic materials.

IV. WORKSHOP AND FINAL OUTCOMES

To promote a wider impact, the TRaMM project will also organise a workshop, toward the end of its funding period (i.e. Fall 2023 - Winter 2024), where stakeholders, other NMIs, academia, any interested parties will be invited to join the project participants to share the experience developed during the project. The desired outcomes will be to analyse future routes for improving the collaboration at the EU level while further extending the measurement and calibration capabilities on magnetism and magnetic properties of materials and for approaching standardisation bodies with the intendment of driving the development of new standards and regulations at the international level toward the stakeholders requirements. All interested parties are invited to attend the workshop and can get in touch with the project participants for further information and details. The participation in the workshop will be free, and it will also be possible to join it online, although in-person participation is recommended for the best possible interaction among participants. This will also be an opportunity to draft possible applications to future funding calls. Details of the final workshop will be made available in due time on the project website [36].

ACKNOWLEDGMENTS

This project 21SCP02 TRaMM has received funding from the EMPIR programme co-financed by the Participating States.

REFERENCES

[1] M.J.S. Johnston, "Review of electric and magnetic fields accompanying seismic and volcanic activity", Surveys in Geophysics, vol. 18, 1997, pp. 441-476, doi: 10.1023/A:1006500408086.

[2] K.L. Verosub, A.P. Roberts, "Environmental magnetism: past, present, and future", J. Geophysical Research, vol. 100, 1995, pp. 2175-2192, doi: 10.1029/94JB02713.

[3] Y. Li, H. Cheng, Z. Alhalili, G. Xu, G. Gao, "The progress of magnetic sensor applied in biomedicine: a review of non-invasive techniques and sensors", J. Chinese Chem. Soc., vol. 68, 2021, pp. 216-227, doi: 10.1002/jccs.202000353.

[4] N.M. Shupak, F.S. Prato, A.W. Thomas, "Therapeutic uses of pulsed magnetic-field exposure: a review", URSI Radio Science Bulletin, vol. 2003, 2003, pp. 9-32, doi: 10.23919/URSIRSB.2003.7909506.

[5] E.A. P'erigo, G.. Hemery, O. Sandre, D. Ortega, E. Garaio, F. Plazaola, F.J. Teran, "Fundamentals and advances in magnetic hyperthermia", Appl. Phys. Rev., vol. 2, 2015, pp. 041302, doi: 10.1063/1.4935688.

[6] A. Ahlbom, "A review of the epidemiologic literature on magnetic fields and cancer", Scand. J.

Work Environ. Health, vol. 14, 1998, pp. 337-343, https://www.jstor.org/stable/40965589.

[7] P. Levallois, "Hypersensitivity of human subjects to environmental electric and magnetic field exposure: a review of the literature", Env. Heath Persp., vol. 110, 2002, pp. 613-618, doi: 10.1289/ehp.02110s4613.

[8] D.A. Savitz, "Overview of occupational exposure to electric and magnetic fields and cancer: advancements in exposure assessment", Env. Health Persp., vol. 103, 1995, pp. 69-74, doi: 10.1289/ehp.95103s269.

[9] "Magnetic Materials Market by Type (Semi-Hard Magnet, Soft Magnet, Hard/Permanent Magnet) & by Application (Automotive, Electronics, Industrial, Power Generation, and Others) - Global Forecasts to 2020", report code CH 3238, March 2016, https://www.marketsandmarkets.com/Market-Reports/magnetic-materials-397.html

[10] I. Andreu, E. Natividad, "Accuracy of available methods for quantifying the heat power generation of nanoparticles for magnetic hyperthermia", Int. J. Hyperthermia, vol. 29, 2013, pp. 739-751, doi: 10.3109/02656736.2013.826825

[11] V.I. Shubayev, T.R. Pisanic II, S. Jin, "Magnetic nanoparticles for theragnostics", Adv. Drug Delivery Rev., vol. 61, 2009, pp. 467-477, doi: 10.1016/j.addr.2009.03.007.

[12] A.G. Leone, A.A.P. Mansur, H.S. Mansur, "Advanced functional nanostructures based on magnetic iron oxide nanomaterials for water remediation: a review", Water Res., vol. 190, 2021, pp. 116693, doi: 10.1016/j.watres.2020.116693.

[13] R.D. Ambashta, M. Sillanpää, "Water purification using magnetic assistance: a review", J. Haz. Mat., vol. 180, 2010, pp. 38-49, doi: 10.1016/j.jhazmat.2010.04.105.

[14] W. Irnich, "Electronic security systems and active implantable medical devices", Pacing and clinical electrophysiology, vol. 25, 2002, pp. 1235-1258, doi: 10.1046/j.1460-9592.2002.01235.x.

[15] V. Zhukova, P. Corte-Leon, J.M. Blanco, M. Ipatov, J. Gonzalez, A. Zhukov, "Electronic surveillance and security applications of magnetic microwires", Chemosensors, vol. 9, 2021, pp. 100, doi: 10.3390/chemosensors9050100.

[16] C. Morón, C. Cabrera, A. Morón, A. García, M. González, "Magnetic sensors based on amorphous ferromagnetic materials: a review", Sensors, vol. 15, 2015, pp. 28340-28366, doi: 10.3390/s151128340.

[17] Y. Wang, J.Li, D. Viehland, "Magnetoelectrics for magnetic sensor applications: status, challenges and perspectives", Materials Today, vol. 17, 2014, pp. 269-275, doi: 10.1016/j.mattod.2014.05.004.

[18] S. Zuo, H. Heidari, D. Farina, K. Nazarpour, "Miniaturised magnetic sensors for implantable magnetomyography", Adv. Materials Tech., vol. 5, 2020, pp. 2000185, doi: 10.1002/admt.202000185.

[19] S. Wei, X. Liao, H. Zhang, J. Pang, Y. Zhou, "Recent progress of fluxgate magnetic sensors: basic research and application", Sensors, vol. 21, 2021, pp. 1500, doi: 10.3390/s21041500.

[20] B. Cao, K. Wang, H. Xu, Q. Qin, J. Yang, W. Zheng, Q. Jin, D. Cui, "Development of magnetic sensor technologies for point-of-care testing: fundamentals, methodologies and applications", Sensors and Actuators A: Physical, vol. 312, 2020, pp. 112130, doi: 10.1016/j.sna.2020.112130.

[21] C.M. Leung, J. Li, D. Viehland, X. Zhuang, "A review on applications of magnetoelectric composites: from heterostructural uncooled magnetic sensors, energy harvesters to highly efficient power converters", J. Phys. D: Appl. Phys., vol. 51, 2018, pp. 263002, doi: 10.1088/1361-6463/aac60b.

[22] F. Yang, L. Du, H. Yu, P. Huang, "Magnetic and electric energy harvesting technologies in power grids: a review", Sensors, vol. 20, 2020, pp. 1496, doi: 10.3390/s20051496.

[23] L. Sun, M. Cheng, H. Wen, L. Song, "Motion control and performance evaluation of a magnetic-geared dual-rotor motor in hybrid powertrain", IEEE Transactions on Industrial Electronics, vol. 64, 2017, pp. 1863-1872, doi: 10.1109/TIE.2016.2627018.

[24] https://msu.euramet.org/current_calls/scp_2021/

[25] https://www.magnetometry.eu

[26] https://magnetism.eu

[27] https://www.bipm.org/kcdb/cmc/quicksearch?includedFilters=&excludedFilters=cmcBranches.Density%2CcmcBranches.Fluid+flow%2CcmcRmo.APMP%2CcmcRmo.COOMET&page=0&keywords=magnetic

[28] MagNaStand Final Publishable Report: https://www.euramet.org/download/?L=0&tx_eurametfiles_download%5Bfiles%5D=41169&tx_eurametfiles_download%5Bidentifier%5D=%252Fdocs%252FEMRP%252FJRP%252FJRP_Summaries_2016%252FNormative%252F16NRM04_Final_Publishable_Report.pdf&tx_eurametfiles_download%5Baction%5D=download&tx_eurametfiles_download%5Bcontroller%5D=File&cHash=887a8ca2d84cc6137aef3d013cfc73e9

[29] ISO/TS 198071 Nanotechnologies Magnetic nanomaterials Part 1: Specification of characteristics and measurements for magnetic nanosuspensions. International Organisation for Standardisation, 2019.

[30] ISO/TS 198072 Nanotechnologies Magnetic nanomaterials Part 2: Specification of characteristics and measurements for nanostructured superparamagnetic beads for nucleic acid extraction. International Organisation for Standardisation, under development.

[31] Kanika, G. Kedawat, S. Singh, B.K. Gupta, *A novel approach to design luminomagnetic pigment formulated security ink for manifold protection to bank cheques against counterfeiting*, Adv. Mater. Techn. **6** (2021) 2000973, doi 10.1002/admt.202000973.

[32] H. Zhang, J.-Y. Xia, X.-L. Pang, M. Zhao, B.-Q. Wang, L.-L. Yang, H.-S. Wan, J.-B. Wu, S.-Z. Fu, *Magnetic nanoparticle-loaded electrospun polymeric nanofibers for tissue engineering*, Mat. Sci. Eng. C **73** (2017) 537-543, doi 10.1016/j.msec.2016.12.116.

[33] J. Govan, *Recent advances in magnetic nanoparticles and nanocomposites cor the remediation of water resources*, Magnetochemistry **6(4)** (2020) 49, doi 10.3390/magnetochemistry6040049.

[34] JZ. Hedayatnasab, F. Abnisa, W.M.A. Wan Daud, *Review on magnetic nanoparticles for magnetic nanofluid hyperthermia application*, Materials and Design **123** (2017) 174-196, doi 10.1016/j.matdes.2017.03.036.

[35] J. Alam, C. Bran, H. Chiriac, N. Lupu, T.A. Óvári, L.V. Panina, V: Rodionova, R: Varga, M. Vazquez, A. Zhukov, *Cylindrical micro and nanowires: fabrication, properties and applications*, J. Magn. Magn. Mater. **513** (2020) 167074, doi 10.1016/j.jmmm.2020.167074.

[36] https://www.tracemag.eu

[37] https://www.youtube.com/@EURAMET-TRaMM/featured

26th IMEKO TC4 International Symposium
24th International Workshop on ADC and DAC Modelling and Testing
IMEKO TC-4 2023
Pordenone, Italy / September 20-21, 2023

A new type of rack for the clamp ammeter

Hongrui Yan[1], Xinyan Wang[1], Xiao Liu[1], Jianbo Liu[1], Qian Chen[1], Bin Deng[1]

[1]*Shandong Engineering Research Center of Reliability Evaluationfor Electric Energy Metering Devices, Shandong Institute of Metrology, No.28, Qianfoshan East Road, 250014 Jinan, China*
yhr1986@126.com

***Abstract* – In order to improve the calibration ability of the clamp ammeter, realize the simultaneous measurement of single-phase, three-phase and multiple clamp ammeters，and provide technical support for realizing more efficient real-time monitoring of power, this paper analyzed the measurement methods and problems of the clamp ammeters, and studied the measurement principle of the clamp ammeters, then designed a new type of rack for the clamp ammeter. The measurement has been proved that the rack for the clamp ammeter is accurate and efficient.**

***Keywords* – clamp ammeter , measurement, hanging rack, real-time monitoring**

I. INTRODUCTION

The clamp ammeter is a kind of instrument that measures the current value by surrounding a current-carrying conductor by a magnetic circuit which can be opened and closed. It has the characteristics of non-contact measurement and simple operation, and is mainly used in electrical monitoring and measurement of scientific research departments in various industrial fields such as power, transportation, elevators, energy, and so on. In this paper, after considering the influence of the simultaneous measurement of multiple current clamps and the position of the wire through the center on the measurement results of the clamp meter, a new hanging rack is designed, which greatly improves the measurement ability to the clamp ammeter.

II. WORKING PRINCIPLE OF THE CLAMP AMMETER

The clamp ammeter is composed of an ammeter and a current transformer. The iron core of the current transformer can be opened when the wrench of the current clamp is tightened. The wire through which the measured current passes can pass through the open gap of the iron core without cutting off. When the wrench is released, the iron core is closed[1,2]. The tested circuit wire passing through the iron core becomes the primary coil of the current transformer, and the current passing through induces the current in the secondary coil, so that the ammeter connected to the secondary coil can measure the current in the tested wire.

III. INFLUENCE OF MEASUREMENT ACCURACY OF CLAMP AMMETER

The eccentricity and inclination of the current-carrying conductor can lead to uneven magnetic flux distribution along the cross-section of the transformer coil and unequal magnetic permeability along the circumference of the core, thus affecting the measurement accuracy of the clamp ammeter [3] .

The measured wire should be adjusted to the geometric center of the clamp as much as possible. If the measured wire deviates too much from the center, the magnetic induction strength produced by the clamp ammeter core will change significantly, which will directly affect the accuracy of the measurement. Generally, the measurement errors caused by improper positioning of the measured wire in the clamp can reach 2% to 5%.

According to Ampere's Law, the magnetic induction strength around an infinitely long cylinder conductor perpendicular to the plane of the current transformer coil's geometric center [4] is

$$B = \mu_0 I/2\pi r \quad (1)$$

In formula, μ_0 is the vacuum permeability, I is the current of the conductor, and r is the radius of the center circle of the current transformer coil.

The magnetic flux on the coil cross section S is given by:

$$\Phi = \mathrm{B}S_{\perp} = \mu_0 S_{\perp} I/2\pi r \quad (2)$$

In formula, $S_{\perp}$ is the projected area of the cross section of the coil perpendicular to the direction of the magnetic field. which is not necessarily the entire area of the coil, but the effective perpendicular area located in the magnetic field portion.

When B is not perpendicular to S:

$$\Phi = BS_{\perp} = BScos\theta \quad (3)$$

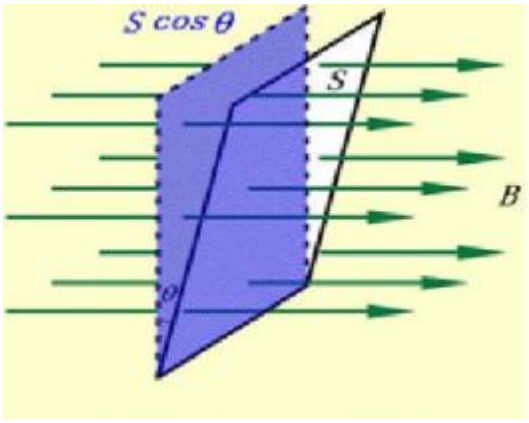

Fig. 1.The plane is not perpendicular to the direction of the magnetic field

As can be seen from the above formulas, the magnitude of the magnetic flux was related to the central circle radius of the current transformer coil and the effective perpendicular area of the coil in the magnetic field portion. Therefore, to ensure measurement accuracy when using a clamp meter, the measured wire should be perpendicular to the clamp.

IV. DESIGN OF A CLAMP AMMETER HANGING RACK

A. *Key lssues*

Realized simultaneous measurement of single-phase, three-phase and multiple clamp ammeters.

Adjusted and fixed the position of the clamp ammeter, so that the wire just passed through the geometric center of the clamp mouth and was perpendiculared to the clamp mouth.

B. *Design ideas*

For small mouth clamp ammeters: if only a single current line can pass throug，select directly clamped.

For large mouth clamp ammeters: The adjustable insulation rods are designed to adjust the position of the clamp ammeter up and down; the sliding insulation clasps are added on the insulation rod to fix the clamp ammeter.

C. *Structural composition*

The clamp ammeter hanging rack is composed of three adjustable insulating rods, three 100A copper rods, three 10A copper rods, six insulation clasps, two insulation plates, an aluminum alloy bracket, screws, and gaskets, as shown in Figure 2.

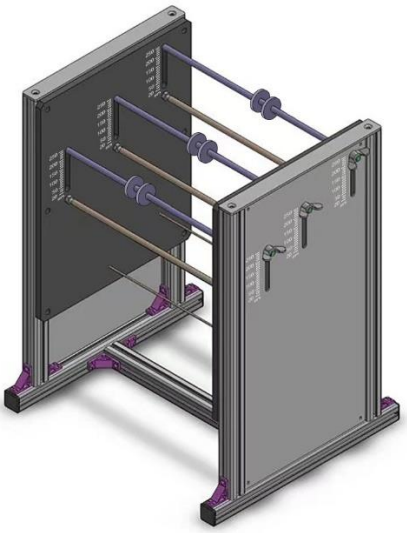

Fig. 2. Image of a rack for the clamp ammeter.

The three 100A and three 10A copper rods were fixed on the insulating plates at both ends respectively with screws.One end of the 100A and 10A current wires was fixed on the 100A and 10A copper rods with screws and gaskets, and the other end was led out from the bottom to be connected to the current source.

The two insulating plates were fixed and supported by the aluminum alloy bracket, and the outer sides were also fastened by the aluminum alloy panels, which were solid and beautiful. The insulating rods were fixed on the outer aluminum alloy panels with screw caps, to facilitate the adjustment of the current clamp position up and down during the test, the insulation clasps were used to hold the clamp ammeter, so that the wire just passed through the geometric center of the clamp mouth. In addition, the adjustment of the insulation rods were marked with scale, which can realize accurate adjustment according to the radius of the clamp ammeter.

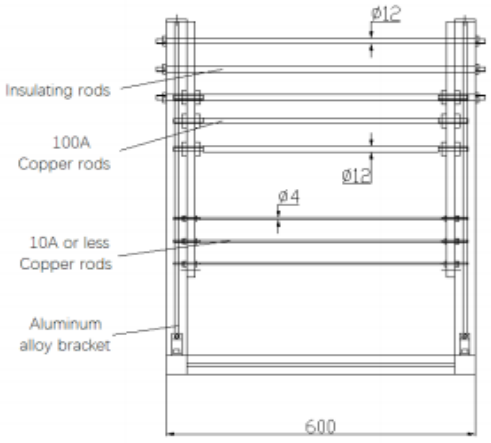

Fig. 3. Frontal structure diagram of the rack for clamp ammeter.

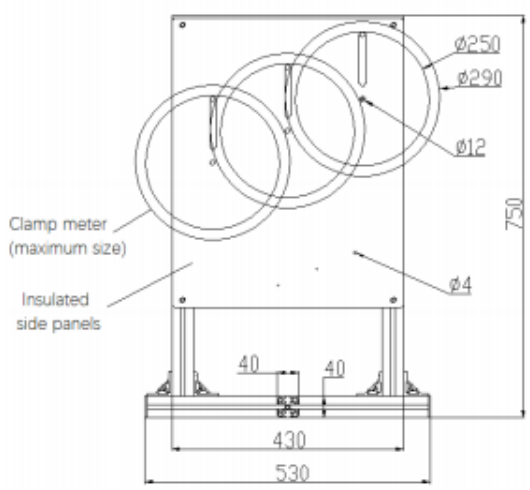

Fig. 4. Side structure diagram of the rack for clamp ammeter.

D. Method of application

For 10A and below small clamp ammeters, clamp them directly onto the 10A copper rods, and test them by 10A and below current. When hanging small current clamp ammeters, it should not be too compact to prevent interference.

For more than 10A large clamp ammeters, the clamp mouth is generally larger. To hang them, both 100A copper rods and insulating rods should be completely threaded into the clamp mouth. The clamp ammeter were secured with insulation clasps. By adjusting the position of the insulating rod, ensure that the 100A copper rod can be passed through the geometric center of the large clamp ammeters and be perpendiculared to the clamp mouth.Then, test it by passing current. When hanging large clamp ammeters, it should also not be too compact to prevent interference.

V. MEASUREMENT VERIFICATION

A. Calibration basis

JJF 1075-2015 "Calibration Specification for Clamp Ammeters"[5].

B. Environmental conditions

Ambient temperature: (20±2)℃; Relative humidity: (55±3)% .

C. Measurement standards

Three-phase energy meter inspection device, model: NST-3500, current range: 3×(0.01～100)A.

Three-phase standard energy meter, model: RD41-233, current range: 3×(0.005～100)A.

D. Tested object

Clamp type power meter, current range: ACI (0～100)A, accuracy: ±0.3%rdg.

Clamp type energy meter on-site calibration device, current range: ACI (0～5)A, accuracy: ±0.2%rdg.

E. Measurement method

The standard meter comparison method was adopted, the three-phase standard energy meter was connected to the current circuit of the rack for clamp ammeter, and clamp ammeter was measured by using the hanging rack and current wire respectively. By comparing with the current value of the three-phase standard energy meter, the measurement accuracy of the two methods was determined.

F. Measurement Results

Under the same conditions, measurements were taken at the specified current point after preheating. Restart the current before each measurement, and independently repeat each measurement for 10 times to obtain the data.

Table 1. Current standard value

The output value of the three-phase energy meter inspection device	Displayed value of the Three-phase standard energy meter		
	Phase A	Phase B	Phase C
5A	4.99992A	4.99994A	4.99995A
50A	49.9989A	49.9991A	49.9986A

Table 2. Measurement results of the rack for the clamp power meter

Number of measurements	Current 50A		
	Phase A	Phase B	Phase C
1	49.995A	49.994A	49.996A
2	49.994A	49.993A	49.997A
3	49.995A	49.994A	49.996A
4	49.994A	49.995A	49.996A
5	49.995A	49.994A	49.995A
6	49.995A	49.996A	49.997A
7	49.996A	49.994A	49.996A
8	49.995A	49.995A	49.997A
9	49.996A	49.994A	49.998A
10	49.995A	49.994A	49.996A
y	49.9950A	49.9943A	49.9964A

$s(y_i)=\sqrt{\frac{\sum_{i=1}^{n}(y_i-\bar{y})^2}{n-1}}$	0.0007A	0.0008A	0.0008A
Note: Adjust the insulating rods so that the 100A copper rods passes exactly through the geometric center of the jaws.			

Table 3. Measurement results of the rack for the clamp energy meter on-site calibration device

Number of measurements	Current 5A		
	Phase A	Phase B	Phase C
1	4.9995A	4.9996A	4.9996A
2	4.9994A	4.9991A	4.9991A
3	4.9997A	4.9995A	5.0001A
4	4.9997A	4.9999A	4.9995A
5	4.9993A	4.9995A	4.9999A
6	4.9995A	4.9995A	4.9995A
7	4.9991A	4.9992A	4.9992A
8	4.9995A	4.9995A	4.9995A
9	4.9997A	4.9998A	5.0002A
10	4.9993A	4.9999A	4.9992A
y	4.99947A	4.99955A	4.99958A
$s(y_i)=\sqrt{\frac{\sum_{i=1}^{n}(y_i-\bar{y})^2}{n-1}}$	0.0002A	0.0003A	0.0004A
Note: Hang the clamp ammeters directly on the 10A copper rods.			

Table 4. Measurement results of the clamp power meter using current line

Number of measurements	Current 50A		
	Phase A	Phase B	Phase C
1	49.997A	50.002A	49.991A
2	49.991A	49.992A	49.994A
3	49.995A	49.994A	49.996A
4	49.989A	49.988A	49.987A
5	49.995A	49.992A	49.995A
6	49.990A	49.994A	49.989A
7	49.996A	49.988A	49.993A
8	49.992A	49.995A	49.991A
9	49.996A	49.987A	49.990A
10	49.988A	49.992A	49.994A
y	49.9929A	49.9924A	49.9920A
$s(y_i)=\sqrt{\frac{\sum_{i=1}^{n}(y_i-\bar{y})^2}{n-1}}$	0.0033A	0.0024A	0.0029A
Note: Hang the clamp ammeters directly on the current lines.			

Table 5. Measurement results of the clamp energy meter on-site calibration device using current line

Number of measurements	Current 5A		
	Phase A	Phase B	Phase C
1	4.9994A	4.9991A	4.9992A
2	4.9993A	4.9992A	4.9995A
3	4.9994A	4.9996A	5.0002A
4	4.9998A	4.9997A	4.9987A
5	4.9989A	4.9996A	4.9991A
6	4.9995A	4.9986A	4.9996A
7	4.9997A	4.9996A	5.0001A
8	4.9995A	4.9987A	4.9989A
9	4.9989A	4.9985A	5.0001A
10	4.9987A	4.9989A	4.9997A
y	4.99931A	4.99915A	4.99951A
$s(y_i)=\sqrt{\frac{\sum_{i=1}^{n}(y_i-\bar{y})^2}{n-1}}$	0.0004A	0.0005A	0.0005A
Note: Hang the clamp ammeters directly on the current lines.			

G. Result evaluation

Table 6. Summary of measurement results with small clamp ammeters

5A / Phase	Phase A	Phase B	Phase C
The difference from the standard value and the rack measurements	-0.00045A	-0.00039A	-0.00037A
Standard deviation value of the rack measurements $S_1(y_i)$	0.0002A	0.0003A	0.0004A
The difference from the standard value and the current line measurements	-0.00061A	-0.00079A	-0.00044A
Standard deviation of the current line measurements $S_2(y_i)$	0.0004A	0.0005A	0.0005A

Table 7. Summary of measurement results with large clamp ammeters

50A / Phase	Phase A	Phase B	Phase C
The difference from the standard value and the rack measurements	-0.0039A	-0.0048A	-0.0022A
Standard deviation value of the rack measurements $S_1(y_i)$	0.0007A	0.0008A	0.0008A
The difference from the standard value and the current line measurements	-0.0060A	-0.0067A	-0.0066A
Standard deviation of the current line measurements $S_2(y_i)$	0.0033A	0.0044A	0.0029A

The evaluation of the measurement results using the hanging rack was based on the the average y and standard deviation $s(y_i)$. The closer the average value is to the standard value y, the higher the measurement accuracy is. The Smaller standard deviations $s(y_i)$ indicate better measurement repeatability and higher measurement reliability. From the above measurement results, it can be seen that the values obtained using the rack for the clamp ammeter are both accurate and reliable, thus it proves the measurement ability of the rack for clamp ammeters.

VI. CONCLUSION

Through studying the measurement principle of the clamp ammeter, analyzing the measurement methods and existing issues of the clamp ammeter, a new type of rack for the clamp ammeter was designed. The new type of rack for the clamp ammeter could not only achieve simultaneous measurement of single-phase and three-phase clamp ammeters, but also fixed the position of the large clamp ammeter by adjusting the insulation rod accurately up and down and moving the insulation clasps left and right, so as to the 100A copper rods could pass through the center of the clamp mouth and be perpendicular to the plane. This hanging rack reduced interference while achieving accurate measurement, significantly improved the measurement capability of the clamp ammeter.

REFERENCES

[1] Z. Zhang, “Research on modification and application of the clamp ammeter”, Journal of Science and Technology, August 2019, pp.75.

[2] S. Ma, “Evaluation of uncertainty of clip-on ammeter calibration device”, Proceedings of the 2017 Aviation Intelligent Equipment and Test Technology Summit and Academic Exchange Meeting, 2017, pp.289-291.

[3] Y. Pan. et al., “Analysis and evaluation of uncertainty in calibration of clamp ammeters”, Electrical Measurement and Instrumentation, vol 46, No.524, August 2009, pp.76-80.

[4] Y. Hu. et al., “Electromagnetics and Electrodynamics”, Beijing: Science Press, 2014, No.2, pp. 131-134.

[5] JJF 1075-2015 Specification for Calibration of Clamp Ammeters.

26th IMEKO TC4 International Symposium
24rd International Workshop on ADC and DAC Modelling and Testing
IMEKO TC-4 2023
Pordenone, Italy / September 20-21, 2023

Characterization of an accurate phase measurement system using transmission lines

Luca De Vito, Francesco Picariello, Sergio Rapuano, Ioan Tudosa

Department of Engineering, University of Sannio, 82100 Benevento, ITALY
e-mail: {devito, fpicariello, rapuano, ioan.tudosa}@unisannio.it

***Abstract* – This paper deals with the experimental characterization of an accurate phase measurement system using transmission lines as phase reference. In particular, the used prototype implementing the accurate phase measurement system is also described. The prototype characterization aims of assessing the repeatability of the phase measurement and identifying the systematic effects affecting them. Several transmission lines, priory characterized by means of a Vector Network Analyzer, have been used as phase references. The obtained results demonstrated the standard deviation increases with the sine-wave frequency, while systematic effects are clearly visible at 10 kHz and 100 kHz. The maximum obtained standard deviation at 10 MHz is 0.30 °.**

I. INTRODUCTION

In several test procedures, sine-wave signal generators are adopted as sources of excitation for assessing the performance of waveform recorders [1], [2], [3], [4]. Those generators are often used to determine the magnitude and phase of the frequency response of waveform recorders (e.g., oscilloscopes) [5]. In this way, it is possible to compensate for the effect of the front-end on signal acquisition and to guarantee measurement traceability. For example, this is a very important step for calibrating electroshock weapons, as described in [6]. The frequency-sweep technique is the most accurate method used for estimating the magnitude of the frequency response of waveform recorders. However, for assessing the output phase spectrum of a sine-wave generator, the phase of the sine-wave should be measured. As stated in [7], several instruments are available on the market for measuring the phase difference between two isofrequential signals, however, few methods or instruments are available for measuring the phase of signals having different frequencies. Those methods and instruments cannot measure the phase over a wide range of frequencies with a low measurement uncertainty [7].

In [8], a method for accurately measuring the phase of a sine-wave signal is proposed. A proof-of-concept implementation of this method consisting of an Arbitrary Waveform Generator (AWG), an oscilloscope, and a universal digital counter is described in [9]. In this implementation, the AWG provides two outputs, i.e., the sine-wave under test and a pulse train signal synchronized with the sine-wave. Standard deviations in the order of 0.1 ° were obtained for frequencies ranging from 100 Hz to 10 MHz [9]. An improved hardware implementation using an analog multiplier and a voltmeter, is described in [10]. In this case, phase standard deviations of 0.017 ° and 0.0022 ° were obtained at 100 Hz and 1 MHz, respectively [10]. However, both the above-mentioned implementations require a signal generator under test having two output channels.

An implementation of the method [8] for a single input phase measurement instrument was proposed in [5]. In this case, a sampling pulse train signal is provided by a Field Programmable Gate Array (FPGA) board. The synchronization between the pulse train signal and the sine-wave under test is obtained through a 10 MHz reference clock. The obtained standard deviations are in the order of 0.01 ° at 5 °C for frequencies ranging from 100 Hz to 10 MHz, [5]. In the experimental setups used in [10], the standard deviation was assessed on 40 phase measurements by using a universal digital counter as a monitor to provide a coarse estimation of the phase. As reported in [7], the expanded uncertainty of the Keysight 53200A universal digital counter is 0.3 ° from 1 mHz to 100 kHz and 1.5 ° at 10 MHz. To the knowledge of the authors, there is no better reference counter on the market with a wide frequency range. However, it exhibits expanded uncertainties of one or two orders of magnitude higher than the standard deviations of the phase measurements provided by the proposed implementation. For this reason, the counter-based measurements cannot be used as reference. Therefore, the reference instrument has to be replaced with a reference method and reference objects presenting high repeatability phases.

In this paper, the performance of the prototype proposed in [10] is assessed against the measurements of phase deviation obtained by a Vector Network Analyzer (VNA) when the signal is passed through some transmission lines. The aim of the proposed analysis is to identify systematic effects and to assess the standard deviation of the phase measurements for frequencies ranging from 10 kHz to 10 MHz.

The paper is organized as follows. The phase measurement method is described in Section II. Section III reports the adopted prototype implementation. A compari-

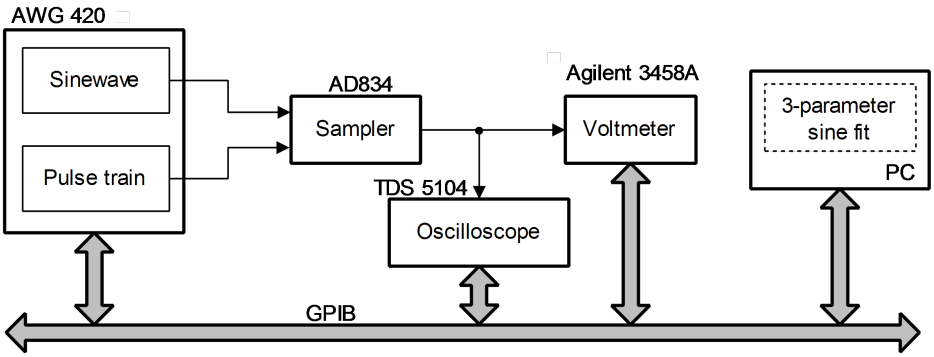

Fig. 1. Prototype implementation of the phase measurement method [10].

son of the obtained phase measurements with the reference ones derived from time propagation delay measurements of transmission lines is discussed in Section IV. The last Section concludes the paper and draws the future steps of the research.

II. PHASE MEASUREMENT METHOD

In this section, the phase measurement method proposed in [8] is summarized. In particular, the method is based on the coherent sampling of the sine-wave signal under test at instants defined by a pulse train signal (i.e., the pulse train and sine-wave signals are synchronized with each other). On the acquired samples, the 3-parameter sine fit method is applied to obtain the phase.

The phase measurement method relies on the following functional blocks: (i) a reference clock source, (ii) the sine-wave source under test, (iii) the pulse train source, (iv) a pulse delay, (v) a pulse selector, (vi) a sampler, (vii) an averaging and digitizing block, (viii) and the sine fit. The sine-wave source provides the signal under test, which is synchronized with the reference clock. Also, the pulse train source provides a signal synchronized with the reference clock, thus both sine-wave and pulse train signals are synchronized with each other. Then, the pulse train signal is delayed of a quantity that is an integer sub-multiple of the sine-wave period. The pulse selector is used for regulating the frequency of the pulse train signal driving the sampler. In particular, its frequency should be an integer sub-multiple of the sine-wave one. In this way, the sampler operates the sampling of the input signal (i.e., the sine-wave under test) in one instant for a sine-wave period and, being the frequency of the pulse train signal a sub-multiple of the sine-wave one, the output of the sampler is a pulse train having a time-integral value proportional to the amplitude of the sine-wave at the sampling instant defined by the pulse train. An averaging operation is performed on the sampler output before the final analog-to-digital conversion. The obtained samples are stored in a vector. A new time delay is imposed on the pulse train and another amplitude measurement is performed. When at least 3 amplitude measurements are acquired, the 3-parameter sine fit method is applied to the stored samples for estimating the phase of the sine-wave considering known its frequency.

III. PROTOTYPE IMPLEMENTATION

The prototype implementing the above-described phase measurement method is the one described in [10] (see Fig. 1). The AWG 420 by Tektronix [11] provides both the sine-wave and the pulse train signals working at the same frequency. The sampler is implemented with a commercially-available analog multiplier integrated circuit, i.e., AD834 [12]. The output of the sampler is a pulse train where the pulse amplitudes are modulated according to the sine-wave amplitudes in the time intervals defined by the pulse duration. In this way, the output signal has an energy proportional to the amplitude of the sine-wave at the instants defined by the pulse train. The Agilent 3458A voltmeter [13], configured for true-root mean square (true-rms) measurements, is used for quantifying this energy. The oscilloscope TDS 5104 by Tektronix [14] is used to acquire the sampler output signal, and by thresholding, to identify the sign of the associated true-rms measurement.

A MATLAB application has been developed for managing all the instruments, via General Purpose Interface Bus (GPIB), and for performing the 3-parameter sine fit on the true-rms measurements according to the imposed pulse train delays and the sine-wave frequency.

IV. PHASE MEASUREMENTS OF TRANSMISSION LINES

An experimental setup was implemented to investigate if the phase measurements provided by the prototype are affected by systematic effects. To this aim, transmission lines have been adopted for introducing phase shifts according to their exhibited time propagation delays. The test bench used for this analysis is depicted in Fig. 2. The Tektronix AWG 420 provides the sine-wave to the Quad Serial Loop Rev.B transmission line board by Xilinx. The transmission line board consists of five lines of nominal length

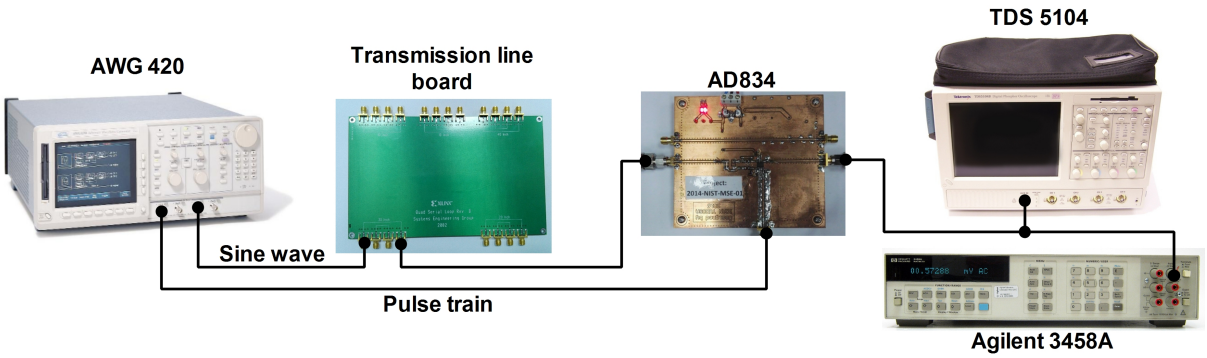

Fig. 2. Experimental setup used for the phase measurements using the transmission lines.

254 mm, 381 mm, 508 mm, 762 mm, and 1016 mm, that allows imposing five phase delays to the sine-wave. The phase measurement prototype based on the analog multiplier is used for measuring the sine-wave phase at the output of the transmission line. All the phase measurements have been referred to the one obtained by considering a short circuit instead of the transmission line. To characterize the transmission line, the Agilent E5071B network analyzer [15] has been used. In particular, for each transmission line, magnitude, phase, and propagation delay measurements for S_{21} parameter have been performed. The measurements are provided with respect to the magnitude, phase, and propagation delay measurements with the port wires of the network analyzer in a short circuit.

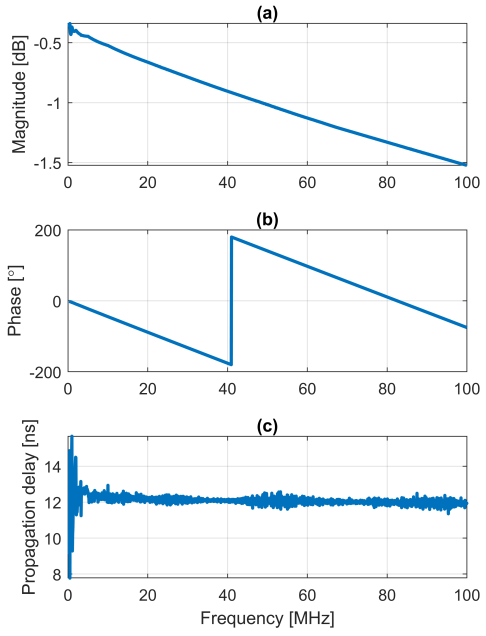

Fig. 3. Results of the S_{21} characterization of the 1016 mm transmission line: (a) magnitude, (b) phase, and (c) propagation delay.

For example in Fig. 3, the magnitude, phase, and propagation delay measurements for 1016 mm transmission line are depicted up to 100 MHz. As reported in [15], the VNA can perform measurements from 300 kHz to 8.5 GHz, thus, since the phase measurements are performed at 10 kHz, 100 kHz, 1 MHz, and 10 MHz, they have been derived from the propagation delay, by considering it constant with the frequency, as follows:

$$\phi = \Delta_T \cdot f, \tag{1}$$

where Δ_T is the measured propagation delay, and f is the frequency. The VNA exhibits a low accuracy for propagation delay measurements at frequencies up to 10 MHz, [15] (i.e., it is around 1 ns at 300 kHz, and decreases to 0.1 ns at 10 MHz). Thus, considering the propagation delays of the transmission lines constant in the bandwidth of analysis, the propagation delay measurements were obtained as the mean of the delays in the frequency range of 10 MHz to 90 MHz, and their variabilities were assessed from their standard deviations. In Tab. 1, the obtained propagation delay measurements and their type-A uncertainties for each transmission line are summarized. The uncertainty for the phase measurement has been assessed by applying the law of propagation of uncertainty to (1):

$$u_\phi = \phi \cdot \sqrt{u^2_{\Delta_T}/\Delta^2_T + u^2_f/f^2}, \tag{2}$$

Table 1. Propagation delays measured with the Agilent E5071B network analyzer.

Transmission line length [mm]	Propagation delay [ns]
254	2.01 ± 0.04
381	2.91 ± 0.04
508	3.84 ± 0.04
762	5.65 ± 0.04
1016	7.47 ± 0.04

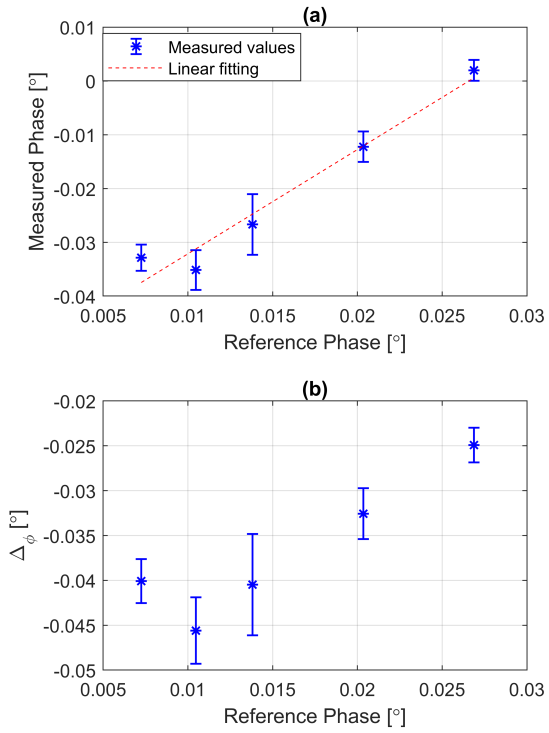

Fig. 4. Obtained phase measurements vs. reference phase measurements at 10 kHz with the five transmission lines.

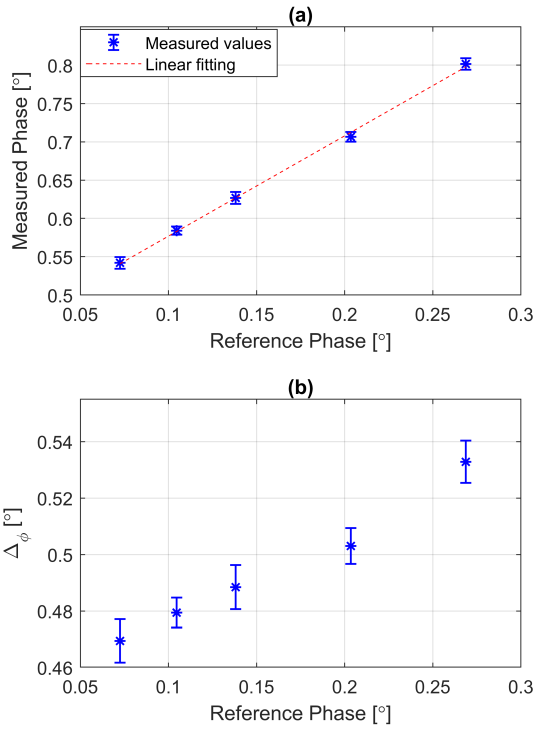

Fig. 5. Obtained phase measurements vs. reference phase measurements at 100 kHz with the five transmission lines.

where u_{Δ_T} is the type-A uncertainty reported in Tab. 1 and u_f is 5 ppm of the measured frequency f as reported in [15]. For assessing the repeatability of the phase measurements provided by the phase measurement prototype, 40 phase estimates are performed for each transmission line.

In particular, for the sine-wave frequency of 10 kHz, the following parameters were used to configure the phase measurement: the pulse duration was 10 μs, the sine-wave and pulse train amplitudes were 2 V, and the integration time for the true-rms measurements was 2 s. In Fig. 4a, the measured phases against the reference ones derived from the propagation delay measurements are depicted. The maximum obtained standard deviation is 0.0019 ° for the transmission line of 508 mm length, against the uncertainty of 0.00014 ° of the reference phase measurements obtained according to (2). Fig. 4b shows that the differences between the measured phases and the reference ones (i.e., Δ_ϕ) clearly increase with the reference phase, thus concluding that systematic effects affect the performed phase measurements at 10 kHz.

Fig. 5 reports the results obtained at 100 kHz with a pulse duration of 1 μs. Even in this case, the phase measurements are affected by systematic effects, and the maximum obtained standard deviation is 0.0026 ° for the transmission line of 508 mm length.
At the sine-wave frequency of 1 MHz, the maximum obtained standard deviation increased at 0.047 °, which is obtained for the transmission line of 762 mm length. In this case, the phase measurements do not show clear systematic effects (see Fig. 6).

Even for the sine-wave frequency of 10 MHz, the phase measurements seem not affected by systematic effects as depicted in Fig. 7. However, as expected, the maximum standard deviation increases by one order of magnitude with respect to the sine-wave frequency of 1 MHz (i.e., 0.30 ° for the transmission line of 254 mm).

In conclusion, the phase measurements are clearly affected by systematic effects at 10 kHz and 100 kHz, while at 1 MHz and 10 MHz, due to the increased standard deviations, the Δ_ϕ trends could be covered by the variability of the phase measurements.

V. CONCLUSION AND FUTURE WORK

In this paper, an experimental setup for measuring the phase delay introduced by transmission lines using a hardware prototype for measuring the phase of a sine-wave signal provided by at the output port of generator and was described. To guarantee measurement traceability, the propagation delays for all the transmission lines were measured

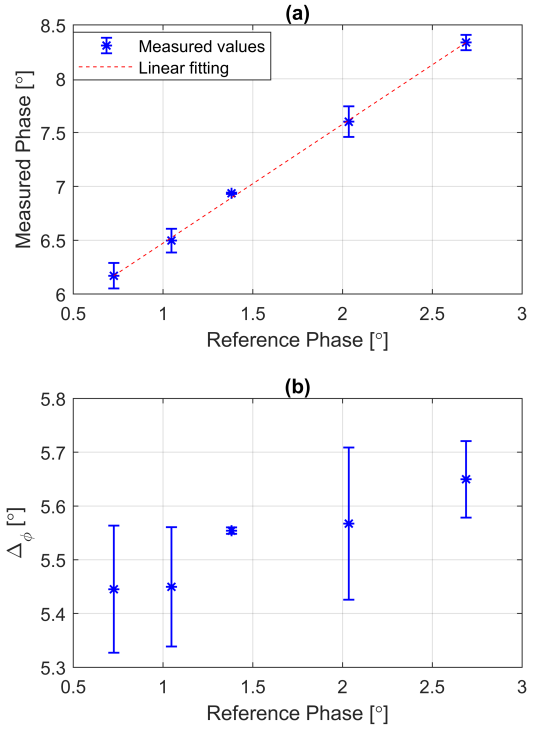

Fig. 6. Obtained phase measurements vs. reference phase measurements at 1 MHz with the five transmission lines.

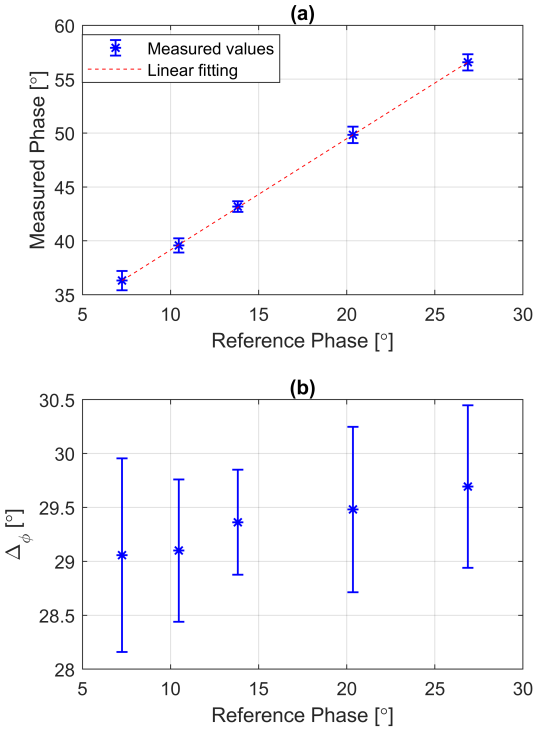

Fig. 7. Obtained phase measurements vs. reference phase measurements at 10 MHz with the five transmission lines.

by means of a network analyzer, a commercially available bench-top instrument. The obtained results for a sine-wave frequency from 10 kHz to 10 MHz were discussed. From the obtained results it was demonstrated that systematic effects affect the phase measurement performed by the prototype at 10 kHz and 100 kHz, while they were not clearly visible at 1 MHz and 10 MHz. Furthermore, the obtained standard deviations of the phase measurements were increased with the sine-wave frequency. In particular, at 10 kHz, it was 0.0019 °, while at 10 MHz, it has reached the value of 0.30 °. In particular at 1 MHz, the maximum obtained standard deviation is 0.047 ° against the value of 0.0022 ° reported in [10]. This growth of one order of magnitude of the standard deviation could be due to the fact that the phase delay measurement is obtained from two phase measurements one with the transmission line and the other with the short circuit. Furthermore, when the transmission line is inserted, the sinewave amplitude at the input of the analog multiplier is attenuated with respect to the one used in [10]. Future work will be directed to: (i) investigate the cause of systematic effects at 10 kHz and 100 kHz, (ii) implement a compensation method for the systematic effects, and (iii) to reduce the standard deviation of the phase measurements at 1 MHz and 10 MHz.

ACKNOWLEDGEMENT

The research presented in this paper has been supported by grant 70NANB19H074 “An electro/optical phase measurement system for the characterization of electroshock weapon electrical sources” awarded by the National Institute of Standards and Technology (NIST), USA.

The Authors thank Nicholas G. Paulter for his assistance with methodology and significant advice during research.

REFERENCES

[1] “1057-2017 - IEEE Standard for Digitizing Waveform Recorders”, 26 January 2018, available online: https://ieeexplore.ieee.org/document/8291741

[2] P.D.Hale, D.F.Williams, A.Dienstfrey “Waveform metrology: signal measurements in a modulated world”, Metrologia, vol.55, (2018), pp. s135-s151.

[3] W.L.Gans, “Dynamic calibration of waveform recorders and oscilloscopes using pulse standards”, in IEEE Transactions on Instrumentation and Measurement, vol.39, No.6, pp.952-957, Dec. 1990.

[4] S.Gustafsson, M.Thorsell, J.Stenarson, C. Fager, “An oscilloscope correction method for vector-corrected RF measurements”, in IEEE Transactions on Instrumentation and Measurement, vol.64, No.9, pp.2541-2547, Sept. 2015.

[5] I.Tudosa, F.Picariello, P.Daponte, L.De Vito, S.Rapuano, N. G.Paulter, “Prototype of high accuracy single input phase measurement instrument”, Measurement, Elsevier, vol.201, 30 September 2022.

[6] N. G.Paulter, D R.Larson, “A reference measurement system for electroshock weapons”, National Institute of Standards and Technology (NIST), 3 June 2013.

[7] E.Balestrieri, L.De Vito, F.Picariello, S.Rapuano, I.Tudosa, “A review of accurate phase measurement methods and instruments for sinewave signals”, ACTA IMEKO, vol.9, No.2, pp.52-58, June 2020.

[8] N. G.Paulter, “Method for Measuring the Phase Spectrum of the Output of a Frequency Source Used in the Calibration of an Electroshock Weapon Characterization System”, Journal of Research of the National Institute of Standards and Technology, vol.122, No.35, 19 September 2017.

[9] S.Rapuano, P.Daponte, L.De Vito, F.Picariello, I.Tudosa, N.Paulter, “A Phase Measurement Method to Guarantee the Traceability of the Calibration Systems”, 2020 Conference on Precision Electromagnetic Measurements (CPEM), Denver, CO, USA, 24-28 August 2020, pp.1-2.

[10] F.Picariello, I.Tudosa, L.De Vito, S.Rapuano, N. G.Paulter, “An Initial Hardware Implementation of a New Method for Phase Measurement of Sinewave Signals”, 2019 11th International Symposium on Advanced Topics in Electrical Engineering (ATEE), Bucharest, Romania, 28-30 March 2019, pp. 1-6.

[11] AWG 420 by Tektronix. Available online: https://www.tek.com/en/awg410-manual/awg410-awg420-awg430-user-manual

[12] AD834 by Analog Device. Available online: https://www.analog.com/en/products/ad834.html

[13] Agilent 3458A digital multimeter. Available online: https://www.keysight.com/us/en/product/3458A/digital-multimeter-8-5-digit.html

[14] Oscilloscope TDS 5104 by Tektronix. Available online: https://www.tek.com/en/datasheet/tds5000-series-digital-phosphor-oscilloscope

[15] Agilent E5071B network analyzer. Available online: https://www.keysight.com/us/en/product/E5071B/ena-rf-network-analyzer.html

26th IMEKO TC4 International Symposium
24th International Workshop on ADC and DAC Modelling and Testing
IMEKO TC-4 2023
Pordenone, Italy / September 20-21, 2023

Study on Calibration Method for Emergency Lighting and Evacuation Indicating System

Bin Deng[1], Ze-Xin Guan[1], Dong-Sheng Zhao[2], Xue-Feng Ma[1], Ru Jia[1], Hong-Rui Yan[1],

Hai-Long Xu[2] ,Guang-Kun Dong[2], Fan-Li Kong[2]

[1] 1st Shandong Engineering Research Center of Reliability Evaluation for Electric Energy Metering Devices，Shandong Institute of Metrology ,250131, No. 28, QianfoShan East Road, Jinan,Shandong,China ,dengbin0105@sina.com
[2] 2nd Shandong Institute of Metrology and Science 250131, No. 28, QianfoShan East Road, Jinan,Shandong,China , 1070249558@qq.com

Abstract

The quality inspection department regularly conducts spot checks on the quality issues of the fire emergency lighting and evacuation indication system, and detects the internal power supply voltage, emergency time, charging and discharging voltage, charging and discharging current, and other metrological characteristics of the system to ensure that the metrological characteristics of the system meet the requirements of national standards. However, there is a lack of reliable calibration methods and devices in China. In order to solve the problem of quantity traceability of detection devices for fire emergency lighting and evacuation indication systems, a calibration method for detection devices for fire emergency lighting and evacuation indication systems is studied.

Keyword

Evacuation indicating system
Emergency time
Metrological characteristics
Calibration method
Quantity traceability.

I. INTRODUCTION

With the rapid development of China's social economy and the acceleration of urbanization, there are more and more large-scale urban complex buildings, and the attendant fire safety management issues cannot be ignored. In accordance with the detection requirements of GB 17945-2010 "Fire Emergency Lighting and Evacuation Indication System" and GB 51309-2018"Fire emergency lighting and evacuation indication system technical standards"[1]. In fire-fighting facilities, the fire emergency lighting and evacuation indication system is a very important part, which can not only provide lighting during fire-fighting operations, but also provide assistance for evacuating people [2].

The design of fire emergency lighting and evacuation indication system products need to meet the technical requirements of currently implemented fire protection standards and design specifications to ensure the stability and reliability of the operation of the fire emergency lighting and evacuation indication system [3]. In the system of fire emergency lighting and evacuation instruction, the metrological characteristics of fire emergency lighting products are checked to see if they meet the requirements, test items include emergency time, charge and discharge voltage, charge and discharge current, power supply, etc.

In recent years, with the continuous innovation of lighting and evacuation indication systems. The accuracy of the detection device of the fire emergency lighting and evacuation indication system is also improved. At present, there is a lack of reliable calibration methods and devices in China. In order to solve the problem of traceability of the measurement value of the detection device of the fire emergency lighting and evacuation indication system in the quality inspection department[4]. After investigation and research in the field of fire-related emergency lighting products and measuring devices. A calibration method of fire emergency lighting and evacuation indication system is studied. Develop a comprehensive fire emergency lighting and evacuation indication calibration device.

II. CALIBRATION METHOD

According to the testing requirements of GB 17945-2010 "Fire Emergency Lighting and Evacuation Indication System", the technical indicators of the fire emergency lighting lamp detector should meet the requirements of Table 1.

The main metering characteristics include emergency conversion time, emergency working time, DC charging voltage, DC discharge voltage, DC charging current, DC discharge current, test temperature and test humidity.

Table 1. Technical specifications of the detector

Parameter	Technical specification
Emergency switch time (general area)	MPE: ± 0.5 s
Emergency switch time (high risk area)	MPE: ±0.025 s
Emergency working hours	MPE: ±0.1 s the emergency time is not less than 90 min
DC charging voltage	MPE: ±0.1%
DC discharge voltage	MPE: ±0.1%
DC charging current	MPE: ±0.2%
DC discharge current	MPE: ±0.2%
AC voltage output	MPE: ±1%
Test temperature	MPE: ±2 ℃
Test humidity	MPE: ±5 %RH

A. Delay time test system

The calibration of the delay time test system can directly calibrate the delay time of emergency switching time .The calibration of emergency switching time is shown in Figure 1. The working principle of the fire emergency lighting fixture detector for emergency switching time detection , one end is connected to a start switch (solid state relay).

It utilizes the fast response characteristics of the solid-state relay. When a sudden power failure occurs, it switches from charging mode to discharging mode, and the charging current circuit is zero, triggering a timing start circuit to turn on the start signal[5].The other end is connected to a photoelectric sensor. When the emergency light comes on momentarily, the circuit is in the discharge mode, triggering the timing end circuit and starting the stop signal.

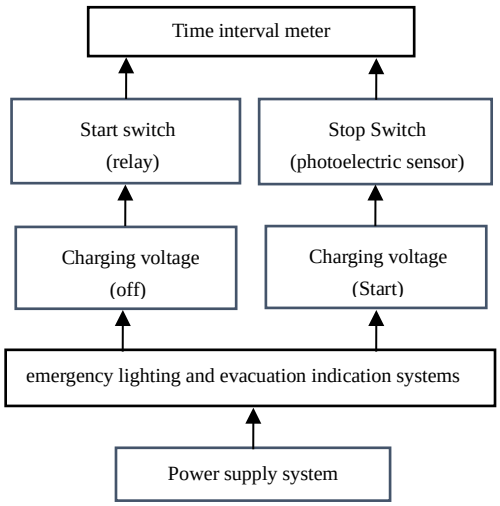

Fig.1. emergency switching time

The calibration of emergency working time is shown in Figure 2.The detection principle of the emergency working time of the fire emergency lighting lamp detector is as follows, one end connect a photoelectric sensor at one end, and when the emergency lamp is momentarily lit, the circuit is in the discharge mode, triggering a timing start circuit to turn on the start signal. The other end is connected to a solid-state relay. When the set time is reached, the charging circuit voltage is turned on, and the circuit is in charging mode. When the charging current reaches a constant value, the timing end circuit is triggered to start the stop signal.

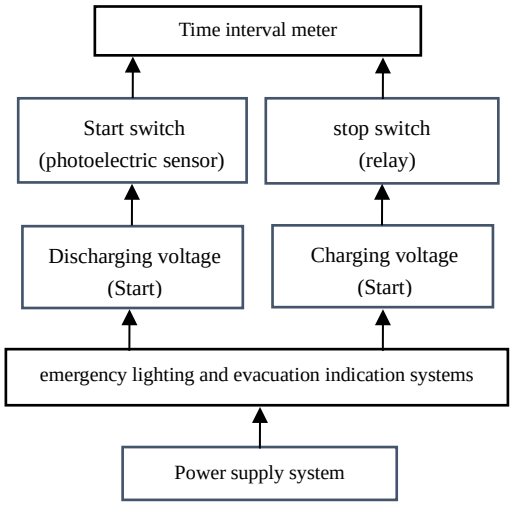

Fig.2. emergency working time

B. Calibration of AC output voltage

The fire emergency lighting lamp detector controls the output of AC stabilized power supply. It controls the output of AC voltage X_1. The AC digital voltmeter measures the output voltage X_0 at both ends. After the output is stable, the output value is recorded and the measurement result is calculated.

C. Calibration of DC charging and discharging voltage

For DC charging voltage calibration, using the DC standard voltmeter method, it sets the constant voltage charging mode, connects the DC digital voltmeter in parallel to both ends of the detector's output voltage, compares the voltage value X_1 displayed by the DC digital voltmeter X_0 and the calibrated fire emergency lighting fixture detector, and calculates the measurement results.

For DC discharging voltage calibration, using the DC standard voltmeter method. It sets the constant current discharge mode, connects a DC digital voltmeter in parallel to both ends of the output voltage of the tester, compares the voltage value X_1 displayed by the DC digital voltmeter X_0 and the calibrated fire emergency lighting fixture detector, where U is the DC digital voltmeter, and calculates the measurement results[6].

D. Calibration of DC charging and discharging current

For DC discharging current calibration, using the DC digital ammeter method, as shown in Figure 3. It sets the DC electronic load to the constant resistance mode. The electronic load is connected first, and then starting the calibrated fire emergency lighting fixture detector to output the current. After the current stabilizes, recording the DC digital ammeter reading and the current indication of the calibrated fire emergency lighting fixture detector, and calculating the measurement results.

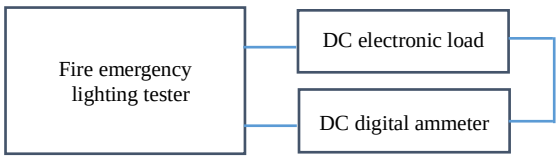

Fig.3. DC discharging current

For DC charging current calibration, using the DC digital ammeter method, as shown in Figure 4. It sets the calibrated fire emergency lighting detector to constant current charging mode. It sets the DC stabilized voltage to the constant voltage mode. The DC stabilized power supply output first, and then starting the calibrated tester. After the current output is stable, recording the current readings of the DC digital ammeter and the calibrated tester, and calculating the measurement results.

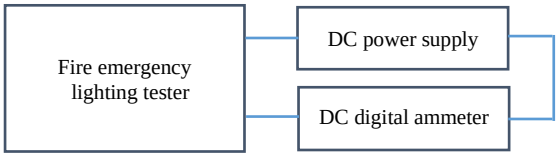

Fig.4. DC charging current

E. Calibration of ambient temperature and humidity

As the test system requires emergency time testing in a sealed environment, the box of the test system is an environmental temperature and humidity box. Refer to the test point layout method in the JJF1101-2019 Environmental Test Equipment Temperature and Humidity Calibration Specification.The location of the test points is shown in Figure 5.

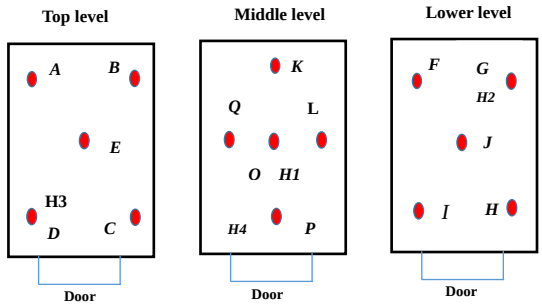

Fig.5. Layout measurement points

Test point N=15, (O, A, B, C, D, F, G, H,I,J,K,L,Q,P), where in test point O is arranged at the geometric center of the working space of the test box, and other test points are arranged in layers at the eight corners of the upper and lower layers of the test box. The distance from the test point to the box wall is 1/8 of the length of the opposite side of the inner wall of the test box. Refer to the temperature wiring diagram and place the humidity sensor in a suitable location. After stabilization, calibrate the humidity in the test box. Humidity test points with H1,H2,H3,H4 characters.

III. DESIGN OF CALIBRATION DEVICE

A. Measuring principle

As shown in Figure 6, the fire emergency lighting lamp detector is mainly composed of a microcomputer control system, a DC unit (DC regulated output), a discharge unit (DC electronic load), a charge and discharge control unit, and a measurement unit to achieve the detection of fire emergency lighting lamps. The main detection parameters include emergency conversion time, emergency working time, DC charging voltage, DC discharge voltage, and DC charging current DC discharge current, environmental test temperature, and environmental test humidity [7].

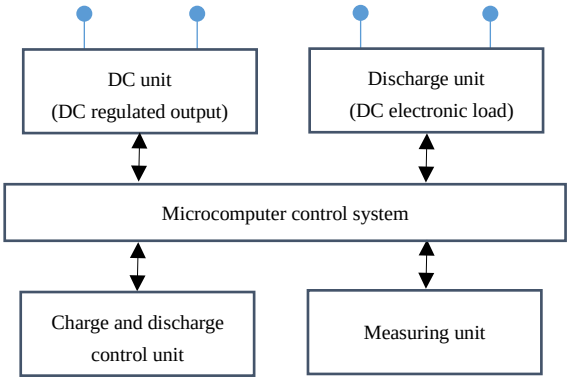

Fig.6. Measuring principle

B. Design of emergency time

The system timing control CPU circuit uses the STM32F405RGT6 chip, as shown in Figure 7.It completes the timing measurement of time, control of display, key input, control of DC voltage source, control of output AC source, and other functions. The clock uses a 10MHz thermostatic crystal oscillator.

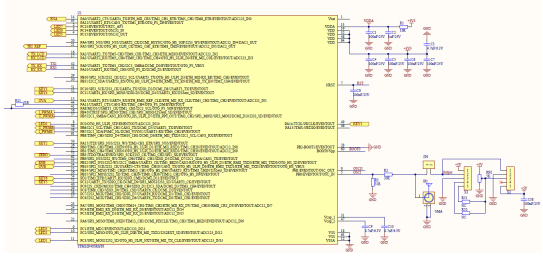

Fig.7. Timing control circuit

C.Design of AC programmable power supply

A self-developed control program using a MEGA48PA control chip as shown in Figure 8. Adopting unipolar SPWM modulation method, where H_ A、H_ B is high-frequency drive (40kHz), H_ C、H_ D is a low frequency drive (50Hz). CURR is the H-bridge overcurrent signal input, and EN is the input enable. After receiving a valid signal, an AC output voltage is established.

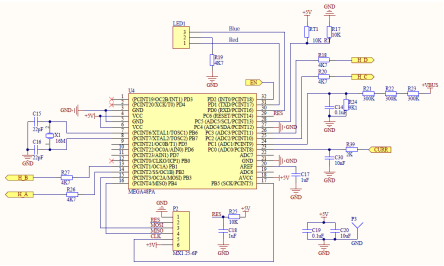

Fig.8. AC output voltage *circuit*

The design of the isolation drive circuit is shown in Figure 9. The SI8235 is based on a magnetic isolation gate driver, with an isolation voltage greater than 1500 V, and an output of a totem pole structure, with an output current of up to 4 A.

The VDDA adopts a bootstrap power supply mode. When the lower tube is turned on, a voltage of +12 V charges C9 and C10 through R14 and D14, a set of isolated drive circuits is saved.

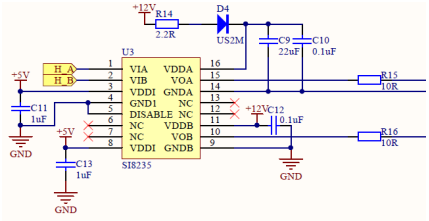

Fig.9. Isolated drive circuits

D. Design of program controlled

DC output power supply Q11 (27N80) is used to adjust the MOS transistor as shown in Figure 10.

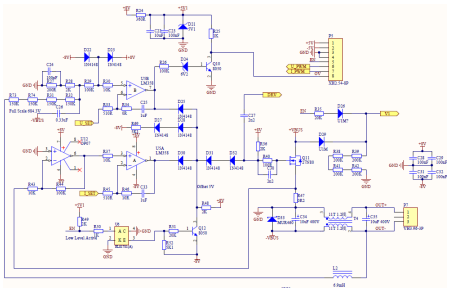

Fig.10. Linear adjustable power supply circuit

The basic principle is to change the voltage of the gate electrode, thereby changing the equivalent resistance of the MOS to complete the voltage adjustment. A part of U5 is an output current regulator, and the B part of U5 is an output voltage regulator. Both are PI regulators, and C25 and C33 are integral capacitors to ensure no steady-state error in the output voltage (current). U_ PWM，I_ PWM is a given signal for output voltage and output current, respectively.The design of the adjustable power fast switch for the emergency time measurement device is shown in Figure11.

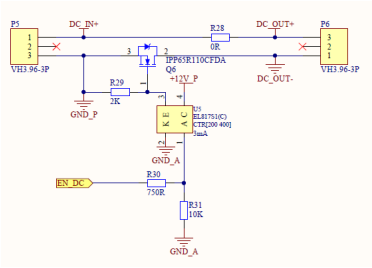

Fig.11. Fast switching circuit of adjustable power

The output voltage adjustment speed of the existing programmable DC power supply is relatively slow (generally using a time of 100 ms), and it is not possible to quickly establish the set voltage. This device adds MOS switch control output on the basis of existing programmed DC voltage, and can quickly establish a set voltage (using time of 100 μs) And can meet the requirements for fast setting of the power supply voltage of the time relay measurement system.

Adopting a composite mechanism of soft switching resonant switching power supply and linear power supply, utilizing the advantages of high efficiency of switching power supply, as well as the advantages of small ripple coefficient, high accuracy, and fast response of linear regulated power supply, the output of 10 V to 400 V DC regulated power supply is realized, with accuracy of 0.01% and stability of 0.005%.

IV. UNCERTAINTY ANALYSIS

Using this calibration method, a fire emergency lighting detector is calibrated. The fire emergency lighting detector models are XFDJ-2 and YDJ-1.

Table 2. Test data

Model	Parameter	Display value	Actual value	Uncertainty (k =2)
XFDJ-2	switch time	261 ms	260.8 ms	1.2 ms
YDJ-1	switch time	258 ms	257.4 ms	1.2 ms
XFDJ-2	Working time	10 min	10 min 0.1 s	0.2 s
YDJ-1	Working time	10 min	10 min 0.1 s	0.2 s
XFDJ-2	DC charging voltage	12.00 V	12.00 V	0.01 V
YDJ-1	DC charging voltage	12.00 V	12.01 V	0.01 V
XFDJ-2	DC charging current	76.22 mA	76.19 mA	0.08 mA
YDJ-1	DC charging current	76.20 mA	76.18 mA	0.08 mA
XFDJ-2	Temperature	20.1 ℃	20.1 ℃	0.1 ℃
YDJ-1	Temperature	20.1 ℃	20.1 ℃	0.1 ℃
XFDJ-2	Humidity	50.3 %RH	50.2 %RH	2.0 %RH
YDJ-1	Humidity	50.2 %RH	50.4 %RH	2.0 %RH

The emergency conversion time, emergency working time, DC charging voltage, DC discharge voltage, DC charging current, DC discharge current, and AC power output voltage are shown in Table 2. Compared with other calibration devices, the calibration device can meet the technical requirements for calibration of fire emergency lighting tester, and can carry out the calibration of fire emergency lighting tester.

Taking emergency switching time as an example, the sources of measurement uncertainty for calibration devices are analyzed, mainly including standard uncertainties introduced by factors such as the maximum allowable error of time interval meters, measurement repeatability, allowable error of photoelectric sensors, and solid-state relay contact switches. Within the measurement range 1 μs to 100 s, the fire emergency lighting lamp detectors are evaluated to have the same source.

A.Uncertainty component introduced by allowable error limit of time interval measuring instrument

According to the technical indicators of time interval measuring instrument, the maximum allowable error of the time interval: ± 0.1 μs , which is qualified after verification and evaluated according to class B. Assuming uniform distribution and inclusion factor k be equal to $\sqrt{3}$, uncertainty is equal to 0.06 μs.

B.Uncertainty component introduced by measurement repeatability

Under the specified conditions, use the time interval measuring instrument to make six repeated measurements on the calibration device, with the data being:260.8 ms, 261.2 ms, 261.4 ms, 261.5 ms, 260.9 ms, 261.3 ms and 269.2 ms. According to class a evaluation, the standard uncertainty introduced is calculated by Bessel formula, uncertainty is equal to 0.28 ms.

C.Uncertainty component introduced by the photoelectric sensor sensitivity

The standard uncertainty introduced by photoelectric sensor sensitivity which is based on the response time of the photosensitive transistor, the maximum allowable error introduced by photoelectric sensor shall not exceed 5 μs. Assuming uniform distribution and inclusion factor k be equal to $\sqrt{3}$, uncertainty is equal to 2.9 μs .

D.Uncertainty component introduced by asynchronous switching relay

The standard uncertainty introduced by asynchronous switching relay, the maximum allowable error introduced by asynchronous switching relay shall not exceed 1 ms. Assuming uniform distribution and inclusion factor k be equal to $\sqrt{3}$, uncertainty is equal to 0.58 ms .

E.Synthetic standard uncertainty

The above standard uncertainty components are not related to each other, so the synthetic standard uncertainty is equal to 0.6 ms.

F.Extended uncertainty

Take k be equal to 2 , Extended uncertainty be equal to 1.2 ms.

V. CONCLUSION

In order to solve the problem of quantity traceability of detection devices for fire emergency lighting and evacuation indication systems, this article analyzes the detection requirements of GB17945-2010 "Fire Emergency Lighting and Evacuation Indication System", and GB51309-2018 "Fire Emergency Lighting and Evacuation Indication System Technology", investigates the technical parameters of fire emergency lamp detectors on the market, studies a calibration method for fire emergency lighting lamp detectors, and designs a set of calibration devices[8], field test and measurement comparison show that this calibration device can meet the traceability requirements of the fire emergency lighting lamp detector and can be used as a measurement standard.

REFERENCES

[1]Standardization Administration of China. “Fire emergency lighting and evacuation indication system”,GB 17945-2010[S]. Beijing: China Standard Press,2010:1-3.

[2]Zheng G. Application of intelligent fire emergency lighting system in electrical design of civil buildings [J] . Architecture and budget, 2020.10 : 73-75.

[3]Luo X. （ 2021 ） Application of intelligent fire emergency lighting system in electrical design of civil buildings [J] . Engineering research,6(6) : 223-224.

[4]Ministry of Emergency Management of the People's Republic of China. Fire emergency lighting and evacuation indication system technology, standard: GB 51309-2018[S] . Beijing: China Planning

[5]Wu Zhen, Wu Jun “Design and application of gap measurement system based on DSP and FPGA ”, Instrumentation technology and sensors, vol.68，No.9 Sep.2008, pp.68-69.

[6]Liu Dongbin ,“Design and implementation of high precision time interval measurement system based on FPGA ”, Journal of missiles and guidance, vol.29， No.2 Apr.2009, pp.99-302.

[7]Bai X.(2021) Design of emergency lighting and evacuation indication system for theater building fire fighting, and discussion [J] . Modern building electric, 12(9) : 23-27.

[8]Liu Deliang, Wei Guangjun, “Research on ignition time measurement of a missile based on FPGA”, Computer measurement andcontrol,vol.19,No.6, Dec.2011,pp.1394-1396.

26th IMEKO TC4 International Symposium
24rd International Workshop on ADC and DAC Modelling and Testing
IMEKO TC-4 2023
Pordenone, Italy / September 20-21, 2023

Towards new IEC standards for the electrical characterization of graphene

Alessandro Cultrera[1,2], Luca Callegaro[1], Danilo Serazio[1], Norbert Fabricius[2,3]

[1]*INRIM – Istituto Nazionale di Ricerca Metrologica, strada delle Cacce 91, 10135 Turin, Italy*
[2]*ISC –International Standards Consulting GmbH & Co. KG, Verdistrasse 15A, D-30989 Gehrden, Deutschland*
[3]*IEC – International Electrotechnical Commission, Technical Committee 113 "Nanotechnology for electrotechnical products and systems"*

***Abstract* – New IEC technical specifications, for the standardized assessment of the sheet resistance R_S of monolayer graphene, recently published in June 2023 are here presented. These new standards of the series IEC TS 62607-6-xx describe protocols for the application of the contact methods i) in-line four point probe and ii) van der Pauw. The general IEC context of the main development steps for standards and and example of the scientific experiments used as input for the standard development are also presented.**

I. INTRODUCTION

Once graphene was unambiguously isolated in laboratory in 2004 [1], immediately academic research focused on its basic properties and industry begun to develop and place on the market several types of graphene and related products. The field progressed on even more encouraging results since the first evidence on academic journals of large-scale graphene synthesis [2] by chemical vapour deposition (CVD) in 2009. Still today, graphene used in academic research is hardly comparable to the raw materials offered by the industrial providers. Even within the same laboratory or industrial firm, repeatability and definition of materials' representative parameters (key control characteristics) is an issue that still holds. In fact, many available synthesis processes – such as mechanical exfoliation, chemical vapour deposition and reduction of graphene oxide dispersion, yield "graphene" with very different properties: graphene synthesized in labs rather than the one produced in industry has flakes of different size, possibly containing several types of defects and chemical contamination; research on scalable graphene is indeed facing a reproducibility gap [3].

For a successful uptake of products involving graphene and related materials, the availability of international standards is essential to define the key material properties and the appropriate measurement protocols. Within this framework, at the International Electrotechnical Commission, the Technical Committee 113 "Nanotechnology for electrotechnical products and systems" (IEC/TC 113) added the standardization of graphene and related materials into its work programme as early as 2012. The task was allocated to the Working Group 8 "Graphene related materials/Carbon nanotube materials". Currently, 36 graphene standards either published or under development within the IEC/TC 113. This TC established a liaison with the GRACE [1] research consortium [4], and since 2017 several standards about the electrical characterisation of graphene were initiated within this interaction, see the BOX 1 below.

BOX 1 - Standards Titles

IEC TS 62607-6-10:2020 Nanomanufacturing - Key control characteristics - Part 6-10: Graphene - sheet resistance: Terahertz time-domain spectroscopy.

IEC TS 62607-6-7:2023 Nanomanufacturing - Key control characteristics - Part 6-7: Graphene - Sheet resistance: van der Pauw method.

IEC TS 62607-6-8:2023 Nanomanufacturing - Key control characteristics - Part 6-8: Graphene - Sheet resistance: in-line four-point probe.

IEC TS 62607-6-25 Nanomanufacturing - Key control characteristics - Part 6-25: Two-dimensional materials - Variation of doping concentration: Kelvin Probe Force Microscopy.

IEC TS 62607-6-10:2020 has been already published in 2020 [5], IEC TS 62607-6-7 and IEC TS 62607-6-8 have been published in June 2023 [6, 7], while IEC TS 62607-6-25 is scheduled for 2024 [8]. The technical input for the establishment of the new work item proposals that are now the presented draft/published technical specifications, emerged in good part from the interaction between the

[1]EMPIR 16NRM01 GRACE "Developing electrical characterisation methods for future graphene electronics". EMPIR is the European Metrology Programme for Innovation and Research, funded by EURAMET, the European Association of National Metrology Institutes.

GRACE research consortium an IEC/TC 113. Concerning the scientific and experimental work that backed the standards development, it is worth mentioning that the liaison between IEC/TC 113 and GRACE consortium did not restrict the publication of scientific results. In fact, within the GRACE project time span, two good practice guides [9, 10] and several papers about characterisation of graphene (e.g. [11, 12]) were published as open source documents by the GRACE consortium.

In the following and at the conference, the new standards IEC TS 62607-6-7:2023 (in-line four point probe method) [6] and IEC TS 62607-6-8:2023 (van der Pauw method) [7] will be presented and their technical background discussed.

II. GRAPHENE KEY CONTROL CHARACTERISTICS

A key control characteristic (KCC) is a property of a material or an intermediate product that can affect the safety or the compliance with regulations, performance, quality, reliability or subsequent processing of the final product. Graphene related KCC include mechanical (elastic modulus), electrical (carrier density, carrier mobility, sheet resistance), chemical (metallic impurity content) and biological (skin sensitisation) ones. KCC may or may not already have been assigned a corresponding standard for their measurement. Some basic KCC are considered mandatory by IEC for all types of graphene and related material. For example, the indication of the availability of the safety documentation (MSDS data) or the manufacturing method. On the other hand, different forms of graphene may require different subsets of KCC to be defined. In the case of chemically exfoliated graphene oxide dispersion, the KCC Carbon-Oxygen ratio (C/O) is considered relevant (it shall be characterised following the standard IEC TS 62607-06-21:2022 [13] wherever needed). The same does not hold for chemical vapour deposited monolayer graphene, for which the KCC sheet resistance (R_S) is relevant instead; CVD graphene shall be characterised following available standards of the series IEC 62607-06-xx , e.g. IEC TS 62607-06-23 (Hall bar method) or the recently published IEC TS 62607-06-8 (van der Pauw method).

III. IEC STANDARDS DEVELOPMENT PROCESS

The development of the standards IEC TS 62607-6-7 and IEC TS 62607-6-8 followed the IEC workflow (see Sec. 2.1.3.1. in [14]). The main development stages are summarized in Fig. 1, the document types abbreviations are reported in the BOX 2. The process starts at the *preliminary* stage, with a standardisation topic of potential interest presented by either a TC member or an invited external expert. The topic eventually becomes a Preliminary Work Item (PWI) and is discussed at TC level within the *proposal* stage. If approved, the PWI becomes a New Work Item Proposal (PNW) which is then assigned a project leader (usually the author of the proposal itself); a project team (PT) is also formed on the basis of voluntary participation of other TC members. The PT works on a first working draft (WD) of the technical specification. When the WD prepared at PT level is considered mature enough, the technical discussion proceeds, at TC level, during the *committee stage* by iterative editing of the committee draft (CD) versions of the standard. During the technical discussion, the PT meet periodically, resolving the TC comments to the CD, eventually adding experimental and theoretical elements to bolster the document; the *committee* stage may take several iterations before the document is considered ready for the *approval* stage, where Draft Technical Specification (DTS) is considered in terms of technical contents (a DTS may also be returned to the CD stage for solving technical flaws). Once the technical discussion is concluded, two cases may occur. For Technical Specifications (lower level of consensus required) the DTS is approved for *publication* (APUB); at a higher level of consensus (required for International Standards) the DTS is approved as Committee Draft for Vote (CDV) and later, if the vote is positive, as Final Draft International Standard (FDIS) which enters the *publication* stage. Editorial and copyright revision is made on APUB documents, prior the publication as IEC documents. Each IEC standard is assigned a stability date, within which the document can be confirmed, revised, or withdrawn.

BOX 2 - Abbreviations

TS Technical Specification;

IS International Standard;

PWI Preliminary Work Item;

PNW New Work Item Proposal.;

WD Working Draft;

CD Committee Draft;

DTS Draft Technical Specification (TS);

CDV Committee Draft for Vote (IS);

FDIS Final Draft International Standard (IS);

APUB Approved For Publication;

IEC Published standard;

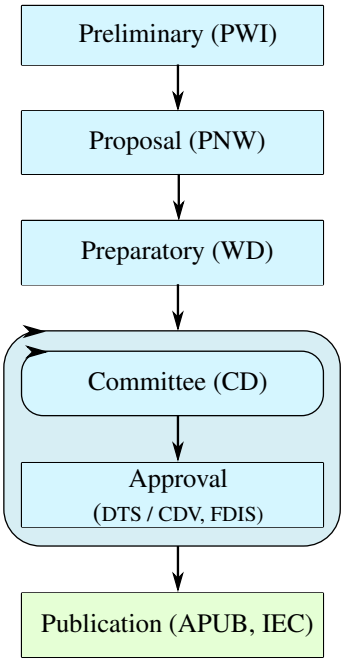

Fig. 1. Stages for the development of IEC standards. Abbreviations are defined in BOX 2. The circulating arrows enclosing "Committee" and "Approval" represent stages where iterative discussion and revision typically occur.

IV. NEW IEC STANDARDS FOR GRAPHENE SHEET RESISTANCE

CVD graphene is of particular interest for the development of new graphene based electronics, electrotechnical products, integration in established fabrication processes and sensors. Concerning this type of graphene, the new standards IEC TS 62607-6-7 [6] and IEC TS 62607-6-8 [7], describe standardized measurement protocols for the assessment of graphene's KCC sheet resistance R_S by means of contact methods, respectively the four in-line probe (4PP, [15]) and the van der Pauw methods (vdP, [16]) and represent complementary standards to others of the same series describing non-contact methods (e.g. [5]). The sheet resistance, R_S, is a quantity which can be used as global measure of the local conductivity of a sample with finite geometrical dimensions. In order to check the repeatability of the electrical properties of graphene, R_S is considered a KCC for monolayer CVD graphene. IEC standards TS 62607-6-7 and TS 62607-6-8 explain how to apply standardized methods on large area (mm^2 to cm^2) CVD graphene on rigid insulating support and how to perform a reliable estimation of the sample R_S and the measurement uncertainty, also considering the non-ideal nature of large-area commercial graphene. These two standards give instructions about i) how to prepare and store samples, ii) the required instrumentation specifications, iii) the ambient conditions within which the measurements shall be performed, iv) the standardized procedure to follow to perform the measurements, and v) the interpretation and reporting of the results.

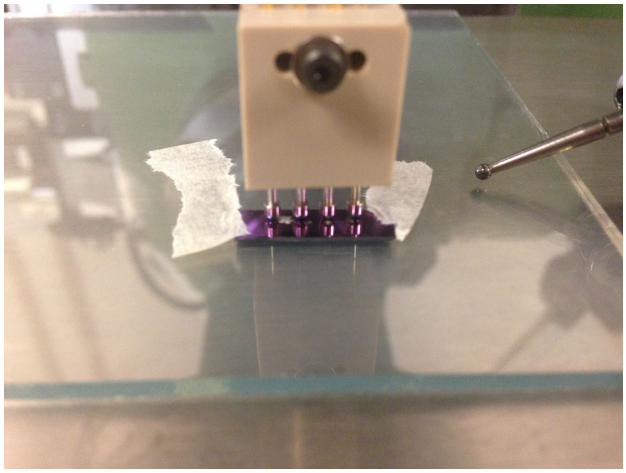

Fig. 2. A graphene sample is standing on an insulating glass slab placed on the balance plate. The test probe is in contact on the sample, while the lever indicator is placed in contact with the glass slab to measure the balance plate vertical displacement.

V. EXAMPLE OF SCIENTIFIC BACKGROUND PROVIDED TO THE PRESENTED STANDARDS

An example of scientific evidence provided IEC/TC 113 for the IEC TS here considered is given in the following. Here is briefly described one of a series of experiments performed during the TS development process, aimed to check the quality and the effect of purely mechanical electrical contacts on CVD graphene to perform multi-terminal electrical measurements. The use of this type of contacts was desirable to avoid any additional fabrication process that would certainly alter the pristine material conditions. To this aim, a custom probe provided of four equally spaced spring-loaded tips with round head profile was used to perform four terminal resistance measurements. The setup also included a digital balance (Sartorius LP8200S) a lever indicator (Mitutoyo 513-404), a 3-axis moving tool and position indicator (Anilam SENC 125 linear transducers, Anilam Wizzard 411 visualizer). An HP 34401 was used in 4-wire (4W) configuration to perform resistance measurements R_{4W} (from which R_S can be calculated). 4W resistance is measured by applying current through the outermost tips of the test probe and measuring the voltage drop between the two innermost tips. The probe standing on the graphene sample, the lever indicator and the balance plate are shown in Fig. 2. The sample was cut from a 4 inches wafer of commercial CVD graphene on Silicon (Pi-Kem Ltd., UK). The wafer was Boron-doped Silicon with thermal oxide coating, with graphene placed on the polished side of the wafer. The tests were performed to

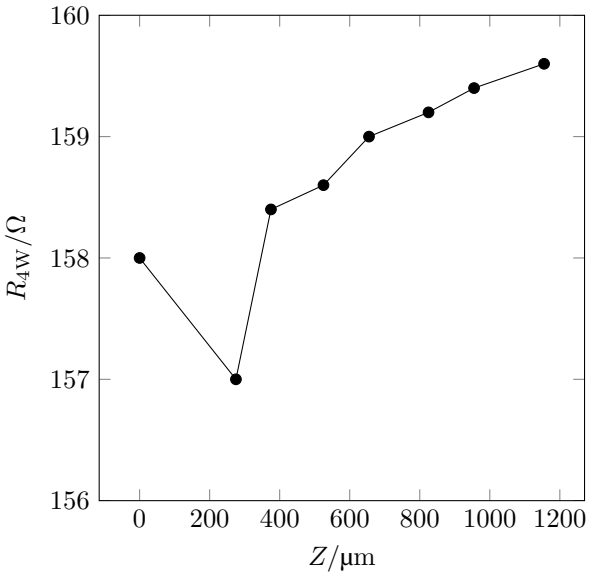

Fig. 3. 4-wire resistance measurements R_{4W} performed on the graphene sample. Error bars representing the type B uncertainty are not shown because negligible in comparison with the vertical axis range. The maximum Z for the used tips is $2.5\,\mathrm{mm}$.

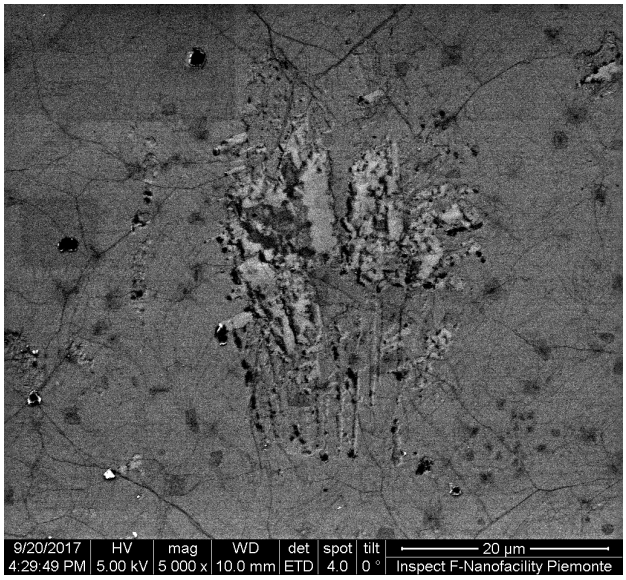

Fig. 4. SEM micrograph of one of the landing spots of the test probe tips on the graphene sample. Graphene grain boundaries and multi-layer seeds are visible as darker profiles and spots. In the center, a footprint of the probe tip is visible. Sign of shear displacement of the tip is visible in the lower part of the footprint. Lighter gray represents areas where graphene was scratched away for the support and Silicon thermal oxide appears.

check the stability and repeatability of the contacts, measuring both the probe spring displacement Z and the resulting weight, while measuring the electrical resistance. The net displacement Z of the tips springs was calculated by subtracting the displacement of the balance plate to the total probe displacement measured by the moving tool. The total applied weight to the sample (proportional to the spring force) was measured by means of the weighting scale placed under the glass slab supporting the sample. The 4W resistance R_{4W} was measured at 8 different spring Z, in the range $0\,\mu m$ to $1155\,\mu m$ (where the position $0\,\mu m$ corresponds to the probe making electrical contact with the graphene) to check whether the applied force influenced the contact quality, and to assess the damage induced by the probe on the graphene layer. The 4W resistance measured placing the probe at the center of the sample was $R_{4W} = 158.65\,\Omega \pm 0.85\,\Omega$. The type B uncertainty calculated from the measuring instrument's specifications was of the order of $0.05\,\Omega$. The small standard deviation of the measurements suggests that the effect of the spring displacement was not critical. Results of this measurements are reported in Fig. 3. The plot shows the larger change in R_{4W} occurring at small Z, up to about $300\,\mu m$, reasonably because the contact is still weak, then the readings stabilize with a slight increment up to the larger considered Z.

After the electric measurements, SEM micrographs were acquired to assess the damage produced by landing the test probe on the sample. The footprint of one of the tips, after reaching the maximum Z is shown in Fig. 4. The scratched area is about $20\,\mu m \times 20\,\mu m$, which is reasonably of the order of the round tip footprint itself. Moreover, at least two different types of damage can be observed: i) areas where graphene was pealed away, in the center of the landing spot (insulating thermal Silicon oxide appears brighter in SEM micrographs), and ii) a few linear shear scratches, at the bottom of the spot probably due to lateral movement of the probe tip. The R_{4W} increment in plot of Fig. 3 could be ascribed to the increasing damage produced by the unavoidable lateral displacement of the probe. This and other similar tests (e.g. repeatability of the contacts by raising and landing repeatedly the probe on the same spots) suggested that mechanical contacting on monolayer graphene sheets on rigid supports was a viable method to be used in standardized protocols, also considered that commercial test probes already available on the market could be directly employed for the task by most laboratories.

VI. CONCLUSION

The laboratory exploration of new concepts based on original ideas is absolutely valuable for the scientific progress, nevertheless, standardization is fundamental to bring scientific advances into production. The presented new standards IEC TS 62607-6-7 and IEC TS 62607-6-8 for the electrical characterisation of CVD graphene can contribute

to the establishment of shared good practices and standardized measurement protocols respectively in research labs and industry.

VII. ACKNOWLEDGEMENTS

The work has been done within the Joint Resarch Project EMPIR 16NRM01 GRACE – Developing electrical characterisation methods for future graphene electronics. This project has received funding from the EMPIR programme co-financed by the Participating States and from the European Union's Horizon 2020 research and innovation programme.

VIII. *

References

[1] K. S. Novoselov, A. K. Geim, S. V. Morozov, D. Jiang, Y. Zhang, S. V. Dubonos, I. V. Grigorieva, A. A. Firsov, Electric field effect in atomically thin carbon films, Science 306 (5696) (2004) 666–669.

[2] X. Li, W. Cai, J. An, S. Kim, J. Nah, D. Yang, R. Piner, A. Velamakanni, I. Jung, E. Tutuc, et al., Large-area synthesis of high-quality and uniform graphene films on copper foils, Science 324 (5932) (2009) 1312–1314.

[3] P. Bøggild, Research on scalable graphene faces a reproducibility gap, Nature Communications 14 (1) (2023) 1126.

[4] L. Callegaro, C. Cassiago, A. Cultrera, V. D'Elia, D. Serazio, M. Ortolano, M. Marzano, O. Kazakova, C. Melios, F. Raso, et al., Grace: Developing electrical characterisation methods for future graphene electronics, in: 2018 Conference on Precision Electromagnetic Measurements (CPEM 2018), IEEE, 2018, pp. 1–2.

[5] IEC, Geneve, Switzerland, IEC TS 62607-6-10:2021, Nanomanufacturing - Key control characteristics - Part 6-10: Graphene - Sheet resistance: Terahertz time-domain spectroscopy.

[6] IEC, Geneve, Switzerland, IEC TS 62607-6-7:2023, Nanomanufacturing - Key control characteristics - Part 6-7: Graphene - Sheet resistance: van der Pauw method.

[7] IEC, Geneve, Switzerland, IEC TS 62607-6-8:2023, Nanomanufacturing - Key control characteristics - Part 6-8: Graphene - Sheet resistance: in-line four-point probe.

[8] IEC, Geneve, Switzerland, IEC TS 62607-6-25, Nanomanufacturing - Key control characteristics - Part 6-25: Two-dimensional materials - Variation of doping concentration: Kelvin probe force microscopy.

[9] A. Cultrera, A. Fabricius, A. Catanzaro, L. Callegaro, Good Practice Guide on the electrical characterisation of graphene using contact methods, Accepted by EURAMET as deliverable for 16NRM01 EMPIR GRACE, https://arxiv.org/abs/2007.13348, 2020.

[10] A. Catanzaro, A. Fabricius, A. Cultrera, O. Kazakova, Good Practice Guide on the electrical characterisation of graphene using non-contact and high-throughput methods, Accepted by EURAMET as deliverable for 16NRM01 EMPIR GRACE, https://arxiv.org/abs/2007.14047, 2020.

[11] A. Cultrera, D. Serazio, A. Zurutuza, A. Centeno, O. Txoperena, D. Etayo, A. Cordon, A. Redo-Sanchez, I. Arnedo, M. Ortolano, et al., Mapping the conductivity of graphene with Electrical Resistance Tomography, Scientific Reports 9 (1) (2019) 10655.

[12] C. Melios, N. Huang, L. Callegaro, A. Centeno, A. Cultrera, A. Cordon, V. Panchal, I. Arnedo, A. Redo-Sanchez, D. Etayo, et al., Towards standardisation of contact and contactless electrical measurements of CVD graphene at the macro-, micro-and nano-scale, Scientific Reports 10 (1) (2020) 3223.

[13] IEC, Geneve, Switzerland, IEC TS 62607-6-21:2020, Nanomanufacturing - Key control characteristics - Part 6-21: Graphene - Elemental composition, C/O ratio: X-ray photoelectron spectroscopy.

[14] IEC, Geneve, Switzerland, ISO/IEC Directives part 1, Procedures for technical work, 2022.

[15] F. Smits, Measurement of sheet resistivities with the four-point probe, Bell System Technical Journal 37 (3) (1958) 711–718.

[16] L. J. van der Pauw, A method of measuring the resistivity and hall coefficient on lamellae of arbitrary shape, Philips Technical Review 20 (1958) 220–224.

26th IMEKO TC4 International Symposium
24rd International Workshop on ADC and DAC Modelling and Testing
IMEKO TC-4 2023
Pordenone, Italy / September 20-21, 2023

Verification of thermal converters by means of a pulsed Josephson standard

Krzysztof Kubiczek[2], Paolo Durandetto[1], Pier Paolo Capra[1], Claudio Francese[1], Marco Lanzillotti[1], Luca Roncaglione[1], Marian Kampik[2], Andrea Sosso[1]

[1]*INRiM - Istituto Nazionale di Ricerca Metrologica, strada delle Cacce 91, Turin, Italy, E-mail: p.durandetto@inrim.it, p.capra@inrim.it, c.francese@inrim.it, m.lanzillotti@inrim.it, l.roncaglione@inrim.it, a.sosso@inrim.it*

[2]*Department of Measurement Science, Electronics and Control, Faculty of Electrical Engineering, Silesian University of Technology, Gliwice, Poland, E-mail: krzysztof.kubiczek@polsl.pl, marian.kampik@polsl.pl*

***Abstract* – Starting from 2019 a new central role is played by quantum standards, owing to the redefined SI [1], where electrical units are directly linked to the fundamental constants e (elementary charge) and h (Planck constant). Thus, metrologists are nowadays trying to extend the astonishing accuracy attainable in dc measurements to ac and beyond, moving from sinusoidal toward quantum calibrations of arbitrary signals. Programmable Josephson Voltage Standards are nowadays capable of fulfilling primary metrology requirements only for signals up to few hundreds Hz. Pulsed Josephson standard are instead capable of generating arbitrary waveforms at higher frequencies, so are generally called Josephson Arbitrary Waveform Standards (JAWS). In particular, the capability of generating high spectral purity signals allows high accuracy measurements of the ac-dc difference of thermal converters. We report in the following about our setup for quantum calibrations of thermal converters, first results obtained and open issues.**

I. INTRODUCTION

The impressive improvement in accuracy of dc voltage calibrations attained with Josephson junction arrays is one of the most relevant success of superconductive electronics. Dc Josephson Voltage Standards (JVSs) can generate stable voltages up to 10 V with uncertainties below 1 nV/V [2]. Unfortunately, the generation of ac voltages of similar accuracy is difficult because the output voltage cannot change unless at relatively low rate. Instead, the one-to-one current-voltage (IV) relationship [3] in Programmable Josephson Voltage Standards (PJVS) under microwave irradiation makes it possible to suitably control the voltage by setting the junction bias current. They are realized with many Josephson junctions, connected in series and subdivided in sub-circuits following a power-of-two rule: the total voltage across all sections can thus be binary programmed, equivalently to the technique used in electronic digital-to-analog converters. Among the different technologies proposed for PJVS, we mention SNIS junctions with respectively Nb, Al and AlO_x as superconducting (S), normal (N) and insulating (I) elements, developed at INRiM [4], that proved particularly interesting for operation with He-free systems [5].

However, the step switching speed of PJVS is also limited, thus PJVS are suited to primary metrology generating ac voltages at frequencies up to few hundreds Hz. The resulting transients between consecutive waveform steps deteriorate the accuracy of the rms value calculated from quantum-accurate dc voltages of these steps. To get rid of PJVS limitations, arrays operating with a pulsed, ideally-square wave, microwave bias were developed. The use short pulses rather than a continuous sinusoidal wave allows to suitably modulate the signal frequency over a wide range of frequencies. Exploiting the $\Sigma\Delta$ technique developed for semiconductor electronics, pulsed standards can synthesize arbitrary waveforms with quantum accuracy and guarantee very high spectral purity in signals from digital-to-analog conversion. Quantum-traceable sinewaves of high purity are currently considered to estimate the ac-dc conversion error of thermal converters with unparalleled accuracy, for primary ac voltage metrology [6]. For evaluating the ac-dc transfer difference of a Fluke 792A[1] thermal voltage converter (TVC) we used our cryocooled JAWS system to generate quantum accurate dc and ac signals applied to the input of the TVC.

II. MEASUREMENT METHOD

The highest accuracy in ac voltage measurements are generally attained by means of thermal voltage converters (TVCs), where ac and dc voltages are compared and the rms value is determined from the heating effect of both. However, due to thermoelectric and electromagnetic ef-

[1]Brand names are used for identification purposes and such use implies neither endorsement by INRiM nor assurance that the equipment is the best available in the market.

fects, the TVC is affected by a residual difference of its response to ac and dc, that depends on both the applied voltage and frequency.

The ac-dc transfer difference with its uncertainty, apart from the sensitivity, is one of the most relevant characteristics of the TVC [7]. It is usually calculable by the mathematical model of the construction, depending on its geometrical dimensions, material properties, and physical phenomena. The ac-dc transfer difference depends strictly on the frequency. At the frequency of typically below 100 Hz, the main reasons of the transfer difference are the nonlinear thermal phenomena and insufficient averaging of the temperature of the heater and thermoelectric junctions. In the frequency range of 100 Hz to 10 kHz, the transfer difference is mostly due to thermoelectric effects, which do not occur with the ac voltage provided. At the level of 10 kHz to 1 MHz, the skin effect in the heater and microwave circuits start to be the most essential factors of enlarging of the transfer difference. Finally, above 1 MHz, the microwave phenomena such as reflection, interference, characteristic impedance mismatching, and standing waves as well as residual parameters of the heater determinate the ac-dc transfer difference of the TVC.

In the TVC quantum-based calibration method, the TVC input is connected to the JAWS output, then a proper sequence of different calculable and quantum-defined voltage signals are applied to TVC input. Finally, the TVC output is measured with a high-resolution dc nanovoltmeter. Since the pulsed Josephson standard can generate signals with any arbitrary shape, a wide range of possibilities are available to analyze the TVC behaviour. The typical test follows the sequence dc-ac-dc: by comparing the response in ac with the average of values for dc of opposite polarities, the ac-dc difference can be accurately obtained with drifts and offsets reduction. In some cases, it can be preferable to observe difference in the response to signals at different frequencies, to determine the, so called, ac-ac difference. Sometimes, to eliminate the dc reversal error and other electrothermal phenomena, more sophisticated procedures are used to determine the ac-dc transfer such as ac/dc+/ac/dc-/ac, where dc+ and dc- denote the dc voltages with opposite polarities [8].

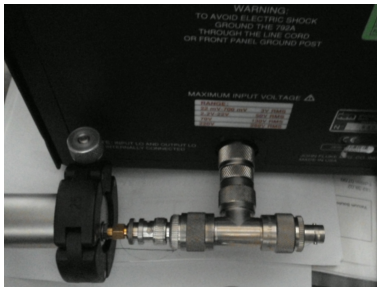

Fig. 1. Short connection of the TVC to the JAWS inside the pulse-tube cryocooler through the vacuum-tight SMA feedthrough.

The JAWS capability to generate pure signals over a wide range of frequency allows to perform this test in a straightforward manner, the measurement accuracy is in any case guaranteed by JAWS principle of operation. However, it is widely recognized that, for increasing frequencies, the most relevant uncertainty contribution in JAWS standards is due to the loading effect of voltage leads [9]. One way to reduce these errors is to use a short voltage cable, though this condition cannot be fully realized in a LHe system, where the cable is more than one meter long. In our cryocooler the cable length is more than halved with respect to a liquid Helium cryostat (typical cryoprobe length > 1 m).

III. CALIBRATION SYSTEM

The setup is realized around a "flexible" cryogen-free refrigeration system [10] that we built to operate both programmable and pulsed standards. The arrays of Josephson junctions we used were realized by PTB with Nb_xSi_{1-x} as barrier material [11]), where Nb and Si relative content (x) is suitably adjusted to get characteristic frequencies around 10-15 GHz at 4.2 K. Our JAWS sample consists of two arrays, with 5000 junctions each, integrated on a $10\,\mathrm{mm}\times10\,\mathrm{mm}$ silicon chip. For each array, junctions are arranged in double stacks and are embedded into the center line of a 50 Ω coplanar waveguide, which ensures a suitable propagation of pulses. The JAWS chip is mounted in a special thermally-conductive cryopackage similar to that described in Ref. [12], designed to enhance heat dissipation in the cryocooler vacuum environment. The copper coldplate that refrigerates the cryopackage hosts a thermometer and a heater to finely monitor and control its temperature. A second thermometer is installed onto the cryopackage, in proximity of the Josephson chip. Transmission of the quantized signal through the probe is generally done with either a coaxial cable or twisted pair, with length around $1.5\,\mathrm{m}$ in liquid He experiments, or even longer in cryocoolers since thermalization requires suitable thermal anchors windings. In this setup we instead used a cryogenic coaxial cable that allowed us to reduce the total length from chip to outer connector down to $0.5\,\mathrm{m}$, a value even lower than in special short He probes. A special SMA vacuum-tight feedthrough is installed onto a flange of the cryocooler vacuum chamber to pick up the Josephson voltage. Figure 1 shows the straight connection from cryocooler output to TVS.

IV. RESULTS

At first, the dc current-voltage (IV) characteristics of the arrays, hence with no pulsed rf-bias, are observed. These have been properly analysed to evaluate the junctions electrical parameters, namely critical current I_c, nor-

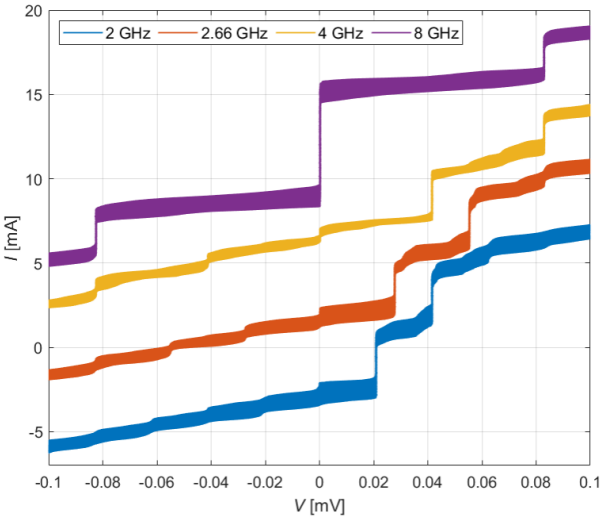

Fig. 2. IV curves of the Josephson array radiated with unipolar pulses of amplitude 1 V, at different repetition frequencies, at 4.5 K.

mal resistance R_n and characteristic frequency $f_c = K_J\, I_c\, R_n$, with K_J the Josephson constant. This characterization is necessary to determine the optimal temperature setpoint, which is related to highest pulses repetition frequency and width as well as to the cryopackage thermal performances. Indeed, optimal pulse amplitude and frequency for wide quantum range depend on critical current and characteristic frequency, which in turn depend on the operating temperature.

In addition, one of the two available JAWS array was investigated as on-chip temperature sensor, in a similar way as described in Ref. [13]. This would ensure the stabilization of the actual chip temperature even when microwave pulses are applied to the junctions, which is particularly critical at lower temperatures, owing to the reduced thermal conduction.

Next, the Josephson array has been microwave-radiated with pulses at different repetition frequencies, but same pulse width, in order to verify the array quantum behavior in the same experimental conditions that will be reproduced for the sinusoidal quantum-based waveform synthesis needed for the TVC calibration. IV curves of the Josephson array at the constant temperature of 4.5 K, radiated with pulses of amplitude 1 V, at different repetition frequencies are plotted in Fig. 2. Wide first-order quantum voltage steps have been obtained for this large frequency range. The effect of the cryocooler-induced temperature fluctuations are visible in the IV characteristics, causing the reduction of the useful quantum step current-amplitude.

V. CONCLUSION

A cryocooled pulse-driven Josephson standard setup for the analysis of TVC properties by means of quantized pure sinewaves was presented. Very small cable loading effect were obtained, thanks to a special short coax. In particular, the preparation of the measurement apparatus and the optimization of operating parameters for the generation of verified quantum signals were discussed. Quantum operation of the standard was demonstrated for both sinusoidal and pulsed rf excitation.

ACKNOWLEDGEMENTS

This research was partially funded by the Polish National Science Center (NCN) [grant no. 2022/06/X/ST7/00014]. Krzysztof Kubiczek is supported by the Foundation for Polish Science (FNP) [grant no. START 036.2022].
The authors are indebted with Dr. O. Kieler of Physikalisch-Technische Bundesanstalt for providing the chips used in this work.

REFERENCES

[1] Stock M, Davis R, de Mirandés E and Milton M J 2019 *Metrologia* **56** 022001
[2] Behr R and Katkov A S 2005 *Metrologia* **42** 01005
[3] Lacquaniti V and Sosso A 2012 Josephson Junctions for Present and Next Generation Voltage Metrology *Modern Metrology Concerns* (InTech)
[4] Lacquaniti V, Cagliero C, Maggi S and Steni R 2005 *Appl. Phys. Lett.* **86** 04–2501
[5] Lacquaniti V, De Leo N, Fretto M, Maggi S and Sosso A 2007 *Appl. Phys. Lett.* **91** 252505
[6] Underwood J M 2018 *Metrologia* **56** 015012
[7] Kubiczek K, Kampik M and Grzenik M 2021 *Measurement* **168** 108439
[8] Kubiczek K, Kampik M and Grzenik M 2022 *Measurement* **201** 111686
[9] Zhao D, van den Brom H E and Houtzager E 2017 *Meas. Sci. Technol.* **28** 095004
[10] Sosso A, Durandetto P, Trinchera B, Kieler O, Behr R and Kohlmann J 2017 *Measurement* **95** 77 – 81
[11] Kohlmann J, Kieler O, Iuzzolino R, Lee J, Behr R, Egeling B and Muller F 2009 *IEEE Trans. Instrum. Meas.* **58** 797–802 ISSN 0018-9456
[12] Durandetto P, Monticone E, Serazio D and Sosso A 2019 *IEEE Trans. Compon. Packag. Manuf. Technol.* **9** 1264–1270
[13] Durandetto P and Sosso A 2021 *Superconductor Science and Technology* **34** 045008

26th IMEKO TC4 International Symposium
24th International Workshop on ADC and DAC Modelling and Testing
IMEKO TC-4 2023
Pordenone, Italy / September 20-21, 2023

Novel 3D Hall sensor and its application in inspection robots

Dragana Popovic Renella[1], Thomas Kaltenbacher[1], Sasa Spasic[1], Andrea Cavelti[2], Giorgio Valsecchi[2], Lennart Nachtigall[2], Marco Hutter[2]

[1] *SENIS Group, Switzerland, info@senis.swiss*
[2] *RSL ETH Zurich, Switzerland, mahutter@ethz.ch*

Abstract – This paper describes a novel CMOS magnetic field sensor that can measure all three magnetic field components (Bx, By, and Bz) simultaneously at a single location. The sensor employs three groups of mutually orthogonal horizontal and vertical Hall-effect elements, each with dedicated biasing circuits and amplifiers. The field sensitive volume of the 3D sensor is very compact, only 100 x 100 µm2, which enables high spatial resolution. The use of CMOS technology ensures high angular accuracy and orthogonality of the three measurement axes. The sensor also employs a spinning-current technique that effectively mitigates issues such as offset, low-frequency noise, and planar Hall effect. The wide analog bandwidth from DC to 300 kHz and built-in temperature sensor make the sensor suitable for various applications, including 3D positioning sensors, proximity sensors, current sensors, and magnetometry. As an example, the paper discusses an application of the 3D sensor for improved adhesion control in inspection robots.

I. INTRODUCTION

Magnetic field sensors are vital for numerous applications across various industries, such as robotics, automotive, and medical fields, where the precise measurement of magnetic fields is critical. While Hall-effect sensors have gained popularity for their ability to measure magnetic fields, conventional sensors have limitations in measuring magnetic fields in all three dimensions simultaneously and at the same location, which is essential to precisely measure high gradient magnetic fields of permanent magnets, electro magnets and magnet assemblies. To address this limitation, a novel CMOS magnetic field sensor has been developed, capable of measuring all three magnetic field components (Bx, By, and Bz) simultaneously at virtually a single spot. The integrated vertical and horizontal Hall elements ensure high angular accuracy and orthogonality of the three measurement axes. The spinning-current technique used in the biasing of the Hall elements reduces issues such as offset, low-frequency noise, and planar Hall effect. This paper presents a compact 3D Hall sensor that has a wide analog bandwidth, high magnetic field resolution, and a built-in temperature sensor. The sensor's versatility makes it suitable for various applications, such as 3D positioning sensors, angular sensors, current sensors, and magnetometry. The paper also outlines an application of the 3D sensor for improved adhesion control in inspection robots.

II. HORIZONTAL AND VERTICAL HALL SENSORS

Hall sensors are commonly used to measure magnetic fields, but traditional Hall sensors only detect fields that act perpendicular to the sensor. To measure in-plane magnetic fields, a vertical Hall plate device must be integrated into the sensor. This idea was first introduced by Popovic [1] over 20 years ago and has been further developed using CMOS silicon technology to improve both horizontal and vertical Hall sensors.

The latest version of the vertical Hall device has a significantly better signal-to-noise ratio than any other vertical Hall device on the market, with a noise voltage spectral density of 0.8µV/Hz at 1kHz after signal processing [2]. The vertical and horizontal Hall elements can be combined in integrated CMOS technology to create various magnetic sensors for a wide range of applications: e.g. a compact 3D Hall sensors for providing a complete picture of the magnetic field environment; a 2D sensor for magnetic angle measurement or Hall sensors for electric current measurements.

III. THE 3D HALL SENSOR SENM3DX

The novel 3D Hall sensor SENM3Dx [3] is an advanced device that is capable of measuring all three components of the magnetic field (Bx, By, and Bz) at a single location simultaneously. The sensor is designed with three groups of mutually orthogonal Hall-effect elements, each of which has its own dedicated biasing circuits and amplifiers. This enables the sensor to have a high spatial resolution of only 100 x 100 µm2, see Fig. 1.

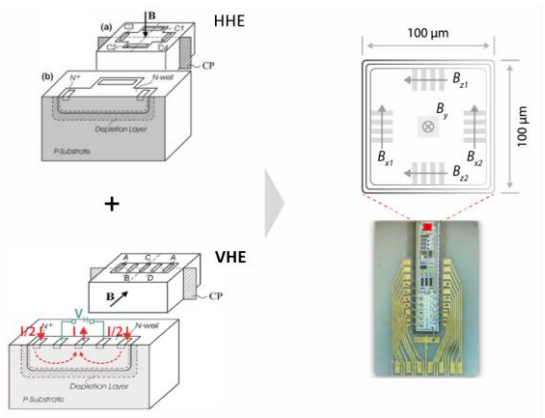

Fig. 1. Horizontal Hall Elements (HHE) and Vertical Hall Elements (VHE) integrated on silicon chip: Small sensitive volume. High mutual orthogonality. Equal performance for HHE and VHE.

The use of complementary metal-oxide-semiconductor (CMOS) technology in the fabrication of both the vertical and horizontal Hall elements and ensures high angular accuracy and orthogonality of the three measurement axes. The sensor also employs a spinning-current technique, which is effective in mitigating issues such as offset, low-frequency noise, and planar Hall effect.

The sensor is characterized by its wide analog bandwidth, ranging from DC to 300 kHz, and includes a built-in temperature sensor. The sensor chip is packaged in non-magnetic QFN28 package, see Fig. 2. These features make the sensor suitable for various applications.

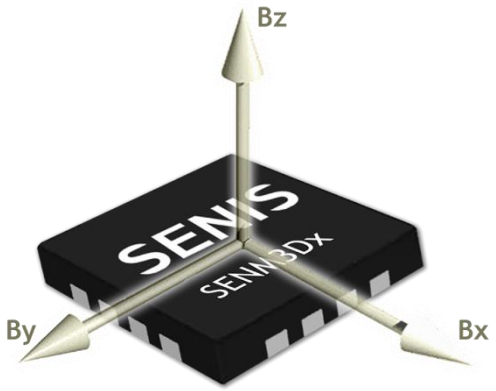

Fig. 2. SENM3Dx sensor packaged in non-magnetic QFN28 package

The RSL at ETH Zürich has integrated a 3D Hall sensor into their inspection robots to significantly enhance adhesion control during wall-climbing, as discussed below.

IV. 3D SENSOR APPLIED IN INSPECTION ROBOTS

Inspection robots are becoming increasingly important for tasks such as maintenance, monitoring, and inspection of critical infrastructure. One of the major challenges in the design and operation of these robots is the need for reliable adhesion control, especially in harsh and unpredictable environments.

To enhance safety, accuracy, efficiency, and cost-effectiveness, climbing robots equipped with electro-permanent magnet (EPM) grippers have been widely adopted [4], [5]. However, these robots are typically heavy and expensive, making it crucial to ensure that they do not fall during operation. To address this issue, obtaining feedback on the actual adhesive force or grip of the EPM to the support structure is essential. This feedback would not only allow for energy-saving during climbing but also enable the avoidance of areas that provide insufficient support. In this context, the proposed method for estimating the magnetic adhesive force utilizes SENIS 3D-magnetic field sensors SENM3Dx.

The 3D sensors are strategically placed on the edge of a gripper foot to probe the fringe field of the EPM. An adhesive force model was developed and a prototype was constructed using the EPM VM65/ND manufactured by NAFSA [6] and four SENM3Dx sensors, as shown in Figure 3 a) and b). The optimal sensor position was determined by electro-magnetic (EM) simulations, which identified the location of maximal magnetic field changes adjacent to the gripper foot housing.

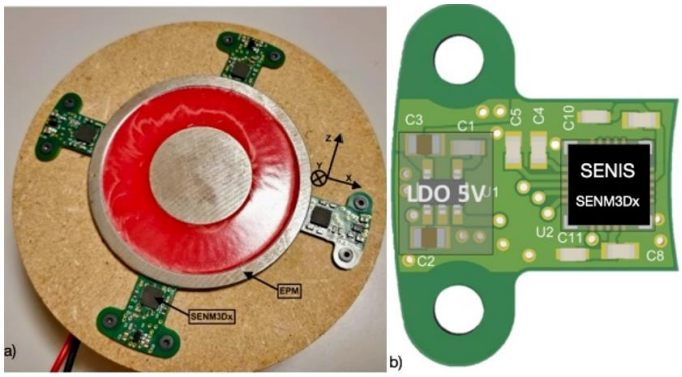

Fig. 3. The gripper foot prototype is shown in the bottom view with four equally distanced SENM3Dx sensors on PCBs and the electro permanent magnet (EPM). The magnetic axis definition is displayed for one sensor in (a), while (b) shows the sensor PCB's bottom view with SENIS® SENM3Dx. Both images are adapted from [4]

By taking into account the complexities of the real world, the adhesive force is influenced by various parameters. In this model, the focus is on four key factors that significantly impact the adhesive force: the strength of

the permanent magnet, the air gap between the EPM and support, the thickness of the support (metal), and the texture of the support surface.

A novel solution involves defining an angle between the X and Y components, which offers valuable insight into air gap distance up to a certain range. Specifically, larger air gaps result in an angle of 90°, as seen in Fig. 4a, whereas for thicker support structures, the angle remains independent of thickness. However, for decreasing air gaps, the relative error in magnetic field component measurements can cause outliers, as shown in Fig. 4a. Therefore, understanding this relationship is key in accurately estimating adhesive force for climbing robots and ensuring their safe and efficient operation.

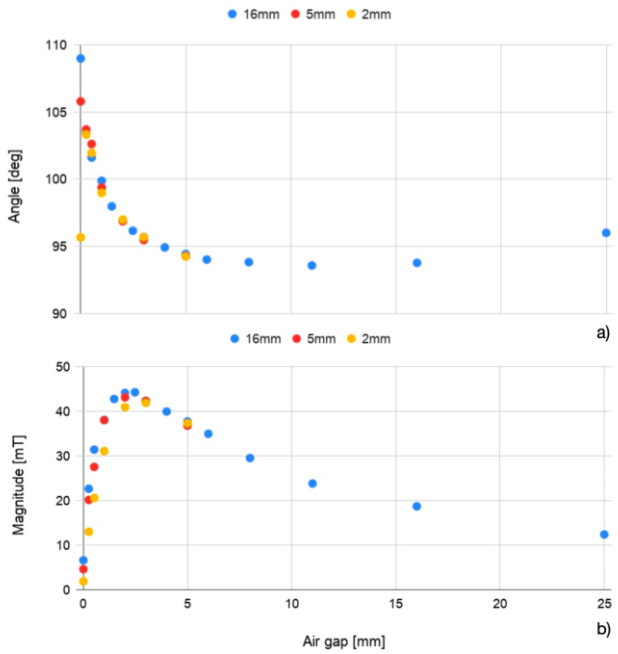

Fig. 4. The magnetic angle is illustrated for various air gaps in (a), while (b) displays the magnetic field magnitude M for different air gaps. A 16 mm thick steel plate was used as support. The image is reprinted from [4]

The X and Y components of the magnetic field amplitude or magnitude M can be used to determine the adhesion force, as it exhibits a nearly linear relationship for small air gaps (see b) Fig. 4). In contrast, the magnetic angle provides less reliable data for estimating the adhesion force compared to the magnetic magnitude, and hence was not utilized in building a simple, linear prediction model. Thus, the magnetic angle can be used to estimate the air gap distance, while the magnetic field magnitude can be used to determine the adhesion force. This is supported by the fact that the adhesion force is roughly proportional to the magnetic field magnitude for a given air gap.

Eqn. 1 presents the adhesion force prediction model, which utilizes data from a 5 mm thick steel plate, based on the magnetic magnitude and an independent force measurement obtained from the 2 mm and 16 mm metal plates. The model is expressed as a function of the air gap width (d), where the subscript indicates the thickness of the metal support. Therefore, the model $F_{5,pred}$ (d) predicts the adhesion force for a 5 mm thick metal plate using the magnetic magnitude (M) and force measurements (F) of 2, 5, and 16 mm thick metal supports.

$$F_{5,pred}(d) = F_2(d) + \frac{F_{16}(d) - F_2(d)}{M_{16}(d) - M_2(d)}\left(M_5(d) - M_2(d)\right) \quad (1)$$

In Fig. 5, the predicted and measured adhesion force values are compared as a function of the air gap distance d, with a maximum relative error of 23%. This level of accuracy is considered acceptable since the magnet's strong adhesion force is chosen for safety reasons. This safety margin allows for the use of the model in real-world applications without further optimization. Additionally, the fast and dynamic responses of the SENM3Dx sensor enable the use of adaptive models that can train and react in real-time. Furthermore, it is highly convenient to obtain adhesion force information from a small, lightweight 3D magnetic field sensor.

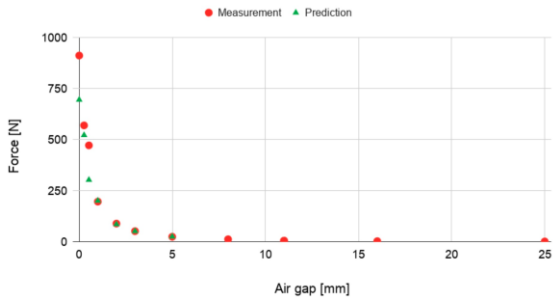

Fig. 5. The performance of the linear prediction model $F_{5,pred}$ is demonstrated, and the model (Prediction) is compared to the measured adhesion force (Measurement) for various air gaps d. The image is reprinted from [4].

V. CONCLUSIONS AND OUTLOOK

This paper presents a novel CMOS magnetic field sensor that can accurately measure all three components of the magnetic field at a single location. The use of three groups of mutually orthogonal vertical and horizontal Hall-effect elements, each with dedicated biasing circuits and amplifiers, ensures high spatial resolution and angular accuracy. The spinning-current technique employed in the

sensor effectively mitigates issues such as offset, low-frequency noise, and planar Hall effect. The wide analog bandwidth and built-in temperature sensor make the sensor suitable for a variety of applications, including 3D position sensing and magnetometry, angular sensing and electrical current sensing.

As an example, an application of the 3D sensor for improved adhesion control in inspection robots is presented. The use of SENIS 3D Hall sensors has proven to be a powerful tool in optimizing the control of magnetic grippers, providing reliable measurements even in high field gradient applications.

With its unmatched performance and precision, SENIS® 3D Hall sensors are poised to play a leading role in the next generation of magnetic measurement solutions. As SENIS continues to push the limits of what is currently possible and available on the market, the range of possibilities for researchers and engineers alike will expand, leading to further advances in magnetometry and sensor technology.

REFERENCES

[1] R. S. Popovic, “Hall Effect Devices”, 2nd Edition, ISBN 9780750308557, published December 1, 2003 by CRC Press

[2] Patent EP14176835.8 Vertical Hall Device (granted: USA, CN, JP, EU). Application: High-resolution CMOS integrated vertical Hall device.

[3] 3D Hall sensor SENM3Dx https://www.senis.swiss/sensors, accessed 15th of March 2023

[4] A. Cavelti, G. Valsecchi, L. Nachtigall, and M. Hutter, “Magnetic gripper feet - Integration of the control electronics and estimation of magnetic adhesive force,” 2020, Student Thesis, RSL, ETH Zurich

[5] EPM: An electro-permanent magnet, also known as EPM, is a special kind of permanent magnet that allows the activation or deactivation of its external magnetic field through the application of an electric current pulse in a wire winding wrapped around a section of the magnet.

[6] https://www.nafsa-solenoids.com/products/holding-electromagnets/round-magnetic/vmnd-series/, accessed 15th of March 2023

26th IMEKO TC4 International Symposium
24th International Workshop on ADC and DAC Modelling and Testing
IMEKO TC-4 2023
Pordenone, Italy / September 20-21, 2023

Atomic density calibration at high-temperature

Erxat Arkin[1], Jiqing Fu[2], Qing He[2], Jia Kong[1]

[1] *Department of physics, Hangzhou Dianzi University,Hangzhou 310018,China*
[2] *Magnetic quality laboratory, National Institute of Metrology, 100029 Beijing,China*

***Abstract* – Calibration of atomic density in vapour cell is very important for high precision quantum metrology and fundamental research. Here we propose to use spin noise spectroscopy(SNS) method for density estimation which would be more reliable than the common density estimation methods based on absorption spectrum or thermodynamic equation. We show our test with different density estimation methods, and show the robustness of SNS method.**

I. INTRODUCTION

Atomic density of alkali vapor is one of the most important parameters of atomic ensemble, which has broad applications in quantum metrology, such as atomic magnetometer [1,2], atomic clock [3], atomic gyroscope [4], and also quantum noise investigation. Our knowledge of atomic density helps to increase measurement sensitivity and accuracy. It is even more crucial for quantum noise study topics that based on atomic interactions to generate quantum entanglement [5] where density calibration determines the standard quantum limit of the system. However, the common density calibration methods are not very suitable for high temperature atomic vapour.

A convenient way of knowing the atomic density is proposed by Alcock [6], based on thermodynamics,

$$n = \frac{1}{T} 10^{21.866 + A - \frac{B}{T}}, \quad (1)$$

where A and B are parameters determined by atomic species. One can easily calculate atomic density with known temperature. However, it is hard to get accurate temperature of atomic vapour.. Firstly, normally we can only measure temperature at the surface of a vapor chamber which can not reflect the real temperature of the alkali vapor. Secondly, there are also limitations on the accuracy of temperature sensors. Absorption spectrum [7] is another way of measuring atomic density, which partly depends on temperature measurements. It gets density information by fitting the absorption spectrum of atoms, which makes it more reliable than thermodynamics methods. However at high temperature, too much absorption makes the spectrum saturated and therefore the fitting results are not reliable any more. Here we propose to estimate alkali vapor's density with spin-noise spectroscopy (SNS) [8], which does not rely on temperature measurement at all, and it can work for both low and high temperature conditions.

II. ATOMIC ABSORPTION SPECTRUM

Absorption spectrum is relatively easy to operate. A laser beam passes through vapor cell with a frequency modulation closed to resonance. The intensity before and after the cell have to be recorded for further calculations.The absorption effects with a given length of alkali vapor are defined by

$$I(z) = I_0 exp(-\alpha(\nu, T)l), \quad (2)$$

where α is absorption coefficient that depends on frequency ν of the incident light and temperature of the vapor chamber, which is defined as

$$\alpha(\nu, T) = \sigma(\nu, T)n(T). \quad (3)$$

where σ is absorption cross section and n is atomic density. We see that the density estimation relies on the measurement of temperature and beam power, but not solely decided by temperature measurement, therefore it can do a better job than thermodynamics equations.

At high temperature conditions, the atomic density is quite high, therefore the absorption effect is so strong that almost all probe power are absorbed on resonance, which makes the fitting results not very reliable. As can be seen in figure 1, above 90 ℃, too much absorption covered the transition details.

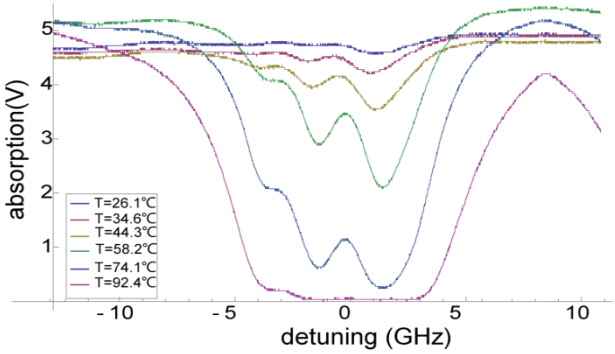

Figure. 1. ***Absorption line versus frequency detuning of probing light under different temperature conditions.***

III. SPIN NOISE SPECTROSCOPY

SNS is a technique to study spontaneous fluctuation of spin system. There are several techniques that have been

applied to measure intrinsic fluctuation of the spin system, such as nuclear magnetic resonance [9,10] and magnetic force microscopy [11,12], but the most used probing technique is Faraday rotation measurement which can transfer information of spin noise to the polarization of an off-resonance probe light. The setup of SNS is relatively easy and very similar to absorption spectrum experiment, where we need to measure the polarization, instead of intensity, of probe beam.

Both photonic noise and atomic noise are included in the SNS signal. For atomic density calibration, we need to get atomic information. On time domain, it is hard to distinguish photonic or atomic noise, but on frequency domain, we could obtain atomic information since they have different frequency dependence. With fast Fourier transformation (FFT), we can get power spectral density (PSD) of the SNS signal, which can be described by Lorentzian function [13]:

$$S(\nu) = S_{ph} + S_{at}\frac{(\Delta\nu/2)^2}{(\nu-\nu_L)^2+(\Delta\nu/2)^2} \quad , \quad (4)$$

where ν_L and $\Delta\nu$ are Lamour frequency and full-width half-maximum (FWHM). S_{ph} is photon shot noise contribution to PSD, which is mainly determined by probe power P. The amplitude of Lorentzian line S_{at} is mainly contributed by atomic spin noise , which is defined as:

$$S_{at} = \frac{4G^2\mathcal{R}^2P^2}{\pi\Delta\nu/2}Var\Theta_{FR} \quad , \quad (5)$$

where G is transimpedance gain; $\mathcal{R}$ is detector responsivity and $Var\Theta_{FR}$ is the variance of Faraday rotation due to light - atom interaction:

$$Var\Theta_{FR} = N\frac{{\sigma_0}^2}{A_{eff}^2}\kappa^2, \quad (6)$$

Here κ is a parameter determined by detuning frequency of probing light and atomic property. σ_0 and A_{eff} are on resonance cross section and effective beam area. N is the number of atoms that interacts with probing light, which is the parameter we want to estimate through SNS technique. We could see that the density estimation is independent of temperature estimation but relies on probe power measurements.

In figure 2 we show SNS and its fitting with Lorentzian line as described above. Integral under the Lorentzian line shape, $S_{at}\Delta\nu/2$, is proportional to N, thus by fitting the noise spectrum we can acquire density of atomic ensemble. Most of the variables are calculable or measurable in fine accuracy, and SNS apparatus is easy to set up, so it's a relatively reliable and convenient method for vapor density calibration at both low and high temperature.

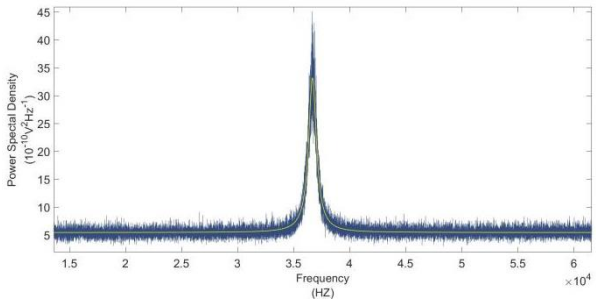

Figure. 2. ***spin noise spectroscopy:*** *Dark blue line is measured spin noise from Rb^{87} vapor at 102 ℃ and under 834.15 nT magnetic field, yellow line is fitting of data with Lorentzian function. Acquisition time is* $\tau_{aqc} = 0.5$ *s with sampling rate of 200 kHz.*

At very high temperature, fast collision among atoms happens, that causes a large spin-exchange rate, Rse, bringing large spin relaxation. However when Lamor frequency induced by exerted magnetic field is much lower spin-exchange rate, ,i.e., $R_{se} \gg \nu_L$,atoms in upper and lower hyperfine levels precess as a bond state. This gives a high signal to noise ratio and narrower linewidth, but with slower-down presession frequency. The precession frequency and magnetic resonance linewidth changes under different spin-exchange rate or precession rate can be illustrated as[9]:

$$\Delta\omega + i\omega_q = \frac{([I]^2+2)R_{se}}{3[I]^2} - \sqrt{-\omega_0^2 - \frac{2i\omega_0 R_{se}}{[I]} + \left(\frac{([I]^2+2)R_{se}}{3[I]^2}\right)^2} \quad (7)$$

where $[I] = 2I + 1$_,and I is nuclear spin, $\omega_0$is the Lamour frequency of atoms. When $R_{se} \gg \omega_0$. the system enters SERF-regime, and the precession rate becomes $\omega_q = \omega_0/q_l$,with slowing down factor q_l.

SNS can also be used as a convenient indicator for atomic ensemble entering spin-exchange relaxation free (SERF) regime, since it gives a magnetic resonance signal with a simpler setup comparing with a full magnetometer setup. In figure 3 we show theoretical prediction based on equation (7) and also experimental results of ω_q from SNS measurements at 176 ℃. We could see the experimental results agree with theory nicely and support for a SERF-regime calibration. Besides, by fitting the experimental data, we could get a more precise density calibration at very high temperature.

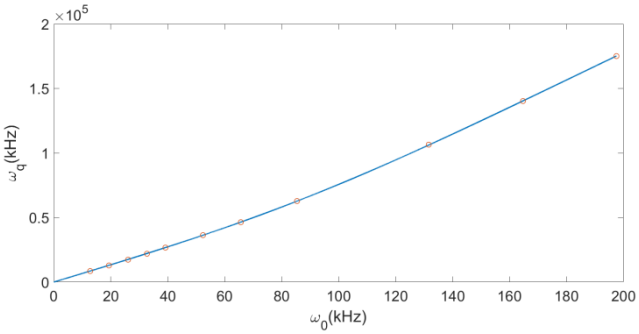

Figure. 3. ***frequency shift in SERF regime:*** *Blue line is the theoretical prediction of Lamour frequency based on equation (7) with fixed* $R_{se} = 4.24 * 10^5 s^{-1}$. *red dots are experimental result acquired at 176 ℃.*

IV. COMPARISON OF DIFFERENT CALIBRATION METHODS

In figure 3 we show the density estimation of three different calibration methods. The black line denotes for estimated vapor density with thermodynamic function. Since the temperature sensor is set at the surface of vapor chamber, it estimates a higher temperature of the atomic vapor. This method should over estimate the atomic density. The purple line shows the density estimated by absorption spectrum. Due to strong absorption effect, and its reliance on temperature estimation it can not give a reliable estimation at high temperatures. Since the density estimation method based on SNS technique relies on the probe power measurements, we did the test under different probe power. As shown in figure 3, the blue, red, green lines stands for density estimation under 2 mW, 3 mW, and 4 mW probe power. We could see, they have good agreement under different power. This shows its robust density estimation ability. We could see at low temperature, the density estimation with different methods can easily be consist with each other, but at high temperature, the accurate density estimation is a crucial problem.

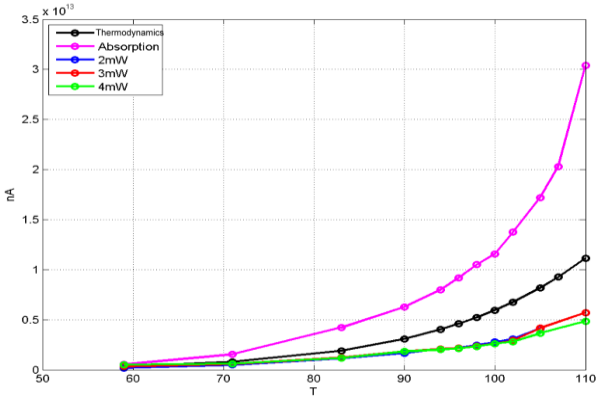

Figure. 3. ***comparison of different density estimation method from 60 ℃ to 110 ℃。***

V. CONCLUSION

In conclusion, we proposed a more reliable atomic density estimation method at high temperature conditions, which is based on SNS technique. We have studied different methods for atomic density estimation, and compared their results in temperature range of 60 ℃ - 110 ℃. We demonstrated the density estimation consistency by using SNS with different probe powers.

REFERENCES

[1] Budker, D., Romalis, M. Optical magnetometry. *Nature Phys* **3**, 227–234 (2007).

[2] C. Troullinou, R. Jiménez-Martínez, J. Kong,V. G. Lucivero, and M. W. Mitchell Phys. Rev. Lett. 127, 193601

[3] Andrew D. Ludlow, Martin M. Boyd, Jun Ye, E. Peik, and P. O. Schmidt Rev. Mod. Phys. 87, 637

[4] Walker, T. G. / Larsen, M. S. Chapter Eight - Spin-Exchange-Pumped NMR Gyroscope 2016 Advances In Atomic, Molecular, and Optical Physics Academic Press p. 373-401

[5] Kong, J., Jiménez-Martínez, R., Troullinou, C. et al. Measurement-induced,spatially-extended entanglement in a hot, strongly-interacting atomic system. Nat Commun 11, 2415 (2020)

[6] Alcock, C. B. / Itkin, V. P. / Horrigan, M. K. Vapour Pressure Equations for the Metallic Elements: 298 – 2500K 1984-07

[7] Weller, Lee / Bettles, Robert J. / Siddons, Paul / Adams, Charles S. / Hughes, Ifan G. Absolute absorption on the rubidium D1 line including resonant dipoleJournal of Physics B: Atomic, Molecular and Optical Physics , Vol. 44, No. 19 p. 195006

[8] Crooker, S. A. / Rickel, D. G. / Balatsky, A. V. / Smith, D. L. Spectroscopy of spontaneous spin noise as a probe of spin dynamics and magnetic resonance 2004-09

[9] Happer, W. / Tam, A. C. Effect of rapid spin exchange on the magnetic-resonance spectrum of alkali vapors *Phys. Rev. A* , Vol. 16 1977-11

[10] Tycho Sleator, Erwin L. Hahn, Claude Hilbert, and John Clarke Phys. Rev. Lett. 55, 1742 – Published 21 October 1985

[11] Rugar, D., Budakian, R., Mamin, H. et al. Single spin detection by magnetic resonance force microscopy. Nature 430, 329 – 332 (2004)

[12] Budakian, R. / Mamin, H. J. / Chui, B. W. / Rugar, D. Creating Order from Random Fluctuations in Small Spin Ensembles 2005

[13] Lucivero, Vito Giovanni / Jim é nez-Mart\inez, Ricardo / Kong, Jia / Mitchell, Morgan W. Squeezed-light spin noise spectroscopy 2016-05

26th IMEKO TC4 International Symposium
24th International Workshop on ADC and DAC Modelling and Testing
IMEKO TC-4 2023
Pordenone, Italy / September 20-21, 2023

DIN SPEC 91411: A standardized representation of magnetic scales

Dr. Jürgen Gerber[1], Dr. Rolf Slatter[2]

[1] *INNOMAG e.V., Ruhe Almend 8, 67655 Kaiserslautern, gerber@innomag.org*
[2] *ITK Dr. Kassen GmbH, Beim Eberacker 3, 35633 Lahnau, R.Slatter@itknet.de*

***Abstract* – When it comes to scales for magnetic length and angle measurement systems, there has been no uniform terminology, no common drawing rules - neither for the mechanical nor for the magnetic parameters - and this has often led to misunderstandings or even errors in de-sign drawings. This primarily affects manufacturers of magnets, magnetic scales and sen-sors as well as machine or device manufacturers. A consortium consisting of a total of 13 companies and research institutions, mainly members of the Innovation Platform for Mag-netic Microsystems INNOMAG e. V., has now developed a DIN SPEC standard for the uni-form representation of magnetic measuring scales.**

I. INTRODUCTION

Magnetic measuring systems are becoming increasingly widespread for the safe detection of movements or positions. The robust, wear-free measuring principle offers numerous advantages over other measuring principles [1 to 6]. Magnetic measuring systems often consist of a field-generating permanent magnet in the form of a measurement scale and a sensor that converts the changes in the magnetic field (strength and/or direction) into electrical output signals via the magnetic scale (Fig. 1). The sensors used are typically based on a magneto resistive or Hall effect [7 to 9].

Measurement scales, in the form of rotary or linear scales, are necessary to realise magnetic measuring systems in combination with one or more sensors (Fig. 2). For the production of magnetic measuring scales, the blanks can be magnetically encoded using different processes (Fig. 3). The material and geometry of the measurement scales are selected according to the requirements of the later place of use and the magnetic coding to be applied.

The magnetic encodings range from simple dipole permanent magnets, to single-track incremental magnetisations in which the measurement scale is described alternately with north and south poles, as well as complex, multi-track magnetisation patterns. The documentation describing the respective measurement scales can there-fore also be correspondingly complex.

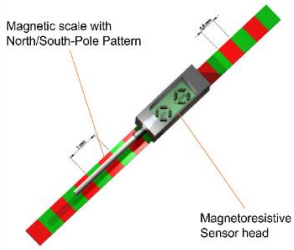

Fig. 1. Magnetic length measuring system consisting of sensor head and scale (Image source: ITK Dr. Kassen GmbH).

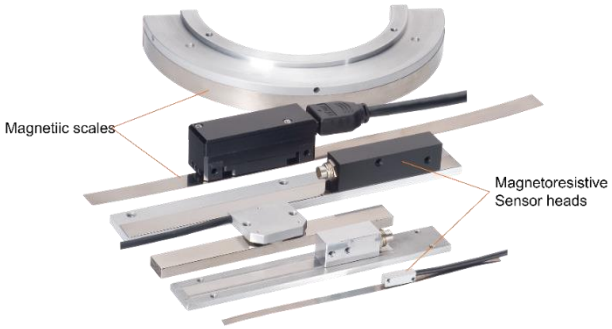

Fig. 2. Magnetic length and angle measuring systems (Image source: ITK Dr. Kassen GmbH).

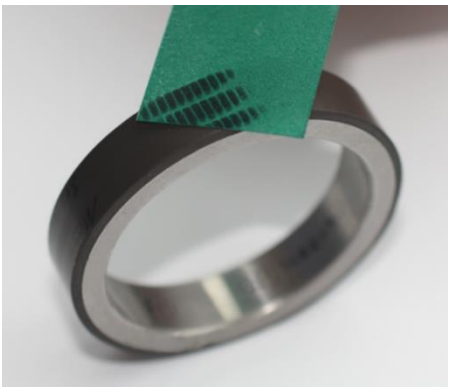

Fig. 3. Magnetisation pattern on a pole ring (Image source: Sensitec GmbH).

II. PROBLEM DEFINITION

There is currently no common terminology or standardised rules for design drawings for the representation of the mechanical and magnetic parameters of magnetic measurement scales (Fig. 4).

Fig. 4. Magnetic measurement scales: Scales (left) and pole rings (right) (Image source: Sensitec GmbH)

The individual steps in the value chain (Fig. 5) are often undertaken by different players and there is usually a need for coordination regarding the mechanical and magnetic properties of the dimensional scale. Incomplete information and different designations lead to misunderstandings and errors that result in lost time and increased costs in the development and application of magnetic measurement systems.

III. SOLUTION APPROACH: DIN SPEC

The creation of a document by means of DIN SPEC is considered to be the shortest way to establish standards on the market directly from research.

DIN SPEC PAS (PAS = "Publicly Available Specification") is a consortium standard that is developed within a few months in small agile working groups and is not subject to outside consensus. The German standards organization DIN ensures that a DIN SPEC does not contradict any existing norms or standards. The standards can also be published internationally and also be the basis for a subsequent “full” DIN standard (Fig. 6).

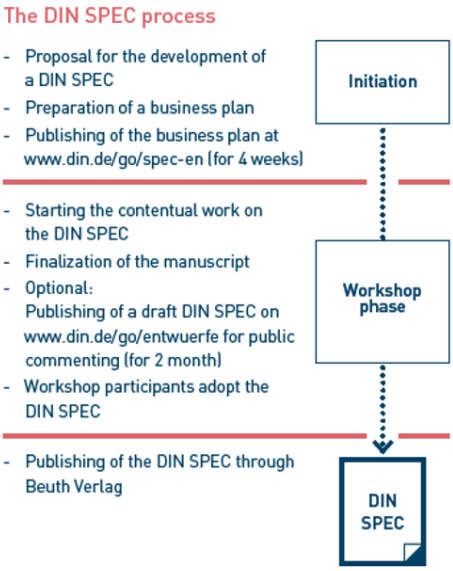

Fig. 6. Creation of a DIN SPEC (Image source: DIN)

DIN currently has more than 150 ongoing and published DIN SPEC according to the PAS procedure. The range of topics includes, for example, terminology, classification, measurement, testing, process and interface standards, guides or reference architecture models on the various innovative topics. The initiators of the standards come from the manufacturing industry, the service sector or from science; they include large companies as well as start-ups and SMEs.

The consortium for DIN SPEC 91411 "Requirements for the technical representation of magnetic dimensional standards in design drawings" consisted of participants (Table 1) covering all stages in the value chain (Fig. 5):

- Magnet manufacturers
- Sensor manufacturers
- Encoder manufacturers
- Research institutions

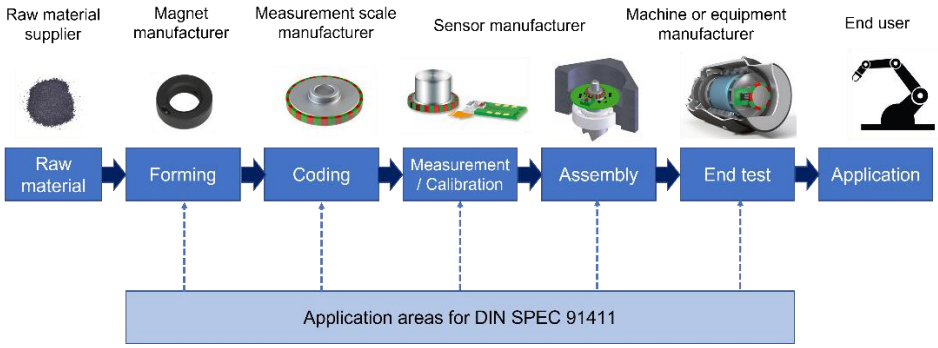

Fig. 5. Areas of application for DIN SPEC 91411

The participants were almost exclusively members of the Innovation Platform for Magnetic Microsystems INNOMAG e. V. (www.innomag.org). This network brings together the interests and potentials of manufacturers, service providers and users as a network. Founded in February 2007, the network is based in Kaiserslautern, Rhineland-Palatinate, and currently has over 40 members.

Table 1. Companies involved in the consortium.

Company	Location
Balluff GmbH	Neuhausen a.d. Fildern
Baumer Hübner GmbH	Berlin
Bundesanstalt für Materialforschung und -prüfung (BAM)	Berlin
Bogen Electronic GmbH	Berlin
Elsoma GmbH	Schwerte
Festo SE & Co. KG	Esslingen
ITK Dr. Kassen GmbH	Lahnau
INNOVENT e. V.	Jena
Fritz Kübler GmbH	Villingen-Schwenningen
Magnetfabrik Bonn GmbH	Bonn
Matesy GmbH	Jena
Sensitec GmbH	Wetzlar
TE Connectivity Sensors Germany GmbH	Dortmund

For the members of INNOMAG e. V., there were five main reasons for creating a DIN SPEC to standard-ise the representation of magnetic dimensional scales:

- Network: The DIN SPEC process promotes exchange with relevant market participants. This leads to further networks with key players: the requirements of manufacturers and customers flow into the common standard.
- Recognised: Well established worldwide, the DIN brand ensures maximum trust in the market. The innovation thus enjoys acceptance among potential users and investors.
- Plug & Play: The DIN SPEC process aligns the innovation with the current state of the art. Users can thus work with the innovation without hurdles.
- Simple: DIN organises the entire DIN SPEC project. This saves time to focus on content and networking
- Fast: DIN SPEC can be created and published within a few months. DIN SPEC prepared ac-cording to the PAS procedure are made available free of charge as a download at www.beuth.de.

IV. RESULTS

The consortium has developed a DIN SPEC standard for the uniform representation of magnetic dimensional standards. A total of 20 employees from 13 companies - mainly members of the Innovation Plat-form of Magnetic Microsystems INNOMAG e.V. - have finally presented a solution to this long-known problem with DIN SPEC 91411 "Requirements for the technical representation of magnetic dimensional standards in design drawings" after almost three years of cooperation.

The creation of DIN SPEC 91411 began in June 2019 at a kick-off meeting in Berlin and originally the document was to be completed by June 2020. Due to the onset of the COVID crisis, there was a significant delay in implementation as it was very difficult at times to organise the necessary project meetings. The draft publication took place in December 2021, after which there was a two-month period during which other interested parties could make additions to complete the document. The final publication of the German-language main document [10] took place in August 2022. The English language translation was published in January 2023.

The new standard has different contents that help to specify the description of magnetic dimensional standards. To set a framework for the DIN SPEC, a new taxonomy of magnetic dimensional standards was developed (Fig. 7).

This taxonomy describes all common dimensional standards and offers designations for an unambiguous assignment of a scale or pole ring and the associated magnetic tracks according to the following parameters:

- Type of measuring standard
- Form
- Track alignment
- Magnetisation
- Track type
- Track length

Subsequently, a glossary or dictionary was created with corresponding symbols, equations, units and auxiliary graphics (Fig. 8) for mechanical and magnetic parameters in relation to dimensional standards (pole rings, scales). The aim was to develop a main document based on this, in which the specification for dimensional standards is defined more precisely and presented more clearly, so that errors and misunderstandings can be avoided in the future.

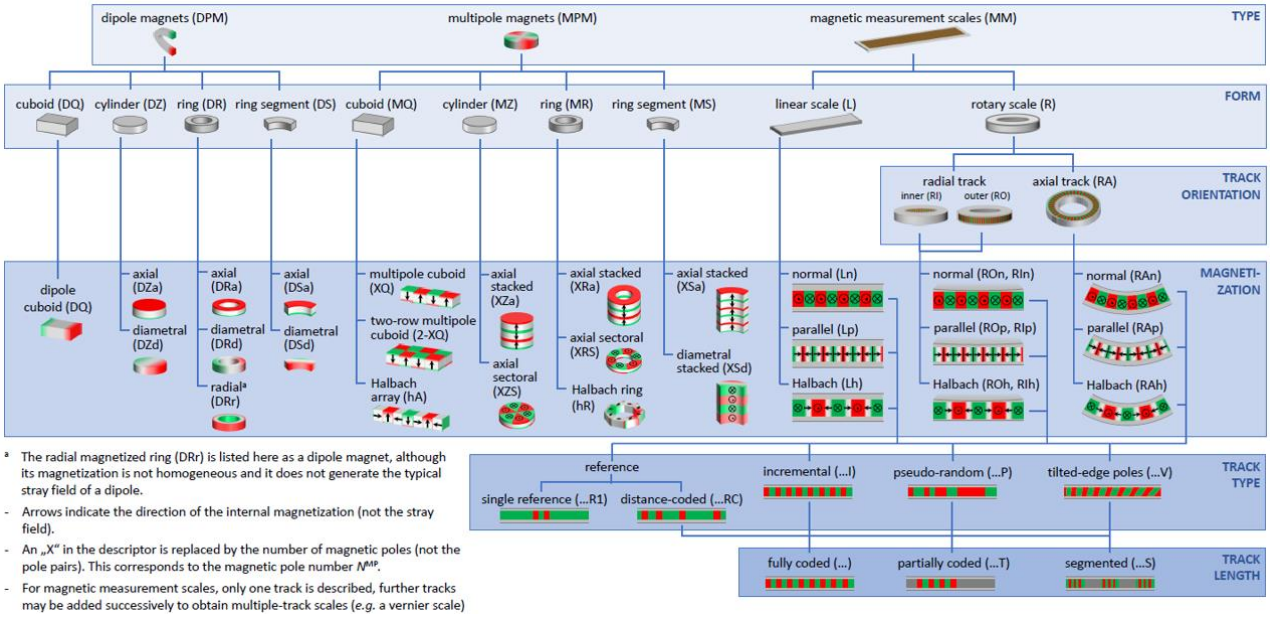

Fig. 7. Taxonomy of magnetic measurement scales (Image source: INNOMAG e.V.)

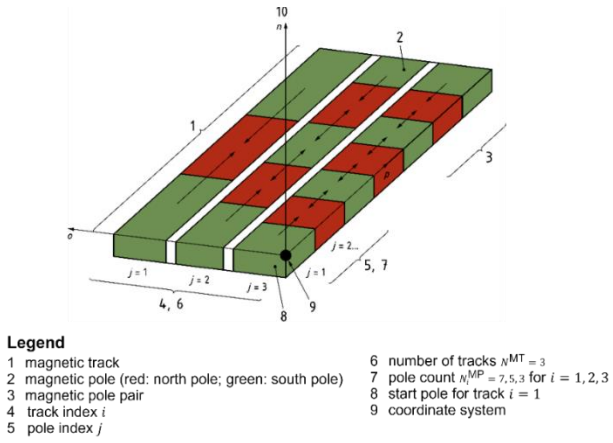

Fig. 8. Auxiliary graphic: Terminology linear scales

To support the practical implementation, the main document was supplemented by several example drawings (Fig. 9). Different types of dimensional standards were shown with the required track, pole and sensor data. Furthermore, the drawings were provided with DIN-compliant form and position tolerances to provide assistance in the mechanical description of the dimensional scale.

V. SUMMARY AND OUTLOOK

Magnetic measuring systems are increasingly used in numerous fields of application. However, there was a lack of standardisation of the representation of magnetic measurement scales. In the creation of DIN SPEC 91411 "Requirements for the technical representation of magnetic measurement scales in construction drawings", a taxonomy, glossary and example drawings were created. DIN SPEC 91411 was successfully published in August 2022 and already actively used by several consortium members. The English version is also now available. The new DIN SPEC standard helps to avoid unnecessary errors in the selection, design and procurement of magnetic measurement scales. The way is the goal: The consortium work not only had the new standard as a result, but also provided a very effective forum for knowledge ex-change between the consortium members. Another DIN SPEC project was started under the auspices of INNOM-AG e. V. as a logical follow-up to DIN SPEC 91411. DIN SPEC 91479 deals with the characterisation of magnetic measurement scales. The aim is to establish a common terminology and define standardised rules for test conditions, measuring equipment and measuring procedures. DIN SPEC 91479 is scheduled for completion during 2023.

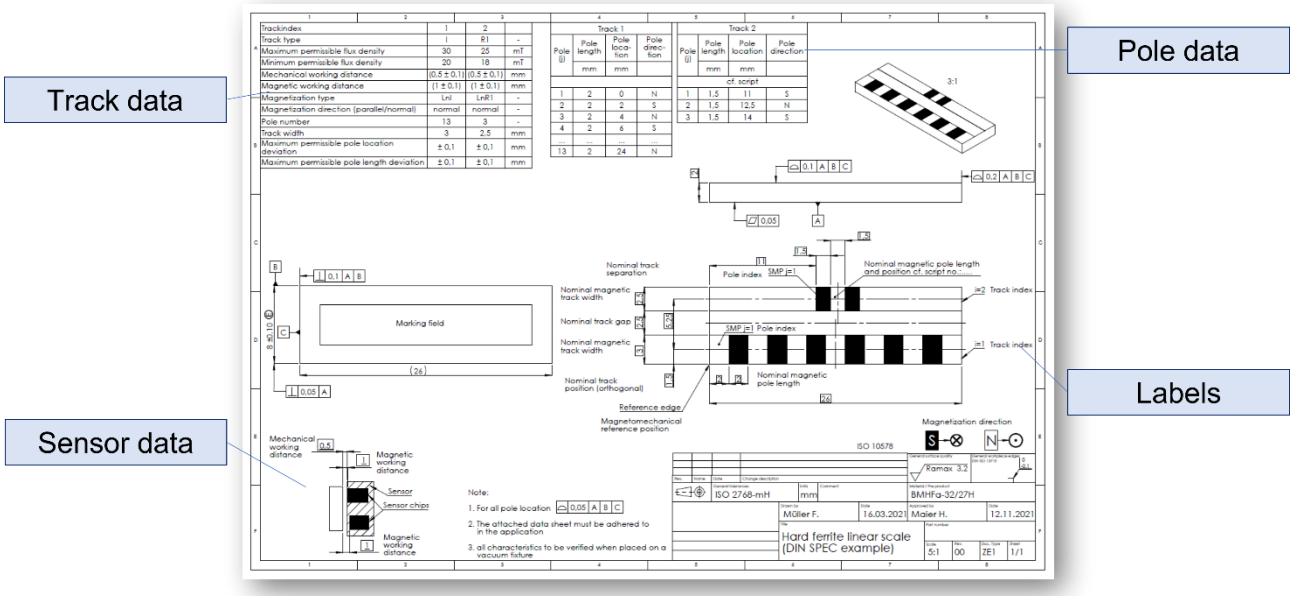

Fig. 9. Example drawing with additional data and labels

VI. REFERENCES

[1] Cassin, W., Kuntze, K. & Ross, G.; Dauermagnete – Mess- und Magnetisiertechnik (3rd ed.), Expert Verlag, Renningen, 2018.

[2] Michalowsky, L. & Schneider, J. (Eds.); Magnettechnik - Grundlagen, Werkstoffe, Anwendungen (3rd ed.), Vulkan Verlag, Essen, 2006.

[3] Schwegler, D. & Rapp, R.; Permanentmagnete - Werkstoffe, Magnettechnik, Anwendungen, Verlag Moderne Industrie, Munich, 2016.

[4] Hilzinger, R. & Rodewald, W.; Magnetic Materials - Fundamentals, Products, Properties, Applications, Publicis Publishing, Erlangen, 2013.

[5] Coey, J.M.D.; Magnetism and Magnetic Materials, Cambridge University Press, Cambridge, UK, 2010.

[6] Cullity, B.D. & Graham, C.D.; Introduction to Magnetic Materials (2nd Edition), IEEE Press/John Wiley, Hoboken, USA, 2009.

[7] Hering, E. & Schönfelder, G. (Eds.); Sensoren in Wissenschaft und Technik - Funktionsweise und Einsatzgebiete, Springer Vieweg, Wiesbaden, 2018.

[8] Schiessle, E.; Industriesensorik - Sensortechnik und Messwertaufnahme (2nd ed.), Vogel Business Media, Würzburg, 2016.

[9] Zielke, D.; Sensorsysteme - Mikrosensoren und ihre Anwendung, Dirk Zielke, Bielefeld, 2019.

[10] DIN SPEC 91411:2002-03 "Requirements for the technical representation of magnetic dimensional standards in construction drawings", Beuth Verlag, Berlin, 2022.

26th IMEKO TC4 International Symposium
24th International Workshop on ADC and DAC Modelling and Testing
IMEKO TC-4 2023
Pordenone, Italy / September 20-21, 2023

Pole positioning for precise magnetic measurement systems

Sebastian Rivera[1], Dr. Rolf Slatter[2]

[1,2] *1st ITK Dr. Kassen GmbH, Beim Eberacker 3, 36533 Lahnau- Germany, s.rivera@itknet.de*

***Abstract* – Modern drive systems rely in terms of accuracy and robustness on the quality of the used position sensors. For high accuracy applications optical position sensors are dominating the market with a trend towards more magnetic systems as their robustness in the field is superior compared to the optical counterparts. While the sensor itself has a great impact on system accuracy, the used scale or pole wheel is of similar importance when evaluating system architectures. ITK presents in this paper a machine setup for high accuracy, single pole writing machines either for linear or rotary magnetic scales. Baseline for the software architecture is the newly released DIN SPEC 91411 which unifies the nomenclature for magnetic measurement system. In addition the paper focus on a systematic approach to also measure the magnetic accuracy. Furthermore, new developments in write head design are presented as new hard magnetic coatings require higher fields for magnetization.**

I. INTRODUCTION

In recent years the development of improved magnetoresistive [1] and hall-effect based sensors as well as new techniques for manufacturing improved magnetic scales has led to an increased usage of magnetic angle- and length measurement systems [2]. Such systems typically comprise a linear or rotational magnetic scale in combination with a sensor head incorporating one or more magnetic sensors (Fig. 1). The magnetic scale can feature different patterns of north and south poles to provide incremental or absolute measurement possibilities.

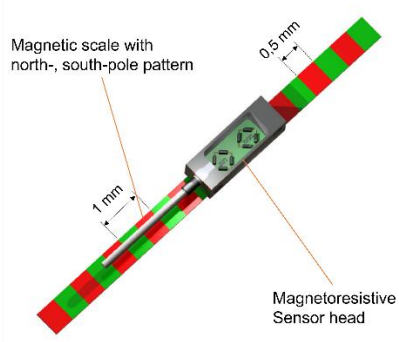

Fig. 1: Typical magnetic length measurement system

A first challenge in the sometimes complex supply chain for magnetic scales is given in the non-unified nomenclature and definitions on how to define drawings and measure the quality of the product. Magnetic scales differ to optical ones in one important aspect, the amplitude of the written pole is not a constant, binary code. For optical scales quality measurements are comparable to any mechanical part which is more complex for the magnetic solutions where amplitude and position depend on the type of measurement sensor and experimental setup.

The quality of the magnetic code depends on a high number of different aspects. Many of the parameters are material or process related, however the definition of who measures in what distance with what sensor is often the main point of discussion between two partners in the supply chain. Just the runout difference of 2 test setups (e.g. outgoing inspection at supplier vs. incoming inspection at customer) with identical reference sensors might have a big impact in comparing measurement results.

In a first step the nomenclature was unified for the supply chain within the recently published DIN SPEC 91411 [3]. In addition to this ITK is again part of the consortium for the second and next DIN SPEC 91479 – characterization of magnetic measurements scales and pole wheels.

Both DIN SPECs form the baseline for machine concepts at ITK and thus provide a guided approach for customers to produce scales and pole wheels (Fig. 2).

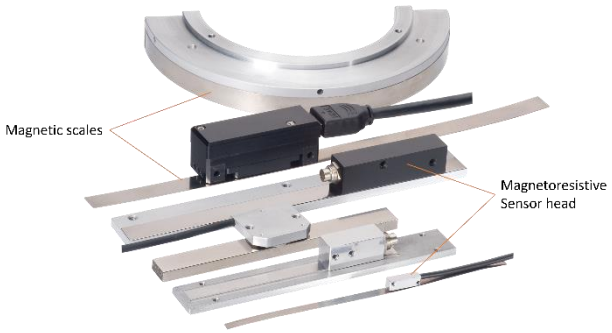

Fig. 2: Typical magnetic scales

The paper provides an overview on how the DIN SPEC

is transferred into the latest standard of magnetization machines and in addition insights for the development of new write heads are provided.

Baseline motivation for ITK in this business sector is derived from a lot of empirical know-how in producing and using magnetic scales. Combined with state-funded projects ITK has used empirical data to feed analytical approaches to understand the different parameters that influence the end result of the scale or pole wheel.

II. MAGNETIZATION MACHINES

ITK offers two fundamental concepts for high precision magnetization machines.
3 provide the DIN SPEC 91411 overview for nomenclature for which ITK's magnetization machines are primarily designed.

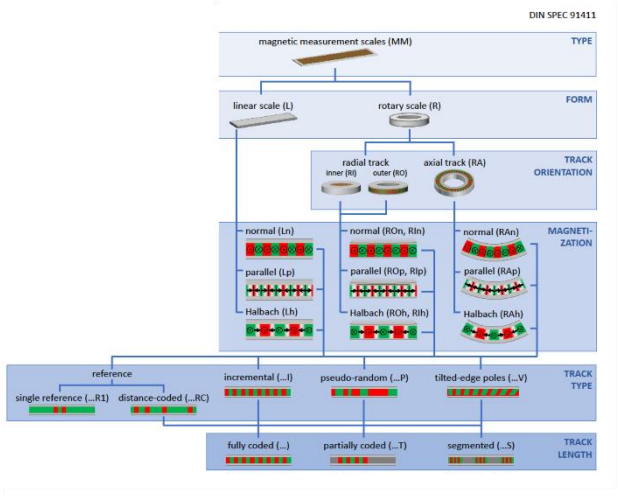

Fig. 3: Extract from DIN 91411[1]

A. RMP – the rotary solution

Apart from the requirement to reflect the nomenclature of DIN SPEC 91411 there is also a requirement for higher accuracy combined with higher flexibility to deal with different pole patterns and different scale geometries. Common features of the new magnetization machine generation are direct drives for the moving axes, high resolution reference measurement systems and powerful graphic interfaces for machine control. 4 provides an overview of the baseline concept and design of ITK's magnetization machines for pole wheels.

Fig. 4: RMP machine

The machine setup is flexibly designed for up to 5 stations with positioning axes in x- and z-directions. All axes are in-house developed and produced. Individualization starts at this point, where customers have differing requirements to the end product. The main design idea is a setup with 3 axes equipped to fulfill the basic functions:

- Runout measurement
- Magnetization
- Magnetic measurement by calibrated Hall sensors

Furthermore, the machine supports on request identification of workpieces (e.g. DMC code) or printing of serial numbers.
Designed as a standalone production machine a communication with the machine can also be realized via OPC UA protocol.

B. LMP – the linear solution

Based on the same principles also magnetic linear scales are highly dependent of the quality of the linear coding. The LMP machines offer a semi-customized solution for each application, assuring coding length as required.

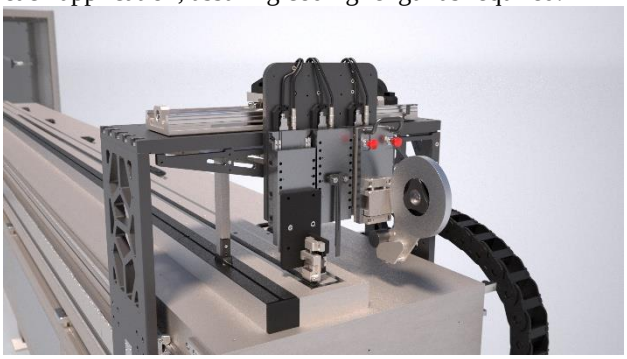

Fig. 51: LMP design

5 shows the basic setup that is a gantry bridge equipped with several functional z-axes for the individual customer needs. The magnetic coding is triggered by a high precision laser interferometer. The drive technology used is the patented ITK linear motors that are not only maintenance free, but also provide a direct driven solution without mechanical backlash.

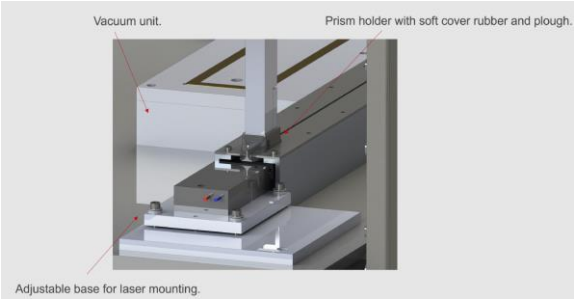

Fig. 6: Details of LMP design

Fig. 6 depicts the design details for the laser interferometer and a metal bar which reflects the beam that moves along with the gantry bridge. The vacuum unit in the background assures flat positioning of the magnetic scale while being processed.

III. WRITE HEAD DESIGN

Magnetization heads or better named write heads are available for either in-plane (ip) or out-of-plane (oop) writing [4]. On the market available solutions were developed years or even decades ago [5] and hardly cope for new requirements that hard magnetic coatings require nowadays.

Within the BMBF-funded KMU Innovativ Project ELM2 the fundamentals and technical limits of currently used inductive write heads for ip writing are analyzed in detail. The development target for a new inductive write head as needed for e.g. pseudo-random code writing process was set to hard magnetic coatings. As such coatings are extremely thin, the common knowledge on magnetism as available for bulk magnets might not be fully applied anymore. Target parameters to meet with the write head were therefore experimentally set combined with a literature analysis on the topic[6]. A simulation based on a carefully selected number of parameters was done iteratively in order to optimize the new write head design.

Variation of core size, core ratio, air gap, etc. lead to an optimized design, the iteration process can be seen in Fig. 7. The ideal design provides a very sharp peak, exceeding the set design targets of 1000kA/m. Within this approach the focus was set on the write head to be able to provide sufficient magnet field for various materials, however it is well known that the interaction between write head and selected material needs to be considered and simulated as well.

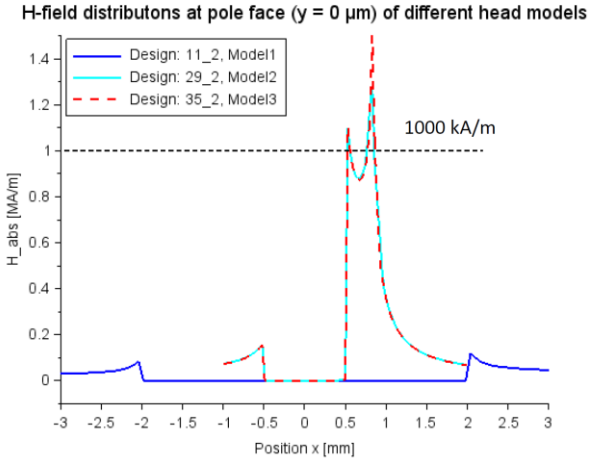

Fig. 7: Iteration of write head designs[4]

The new write head design is currently in final design stage and will be available with first results just before the conference. Results will be presented in the presentation.

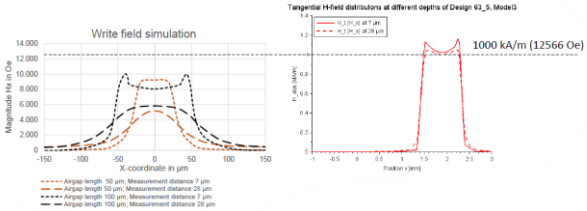

Fig. 8: Comparison of existing vs. new write head[4]

Fig. 8 compares the currently in use write head with the new design by simulation.

The higher magnetic fields are the result of bigger sized write heads. While the overall dimensions were kept, only the width of the write head was significantly changed.

The different write head dimensions are given in Fig.9

and Fig. 10.

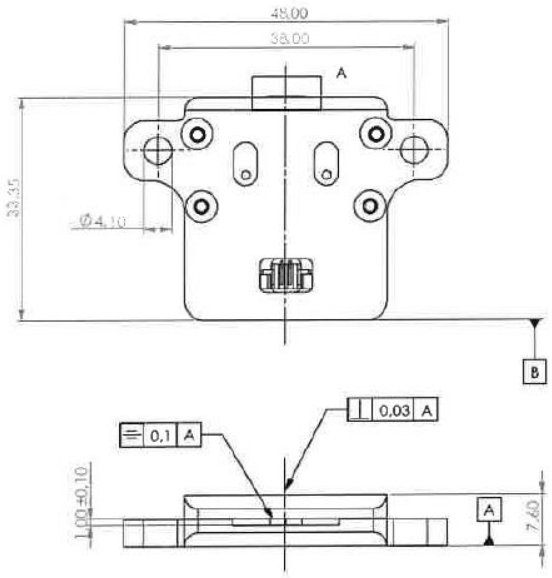

Fig. 9: Outline drawing of former write head

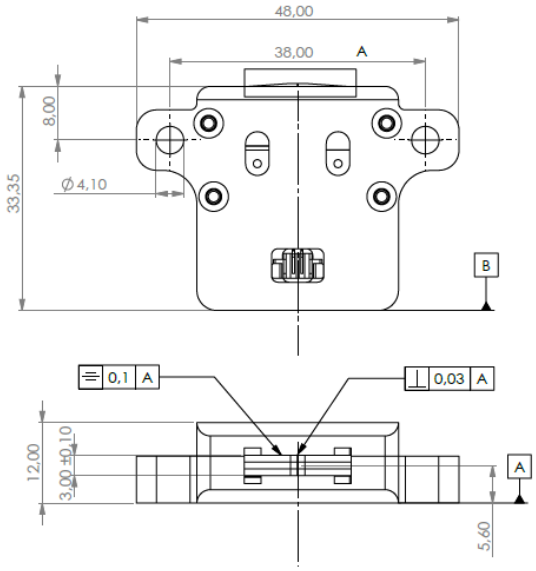

Fig. 10: Dimensions new write head

Simulation results are summarized in Table 1 with the main differentiation results being the higher writing depth and a factor 3 higher writing fields.

Table 1: Old vs. new write head

Parameters	Write field @ Write Depth [kA/m]	Write Depth (nominal) [µm]	Track Width [mm]
MIP in-plane head (for ITK, 3-mm Head)	≥ 477	20	3
MIP out-of-plane head (for ITK, Design 73_2, Model 3)	≥ 1700	110	5

IV. OUTLOOK

The latest generation of magnetization machines are now ready for market entry and will further develop by individual customer needs. First test results with the newly designed write head will be available and presented at the conference.

Acknowledgement:
The work described in this paper has been partly funded within the German state-funded BMBF-project „KMU-innovativ: Entwicklung einer hochpräzisen Linear-Magnetisieranlage für die Beschreibung von magnetischen Maßstäben (ELM2)“ Project No.: 02P21K060

REFERENCES

[1] Paul, J., “True power on magnetic position sensor system with submicron accuracy“, Proc. of 15th MR-Symposium, Wetzlar, 2019

[2] R. Slatter, „High resolution miniaturized magnetic linear measurement systems for small- and micro-actuators”, 12th International Conference for small- and micro-sized actuators”, Würzburg, 2019

[3] DIN SPEC 91411 “Requirements for the technical representation of magnetic measurement scales in design drawings”, Beuth Verlag, July 2023

[4] M.Rechel, P. Taptimthong, “Meilensteintreffen ELM 2, ITK internal document“

[5] C. Möller, U. Loreit, F. Dettmann, „Neues Verfahren zum berührungslosen Magnetisieren von Maßstäben und Polrädern für die MR-Sensorik, Proc. of 5th MR Symposium, Wetzlar, 2001

T. Schrefl, M.E. Schabes, D. Suess, and M. Stehno, „Dynamic Micromagnetic Write Head Fields During Magnetic Recording in Granular Media, IEEE TRANSACTIONS ON MAGNETICS, VOL. 40, NO. 4, JULY 2004

26th IMEKO TC4 International Symposium
24th International Workshop on ADC and DAC Modelling and Testing
IMEKO TC-4 2023
Pordenone, Italy / September 20-21, 2023

Rapid Prototyping of Vehicle Software Defined Functions

Jan Sobotka[1], Jiří Novák[1], Jiří Pinkava[1]

[1]*Czech Technical University in Prague, Prague, Czech Republic, jan.sobotka@fel.cvut.cz*

***Abstract* – A modern car is made up of a considerable amount of software running on many Electronic Control Units interconnected by communication infrastructure. Together it creates a rigid system, which is not easy to modify for running modified or custom code to implement new vehicle functions or gathering scientific data. The paper presents a modified (electric) vehicle architecture allowing rapid prototyping. The architecture enables control of particular vehicle functions by an independent computer, arbitrary vehicle data acquisition, and offers an interface for communication with the driver. Car-dependent and independent layers are used to provide an abstraction and hide details of a specific car model.**

I. INTRODUCTION

Passenger cars are object of research activities focused on many research areas. They include, e.g., vehicle stability control, passenger comfort, simple and advanced driver assistance systems, and so on, up to autonomous driving technologies. Implementing a new algorithm into a standard production car to validate it is often as challenging for an independent researcher as the research itself. Today passenger cars mostly use a domain-oriented architecture of in-vehicle electronic systems, which relies on a high number of Electronic Control Units (ECUs) interconnected by different networking technologies [1]. Details about particular ECUs functionality [2], as well as data communication [3] over the in-vehicle networks, are subject of public access restrictions. In addition, each car manufacturer uses its own architecture of internal electronic systems and in-vehicle networking. The complexity and lack of information for implementation on a real car often lead to the validation of research results on models of the vehicle or its subsystem [4]. These models, either intentionally or by mistake, often miss important aspects of reality, and the validity of the research validation is then limited. In some cases, the research results should be validated by the driver and passengers (user experience); here, the actual implementation of the research result is essential. To provide solution, the HW/SW framework was designed and developed, which hides the vehicle-dependent implementation details. It provides high-level API allowing information acquisition from the vehicle (e.g., vehicle speed, internal and external temperature, seat occupation, air condition settings) and simultaneous control of selected vehicle functionalities (e.g., air condition settings, adaptive cruise control settings, infotainment settings, drive mode settings) in a vehicle (and possibly the vehicle manufacturer) independent way. A new prototype functionality can thus reside on the top of the framework, utilize the data available from vehicle information systems, and control vehicle settings according to the researcher goals.

II. E/E ARCHITECTURE MODIFICATION ANALYSIS

Electronic functionalities are implemented in various ways. It depends on the used E/E (Electrical/Electronic) architecture [1]. Typical vehicle architecture evolves from several isolated systems over communicating specialized ECUs towards general ECUs over time. This section analyzes modification possibilities for the rapid prototyping of new software-defined functionalities.

A. ECU Software Modification

A natural way for rapid prototyping of a new feature is a modification of ECU software. The situation is complicated by two facts. First, running own code on an ECU without manufacturer support is a challenging task [5], as often even the car manufacturer does not have the original source codes available. Second, I/Os are distributed over multiple ECUs; thus, code modification in a single ECU might not be sufficient. For rapid prototyping, it is necessary to have the ability to extend existing code for a new feature. Running its own software on ECU hardware thus leads to the implementation of complete ECU software, including communication with the rest of the car. This is nearly impossible for an independent researcher, so the following methods can be used.

B. Physical Signals Modification

Every vehicle electronics system uses some sensors and actuators. Modification of input signals, as well as output signals, is the first possibility for alternating the system behavior. This approach is widespread in Hardware-in-the-loop (HIL) testing [6]. The disadvantage of this technique is a limited generality. Different types of sensors and actuators require specific solutions. Also, the concurrent usage of I/O for an existing and prototyped function could be problematic.

C. Communication Modification

Modern passenger cars reside on in-vehicle communication. Several communication standards are used. The most commons are CAN/CAN FD, LIN, Automotive Ethernet, and FlexRay. In the rest of the paper, CAN/CAN FD technology is assumed. A widespread scenario is a communication among the ECUs based on the exchange of entities called signals. An example of the signal is outside temperature measured by an ECU and broadcasted to other network nodes by CAN bus [7]. Switch status (pressed/released) checked and transmitted in respective CAN message by one ECU can be another example. The message is received by other ECU and used to control the output as required. To change the switch state, the dedicated communication device that filters and/or modifies the original message and sends a modified one toward the ECU of interest should be used.

D. Service-Oriented Architectures

Not only signal communication is used in modern vehicles. Service-oriented protocols are becoming an integral part of modern cars. These protocols can either be proprietary or open. An example of an open protocol is Scalable serviceOriented MiddlewarE over IP (SOME/IP) [8] as a part of AUTOSAR. A representative of a proprietary protocol can be BAP (Bedien und Anzeigeprotokoll), used in Volkswagen Group vehicles. The advantage of services-oriented communication is that requests for service provided by ECU can come from any other ECU. And thus, the service requests can be generated using a suitable communication interface connected to a bus.

III. CAR ARCHITECTURE FOR RAPID PROTOTYPING

The presented platform for rapid prototyping of new vehicle functionalities uses the principles described above in paragraphs C. and D. Overall architecture is depicted in Fig. 1. The central element is the industrial computer Advantech ARK-3520P. Used technologies require some up-to-date desktop Linux distro. In our case, it is Ubuntu 22.04.

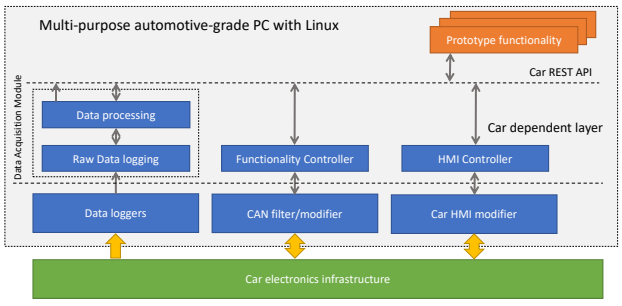

Fig. 1. Car Architecture for Rapid Prototyping

All the platform services are available at the Car REST API [9], which is vehicle (and vehicle manufacturer) independent. The car-dependent layer consists of three modules, providing for vehicle data acquisition, required vehicle functionality control, and access to vehicle infotainment screen (user-defined screens, driver touch responses). Each of these software modules is supported by the hardware modules that physically interfere with the car's functions (see Fig. 2).

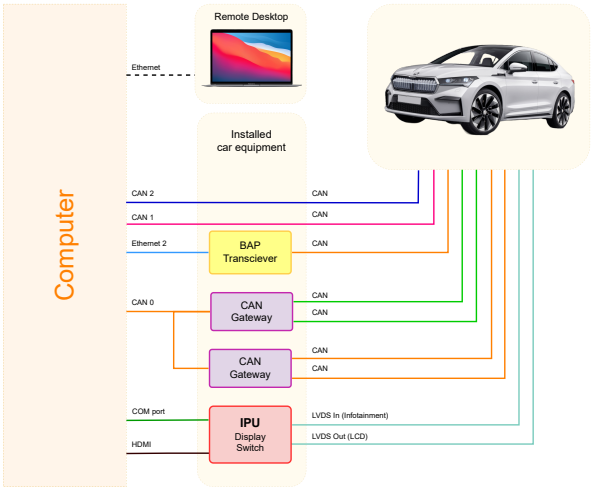

Fig. 2. Car Hardware Setup

A. Data Acquisition Module

The Data Acquisition module is implemented using Data loggers HW layer, consisting of external CAN FD/USB interfaces. They are supported by the native Linux CAN interface SocketCAN. DAQ module receives CAN messages from an in-vehicle network and interprets them using industry-standard .dbc definition file into the physical quantities. Simultaneously the BAP protocol messages (carried in specific CAN messages) are parsed, providing complete information about the vehicle state and activities. The stream of acquired vehicle signals (in JSON format) is pushed to the TCP endpoint configured (using the Car REST API) from the prototyped application. Each signal value is accompanied by its timestamp.

B. Functionality Controller Module

The preferred way to control the car functionalities is real-time manipulation of in-vehicle communication networks. The data manipulation system structure is shown in Fig. 3. To independently control selected vehicle functionalities, the CAN Gateway (GW) modules (providing real-time manipulation with CAN message) are inserted into the internal vehicle communication paths. Their activities (which are independent of specific vehicle functionality that should be initiated) are controlled by a Func-

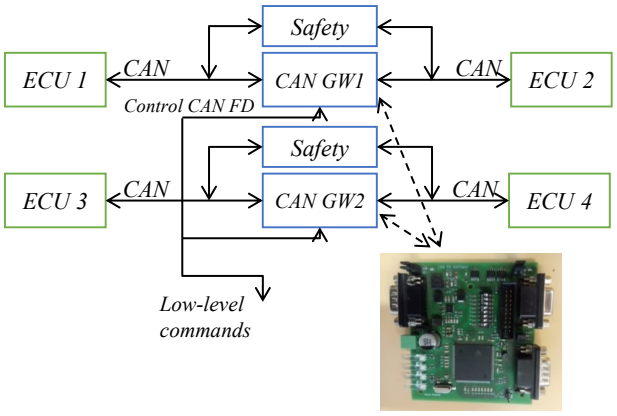

Fig. 3. CAN Gateway Application Principle

tionality Controller module. The CAN Gateway allows blocking/passing selected messages, modifying their content (with respect to some application layer constraints), and transmitting/monitoring chosen messages. The CAN Gateway functionality is vehicle and function independent. Thus the list of supported functionalities can be extended without the GW firmware modification (only the Functionality Controller module will require a software update in such a case). Service oriented communication used to control specific car functionalities is also implemented within this SW module. Each CAN Gateway is equipped with an emergency circuit – in case of any problem, the CAN Gateways are bridged, and the original CAN interconnection is restored to keep the driver and passengers safe.

C. HMI Controller

Human-Machine Interface (HMI) Controller module provides for communication with driver/passengers. It relies on video inserter and CAN GW hardware support. The overall HMI subsystem structure is shown in Fig. 4.

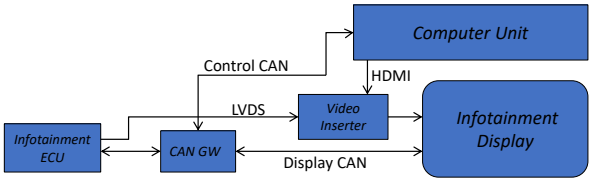

Fig. 4. HMI Control Application Principle

Video inserter is placed between the vehicle Infotainment ECU and its display. It allows switching between the standard video source (Infotainment ECU) and the user prototype generated video (HDMI output of Linux computer). In case the prototype SW needs to use the car display, the display is switched to the prototyped screen, and the user response is awaited (see Figure 5). The display is connected by the FDP-Link interface. The display unit supports touch-screen functionality – user actions are reported from the display to the Infotainment ECU by CAN messages. The CAN GW module is used here again, allowing redirection of touch screen message of interest, when the response on prototype generated screen is expected. Simultaneously it blocks the touchscreen messages transport from display to Infotainment ECU when prototype software generated screen is active (to avoid false car Infotainment ECU reactions).

IV. RESULTS - PLATFORM USAGE EXAMPLES

Rapid-prototyping platform allow its user to design and validate applications that may change the way how drivers use their cars. The application can use information from in-vehicle networks (Data Acquisition subsystem), control selected car functionalities (Functionality Controller subsystem), and use internal user interface (HMI Controller subsystem), all available at the vehicle-independent car REST API. To evaluate the platform's functionality and to show its ease of use, we have designed and implemented two groups of examples. Within the first group, there are classical (rule-based) applications, and within the second, the machine learning (ML) based applications. All the below-described applications can be configured using car HMI.

A. Classical Application Examples

The first example application uses car-provided information about the actual location and external map sources to get information about the tunnels. It implements automated activation of internal air circulation when the car approaches the tunnel and switches it back when the tunnel is left. This functionality can be configured as fully autonomous or user-confirmed. The second example application uses car-provided information about the internal temperature and seats occupation. If the temperature is below the limit, occupied seat heating is activated. The temperature limits and heating level can be configured individually for particular seats. This application can easily be extended to support automated control of seat ventilation if supported by car hardware.

B. Machine Learning based Examples

The third example application again uses the car-provided information about the actual location. Simultaneously it acquires information about the ACC (Adaptive Cruise Control) activity and required car speed (in case the ACC is active). During the training phase, the ML model learns the way the driver uses ACC. When trained, its predictions are used to (de-)activate the ACC and set the required speed (after the simple confirmation from the driver (see Fig. 5). The fourth implemented example is focused on car infotainment. On weekday mornings, the driver

regularly takes the children to school. They always ask him/her to activate the function of playing songs from their mobile phone via infotainment. An ML-based application receives information about the date/time, seat occupation, and infotainment setting. It learns the usage pattern and autonomously activates the audio source to the children's phone when they get on and back to the driver's favorite radio station when they get off.

Fig. 5. Prediction Based ACC Activation Offer

V. CONCLUSION

The platform for rapid prototyping of new vehicle features was presented. It addresses the problem of rapid prototyping or evaluating new software-defined functions, algorithms, and data acquisition on production vehicles. The main capabilities are data acquisition of information available on in-vehicle networks, independent control of selected vehicle functionalities, and HMI access. The used approach can be adapted to vehicles of different manufacturers, but quite detailed information is required. The presented platform was incorporated into Škoda Kodiaq and Škoda Enyaq Coupé RS iV. Thanks to the shared vehicle platforms, it is pretty straightforward to implement the proposed solution into any car of the VW group.

Further rapid prototyping platform development is planned to focus on three areas. First is the usage of SOME/IP services over the Automotive Ethernet within the Functionality Controller. Second is the extension of the platform hardware layer with LIN Gateways. They provide similar services as CAN Gateways described above, but for the LIN networks. Finally, the HMI will be improved to support voice input (instead of touchscreen response, which distracts the driver much more).

ACKNOWLEDGMENT

This research has been realized using the support of Technology Agency of the Czech Republic, programme National Competence Centres, project #TN01000026 Josef Bozek National Center of Competence for Surface Transport Vehicles. This support is gratefully acknowledged.

REFERENCES

[1] A. G. Mariño, F. Fons, and J. M. M. Arostegui, "The future roadmap of in-vehicle network processing: A hw-centric (r-) evolution," *IEEE access*, vol. 10, pp. 69 223–69 249, 2022.

[2] J. Van den Herrewegen, "Automotive firmware extraction and analysis techniques," Ph.D. dissertation, University of Birmingham, 2021.

[3] M. Zago, S. Longari, A. Tricarico, M. Carminati, M. G. Pérez, G. M. Pérez, and S. Zanero, "Recan–dataset for reverse engineering of controller area networks," *Data in brief*, vol. 29, p. 105149, 2020.

[4] X. Pan, C. Zivkovic, and C. Grimm, "Virtual prototyping of heterogeneous automotive applications: matlab, systemc, or both?" in *Proceedings of the 24th Asia and South Pacific Design Automation Conference*, 2019, pp. 544–549.

[5] P. Nasahl and N. Timmers, "Attacking autosar using software and hardware attacks," *2019 Embedded Security in Cars USA*, 2019.

[6] D. d. S. A. Loura, F. F. V. de Melo Ferreira, and R. C. da Costa, "Hardware-in-the-loop alternative approach for an esp verification," SAE Technical Paper, Tech. Rep., 2022.

[7] S. Yong, Y. Ma, Y. Zhao, and L. Qi, "Analysis of the influence of can bus structure on communication performance," in *IoT as a Service: 5th EAI International Conference, IoTaaS 2019, Xi'an, China, November 16-17, 2019, Proceedings 5*. Springer, 2020, pp. 405–416.

[8] D. Martin, L. Völker, and M. Zitterbart, "A flexible framework for future internet design, assessment, and operation," *Computer Networks*, vol. 55, no. 4, pp. 910–918, 2011.

[9] K. Relan, *Building REST APIs with Flask: Create Python Web Services with MySQL*, 1st ed. USA: Apress, 2019.

26th IMEKO TC4 International Symposium
24th International Workshop on ADC and DAC Modelling and Testing
IMEKO TC-4 2023
Pordenone, Italy / September 20-21, 2023

Quantum sampling modular setup for practical power measurements based on a programmable binary Josephson voltage standard

Bruno Trinchera, Paolo Durandetto, Danilo Serazio

INRiM-Istituto Nazionale di Ricerca Metrologica, Strade delle Cacce 91, 10135-Torino, Italy, b.trinchera@inrim.it

***Abstract* – The new quantum SI opens the route to link the base unit definitions to fundamental constants of nature. In the spirit of the quantum SI, a similar traceability route can be implemented for alternating electrical quantities, such as electrical power. Its implementation is summarized in the present paper along with the main steps about the realization of a quantum-based sampling power standard carried out in the framework of the EMPIR project Quantum Power. A programmable Josephson voltage standard (PJVS) based on a 1-V SNS binary array provides the traceability of the power standard. The PJVS has been integrated into an existing sampling power standard and its main purpose is the real-time calibration of high-precision waveform digitizers using a new synchronous quantum power multiplexer (SQPM). Measurement scenarios and experimental characterization aimed at evaluating the gain and phase errors of the system constituents, and in particular of SQPM, are presented.**

I. INTRODUCTION

In the new quantum SI, the quantum effects play a crucial role in the redefinition of the SI units. For example, electrical power measurement could be linked to fundamental constants of nature according to the expression,

$$P = U \cdot I = I^2 \cdot R = \frac{U^2}{R} \quad (1)$$

taking into account the toolbox of electrical quantum effects based on:

- the quantum current standard using the single-electron tunnelling effect (SET), $I = e \times f_{\mathrm{SET}}$;
- the quantum voltage standard using the Josephson effect (JE), $U_{\mathrm{J}} = n f_{\mathrm{J}} \frac{h}{2e}$;
- the quantum resistance standard using the quantum Hall effect (QHE), $R_{\mathrm{H}} = \frac{h}{e^2}$.

where: e is the unit of electric charge, h the Planck constant, n is the product between the Shapiro step order and the number of Josephson junctions, f_{J} is the irradiating microwave frequency and f_{SET} is the frequency controlling individually the tunneling of each electron. Both f_{J} and f_{SET} are traceable to the atomic frequency standard with negligible uncertainty (as low as 1×10^{-10}).

By combining the electrical quantum effects according to the Eq. 1 and substituting U by U_{J} and R by R_H, it is straightforward to get a set of equivalent mathematical expressions, shown in Table 1, linking electrical power to constants of nature, in particular to the product between Planck constant (h) and either one frequency squared or two distinct frequencies, which are in turn traceable to the primary atomic frequency standard.

Table 1. Power standard realization in terms of constants of nature by combining quantum electrical effects.

Quantum Effects Combination	Quantum Current Standard	Quantum Voltage Standard	Quantum Resistance Standard	Quantum Power Standard
JE & SET $\left(P = U_{\mathrm{J}} \cdot I\right)$	ef_{SET}	$nf_{\mathrm{J}}\frac{h}{2e}$		$nf_J f_{SET}\frac{h}{2}$
SET & QHE $(P = I^2 \cdot R_{\mathrm{H}})$	ef_{SET}		$\frac{h}{e^2}$	$f_{\mathrm{SET}}^2 h$
JE & QHE $\left(P = \frac{U_{\mathrm{J}}^2}{R_{\mathrm{H}}}\right)$		$nf_{\mathrm{J}}\frac{h}{2e}$	$\frac{h}{e^2}$	$n^2 f_{\mathrm{J}}^2 \frac{h}{4}$

JE and QHE have been used since 1990 for the practical realization of the Josephson voltage standard (JVS) and quantum Hall resistance standard (QHRS). From a practical point of view, the combination of JVS and QHRS, offers an interesting proof of concept and a straightforward route for establishing quantum traceability for power measurements in the framework of the new quantum SI. However, due to technological limitations, such a combination for practical quantum-based electrical power measurements and calibration purposes has not yet been pursued.

Non-quantum power standards, based on synchronized high precision digitizing multimeters equipped with suitable voltage and current transducers, have been developed and routinely used by NMIs [1] - [2] and

industrial laboratories for practical power measurements with relative uncertainty within 10 µW/VA (coverage factor k=1) at power-line frequency.

A different traceability route using a single electrical quantum standard, i.e. the JVS, and the sampling strategy has been described in [3] - [5]. Inspired by these developments, the same strategy has been revised in the framework of the EMPIR project 19RPT01 - Quantum Power [6]. The goal of the project is to design and realize a quantum power standard (QPS) by integrating existing programmable Josephson standards into sampling power standards.

The realization of the practical quantum sampling electrical power standard has been accompanied by the development of an open source software [7], measurement methods and algorithms suitable to provide real-time electrical power measurements benefiting from permanent integration of the Josephson voltage standard.

The paper is organized as follows: Section II describes the main purposely-built constituents of the quantum sampling wattmeter. Section III deals with the measurement scenarios implemented at the present stage of the development, and section IV reports the experimental results carried out during the testing of QPS constituents.

II. QUANTUM SAMPLING POWER STANDARD

The quantum sampling power standard has been designed and built using the modular concept, which allows the swapping of its main constituents depending on the measurement scenarios.

Figure 1 reports a simplified schematic of the QPS.

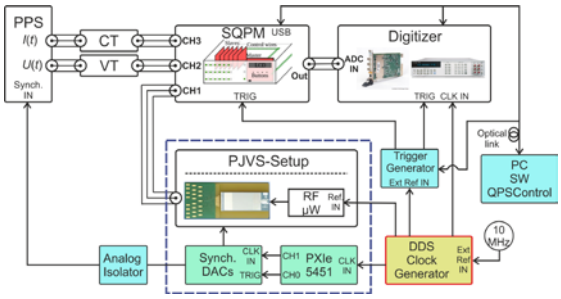

Fig. 1. Schematic diagram of the quantum sampling power standard implemented at INRiM.

Figure 2 reports a photo of the QPS setup developed at INRiM.

A. Programmable binary Josephson voltage standard

The main purpose of the programmable binary Josephson voltage standard (PJVS) is the real-time gain calibration of commercial high precision analog-to-digital converters (ADCs) or digitizing multimeters using staircase approximated sinusoidal waveforms ranging from Hz up to few kHz.

Fig. 2. Photo of the QPS setup.

The PJVS system has been designed and built in the framework of the project [6] using a commercial SNS (superconductor-normal-superconductor) array [8] containing 8192 Josephson junctions (JJs) divided into 14 binary segments in 64 parallel microwave stripline branches. The number of JJs for stripline is 128 and the JJs between each two successive dc contacts are 1, 1, 2, 4, 8, 16, 32,…, 4096. Each segment of the array is current-biased independently using a software-controlled voltage source. For a SNS array containing 8192 JJs, the maximum output voltage at the RF frequency f=70.000000038324 GHz, which is generated by a commercial RF synthesizer, when biased to the first Shapiro step is U=1.1857786427 V. The weight of the low significant bit that correspond to the PJVS voltage resolution is $U_{LSB} = f \cdot h/2e$=144.738369 µV.

The bias electronics used to switch on/off the single binary segments has been realized at INRiM starting from single commercial electronic boards. It has been further improved and updated with a new control software compared to the previous version described in [9]. Two commercial boards with up to 8 individually 16 - bit digital-to-analog converters (DACs) are synchronized to a common clock and trigger signals.

The synchronization signals are provided by an additional high-speed DAC phase locked to the 10 MHz

distributed reference signal coming from the INRiM atomic clock. All DACs boards are fitted in a separate optically isolated PXI chassis controlled by a dedicated PC. In general, up to 16 independent bias outputs are available, 13 of which are used to set the voltages across the array segments to $-V_n$, 0, $+V_n$, where V_n is the voltage of the n-th channel of the bias electronics suitable to drive the n-th array segment to the first Shapiro step.

The remaining outputs can be programmed for synthesis of suitable isofrequential sinusoidal and rectangular waveforms useful for synchronizing external equipment, such as AC generators, phantom power sources (PPSs) or multifunction calibrators to the PJVS bias source. Further details on the construction and characterization of the 1-V PJVS are reported in [9].

B. SQP-Multiplexer

The SQPM has been designed by INTI [10] and several versions have been independently built by the project partners. In general, for the realization of a single SQPM unit up to six independent slave boards are required in the configuration 2-to-1 (2-inputs and 1-output).

The outputs of two single 2-to-1 slave boards can be connected in parallel to form a single 4-to-1 slave board. The slave boards are equipped with photoMos relays, compared to other solid-state relays, introduce lower errors and noise in the measurement system. The SQPM is remotely controlled remotely using a master board based on an Arduino microcontroller connected to the PC by means of an USB interface.

The switching sequence contains the on/off state of the single relays and is prepared via software in a matrix form. It is transferred from the PC to the master board. The on/off aperture time of the relays is controlled by a switching event, which can be generated internally using the internal SQPM clock or by applying an external synchronization signal to its trigger input. To avoid ground loops the trigger input has been optically isolated. Figure 3 shows the full SQPM built at INRiM.

C. Modular sampling power standard

The sampling power standard identified for the integration of both PJVS and QPM is part of the modular power and power quality measurement setup developed at INRiM in the framework of the project 15RPT04-TracePQM. The low frequency (LF) part of the modular power measurement setup employs two synchronized high precision sampling DMM3458A and voltage and current transducers. It has been validated in the EURAMET.EM-K5.2018 international comparison, where a relative measurement uncertainty (k = 1) within 8 μW/VA at any power factor and applied voltage and current 240 V and 5 A, respectively, has been demonstrated [4]. To achieve such a measurement uncertainty, an improved traceability chain has been implemented, where all the single constituents of the modular sampling power setup have been calibrated against dc and ac electrical national standards.

A further step in uncertainty improvement can be achieved by shortening the present traceability chain through the integration of a PJVS for real-time gain and linearity calibration of the digitizers under almost real operating conditions.

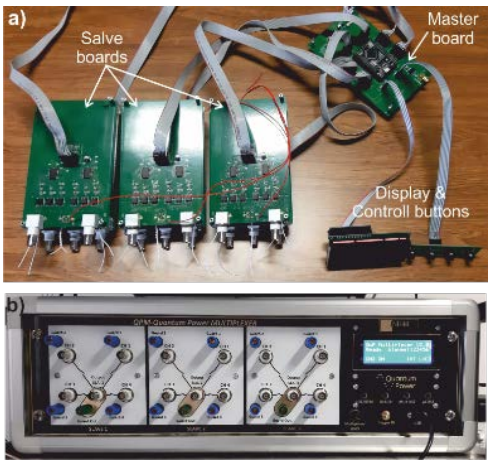

Fig. 3. a) Set of the multiplexer boards. b) photo of the SQPM developed at INRIM composed by three 4-to-1 slave boards.

III. QPS MEASUREMENT SCENARIOS

One of the main features of the QPS concerns the multiplexing strategy. It enables multiple electrical power measurement scenarios ranging from single-phase to three-phase power measurements using a single PJVS and a reduced number of ADCs. A proof of concept on multiplexing strategies is reported in [11]. Below, we report the measurement scenarios that are possible to implement at the current stage of development of the QPS.

A. Testing high precision AC sources and calibrators

As shown in Figure 1, the QPS can be used for the calibration of AC sources and multifunction calibrators using the following configuration:

- $CH1_{SQPM}$ connected to the AC-PJVS output;
- $CH2_{SQPM}$ connected to the output of the device under test (DUT), e.g. AC synthesizer or calibrator;
- SQPM output connected to the ADC input.

The proposed method differs from the differential sampling approach in that it does not require robust synchronization and frequency matching between the DUT and the PJVS. However, in our setup we deal with the configuration in which the DUT is phase-locked to the PJVS setup.

The synchronization is performed by using a dedicated output channel of the PJVS bias electronics, which has been programmed to generate an isofrequential AC signal

to the PJVS. The output clock of the PJVS bias electronic and the sampling clock of the ADC are derived from the same 10 MHz reference signal, thereby coherent sampling can be performed on the serialized waveforms at the SQPM output.

B. Single phase power measurements

Figure 1 reports the schematic diagram for single phase power measurements. The configuration uses a single SQPS slave board (2 channels for $U(t)$ and $I(t)$ signals and 1 channel for the $U_{\mathrm{PJVS}}(t)$ reference signal) and a single ADC.

This configuration is suitable for electrical power measurements using only 33 % of the recorded stream. The synchronization of external phantom power sources to the QPS is obtained as in the previous scenario. Furthermore, extensions to other power measurement scenarios using more than one SQPM slave board and ADC channels are still in the implementation stage of development.

IV. TEST RESULTS

Experimental tests concerning the operation of the QPS as a whole, with particular emphasis to the measurement scenarios described in section 3, have been successfully performed. Moreover, further tests have been conducted to characterize the QPS constituents, particularly the SQPM. Since the SQPM performs the mixing of different analog and quantum AC waveforms into a unique signal stream, its amplitude gain and phase delay errors related to each single channel become relevant and important to keep into consideration when high precision voltage measurements approaching the ppm level or below are required.

The SQPM characterization in terms of amplitude gain and phase errors related to the single channels of the first slave board has been conducted using two different measurement setups. The first setup is dedicated for the measurement of the amplitude gain error of SQPM single channels. It is based on the use of the AC-PJVS and a high precision DMM3458A. The measurement method consists in manually switching a DMM3458 between the input and output of each SQPM channel, while the channel state changes from OFF to ON.

By neglecting the error due to the DMM gain variation between two consecutive measurements, the relative amplitude gain error of each SQPM channel is computed as follows:

$$\varepsilon_{\mathrm{CH}}^{\mathrm{G}} = \frac{U_{\mathrm{CH}}^{\mathrm{ON}} - U_{\mathrm{CH}}^{\mathrm{OFF}}}{U_{\mathrm{PJVS}}} \cdot 1 \times 10^{6} \qquad (2)$$

where: $U_{\mathrm{CH}}^{\mathrm{ON}}$ is the voltage measured at the output of the SQPM slave 1 when the state of channel under test is ON, $U_{\mathrm{CH}}^{\mathrm{OFF}}$ is the voltage measured at input of the channel when its state is OFF, and U_{PJVS} is the theoretical rms value of the staircase Josephson sinusoidal waveform applied at the channel under test.

For the determination of the phase delay error of the SQPM channels a second experimental setup based on a digital phase comparator has been used [12]. The AC signal has been generated with a Fluke 5730A calibrator.

The characterization concerned only the channels of the first SQPM slave board and the results are reported in Figure 4. Error bars corresponds to Type A uncertainty, which is the most dominant component.

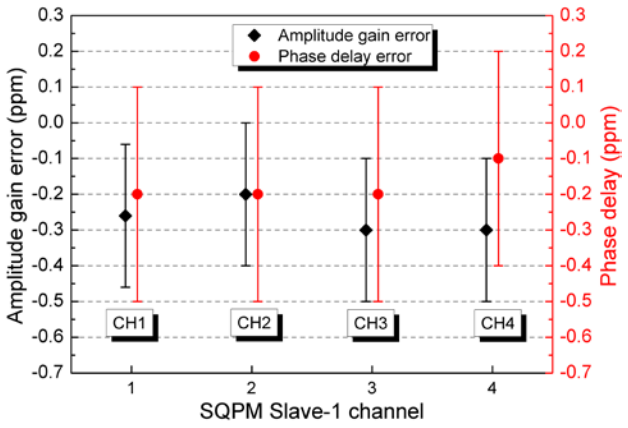

Fig. 4. Amplitude gain and phase delay errors of the channels of the first SQPM slave. Measurements were carried out at 50 Hz and 800 mV.

Further tests concerning the measurement scenarios with the QPS reported in the section 3 are in progress and the main achievements will be presented during the conference.

V. CONCLUSIONS

A quantum sampling modular setup suitable for practical electrical power measurements based on an AC-PJVS has been built and two different measurement scenarios have been preliminary tested.

Dedicated tests have been performed for precise characterization of all channels (CH1, CH2, CH3 and CH4) of the first SQPM slave.

It has been shown that the relative errors of all channels in terms of amplitude gain and phase delay are below 0.5 ppm, whereas Type A uncertainty is within 0.3 ppm. The obtained results are in good agreement with the SQPM design expectations and sufficient for the purpose and pave the way for metrological characterization of different measurement scenarios using the QPS as a whole.

ACKNOWLEDGMENT

This project (19RPT01 Quantum Power) has received funding from the EMPIR programme co-financed by the Participating States and from the European Union's Horizon 2020 research and innovation.

REFERENCES

[1] B. Trinchera and D. Serazio, “A Power Frequency Modular Sampling Standard for Traceable Power Measurements: Comparison and Perspectives” *IEEE Trans. Instrum. and Meas*, vol. 71, pp. 1-8, 2022.

[2] C. Mester, “Sampling primary power standard from dc up to 9 kHz using commercial off-the-shelf components”, *Energies*, vol. 14, no. 8, 2021. [Online]. Available: https://www.mdpi.com/1996-1073/14/8/2203.

[3] B. Djokic, “Low-Frequency Quantum-Based AC Power Standard at NRC Canada”, *IEEE Trans. Instrum. and Meas.*, vol. 62, no. 6, pp. 1699-1703, 2013.

[4] L. Palafox et al., “The Josephson-Effect-Based Primary AC Power Standard at the PTB: Progress Report,” *IEEE Trans. Instrum. And Meas.*, vol. 58, no. 4, pp. 1049-1053, 2009.

[5] Bryan C. Waltrip et al., “AC Power Standard Using a Programmable Josephson Voltage Standard”, *IEEE Trans. Instrum. and Meas.*, vol. 58, no. 4, pp. 1041-1048, 2009.

[6] 19RPT01 – Quantum Power, Quantum traceability for AC power standards, 2020-2023. https://quantumpower.cmi.cz/.

[7] QPsw - Quantum Power software, 2022. https://github.com/KaeroDot/QPsw.

[8] B. Trinchera, et al. , “Development of a PJVS System for Quantum-Based Sampled Power Measurements,” *Submitted to Measurement*, 2023.

[9] B. Trinchera, et al., “On the Synthesis of Stepwise Quantum Waves Using a SNIS Programmable Josephson Array in a Cryocooler,” in *IEEE Trans. Appl. Supercond.*, vol. 27, no. 4, pp. 1-5, June 2017.

[10] M. E. Bierzychudek, et al., “An SSR-based multiplexer for power measurement,” in: *Proc. CPEM*, Wellington, New Zealand, 2022.

[11] M. Šíra, et al., “Multiplexing schemes for quantum power systems,” in: *Proc. CPEM*, Wellington, New Zealand, 2022.

[12] B. Trinchera, D. Serazio and U. Pogliano, “Asynchronous Phase Comparator for Characterization of Devices for PMUs Calibrator,” *IEEE Trans. Instrum. and Meas*, vol. 66, no. 6, pp. 1139-1145, 2017.

26th IMEKO TC4 International Symposium
24th International Workshop on ADC and DAC Modelling and Testing
IMEKO TC-4 2023
Pordenone, Italy / September 20-21, 2023

Analytical Models and Magnetic Position Systems

Michael Ortner[1], Alexandre Boisselet[2], Luiz G. Enger[1], Florian Slanovc[1], Peter Leitner[1], Daniel Markó[1]

[1]*Silicon Austria Labs, Europastraße 12, 9524 Villach, Austria, michael.ortner@silicon-austria.com*
[2]*Infineon Technologies Austria, Siemenstraße 1, 9500 Villach, Austria*

***Abstract* – In this work, we promote the use of analytical solutions for magnetic position system design and analysis, which has become extremely convenient through the development of the open-source Magpylib computational package. We discard three common arguments against this ansatz by showing that analytical models are suitable for dealing with complex shapes, inhomogeneous magnetizations and even material interactions. Accuracy of analytical models is discussed, and the computational performance is demonstrated with three examples, a complex shape, an inhomogeneous magnet, and the calibration of a position system experiment. We find that analytical models can be powerful tools in this context.**

I. INTRODUCTION & MOTIVATION

Magnetic position systems are commonly used to track the motion in mechanical machinery by measuring the relative position between a permanent magnet and a magnetic field sensor. Such systems are widely used in industrial applications due to their robustness, versatility and potential for miniaturization [1, 2]. However, while some basic design patterns for common applications like rotary encoders, linear position systems, and joystick motion are established, advances in sensing and magnet technologies, a large and competitive market, as well as the development of novel applications require a constant modelling effort for improving and optimizing designs.

To meet this demand, commercial finite element environments like Ansys or Comsol are the tool of choice in engineering circles. While finite element computations are well-developed powerful tools, their main disadvantage is the computation speed, which makes it difficult to sweep through design variations and impossible to find optimal designs, when more than two or three variables are involved. Typical position systems deal with 30 - 100 variables that include parameters of geometry, magnetic material, sensor and tolerances.

In this paper, we endorse analytical models for designing a large variety of position systems due to their computational performance and the recent development of the Magpylib package [3], which gives effortless access to performant implementations. We discuss advantages, disadvantages, and accuracy of such models and discard several common arguments against their use that include "only simple geometries", "only simple magnetizations", and "no material interaction".

II. ANALYTICAL MODELS

A permanent magnet corresponds to a spatial magnetization distribution $\mathbf{M}(\mathbf{r})$. The field of such a distribution is simply the sum of the fields of the individual magnetic moments, which can be expressed in a macroscopic continuum approximation [4] as

$$\boldsymbol{B}(\mathbf{r}) = \frac{1}{4\pi} \int \frac{\boldsymbol{\nabla}' \cdot \boldsymbol{M}(\mathbf{r}')(\mathbf{r} - \mathbf{r}')}{|\mathbf{r} - \mathbf{r}'|^3} \mathrm{d}V. \qquad (1)$$

These integrals can be solved analytically in many cases depending on geometry and magnetization. Magnetic field expressions are then reduced to closed forms (polynomial, rational, trigonometric,...), and expressions such as elliptic integrals that are easily evaluated. Solutions that can be found in the literature include cuboid [5], cylinder [6, 7], cone [8], triangle [9], and other basic shapes with homogeneous magnetizations, of which most are implemented in Magpylib. Finding new solutions is an on-going effort.

One major argument against analytical solutions is that only simple geometric forms are possible. This statement ignores the possibilities offered by discretization and superposition. In magnetostatics, arbitrary complex forms can be constructed by combining simple base geometries. While this hinders the performance, in most cases it is possible to find a good compromise in terms of discretization finesse, required accuracy, and computational speed. In this context, the triangle solution must be mentioned, because it does not require a volume mesh, but only a surface approximation. An example of a complex magnet form realized with a triangular mesh is shown in Fig. 1. A B-field computation with Magpylib of this body including 1000 triangular facets takes 1.9 ms on an Intel Core i5-1235U without multiprocessing.

It should also be noted, that for many applications the simple base geometries are sufficient. This is demonstrated by the industry standard DIN SPEC 91411 [10], where these forms are described in detail. The reason for this are mostly off-the-shelf solutions offered by magnet man-

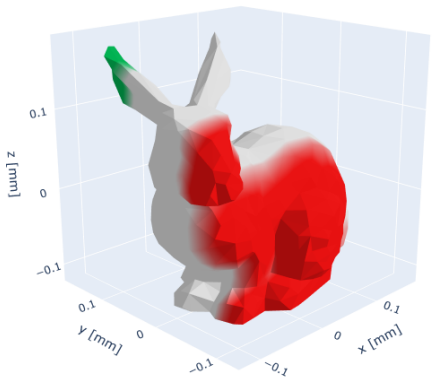

Fig. 1. Complex magnet form realized with triangular surface mesh.

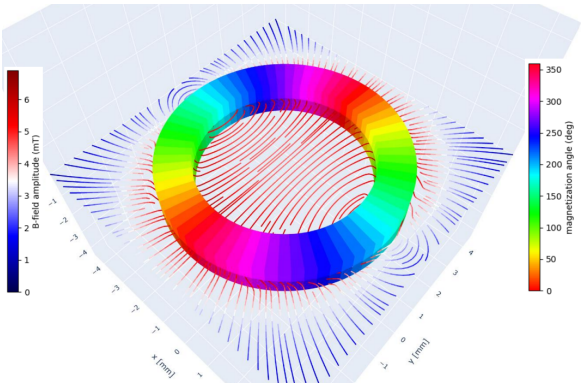

Fig. 2. Approximation of Halbach magnetization and resulting magnetic field.

ufacturers, low costs in fabrication and development, and superior magnetic properties when compared to special geometries realized, e.g., by milling and injection molds of polymer bound magnets [11].

The second argument against using analytical solutions is that magnetizations are often inhomogeneous, for which very limited solutions exist. Specific examples are magnetic multipole rings with a low number of poles, or magnetic scales with thick magnetic material layers that are not magnetized all the way through. While numerical solutions based on direct integration are possible [12], discretization methods based on analytical solutions should not be discarded. Any inhomogeneous magnetization distribution can be approximated by splitting the magnet into small pieces, each with a different homogenous magnetization. An example of this is shown in Fig. 2, where a continuous Halbach cylinder is approximated by a discretized version of 61 base cylinder tile geometries [7]. The homogeneous field on the inside and the fast decay of the field on the outside of the cylinder are clearly visible. This computation of the B-field at 400 grid positions with magnet comprised of 61 cells took less than 5 s on an Intel Core i5-1235U mobile CPU without multiprocessing.

In summary, it can be said that discretzation methods enable analytical solutions for complex forms and inhomogeneous magnetization. The downside is that computation performance is reduced because the field of many cells must be computed. However, this is often mitigated by the ultra-fast computation times of individual base geometries that are about 1-100 µs and the remarkable possibilities for multiprocessing that are discussed below. In addition, the discretization approach is in line with modern open-source meshing tools [13], that generate efficient meshes of complex bodies without much effort.

III. MATERIAL RESPONSE AND ACCURACY

It is often stated that analytical methods cannot be used to compute the effects of material interaction. What is actually meant is that the inhomogeneous magnetization distributions resulting thereof are typically not known. When using finite element tools, the user input is not the magnetization distribution, but a known initial state and material parameters. For permanent magnets, the initial state is “the instant of their magnetization”, and for ideal soft-magnetic materials it is simply zero. The FE environment then solves the magnetization problem, and computes the B-field at the same time.

There are two major effects that must be considered: Demagnetization in hard-magnetic materials ($\mu_r \ll 5$), and magnetization of soft-magnetic materials ($\mu_r \gtrapprox 500$). The first effect is relatively weak because of the low permeabilities of most modern hard magnetic materials. For example, sintered NdFeB typically has a value of $\mu_r \leq 1.05$. The relative error resulting from demagnetization with such materials are estimated in [14] for cubical magnets as 10^{-2}, and less than 10^{-3} when the homogeneous part is compensated. In comparison, FE errors as low as 10^{-4} can only be achieved by immense computational effort. The effect depends on the magnet geometry and on the distance from the magnet. In addition, softmagnetic materials are generally avoided in magnetic position systems because they give external stray fields a position dependence. In combination, this already opens a wide range of applications for working with analytical models in which demagnetization effects play a negligible role.

However, to compute the magnetization distribution of hard and soft materials with arbitrary initial states, it is possible to rely on the Magnetostatic Method of Moments [15], which is a discretization method that solves the interactions between individual cells analytically [16]. The method is demonstrated here using a point-matching interaction (Magpylib H-field computation) to compute the demagnetization of a cuboid magnet with an unfavorable

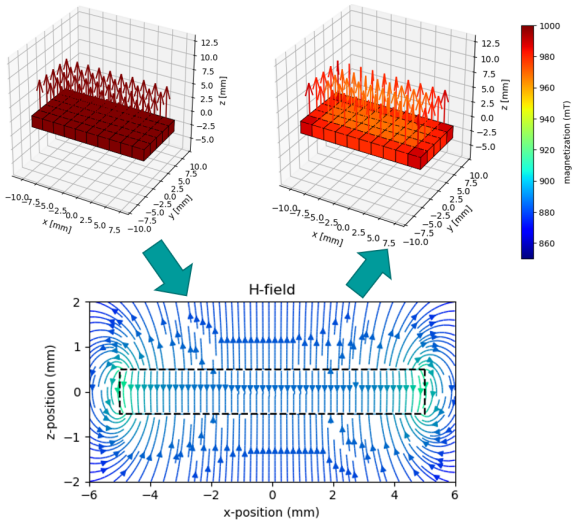

Fig. 3. material response.

shape of 5 x 10 x 1 mm^3 magnetized in z-direction with a remanence field of 1000 mT and an isotropic relative permeability of $\mu_r = 1.05$. The result is shown in Fig. 3. The initial state is a homogeneous magnetization, which creates a strong opposing field inside the magnet which resulting in a change of the magnetization state. One can observe an overall reduction of the magnetization by ≈ 2 %, superposed with a small variation between sides and center of the magnet slab. This method can also be applied to treat softmagnetic bodies.

IV. ADVANTAGE AND PROOF

Magnetic field computations based on analytical solutions have unparalleled computational speed. Individual data points can be obtained in microseconds, which is typically 6-9 orders of magnitude faster than corresponding FE computations, and enables the use of standard global optimization strategies in 10-100 dimensional spaces. There are two types of optimization problems that are regularly encountered with magnetic position systems: (i) finding optimal system designs, which requires the minimization of complex cost functions including system construction constraints, with an excellent example shown in [14], and (ii) the fitting of experimental data to understand experimental tolerances, which is demonstrated below.

Specifically, evolutionary black box optimizers were shown to be highly synergetic with analytical methods [17]. This synergy can be exploited maximally when parallellization is an option. Here, an evolutionary optimizer can make use of many unrelated input points in each generation, which can all be computed in parallel on multiple cores or even computational clusters. The license-free Magpylib is especially useful when computational upscaling is attempted.

We demonstrate the calibration of an experiment in Fig. 4. In this figure, we see a classical linear position

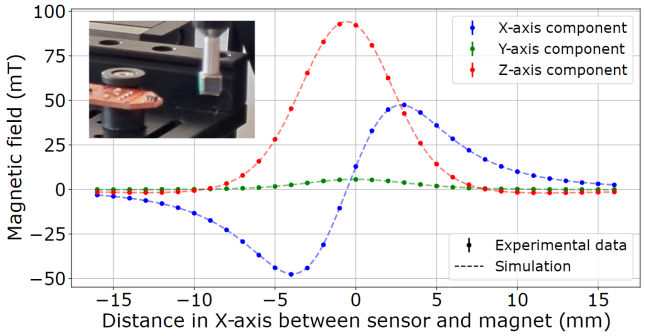

Fig. 4. material response.

system experiment, where a magnet moves linearly with respect to a sensor. The most difficult part in such an experiment is aligning magnet and sensor properly. We fit an analytical model to the experimental data obtained with an Infineon TLE493D 3D Hall sensor, leaving magnet magnetization, sensor displacement, orientation, offset and sensitivities as fitting variables. With 33 data points and 18 fitting variables, a least mean square fit took less than four minutes on an Intel Core i5-1235U mobile CPUs using the SciPy differential evolution algorithm [18, 19] with standard settings and eight workers. The figure shows the excellent alignment between experiment and theory with a relative error below 2.85 %.

V. CONCLUSION

In this paper, we have discarded three classical arguments against the use of analytical solutions for magnetic field computation by demonstrating that analytical models can deal with arbitrary shapes, inhomogeneous magnetizations, and even material response computation. We have demonstrated the performance of analytical solutions by computing the magnetic field of a complex shape and a Halbach cylinder, and by solving a highly complex fitting problem with 18 degrees of freedom. While analytical models are not the answer for every problem, they should be considered as powerful design and fitting tools, at least in pre-development stages to give good starting values to sophisticated yet slow FE-based optimizers.

VI. *

References

[1] CPO Treutler. “Magnetic sensors for automotive applications”. In: *Sensors and Actuators A: Physical* 91.1-2 (2001), pp. 2–6.

[2] Joseph P. Heremans. “Magnetic Field Sensors for Magnetic Position Sensing in Automotive Applications”. In: *MRS Online Proceedings Library* 475.1 (Dec. 1997), pp. 63–74. ISSN: 1946-4274. DOI: 10.1557/PROC-

475-63. URL: https://doi.org/10.1557/PROC-475-63.

[3] Michael Ortner and Lucas Gabriel Coliado Bandeira. "Magpylib: A free Python package for magnetic field computation". In: *SoftwareX* 11 (2020), p. 100466.

[4] John David Jackson. *Classical electrodynamics*. 3rd ed. New York, NY: Wiley, 1999. ISBN: 9780471309321. URL: http://cdsweb.cern.ch/record/490457.

[5] ZJ Yang et al. "Potential and force between a magnet and a bulk Y1Ba2Cu3O7-δ superconductor studied by a mechanical pendulum". In: *Superconductor Science and Technology* 3.12 (1990), p. 591.

[6] Alessio Caciagli et al. "Exact expression for the magnetic field of a finite cylinder with arbitrary uniform magnetization". In: *Journal of Magnetism and Magnetic Materials* 456 (2018), pp. 423–432.

[7] Florian Slanovc et al. "Full analytical solution for the magnetic field of uniformly magnetized cylinder tiles". In: *Journal of Magnetism and Magnetic Materials* 559 (2022), p. 169482.

[8] Van Tai Nguyen. "Analytical computation of the magnetic field of a conical permanent magnet with arbitrarily uniform magnetization". In: *AIP Advances* 10.4 (2020), p. 045208.

[9] D Guptasarma and B Singh. "New scheme for computing the magnetic field resulting from a uniformly magnetized arbitrary polyhedron". In: *Geophysics* 64.1 (1999), pp. 70–74.

[10] Innomag. "Anforderungen an die technische Darstellung von magnetischen Maßverkörperungen in Konstruktionszeichnungen". In: *DIN SPEC 91411* (2022).

[11] John Croat and John Ormerod. "Modern Permanent Magnets". In: (2022). DOI: 10.1016/C2020-0-03162-2.

[12] Thomas Schliesch. *PS-Permagsoft*. URL: http://www.permagsoft.com/index.html.

[13] Christophe Geuzaine and Jean-François Remacle. "Gmsh: A 3-D finite element mesh generator with built-in pre-and post-processing facilities". In: *International journal for numerical methods in engineering* 79.11 (2009), pp. 1309–1331.

[14] Perla Malagò et al. "Magnetic position system design method applied to three-axis joystick motion tracking". In: *Sensors* 20.23 (2020), p. 6873.

[15] Olivier Chadebec, J-L Coulomb, and Fleur Janet. "A review of magnetostatic moment method". In: *IEEE Transactions on magnetics* 42.4 (2006), pp. 515–520.

[16] Paul Heistracher et al. "Hybrid FFT algorithm for fast demagnetization field calculations on non-equidistant magnetic layers". In: *Journal of Magnetism and Magnetic Materials* 503 (2020), p. 166592.

[17] Michael Ortner. "Improving magnetic linear position measurement by field shaping". In: *2015 9th International Conference on Sensing Technology (ICST)*. IEEE. 2015, pp. 359–364.

[18] Pauli Virtanen et al. "SciPy 1.0: fundamental algorithms for scientific computing in Python". In: *Nature Methods* 17.3 (Feb. 2020), pp. 261–272. DOI: 10.1038/s41592-019-0686-2.

[19] Rainer Storn and Kenneth Price. In: *Journal of Global Optimization* 11.4 (1997), pp. 341–359. DOI: 10.1023/a:1008202821328.

26th IMEKO TC4 International Symposium
24th International Workshop on ADC and DAC Modelling and Testing
IMEKO TC-4 2023
Pordenone, Italy / September 20-21, 2023

Crosstalk in Gapped-core Contactless Current Sensor

Noby George[1], Pavel Ripka[1], Václav Grim[1]

[1]*Department of Measurement, FEL, Czech Technical University, Prague, noby.george@fel.cvut.cz*

***Abstract* – A detailed analysis of the crosstalk in the gapped-core current sensor is presented in this paper. The gapped-core current transducer with a magnetic field sensor in the airgap is widely used to measure current in industries and laboratories. We examine the effect of a nearby current-carrying conductor on the performance of the gapped-core transducer, for the first time in this paper. The crosstalk is studied by considering various factors such as angular and linear displacement of the external conductor, core material, and position of the main conductor. A 3D Finite Element Method (FEM) based model is used to analyse the cross talk and results are presented in this paper. This analysis helps the designer to get detailed insight into the effect of the external conductor on the gapped core current transducer.**

I. INTRODUCTION

The gapped core current sensor with a magnetic field sensor in the airgap is used for the measurement of DC and AC currents [1]- [2]. The cut in the magnetic core reduces the saturation effects that otherwise affect the performance of Current Transformers (CT) [3]. The width of the air gap, the material, and shape of the core, and the position of the magnetic field sensor affect the performance of the gapped core current transducer, and it is studied in the literature [4]-[5]. It is also important to analyze the crosstalk from nearby current-carrying conductors because this situation is common in electric vehicles and their chargers where gapped core current transducers are used [6]- [7].

A detailed analysis regarding the crosstalk effect in the gapped core current transducer is presented in this paper. We consider the effect of change in relative permeability of the core, and off-centered measured conductor when an external current is present near (at various linear and angular positions) to the current transducer. The details about the crosstalk effect in the gapped core current transducer are presented in the next section of the paper.

II. CROSSTALK IN GAPPED-CORE CURRENT TRANSDUCER

A gapped-core current transducer with a magnetic field sensor placed in the airgap is shown in Fig.1a. The dimensions of the gapped core and conductors that are used in the 3D-FEM analysis are provided in Fig.1b. The 3D model developed in the Ansys Maxwell software exactly replicate actual gapped core transducer for current measurement. The dimensions provided in Fig. 1b is the dimension of a nanoperm core from Magnetec GmbH [8]. The air gap length of 1.8 mm is required to keep the Hall-Effect [9] or TMR [10] magnetic field sensors in the gap. A 10 A DC current was passed through the conductors during the analysis. The magnitude of flux density at the airgap is proportional to the current in the measured conductor. The change in magnitude of flux density the airgap due to the presence of an external conductor (as shown in Fig.1a.) is prone to introduce error in the measurement. An analysis of the error introduced in the

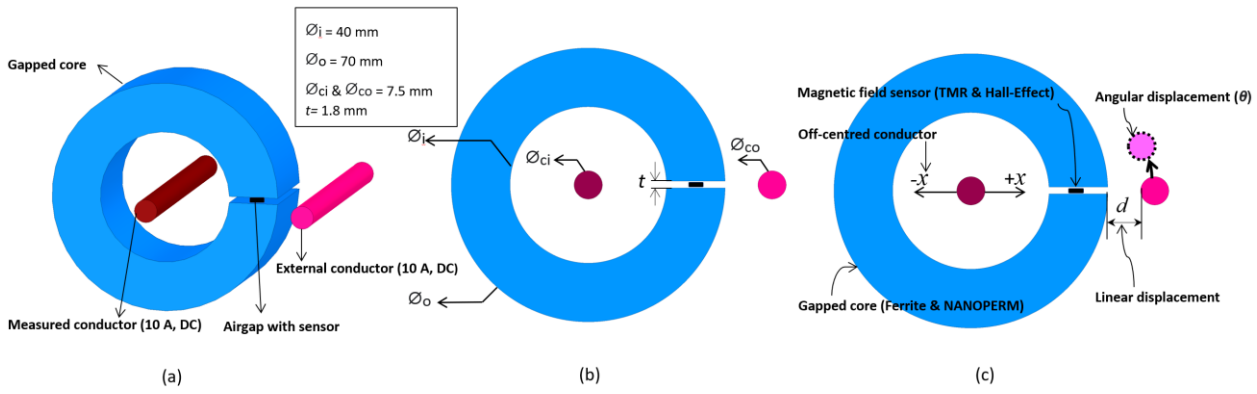

Fig. 1. (a) The gapped-core current transducer with an external conductor. The dimensions of the transducer is provided in (b). The crosstalk by external conductor is analysed for various conditions provided in (c).

measurement due to the crosstalk effect is provided in the following subsections of the paper.

A. Crosstalk in ferrite and nanoperm based gapped cores

The core in the gapped core current sensor is made of materials with high relative permeabilities. We have used ferrite gapped core with a relative permeability of 2100 and Nanoperm (from Magnetec GmbH) with a relative permeability of 10000 [8] in the 3D-FEM analysis. Fig. 2 shows the flux line distribution in the core (relative permeability = 2100) and the air gap when only the external conductor is excited. It is visible in Fig.2 that some of the flux lines choose the path through the airgap. Fig. 3 shows the flux line distribution for a gapped core with a relative permeability of 10000. It is visible from Fig.3 that most of the flux lines use the path as core and none of the lines crosses the air gap. This scenario happens because for the core with low relative permeabilities, the reluctance offered by the core is high (compared to the core with high relative permeability) and this tends the flux lines to cross the air gap. In both cases, the external conductor is in the closest position (d = 0) to the airgap and only the external conductor was excited.

During the FEM analysis, the distance (d, as shown in Fig.1c.) between the gapped core and the external conductor varied from 0 to 20 mm. The error introduced in the measurement due to the change in magnitude of the flux density at the airgap due to the external conductor for each distance is obtained and provided in Fig. 4. It is visible from Fig. 4 that crosstalk error is high if the external conductor is near to the air gap and for the ferrite-gapped core. We found this interesting and analyzed the crosstalk error for different permeabilities of the gapped core and which is provided in Fig.5. The results are presented in Fig.4. shows the importance of selecting a gapped core with higher permeabilities for a low crosstalk effect.

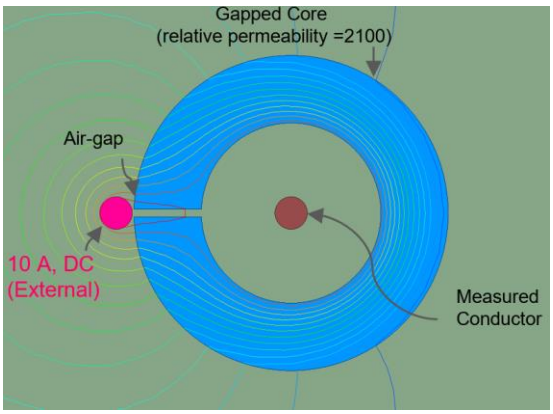

Fig. 2. Fluxline distribution in the ferrite-gapped core transducer when only the external conductor is excited.

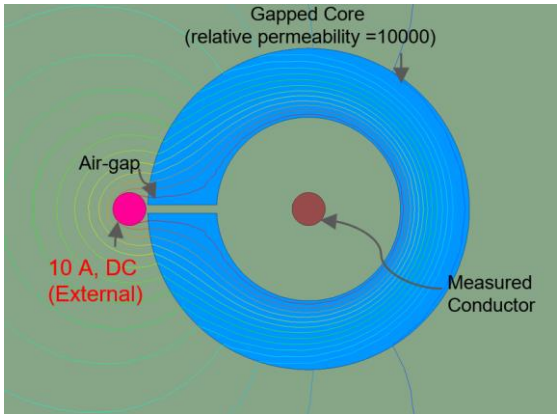

Fig. 3. Fluxline distribution in the nanoperm gapped core transducer when only the external conductor is excited.

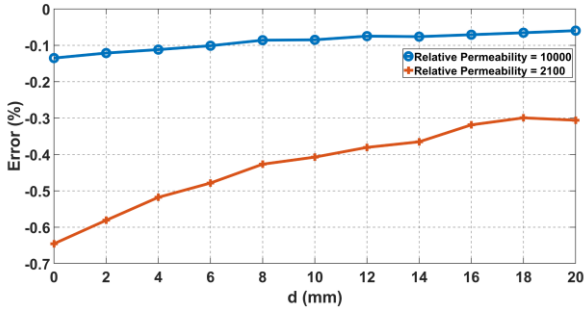

Fig. 4. Crosstalk error characteristics for ferrite and nanoperm core.

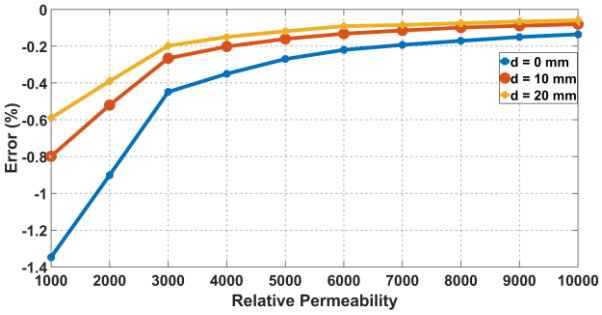

Fig. 5. The crosstalk error for various relative permeability of the gapped core.

B. Crosstalk error for angular displacement of external conductor

The crosstalk error for linear displacement of the external conductor (at different permeabilities of the core) is presented in the previous section. It is also important to analyze the crosstalk error at different angular positions (θ, as shown in Fig.1c.) of the external conductor. The same is analyzed using the 3D-FEM and results are

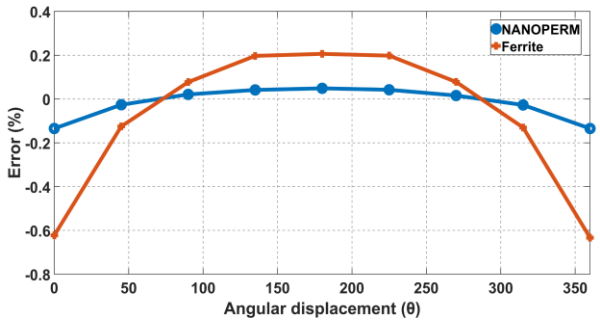

Fig. 6. Crosstalk error at different angualr postion of the external conductor.

provided in Fig. 6. It is visible from Fig. 6 that the crosstalk effect is low for angualr postion of 75 (also 275) degress for the external conductor.

C. Effect of off-centered measured conductor on corsstalk error

The effect of an off-centered measured conductor on the crosstalk error is presented in this section. The measured conductor is moved from its ideal center position (in the gapped core) along the *X*-axis in both directions (as shown in Fig.1c.). The results are presented in Fig.7. shows that the crosstalk is dependent on the position of the measured conductor.

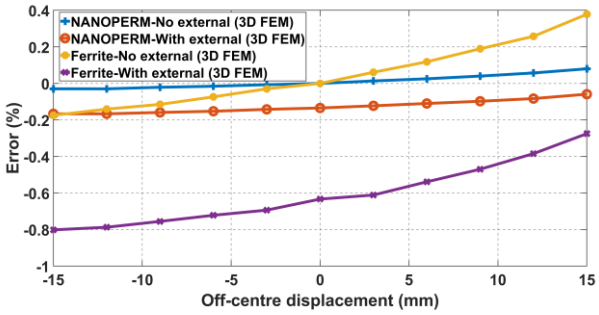

Fig. 7. The effect of off-centered measured conductor on crosstalk by external conductor.

D. Crosstalk in a dual-gapped core current transducer

This section of the paper analyses the crosstalk effect on a dual-gapped core transducer. The dimension of the transducer used for the FEM analysis is shown in Fig. 8. The flux line distribution in the dual-gapped core current transducer is provided in Fig. 9. The FEM analysis showed that the magnitude of the flux density at one airgap increases due to external field but the magnitude of the flux density at second airgap decreases due to external field. This enables to cancel the effect of the external field with the help of differential measurement [11]. So, the crosstalk effect in low permeability single-gapped core can be improved by using a dual-gapped core current transducer, and the same is shown in Fig. 10.

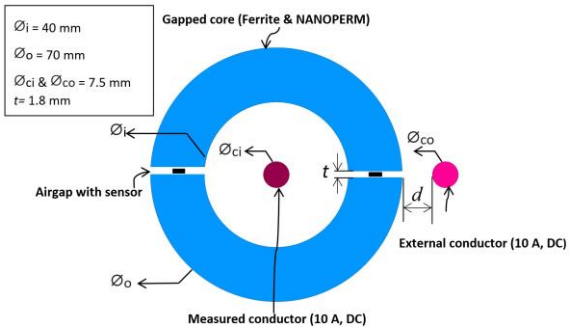

Fig. 8. The gapped core current sensor with two gaps in the core.

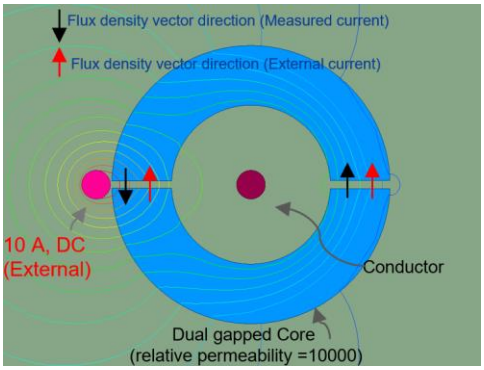

Fig. 9. Fluxline distribution in the nanoperm dual gapped core transducer when only the external conductor is excited.

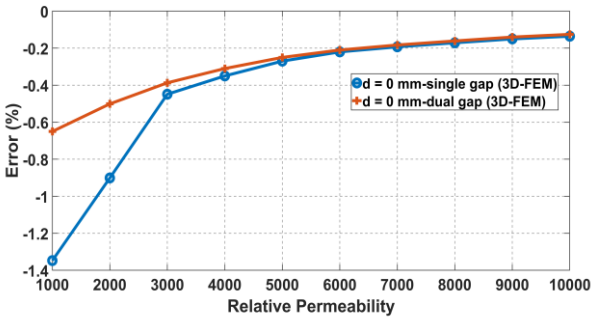

Fig. 10. The comparison of the crosstalk in the single and dual gapped core current transducer.

III. CONCLUSION

The effect of crosstalk from the external conductor in a gapped core current sensor is presented in this paper. The results presented in this paper show that the crosstalk error depends on the relative permeability of the core, the angular and linear position of the external conductor, and

the position of the measured conductor. The NANOPREM core with a relative permeability of 10000 showed better resistance to the crosstalk effect compared to a ferrite core with relative permeability of 2100. The crosstalk effect of single gapped low permeability cores can be improved using dual gapped core current transducers.

REFERENCES

[1] P. Ripka, “Electric current sensors: A review,” Meas. Sci. Technol.,vol. 21, no. 11, pp. 1–23, Sep. 2010.

[2] M. Crescentini, S. F. Syeda and G. P. Gibiino, "Hall-Effect Current Sensors: Principles of Operation and Implementation Techniques," IEEE Sensors Journal, vol. 22, no. 11, pp. 10137-10151, 1 June1, 2022.

[3] M. Davarpanah, M. Sanaye-Pasand and R. Iravani, "A Saturation Suppression Approach for the Current Transformer—Part I: Fundamental Concepts and Design," IEEE Transactions on Power Delivery, vol. 28, no. 3, pp. 1928-1935, July 2013.

[4] R. Rushmer, J. Annis, R.D. Marasch, and G. Voborsky, “Hall Effect Sensor Core With Multiple Air Gaps,” U.S. Patent 9,285,437 B2, Mar. 15, 2016.

[5] D. Geisler, and S. D . Milano, “Current Sensor,” U.S. Patent 10,114,044 B2, Oct. 3, 2018.

[6] A. Patel and M. Ferdowsi, "Current Sensing for Automotive Electronics—A Survey," IEEE Transactions on Vehicular Technology, vol. 58, no. 8, pp. 4108-4119, Oct. 2009.

[7] S. Cong, Hein, I. Ansari, A. Armento, A. Hurlburt, R. Cleveland, and M. Zamieski “Electric Current Sensor for Detecting Leakage Current,” U.S. Patent 11,313,917 B2, Apr. 26, 2022.

[8] “*M-712 MAGNETEC*”, [Online]. Available at: https://www.magnetec.de/en/?s=M-712.

[9] “Datasheet for MLX91209,” Melexis. [Online]. Available: https://www.melexis.com/en/documents/documentation/datasheets/datasheet-mlx91209.

[10] “Datasheet v1.0a TMR2505 - aecsensors.com” [Online]. Available at: https://www.aecsensors.com/components/com_virtuemart/shop_image/product/Magnetic-Tunnelling-Magnetoresistive-TMR-Linear-Sensors/pdfs/TMR2505-Datasheet-EN-V1.0a.pdf.

[11] P. Ripka and A. Chirtsov, "Influence of External Current on Yokeless Electric Current Transducers," IEEE Transactions on Magnetics, vol. 53 (2017), 1-4.

26th IMEKO TC4 International Symposium
24th International Workshop on ADC and DAC Modelling and Testing
IMEKO TC-4 2023
Pordenone, Italy / September 20-21, 2023

Rapid Prototyping of Automotive Magnetic Positioning Systems

Luiz G. Enger[1], Aleš Travnik[1], Peter Leitner[1], Florian Slanovc[1], Daniel Markó[1], Michael Ortner[1]

[1]*Silicon Austria Labs, Europastraße 12, 9524 Villach, Austria, luiz.enger@silicon-austria.com*

***Abstract* – Magnetic position and orientation systems offer the advantages of contactless sensing, high precision, robustness and low cost. They are heavily employed in automotive and industrial applications. The standard development process of such system starts with a simulation that is followed by validation with experimental data. This work presents a platform to which different sensors and magnets can be attached, with complete six degrees of freedom for relative movement. It is thus quite flexible in terms of experiments it can perform. A system calibration scheme based on dipole approximation is presented, yielding sensor tolerances and allowing to compute the field of a corresponding magnet.**

I. INTRODUCTION & MOTIVATION

Magnetic position and orientation (MPO) systems posses several advantages over other position and motion detection systems. They operate with contactless sensing, are thus wear-free and can work immersed in liquids such as motor oil [1]. They combine high-precision, robustness against moisture, dirt and temperature variations, and operate at low power consumption. Permanent magnets and magnetic field sensors are also relatively cheap thanks to large scale production. Due to these properties, MPO systems are extensively used in the automotive industry for engine and transmission control, pedal and steering wheel position sensing, anti-lock brake systems, active suspension and more [2, 3].

The general approach to develop a MPO system is to start with a simulation, followed by obtaining experimental data, which will be used for validation and to improve the simulation. Figure 1 shows common implementations of MPO systems, each requiring a specific setup to run experiments. There is no one-size-fits-all solution. To fill in this gap, a flexible platform to obtain precise experimental data which allows for rapid prototyping of MPO systems targeting automotive applications is proposed. Whereas some work has already been published using robot arms for linear movement and joystick applications or a Stewart platform holding an array of sensors for six degrees of freedom (6DoF) [5, 6, 7], this work presents a platform offering 6DoF with separated modules for translation and rotation movements. This allows more flexibility for different movements and an increased range of motion compared to other platforms.

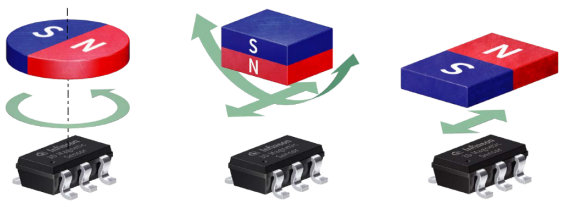

Fig. 1. Typical examples of MPO systems. From [4].

The major issue with magnetic position system testing equipment is the difficult alignment of position and orientation between sensor and magnet, which results from system assembly, but also imperfectly fabricated magnets and sensors themselves. Many schemes have been proposed to achieve such a calibration, all with their advantages and disadvantages [7, 8]. The proposed 6DoF setup requires a (semi-)automatic scheme, that will work with different magnets and sensors to enable fast prototyping and repeated measurements. In this work, we give an overview of the 6DoF setup and demonstrate a novel calibration scheme based on dipole field approximations.

II. PLATFORM FOR MPO PROTOTYPING

Our 6DoF test bench is mechanically designed to achieve a positioning precision of 100 µm, an angular precision of 0.1° while fully realizing 6DoF within a linear range of ±20 mm, and full 360° of rotation. The setup, shown in Fig. 2, consists of a 3D translation stage, onto which the sensor is mounted, and a 3D rotation stage the magnet is attached to. In combination, these two stages realize 6DoF motion. The majority of the pieces holding the test bench together are made from aluminum, since it is nonmagnetic, lightweight and easy to machine. Anodization of the parts was performed to provide a durable finish. The setup is mounted on a high-precision optical bread board, to provide the necessary stability. Each stage is independently controlled with a stepper motor, which in turn is controlled directly from a PC via a USB interface from a low-level Python back-end. The same back-end is used to obtain the sensor data, which allows for a high level of flexibility to operate with different sensors. In Fig. 2, an Infineon TLV493D-A1B6 MS2Go kit is mounted.

To achieve our mechanical precision goal, the mecha-

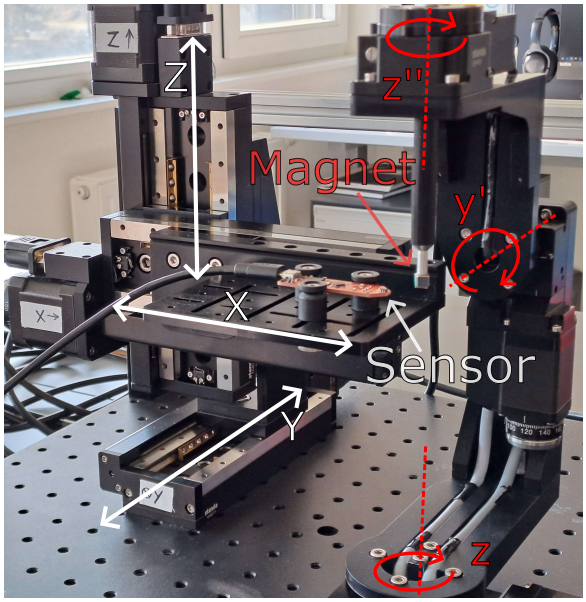

Fig. 2. Photo of the platform, with a sensor mounted onto the translation stage and a cube magnet attached to the tip of a shaft on the rotation stage. Translation axes are highlighted in white and rotation axes in red. Sensor and magnet are indicated.

nical deflection of fabricated components was calculated and accounted for together with fabrication tolerances and assembly errors. The assembly of the test bench follows the left-hand convention, with the thumb pointing up towards positive Z-, straight index finger pointing towards positive Y- and middle finger pointing towards positive X-direction. The 3D rotation motion follows the z-y'-z'' convention for Euler angles considering intrinsic rotations. The 3D translation stage is constructed from three individual linear stages with a single step resolution of 2.5 µm. Like a goniometer, the 3D rotation stage itself is constructed from three individual rotation stages, where the z-rotation has 0.01° single step resolution, whereas y'- and z''- rotations can achieve 0.015° per step. The total range of motion for each translation axis is ±50 mm, and full 360° for the each rotation axis with no limit for the number of revolutions as slip-ring connectors are used to connect the stages.

The Python back-end forwards commands to the motor drivers to physically move the test bench. However, this back-end is not very convenient for purposes including complex relative motions between sensor and magnet. For defining relative paths between sensor and magnet, we make use of the practical Magpylib path standard [9]. A Python front-end translates a Magpylib path, possibly from a virtual experiment, into back-end commands that are needed to generate the desired motion in the experiment. To avoid collisions between individual components of the setup, e.g., between moving and resting stages or between sensor and magnet mounts, a digital twin of the setup was built with PyVista [10]. The digital twin can predict collisions based on given input parameters and allows only valid positions to be passed to the physical test bench.

III. CALIBRATION OF THE PLATFORM

To meet our target precision goal, all tolerances have to be identified, evaluated, and calibrated out. Tolerances can be divided into two main categories: (i) stage assembly tolerances and (ii) system assembly tolerances associated with every new experiment, including the tolerances of magnet, sensor(s) and their respective mounts.

A. *Stage calibration*

Manufacturing and assembly imperfections result in a set of critical errors including stage axes orthogonality, rotational eccentricity and runout. These errors lead to poor positioning and have to be accounted for. This is realized by precise characterization and subsequent correction when translating front-end paths to encoder signals.

For characterization of the test bench, a touch trigger probe model TPA2 is employed [11]. This probe triggers a signal whenever sufficient pressure is applied to its tip, either from the side or from below, with a repeatability of 2 µm. With this probe, the characterization of the above-mentioned tolerances is performed by touching the stages at various points of progress of individual motions.

B. *System calibration scheme*

While the stage tolerances are constants, every MPO system assembly introduces additional errors into the experiment. Those include intrinsic sensor and magnet tolerances like die position and orientation in package, sensing direction orthogonality, offset and gains, geometric imperfections and bad magnetization distributions. There are also tolerances related to how sensor and magnet are mounted onto the stage.

It is crucial for rapid prototyping to find a (semi-)automated calibration procedure with a high level of repeatability, that can, at the same time, flexibly deal with different magnets and sensors. We propose to exploit the fast decay of the magnetic field of higher order moments to find a good mechanical reference between sensor and magnet. In practice, the magnet is positioned at a distance from the sensor such that the latter is unable to distinguish between the magnet and a dipole field, but close enough so that variations can still be detected. A "sweet volume" corresponds to a shell around the sensor where both conditions are fulfilled. Its shape and size depend strongly on the magnet (shape and magnetization) and the sensor (resolution and range) properties.

The magnet is then moved along specific paths inside this "sweet volume" and magnetic field readings are stored. An optimization algorithm subsequently performs a fit of the experimental data to the computed field values for a dipole source. The tolerances of interest are used as fitting parameters.

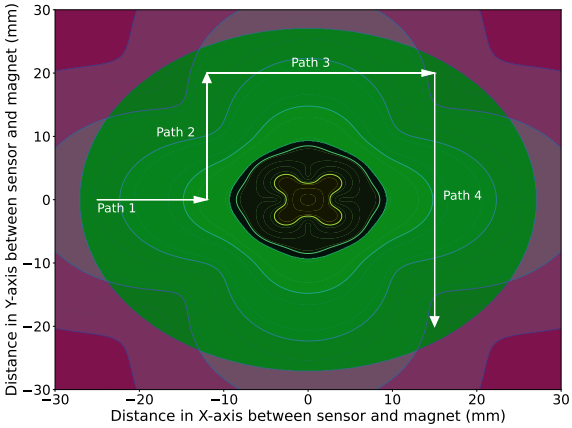

Fig. 3. Black zone: difference between dipole field and cube magnet field amplitudes is above sensor resolution. Red zone: field amplitude is below sensor resolution. Green zone: area in which the cube magnet can be effectively considered as a dipole, the sweet volume.

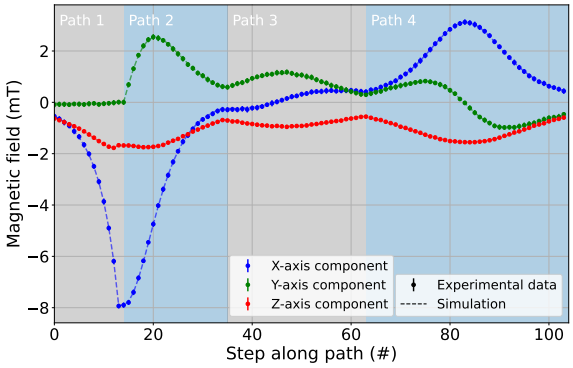

Fig. 4. Optimized dipole fit with average and standard deviation of 64 sensor readings at each position, with a step size of 1 mm.

C. Experimental calibration

For an ideal cube magnet of 5 mm long edges, magnetized in Z-direction with a remanence of 1000 mT and at an airgap of 5 mm from sensor, Fig. 3 shows the sweet volume of a TLV493D-A1B6 sensor at $Z = 0$ mm. A movement inside this volume is also defined, and Fig. 4 depicts the optimized fit between sensors readings and dipole field. Data was acquired using an off-the-shelf cube magnet.

A differential evolution algorithm was used [12, 13]. The optimization parameters were die position, orientation, sensitivity and offset as well as dipole moment for each XYZ component. After optimization, the maximum relative error in field amplitude amounts to 6.4% with an average of 2.0%. As the magnet was kept at a distance from the sensor, its field amplitude is smaller and stray fields have an increased effect on sensor readings. However, such effects were not taken into account for the evaluation of the sweet volume.

D. Proof of concept

A 1D linear motion MPO system was chosen to demonstrate the concept [5, 14]. Figure 5 displays the effective sweet volume after the dipole calibration. The optimized values of the dipole moment were used to calculate the magnetization of an equivalent cube magnet of 5 mm long edges. This has the drawback of considering a homogeneous magnetization and a perfect geometry for the magnet, and that the corresponding dipole is located at its center. The sensor Z position was also corrected. A linear path is defined, moving outside the sweet volume. With the same magnet previously used, sensor readings were obtained from $X = -16$ mm to $X = 16$ mm with a 1 mm step size. Figure 6 presents the comparison between experimental data and the calculated field of a cube magnet.

The maximum relative error in field amplitude was 15%. Differences between experiment and simulation arise outside the sweet volume as an ideal cube magnet was considered for field calculation. If information such as dimension and magnetization distribution is available from a previous magnet characterization, calculated field values will be closer to the experimental data. The presented scheme does not provide calibration of the magnet itself.

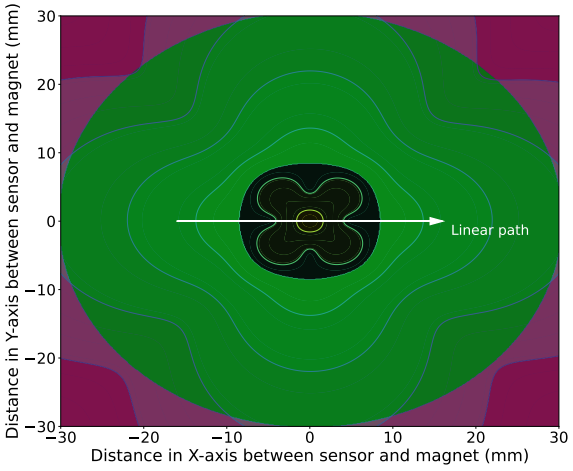

Fig. 5. Linear path crossing the region where sensor detects a difference between the field of a cube magnet and that of a dipole.

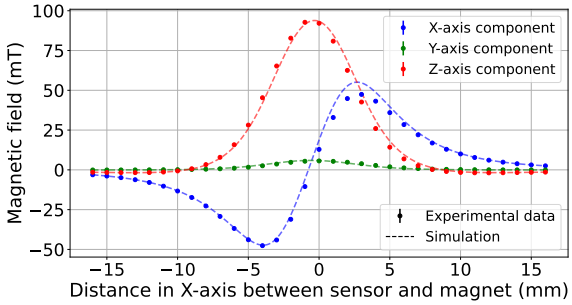

Fig. 6. Parameters from the optimized fit of a dipole field were used to calculate the field of a cube magnet.

IV. CONCLUSION

Positioning systems based on magnetic field sensing of a permanent magnet present several advantages over other systems such as low cost, low power consumption, robustness against hazardous environments and are wear-free due to contactless sensing. This work presented the assembly and discussed the calibration of a platform with six degrees of freedom movement, capable of reproducing every possible relative position and motion between a magnetic field sensor and a permanent magnet. Special attention was given to a system calibration scheme based on a dipole field approximation. This scheme yields the tolerances of the magnetic sensor in a MPO system and the corresponding dipole moment values of a magnet moving inside a sweet volume. Those results can be used to calculate the actual magnetic field of the magnet, although the error increases outside the sweet volume as a magnet with ideal geometry and magnetization distribution is considered. The calibration can be further improved with data obtained from the characterization of the magnet itself and by taking into account other effects such as from stray fields.

REFERENCES

[1] Joseph P. Heremans. "Magnetic Field Sensors for Magnetic Position Sensing in Automotive Applications". In: *MRS Online Proceedings Library* 475.1 (Dec. 1997), pp. 63–74. ISSN: 1946-4274. DOI: 10.1557/PROC-475-63. URL: https://doi.org/10.1557/PROC-475-63.

[2] C.P.O Treutler. "Magnetic sensors for automotive applications". In: *Sensors and Actuators A: Physical* 91.1 (2001). Third European Conference on Magnetic Sensors & Actuators., pp. 2–6. ISSN: 0924-4247. DOI: https://doi.org/10.1016/S0924-4247(01)00621-5. URL: https://www.sciencedirect.com/science/article/pii/S0924424701006215.

[3] Udo Ausserlechner, Armin Satz and Ferdinand Gastinger. *Magnetic position sensors, systems and methods*. US11287252B2. Sept. 2020. URL: https://patents.google.com/patent/US11287252B2/.

[4] Infineon Technologies AG. *XENSIV™ - sensing the world*. Nov. 2022.

[5] Michael Ortner, Marcelo Ribeiro and Dietmar Spitzer. "Absolute Long-Range Linear Position System With a Single 3-D Magnetic Field Sensor". In: *IEEE Transactions on Magnetics* 55.1 (2019), pp. 1–4. DOI: 10.1109/TMAG.2018.2870597.

[6] Perla Malagò et al. "Magnetic Position System Design Method Applied to Three-Axis Joystick Motion Tracking". In: *Sensors* 20.23 (2020). ISSN: 1424-8220. DOI: 10.3390/s20236873. URL: https://www.mdpi.com/1424-8220/20/23/6873.

[7] Daniel Cichon et al. "A Hall-Sensor-Based Localization Method With Six Degrees of Freedom Using Unscented Kalman Filter". In: *IEEE Sensors Journal* 19.7 (2019), pp. 2509–2516. DOI: 10.1109/JSEN.2018.2887299.

[8] Stefano Lumetti et al. "Computationally Efficient Magnetic Position System Calibration". In: *Engineering Proceedings* 2.1 (2020). ISSN: 2673-4591. DOI: 10.3390/ecsa-7-08219. URL: https://www.mdpi.com/2673-4591/2/1/72.

[9] Michael Ortner and Lucas Gabriel Coliado Bandeira. "Magpylib: A free Python package for magnetic field computation". In: *SoftwareX* (2020). DOI: 10.1016/j.softx.2020.100466.

[10] Bane Sullivan and Alexander Kaszynski. "PyVista: 3D plotting and mesh analysis through a streamlined interface for the Visualization Toolkit (VTK)". In: *Journal of Open Source Software* 4.37 (May 2019), p. 1450. DOI: 10.21105/joss.01450. URL: https://doi.org/10.21105/joss.01450.

[11] Kurokesu. *TPA2*. URL: https://wiki.kurokesu.com/books/tpa2 (visited on 30/03/2023).

[12] Pauli Virtanen et al. "SciPy 1.0: fundamental algorithms for scientific computing in Python". In: *Nature Methods* 17.3 (Feb. 2020), pp. 261–272. DOI: 10.1038/s41592-019-0686-2.

[13] Rainer Storn and Kenneth Price. In: *Journal of Global Optimization* 11.4 (1997), pp. 341–359. DOI: 10.1023/a:1008202821328.

[14] Florian Slanovc, Dieter Suess and Michael Ortner. "Designing Airgap-Stable Magnetic Linear Position Systems". In: *IEEE Transactions on Magnetics* 58.9 (2022), pp. 1–5. DOI: 10.1109/TMAG.2022.3188474.

26th IMEKO TC4 International Symposium
24th International Workshop on ADC and DAC Modelling and Testing
IMEKO TC-4 2023
Pordenone, Italy / September 20-21, 2023

Custom Synthesizable VHDL Processor for Embedded Capacitive Angle Sensor Data Processing

Milos Drutarovsky[1], Ondrej Benedik[2], Miroslav Sokol[1], Pavol Galajda[1], Jan Saliga[1], Jan Ligus[2], Cristian D Stratyinski[2]

[1]*Technical University of Kosice, Letna 1/9, 042 00 Kosice, Slovakia, Milos.Drutarovsky@tuke.sk*
[2]*CTRL Ltd., Omska 14, 040 01 Kosice, Slovakia, Cristian.Stratyinski@ctrl1.eu*

***Abstract* – We describe custom architecture of a small synthesizable soft processor for the next generation of proprietary capacitive angle sensor (CAPSE) developed by CTRL company for space applications. We process data streams from ADCs by custom developed 16-bit processor. The processor is written in platform independent VHDL code. It uses a small Leros (soft processor) control unit and several custom coprocessors including CORDIC, fixed-point fractional multiplier, and adder with barrel shifter optimized for fractional fixed-point arithmetic. We describe architecture of the proposed processor and present the results of developed custom processor mapping to the target FPGA circuit. The complete processor occupies only ∼2100 Logic Elements in target FPGA and complete firmware has less than 220 instructions. For a 10 kHz sampling rate, it requires less than 3 MHz system clock frequency.**

Fig. 1. CAPSE sensor prototype with embedded RadHard microcontroller.

I. INTRODUCTION

The robust and reliable measurement of the absolute angle of rotation has an important role in positioning systems in space mechanisms in order to check and control the position of the mechanism moving parts. Position sensors have a significant impact on the performance, functionality, and reliability of space mechanisms and space missions. Capacitive encoders are quite attractive because they can be easily manufactured as small units with simple construction and low power consumption [1]. The proprietary capacitive sensor CAPSE shown in Fig. 1 was developed by CTRL company [2], within ESA supported activity.

CAPSE is a contactless angular sensor, that measures the rotation angle between its rotor mechanical part and its stator mechanical part. The uniqueness of the design is a measurement of absolute angle values, low susceptibility to vibration, temperature error canceling, working in vacuum/air or lubricant conditions, small particles do not affect the performance, easy and fast design scalability, manufacturing and its integration.

The ultimate future goal of CAPSE development is to replace the currently used RadHard microcontroller (MCU) used in CAPSE Engineering Qualification Model (EQM) by a custom digital Application Specific Integrated Circuit (ASIC). In this paper we describe the first step in this effort, the developed custom synthesizable VHDL processor with specialized peripherals implemented for efficient processing of signals acquired by Analog to Digital Converters (ADCs) from CAPSE sensor. We mapped our custom processor into FPGA as a proof of concept in the first stage of future ASIC development in the actual CAPASIC project.

II. EXPERIMENTAL CAPASIC HARDWARE

The CAPASIC project moves main processing functions (data preprocessing of 3 separate digitized analog input channels, math for angle computation, angle linearization, interfaces and status of computation monitoring) into the custom digital Hardware (HW). We describe proposed custom HW in synthesizable VHDL and map it currently into the off-the-shelf FPGA circuit. This allows us to map, test and optimize the main CAPASIC functionality (referred to

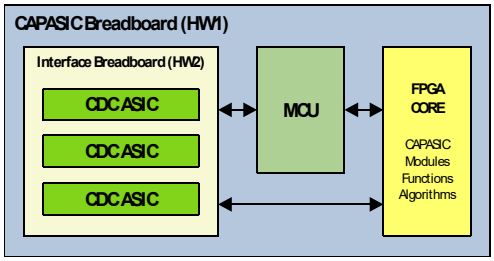

Fig. 2. Experimental CAPASIC hardware.

as FPGA CORE in further text and shown in Fig. 2) already in current project development stage with real capacitive analog sensor prototype.

A. *Analog interface board*

The analog Interface Breadboad (HW2) uses 3 separate ADCs for data acquisition. The ESS214D [3] rad-hard tolerant capacitive sensor signal conditioner integrated circuit (CDC) realized as ASIC includes also sigma-delta ADC. The inputs of CDC ASICs connect directly to the analog capacities of absolute CAPSE rotary encoder. The HW2 provides digital data representing actual values of 3 monitored capacities in real-time. Developed and implemented FPGA CORE algorithms are not limited only to the used CDC ASIC, and, in principle, we can use also other sigma-delta ADCs in future designs.

B. *MCU based development interface*

The MCU provides flexible development interface for transformation of CDCs data to the format required by FPGA CORE development and testing of the interface. For development we use off-the-shelf development board with ARM based MCU. It provides us the following main functionality:

- I2C (optionally SPI) for interface to CDC ASICs.
- Parallel I/O (PIO) for communication with FPGA CORE.
- UART interface for debugging and development.

III. ARCHITECTURE OF PROPOSED FPGA CORE

The main function of the FPGA CORE (shown in Fig. 3) is real-time processing of 3 acquired parallel data streams provided by CDCs. The FPGA CORE performs main signal processing functionality required for computation of actual angle α from acquired CDC data streams in real-time. The main time-critical tasks executed by FPGA CORE are:

- Sequentially read all input data streams from PIO interface with required resolution.

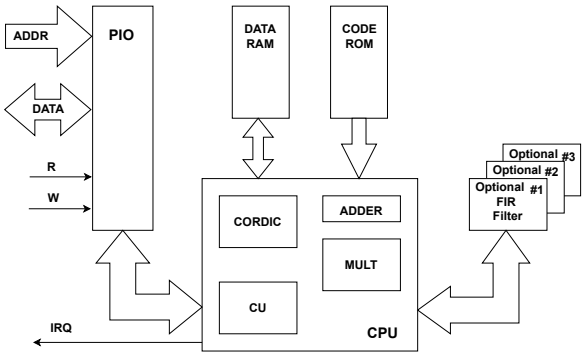

Fig. 3. Block diagram of FPGA CORE hardware.

- Optionally filter input data by decimation FIR filter. Former CAPSE MCU implementation uses a simple averaging FIR filter so we added this block as an option to the FPGA CORE. This block is currently not used.
- Preprocessing (DC offset removing, gain compensation, component transformation) of acquired data from ADCs.
- Compute angle of rotation α by using trigonometric $\arctan()$ function.
- Compensate non-idealities of analog part by piecewise linear correction of computed angle.
- Post-process output data (output data formatting, providing status information about quality of input data).

The FPGA CORE consists of several hardware blocks:

A. *Control Unit (CU)*

A simple CU is required for the control of datapaths implemented as separate external HW blocks. We selected a simple 16-bit Leros processor available as VHDL based soft/processor [4]. It has Harvard architecture with separate Program Memory (PM) and Data Memory (DM), small number ($\sim$20) of really used instructions and can be easily extended. The small and fully customizable Leros design is relatively slow but it is not a bottleneck for overall performance as main data processing tasks are executed by the external datapaths.

B. *Fixed-point 16-bit hardware multiplier*

We use a standard Booth's algorithm based fractional signed 16-bit fixed-point multiplier (MULT) as an external HW coprocessor for implemented CU. It uses input data scaled into fractional (-1,1) interval similarly as is done in a typical fixed-point digital signal processor. The MULT is connected to the external peripheral address and data buses of CU and provides 16-bit signed result (the high significant word) in fractional format. The CU has access also

to the low significant word of multiplication result, but due to proper scaling of data in implemented algorithms, it is not required in the final data processing algorithms. The MULT is implemented as a pure combinatorial circuit and provides result with latency of 1 CU clock cycle.

C. *Fixed-point 32-bit adder*

A 32-bit fixed-point adder (ADDER) is used as an additional external HW coprocessor for implemented CU. It contains also parallel barrel shifter for fast extraction of properly scaled 16-bit output words out of the input 32-bit ADC ones. This coprocessor enables fast removing of DC offsets from input data streams and selection of 16 most significant data bits after DC offset removing. The CDC ASIC uses a sigma delta ADC with up to 32-bit configurable output word-length, but in principle, any ADC with compatible word-lengths can be used.

D. *CORDIC coprocessor*

Implemented signal processing algorithm requires computation of trigonometric function

$$\alpha = \arctan\left(\frac{Y}{X}\right) \tag{1}$$

for evaluation of angle of rotation α in all 4 quadrants, where Y and X are represented as fractional fixed point numbers. A sequential CORDIC (COordinate Rotation DIgital Computer) algorithm [5] based fixed-point coprocessor with 16-bit input/output interface uses a modification of VHDL code from [6]. The CORDIC interfaces to the external peripheral address and data buses of CU and provides 16-bit resolution in full 2π radians angle range. The internal precision of computation and number of iterations of CORDIC are configurable before synthesis. Actually used values are 20 bits for the width of internal CORDIC datapath and 16 iterations (clock periods). These values ensure lower overall errors than required by the actual specification. The CORDIC coprocessor uses the same clock as CU, but in principle, we can use also higher separate clock signal.

E. *Parallel interface with interrupt handling (PIO)*

The PIO interface to an external MCU is implemented as a set of two separate small Dual-Port Memories (DPMs). DPM_1 is used for CU $\rightarrow$ MCU direction (CU can write only, MCU can read only) and DPM_2 is used for MCU $\rightarrow$ CU one (MCU can write only, CU can read only). Additionally, the CU has read only access to the PIO STATUS register. The DPM_1 has only four 16-bit words $DATA_{0-3}$ addressed by address bits ADDR(1:0) and mapped to the specific address locations. The DPM_2 has eight 16-bit words $DATA_{0-7}$ in order to support efficient transfer of 3 data channels from MCU to CU. The CU signalizes by interrupt line (sets IRQ) to the MCU automatically by writing to the specific DATA register in DPM_1. The MCU clears automatically pending IRQ by writing to the specific DATA register in DPM_2. The external MCU interface uses a set of standard signals: 16-bit ADDRES bus, 16-bit DATA bus, RD, WR and IRQ. The PIO block is mapped to the I/O space of CU. The CU can read actual status of IRQ (properly synchronized to the CU clock domain) that is mapped to the STATUS register.

We assume the MCU clock is not synchronous with the CU clock. For reliable cross domain clock crossing we use "Flancter" based hardware synchronization circuit [7] and HW controlled interrupt line.

F. *Optional decimation FIR filter*

A FIR filter can be used for additional filtration of input data streams in order to suppress input noise and increase input data resolution. Filtration is currently not yet implemented and optional simple averaging is computed by CU.

G. *Optional UART*

A simple Universal Asynchronous Receiver-Transmitter (UART) is actually connected to the CU. We use UART for communication with an external computer during development and debugging of complete HW and Firmware (FW) design. The UART will be removed from the final stable design.

IV. FIRMWARE OF THE PROPOSED FPGA CORE

The FPGA CORE functionality follows developed mathematical expressions already tested in the former experimental CAPSE MCU implementation. The experimental MCU implementation used floating-point implementation.

The proposed CAPASIC implementation maps these algorithms into digital FPGA CORE HW blocks with the aim to decrease overall HW complexity and maintain required precision of computation with small HW resource requirements. Hence, we use fractional fixed-point arithmetic in all implemented signal processing algorithm steps mapped into the FPGA CORE shown in Fig. 4.

The implemented algorithms are controlled by CU firmware stored in the PM of implemented CU. The PM contains less than 256 CU instructions that are encoded as a simple loop even without subprogram calls (although subroutine calls are also supported in Leros CU). The firmware is written in assembler of Leros CU. The instructions are used for mapping of intermediate data to/from described hardware coprocessors and reading (and waiting) of corresponding status information.

The implemented firmware supports also a "boot phase" during which all relevant parameters are downloaded from an external MCU via PIO interface to the DM of CU. These parameters include:

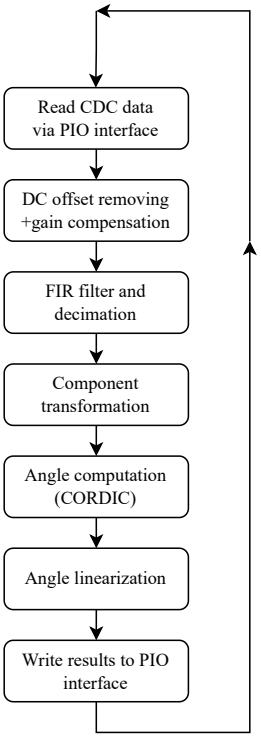

Fig. 4. Flowchart of implementd signal processing algorithms steps.

- Offsets and gains for compensation of errors of input analog sensor parts.
- System parameters used for monitoring status of input data. The firmware also monitors and reports in real-time (via status register) some fault conditions caused by fault input data.
- Calibration constants for simple piece-wise linearization. The firmware supports N_{seg}=8, 16, 32 and 64-point linearization.

Currently used Leros HW implementation supports up to 256 words of DM with memory words that are directly mapped as CU registers. The complete FW uses only 20 DM words for all implemented signal processing steps except for linearization routine. We implemented a simple linearization routine [8] with correction curve based on N_{seg} piece-wise linear segments. We adapted correction coefficients for usage of fractional fixed-point multiplier. In contrast to [8], we use calibration coefficients that minimize Minimum Min Square Error (MMSE) in each of N_{seg} segments. The linearization routine requires 2 additional DM words per one linearization segment. This limits support for max $N_{seg} = 64$-point linearization in available DM with 256 words.

V. EXPERIMENTAL RESULTS

We implemented all described blocks as parametrized VHDL code and we do not use specific FPGA HW blocks. E.g., usage of embedded FPGA multipliers was intentionally disabled in order to enable porting of developed VHDL code to the future ASIC design. We prepared VHDL testbench files for independent testing of all developed HW blocks in Modelsim simulator. Functional and timing simulations (after mapping to the low-cost MAX 10 FPGA) were performed in Modelsim to confirm proper functionality of implemented blocks. Mapping and placement & route to the specific FPGA HW were done by Intel Quartus CAE tool. The expected functionality in selected FPGA was confirmed. Prepared testbenches can be used for testing critical paths of implemented HW blocks in the target FPGA.

As the next step, all developed HW blocks were connected and mapped to the specified peripheral memory locations of Leros CU. The complete FPGA CORE with debug UART occupies 2200 Logic Elements (LEs) in the target MAX 10 FPGA hardware. This number includes also LEs used for storage of firmware that is mapped to the synthetized HW and not stored in embedded FPGA Block Memories (BMs). Resources required for implementation of specific coprocessors are shown in Table 1 (ADDER includes also barrel shifter, CU includes also stored FW).

Table 1. FPGA resources required for implementation of specific parts of developed FPGA CORE

MULT	CORDIC	ADDER	CU
425 LEs 0 BM	444 LEs 0 BM	300 LEs 0 BM	512 LEs 2 BMs

We used data acquired from analog sensor testbench developed in previous CAPSE project for extensive testing of developed custom processor digital hardware. The raw input data for angle rotation $\alpha \in \langle 0, 2\pi \rangle$ acquired by three 20-bit ADCs are shown in Fig. 5. The input raw data have slightly different offsets and require also different gains compensation for each of 3 processed ADC channels. The differences are caused by imperfections of analog sensor sections and they are decreased by algorithms implemented in CU firmware. The final computed angle errors for $N_{sec} = 8$ and $N_{sec} = 32$ are shown in Fig. 6.

We tested our complete custom processor also on DE10-Lite FPGA development board with CU clock generated by FPGA PLL clock block. The extensive hardware tests confirmed proper functionality of developed custom processor and its long-term reliable and stable operation.

Complete data processing (without decimation filtration) shown in Fig. 4 takes 212 CU clock cycles (actual FW has 238 instructions). For an expected sampling frequency F_s = 10 kHz the CU system clock frequency of

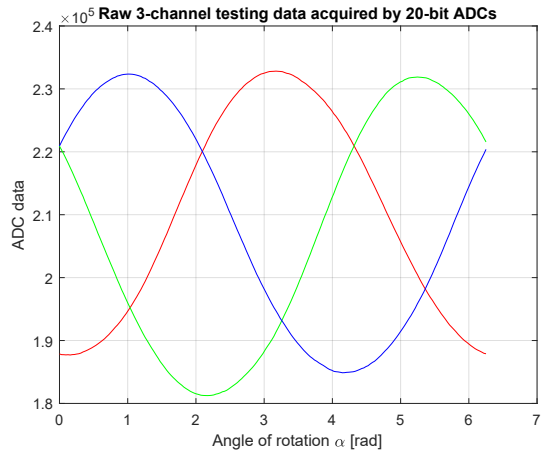

Fig. 5. Three channel testing data acquired from analog testbench by 20-bit ADCs during complete 2π radian rotation.

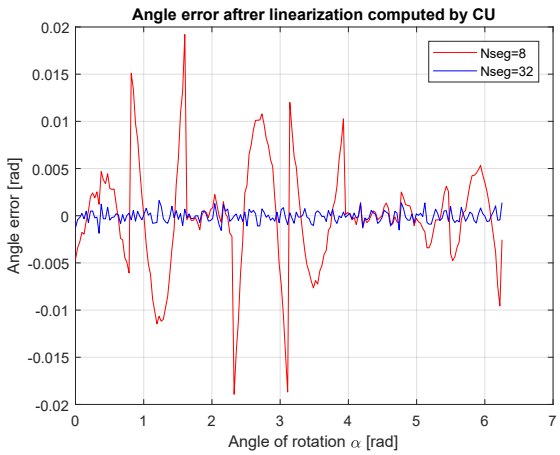

Fig. 6. Angle error of actual angle position α computed by developed processor in fixed-point arithmetic.

only $\sim$2.2 MHz is required. This is significantly lower frequency than the one required for previous MCU implementation. The overall precision of computed angle α by digital part is better than 13 bits that was required according to the specified design requirements.

VI. CONCLUSIONS

We described architecture of a small custom soft processor for proprietary capacitive angle sensor written in synthesizable VHDL. The final custom processor occupies $\sim$2100 LEs (without debug UART) and uses only 2 BMs in the target FPGA. The complete firmware has less than 250 CU instructions. Developed processor HW and FW can replace standard MCU used in former CAPSE prototype with significantly lower clock frequency in comparison with former MCU implementation. We mapped current version of developed processor to the specific Intel FPGA and fully tested in Intel Quartus and Modelsim CAE tools as well as in the target off-the-shelf FPGA development board. We can use prepared set of VHDL testbenches for efficient testing of developed processor HW and FW with acquired real data records in further stages of development. The complete design provides better than required 13-bit precision in 2π radians angle range. By changing internal parameters of implemented coprocessors (before synthesis) we can increase overall precision at the expense of additional HW resources. We will use our stable and tested VHDL code of developed custom processor as the main signal processing block in further CAPSE sensor development in the actual CAPASIC project.

ACKNOWLEDGMENTS

This work was supported also by the Science Grant Agency of the Slovak Republic (project No. 1/0413/22) and by the Slovak Research and Development Agency under Contract No. APVV-22-0400.

REFERENCES

[1] X. Fan, Z. Yu, K. Peng, and Z. Chen, "A compact and high-precision capacitive absolute angular displacement sensor," *IEEE Sensors Journal*, vol. 20, no. 19, pp. 11 173–11 182, 2020.

[2] "CTRL Ltd." http://www.ctrl1.eu.

[3] *ESS214D Radiation tolerant Capacitive Sensor Signal Conditioning IC*, ES Systems, 2020, rev. 1.

[4] M. Schoeberl, "Leros: A tiny microcontroller for FPGAs," in *Proc. of 21st International Conference on Field Programmable Logic and Applications*, ser. FPL, Sep 5–7, 2011, pp. 10–14.

[5] P. K. Meher, J. Valls, T. Juang, K. Sridharan, and K. Maharatna, "50 years of cordic: Algorithms, architectures, and applications," *IEEE Trans. on Circuits and Systems*, vol. 56, no. 9, pp. 1893–1907, 2009.

[6] "VHDL-extras library," https://github.com/kevinpt/vhdl-extras.

[7] R. Weinstein, *Application Note: The "Flancter"*, http://fpgacpu.ca/fpga/Flancter_App_Note.pdf, Memec Design, July 2000.

[8] *ZMID4200 Calibration and Linearization Manual – Analog Output*, https://www.renesas.com/us/en/document/mas/zmid4200-manual-cal-linearization-analog-out, Renesas, October 2020, rev 5.0-1.

26th IMEKO TC4 International Symposium
24th International Workshop on ADC and DAC Modelling and Testing
IMEKO TC-4 2023
Pordenone, Italy / September 20-21, 2023

Practical limitations of accurate magnetic measurements in industrial applications

A.Stuck, M. Mijalkovic, M.Vidojevic, D. Popovic

Senis Group, Neustr. 5a, 6340 Baar, Switzerland, info@senis.swiss

***Abstract* – The fundamental factors that limit the accuracy of magnetic measurements for field strengths typically encountered in industrial measurements of permanent magnets are discussed. In regions where magnetic fields can be considered homogenous, the accuracy of the measurement is limited by the stability of the magnetometer, the accuracy of its calibration, and the orthogonality of the sensor. However, the field-sensitive volume's size and the measurement axis's orthogonality determine the total accuracy in the near-field region of small magnetic structures. Using measured magnetic images from encoder structures, it is shown that accurate measurements are achieved only by measuring all 3 magnetic field components in a tiny volume.**

I. INTRODUCTION

Magnets are vital in numerous industries, including automotive, electronics, aerospace, and medical [1]. To ensure optimal performance and quality in production, it is crucial to have precise knowledge of the magnetic field distributions of magnetic devices. As the need for magnetic systems that are stronger, smaller, and more intricate grows, measuring magnetic fields with precision has become more exacting. As a result, magnetic measurement systems must become more accurate and faster to keep up with these demands.

This paper discusses the fundamental factors that limit the accuracy of magnetic measurements for field strengths typically encountered when measuring permanent magnets in industrial applications, ranging from a few milliteslas (mT) to several teslas (T). Understanding these limitations and adequately accounting for them makes it possible to obtain highly accurate and repeatable measurements of such magnets, even in challenging industrial environments.

Magnetic fields are inherently three-dimensional, with a specific strength and direction at every point in space. Unlike electrical fields, the distribution of magnetic fields cannot be characterized by a simple scalar function such as voltage. Measuring all three magnetic field components accurately and locally is therefore unavoidable to correctly describe real magnetic systems and draw valid conclusions. This, however, presents a significant challenge for magnetic measurement systems known as magnetometers.

II. MECHANICAL AND ELECTRONIC LIMITATIONS

A magnetometer must be stable, with low drift, and not affected by the external temperature to ensure accurate measurement. The instrument's mechanics should be simple and solid, providing a well-defined point in space for measurements to be taken. NMR-based magnetometers are precise and stable because they rely on the fundamental principle of nuclear magnetic resonance. However, NMR measurements do not provide information about the direction of the magnetic field and are not local. On the other hand, Hall-based magnetometers provide accurate local information about the field's strength and direction, and they can measure both DC and AC magnetic fields in real-time. Well-designed Hall-based magnetometers compensate for temperature effects and stabilize the drift of the electronics to the extent that their measurements remain accurate within a few 100ppm or less over at least one year. This makes Hall-based magnetometers the instruments of choice for advanced research, development, and industrial applications [2].

III. HOW CALIBRATION AFFECTS MEASUREMENT ACCURACY

Most magnetometers require calibration against a known reference in a homogeneous field at DC. In this situation, the size of the instrument's field-sensitive volume (FSV) does not affect its calibration. However, in real-world scenarios where magnetic fields have strong gradients, the size of the FSV can significantly impact the accuracy of the measurements. For example, suppose a magnetic field has a periodic variation along a straight line with a period of Λ. In that case, the measurement error ε due to the size of the FSV is given by equation 1:

$$\varepsilon = 1 - \cos\left(\frac{\pi W}{\Lambda}\right) \qquad (1)$$

Where W is the width of the FSV along the line. Specifically, a 150µm long sensor will inaccurately measure a periodic magnetic structure with a 10mm period by approximately 0.1%. Although seemingly minor, high-precision magnetometers are accurate to 0.1% or better in homogenous magnetic fields. In our example, the size of the FSV doubles the total error of the measurement, as the FSV error is systematic rather than statistical.

IV. THE IMPORTANCE OF THE FIELD-SENSITIVE VOLUME

To quantify measurement errors caused by the FSV in actual magnetic structures of small size, we used a high-precision mapper from SENIS AG, Switzerland [3], to scan a magnetic encoder tape. This mapper can measure the entire magnetic field of a sample over large volumes with positional repeatability better than 10µm. The SENIS Hall Sensor has an FSV of 100µm x 100µm x 10µm and can measure all three components of the magnetic field simultaneously within this volume, with an absolute accuracy of better than 100µT. To achieve unprecedented resolution in one direction, the sample was scanned so that the smallest dimension of the FSV, i.e., 10µm, was moved along the long side of the sample. Fig. 1 illustrates the measured magnetic distribution over an area of about 5.5cm x 1.5cm, with the three components of the field presented in separate images of red, green, and blue. The combined full-color image depicts the entire magnetic field vector. The fourth image (purple) shows B_{tot}, the field's strength.

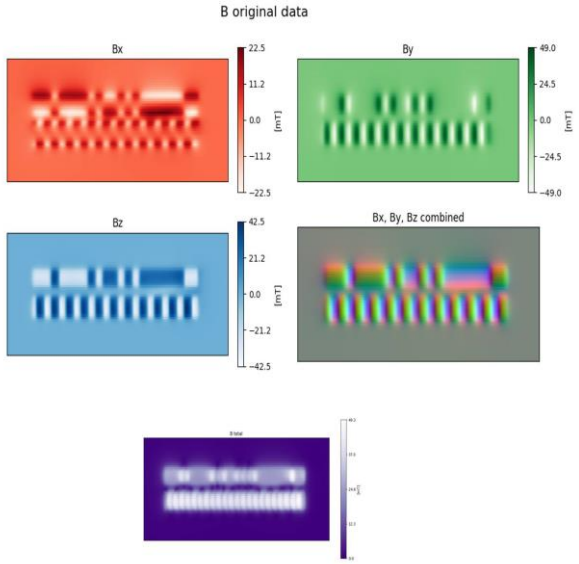

Fig1. Measured magnetic field of an encoder. Red/green/blue are the images of B_x,B_y and B_z. The full color image is the B-vector, the strength of the field B_{tot} is shown in purple.

This measurement reveals two distinct structures: a regularly modulated stripe with a periodicity of 4mm located beneath an irregularly coded strip. The primary directional components are B_y and B_z, with a weaker B_x component. In the full-color image, it is evident that the direction of the magnetic field rotates continuously along the periodic structures, primarily in the B_y and B_z plane. However, the Bx component dominates along the upper and lower edges of the stripes. Although this magnetic encoder may appear simple, its three-dimensional magnetic pattern is intricate. The strength of the magnetic field varies significantly in a localized manner, and the direction of the magnetic field continuously changes from one point to another within a small volume.

Fig. 2 displays the field strength along the center of the lower regular stripe, with the sensing width in the scanning direction measuring only 10µm. By averaging the original data over a given distance D along the center line, we can compare the averaged data with the measured signal strength at the central point to obtain the actual relative error for a sensor with width D. Fig. 3 shows the results.

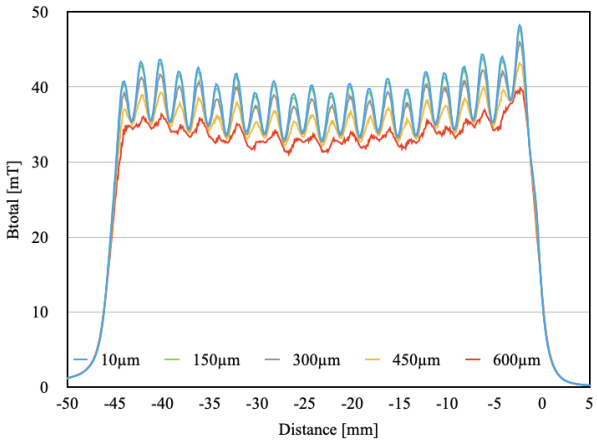

Fig2. Amplitude of the magnetic field for different widths (10µm, 150µm, 300µm, 400µm, and 600µm) of the FSV along the center line of the lower strip.

Even for a tiny sensor of 150µm width, the error associated with the size of the magnetic sensor is greater than 1%. It increases significantly with the width of the FSV. For a 600µm wide FSV, the error related to size is nearly 20%, without considering the inaccuracies of the sensor itself. In fig. 3, these measured errors are compared to the errors that would be expected based on the simple theory presented in equation 1.

The measured errors are nearly twice as large as what simple theory predicts. This discrepancy is due to the complexity of the magnetic structure and depends on the particular case. Theoretical models tend to underestimate the actual errors and should therefore be understood to provide conservative estimates only. This is especially true for small and/or complex magnetic systems. To accurately characterize such systems, measuring all three magnetic field components as precisely and locally as possible is therefore mandatory.

As this simple example shows, it is essential to consider the FSV size carefully when using magnetometers for specific applications. Unfortunately, it is not possible to provide a universal estimation of the total measurement errors for a given measurement system because they depend on various factors, such as the size and orientation of magnetic structures in relation to the sensor itself (distance to the sample, size, and orientation of the FSV for example). Therefore, estimating these errors on a case-

by-case basis is necessary. Especially in small, complex magnetic systems or if strong field gradients are present, i.e. in the near-field region of a magnet, the FSV size can be the dominant factor strongly limiting the measurements' total accuracy. In the far-field region, gradients are typically too small for the FSV size to affect the measurement.

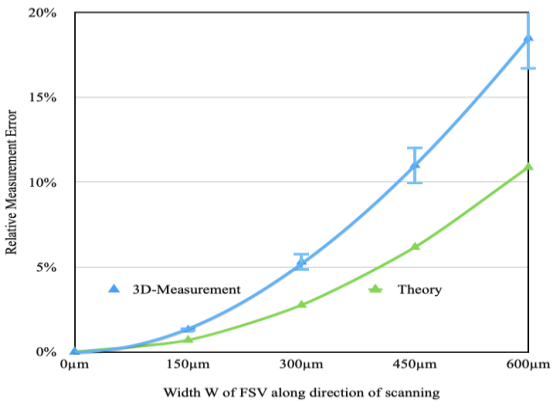

Fig3. Impact of sensor size on measurement error of small magnetic structures

V. ANGLES AND ACCURACY

Magnetic fields are directional, so sensors must be correctly oriented or measure all field components in a small volume to ensure accuracy. Most magnetic field detection technologies, except for NMR, which measures field strength, are only sensitive to one or two field components. As a result, they need to be integrated into sensor systems to obtain the complete 3D information necessary for precise field distribution measurements. When measuring only one or two field components, the manufacturer and the user must ensure the sensor is aligned with the magnetic field vector. Even a slight misalignment of 5° between the field and the sensor will result in a relative measurement error of 0.4%. This effect is also present in homogenous fields. It, therefore, similarly affects near-field and far-field measurements.

The cost and technology limitations for arranging multiple sensors in the same package restrict the FSVs to approximately 1x1x1mm today. This limits the application of such systems to measuring larger fields with small gradients. Semiconductor manufacturing technology is required to build tiny, fully integrated magnetic sensors with smaller FSVs in three dimensions which are capable of measuring intricate high gradient magnetic fields.

Regardless of how multiple sensors are arranged to measure all three directions in space, care must be taken to ensure these sensors point in orthogonal directions. Even minor deviations from orthogonality can significantly impact total field values. Generally, a non-orthogonality of 0.1° between individual sensor axes in an integrated 2D or 3D sensor will lead to an error of at least 0.1% for the total field value somewhere in space. Higher accuracies require measuring along a known given sensor direction or an absolute but not local measurement, such as NMR.

VI. CONCLUSIONS AND OUTLOOK

The accuracy of magnetic field measurements in industrial applications depends on three key factors: First, the magnetometer's mechanics and electronics must be precise and stable; second, the magnetometer must be capable of measuring all three magnetic field components within a small field-sensitive volume, and third, the sensing directions (x,y, and z) must be perpendicular.

Through analysis of magnetic measurements from an encoder, we have shown that for intricate magnetic fields with high gradients, the field-sensitive-volume size can become the dominant factor in measurement accuracy. While magnetometers can have calibrated accuracies of better than 0.1%, non-orthogonality can add several 0.1% to that error. However, careful selection of the measurement instrument and the setup is required to contain the influence of FSV error well within 1%. This is particularly important for near-field measurements of small magnets, where these limitations become significant. But if, for example, one measures the far field or the surface of a large homogeneous magnetic structure, the FSV error can be ignored. In the region far away from the magnet, only the errors caused by non-orthogonality and calibration of the sensor itself remain.

As miniaturization continues to be a prevalent trend across various industries, the need for precise measurement of complex and minute magnetic fields is expected to increase. Manufacturers must, therefore, consider the impact of FSV and non-orthogonality errors in their products to meet this demand. At Senis, we offer the only Hall-based magnetometers and field mappers that can accurately measure all three field directions in a minimal volume. Our latest device, the magnetic camera, boasts 16,000 pixels, each pixel having an FSV of 27 x 9 x 4 micrometers. This small FSV enables accurate measurement of the near field of tiny magnets. This instrument can fully characterize a magnet by concurrently measuring the field distribution at 16,000 points within seconds.

REFERENCES

[1] Magnetic Materials Market - Global Industry Assessment & Forecast, Market Report from Vantage Market Research, 2022

[2] R. S. Popovic, “Hall Effect Devices”, 2nd Edition, ISBN 9780750308557, published December 1, 2003, by CRC Press

[3] For more information about Senis, visit: www.senis.swiss

26th IMEKO TC4 International Symposium
24rd International Workshop on ADC and DAC Modelling and Testing
IMEKO TC-4 2023
Pordenone, Italy / September 20-21, 2023

A 10 V PJVS-based DC voltage realization at INRiM

Paolo Durandetto[1], Bruno Trinchera[1], Danilo Serazio[1], Emanuele Enrico[1]

[1]*INRiM - Istituto Nazionale di Ricerca Metrologica, Strada delle Cacce 91, Torino (Italy), p.durandetto@inrim.it*

***Abstract* – A 10 V DC quantum voltage calibration system, based on a programmable Josephson voltage standard (PJVS) operating in liquid helium, has been recently set-up and tested at INRiM. The PJVS system is partly-commercial and is based on a 10 V superconductor-normal metal-superconductor (SNS) array of 69631 Josephson junctions operated on the first Shapiro steps. The goal is to establish a new high-reliability quantum voltage standard for the DC calibration of solid-state voltage sources and digital voltmeters (DVMs). The paper reports the PJVS system description and first experimental testings and calibrations, preparatory to the future participation to international comparisons as final validation of the novel system.**

I. INTRODUCTION

Quantum-based voltage standards exploiting the inverse AC Josephson effect have been developed since the 1980s to either *reproduce* or *realize* the voltage unit (V) up to the 10 V level [1], and today are still under further improvement. Nowadays, turnkey systems based on Josephson voltage standards (JVSs) with both DC and AC capabilities are commercially-available and widespread within National Metrology Institutes (NMIs) and most-advanced calibration laboratories [2]. The first 10 V JVSs were based on SIS Josephson junctions (JJs) with insulating barrier and zero-current overlapping steps, which prevented them to be rapidly and easily programmed to generate the desired quantum voltage value. Also, quantum operating margins, i.e. the current-width of Shapiro steps, are generally lower than 50 µA, thus proper filtering is required to prevent uncontrolled transitions between the overlapping voltage steps during calibrations. Despite this, SIS-JVSs are still operational at some NMIs as primary voltage standard, though are being gradually replaced by new-generation Programmable JVSs (PJVSs) [3]. These are based on SNS JJs with a single-valued current-voltage relation and quantum operating margins easily larger than 1 mA. Besides replacing SIS arrays as novel primary DC voltage standards, PJVS arrays can also be used for routine DC and AC voltage calibrations up to the kHz range with voltage resolution equal to the voltage generated by a single JJ, i.e. about 145 µV at 70 GHz [4].

At Istituto Nazionale di Ricerca Metrologica (INRiM), we are setting up a 10 V DC quantum voltage calibration system based on a PJVS operating in liquid helium and driven at frequencies around 70 GHz. This paper presents the basic commercial 10 V DC PJVS system recently acquired from Supracon AG[1] and the further integration made at INRiM to make it fully operational. The basic PJVS system lacks of some features that are vital for a complete quantum-based DC voltage measurement system, in particular with regards to the calibration of DC voltage sources. Hardware and software components for covering this missing part have been developed in-house using existing commercial instrumentation and home-made equipment. These include a digital nanovoltmeter, a liquid helium (LHe) dewar, a home-made low-thermal manually-operated scanner, and a Python software for measurement acquisition and automated data analysis. The complete 10 V PJVS system is described below, along with first measurement characterizations and DC validation through the calibration of solid-state voltage standards.

II. PJVS-BASED MEASUREMENT SYSTEM

In the following we report details about the main parts constituting the quantum voltage measurement system, which is shown in Fig. 1.

A. *10 V PJVS device*

PJVS arrays generate quantized voltages (V_{PJVS}) through the current-controlled activation/deactivation of M sub-arrays, according to Eq. 1

$$V_{\mathrm{PJVS}} = \sum_{i=1}^{M} N_{\mathrm{JJ}}(i)\, n(i)\, K_{\mathrm{J}}^{-1}\, f_{\mathrm{rf}} \qquad (1)$$

with $N_{\mathrm{JJ}}(i)$ the number of JJs in the i^{th} sub-array, $n(i)$ the selected Shapiro step order of the i^{th} sub-array, K_{J} the Josephson constant, and f_{rf} the frequency of the applied microwave bias.

The PJVS device is a Supracon *almost*-binary array [5] with 69 631 SNS JJs. The N-layer is made of amorphous

[1]Brand names are used for identification purposes and such use implies neither endorsement by INRiM nor assurance that the equipment is the best available in the market.

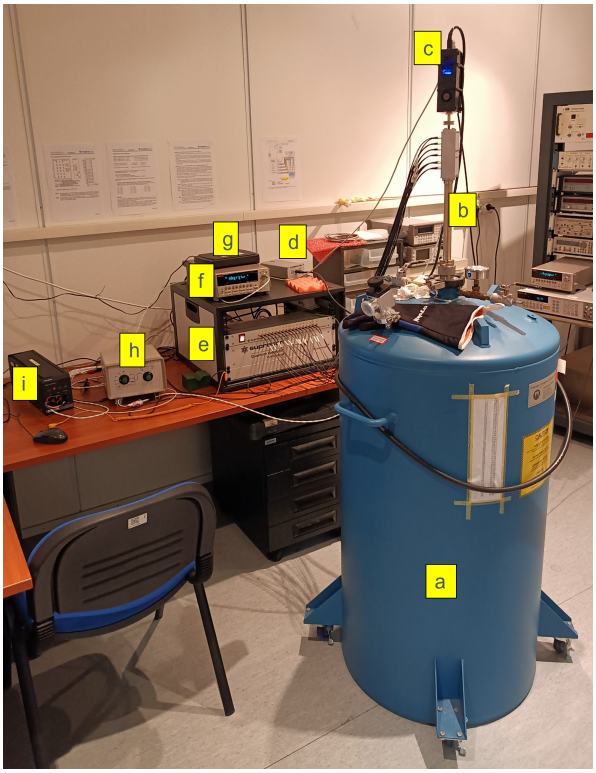

Fig. 1. Photograph of the 10 V PJVS-based measurement system. a) 60 L LHe dewar; b) Supracon cryoprobe immersed into the LHe, PJVS at the lower end and electrical connection box on the top side; c) 70 GHz synthesizer and d) power supply unit; e) rack with Supracon 18-channel bias source and floating power supply; f) Keithley 2182A nanovoltmeter; g) optically-isolated USB hub; h) low-thermal scanner; i) voltage source under calibration (Fluke 732B). Laptop not shown.

Nb_xSi_{1-x}, trimmed for 70 GHz irradiation [6]. The PJVS main parameters are: critical current of 8.0 mA at 4.2 K; $n = 0$ step width larger than 2 mA; $n = \pm 1$ step width of 1.3 mA, centered at 9 mA. The array contains $M = 17$ sub-arrays of series-connected JJs, each of which can be independently biased to a given Shapiro step. The array is structured with an almost-binary segmentation to limit the number of JJs required to reach the 10 V voltage target, that would be almost doubled with a true-binary segmentation [7]. The implemented array segmentation also enables to accurately verify the quantum operation with nV resolution.

B. *Cryogenic equipment*

The PJVS chip is installed on the lower end of a cryoprobe and is magnetically shielded by a cryoperm can. The cryoprobe has been designed for operation with a 60 L LHe dewar. It is made of a low conductivity stainless steel tube and internally houses an oversized circular waveguide for microwave transmission, as well as the wirings for sub-arrays bias and quantum voltage transfer. On the top side of the cryoprobe, an electrical connection box presents 17 SMB connectors for the sub-arrays biasing, a WR-12 flange for the microwave transmission, a 2-poles port for the Josephson voltage pick-up, and a 6-poles port for an additional quantum voltage pick-up and for biasing an integrated resistive heater mounted close to the PJVS chip, useful for quick JJ defluxing.

C. *Multi-channel bias source*

The bias-current to drive each PJVS sub-array is provided by a 18-channel voltage generator built by Supracon AG. The main specifications of this bias source can be found in Ref. [8]. In our system, 17 out of the available 18 channels are used to drive the 17 sub-arrays.
To guarantee the PJVS array electrical isolation from the Earth ground, the Supracon system features a floating supply to power the 18-channels bias source. Moreover, the power supply is equipped with a second DC power source at 18 V suitable to energize the aforementioned defluxing heater by simply pushing a dedicated button on the front panel for few seconds. An USB galvanic isolator and a USB-optical hub are employed for isolating the PJVS array from ground as well as minimizing the number of USB-connections to the laptop.

D. *Microwave synthesizer*

The required microwave power is provided by a commercial synthesizer[2] designed for 70 GHz Josephson voltage standards. The frequency range is 69.5 GHz to 70.5 GHz with 1 kHz resolution, whereas the maximum power level is about 250 mW, largely enough to drive common PJVS arrays. Frequency and power are set via software, and the synthesizer is USB-connected through the optical hub. The synthesizer comes with an external power supply unit (PSU), which can be in turn either DC or AC powered depending on the need. The synthesizer is equipped with a WR-12 flange for the 70 GHz signal output and a BNC input for the required 10 MHz reference time-base, which in our setup is provided by the INRiM Time and Frequency department.

E. *Nanovoltmeter / Null-detector*

The Supracon basic PJVS system employs a commercial nanovoltmeter to perform the usual array performance tests, i.e. verification of critical current and quantum margins (Sec. F). Also, the same nanovoltmeter can be used as a null-detector for the calibration of voltage sources through a multi-step differential measurement strategy. In our system, a Keithley 2182A is employed for both functions, though a different high-accuracy null-detector, e.g.

[2]ELVA SYN-E-69.5-70.5

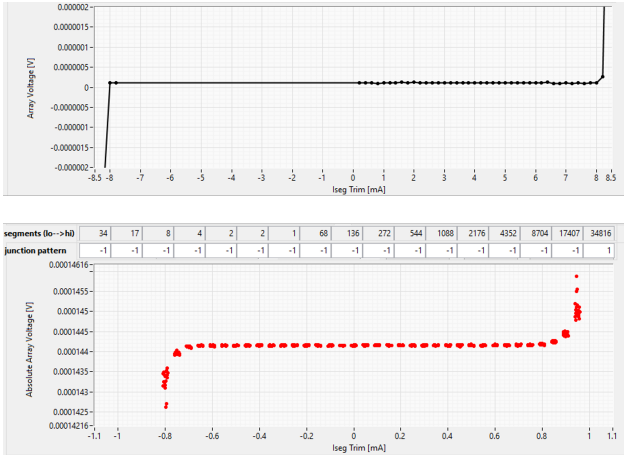

Fig. 2. PJVS array performance tests executed with the Supracon software. Top: plot of critical current test (no microwave). Bottom: plot of high-resolution quantum test with microwave at 69.65 GHz and 58 mW, set via the Supracon software, showing quantum margins larger than 1 mA.

an analog nanovoltmeter, may be employed for the calibration of voltage sources (Sec. G.) as well as to perform direct comparisons between Josephson voltage standards with ultimate accuracy [9].

F. *Supracon software*

The employed electronic instrumentation is properly software-controlled in order to automate both data acquisition and real-time analysis as much as possible.. The purchased system comes with a closed-source basic software to control multi-channel bias source, microwave synthesizer and nanovoltmeter. Supracon software is employed to check the PJVS array performances, i.e. critical current, step width and quantum test (see Fig. 2), to automatically optimize microwave frequency and power, and to suitably current-drive the sub-arrays to produce the quantized voltage V_{PJVS} programmed via the user interface.
Supracon software also allows to perform the calibration of gain and non-linearity of a wide range of commercial digital voltmeters (DVMs), including the "internal" Keithley 2182A nanovoltmeter and the widespread Keysight 3458A digital multimeter. Gain factors of the internal nanovoltmeter are saved into a configuration file and exploited by Supracon software to correct the measured value for each nanovoltmeter range up to 10 V. Finally, the acquired Supracon software comes with a TCP option to enable it to be externally-controlled with another home-built computer application.

G. *INRiM software*

Supracon commercializes hardware and software tools for DC voltage source calibrations as an additional option to the purchased basic PJVS system. Hence, a software written in Python has been developed at INRiM to work together with the basic Supracon software: INRiM software extends the full system capabilities with a tool for the calibration of a voltage source through the implementation of differential measurement schemes exploiting the same Keithley 2182 nanovoltmeter employed by the Supracon software, but it also leaves open the possibility of using a different null-detector. INRiM software exploits the Supracon TCP option to indirectly control the PJVS to generate the required voltage levels V_{PJVS}, without the need of dealing with two separate graphical interfaces at the same time. Moreover, PJVS quantization can be further verified during the voltage source calibration by slightly trimming the PJVS bias currents, typically in steps of $\pm 0.1\,\mathrm{mA}$. Finally, the INRiM software also enables internal nanovoltmeter gain correction using calibrated gain factors read from the Supracon software configuration file.

III. CALIBRATION OF A DC VOLTAGE SOURCE

The implemented measurement system is illustrated in Fig. 3.

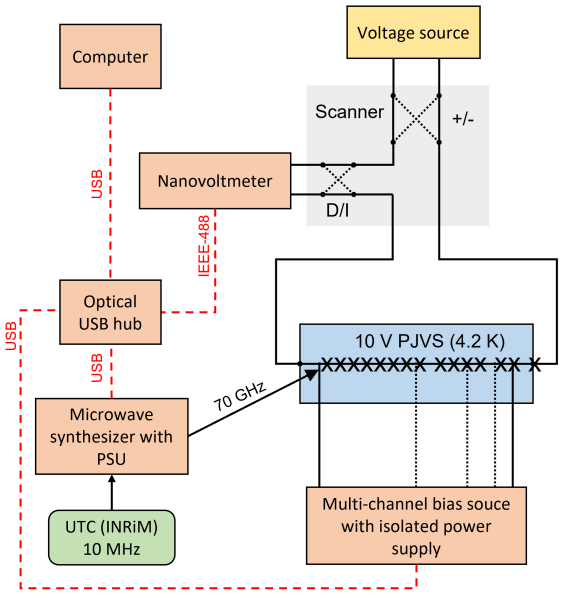

Fig. 3. Graphical representation of the 10 V PJVS system for the calibration of a DC voltage source through the differential measurement scheme.

At the current stage, a manual low-thermal electromotive forces (EMFs) scanner with both voltage source output polarity (+ or -) and nanovoltmeter input position (direct or

indirect) reversal capabilities is employed. In the future, a remotely-controlled scanner will be integrated in the system to fully automate and speed-up the calibration as well as to reduce possible heating effects related to the manual operation.

As customary, the calibration of a solid-state voltage standard requires the offsets cancellation in the measurement circuit, which are mostly due to thermal EMFs appearing between the PJVS array in LHe and the room temperature equipment. In a properly-designed measurement circuit, thermal offsets lower than 1 µV are attained by using low Seebeck coefficient materials, by minimizing the number of connections and by reducing temperature gradients between the two equal branches of the closed loop. It is also worth to mention that the accurate knowledge of the thermodynamic temperature is not needed, but rather the overall thermal stability during the calibration is required. Besides thermal offsets, attention should also be paid to possible ground-loops or EMI-coupling effects, which may introduce additional systematic errors which depend on the null-detector polarity. To compensate for these possible systematic errors, the difference between PJVS and source voltages is measured in different circuit configurations using the low-thermal scanner and the reversal strategy. The PJVS polarity reversal does not require a physical switch and is easily accomplished through a dedicated software function. To avoid the nanovoltmeter overloading due to the non-simultaneous source and PJVS polarity reversals, the nanovoltmeter input is shorted prior to each voltage inversion and restored right after. Finally, in case of significant thermal EMFs variations, a proper calibration scheme can be implemented to cancel the contribution of offsets linearly changing with time, which consists in repeating the normal measurement sequence in the opposite way.

Preliminary calibration tests have been carried out to verify the correct operation of overall measurement system and employed procedures. The device under calibration was a Fluke 732B solid-state voltage source, with 1.018 V and 10 V nominal outputs. Microwave frequency and power were set to the optimal values attained with the Supracon software, i.e. 69.65 GHz and 56 mW. Two distinct calibration strategies have been adopted: i) a 4-steps sequence with both sources and nanovoltmeter reversals (+D, +I, -I, -D); ii) a faster 2-steps sequence with only sources polarity reversal (+D,-D), hence always keeping the null-detector switch in the direct mode (D). The calibration results at 10 V and 1.018 V nominal outputs are shown in Fig. 4. It can be seen that the measurements performed with the different polarity-reversals sequence are consistent within each other, therefore possible deviations related to the null-detector polarity are not significant.

Error bars represent the standard deviation of the mean of five repeated measurements. However, it is widely recognized that the calibration uncertainty of commercial

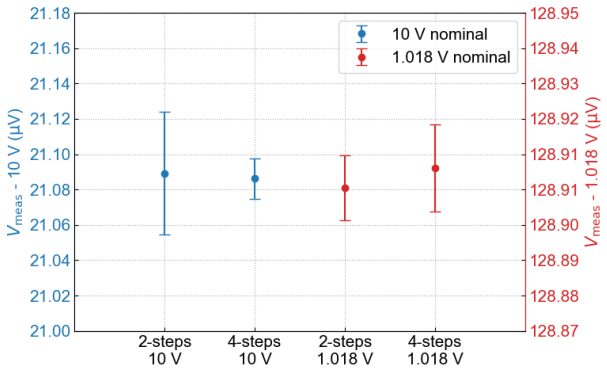

Fig. 4. Difference between source calibrated voltage and nominal voltage, at 10 V (left axis, blue) and 1.018 V (right-axis, red). Each voltage output has been calibrated following two distinct measurement schemes with either two (+D, -D) or four (+D, +I, -I, -D) reversal steps. Suppression of time-dependent offsets was not necessary. Error bars represent the standard deviation of the mean of five repeated measurements.

Zener-diode voltage references is dominated and limited by their inner flicker noise [10], which is likely to underestimate the actual random effects when the standard deviation of the mean is considered, especially for long measurement times. To account for the presence of the Zener flicker noise, a type-A uncertainty contribution not lower than 100 nV for the 10 V output is usually assumed [10]. With regards to type-B uncertainty contributions, these are associated to: i) null-detector gain and non-linearity; ii) uncompensated thermal offsets; iii) leakage resistances; iv) microwave frequency. A preliminary uncertainty budget, including both type-A and type-B sources, is shown in Tab. 1.

Uncertainty source	**Uncertainty (nV)**
Type A	
Noise (flicker)	150
Type B	
Nanovoltmeter	20
Uncompensated offsets	10
Leakage	< 1
Microwave frequency	< 0.1
Combined standard uncertainty (*k*=1)	**151.7**

Table 1. Preliminary uncertainty budget of the 10 V nominal output of the Fluke 732B calibrated with the PJVS system.

IV. CONCLUSION

A 10 V PJVS-based DC voltage calibration system has been recently purchased, integrated and tested at INRiM. It will serve as basis for the realization of the primary DC voltage standard linking the Italian voltage unit to the new quantum-based International System of Units. The optimal performances of the array have been verified. Also, actual quantization of PJVS-segments has been tested at the nV-level using the nanovoltmeter as null-detector. First calibration tests of a solid-state voltage source provide satisfactory results in terms of repeatability and overall uncertainty. Interlaboratory comparisons are foreseen to provide a final validation of the implemented quantum voltage measurement system.

REFERENCES

[1] C. A. Hamilton, "Josephson voltage standards," *Rev. Sci. Instrum*, vol. 71, no. 10, pp. 3611–3623, 2000.

[2] B. Jeckelmann and B. Jeanneret, *The application of the Josephson and quantum Hall effects in electrical metrology*. IOS Press, 2007, vol. 166, pp. 135–179.

[3] A. Rüfenacht, N. E. Flowers-Jacobs, and S. P. Benz, "Impact of the latest generation of Josephson voltage standards in ac and dc electric metrology," *Metrologia*, vol. 55, no. 5, p. S152, 2018.

[4] B. Trinchera, D. Serazio, P. Durandetto, L. Oberto, L. Fasolo *et al.*, "Towards a novel programmable Josephson voltage standard for sampled power measurements," in *Proceedings of 25th IMEKO TC4 International Symposium*. IMEKO, 2022, pp. 1–6.

[5] F. Müller, T. J. Scheller, J. Lee, R. Behr, L. Palafox, M. Schubert, and J. Kohlmann, "Microwave design and performance of PTB 10 V circuits for the programmable Josephson voltage standard," *World J. Condens. Matter Phys.*, vol. 4, no. 03, p. 107, 2014.

[6] F. Müller, T. Scheller, R. Wendisch, R. Behr, O. Kieler, L. Palafox, and J. Kohlmann, "NbSi barrier junctions tuned for metrological applications up to 70 GHz: 20 V arrays for programmable Josephson voltage standards," *IEEE Trans. Appl. Supercond.*, vol. 23, no. 3, pp. 1 101 005–1 101 005, June 2013.

[7] P. Durandetto and A. Sosso, "Non-conventional PJVS exploiting first and second steps to reduce junctions and bias lines," *IEEE Trans. Instrum. Meas.*, vol. 69, no. 4, pp. 1294–1301, 2020.

[8] M. Starkloff, H. Preissler, and M. Schubert, "Compact 18-channel bias source for 10 V programmable Josephson voltage standard arrays," in *2020 Conf. Precis. Electromagn. Meas. (CPEM)*. IEEE, 2020, pp. 1–2.

[9] A. Rüfenacht, Y. Tang, S. Solve, A. E. Fox, P. D. Dresselhaus, C. Burroughs, R. E. Schwall, R. Chayramy, and S. Benz, "Automated direct comparison of two cryocooled 10 volt programmable Josephson voltage standards," *Metrologia*, 2018.

[10] R. Chayramy, S. Yang, O. Power, and S. Solve, "Metrology of zener-based secondary voltage standards," *Meas. Sci. Technol.*, vol. 32, no. 10, p. 105019, 2021.

26th IMEKO TC4 International Symposium
24th International Workshop on ADC and DAC Modelling and Testing
IMEKO TC-4 2023
Pordenone, Italy / September 20-21, 2023

Quantum magnetometry with OPM: Novel applications in non-destructive testing?

Andreas Blug[1], Kerstin Thiemann[1], Simon Philipp[2], Thomas Straub[2], Alexander Bertz[1]

[1] *Fraunhofer Institute for Physical Measurement Techniques IPM, Freiburg, Germany.*
E-mail: prename.name@ipm.fraunhofer.de, e.g., andreas.blug@ipm.fraunhofer.de
[2] *Fraunhofer Institute for Mechanics of Materials IWM, Freiburg, Germany*
E-mail: prename.name@iwm.fraunhofer.de

Abstract **– Microfabricated optically pumped magnetometers (OPM) are a novel class of commercially available quantum magnetometers combining high sensitivity with high dynamic range. In non-destructive testing (NDT) this should enable new applications like measuring stray fields arising from small stress concentrations affecting local magnetization. In ferromagnetic steel the sensitivity of OPM is sufficient to measure magnetization from critical stresses for crack initiation in submillimeter volumes. However, OPM, as they are built today, require additional components like magnetic flux guides to control the measurement volume in NDT systems. The improvement of spatial resolution with such a flux guide is demonstrated using neighbored weld seams as an example for stress concentrations.**

I. INTRODUCTION

Quantum magnetometers like OPM exploit fundamental physical constants so that no calibration is required and quantum techniques as entanglement or spin squeezing to achieve a higher statistical precision than classical approaches [1, 2]. This results in robust and highly sensitive devices with extraordinary dynamic range close to the physical limits [3]. OPM measuring magnetic fields by their interactions between resonant light and atomic vapor have evolved rapidly during the past two decades. Modern ones, as they became commercially available in recent years, are microfabricated systems consisting of one or more small vapor cells (~ 1 mm³) of gaseous helium or alkali atoms that are pumped by a laser to spin states similar to atomic clocks [4-7]. They measure spins collectively precessing around the magnetic field direction with the so-called Larmor frequency. Depending on the read-out mechanism, different sensitivities and measurement ranges are achieved. Table 1 lists specifications of some commercially available OPM sensors which might be interesting for applications in the field of non-destructive testing (NDT). They achieve similar sensitivities as superconducting quantum interference devices (SQUIDs), but without complex and expensive cryogenic cooling.

Table 1. Some commercially available OPM sensors.

	Fieldline V3 [8]	Mag4Health He-4-mag. [9]	QuSpin total-field mag. [10]
Gas	Rb	^{4}He	Rb
B-field	single axis	vector xyz	scalar
Sensitivity	15 fT/√Hz	40 fT/√Hz	3 pT/√Hz
Dyn. range	50 nT	250 nT	100 µT
Bandwidth	250 Hz	2 kHz	500 Hz
Size [mm³]	13x15x36	20x20x50	12x18x36

As passive magnetic NDT methods like “metal magnetic memory” (MMM) measure local variations of magnetization due to stress or microscopic structure within a volume in ferromagnetic materials, OPM are beneficial to decrease that measurement volume [11-13], i.e., to increase either lateral resolution for stress concentration measurement or depth resolution for structural changes like martensite-austenite transitions in hardening layers. The major challenges for using these systems are to control the measurement volume and to suppress ambient perturbations from microtesla to picotesla scale. A particular benefit would be to measure stress concentrations with a submillimeter resolution because such stress concentrations are the precondition for crack initiation [14, 15].

II. PIEZOMAGNETIC FATIGUE TESTING

A first setup to learn about the evolution of magnetic signals over the lifetime of a material is shown in Fig. 1. It combines a cyclic fatigue setup with a OPM in a shielded environment. As shown in Fig. 1a, the specimen is mounted on ceramic rods where the right end is moved by a piezo actor and the left is connected to a force measurement cell. The zero-field OPM measures the vertical component of the magnetic stray field B varying with force F and strain ε [16]. The coils on the inner layer of the magnetic shield control the magnetic environment

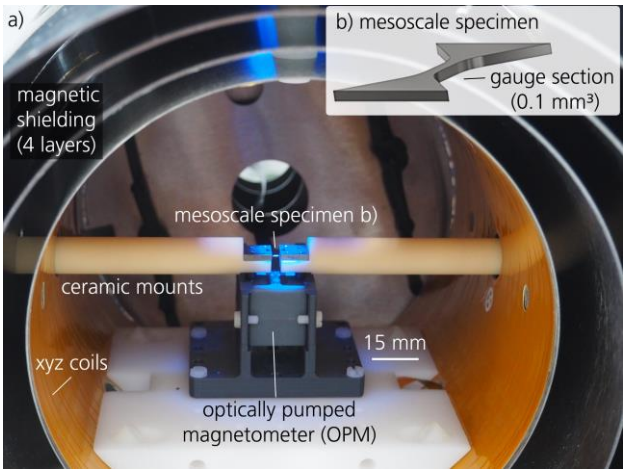

Fig. 1. a) Setup for piezomagnetic fatigue testing with mesoscale specimen (b). Magnetic signals arise from the gauge section with a volume of 0.6x0.4x0.4 mm³.

of both, specimen and OPM sensor. In contrast to similar experiments with classical magnetometers [17, 18], the gauge section of the specimen can where fatigue damage accumulates can be decreased from cm to sub-mm scale which makes it much easier to link events in the magnetic signal to metallographic characterizations. The noise within the shielding is below 1 pT at a measurement rate of 100 Hz, even if the sample is moved.

Fig. 2 shows the evolution of the mechanical hysteresis (F-ε) and of the piezomagnetic hysteresis (B-ε) over the lifetime of a ferritic steel specimen. A 5%-drop of force amplitude is used as end-of-life criterion [19]. The complete signals over the lifetime of 140 cycles are drawn light grey; some of them are colored to illustrate the evolution. Up to that point, microscopic defects like dislocations, grain boundaries, precipitates, and non-magnetic inclusions are accumulated in the material without crack initiation and the stiffness of the sample is not altered significantly. Therefore, force F hardly changes apart from some hardening in the beginning. In the piezomagnetic curve, two major effects are visible: firstly, the major change in magnetic stray field B occurs in the elastic parts of the mechanical hysteresis, i.e., the steep slopes in the mechanical hysteresis (F-ε). This corresponds to the stress response of magnetization of the material [20]. Secondly, the amplitude of the piezomagnetic hysteresis varies much stronger over the lifetime than the force signal due to pinning effects between fatigue damage and magnetic domain walls.

For NDT applications, these experiments demonstrate that OPM can resolve the variation of the magnetic stray field corresponding to yield condition in a volume of 0.1 mm³, i.e., on a submillimeter scale. The amplitude of the magnetic stray field varies by about 5 nT between positive and negative yield stress. However, the lateral resolution is defined by the distance between the vapor cell

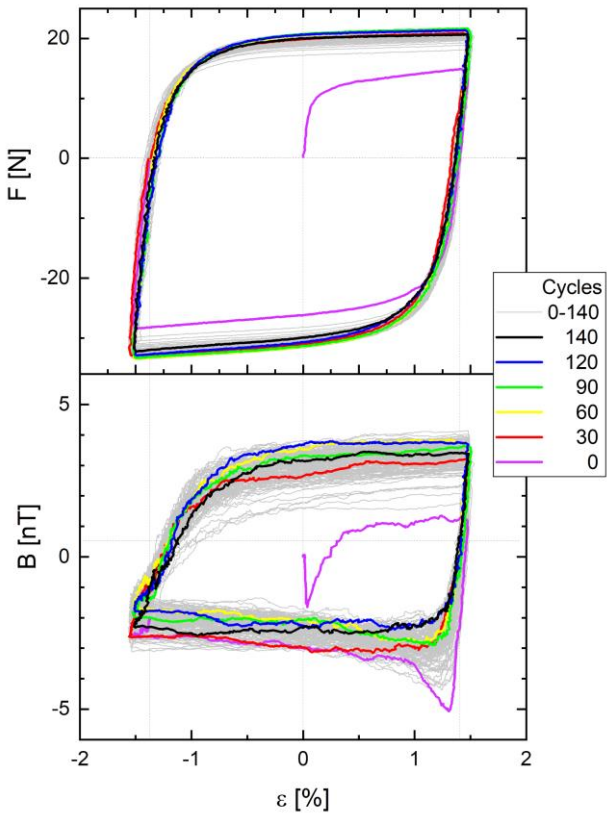

Fig. 2. Piezomagnetic fatigue signals for a ferritic steel specimen. End-of-life criterion is a 5% drop of force. Mechanical hysteresis (F-ε) of force F and strain ε, and piezomagnetic hysteresis (B-ε) of magnetic stray field B and strain ε.

inside the sensor, where the magnetic field is measured, and the specimen surface. In the setup of Fig. 1 it is about 12 mm – the minimum distance between vapor cell and sensor surface is about 6 mm. Therefore, additional components like pick-up coils or flux guides are required to control the measurement volume.

III. SPATIAL RESOLUTION AT WELD SEAMS

To confine the measurement volume, Kim and Savukov used flux guides from Mn-based ferrites to measure the lateral component of the magnetic field with high spatial resolution of 0.25 mm [21]. For the setup in Fig 3a, we use a different flux guide geometry measuring the normal component of the external magnetic field [22]. This geometry should be appropriate for NDT of ferromagnetic specimen as their inner magnetic field is refracted towards the normal at the surface due to their high magnetic permeability μ_r. The setup in Fig 3a uses a similar shielding as the fatigue trials Fig. 1. The zero-field OPM is embedded in a 3D printed structure holding a flux guide with a conically shaped tip.

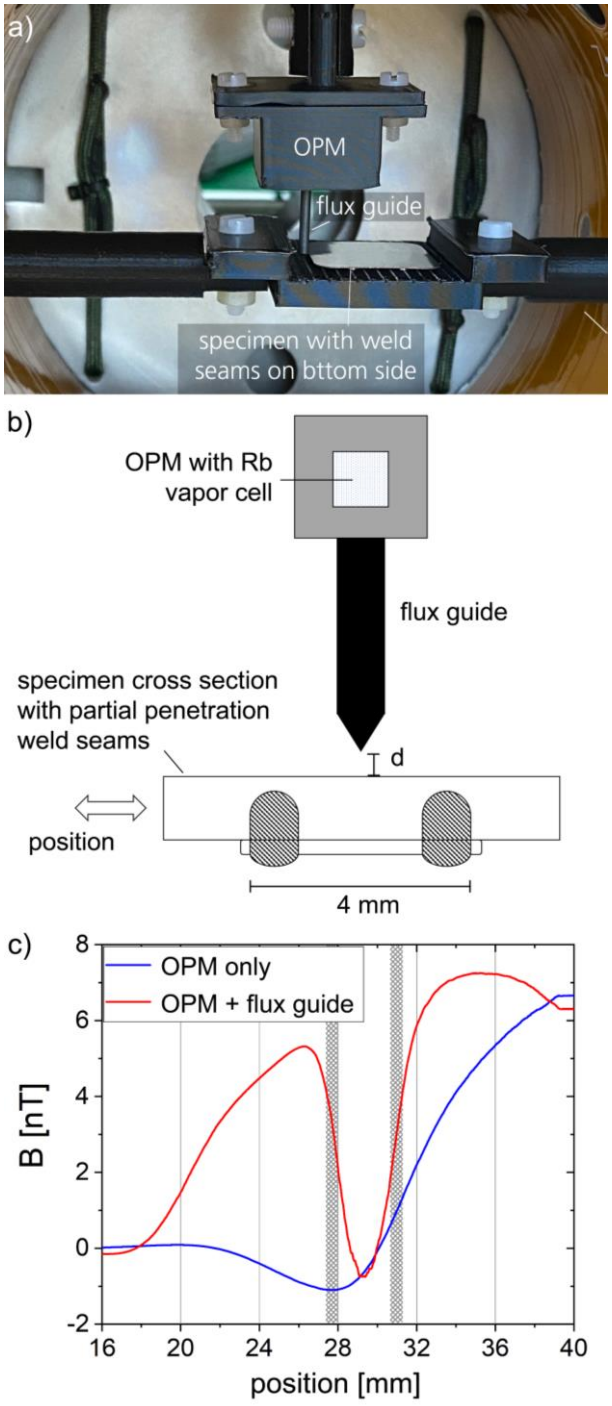

Fig. 3. Detection of two partial penetration weld seams separated by 4 mm. A): image of the setup with OPM, flux guide and specimen. B) sketch of OPM with Rb vapor cell, flux guide, and cross section of a moving specimen with weld seams. C) distribution of magnetic stray field B measured with (red) and without flux guide (blue).

To demonstrate the improvement of spatial resolution, a steel sample with two neighbored partial penetration weld seams serving as localized stress concentrations due to thermal expansion [23 - 25]. As sketched in Fig. 3b, the weld seams are separated by 4 mm, attaching a second layer of ferromagnetic steel. No heat affected zone is visible on the bottom of the sample so that the distance d between sample and tip of the flux guide remains constant when the sample is moved. The diameter of the flux guide is 1.5 mm.

The comparison between the measurements with the OPM sensor only guided close to the sample (blue) and the combination of OPM and flux guide (red) is shown in Fig. 3. In both cases, the distance d between sample surface and OPM housing in the first case and flux guide in the second case is estimated visually to about 1 mm. The sample has a magnetic gradient across the scanned line. However, the expected pairwise symmetry of the weld seams is only visible in the magnetic signal acquired with flux guide. Due to the flux guide, the noise level rises from 0.5 to 2 pT, but with increased lateral resolution in the range of about 2 mm at the depth of the weld seam. By further optimizing the flux guide geometry, it should be possible to achieve sub-millimeter spatial resolution in this configuration.

IV. DISCUSSION

Microfabricated optically pumped magnetometers (OPM) are among the first commercially available quantum sensors. Total-field OPM have an exceptional dynamic range with a sensitivity of 3 pT/√Hz in an environment of 100 µT, i.e., in earth magnetic field. Zero-field OPM based on Rb or He vapor cells achieve sensitivities below 100 fT/√Hz – similar to SQUIDs, but without cryogenic cooling which simplifies high-sensitive magnetometry systems enormously. Due to these properties, OPM sensors open new applications in magnetic NDT.

In the piezomagnetic fatigue experiments, the magnetic stray field from a volume of only 0.1 mm³ varying by 5 nT is measured at a specimen from ferritic steel. The magnetic signal is much more sensitive to the accumulation of damage in the sample's gauge area than the stress-strain signal, which is a first step towards a magnetic fingerprint for mechanical degradation. The noise level of 0.5 pT without and of 2 pT with flux guide is also sufficient to measure critical stress concentrations arising from weld seams or material defects as precondition for crack initiation. Here, a flux guide is required to confine the measurement volume so that residual stresses of two neighbored weld seams separated by 4 mm could be resolved. With some optimization, sub-millimeter resolution appears feasible.

To test ferromagnetic devices in industrial environments, key components like flux guides, shielding, and low-stray-field actuators must be developed. Doing

that, the result can be a new generation of non-destructive testing systems estimating the remaining lifetime in maintenance or in the production if higher levels of functional safety are required or to assess the quality of critical weld seams.

ACKNOWLEDGEMENTS

This work was supported as a Fraunhofer LIGHTHOUSE PROJECT (QMag). We acknowledge financial support from the Ministry of Economic Affairs, Labor and Housing of the State of Baden-Württemberg, Germany. Thanks also to Ralph Sperling from Fraunhofer IMM for manufacturing the flux guides.

REFERENCES

[1] D. Budker, M. Romalis, “Optical magnetometry,” nature physics, vol. 3, pp. 227–234, 2007.

[2] L. Pezzè, A. Smerzi, M. K. Oberthaler, R. Schmied, P. Treutlein, “Quantum metrology with nonclassical states of atomic ensembles,” Rev. Mod. Phys., vol. 90, no. 3, p. 99, 2018.

[3] M. W. Mitchell, S. Palacios Alvarez, “Colloquium: Quantum limits to the energy resolution of magnetic field sensors,” Rev. Mod. Phys., vol. 92, no. 2, 2020.

[4] S. Knappe, O. Alem, D. Sheng, J. Kitching, “Microfabricated Optically-Pumped Magnetometers for Biomagnetic Applications,” J. Phys.: Conf. Ser., vol. 723, p. 12055, 2016.

[5] V. Shah et al., “Fully integrated, standalone zero field optically pumped magnetometer for biomagnetism,” Proc. SPIE 10548, p. 51, 2018.

[6] F. Bertrand et al., “A 4He vector zero-field optically pumped magnetometer operated in the Earth-field,” The Review of scientific instruments, vol. 92, no. 10, p. 105005, 2021.

[7] N. V. Nardelli, A. R. Perry, S. P. Krzyzewski, S. A. Knappe, “A conformal array of microfabricated optically-pumped first-order gradiometers for magnetoencephalography,” EPJ Quantum Technol., vol. 7, no. 1, p. 664, 2020.

[8] HEDscan V3 spec sheet, Fieldline Inc., 4845 Sterling Drive, 200, Boulder CO 80301, USA. https://fieldlineinc.com/ (accessed: Mar. 30, 2023)

[9] Mag4Health SAS, 9 Avenue Paul Verlaine, 38100 Grenoble, F, He-4 magnetometer. [Online]. https://www.mag4health.com/product/ (accessed: Mar. 23, 2023).

[10] QuSpin, Inc., 331 South 104th Street, Louisville, CO 80027, Quspin QTFM Gen-2. [Online]. https://quspin.com/qtfm-gen-2/ (accessed: Mar. 23, 2023).

[11] Z. D. Wang, Y. Gu, Y. S. Wang, “A review of three magnetic NDT technologies,” Journal of Magnetism and Magnetic Materials, vol. 324, no. 4, pp. 382–388, 2012.

[12] M. Roskosz, M. Bieniek, “Evaluation of residual stress in ferromagnetic steels based on residual magnetic field measurements,” NDT & E International, vol. 45, no. 1, pp. 55–62, 2012.

[13] N. Sonntag, B. Skrotzki, R. Stegemann, P. Löwe, M. Kreutzbruck, “The Role of Surface Topography on Deformation-Induced Magnetization under Inhomogeneous Elastic-Plastic Deformation,” Materials (Basel, Switzerland), vol. 11, no. 9, 2018.

[14] S. Gustafson et al., “Quantifying microscale drivers for fatigue failure via coupled synchrotron X-ray characterization and simulations,” Nature communications, vol. 11, no. 1, p. 3189, 2020.

[15] P. Ferro, “The local strain energy density approach applied to pre-stressed components subjected to cyclic load,” Fatigue Fract Engng Mater Struct, vol. 37, no. 11, pp. 1268–1280, 2014.

[16] P. A. Koss et al., “Optically Pumped Magnetometer Measuring Fatigue-Induced Damage in Steel,” Applied Sciences, vol. 12, no. 3, p. 1329, 2022, doi: 10.3390/app12031329.

[17] A. Ouaddi et al., “Passive piezomagnetic monitoring of structures subjected to in-service cyclic loading: Application to the detection of fatigue crack initiation and propagation,” AIP Advances, vol. 11, no. 1, p. 15344, 2021.

[18] S. Bao, T. Erber, S. A. Guralnick, W. L. Jin, “Fatigue, Magnetic and Mechanical Hysteresis,” Strain, vol. 47, no. 4, pp. 372–381, 2011.

[19] K. Thiemann et al. "Using optically pumped magnetometers to identify initial damage in bulk material during fatigue testing." Quantum Technologies 2022. Vol. 12133. SPIE, 2022.

[20] D. C. Jiles, “Theory of the magnetomechanical effect,” J. Phys. D: Appl. Phys, no. 28, p. 1537, 1995.

[21] Y. J. Kim, I. Savukov, “Ultra-sensitive Magnetic Microscopy with an Optically Pumped Magnetometer,” Scientific reports, vol. 6, p. 24773, 2016.

[22] U. Poppe et al., “High temperature superconductor dc-SQUID microscope with a soft magnetic flux guide,“ Jpn. J. Appl. Phys. 17(5), S191-S195 (2004).

[23] R. Stegemann et al., “Influence of the Microstructure on Magnetic Stray Fields of Low-Carbon Steel Welds,“ J Nondestruct Eval 37(3), 1821 (2018).

[24] F. Giudice, A. Sili, “A theoretical approach to the residual stress assessment based on thermal field evaluation in laser beam welding,” Int J Adv Manuf Technol, vol. 123, 7-8, pp. 2793–2808, 2022.

[25] A. Blug et al., “The full penetration hole as a stochastic process: controlling penetration depth in keyhole laser-welding processes,” Appl. Phys. B, vol. 108, no. 1, pp. 97–107, 2012.

26th IMEKO TC4 International Symposium
24th International Workshop on ADC and DAC Modelling and Testing
IMEKO TC-4 2023
Pordenone, Italy / September 20-21, 2023

Power System Frequency and ROCOF Measurement by Means of Electronic Instruments

Daniel Belega[1], Gabriel Găspăresc[1]

[1]*Department of Measurements and Optical Electronics, University Politehnica Timisoara, Bv. V. Parvan, Nr. 2, 300223, Timisoara, Romania, emails: daniel.belega@upt.ro, gabriel.gasparesc@upt.ro*

***Abstract* – In this paper the accuracy of the power system frequency measurement achieved by means of two commonly used electronic instruments, which are a universal counter and a bench top digital multimeter, are investigated under steady-state conditions in the case of synthetized and real-life power system signals. Moreover, the accuracy of the Rate-Of-Change Of Frequency (*ROCOF*) estimates achieved by means of the frequency measurements is analyzed. The results obtained by both instruments are compared with each other. In addition, from the achieved measurements some remarks are drawn.**

I. INTRODUCTION

One of the most important parameters of an electrical waveform is its frequency. It is often used in the modern power systems for control and protection purposes. In these applications the frequency should be estimated in real-time with high accuracy. To this aim there have been proposed different time-domain and frequency-domain algorithms [1]-[5]. To achieve high accuracy, they compensate the contribution of the spectral interference due to the frequency image component, harmonics, and interharmonics, which affect any real-life electrical waveforms. Another possibility to estimate the frequency is to use electronic instruments. The commonly used instruments for frequency measurement are the reciprocal Universal Counters (UCs) and the Digital MultiMeters (DMMs). They measure the frequency by using the same technique. The aim of this paper is to investigate the accuracy of the frequency estimates achieved by using two such instruments under different steady-state conditions in the case of synthetized and real-life power system signals. These conditions are the off-nominal frequency, harmonics, and Out-Of-Band Interferences (OOBI). The used instruments are the reciprocal UC BK1823A [6] and the DMM Keysight 34465A [7]. The BK1823A has only fixed gate time (*GT*) values, which are 0.01 s, 0.1 s, 1 s, and 10 s. The Keysight 34465A is a bench top DMM with 6½ digits. It measures frequency by using the principle of the reciprocal universal counter. The Keysight 34465A also has fixed *GT* values, which are the same as in the case of BK1823A and, supplementary, 1 ms value. It should be remarked that the price of the Keysight 34465A is about four-times higher than that of the BK1823A.

Also, the Rate-Of-Change-Of Frequency (*ROCOF*) parameter is estimated by means of the obtained frequency estimates. As accuracy parameters the Frequency Error (*FE*) and the Rate of change of the Frequency Error (*RFE*) or the *ROCOF* error are used. The *FE*s and *RFE*s achieved by both instruments are compared with each other.

The analysis performed in this work is very important since it allows the researchers to compare the accuracies of the proposed frequency estimators also with those achieved using such instruments. The presented measurements can be easily reproduced.

II. THE PERFORMED MEASUREMENTS

The nominal frequency is f_0 = 50 Hz. For both instruments the *GT* is fixed to 0.01 s or 0.1 s, in order to achieve a fast measurement. The frequencies measured by the BK1823 are acquired via an RS232 interface using the software developed by the manufacturer. In the case of the Keysight 34465A the measured frequencies are acquired via an USB interface by means of the PathWave BenchVue software developed by Keysight [8].

Unfortunately, the time between two successive readings, which is available for the user, is not the same, and so, we cannot achieve a fixed reporting rate by any of these instruments. The average reporting rate for the BK1823A is about 4 readings/s, while for the Keysight 34465A it is about 15 readings/s.

The test signals are provided by the Keysight EDU33212A function/arbitrary waveform generator [9]. That generator has the facility to combine the signals generated at both outputs into one signal. That facility is used in this work to generate a sinewave affected by a harmonic or an interharmonic. The Keysight EDU33212A generator has a very high frequency stability, of about ±(1 *ppm of setting*) for the frequencies used in the performed tests. Therefore, we will consider that the true frequency is equal to the setting one. In each test there are measured M = 1000 values of signal frequency.

The parameter *FE* is computed by the expression:

$$FE_k(\text{Hz}) = f_k - f, k = 1, 2, \dots, M-1 \qquad (1)$$

in which f_l is the lth measured frequency and f is the true frequency.

Since in the steady-state conditions the frequency is not changed the parameter *RFE* is equal to the parameter

ROCOF, which are computed as:

$$RFE_k\ (\mathrm{Hz/s}) = ROCOF_k(\mathrm{Hz/s}) = \frac{f_{k+1}-f_k}{T},\ k = 1, 2, \ldots, M-1 \qquad (2)$$

where T is the time between two successive readings. Then, the maximum of the absolute value of the magnitudes of the parameters *FE* and *RFE*, $|FE|_{max}$ and $|RFE|_{max}$, are computed.

The amplitude of the generated sinewave is equal to 8 V.

In the following we will present the results achieved by both instruments under the considered conditions.

A. Steady-state conditions

• off-nominal frequency condition

GT is equal to 0.01 s. The results achieved by both instruments at 45 Hz, 48 Hz, 50 Hz, 52 Hz, and 55 Hz frequencies are given in Table 1 and the histograms corresponding to the frequency f = 52 Hz achieved for the frequency measurements obtained by both instruments are shown in Fig. 1.

Table 1. $|FE|_{\max}$ and $|RFE|_{max}$ achieved by both instruments when GT = 0.01 s under off-nominal frequency condition.

Frequency (Hz)	UC BK1823A		DMM Keysight 34465A	
	$\|FE\|_{\max}$ (mHz)	$\|RFE\|_{\max}$ (Hz/s)	$\|FE\|_{\max}$ (mHz)	$\|RFE\|_{\max}$ (Hz/s)
45	2.0	0.009	17.0	0.41
48	3.0	0.017	15.0	0.36
50	2.0	0.014	13.0	0.32
52	3.0	0.014	16.0	0.38
55	2.0	0.009	20.0	0.46

From the results given in Table 1 it follows that the frequency and *ROCOF* are more accurate measured by using the BK1823A than the Keysight 34465A. Moreover, from Fig. 1 it can be observed that the BK1823A provides a smaller number of different frequency values as compared with the Keysight 34465A. This observation holds also for the *ROCOF* estimates.

• harmonics condition

GT is equal to 0.01 s. The results achieved by both instruments in the case of the 2nd, 3rd, 5th, and 7th harmonics are given in Table 2. The amplitude of each considered harmonic is equal to 10% of the fundamental amplitude.

From the results given in Table 2 it follows that the frequency and *ROCOF* measurements achieved by using the BK1823A are more accurate than those achieved by using the Keysight 34465A. Also, by comparing the results given in Table 1 when f = 50 Hz with those given in Table 2 it follows that the harmonics has a very small contribution on the frequency measurements achieved by both instruments.

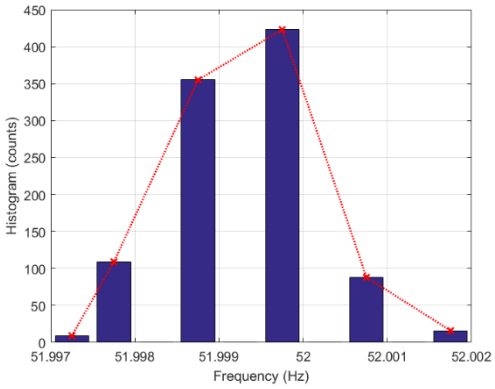

(a)

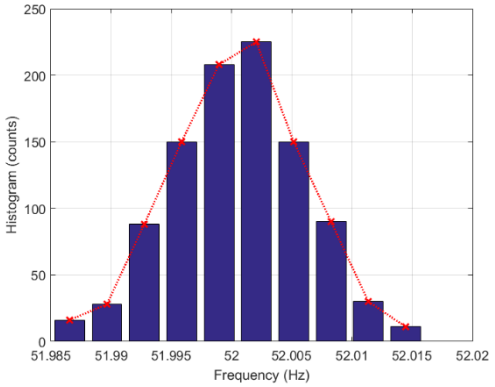

(b)

Fig. 1. Histograms of the frequency measurements achieved by the BK1823A (a) and the Keysight 34465A (b) when GT = 0.01 s and f = 52 Hz. M = 1000 measurements.

Table 2. $|FE|_{\max}$ and $|RFE|_{max}$ achieved by both instruments when GT = 0.01 s under harmonics condition.

Harmonic	UC BK1823A		DMM Keysight 34465A	
	$\|FE\|_{\max}$ (mHz)	$\|RFE\|_{\max}$ (Hz/s)	$\|FE\|_{\max}$ (mHz)	$\|RFE\|_{\max}$ (Hz/s)
2nd	2.0	0.013	15.0	0.36
3rd	2.0	0.013	11.0	0.27
5th	2.0	0.017	9.0	0.23
7th	2.0	0.013	8.0	0.19

• out-of-band interference (OOBI) condition

Two test signals which contain the fundamental component and an interharmonic are considered. In the first test signal the frequency of the fundamental component is equal to 47.5 Hz, while that of the interharmonic is equal to 25 Hz. In the second test signal the frequency of the fundamental component is equal to 52.5 Hz, while that of the interharmonic is equal to 75 Hz.

The interharmonics amplitude is equal to 10% of the amplitude of the fundamental component. The results achieved when GT = 0.01 s and 0.1 s are reported in Table 3.

Table 3. $|FE|_{max}$ and $|RFE|_{max}$ achieved by both instruments when GT = 0.01 s and GT = 0.1 s under out-of-band interference condition.

Sinewave and interharmonics frequencies and GT	UC BK1823A		DMM Keysight 34465A	
	$\|FE\|_{max}$ (mHz)	$\|RFE\|_{max}$ (Hz/s)	$\|FE\|_{max}$ (mHz)	$\|RFE\|_{max}$ (Hz/s)
47.5 Hz & 25 Hz GT = 0.01 s	1123.0	8.27	1567.0	58.74
47.5 Hz & 25 Hz GT = 0.1 s	202.4	1.74	286.1	2.97
52.5 Hz & 75 Hz GT = 0.01 s	1774.0	7.10	1600.0	54.46
52.5 Hz & 75 Hz GT = 0.1 s	307.0	2.09	265.0	2.27

When GT = 0.1 s the errors achieved by both instruments are smaller as compared with those achieved when GT = 0.01 s, but they are still high. A further reduction of the achieved errors can be achieved by filtering. In Table 4 there are given the results achieved when GT = 0.1 s and a six-order band-pass filter is applied to the analyzed signal. That filter was obtained by connecting three two-order Butterworth band-pass filters in series. The two-order band-pass filter was implemented by means of the universal filter UAF42 [9]. The band-pass of this filter is [40, 60] Hz. The histograms corresponding to the second signal test for the frequency measurements achieved by both instruments are shown in Fig. 2.

Table 4. $FE|_{max}$ and $|RFE|_{max}$ achieved by both instruments when GT = 0.1 s and using a filter under out-of-band interference condition.

Sinewave and interharmonics frequencies	UC BK1823A		DMM Keysight 34465A	
	$\|FE\|_{max}$ (mHz)	$\|RFE\|_{max}$ (Hz/s)	$\|FE\|_{max}$ (mHz)	$\|RFE\|_{max}$ (Hz/s)
47.5 Hz & 25 Hz	8.60	0.06	64.00	0.83
52.5 Hz & 75 Hz	33.30	0.20	30.00	0.31

By filtering the accuracy of the frequency and *ROCOF* measurements achieved by both BK1823A and Keysight 34465A increases very much. In most situations the smallest errors are achieved by using BK1823A.

In Fig. 2 it can be seen that about half of the frequency measurements achieved by both instruments are very close to 52.5 Hz. Also, it is worth noticing that in the case of the BK1823A more different frequency values are achieved as compared with the case of a pure sinewave (see Fig. 1(a)).

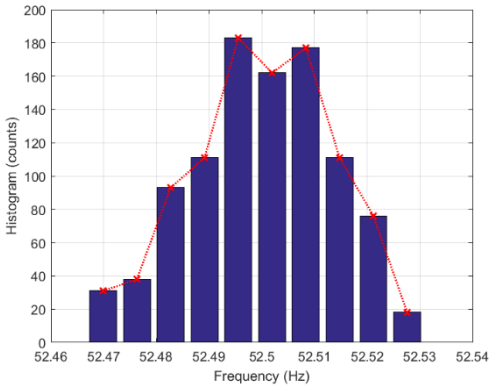

(a)

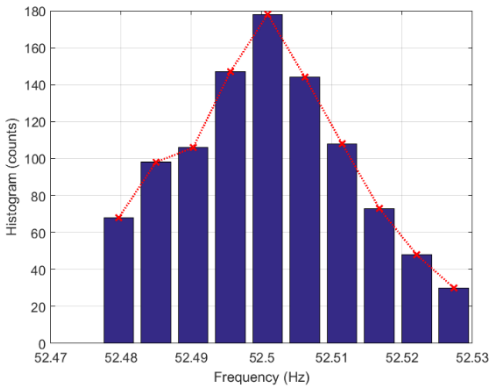

(b)

Fig. 2. Histograms of the frequency measurements achieved by the BK1823A (a) and the Keysight 34465A (b) when GT = 0.1 s in the case of a sinewave of frequency f = 52.5 Hz affected by an interharmonic of 75 Hz frequency, applied to a six-order band-pass filter. Amplitude of interharmonic equal to 10% of that of the fundamental component, M = 1000 measurements.

Moreover, measurements of a real-life power system frequency and *ROCOF* by means of both instruments have been carried out. The analyzed signal has been achieved from the power system through a step-down voltage transformer. Also, a hair dryer is connected to the same power source. Fig. 3 shows the spectra of the power signals obtained when the hair dryer is off (Fig. 3(a)) and on (Fig. 3(b)). In Fig. 3 it can be observed that the hair dryer introduces also even harmonics in the signal spectrum. The most important ones are the 2nd and 4th harmonics. M = 1000 frequency measurements are performed by both instruments with GT = 0.01 s when the hair dryer is on. The statistical results of the frequency and *ROCOF* measurements achieved by using each instrument are given in Tables 5 and 6. From Table 5 it results that the mean values of the frequency measurements achieved by both instruments are very close. Also, the maximum differences between the mean and the extreme values of the frequencies achieved by the BK1823A and the Keysight 34465A are about 51 mHz and 63 mHz, respectively. Conversely, the statistical efficiency of the *ROCOF* measurements achieved by using the BK1823A is higher than that achieved by using the Keysight 34465.

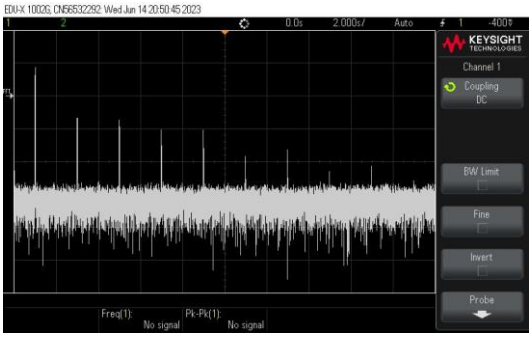

(a)

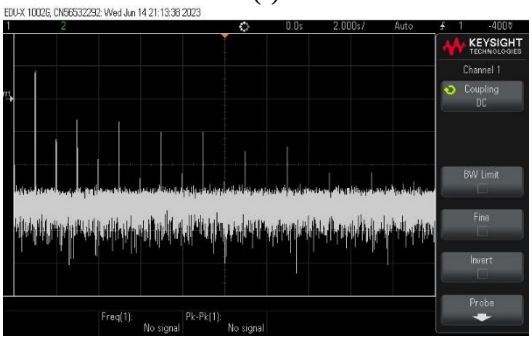

(b)

Fig. 3. Spectra of the real-life power system signals obtained when a hair dryer is off (a) and on (b).

Table 5. Statistical results of the frequency measurements achieved by both instruments when GT = 0.01 s in the case of real-life power system signals obtained when a hair dryer is on.

Parameter	UC BK1823A	DMM Keysight 34465A
Minimum (Hz)	49.963	49.978
Maximum (Hz)	50.060	50.050
Mean (Hz)	50.012	50.015
Std. dev. (Hz)	0.016	0.013

Table 6. Statistical results of the ROCOF measurements achieved by both instruments when GT = 0.01 s in the case of real-life power system signals obtained when a hair dryer is on.

Parameter	UC BK1823A	DMM Keysight 34465A
Minimum (Hz/s)	-0.26	-0.81
Maximum (Hz/s)	0.26	0.70
Mean (Hz/s)	-6.56E-5	-4.30E-3
Std. dev. (Hz/s)	0.08	0.81

Figs. 4 and 5 show the histograms of the frequency and *ROCOF* measurements achieved by both instruments. It can be observed that for both frequency and *ROCOF* there are many different measurement values achieved by each instrument. Furthermore, the skewness and Kurtosis coefficients of the performed data measurements have been computed. Thus, for the frequency measurements achieved by the BK1823A and the Keysight 34465A they are about -0.07 and 3.18 and -0.02 and 2.67, respectively, while for the *ROCOF* measurements they are about -0.10 and 3.20 and -0.07 and 2.97, respectively. Thus, the distributions shapes of data measurements are relatively close to a normal one.

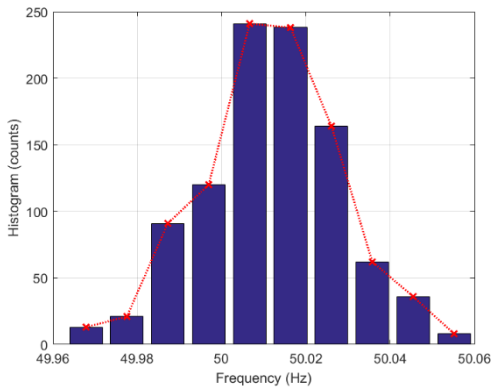

(a)

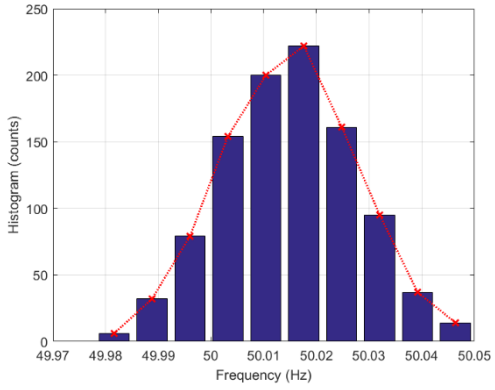

(b)

Fig. 4. Histograms of the frequency measurements achieved by the BK1823A (a) and the Keysight 34465A (b) when *GT* = 0.01 s in the case of real-life power system signals obtained when a hair dryer is on. *M* = 1000 measurements.

III. CONCLUSIONS

In this work the power system frequency accuracies achieved by a reciprocal universal counter – BK1823A, and a bench top DMM - Keysight 34465A, have been compared with each other under different steady-state conditions in the case of synthetized and real-life power system signals. Moreover, the *ROCOF* parameter achieved based on the frequency measurements provided by both instruments at their reporting rates has been estimated. It has been shown that by using the BK1823A more accurate frequency and *ROCOF* measurements are achieved than when the Keysight 34465A is used. Also, it has been shown that the measurements achieved by using both instruments are not affected by harmonics, but they are very much affected by interharmonics. To avoid the contribution of the interharmonics on the frequency and *ROCOF* measurements the *GT* should be increased, and the analyzed signal should be filtered.

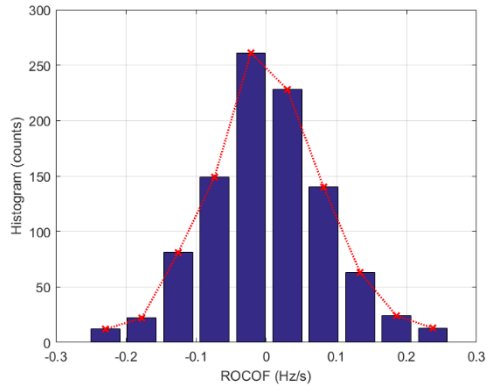

(a)

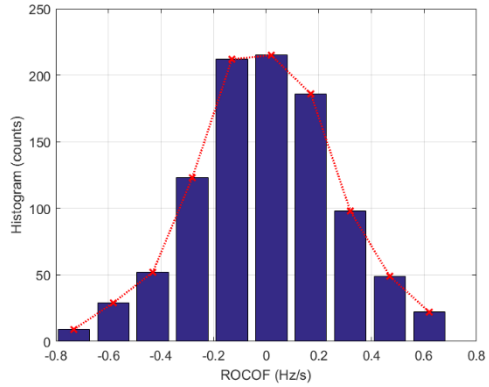

(b)

Fig. 5. Histograms of the *ROCOF* measurements achieved by the BK1823A (a) and the Keysight 34465A (b) when *GT* = 0.01 s in the case of real-life power system signals obtained when a hair dryer is on. *M* = 1000 measurements.

REFERENCES

[1] T. S. Sidhu, "Accurate measurement of power system frequency using a digital processing technique", IEEE Trans. Instrum. Meas., vol. 48, no. 1, Feb. 1999, pp. 75-81.

[2] J.Z. Yang and C.W. Liu, "A precise calculation of power system frequency", IEEE Trans. Power Del., vol. 16, no. 3, Jun. 2001, pp. 361-366.

[3] Y. Xia, Y. Hu, K. Wang, Z. Blazic, D. P. Mandic, "A complex least squares enhanced smart DFT technique for power system frequency estimation", IEEE Trans. Power Del., vol. 32, no. 3, June 2017, pp. 1270-1278.

[4] M. D. Kušljević, J. J. Tomić, "Multiple-Resonator-Based Power System Taylor-Fourier Harmonic Analysis", IEEE Trans. Instrum. Meas., vol. 64, no. 2, Feb. 2015, pp. 554-563.

[5] D. Belega, D. Macii, D. Petri, Power System Frequency Estimation Accuracy of Improved DFT-based Algorithms over Short Intervals, in Proc. IEEE. AMPS workshop, Aachen, Germany, 28-30 Sept. 2016.

[6] BK Precision, BK1823 Instruction Manual, 2015.

[7] Keysight, Truevolt Series Digital Multimeters, 2013-2015.

[8] Keysight, PathWave BenchVue Sofware. Control. Automate. Simplify, July 2022.

[9] Keysight, EDU33210 Series Trueform Arbitrary Waveform Generators, 2021.

[10] Texas Instruments, UAF42 – Universal Active Filter, Data Sheet, 1998.

26th IMEKO TC4 International Symposium
24th International Workshop on ADC and DAC Modelling and Testing
IMEKO TC-4 2023
Pordenone, Italy / September 20-21, 2023

Introducing the SENIS SENCS1Dx: A Novel Current Sensor IC with Ultra-High Bandwidth and Exceptional Magnetic Resolution

Radivoje S. Popovic[1], Dragana Popovic Renella[1], Sasa Dimitrijevic[1], Bojan Milenkovic[1], Sasa Spasic[1]

[1] *SENIS Group, Switzerland, info@senis.swiss*

Abstract – This paper introduces a novel magnetic sensor IC for current sensing applications. The magnetic sensing function is based on the combination of the Hall effect devices for DC and low frequency fields, and an inductive coil for high frequency fields. The sensor IC incorporates a horizontal Hall device and a planar coil for the magnetic field perpendicular to the chip surface; and a vertical Hall device that can be combined with an external coil for the magnetic field parallel to the chip surface. The integrated signal processing electronics contains innovative circuits based on the switched capacitors, which combines the Hall and coil signals in a convenient, stable and reproducible way. The new sensor features the frequency bandwidth from DC to 1MHz and the equivalent magnetic field noise 40μTrms.

I. INTRODUCTION

Electric current sensors [1] are crucial components in a range of industrial applications, including power generation, automotive, and consumer electronics industries. Accurate current measurements are essential for ensuring safety, efficiency, and performance in many apparatuses. One of the most important types of current sensors incorporates the magnetic sensor based on the Hall effect. The Hall elements allow for easy integration into a CMOS IC, making them compact, cost-effective, and energy-efficient. The basics of the Hall effect sensors are described, for example, in [2]-[3].

Practical implementations of Hall-based current sensors have limited bandwidths, typically from DC to less than 250 kHz [4]. The frequency limit comes about because of the use of the so-called spinning-current technique for cancelling offset of the Hall device [3]. To increase the bandwidth, a Hall element may be combined with an inductive coil, with the Hall sensor covering only the low-frequency sub-band [5]. In ref. [6] is described such a broadband magnetic sensor consisting of a hybrid combination of an integrated spinning-current, Hall sensor and a small coil on a printed-circuit board. The outputs of the Hall and Coil signal paths are then summed up, which results in the frequency response of the hybrid sensor from DC to 3MHz, with the magnetic-equivalent noise 210μTrms.

In a magnetic sensor based on Hall-Coil combination, the respective signals pass through a first-order low-pass filter (further: LPF). The cut-off frequency of the LPF defines the cross-over frequency of the Hall and Coil signals, and also contributes to the effective gain of the Coil signal path. In order to get a flat frequency response of a magnetic sensor based on a Hall-Coil combination, the respective effective magnetic sensitivities of the two signal paths must be equal. Since the magnetic sensitivity of each of the two sensor signal paths depends on a few different parameters, it is not easy to ensure the stability and flatness of the frequency response of such a magnetic sensor over a large temperature range.

In this paper, we present a novel integrated magnetic sensor for current sensor applications, the SENIS® type SENCS1Dx, also known as ANYCS [7]. Similarly as the sensors described in refs. [5] and [6], this sensor is based on a combination of a Hall device and an inductive coil, and, therefore, features exceptionally high frequency bandwidth and low noise. Moreover, our new magnetic sensor has an innovative structure of the supporting electronic circuits [8], which allows for achieving a flat and stable frequency response over a large temperature range.

II. OPERATION PRINCIPLE OF THE MAGNETIC SENSOR SENCS1DX

The SENIS' magnetic field sensor SENCS1Dx is based on a combination of two different magnetic field sensor devices, a Hall device, and an inductive coil.

For an AC magnetic field, the output voltage of the Hall signal chain is approximatively given by

$$Vhall(t) = Gh * Si * Ih * Bm * \cos(\omega t) \quad (1)$$

where Gh denotes the gain of the amplifiers in the Hall signal chain, Si - the current-related magnetic sensitivity of the Hall device, Ih – the biasing current of the Hall element, Bm - the amplitude of the AC magnetic induction, and ω - the angular frequency of the B-field.

At low frequencies, the magnitude of the output signal of the Hall signal chain in Eq. (1) is independent of frequency; but, due to the spinning current technique, the frequency independence extends only to a few 10s of 100s kHz.

The voltage induced in the coil by a time-variable magnetic field is given by the Faraday's law. For an AC magnetic field, the output of the coil chain, the signal is given by

$$Vind(t) = Gc * A * Bm * \omega * \sin(\omega t) \quad (2)$$

where Gc denotes the gain of the amplifiers in the coil signal chain, and A denotes the effective area of the coil. The sign of the gain Gc is chosen so that the inductive signal advances in phase for $\pi/2$ with respect to the Hall signal.

The amplitude of the signal of the coil chain (2) is proportional with its frequency. Since in the coil signal chain there is no switching operation, there is no such a severe bandwidth limitation at higher frequencies as that in the Hall signal chain; therefore, Eq. (2) is valid up to several MHz.

The frequency dependence of the coil signal (2) can be conveniently eliminated by passing this signal trough a low-pass filter of the first order. At frequencies much higher than the cutoff frequency of this filter, the "gain" of the filter is inversely proportional with the frequency. Therefore, at higher frequencies, this filter cancels out the frequency dependence of the coil signal.

In SENCS1Dx, the amplified Hall signal, Eq. (1), and the amplified coil signal, Eq. (2), are added together, and then this common Hall+Coil signal passes through a first-order low-pass filter. Then, in the common signal, the Hall contribution dominates at DC and low frequencies up to the cutoff frequency of the low-pass filter (fc); whereas the coil contribution dominates at frequencies higher than fc. Figure 1 illustrates the frequency dependence of various signals in SENCS1Dx.

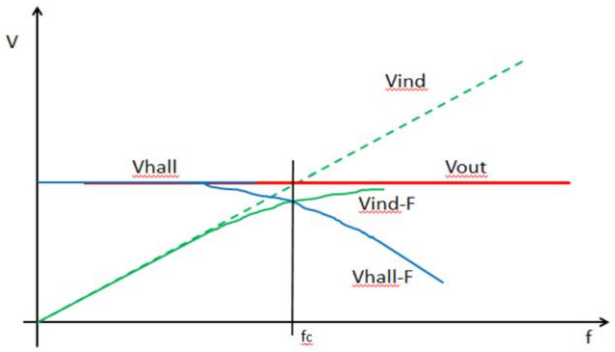

Fig. 1. The Frequency dependences of the amplitudes of the signals in the magnetic sensor based on a Hall-Coil combination. Notation: Vhall: non-filtered Hall voltage; Vhall-F: Hall voltage after low-pass filtering; Vind: Non-filtered voltage of the inductive coil, Vind-F: Voltage of the inductive coil after low-pass filtering; Vout: The sum of Vhall and Vind after low-pass filtering; fc: The cutoff frequency of the low-pass filter

The cutoff frequency of the low-pass filter (fc) should be chosen so as to be equal with the frequency at which the amplitudes of the Hall signal and that of the inductive signals are equal. This frequency corresponds to the crossing point of the lines Vhall and Vind in Fig. 1. The final result is that the amplitude of the common signal Vout is independent on the signal frequency. For details – see below the next section.

Therefore, the role of the low-pass filter is to provide frequency independence of the common signal; this low-pass filter does not limit at all the frequency bandwidth of the common signal. However, it does limit the bandwidth of the noise in the common signal, exactly as it limits the signal bandwidth of the Hall part of the common signal.

The noise bandwidth of the common Hall-Coil signal (fc) might be at least 25 times smaller than the bandwidth of an only-Hall magnetic sensor (f-ch); therefore, the noise of a Hall-Coil sensor could be at least 5 times lower than that of an only-Hall magnetic sensor.

III. THE RELATIONSHIP AMONG THE PARAMETERS OF THE HALL CHAIN, COIL CHAIN, AND THE LOW PASS FILTER

The voltages Vhall (1) and Vind (2) can be represented in the complex forms by the phasors

$$pVh = Gh * Si * Ih * Bm \quad (3)$$

$$pVi = j * \omega * Gc * A * Bm \quad (4)$$

Let the transfer characteristic of the LPF be given by

$$(Vout/Vin) = Gf / (1 + j * \omega * Tf) \quad (5)$$

where Gf denotes its voltage gain and Tf is the time constant of the filter. Then, if we apply as the input voltage of the filter the sum of the voltages (3) and (4), the phasor of the output voltage of the filter will be

$$pVout = Gf * Si * Ih * Bm * [(1 + j * \omega * Gc * A / (Gh * Si * Ih)] / (1 + j * \omega * Tf) \quad (6)$$

In this equation, the terms $[(1 + j * \omega * Gc * A / (Gh * Si * Ih)] / (1 + j * \omega * Tf)$ will cancel out if we chose the parameters of the Hall chain, coil chain, and of the low-pass filter so that the following equation is fulfilled:

$$Tf = Gc * A / (Gh * Si * Ih) \quad (7)$$

or, since the cutoff frequency is related to the time constant, $fc = 1 / (2 \pi * Tf)$, the condition (7) can be expressed as

$$fc = Gh * Si * Ih / (2 * \pi * A * Gc) \quad (8)$$

Then Eq. (6) reduces to

$$pVout = Gf * Si * Ih * Bm \quad (9)$$

This means that, if Equation (8) is fulfilled, the output voltage of the filter Vout will be independent of frequency, as illustrated in Fig. 1, and it will be in phase with the magnetic field signal.

In order to enaible the fulfillment of Eq. (8) in spite of the fabrication tolerances, the gains Gh and Gc of the SENCS1Dx are made adjustable. During the calibration process of the SENCS1Dx, these two gains are adjusted so as to give both desired magnetic sensitivity and flat frequency response of the magnetic sensor. However, in Eq. (8), each of the parameters fc, Si, and Ih, might have different and non-linear temperature dependences, which would make dificult keeping Eq. (8) valied over a large temperature range. We solved this difficulty by implementing the corresponding supporting circuits in the form of the switched capacitor circuits that make Ih and fc proportional to the same stable clock frequency [8].

IV. STRUCTURE OF THE SENCS1DX

The SENCS1Dx current sensor incorporates integrated Hall devices, coils, analog signal processing channels, control logic, and ADC. Figure 2 depicts the sensor chip's block diagram, including the horizontal and vertical Hall elements (X) and their corresponding coils (H and V). While the horizontal coil is integrated into the chip, the vertical coil is separate and can be added off-chip.

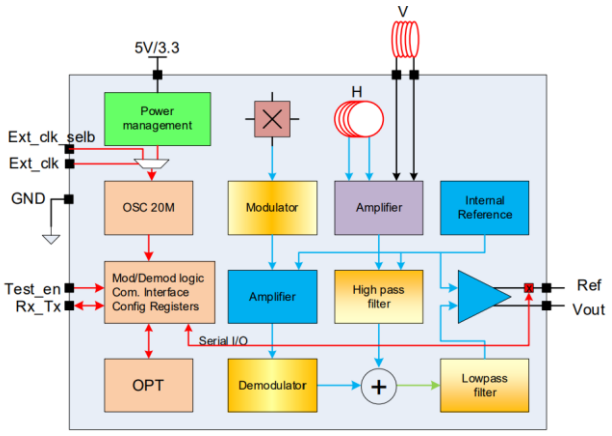

Fig. 2. Block diagram of SENCS1Dx

The sensor architecture employs both SENIS horizontal and vertical Hall elements, which offer the industry's most exceptional magnetic resolution [9]. With this dual Hall element configuration, the sensor can sense magnetic fields along any desired axis (perpendicular to, or parallel with the chip surface), thereby earning the name ANYCS.

V. EXPERIMENTAL RESULTS

The SENCS1Dx chips are fabricated in a high-voltage 0.18µm CMOS technology.

Fig. 3 shows the layout of the chip.

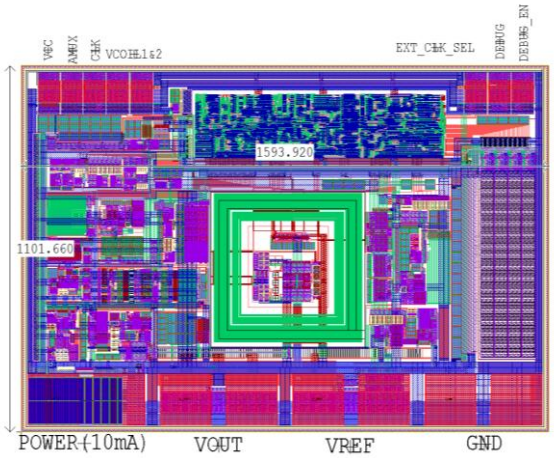

Fig. 3. The layout of the SENCS1Dx. The big square (green) in the middle is the planar coil. The horizontal and vertical Hall elements are situated in the coil.

In Table 1 we summarize the main test conditions and test results of the SENCS1Dx.

Fig. 4 shows the relative variation of the magnetic sensitivity of the SENCS1Dx as a function of the frequency of the magnetic field. The curve is reasonably

flat over the whole sensor bandwidth, from DC to 1MHz.

Table 1. Test conditions and performance parameters

Parameter	Symbol	Value	Unit
Power supply Voltage	VCC	5	V
Current @VCC	IVCC	9.8	mA
Hall biasing current	Ibias	0.96	mA
Hall Low Pass filter	LP	2	kHz, @Fclk=8MHz
Coil High pass filter	HP	100	Hz
Oscillator	Fclk	8	MHz
Magnetic field range	FS	5	mT
Magnetic sensitivity	S	210	V/T
Output voltage noise	Vn	9	mVrms
Eq. magnetic noise	Bn	40	uTrms

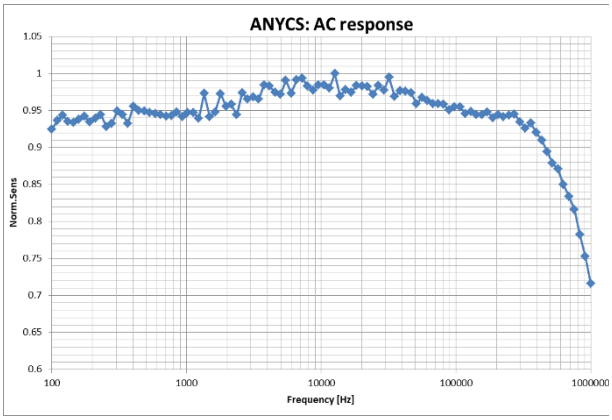

Fig. 4. Frequency response

Fig. 5 illustrates the noise spectral density over the sensor frequency bandwidth. As expected, most of the noise appears at the frequencies below the cutoff frequency of the low-pass filter.

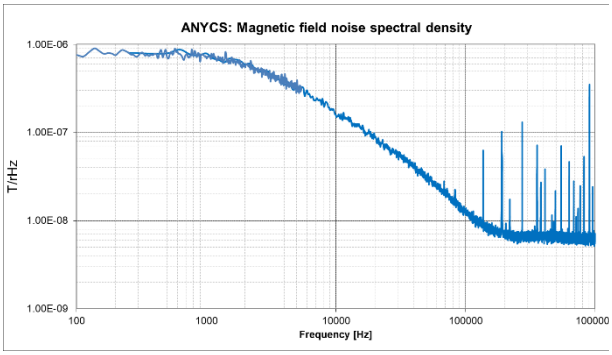

Fig. 5. The equivalent magnetic field noise spectral density

In a separate measurement, we made a histogram of the noise voltage over the whole sensor bandwidth (DC to 1MHz), which reviled the standard deviation of 9mV. This corresponds to the equivalent input magnetic field noise of 40µTrms.

VI. CONCLUSIONS AND OUTLOOK

Based on the known concept of the combination Hall-Coil [5], [6], and new ideas [7], [8] that support its implementation, we developed the new integrated magnetic sensor, the SENIS® SENCS1Dx, also known as ANYCS, with extraordinary features: Magnetic sensitivity direction either perpendicular to, or parallel with the chip surface, frequency bandwidth from DC to 1MHz, equivalent magnetic field noise 40uT, and high stability against temperature changes. The SENCS1Dx is a fully integrated sensor for the magnetic field perpendicular to the chip surface, whereas for the magnetic field parallel with the chip surface, it should be combined with a suitable external coil.

With its unique performance, the SENIS ANYCS sensor is poised to revolutionize electric current measurement solutions. Its first applications are expected in electric bicycles, AC magnetic field monitoring for green cars stations, and power electronics, among others. High-accuracy measurement with SENIS sensors is moving the limits of what is currently possible and available on the market, leading to further advances in sensor technology and applications.

REFERENCES

[1] P. Ripka, “Electric current sensors: a review”, Measurement Science Technolology, 2010

[2] R. S. Popovic: "Hall-effect devices", Journal for Sensors and Actuators, Volume 17, Issues 1-3, 1989

[3] R. S. Popovic "Hall Effect Devices", 2nd Edition CRC Press Taylor & Francis Group, LLC 2003, ISBN: 978-1-4200-3422-6

[4] MLX91208, 250 kHz IMC-Hall® current sensor IC with enhanced thermal and lifetime stability, 2022

[5] N. Karrer, P. Hofer-Noser, “Device with wide passband for measuring electric current intensity in a conductor”, Patent US 6,366,076 B1, 2002

[6] J. Jiang, K.A.A. Makinwa, “Multipath Wide-Bandwidth CMOS Magnetic Sensors”, IEEE J. Solid-State Circuits. (2016) 1–12. doi:10.1109/JSSC.2016.2619711

[7] SENIS® ANYCS current sensor IC with high bandwidth from DC-1MHz, www.senis.swiss, 2023

[8] Patent 2022110921071100DE, “Magnetfeldsensorsystem mit einem temperaturgangskompensierten Ausgangssignal sowie Verfahren für die Temperaturgangskompensation eines Ausgangssignals eines Magnetfeldsensorsystems”, 2022

[9] Patent EP14176835.8, “Vertical Hall Device”, 2016

26th IMEKO TC4 International Symposium
24th International Workshop on ADC and DAC Modelling and Testing
IMEKO TC-4 2023
Pordenone, Italy / September 20-21, 2023

The Design of Vehicle Surround View Monitor

Antonia Juskova and Ondrej Kovac

Technical University of Kosice, Letna 9, 04200 Kosice, Slovakia
e-mail addresses: ondrej.kovac@tuke.sk, antonia.juskova@student.tuke.sk

***Abstract* – In this paper, the technology and design of a driving assistant called the Surround View Monitor (SVM) are discussed. The procedures used to create a unified, bird's-eye view are presented, which involve stitching images captured by strategically placed cameras on the vehicle. The proposed algorithm was successfully implemented on a car model and involves various stages, including camera calibration, photometric and perspective correction, scale planar transformation, and final image stitching. The paper should be considered student work and it is positioned as the foundation for the authors' future scientific work in the field of automated parking systems.**

I. INTRODUCTION

Sensing and communication between the environment and the vehicle are key challenges in the automotive industry [1]. The constantly increasing number of vehicles in traffic cause more emphasis on traffic safety and driving comfort [2]. Today's vehicles consist of newer and more sophisticated driving assistants referred to as Advanced Drivers Assistance Systems (ADAS). ADAS use advanced knowledge about the surrounding environment obtained by radars, lidars, cameras, or map databases [1]. Adaptive cruise control, driver drowsiness detection, and park assists are among many driver assistance systems which are frequently used in current vehicles. Advanced camera systems, such as SVM, are considered ADAS as well [2]. The surround view systems market was valued at 3.8 billion and probably reach 9.9 billion USD by 2027 [3]. This shows that development in this area of the automotive industry is economically interesting. SVM systems offer a 360° overview of the entire surrounding of the vehicle from a bird's eye perspective [2]. The first SVM was introduced by Nissan car division Infinity and was presented by the name Around View monitor [4]. Later, other manufacturers also started developing this technology. For example, Toyota introduced this system as Bird's View Camera or Chevrolet as Surround View [4]. SVM uses four wide-angle cameras strategically placed on the vehicle [2]. These cameras catch the entire surrounding of the vehicle. The control unit performs all the operations needed to transform images and stitches them into a unified, bird's eye view image.

II. CAMERA CALIBRATION

For capturing as much of the vehicle's surrounding as possible 160° wide-angle cameras are used. Wide-angle or fish-eye cameras are very popular and widely used types of cameras in robotic and computer vision [5]. These cameras provide wide fields of view, which allows for mapping a greater field of the 3D visual scene. Those wide-angle camera lenses produce significant visual distortion [6]. Approximation by a standard camera model may not be sufficient for those cameras. Using this model for wide-angle cameras may cause significant information loss in calibrated images. The lenses of these cameras are designed to capture a semi-spherical field of the 3D area. This view cannot be projected into the image plane by perspective correction. There are several methods of calibrating omnidirectional cameras. The crucial part of calibration is choosing a suitable camera model [5]. Most models of camera projection are estimated by the known geometry of captured objects or patterns, such as straight lines, angles, or planes**Chyba! Nenalezen zdroj odkazů.**. The projection of any camera can be approximated by an omnidirectional camera model [7]. The omnidirectional camera model is defined by two planes: the sensor plane and the image plane. The point from the 3D visual scene is projected into the sensor plane as a point $\boldsymbol{u}''$ defined by coordinates u'' and v''. The relationship between the 3D world and sensor plane can be mathematically described by imaging function $\boldsymbol{g}$. This function can have various forms and depends on lens type or construction. Projection between point $\boldsymbol{X}$ and point $\boldsymbol{u}''$ is defined by function $\boldsymbol{g}$ as:

$$\boldsymbol{g}(u'', v'') = (u'', v'', f(u'', v''))^T \quad (1)$$

$$f(u'', v'') = a_0 + a_1\rho'' + \cdots + a_N\rho''^N \quad (2)$$

Where $\rho'' = \sqrt{u''^2 + v''^2}$.

After camera projection and digitalization, point $\boldsymbol{u}''$ is mapped into the image plane as a point $\boldsymbol{u}'=(u,' v')^T$. The relationship between these two points in the sensor and image plane is defined as:

$$\boldsymbol{u}'' = \boldsymbol{A}\boldsymbol{u}' + \boldsymbol{t} \quad (3)$$

where $\boldsymbol{A}$ is a 2×2 matrix, **t** is a 2×1 vector.

By combining these two relationships, the projection of an omnidirectional camera model can be expressed:

$$\lambda \begin{bmatrix} u'' \\ v'' \\ w'' \end{bmatrix} = \lambda\, \boldsymbol{g}(\boldsymbol{u}'') = \lambda \begin{bmatrix} \boldsymbol{A}\boldsymbol{u}' + \boldsymbol{t} \\ f(u'', v'') \end{bmatrix} = \boldsymbol{P}.\boldsymbol{X} \qquad (4)$$

where λ is a non-zero scalar factor.

The goal of omnidirectional camera calibration is an estimation of $\boldsymbol{g}$ function parameters $a_0 \dots a_N$, matrix $\boldsymbol{A}$, and vector $\boldsymbol{t}$. During the calibration process, images of the checkerboard pattern are captured from several different positions. The checkerboard pattern has a known geometry and it's widely used in calibration techniques.

a) b)

Figure 1 Calibration process (a) distorted image and (b) calibrated undistorted image.

The result of calibration is shown in Figure 1b. As is shown, the camera distortion is partially eliminated. Changes are obvious mainly in displaying straight lines, which are not curves anymore.

III. PHOTOMETRIC ALIGNMENT

The brightness and color intensity of the same objects captured by several cameras may be in each picture different. This is caused due to different characteristics of cameras and lighting. Each of these cameras performs automatic exposure (AE) and automatic white balance (AWB) independently [8]. The mismatch of brightness and color intensities can cause noticeable boundaries mainly between nearby images. This mismatch can be reduced by the histogram equalization method.

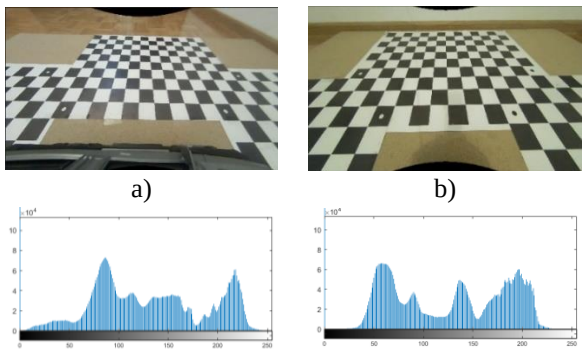

a) b)

c) d)

Figure 2 Differences of brightness intensity (a) reference, (b) input image (c) reference, and (d) input histogram.

Histogram equalization is a method that transforms brightness intensity on each level according to the desired brightness distribution. This method creates a map based on a histogram of the reference image. Histograms of input images are changed based on the map derived from the reference image histogram [9]. This method redistributes pixels on each brightness level into new adapted values. Redistribution causes the input histogram's brightness values to be as close as possible to the values in the reference histogram [10]. The map function for histogram equalization can be derived from the distribution functions of an input image $\overline{DF}_{if}$ and reference image $\overline{DF}_{rf}$. Mapping aims to find for each intensity value i, a new intensity value j so that the difference between $\overline{DF}_{if}(i)$ and $\overline{DF}_{rf}(j)$ is minimal [11]. This can be described as follows:

$$\left|\overline{DF}_{zf}(i) - \overline{DF}_{rf}(j)\right| = min\left|\overline{DF}_{zf}(i) - \overline{DF}_{rf}(k)\right| \quad (5)$$

Based on minimalization, it is possible to create a mapping matrix M_{zf}. This matrix describes the mapping of pixels with intensity i to new intensity j as $M_{zf}(i) = j$. This method can be used for derivating the mapping matrix for each input image and each color depth. The result of this operation is a new normalized image with different colors and brightness intensity (Figure 4.). The probability of pixels occurrence with a certain brightness is closer to the probability of occurrence obtained from the reference image [10].

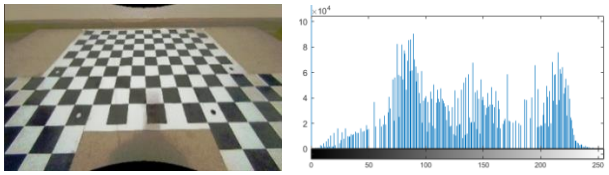

a) b)

Figure 3 Result of histogram equalization, the normalized (a) image, and (b) histogram.

IV. PERSPECTIVE CORRECTION

Perspective correction is an important image-processing task in computer vision. This operation can adjust distortion created by shooting from different angles and distances [12]. Perspective correction is image transformation from one plane view to another plane view which is desired by the application. In surround view, all captured images need to be transformed into the front-parallel plane from the view of the virtual camera placed above the vehicle. One of the options for performing such a transformation is a homogenous perspective transformation. Homogeneous perspective transformation is an image transformation technique, where points of the input plane are transformed into new points in the output plane [13]. This transformation is defined by the transformation matrix $\boldsymbol{H}$ which transforms point $\boldsymbol{x}$ in input plane to coresponded point $\boldsymbol{x}'$ in output plane. The

homography matrix $\boldsymbol{H}$ has 9 entries, but is defined only up to scale [14]. Homography between two corresponding points can be defined by (6).

$$\begin{bmatrix} x_1' \\ x_2' \\ x_3' \end{bmatrix} = \begin{bmatrix} h_{11} & h_{12} & h_{13} \\ h_{21} & h_{22} & h_{23} \\ h_{31} & h_{32} & 1 \end{bmatrix} \begin{bmatrix} x_1 \\ x_2 \\ x_3 \end{bmatrix} \tag{6}$$

where $(x_1, x_2, x_3)^T$ are coordinates of a homogenous point in the input plane, $(x_1', x_2', x_3')^T$ are coordinates of a homogenous point in the output plane, and $h_{11} \ldots h_{32}$ are degrees of freedom of the matrix $\boldsymbol{H}$. As stated in the equation, it is necessary to calculate 8 degrees of freedom to estimate homography. Direct linear transformation (DLT) can be used to calculate unknown entries. For estimation with DLT, it is a necessity to choose four corresponding points in both planes.

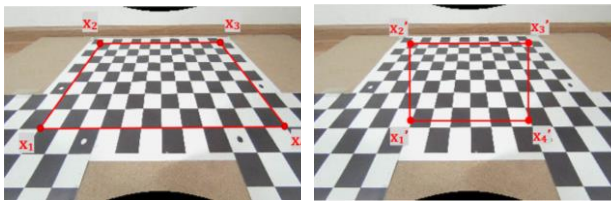

a) b)

Figure 4 Coresponding points for DLT, (a) input plane, (b) output plane.

For each point correspondence $x_i \leftrightarrow x_i'$ is necessary to compute the matrix $\boldsymbol{A_i}$:

$$\boldsymbol{A_i} = \begin{bmatrix} x_i & y_i & 1 & 0 & 0 & 0 & -x_i x_i' & -y_i x_i' \\ 0 & 0 & 0 & x_i & y_i & 1 & -x_i y_i' & -y_i y_i' \end{bmatrix} \tag{7}$$

From each point correspondence, two equations are obtained. With four 2×9 matrices $\boldsymbol{A_i}$ a single 8×9 matrix can be assembled. The following equation (8) represents DLT using point correspondence. The matrix $\boldsymbol{H}$ is vectorized into $\boldsymbol{h}$ as follows.

$$\boldsymbol{h} = (h_{11}, h_{12}, h_{13}, h_{21}, h_{22}, h_{23}, h_{31}, h_{32})^T \tag{8}$$

$$\boldsymbol{A}.\boldsymbol{h} = \begin{bmatrix} \boldsymbol{A_1} \\ \boldsymbol{A_2} \\ \boldsymbol{A_3} \\ \boldsymbol{A_4} \end{bmatrix} \boldsymbol{h} = 0 \tag{9}$$

The unknown entries of vector $\boldsymbol{h}$ can be calculated by the least squares solution (10).

$$\boldsymbol{h} = (\boldsymbol{A}^T \boldsymbol{A})^{-1} \boldsymbol{b} \boldsymbol{A}^T \tag{10}$$

Where $\boldsymbol{b} = (x_1', y_1', x_2', y_2', x_3', y_3', x_4', y_4')^T$.

By this algorithm, it is possible to calculate the transformation matrix of the homography $\boldsymbol{H}$ for all four images. By multiplying all points in the image with the matrix $\boldsymbol{H}$, these are transformed into equivalent points in the output image.

Figure 5 Input image after perspective correction

The transformed image (Figure 6.) represents the input image after perspective correction performed from the perspective of the front-parallel plane above the vehicle. Before stitching images into one unified image, scale transformation of images must be performed.

V. SCALE TRANSFORMATION

After perspective correction, it may happen that The size of the same objects captured by the 4 cameras may not be the same and problems may arise, especially during final image stitching. The goal of planar scale transformation is to match the scale of the images. This transformation is defined by scale factors s_x and s_y. For scale alignment of four views, a checkerboard pattern can be used (Figure 7). From each image, the width and height of the checkerboard pattern can be obtained from corner points. Based on these values, it is possible to calculate the average height and width. These average values represent the unified dimensions of the checkerboard pattern in each image. Thus, the scale matrix based on the checkerboard can be rewritten as follow:

$$S = \begin{bmatrix} E_x/(x_3 - x_2) & 0 & 0 \\ 0 & E_y/(y_2 - y_1) & 0 \\ 0 & 0 & 1 \end{bmatrix} \tag{12}$$

Where E_x is mean width and E_y is mean height.

The matrix S is subsequently used for the scale unification of all 4 images. The scaling factors for a particular image can be calculated from the mean values and checkerboard dimensions in the actual image.

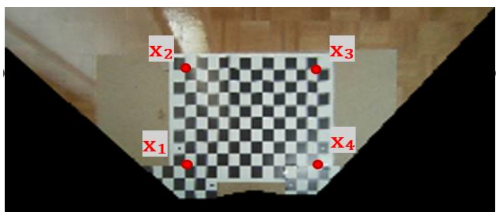

Figure 6 Checkerboard corner points

VI. STITCHING IMAGES

Finding the most accurate match between images is a very important part of image stitching. Defining common points between two adjacent images is a necessity. These common points indicate how joining should be performed. One of the image stitching methods is an algorithm based on imaginary diagonals that define where adjacent views should intersect. In this algorithm, only two points in each adjacent image must be entered. These common points define the imaginary diagonals, which represent the same point within adjacent frames. This is shown in Figure 8.

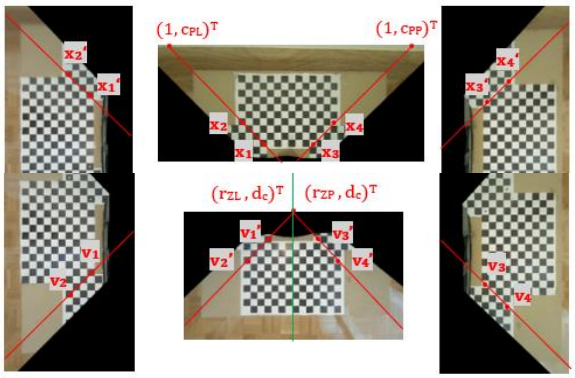

Figure 7 Common points for image stitching

Finally, all images are mapped into one image. The view of the vehicle's front camera can be chosen as the main image. This image also represents the resulting plane of the surrounding view so the resolution must be increased. The resolution must be large enough to map all the remaining images onto it. The remaining images need to be rotated and moved to the specified coordinates. Before joining, the two corresponding common points must lie approximately on the same coordinates. Based on these points, it is necessary to calculate the incremental step (IS). IS is a value that represents how many pixels need to be added/subtracted on each row of the image. The result of the joint appears as a straight line passing through the common points (Figure 8).

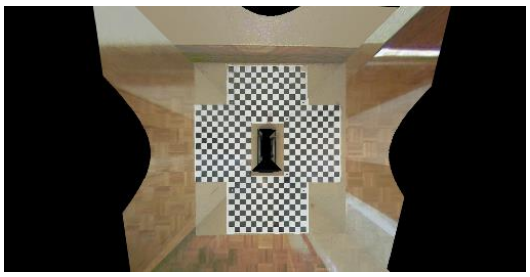

Figure 8 Unified joined image

Next, it is necessary to calculate where the given incremental step should be added/subtracted. In the case of connecting the front, right and left images, it is necessary to calculate the coordinates of the columns c_{PP} and c_{PL}. These coordinates define in which column the pixels from one adjacent image should be added and where from the other (Figure 7). In the case of stitching the rearview, it is necessary to calculate the lines r_{ZP} and r_{ZL}. These lines define where the rear image should be mapped.

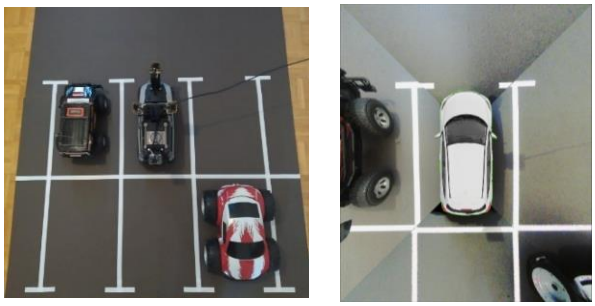

a) b)

Figure 9 Estimation of the vehicle surrounding, (a) actual scenery, (b) estimated scenery.

The result of this process is a unified view from a bird's perspective. This view still needs to be cropped to the immediate surroundings of the vehicle. For a better understanding of the perspective, the image of a car can be placed in the middle of the image.

VII. PRACTICAL IMPLEMENTATION

For demonstration purposes, the prototype of a surround-view system was proposed. The software was implemented in MATLAB and partially in Python. The images are acquired by a Raspberry Pi via Python script which captures the images with the highest possible resolution. The images are sent to the MATLAB environment via the local network. Image processing and transformation functions are performed in MATLAB.

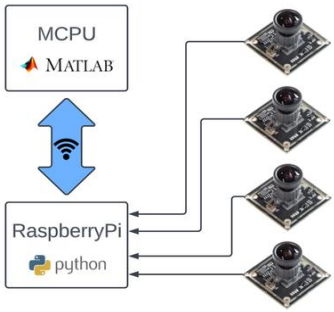

Figure 10 Surround-view system

The prototype uses four wide-angle cameras B0202 with a 160° field of view. The cameras are connected to Raspberry Pi's USB inputs, which are used for image acquisition. For image processing, some functions of the MATLAB Image Processing Toolbox are used, such as checkerboard pattern recognition, fish-eye camera parameters estimation, and 2D image transformation with a specified matrix.

VIII. FUTURE WORK

The final view obtained by the proposed system can be used as a zero-level driver assistant. Based on a bird's eye view it is possible to evaluate the environment around the vehicle. Surround-view cameras can be also used as a sensor system for higher-level ADAS such as park assist or as a redundant sensor in autonomous vehicles. The image can be simply converted into an occupancy binary map, which indicates free or occupied space. Based on the binary values it is possible to track objects in the surroundings of the vehicle and use it for measuring distance from obstacles in parking warning systems. This representation of the environment can be also used for parking space measurement or trajectory estimation in informative parking assistance. Provided that there is suitable lighting, these functions can also be used for semi-automatic and automatic parking systems.

IX. CONCLUSION

This article details the process of implementing a vehicle surround view monitoring system, also known as the bird's eye view. The proposed system utilizes output from four cameras mounted on all sides of a vehicle and includes camera calibration, histogram equalization, perspective projection, and image stitching. In the system calibration process, an automatic checkerboard pattern recognition function is used. By automating these steps, it is possible to eliminate errors and inaccuracies in the manual marking of corner points on the checkerboard pattern by the user. The proposed algorithm was successfully implemented on a car model. The bird's eye view generated by this system can be utilized as a sensor system for parking assistance, a critical aspect of which involves estimating obstacles and maneuvering between them. Existing parking systems rely solely on ultrasound or lidar sensors, which may provide incomplete information about a vehicle's surroundings, increasing the risk of collision. The proposed bird's eye view system is positioned as the foundation for the authors' future work in the field of automated parking systems.

ACKNOWLEDGMENT

The work is a part of the project supported by the Science Grant Agency of the Slovak Republic (No. 1/0413/22).

REFERENCES

[1] Galvani, M. "History and future of driver assistance." 2019 IEEE Instrumentation Measurement Magazine, 22(1), str. 11–16, doi:10.1109/mim.2019.8633345.

[2] X. Yan, L. Wang,Y. Li, "A Calibration Method for the Surround-View Parking Assistant System," 2020 IEEE 11th ICSESS, Beijing, China, 2020, pp. 485-488, doi: 10.1109/ICSESS49938.2020.9237687.

[3] Imarc. (2022) Automotive Surround View Systems Market (Report ID: SR112023A1650). Retrieved from Imarc database.

[4] Howard, Bill. "Why are car surround view cameras and why are they better than they need to be," Extremetech, 18-07-2014, [cit. 25-03-22]. Available at: <https://www.extremetech.com/extreme/186160-what-are-surround-view-cameras-and-why-are-they-better-than-they-need-to-be...>.

[5] Urban, Steffen. Leitloff Jens. "Improved Wide-Angle, FishEye and Omnidirectional Camera Calibration," ISPRS Journal of Photogrammetry and Remote Sensing, Vol. 108, 2015, pp. 72-79, ISSN 0924-2716, DOI: 10.1016/j.isprsjprs.2015.06.005.

[6] J. Kannala and S. S. Brandt, "A generic camera model and calibration method for conventional, wide-angle, and fish-eye lenses," in IEEE Transactions on Pattern Analysis and Machine Intelligence, vol. 28, no. 8, pp. 1335-1340, Aug. 2006, doi: 10.1109/TPAMI.2006.153.

[7] Scaramuzza, D., A. Martinelli, and R. Siegwart. "A Toolbox for Easy Calibrating Omnidirectional Cameras." Proceedings to IEEE International Conference on Intelligent Robots and Systems, (IROS). Beijing, China, October 7–15, 2006.

[8] K. Lee, D. Kim, H. Do, J. Kim, and K. Chae, "Effective Photometric Alignment for Surround View Monitoring System," *2019 IEEE 9th International Conference on Consumer Electronics (ICCE-Berlin)*, Berlin, Germany, 2019, pp. 390-391, doi: 10.1109/ICCE-Berlin47944.2019.8966185.

[9] Komal, Vij & Yaduvir, Singh. (2011). Enhancement of Images using Histogram Processing Techniques. International Journal of Computer Technology and Applications. 02.

[10] Grundland, M., Dodgson, N. Color histogram specification by histogram warping. Proceedings of SPIE 5667, 2005 s. 610-621. DOI: 10.1117/12.596953

[11] Chen, Ch. Ishikawa, H. Histogram Matching Extends Acceptable Signal Strenght Range on Optical Coherence Tomography Images. Invest Ophthalmol Vis Sci. 2015;56:3810–3819. DOI:10.1167/iovs.15-16502.

[12] Li, Zeying, et al. "Resource-Efficient Hardware Implementation of Perspective Transformation Based on Central Projection." *Electronics* 11.9 (2022): 1367.

[13] HARTLEY, Richard; ZISSERMAN, Andrew. 2004. Multiple View Geometry in Computer Vision, ver. 3. Cambridge: Cambridge University Press. ISBN 978-0-511-811-685.

[14] Agarwal, Anubhav; Jawahar, C.; Narayanan, P. A survey of Planar Homography Estimation Techniques. International Institute of Information Technology, Hyderabad, India, 2005.

26th IMEKO TC4 International Symposium
24th International Workshop on ADC and DAC Modelling and Testing
IMEKO TC-4 2023
Pordenone, Italy / September 20-21, 2023

Case study of NI G Web technology application for remote educational laboratory

Jozef Kromka, Levente Fekete, Jan Saliga

Technical University of Kosice, Letna 9, 04200 Kosice, Slovakia
jozef.kromka@tuke.sk, levente.fekete@student.tuke.sk, jan.saliga@tuke.sk

***Abstract* – Over the years, numerous web-based remote laboratories have been developed, providing a practical solution for offering hands-on training and education in various scientific fields, especially in online settings. This article outlines the initial design of a LabVIEW-based remote laboratory with a web interface created using a novel technology, National Instruments' (NI) G Web Development Software. In addition, a reservation system was implemented to manage access to the remote laboratory's web interface, allowing access only at specific times.**

I. INTRODUCTION

Remote laboratories [1] have become a popular tool for teaching electronics and other STEM (Science, Technology, Engineering, Math) subjects in recent years [2]. These laboratories allow students to access real laboratory equipment and experiments from any location with an internet connection, providing a more flexible and accessible learning experience. The use of remote laboratories in electronics education has shown promise in improving students' understanding of the subject while providing a more engaging and interactive learning experience [3]. Since the COVID-19 pandemic has posed significant challenges for experimental laboratory classes [4]–[6], the popularity of remote laboratories in education has risen even more [7]–[9].

In recent years, numerous web-based remote laboratories have been developed and implemented in educational settings. These laboratories enable students to conduct measurements and experiments from their homes, without the need for physical attendance at a laboratory.

One e-learning measurement laboratory was developed in [10]. This laboratory offers the opportunity to access remote measurement laboratories and allows students to engage in various didactic activities associated with measurement experiments. The fundamental element of the software architecture is the integration of the Learning Management System with the remotely accessible measurement laboratories, accomplished through web services and a thin client paradigm.

Another remote laboratory for Field Programmable Gate Array (FPGA) experiments was introduced in [11]. The laboratory enables the execution of experiments both through a web interface over the Internet and locally within the classroom. The system has been specifically designed for advanced digital design and signal processing courses, utilizing sophisticated FPGA platforms. By leveraging this system, students gain complete access to laboratory equipment, advanced software licenses, and FPGA platforms remotely, utilizing standard web browsers and a conventional remote desktop interface.

In yet another study [12], a remote laboratory known as ADCWAN (Analog to Digital Converters on Wide Area Network) was introduced as a comprehensive hardware and software platform specifically designed for testing Analog to Digital Converters (ADC). This remote laboratory offers versatility for both educational purposes and scientific experimentation. ADCWAN employs a Moodle server and a custom Java applet to facilitate access to the authentic measurement laboratory. The overarching objective of this proposed remote laboratory is to enable the scientific training of young researchers, facilitate the dissemination of knowledge, and enable the comparison of metrological information. By providing a combination of theoretical resources and practical tools, ADCWAN allows for the characterization of ADC through various experimental tests.

While the previously mentioned remote laboratories have a web interface, it should be noted that their interface must be created for that specific laboratory and equipment. This means that they are not entirely versatile and may not be fully compatible with all laboratory functions. Therefore, it is crucial to develop a flexible web interface that can be adapted to different laboratory setups, providing more versatility for educational purposes.

By using one programming environment for both the web page and communication with laboratory equipment, such as LabVIEW, these obstacles could be overcome. This approach provides the advantage of seamless integration between the web interface and laboratory equipment, making it possible to design a more versatile and functional remote laboratory. A Remote laboratory developed in LabVIEW that features the web interface was already developed by authors in [13] and [14]. However, the previous remote laboratory web interface used an outdated technology that required the use of a large plugin and an Internet Explorer browser that is no longer supported.

To overcome the shortcomings of the previously

mentioned systems, we present a remote laboratory system developed in LabVIEW that features a web interface for online access. The novelty of the proposed remote laboratory lies in the development of its web interface utilizing the new technology of NI G Web Development Software. The web interface of the remote laboratory is further enhanced by a reservation system developed by Levente Fekete, a final-year student at the Technical University of Košice. The proposed remote laboratory system allows students to remotely access and control data acquisition (DAQ) devices and conduct experiments using a web browser.

The article is structured as follows: Section II presents the remote laboratory's general design, along with a system block diagram and description of its web interface. Primary conclusions and planned full article extensions regarding the proposed remote laboratory, as well as possible future developments, are outlined in Section III.

II. LABORATORY ARCHITECTURE DESIGN

The remote laboratory consists of three main components. The first component is a LabVIEW program that controls the DAQ card. The second component is a webpage interface developed using G Web development software, which communicates with the LabVIEW program. The third component is a reservation system that manages access to the remote laboratory. In the first subsection of this section, a brief description of the programming environments and DAQ devices utilized in the development of the remote laboratory will be provided. This will be followed by a detailed outline of the remote laboratory's design and a description of its web interface and reservation system.

A. Programming environment and NI DAQ devices

As already mentioned, the remote laboratory was developed using LabVIEW [15] and G Web development software [16], which are established programming environments commonly used in scientific research and engineering. LabVIEW provides a programming language and development environment that enables scientists and engineers to design, control, and test complex systems using graphical programming techniques. In contrast, G Web development software is a novel web application development environment, first introduced in 2021, that allows users to create dynamic web pages and web applications using a graphical interface. The integration of LabVIEW and G Web development software offers researchers and engineers an efficient way to develop and deploy web-based control and monitoring systems. With LabVIEW, users can design the underlying control and monitoring algorithms for their systems. On the other hand, with G Web development software, they can create an intuitive web interface to interact with those systems.

The remote laboratory was designed to be compatible with NI DAQ devices, which offer high accuracy, resolution, fast sampling rates, and flexible connectivity options, making them suitable for a wide range of applications. A major advantage of NI's DAQ devices is their compatibility with LabVIEW. The standardized programming of NI DAQ cards in LabVIEW enables users to easily connect any card to the remote laboratory or upgrade to a newer model, providing greater flexibility and accessibility.

B. Remote laboratory design

The block diagram of the proposed remote laboratory is shown in Fig. 1.

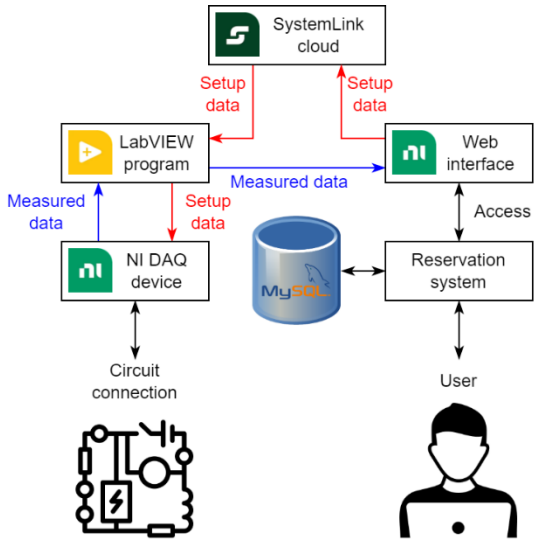

Fig. 1. Block diagram of the remote laboratory design

The remote laboratory's functionality relies on a LabVIEW program which serves as the main control system. The LabVIEW program is used to create signal sample data based on information obtained from the SystemLink [17] cloud. The data includes the amplitude, frequency, number of samples, and waveform shape required to generate the desired signal. The program then generates this signal and sends it to the DAQ card. Additionally, the program reads measured data from the DAQ card and transmits it using HTTP GET. This method is preferred over SystemLink due to its inability to transmit multi-track signal data.

The web interface of the laboratory is shown in Fig. 2.

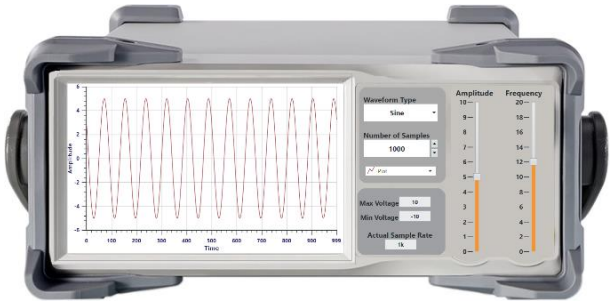

Fig. 2. Web interface of the remote laboratory

The interface consists of two components: a signal setup section and a waveform graph section. The interface is displayed on the screen of an oscilloscope for aesthetic purposes. The creation of the HTML webpage involved the use of the G Web development software. The page allows users to input information about the desired generated signal. This information is then transmitted to the SystemLink cloud for processing. The use of the SystemLink cloud ensures that the transmission of data remains secure, as well as minimizes any potential errors that could arise. Furthermore, the server also loads data from the HTTP GET request that is issued by the main LabVIEW program. This data is used to update the HTML webpage with relevant information regarding the measured signal. Overall, the webpage functionality enables users to modify the generated signal and observe the measured signals in near real-time.

The reservation system of the remote laboratory is implemented in PHP. As shown in Fig. 1 the reservation system is connected to a MySQL database, which contains the login credentials of all users, as well as their reservation times. The reservation system interface includes three pages. The first page is the home page, which allows users to log into the reservation system. The second page displays the available reservation times for the remote laboratory and enables users to make reservations. The third page lists all the reservations made by the logged-in user, including expired reservations. Once a user makes a reservation and opens this page at the scheduled reservation time, the system redirects the user to the web interface of the remote laboratory. Conversely, when the reservation time expires, the user is redirected to the home page of the reservation system.

III. CONCLUSION AND FUTURE WORK

In summary, this paper presented a preliminary design of a LabVIEW-based remote laboratory with a web interface created using the innovative NI G Web Development Software. The study demonstrates that this technology has the potential to create a high-quality web interface for remote laboratories. Also, the implementation of a reservation system has enhanced the functionality and user-friendliness of the proposed remote laboratory. Overall, the proposed remote laboratory has the potential to serve as a valuable teaching tool in experimental electronic classes.

Future work is directed to: (i) implementing the system functionality that enables more than one device to be connected simultaneously, which would enhance the collaborative potential of the remote laboratory, (ii) implementing the ability to export measured data, which would enable students to analyze and manipulate the data outside of the remote laboratory environment, and potentially facilitate more in-depth analysis and experimentation, (iii) developing a more advanced signal setup that includes the ability to import user-defined signals, which would enable students to experiment with custom signal configurations and expand the range of experimental possibilities, and (iv) evaluating the usability and effectiveness of the remote laboratory through surveys, which would enable the collection of feedback from users and facilitate the identification of areas for improvement and refinement.

ACKNOWLEDGMENT

The work is a part of the project supported by the Science Grant Agency of the Slovak Republic (No. 1/0413/22).

REFERENCES

[1] S. Martin, A. Fernandez-Pacheco, J. A. Ruipérez-Valiente, G. Carro, and M. Castro, “Remote Experimentation Through Arduino-Based Remote Laboratories,” *IEEE Revista Iberoamericana de Tecnologias del Aprendizaje*, vol. 16, no. 2, pp. 180–186, May 2021.

[2] I. E. Allen and J. Seaman, “Grade Level: Tracking Online Education in the United States,” Babson Survey Research Group, Feb. 2015. Accessed: Mar. 27, 2023. [Online]. Available: https://eric.ed.gov/?id=ED572778

[3] A. Van den Beemt, S. Groothuijsen, L. Ozkan, and W. Hendrix, “Remote labs in higher engineering education: engaging students with active learning pedagogy,” *J Comput High Educ*, Aug. 2022. Accessed: Mar. 23, 2023. [Online]. Available: https://doi.org/10.1007/s12528-022-09331-4

[4] J. Kromka, O. Kovac, I. Gladisova, and L. Michaeli, “The Impact of the COVID-19 on the Electronics Students of the Technical University of Košice,” in *2021 19th International Conference on Emerging eLearning Technologies and Applications (ICETA)*, Košice, Slovakia, Nov. 2021, pp. 204–210. Accessed: Mar. 14, 2022. [Online]. Available: https://ieeexplore.ieee.org/document/9726672/

[5] J. Svatos, J. Holub, J. Fischer, and J. Sobotka, “Online teaching at CTU in Prague aka university under COVID restrictions,” *Measurement: Sensors*, vol. 18, 2021.

[6] J. Svatos, J. Holub, J. Fischer, and J. Sobotka, “Online teaching of practical classes under the Covid-19 restrictions,” *Measurement: Sensors*, vol. 22, 2022.

[7] F. Valencia de Almeida *et al.*, “Teaching Digital Electronics during the COVID-19 Pandemic via a Remote Lab,” *Sensors*, vol. 22, no. 18, Art. no. 18, Jan. 2022.

[8] R. A. Abumalloh *et al.*, “The impact of coronavirus pandemic (COVID-19) on education: The role of virtual and remote laboratories in education,” *Technology in Society*, vol. 67, p. 101728, Nov. 2021.

[9] M. Youssef, E. L. McKinstry, A. Dunne, A. Bitton, A. G. Brady, and T. Jordan, “Developing Engaging

Remote Laboratory Activities for a Nonmajors Chemistry Course During COVID-19," *J. Chem. Educ.*, vol. 97, no. 9, pp. 3048–3054, Sep. 2020.

[10] G. Andria *et al.*, "Remote Didactic Laboratory 'G. Savastano,' The Italian Experience for E-Learning at the Technical Universities in the Field of Electrical and Electronic Measurement: Architecture and Optimization of the Communication Performance Based on Thin Client Technology," *IEEE Transactions on Instrumentation and Measurement*, vol. 56, no. 4, pp. 1124–1134, Aug. 2007.

[11] M. Drutarovský, J. Šaliga, L. Michaeli, and I. Hroncová, "Remote laboratory for fpga based reconfigurable systems testing," in *Proceedings of the 19th IMEKO World Congress Fundamental and Applied Metrology*, 2009, vol. 2, pp. 1185–1189.

[12] M. Corrado, L. De Vito, H. Ramos, and J. Saliga, "Hardware and software platform for ADCWAN remote laboratory," *Measurement: Journal of the International Measurement Confederation*, vol. 45, no. 4, pp. 795–807, 2012.

[13] L. Michaeli, M. Godla, and J. Šaliga, "Remote access cost effective measurement stand for teaching basic electronic circuits," in *Proceedings of the 6th IEEE International Conference on Intelligent Data Acquisition and Advanced Computing Systems: Technology and Applications, IDAACS'2011*, 2011, vol. 1, pp. 188–191.

[14] L. Michaeli, J. šaliga, I. Andráš, P. Dolinský, and M. Gamcová, "The laboratory stands with remote access for teaching of the experimental courses," in *Proceedings of the 22nd IMEKO TC4 International Symposium and 20th International Workshop on ADC Modelling and Testing 2017: Supporting World Development Through Electrical and Electronic Measurements*, 2017, vol. 2017-September, pp. 229–233.

[15] National Instruments, "What is LabVIEW? Graphical Programming for Test & Measurement." https://www.ni.com/en-us/shop/labview.html (accessed Mar. 30, 2023).

[16] National Instruments, "What is G Web Development Software?" https://www.ni.com/en-us/shop/electronic-test-instrumentation/programming-environments-for-electronic-test-and-instrumentation/what-is-g-web-development-software.html (accessed Mar. 30, 2023).

[17] National Instruments, "What Is SystemLink Software?" https://www.ni.com/cs-cz/shop/electronic-test-instrumentation/application-software-for-electronic-test-and-instrumentation-category/systemlink.html (accessed Mar. 31, 2023).

26th IMEKO TC4 International Symposium
24th International Workshop on ADC and DAC Modelling and Testing
IMEKO TC-4 2023
Pordenone, Italy / September 20-21, 2023

Phase measurement methods based on timer modules

Sanja Mandić[1], Dragan Pejić[1], Đorđe Novaković[1], Marjan Urekar[1], Platon Sovilj[1]

[1] *University of Novi Sad, Faculty of Technical Sciences, sanja.mandic@uns.ac.rs, pejicdra@uns.ac.rs, djordjenovakovic@uns.ac.rs, urekarm@uns.ac.rs, platon@uns.ac.rs*

***Abstract* – In this article, the methods of measuring the relative phase difference between two simple periodic signals, based on timer modules, are considered, with an analysis of a measurement system, its following problems, and proposed solutions. The basic motivation for this research is the necessity for a very precise and accurate measurement of the relative phase difference between the voltage signal and current signal of a two-channel source, when there is a degradation of the phase in the output stage of a two-channel source. To compensate for the deviation of the measured and real phase angle of voltage and current at the output of a two-channel source, phase measurement can be realized with timer modules. This approach requires the conversion of relatively high voltage and current into periodic pulse (rectangular) waves compatible with working with timer modules, and this conversion is achieved by utilizing comparators. Although the timer approach gives excellent results in measuring time intervals, they are rarely applied in phase measurement due to several important problems that appear during the conversion of analog signals into digital signals - the impact of analog noise, an offset of the comparators, as well as asymmetric low-pass filters intended for noise reduction.**

I. INTRODUCTION

In practical applications, there is a frequent need for the measurement of the phase difference between two signals of the same frequency [1-3]. Moreover, it is often necessary to measure the relative phase between two signals rather than the absolute phase of either individual signal [1-3].

According to [2], the methods for relative phase measurement can be divided into three distinct groups: event-counting methods, modulation-based methods, and sampling-based methods. Table 1 provides an overview of these methods along with the corresponding instrumentation employed.

A typical two-channel source of voltage and current commonly comprises several components, including a two-channel function generator, a voltage amplifier, a transconductance amplifier, a voltage output stage and a current output stage. The primary function of the voltage amplifier is to amplify voltage signal (order of magnitude - V) to a higher voltage level (order of magnitude – 10 V or 100 V). The transconductance amplifier converts the voltage signal (order of magnitude - V) to the corresponding current signal (order of magnitude – A).

Table 1. Relative phase measurement methods overview.

Methods	Instrumentation
Event-counting methods	Universal counter
Modulation-based methods	Vector Signal Analysers (VNA) Phase-to-Voltage Converters (PVC) Interferometers
Sampling-based methods	Phasor measurement units (PMU)

Table 2. One solution for correcting the effect of degradation of the relative phase difference.

Step	Description
1	Defining an initial relative phase difference in the input stage of the two-channel source.
2	Measurement of the relative phase difference of the voltage and current at the output of the two-channel source.
3	Determining the deviation of the measured relative phase difference from the initially defined relative phase difference.
4	Correction of relative phase difference deviation.

In the low-voltage stage, the relative phase difference can be achieved with high metrological performances,

however, degradation of the relative phase difference occurs in the amplifying stage.

The degradation of the relative phase difference requires the implementation of correction and one correction-oriented solution consists of the steps elucidated in Table 2.

Converting a simple periodic signal into a pulse (rectangular) wave can be achieved by using a comparator. In an optimal situation, the duty cycle of this pulse wave is 50 %. However, in the presented system, several problems arise.

Firstly, the presence of high-frequency noise, which is added to the comparator input simple periodic signal, causes multiple passings of the signal through zero, ie. reference value, which results in the appearance of multiple rising and falling edges in the output pulse wave - so-called "bouncing". The solution to the problem of the presence of noise in the current and voltage signal can be approached in two ways: by using a comparator with hysteresis or using a low-pass filter. The hysteresis of the comparator is achieved by the positive feedback of the operational amplifier, using two resistors. The implementation of the low-pass filter involves the use of a passive low-pass filter configuration, consisting of one resistor-capacitor pair. Additional problems arise if the hysteresis of the comparator is set in such a way that no pulse wave can be generated at the output of the comparator, or if the RC value of the low-pass filters differs between two channels which results in different phase shifts in each channel.

Additionally, the offset of the comparator leads to a deviation of output pulse wave duty cycle from 50 %. The voltage offset at the input of the comparator is one of the characteristics of real comparators which should be included in the modeling of the measurement system. The output signal will be changed from low voltage level to high voltage level when the amplitude of the input simple periodic signal reaches the value of comparator voltage offset. Consequently, the voltage offset induces variations of the output pulse wave duty cycle (that is, the time duration of high and low voltage levels during the output signal period).

II. MEASUREMENT SYSTEM

Two proposals for solving the problems that arise when measuring the phase of timer methods, therefore, imply the use of:

a) Comparator with hysteresis
b) Low-pass filter and comparator without hysteresis

Therefore, two systems were considered in the paper. Both proposed measurement systems consist of two measurement channels. Each channel has a simple periodic analog signal at the input and a pulse (rectangular) wave at the output (Table 3).

The comparator is the fundamental element in each channel. The analysis of the impact of the comparator offset voltage, as well as the investigation into the influence of comparator hysteresis (modeled using resistors in a positive feedback loop), were key focal points in the analysis of the first proposed measurement system. On the other hand, the assessment of the influence of the comparator offset voltage and a low-pass filter's influence were the primary areas of interest in the analysis of the second proposed measurement system.

Table 3. Phase measurement method based on timer module: measurement channel structure.

Measurement channel input	*Simple periodic analog signal*
Measurement channel output	*Pulse (rectangular) wave*
Measurement channel elements	*Comparator*
	Comparator offset voltage
	a) Comparator hysteresis resistors *b) Comparator input low-pass filter*
	Comparator input switching element
	Comparator output inverter

From the standpoint of measurement error reduction, the key elements of each channel are comparator input switching elements (which have the role of switching the inputs connected to the comparator in appropriate time intervals) and comparator output inverters (which have the role of inverting comparator output in appropriate time intervals).

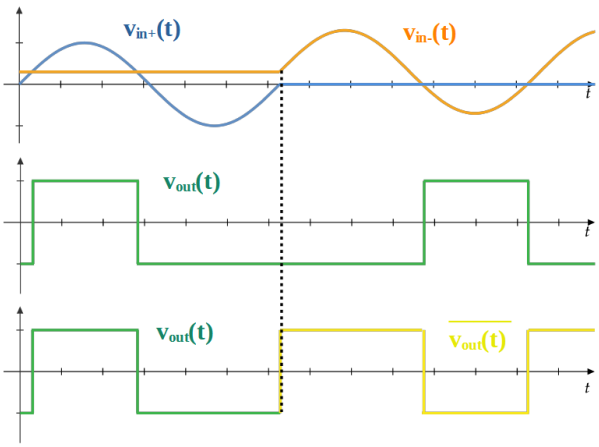

Fig. 1. Proposed solution to the problem due to the comparator offset: changing the comparator input and inverting the comparator output.

In order to solve the problem of the comparator offset voltage that causes deviation of the duty cycle of the

pulse wave (from 50 %), a method is proposed that consists of successively changing the comparator input and inverting the comparator output (Figure 1). Namely, during a time interval lasting one period of the input simple periodic signal, the input simple periodic signal is applied to the non-inverting input of the comparator, while the ground is connected to the inverting, offset input. In the upper graph from Figure 1, the voltages at the comparator inputs are shown in two consecutive periods, where the value of the offset voltage is positive. The logic level of the output signal, due to the presence of an offset on the inverting input, does not change when the value of the input signal is zero, but when the amplitude of the simple periodic input signal reaches a certain value greater than zero (offset voltage), the duration of the high voltage level at the output is shorter compared to the duration of the low voltage level.

During the subsequent time interval of one period of the input signal, the signals at the comparator inputs alternate, i.e., the ground is connected to the non-inverting input of the comparator, while the inverting input supplies a periodic signal, the amplitude of which is affected by the offset of the comparator. In this case, due to the amplitude of the simple periodic signal increased by the offset voltage at the inverting input, in most of the period the voltage at the non-inverting input of the comparator is lower than the voltage at the inverting input of the comparator, and during the second period, the duration of the low voltage level in the output signal is longer than the duration of the high voltage level. In order to achieve a total duty cycle of 50 % in the entire output signal for the given two periods, during the second period the output pulse wave is inverted. The output signal is shown in the lower graph in Figure 1.

III. RESULTS

Extensive simulations and experiments based on the described measurement systems were performed. The simulation analysis involved consideration of the influence of individual problems on the phase error, as well as the influence of a combination of problems.

The phase measurement error as a result of the comparator voltage offset and comparator hysteresis, according to the simulation setup of the first measurement system, before and after applying the method of changing the comparator input and inverting the comparator output is presented in Figure 2. In Figure 2. R2 is the value of the comparator hysteresis resistor. The phase measurement error as a result of the comparator voltage offset and difference of low-pass filters, according to the simulation setup of the second measurement system, before and after applying the method of changing the comparator input and inverting the comparator output is presented in Figure 3. Rx in Figure 3. presents the resistance value in the low-pass filter.

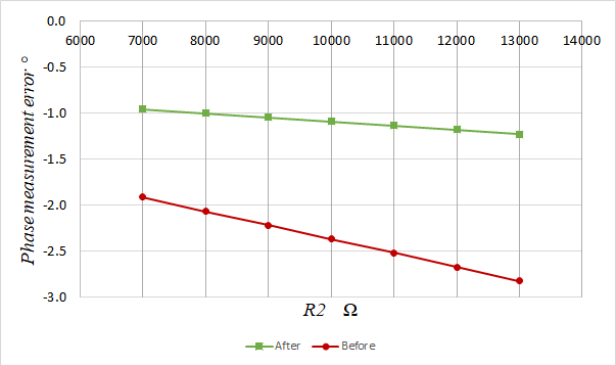

Fig. 2. Simulation results: phase measurement error related to the comparator offset and comparator hysteresis before and after applying the method of changing the comparator input and inverting the comparator output.

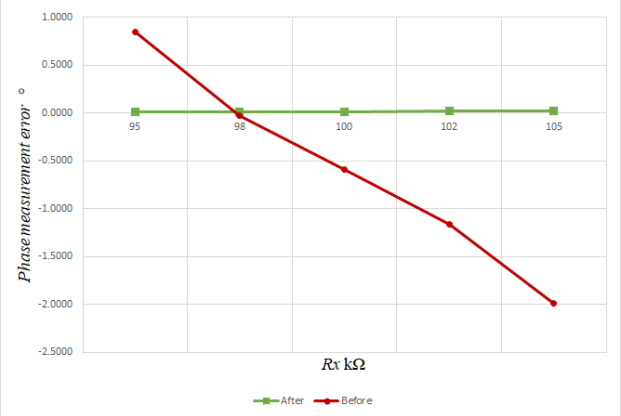

Fig. 3. Simulation results: phase measurement error related to the comparator offset and low-pass filter difference before and after applying the method of changing the comparator input and inverting the comparator output.

As the second proposed measurement system, which involves the use of comparators without hysteresis and low-pass filters, showed better performance through simulations, the hardware implementation of this system was carried out, and a series of experiments were performed.

Table 4. Phase measurement system configuration.

Case	Channel 1 comparator			Channel 2 comparator		
	IN-	IN+	OUT	IN-	IN+	OUT
1	V_{in1}	GND	V_{out1}	V_{in2}	GND	V_{out2}
2	GND	V_{in1}	$\overline{V_{out1}}$	GND	V_{in2}	$\overline{V_{out2}}$
3	V_{in2}	GND	V_{out2}	V_{in1}	GND	V_{out1}
4	GND	V_{in2}	$\overline{V_{out2}}$	GND	V_{in1}	$\overline{V_{out1}}$

Measured time intervals between the falling edges of the output pulse wave related to the input simple periodic signal phase, according to the experimental setup of the measurement system, are presented in Figure 4. The experimental setup includes four system configuration cases, described in Table 4.

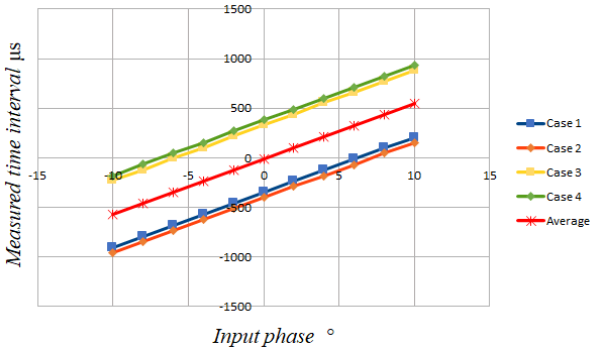

Fig. 4. Experimental results: measured time intervals between the falling edges of the output pulse wave related to the input simple periodic signal phase.

IV. DISCUSSION AND CONCLUSION

At first, simulation results indicated that phase measurement error related to the comparator offset and difference between the low-pass filters decreased, after applying the method of changing the comparator input and inverting the comparator output.

Under the influence of the systematic error due to the difference between the low-pass filters and the comparator offset, in cases 1, 2, 3, and 4, an offset of the time shift phase-related dependence is observed. If cases 1 and 3 are observed, the same configurations of the + and - inputs of the comparators are noticed. However, the simple periodic signals fed to the comparators are changed, which also applies to cases 2 and 4. It is observed that the value of the systematic error is approximately the same for cases 1 and 3, while the sign of the systematic error is the opposite. Also, the value of the systematic error is approximately equal, but of the opposite sign, for cases 2 and 4. It is possible to conclude that due to the application of the input signal-changing method, the systematic error changes its sign, and by averaging the value of the measured time interval, we eliminate the influence of the systematic error.

Therefore, the system in practical implementation shows the performance predicted by the simulation analysis and gives desirable results, that is, the proposed solution successfully eliminates errors caused by the comparator offset and the difference of the low-pass filters on two channels.

Further development of the experimental measurement system is planned, and it involves integrating the implemented system with a microcontroller system, and the use of timer/counter modules of the microcontroller to measure the time shift of the signal.

REFERENCES

[1] Webster, J.G., & Eren, H. (Eds.). (2014). Measurement, Instrumentation, and Sensors Handbook (Chapter "Phase Measurement" by Peter O'Shea). CRC Press.

[2] Balestrieri, Eulalia, De Vito, Luca, Picariello, Francesco, Rapuano, Sergio, Tudosa, Ioan. "A review of accurate phase measurement methods and instruments for sinewave signals." Acta IMEKO 9.2 (2020): 52-58, doi: 10.21014/acta imeko.v9i2.802.

[3] Zupunski, I. Z., Holicek, L. M., i Vujicic, V. V. "Power-factor calibrator." IEEE transactions on instrumentation and measurement 46.2 (1997): 408-411.

26th IMEKO TC4 International Symposium
24th International Workshop on ADC and DAC Modelling and Testing
IMEKO TC-4 2023
Pordenone, Italy / September 20-21, 2023

Metrology and Capacity Building in Higher Education: Project Knowledge Triangle for a Low Carbon Economy (KALCEA)

Platon Sovilj[1], Sanja Mandić[1], Dragan Pejić[1], Đorđe Novaković[1], Marjan Urekar[1]

[1] *University of Novi Sad, Faculty of Technical Sciences, Serbia, platon@uns.ac.rs, sanja.mandic@uns.ac.rs, pejicdra@uns.ac.rs, djordjenovakovic@uns.ac.rs, urekarm@uns.ac.rs*

***Abstract* – The threat of climate change and the global challenges in the energy sectors, led the countries all over the world to consider investing in low-carbon energy projects. Hence, renewable energy technologies, storage technologies, smart electric energy grids, energy efficiency aspects and other similar issues, are some of the main aspects which can lead into the direction of large-scale decarburization. The Knowledge Triangle (KT) methodology points out the significance of jointly organized research, education and innovation processes, and importance of the linkages between these processes. The role of metrology infrastructure in project "Knowledge triangle for a low carbon economy" (acronym KALCEA), because appropriate metrology infrastructure is one of the crucial elements in KALCEA related innovation and technology aspects.**

I. INTRODUCTION

The threat of climate change[1] and the global challenges in the energy sectors, led the countries all over the world to consider investing in low-carbon energy [2] projects. Renewable energy technologies, storage technologies, smart electric energy grids, energy efficiency aspects and other similar issues, are some of the main aspects which can lead into the direction of large-scale decarburization. The Knowledge Triangle (KT) approach emphasizes the significance of jointly organized research, education and innovation processes, and importance of the linkages between these processes.

Academic actors in the KT approach are at the center of the innovation network, in which extended capacities, high level of integration and leadership are preconditions for building up innovation performance. By founding the Knowledge and Innovation Centres (KIC) the existing institutional capacities of the high education institutions will be built up with goal to make prerequisites for implementation of the knowledge triangle activities. KICs will provide area where concepts, skills, and knowledge from various partners in the field of energy can be transferred effectively to the innovation.

The role of metrology in capacity building in higher education is emphasized in project "Knowledge triangle for a low carbon economy" (acronym KALCEA[3]), because appropriate metrology infrastructure is one of the crucial elements in KALCEA related innovation and technology areas.

Successful communication, business, and even the existence of economic, scientific and a number of other organizations depends to a considerable extent on the appropriate support of specialized organizations in the fields of standardization, metrology, quality, conformity assessment, i.e. certification and intellectual, i.e. industrial property.

The mentioned areas are interconnected, whereby the area of conformity assessment, ie certification, rests on the area of product realization (of appropriate quality), and is conditioned by the area of accreditation, ie authorization from competent organizations.

Given the complexity and specificity of the fields of standardization, metrology, accreditation, conformity assessment (certification) and intellectual property, as well as their pronounced legislative arrangement, activities in these areas require appropriate institutional support.

The aforementioned support in our country has so far mainly rested on certain state bodies and organizations with relatively little involvement of regional organizations (eg in some regional chambers of commerce). A somewhat greater participation of economic and other organizations was observed in the domain of consulting for the areas of quality management systems, environmental protection management systems and other management systems in the organization, as well as in the domain of conformity assessment (certification), which relies on accredited and authorized

laboratories.

However, it should be pointed out that even such involvement of economic and other organizations was not sufficiently directed and coordinated, which, in certain cases, caused unnecessary duplication of (poorly used) capacities, but also insufficient representation in certain areas.

The strict requirements of regulations and standards, but also of users, i.e. the market, require that, in order to ensure the required quality of systems, processes and products (services), an appropriate dispersed network of (regional) institutions competent to provide appropriate support for effective and efficient work must be provided in the areas of standardization, metrology, quality and conformity assessment (certification), as well as in the area of intellectual and industrial property.

II. INFRASTRUCTURE OVERVIEW

The technical-technological infrastructure, viewed in this case from the point of view of the region, would represent institutional support for ensuring the quality of systems, processes and products (services), as well as the protection of intellectual, and above all, industrial creativity.

The aforementioned institutional support, from the point of view of consulting, providing and disseminating information, providing services and training staff, would refer to the following areas:

- standardization;
- metrology;
- conformity assessment (certification), including associated accredited and authorized laboratories;
- intellectual and especially industrial properties.

Support from the mentioned areas is, in essence, fundamental support in the areas of system, process and product (service) quality.

The Faculty of Technical Sciences, as part of the Feasibility Study of the establishment of the Regional Center for Standardization and Certification, defined the basic guidelines for the establishment of a wider body that should unite all aspects of the technical-technological infrastructure of the region.

Considering the real situation and the existence of part of the necessary infrastructure at the Faculty of Technical Sciences in Novi Sad, in the aforementioned Feasibility Study of the establishment of the Regional Center for Standardization and Certification, it is proposed that the part dealing with certification be located at the Faculty of Technical Sciences, where there are already laboratories that on a large scale they can satisfy the initial requirements for product certification in the region.

By unifying existing laboratories and developing new ones according to the needs of the region's economy, a strong technical-technological basis will be created for overcoming the technical barriers that exist in trade with developed countries.

III. CENTER OF METROLOGY – MISION, VISION AND AIMS

The regional center of technical-technological infrastructure is intended for the provision of certain information, advisory and other services in the fields of standardization, metrology, accreditation, conformity assessment (certification) and intellectual, and especially industrial property, which meet the needs in these areas, economic, scientific and other organizations in the region and, if necessary, in Serbia as well.

At the moment, there is no such organization in the area of Vojvodina, and in all of Serbia, for some of the mentioned areas, there are only a few organizations, which is insufficient to meet the real needs that ensure modern business on the domestic and foreign markets.

The vision of the Center implies that the Center will be built as a modern, flexible organization, which functions with optimal use of available resources and maximum satisfaction of the region's needs in the areas of standardization, metrology, conformity assessment (certification) and intellectual, especially industrial property.

The development of the Center will be directed in accordance with the realistically determined needs in the mentioned areas, but also with the provided material and other basis, acquired through its own functioning.

The main goal of the Center is to provide a neutral and competent organization for the provision of information and consulting services in the fields of standardization, metrology and intellectual property, as well as in the field of conformity assessment (certification), which is accredited in that field by the Accreditation Body of Serbia, i.e. authorized by the authorities state authorities, for the certification of certain products, that is, systems and services.

In accordance with the stated basic goal, in the management of the processes in the Center, which should ensure the satisfaction of the defined Mission, Vision, or Policy of the Center, are the following goals:

- Provision of satisfactory resources, primarily in terms of staff, equipment, business, or work space; work methods and procedures, as well as appropriate financial resources;
- Combining system knowledge, modern technology and user needs in the conception and implementation of services, with the aim of providing users with relevant and high-quality services, aligned with applicable regulations, that is, standards;
- Expanding the circle of users and creating solid cooperation with them;

- Selection of organizations and individuals - collaborators of the Center, in accordance with their ability to meet the demands of the Center and the demands of its users;
- Achieving a business relationship with partners, in terms of strict compliance with assumed obligations and fair consideration of own and partner's interests;
- Directed development in areas for which there is expressed interest, basic resources and realistically expected, acceptable results;
- Systematically arranged and systematically managed documentation of the work process and work subject;
- Improvement of the work process and appropriate methods and procedures, i.e. development of the Center in accordance with real needs and provided resources;
- Provision of conditions for permanent education, motivated and responsible work of staff.

The center, as a regional body, will carry out high-quality, effective and efficient work in the aforementioned areas, with an acceptable price and short deadlines, which is extremely important for proving the competence of the economy, achieving defined and repeatable product quality and achieving, not only competitive prices and other effects, but in general the placement of products on the domestic, and especially European and world markets.

The operation of the Center implies the provision of appropriate financial results, as compensation for the services rendered. However, the Center will not aim to achieve high profits, but only funds to cover its own functioning and targeted development.

By combining and using existing human, technical and other resources, with a slight addition of those resources, the Center will ensure rational use of those resources and visible effects for economic, scientific and other organizations, as well as for individuals and the social community as a whole.

IV. CONCLUSION

On the territory of the region, there is a great need for the implementation of standards in business, as well as the certification of products and services of a large number of companies. The existing infrastructure in this area is very scarce and insufficiently connected, there is still a small number of accredited laboratories (for a large number of products and services that are key in the region, primarily in food processing, there is not a single laboratory that can calibrate products and measuring instruments , that is, it certifies products and services).

By comparing the situation here and in the immediate surroundings, we come to the conclusion that an urgent institutionalized solution is needed in this area, in order not to lose a step further. By forming the Center for Metrology, which unites the information base of companies, people, products and services from one (users of the Center's services), and laboratory and other infrastructure, companies and specialists for certain areas, who are trained to provide certain services in the field of work, in one place Center (training for the application of standards, certification of systems, products and services, etc.), on the other hand, will ensure significant progress in the adoption of international norms in business and will ensure the competence of products from the region on the European market.

REFERENCES

[1]Change, M. Sc Sem-II Climate. "Climate change." (2017).

[2]Albino, Vito, et al. "Understanding the development trends of low-carbon energy technologies: A patent analysis." Applied energy 135 (2014): 836-854.

[3]Zabasta, Anatolijs, et al. "Development of KALCEA Novel Collaborative Platform for Sustainable Development of Western Balkan Countries." International Conference on Interactive Collaborative Learning. Cham: Springer International Publishing, 2022.

26th IMEKO TC4 International Symposium
24th International Workshop on ADC and DAC Modelling and Testing
IMEKO TC-4 2023
Pordenone, Italy / September 20-21, 2023

Digital Stochastic Measurement and Industry 4.0

Platon Sovilj[1], Dragan Pejić[1], Marjan Urekar[1], Sanja Mandić[1],

[1] *University of Novi Sad, Faculty of Technical Sciences, Serbia, platon@uns.ac.rs, pejicdra@uns.ac.rs, urekarm@uns.ac.rs, sanja.mandic@uns.ac.rs*

***Abstract* – Digital stochastic measurement methods were developed in the past, with the focus onto "measurement over interval" strategy and use of stochastic dither signals. These methods obtained the increase of effective precision from low-precission A/D converters. Combination of simple analog hardware and state-of-art digital modules makes these methods suitable in many applications.Development of 4th industrial revolution (often named as Industry 4.0 concept) is extensivelly based on communication technologies advancement. This advancement enhanced microprocessor and integrated circuits based technology capabilities. The concept of digital stochastic measurement has many advantages which can be applied in Industry 4.0 concept.**

I. INTRODUCTION

Stochastic digital measurement approach is the name for a special approach of signal measurement which, with the use of an A/D converter and the addition of a stochastic dither, has as its main feature measurement over an interval, in contrast to classic digital measurement which is based on point measurement. The stochastic digital measurement approach proves to be suitable not only for measuring time-invariant and simple-periodic signals, but also for measuring harmonics of a stationary signal, with controlled noise suppression.

Development of 4th industrial revolution (often named as Industry 4.0 concept) is extensivelly based on new communication technologies development. This development further extended microprocessor and integrated circuits based technology capabilities. The concept of digital stochastic measurement has many characteristics which can be used for challenges noticed in Industry 4.0 concept.

II. FUNDAMENTALS OF DIGITAL STOCHASTIC MEASUREMENT

In [1] high-precision stochastic Watt-hour meter is proposed. It was based on a stochastic measurement method, containing circuits for analog addition, stochastic dither signal added to the iinputs, analog comparators, analog level limitters and logical multiplzing circuits. Accuracy limit of this high-precision stochastic Watt-hour meter is considered. The device main hardware elements are presented at Figure 1.

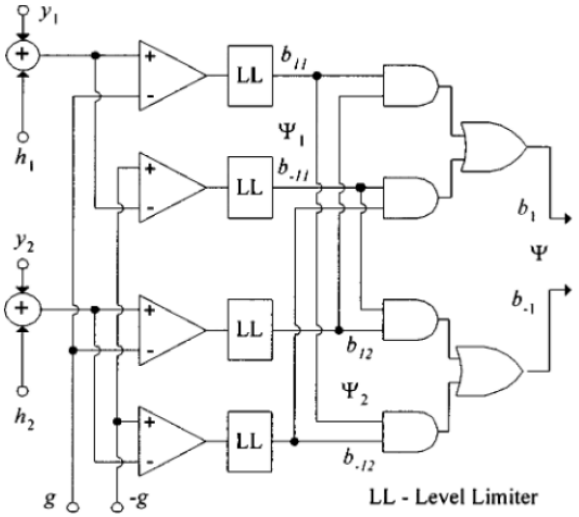

Fig. 1[1]. Main hardware elements of the high-precision stochastic Watt-hour meter. It contains circuits for analog addition, stochastic dither signal added to the iinputs, analog comparators, analog level limitters and logical multiplying circuits

In [2] further generalization of low-frequency true RMS instrument based on stochastic measurement approach is considered. It was based on an improved stochastic measurement method, containing also circuits for analog addition, stochastic dither signal added to the iinputs, but analog comparators, analog level limitters and logical multiplying circuits are replaced with 6-bit A/D converter and FPGA structure (Figure 2).

Microcontroller is getting outputs from FPGA structure and, after basic processing, forward them to the computer by serial communication channel. Prototype instrument and FPGA based core block diagram are presented at

Figure 3. FPGA structure is consisted of A/D driver, LFSR register, synchro element, counter, appropriate memory and implementation of multipliers and accumulators, digital multiplexers and UART communication module.

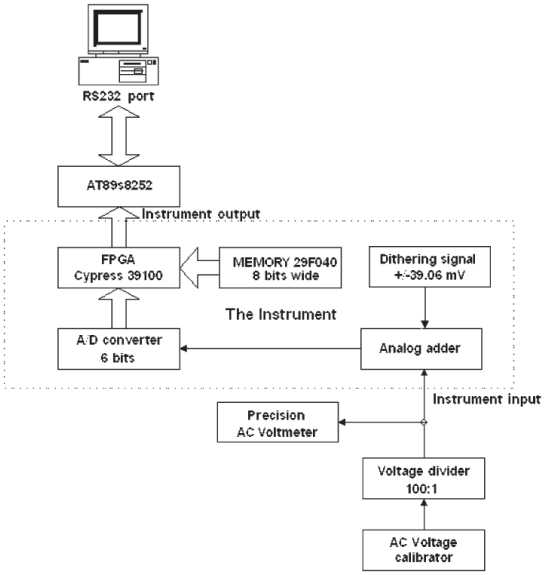

Fig. 2[2]. Further generalization of low-frequency true RMS instrument based on stochastic measurement approach: instrumentation block diagram.

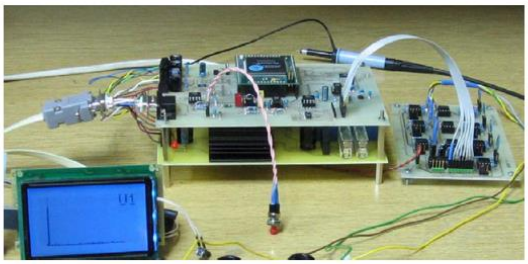

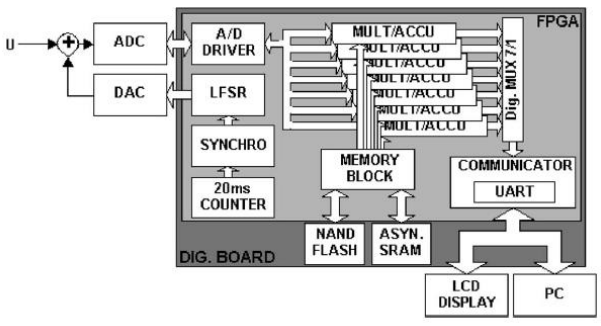

Fig. 3[2]. Further generalization of low-frequency true RMS instrument based on stochastic measurement approach: prototype instrument and FPGA based core block diagram.

III. DEVELOPMENT OF DIGITAL STOCHASTIC INSTRUMENTATION AND INDUSTRY 4.0

A stochastic instrument is proposed in [3] for stochastic measurement of harmonics at low signal-to-noise ratio (Figure 4). Relative standard uncertainty for both Gaussian and uniform noise is simulated and averaged (Figure 5) indicating the further direction of stochastic instrumentation development.

Fig. 4[3]. A stochastic instrument proposed in [3] for stochastic measurement of harmonics at low signal-to-noise ratio.

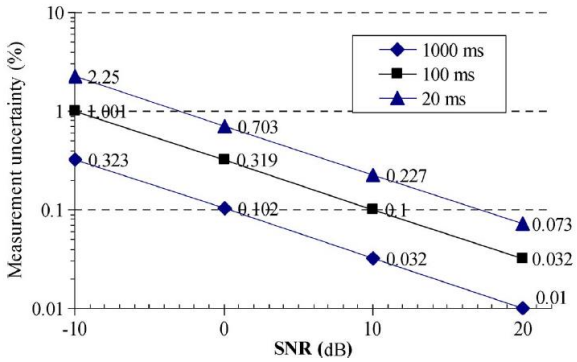

Fig. 5[3]. Relative standard uncertainty for both Gaussian and uniform noise (simulation average) of a stochastic instrument proposed in [3] for stochastic measurement of harmonics at low signal-to-noise ratio.

The research described in [4] evaluated one

implementation of digital stochastic measurement of non-stationary signal (Figure 6). The simulations and experiments showed well agreement with the developed formula for measurement uncertainty limit.

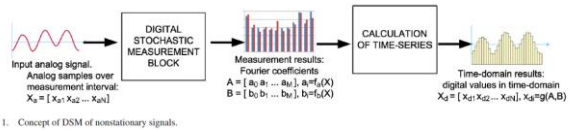

Fig. 1. Concept of DSM of nonstationary signals.

Fig. 6[4]. Digital stochastic measurement of a non-stationary signal with an example of EEG signal measurement: instrumentation block diagram.

The research described in [5] evaluated a design of low power stochastic sensor in IoT, IIoT and Industry 4.0 environments. The sensor model (Figure 7) is consisted of transducing element, digital stochastic measurement module and IioT module.

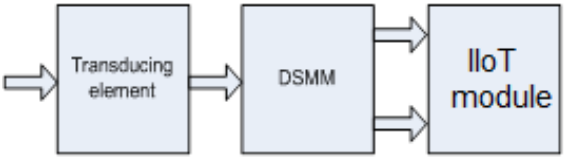

Fig. 7[5]. Model of a single stochastic sensor with IIoT module for industrial applications (SSUIA).

IV. CONCLUSION

Stochastic digital measurement strategy is the name for a special set of methods of signal measurement which, with the application of an A/D converter and the addition of a stochastic dither signal, has as its key characteristics measurement over an interval, which is opposite to typical digital measurement which is based on measurement in a point. The stochastic digital measurement strategy appears to be usefull not only for measuring time-invariant and simple-periodic signals, but also for measuring harmonics of a stationary signal, with determined noise suppression.

Development of 4th industrial revolution (often named as Industry 4.0 revolution) is mainly based on new communication technologies development. This development further extended microprocessor and integrated circuits based technology characteristics. The strategy of digital stochastic measurement has many usefull properties which can be applied for solving problems present in Industry 4.0 concept.

REFERENCES

[1]D. Pejic, V. Vujicic, “Accuracy limit of high-precision stochastic Watt-hour meter,” IEEE Trans. Instrum. Meas., vol. 49, pp. 617-620, June 2000.

[2]V. Pjevalica and V. Vujičić, “Further generalization of low-frequency true RMS instrument,” in Proc. Instrumentation and Measurement Technology Conference IMTC 2005, pp. . May 2005.

[3]B. Santrač, M. A. Sokola, Z. Mitrović, Ivan Župunski and V. Vujičić, “A Novel Method for Stochastic Measurement of Harmonics at Low Signal-to-Noise Ratio”, IEEE Trans. Instrum. Meas., vol. 58, pp. 3434-3441, Oct. 2009.

[4]P. Sovilj, S. Milovancev, and V. Vujicic, “Digital stochastic measurement of a nonstationary signal with an example of EEG signal measurement,” IEEE Trans. Instrum. Meas., vol. 60, no. 9, pp. 3230–3232, Sep. 2010.

[5]Marjan Urekar, Platon Sovilj, Ivan Gutai, Dragan Pejic, Bojan Vujicic, Djordje Novakovic, “Low Power Stochastic Sensor in IoT, IIoT and Industry 4.0 Environments”, 24th IMEKO TC4 International Symposium, 22nd International Workshop on ADC and DAC Modelling and Testing, IMEKO TC-4 2020, Palermo, Italy, September 14-16, 2020.

26th IMEKO TC4 International Symposium
24th International Workshop on ADC and DAC Modelling and Testing
IMEKO TC-4 2023
Pordenone, Italy / September 20-21, 2023

Decoding Cognitive Processes in Arithmetic Tasks: An EEG-Based Convolutional Neural Network Model

Nikola Petrović[1], Lemana Spahić[2], Sanja Mandić[1], Platon Sovilj[1]

[1] *Faculty of Technical Sciences, University of Novi Sad, Novi Sad, Serbia, petrovicnikola@uns.ac.rs, sanja.mandic@uns.ac.rs, platon@uns.ac.rs*
[2] *Verlab Research Institute for Biomedical Engineering, Medical Devices and Artificial Intelligence, Sarajevo, Bosnia and Herzegovina, lemana@verlabinstitute.com*

***Abstract* – In this study, we introduce a novel system, developed in Python, for classifying cognitive processes based on EEG signals. The system employs a Convolutional Neural Network (CNN) trained on a dataset comprising 4-minute EEG recordings from 30 subjects. Each EEG sample processed for CNN input is 0.5 seconds long and is transformed into EEG power levels for each channel. The primary achievement of this research is the successful use of the CNN to classify whether a subject is performing a cognitive task well or poorly. The system's performance has been validated by experts in cognitive neuroscience and psychology, and its results have been benchmarked against state-of-the-art studies in the field. This work represents a significant**
contribution to the field of EEG-based cognitive process classification, demonstrating the effective integration of machine learning techniques and neuroscience data.

I. INTRODUCTION

Electroencephalography (EEG) is a non-invasive technique for measuring the electrical activity of the brain, widely used in research, medical diagnostics, and therapy . EEG signals are used for the detection and analysis of patterns of electrical brain activity, which are typically divided into four basic frequency ranges: delta (0.5-4 Hz), theta (4-8 Hz), alpha (8-13 Hz), beta (13-30 Hz), and gamma (30-45 Hz) [1]. Each frequency range is associated with different cognitive states and functions. For example, alpha rhythm is often linked to relaxation and closed eyes, while beta rhythm is associated with active thinking and task focus.

Quantitative electroencephalography (QEEG) is a technique that uses mathematical analyses to process and analyze EEG signals [2]. QEEG can be used to identify anomalies in brain electrical activity, including changes in signal amplitude and phase, localization of signal generators, and functional connections between different brain regions [3]. QEEG can be useful in the diagnosis and monitoring of various neurological disorders, such as epilepsy, schizophrenia, dementia, and autism [2]. EEG is used in the study of cognitive processes, such as attention, memory, emotions, speech, and problem-solving skills [4]. Moreover, EEG is widely used in sleep research and studies investigating the impact of sleep on cognitive functions [5].

By using EEG as a measurement method, it is possible to record brain activity in real-time, allowing researchers to study the dynamic processes occurring in the brain during different cognitive and emotional states. This can contribute to a better understanding of how the brain functions and the development of new therapies and interventions for neurological and psychiatric disorders [6].

In the realm of neuroscience, artificial intelligence (AI) has become a potent tool that offers fresh approaches to deciphering the intricate data produced by research on the human brain. AI presents exciting possibilities for improving the interface between humans and technology, neurological condition detection and treatment, and brain research. It also brings along fresh difficulties, like the requirement for sizable, high-quality datasets and the understanding of intricate model results. AI, particularly machine learning and deep learning algorithms, can process and analyze neuroimaging data (like MRI or fMRI scans) more efficiently and accurately than traditional methods. They can detect patterns and anomalies that might be missed by the human eye, aiding in the diagnosis and monitoring of neurological disorders like Alzheimer's, Parkinson's, and multiple sclerosis. AI plays a crucial role in the development of BCIs, devices that translate neuronal information into commands capable of controlling software or hardware. Machine learning algorithms can be used to decode the user's intent from the patterns of their brain activity. AI can help model the structure and function of biological neural networks. These models can provide insights into how neurons interact and communicate, aiding our understanding of brain function and behavior. AI can expedite the process of drug discovery for

neurological disorders by predicting the effectiveness of potential compounds and identifying potential side effects. AI can also be used to create predictive models for neurological outcomes based on a variety of data, including genetic information, environmental factors, and lifestyle habits. This can help in early detection and prevention of neurological disorders [7]

Bashivan et al. propose a different approach, using Deep Recurrent-Convolutional Neural Networks (R-CNNs) for learning representations from multi-channel EEG time-series. They transform EEG activities into a sequence of topology-preserving multi-spectral images, and then train a deep R-CNN to learn robust representations from the sequence of images. The goal was to find features that are less sensitive to variations and distortions within each dimension. In summary, both papers propose novel deep learning approaches for EEG data analysis, but they differ in their methods and applications [8]. Schirrmeister et al. focus on ConvNets and their visualization for EEG decoding, while Bashivan et al. use R-CNNs to learn robust representations from EEG data. Both methods show promising results, demonstrating the potential of deep learning techniques in EEG analysis and brain-computer interfaces [9]. Paper by Roy et al. provides a comprehensive review of the application of deep learning in EEG analysis. Instead of focusing on a specific model, the authors analyze a broad range of studies, highlighting trends, challenges, and recommendations for future research in the field. They emphasized the importance of model inspection, especially in clinical settings, and the need for transparency and reproducibility in DL-EEG studies [10].

This paper presents the development and validation of a system for the analysis and processing of electroencephalographic (EEG) signals with the aim of classifying the cognitive states of subjects. The aim of this research is to develop a benchmark for effective utilization of AI in the realm of neuroscience to enable and expedite future research endeavors.

II. METHODOLOGY

The methodology for the development and validation of a system for analysis and processing of EEG signal for classification of cognitive state of subjects is very complex and requires a series of interconnected steps where the success of each phase of development is dependent upon the performance of the previous module. The detailed flowchart of methodology is depicted in Fig. 1.

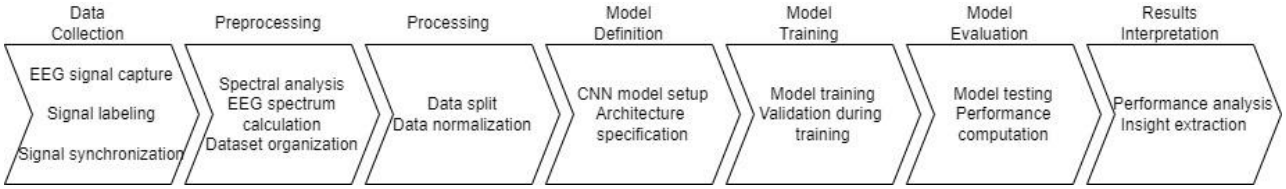

Fig. 1. Model loss over 50 epochs during training

A. Data Import

The initial step in our methodology is the importation of the necessary data for our study. This data consists of electroencephalogram (EEG) signals, which are electrical activities generated by the brain and recorded from the scalp. These signals are stored in European Data Format (EDF) files, a common format for storing biomedical signals.

The EEG data are loaded into the Python environment using the mne library, which is specifically designed for processing and visualizing EEG data. This library provides a function mne.io.read_raw_edf that reads the EDF files and converts them into a format that can be manipulated in Python.

B. Data Processing

The data processing stage is crucial in preparing the raw EEG signals for further analysis and classification. The primary technique used in this stage is the Short Time Fourier Transformation (STFT). The STFT is a powerful tool for analyzing the frequency content of non-stationary signals, such as EEG signals, which change their frequency content over time [11]. The STFT works by dividing the continuous EEG signal into smaller, overlapping segments, and then applying the Fourier Transform to each segment. This results in a time-frequency representation of the signal, which provides information about the signal's frequency content at each point in time. In addition to the STFT, the average power levels of each EEG spectrum range are also extracted. The average power level in each EEG frequency band is computed by integrating the power spectral density over the frequency range of the band. This results in a single value for each band, which represents the average power of the EEG signal in that frequency range. These values serve as features for the machine learning model, providing it with information about the spectral content of the EEG signals.

C. Data Organization for the Machine Learning Model

Once the features have been extracted from the EEG signals, they need to be organized in a way that can be easily processed by the machine learning model. In this project, the features are organized into a 2D array, where the first dimension represents the EEG power levels in the different frequency bands, and the second dimension represents the EEG channels. Each row in the 2D array corresponds to a different EEG channel, and each column corresponds to a different frequency band. The value in each cell of the array is the average power level of the corresponding frequency band in the corresponding EEG channel.

In addition to the 2D array of features, each array is associated with a binary value that indicates whether the subject was performing well or poorly. This binary value serves as the label for the machine learning model, providing it with information about the desired output for each set of features. By organizing the data in this way, the machine learning model can learn to recognize patterns in the EEG power levels across different frequency bands and channels, and use these patterns to predict whether a subject is likely to perform well or poorly. This organization of data is crucial for the successful training and performance of the machine learning model.

D. Machine Learning Model

The machine learning model used in this study is a Convolutional Neural Network (CNN), a type of artificial neural network that is particularly effective for processing grid-like data, such as time-series and image data. The CNN is implemented using the keras library, a high-level neural networks API that allows for easy and fast prototyping of neural networks. The model consists of several layers:

- Convolutional Layer: This is the first layer of the CNN. It performs a convolution operation on the input data using a set of learnable filters, each producing one feature map in the output. This layer is implemented using the Conv2D class from keras.layers.
- Max Pooling Layer: This layer reduces the spatial size of the feature maps, thereby reducing the amount of parameters and computation in the network. It operates by sliding a window over the input and selecting the maximum value in each window. This layer is implemented using the MaxPooling2D class from keras.layers.
- Flatten Layer: This layer flattens the input into a one-dimensional array, which can be fed into the fully connected layer. This layer is implemented using the Flatten class from keras.layers.
- Fully Connected Layer: This layer performs classification based on the features extracted by the previous layers. It is implemented using the Dense class from keras.layers.
- Output Layer: This is the final layer of the CNN. It produces the output of the model, which corresponds to the class predictions. This layer is also a fully connected layer and uses the softmax activation function to produce a probability distribution over the classes.

Once the model is defined, it is trained on the EEG data using the fit method of the Sequential class. This method adjusts the model's weights based on the training data and the corresponding labels.

The model is trained using the Adam optimization algorithm, a variant of stochastic gradient descent that has been shown to work well in practice. The loss function used is categorical cross-entropy, which is suitable for multi-class classification problems.

During training, the model's performance is evaluated on a validation set, which is a subset of the training data not used for updating the model's weights. This provides an estimate of the model's performance during training and allows for the early stopping of training if the model's performance on the validation set stops improving.

After training, the model's performance is evaluated on the testing set using the evaluate method of the Sequential class. This method computes the loss and any metrics specified during the model's compilation on the testing data. The performance of the model is evaluated in terms of accuracy, which is the proportion of correct predictions made by the model. The accuracy is computed using the accuracy_score function from the sklearn.metrics module.

E. Results interpretation

The final step in the methodology is the interpretation of the results. This involves analyzing the model's performance and identifying any patterns or insights that can be derived from the results. The accuracy of the model provides a measure of how well the model is able to classify the EEG signals based on the quality of the count. A high accuracy indicates that the model is effective at distinguishing between "good count quality" and "bad count quality" signals. In addition to accuracy, other metrics such as precision, recall, and the F1 score can be computed to provide a more comprehensive view of the model's performance. These metrics can be computed using the corresponding functions from the sklearn.metrics module. The results can also be visualized using confusion matrices and ROC curves, which provide a graphical representation of the model's performance. These visualizations can be created using the plot_confusion_matrix and plot_roc_curve functions from the sklearn.metrics module. Finally, the results can be interpreted in the context of the problem domain

III. RESULTS AND DISCUSSION

The EEG data used in this study consisted of 0.5-second segments from 23 channels, providing a rich and complex dataset for the model to learn from. The use of short segments of data is advantageous in that it allows for the classification of cognitive states in real-time, a critical requirement for many applications of EEG data, such as brain-computer interface systems and neurofeedback systems.

Our study demonstrated the utility of several data preprocessing and analysis techniques. For instance, we used Short-Time Fourier Transform (STFT) to convert the EEG time series data into the frequency domain, allowing us to extract power spectral density features for each frequency band (delta, theta, alpha, beta, and gamma). These features were then used as input to the CNN model. This approach allowed us to capture the spectral characteristics of the EEG data, which are known to be associated with different cognitive states.

The results of our study demonstrate the efficacy of a convolutional neural network (CNN) model in classifying cognitive states based on electroencephalogram (EEG) data. The model was trained and validated on EEG data collected during a mental arithmetic task, a well-established cognitive task that engages several cognitive processes, including working memory, attention, and numerical processing.

The training process of the convolutional neural network (CNN) model was a critical aspect of our study. The model was trained over 50 epochs, with the training data split into a training set (80%) and a validation set (20%). This split allowed us to monitor the model's performance on unseen data during the training process, providing an indication of the model's ability to generalize to new data.

The training process was guided by the binary cross-entropy loss function, a suitable choice for our binary classification task. The Adam optimizer was used to minimize this loss function. Adam, an algorithm for first-order gradient-based optimization, is widely used in deep learning models due to its efficiency and low memory requirements.

During the training process, we observed a consistent decrease in both training and validation loss (Figure 2), indicating that the model was learning to classify the cognitive states based on the EEG data effectively. The training loss decreased from 0.565 in the first epoch to 0.212 in the 50th epoch. Similarly, the validation loss decreased from 0.533 to 0.183 over the same period. These trends suggest that the model was not overfitting the training data, as evidenced by the concurrent decrease in validation loss.

Figure 2. Model loss over 50 epochs during training

Furthermore, we employed a variety of techniques to optimize the performance of our model. These included the use of dropout layers to prevent overfitting, max pooling layers to reduce the dimensionality of the data, and an early stopping callback to halt training when the validation loss ceased to decrease. These techniques contributed to the robust performance of our model.

To further prevent overfitting, we employed dropout layers in our model. Dropout is a regularization technique that randomly sets a fraction of input units to 0 at each update during training, which helps to prevent overfitting by ensuring that the model does not rely too heavily on any single feature. In our model, a dropout rate of 0.25 was used after the convolutional and max pooling layers, and a rate of 0.5 was used before the final dense layer.

In addition to monitoring the loss during training, we also tracked the model's accuracy on the training and validation sets. The model achieved a final training accuracy of 89.6% and a validation accuracy of 92.1% (Figure 3). These high accuracy rates, along with the low loss values, indicate that the model performed well on both the training and validation sets.

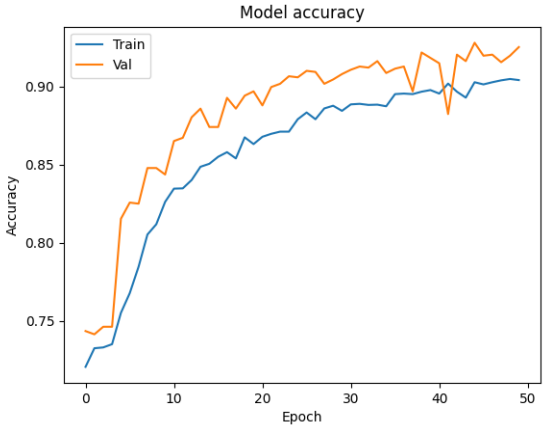

Figure 3. Model accuracy over 50 epochs during training

To evaluate the model's performance in more detail, we constructed a confusion matrix based on the model's predictions on the validation set (Figure 4). The confusion matrix provides a comprehensive overview of the model's performance, showing the number of true positives, true negatives, false positives, and false negatives. This information can be used to calculate various performance metrics, such as the F1 score and Matthews Correlation Coefficient (MCC), providing a more nuanced understanding of the model's performance than accuracy alone.

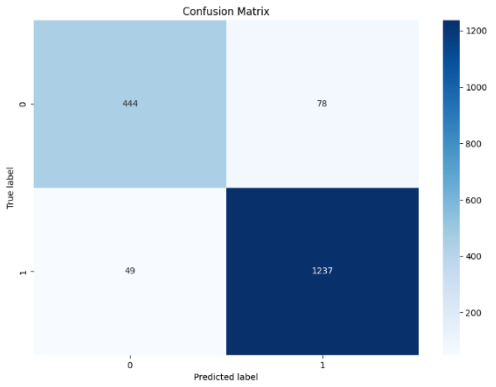

Figure. 4 Confusion matrix for the validation sample of the dataset (TP = 12337, TN = 444, FP = 78, FN = 49).

Sensitivity measures the proportion of actual positives that are correctly identified which in this case is 96.2%. Specificity measures the proportion of actual negatives that are correctly identified, in the case of this model it is 85%. Accuracy is the ratio of correctly predicted observations to the total observations and for the respective model it is 93%. In order to validate the perceived accuracy, the F1 score, which is the the weighted average of Precision and Recall, useful for uneven class distribution and MCC which is a measure of the quality of binary classifications, advantageous over F1 score as it takes into account true and false positives and negatives and is generally regarded as a balanced measure which can be used even if the classes are of very different sizes were used. The F1 score and MCC for the respective model 96.2% and 82.7% respectively.

The model's performance was evaluated by experts in the fields of psychology and machine learning, who rated the system as correct and suitable for further development and improvement. This expert validation lends further credibility to our results and underscores the potential of our model for future research and applications.

One of the significant outcomes of this research is the optimization of the system for real-time classification of cognitive states. This feature opens up new avenues for the application of this system in Brain-Computer Interface (BCI) systems with real-time activity and Neurofeedback systems. The ability to classify cognitive states in real-time can significantly enhance the functionality and effectiveness of these systems, making this research a valuable contribution to the field.

IV. CONCLUSION

The developed model has demonstrated robustness and a significant potential for application in the field of cognitive sciences. The model, based on Convolutional Neural Networks (CNNs), was trained to classify cognitive states during arithmetic tasks using EEG data. The EEG data, collected from 23 channels with a time length of 0.5 seconds, was transformed into frequency bands, namely delta, theta, alpha, beta, and gamma, which are known to be associated with different cognitive processes.

The model was trained over 50 epochs, demonstrating a convergence to an impressive 94% validated accuracy and a low validated loss of 15%. The training process was carefully monitored and adjusted using early stopping and learning rate reduction techniques to prevent overfitting and ensure the model's generalizability to unseen data. The model's performance was further validated by experts in the fields of Psychology and Machine Learning, affirming its correctness and suitability for further development and improvement.

The model's performance metrics, including sensitivity, specificity, accuracy, F1 score, and Matthews Correlation Coefficient (MCC), were calculated based on the confusion matrix. The model achieved a high sensitivity of 0.962, specificity of 0.850, accuracy of 0.932, F1 score of 0.962, and MCC of 0.827. These metrics indicate that the model is highly effective in correctly classifying both the positive and negative classes, with a balanced performance even in the presence of class imbalance.

The success of this model opens up exciting possibilities for its application in real-time Brain-Computer Interface (BCI) systems and Neurofeedback systems. It provides a robust foundation for the development of future models aimed at understanding and interpreting cognitive phenomena in psychology, neurology, and cognitive neuroscience.

This work has demonstrated the feasibility and effectiveness of using deep learning models, specifically CNNs, for the classification of cognitive states based on EEG data. The model's high performance, coupled with

its potential for real-time application, makes it a valuable tool for advancing research in cognitive sciences. Future work could focus on refining the model with larger datasets, exploring other neural network architectures, and applying the model to other cognitive tasks and conditions.

REFERENCES

[1] A. Hamad, E. H. Houssein, A. E. Hassanien, and A. A. Fahmy, "Feature extraction of epilepsy EEG using discrete wavelet transform," in 2016 12th international computer engineering conference (ICENCO), 2016: IEEE, pp. 190-195.

[2] L. L. Popa, H. Dragos, C. Pantelemon, O. V. Rosu, and S. Strilciuc, "The role of quantitative EEG in the diagnosis of neuropsychiatric disorders," Journal of medicine and life, vol. 13, no. 1, p. 8, 2020.

[3] L. Billeci et al., "On the application of quantitative EEG for characterizing autistic brain: a systematic review," Frontiers in human neuroscience, vol. 7, p. 442, 2013.

[4] L. E. Ismail and W. Karwowski, "Applications of EEG indices for the quantification of human cognitive performance: A systematic review and bibliometric analysis," Plos one, vol. 15, no. 12, p. e0242857, 2020.

[5] M. Diykh, Y. Li, and S. Abdulla, "EEG sleep stages identification based on weighted undirected complex networks," Computer methods and programs in biomedicine, vol. 184, p. 105116, 2020.

[6] N. Sciaraffa et al., "Validation of a light EEG-based measure for real-time stress monitoring during realistic driving," Brain sciences, vol. 12, no. 3, p. 304, 2022.

[7] C. Surianarayanan, J. J. Lawrence, P. R. Chelliah, E. Prakash, and C. Hewage, "Convergence of Artificial Intelligence and Neuroscience towards the Diagnosis of Neurological Disorders—A Scoping Review," Sensors, vol. 23, no. 6, p. 3062, 2023.

[8] P. Bashivan, I. Rish, M. Yeasin, and N. Codella, "Learning representations from EEG with deep recurrent-convolutional neural networks," arXiv preprint arXiv:1511.06448, 2015.

[9] R. T. Schirrmeister et al., "Deep learning with convolutional neural networks for EEG decoding and visualization," Human brain mapping, vol. 38, no. 11, pp. 5391-5420, 2017.

[10] Y. Roy, H. Banville, I. Albuquerque, A. Gramfort, T. H. Falk, and J. Faubert, "Deep learning-based electroencephalography analysis: a systematic review," Journal of neural engineering, vol. 16, no. 5, p. 051001, 2019.

[11] C. Mateo and J. A. Talavera, "Bridging the gap between the short-time Fourier transform (STFT), wavelets, the constant-Q transform and multi-resolution STFT," Signal, Image and Video Processing, vol. 14, no. 8, pp. 1535-1543, 2020.

26th IMEKO TC4 International Symposium
24th International Workshop on ADC and DAC Modelling and Testing
IMEKO TC-4 2023
Pordenone, Italy / September 20-21, 2023

Demonstration stand for non-destructive conductive material defect inspection by eddy current

Jan Saliga[1], Pavol Kababik[2], Ondrej Kovac[1], Alena Pietrikova[1]

[1] *Technical University of Kosice, Letna 9, 042 00 Kosice, Slovakia, {jan.saliga, ondrej.kovac, alena.pietrikova}@tuke.sk*
[2] *Magna Electronics Slovakia s.r.o. 044 58 Kechnec 265, Slovakia, pavol.kababik@magna.com*

***Abstract* – To aid in the education of master's level electronic engineering students in our department, we have developed a simple stand that utilizes eddy currents for the non-destructive testing of conductive materials. This method is commonly used for detecting various cracks in the material. The purpose of the stand is to demonstrate the basic idea of such testing during laboratory exercises. The article details the design and implementation of the measuring stand, which includes a measuring device, reference test samples, and accessories. The measuring device is based on the myRIO DAQ device by NI and features a sensing probe that contains an excitation coil, a GMR magnetoresistor AA002-02, and a laser motion sensor. The control software for myRIO was developed in LabVIEW and utilizes both the processor and FPGA in myRIO.**

I. INTRODUCTION

The eddy current method is a universal non-destructive measurement method for detecting surface, subsurface, and internal material defects [1]. The idea is not new, professional instrumentation can be found in the market and many improvements and variants of the principle itself have been proposed and developed over the years, e.g. [2], or in combination with other test methods, e.g., [3]. The material suitable for testing must be electrically conductive, but it does not have to be ferromagnetic. The fundamental concept behind this type of testing involves subjecting the material under examination to a fluctuating electric current, commonly referred to as an eddy current. This current is induced by the alternating magnetic field generated by the excitation coil. The principle of the eddy current excitation is shown in Fig. 1.

The excitation coil is powered by alternating current in a frequency range typically from 100Hz to 10MHz [1]. The current produces a magnetic field which induces an eddy current in the near conductive material. Copper wire is used to create the air coil, which can take on various shapes and typically consists of 10 to 500 turns.

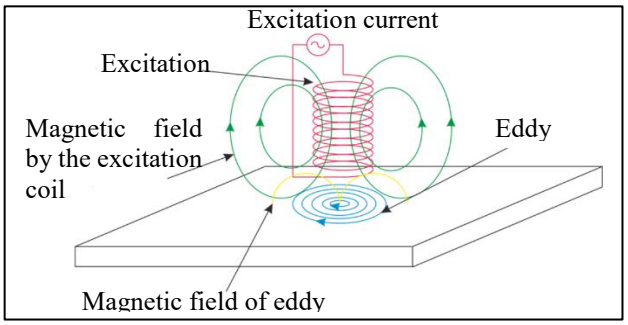

Fig. 1. The principle of induction of eddy current

The eddy currents are in the form of closed current loops in the planes perpendicular to the primary magnetic field induced by the excitation current. The induced eddy current is also called the reaction current. The primary magnetic field is affected by the reaction current, which in turn impacts the primary current. The effect depends on the electrical conductivity of the tested material, permeability, and dimensions of the test sample as well as on other factors such as coil properties, etc. but those can be supposed constant in a simplified model of testing. Changes in the magnetic field indicate a change in the properties of the tested material. Changed properties are mostly caused by a structural defect in the material. Detection is commonly possible for defect dimensions from about 0.1mm located at different material depths.

There are 3 possible ways to detect changes in the magnetic fields:

- monitoring current in the excitation coil,
- using additional sensing coils,
- sensing magnetic field by a magnetic field sensor such as a giant magnetoresistive (GMR) sensor[4].

Due to its sensitivity, affordability, and ease of integration, the NVE AA002-02 GMR sensor [5] was selected for use in the development of the demonstration stand.

II. DESIGN OF THE DEMONSTRATION STAND

The main aim of the demonstration stand design was to develop a very basic, easy-to-use prototype, which can be utilized in laboratory exercises of master students of electronics to demonstrate the principle of testing defects in conductive materials. The block diagram of the developed instrument is shown in Fig. 2.

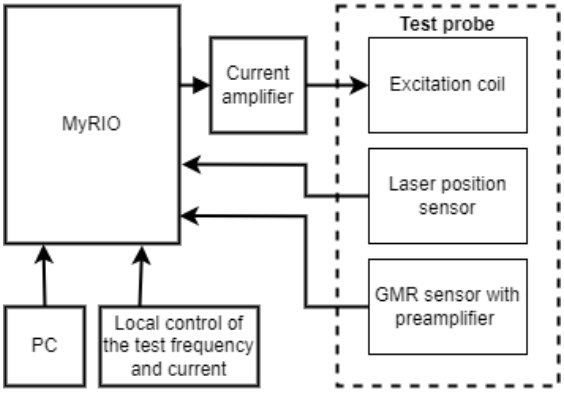

Fig. 2. Block diagram of the instrument.

A. Hardware

The instrumentation is open for students to look inside and perform additional changes and improvements. To simplify the educational process, the myRIO DAQ device by NI [6, 7] is used as the core of the instruments. MyRIO is intended as an embedded system for education and includes analog inputs, analog outputs, digital I/O lines, a Xilinx FPGA, a dual - core ARM Cortex - A9 processor, WiFi support, and other hardware components such as LEDs, push buttons, and an onboard accelerometer. It can be programmed in LabVIEW or C.

Additional external components, including a current amplifier and probe with an excitation coil, a laser position sensor, and a GMR sensor, are integrated with the myRIO. The myRIO is linked to the control PC via the internet. The main tasks of myRIO hardware and software are:

- To generate an exact sinewave to excite the excitation coil in the test probe. To achieve the exact timing of sinewave, FPGA calculates and generates samples of sinewave, which are converted by DAC in myRIO to an analog signal, filtered, converted to current, and amplified by a current amplifier. The amplitude and frequency of excitation sinewave current are set by the local controls in the instrument or remotely as well.
- To sense, digitize, and analyze the signal from the GMR sensor in the probe, which is sensing magnetic field given by a combination of vectors of excitation field and field produced by eddy current in the tested material. The analysis consists of an evaluation of the magnitude and phase of sensed sinewave in comparison with reference sinewave generated by FPGA. The results are transferred together with information about the placement and movement of the test probe to the PC across WiFi.
- To follow the movement and position of the test probe, which is sensed by the laser position sensor.

The more detailed structure of the instrument is in Fig. 3.

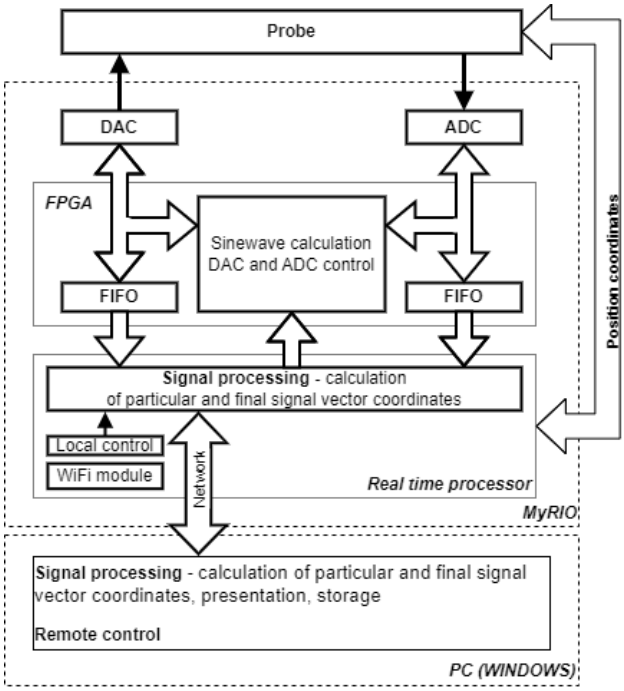

Fig. 3. Instrument hardware and software architecture.

The basic test probe (Fig. 4) consists of an excitation coil, GMR sensor, and preamplifier.

Fig. 4. The basic probe without positioning sensor.

The coil was realized as an air coil with a diameter of 60mm, and 60 winds of Cu wire with a diameter of 0.4mm. In the center of the coil, the GMR sensor is placed, and all are mechanically fixed and protected as it is shown in Fig. 4. To demonstrate the effects of excitation coil design, an alternative planar coil with an integrated GMR sensor was realized (Fig. 5).

The signal from the GMR sensor is filtered by a high pass filter and amplified using instrumentation amplifier LT1167. The advanced version of probes (Fig. 6) is equipped with a laser position sensor.

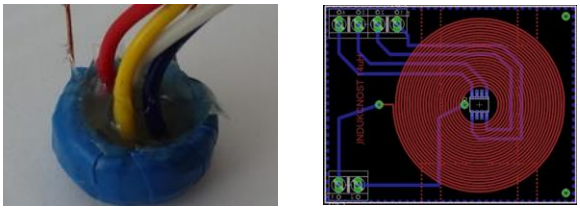

Fig. 5. Air coil with integrated GMR (in the left) and design of planar coil with GMR (in the right).

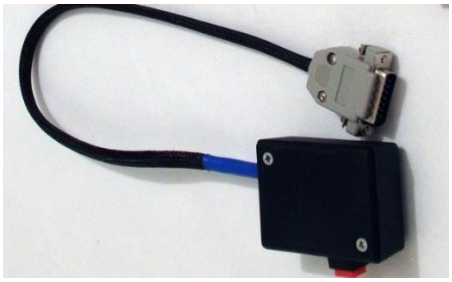

Fig. 6. The advanced probe equipped with a laser position sensor

The position of the probe over the material under test is sensed by the laser sensor ADNS-9800 connected to the Teensy 2.0 board (Fig. 7).

a)

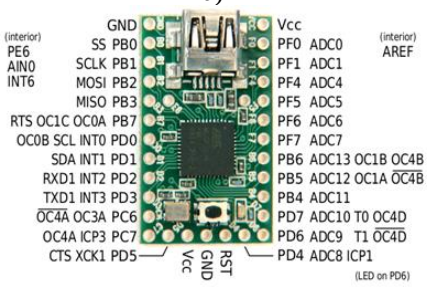

b)

Fig. 7. a) Laser sensor ADNS-9800 and b) Teensy board.

The Teensy board software controls the laser sensor and calculates the actual probe position coordinates from data acquired from the laser sensor. The coordinates are transmitted to myRIO to complete information about performed measurements. Before measurement, the positioning system is calibrated. The reference position of the probe is acquired and stored in myRIO memory to easy detection of a probe position when moving.

The excitation coil is powered by a current amplifier converting the voltage signal generated by FPGA and DAC in myRIO (Fig. 8).

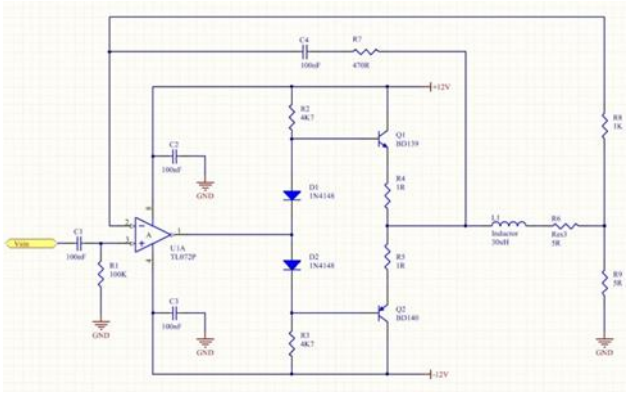

Fig. 8. The schematic diagram of the current amplifier for the excitation coil

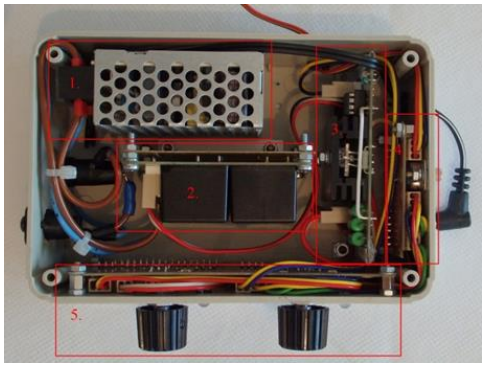

a)

b)

Fig. 9. The core unit of the instrument – a) inside view and b) overall appearance.

The core unit of the developed instrument is shown in Fig. 9. myRIO is placed on the top of the box. The box contains power source (1, 2), current amplifier (3), local control board (5) to set of frequency and amplitude of excitation sinewave, and connector for connection of myRIO and probe.

B. Software

The software was developed in LabVIEW and partially in C. LabVIEW was used for the development of the application for PC with Windows, for the processor in

myRIO as a real-time application (LabVIEW Real Time), and for FPGA in myRIO (LabVIEW FPGA). Language C was used for the Teensy 2.0 board.

The structure of the developed software is in Fig. 3. The communication between myRIO and PC uses network variables. FPGA structure ensures precise timing of excitation sinewave by DAC in myRIO. The calculated excitation sinewave samples as well as the signal acquired by myRIO ADC from the GMR sensor are transferred to real-time signal processing software in myRIO. The vector (magnitude and phase) of the acquired signal is estimated and subtracted from the excitation vector (sinewave). The coordinates of resulted vector characterizing the transfer of signal from the excitation coil to the GMR sensor through tested material are calculated and transferred to PC optionally together with probe position coordinates.

Software in PC visualizes these data in plots – course history of magnitude and phase of the difference vector in time with and without position coordinates. Also, the history of changes in the vector is shown in the plot. The actual values of magnitude and phase of excitation and acquired signal together with the difference vector are indicated in numerical indicators. The software also allows setting the frequency, magnitude, and offset of the excitation signal. The front panel of the PC software is in Fig. 10.

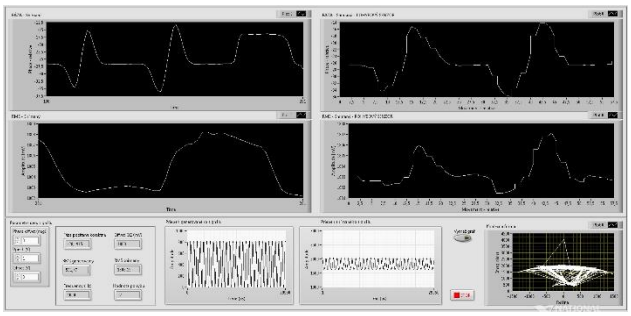

Fig. 10. Front panel of PC software

III. EXPERIMENTAL RESULTS

To experimentally demonstrate the principle of conductive material defect inspection a few aluminum test plates with artificial cracks of various sizes were realized. An example is in Fig. 11. The aluminum plate has a few milled slots with a width of 2mm and depth of 2, 4, 6, and 8mm. Using the developed instrument and experimental aluminum plates, students can perform measurements at various conditions – various cracks, frequencies, amplitudes, and offsets of excitation sinewave and different probes. Two examples of results are in Fig. 12 and 13.

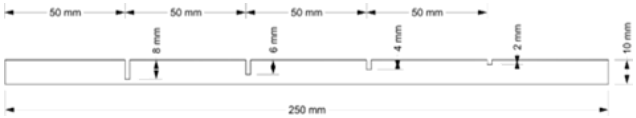

Fig. 11. The side view of the testing aluminum plate with milled slots.

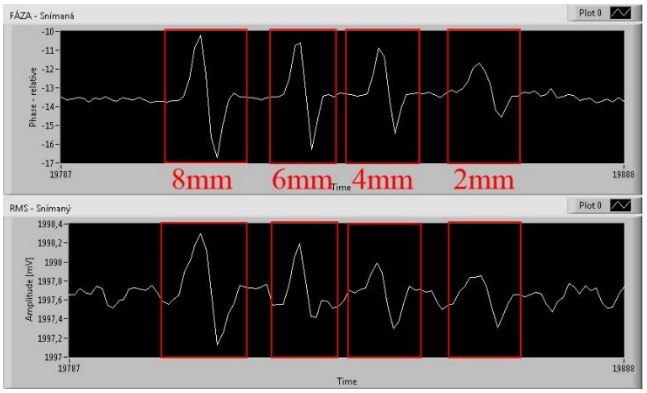

Fig. 12. Magnitude and phase achieved at the testing plate in, frequency and amplitude of excitation signal were 2000Hz and 1V.

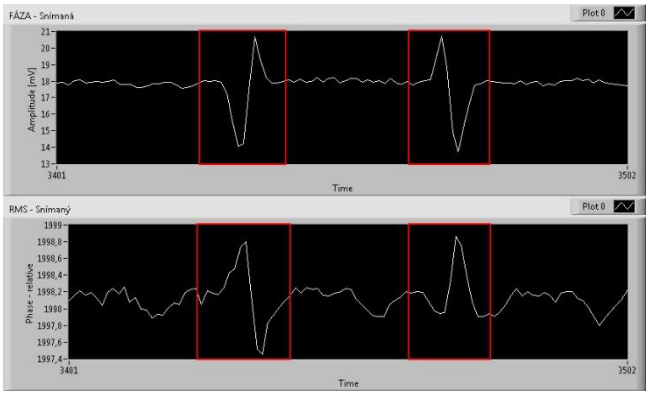

Fig. 13. Detail of magnitude and phase achieved at the testing plate, frequency, and amplitude of excitation signal was 1000Hz and 1V, the slot with the depth 6mm, the probe was moving from right to left and then in opposite.

IV. IMPLEMENTATION IN EDUCATION

The realized system has been implemented in experimental exercises in the course "Advanced measurement system" taught in the master study program "Automotive electronics". A short electronic guide covering the basic theory of non-destructive testing principles, a description of the measuring stand, and a list of experimental tasks have been created and are accessible to students in advance. Before conducting experimental measurements, students must complete the following tasks:

- To understand the basic theory of non-destructive testing of conductive materials based on eddy current and sensing magnetic field generated by the current. The theory is a part of the the short electronic guide.
- To familiarize with the design and structure of hardware of the measuring systems using the guide.

- To familiarize with the control software of the stand at the user level.

The on-site experimental exercise begins with a short test implemented in Moodle to evaluate the entrance knowledge of students. The result of the test is then included in the final evaluation of students achieved on the stand.

The on-site tasks of students are:

- To meet with the experimental stand, hardware, and software using the guide.
- To measure near the center of the aluminum plate without breaks. This may be supposed as a reference.
- To perform measurements on the aluminum plates with different depths and widths (see an example of such plate in Fig. 11). The measurements are performed on both sides of the plates. The students have to evaluate how the measured signals depend on break sizes and probe position.
- To perform measurements on the edge of the plate with and without connecting the plate to another plate.

The results of measurements can be saved in graphical form on a PC. The knowledge and results achieved by students are evaluated later after performing other experimental measurements on other stands, e.g., measurement of temperature using different sensors, etc.

At the end of a measurement round consisting also from other tasks and test stands, the students choose by lot a stand and prepare the PowerPoint presentation. Subsequently they defend it in front of other students and teacher. The final evaluation of each student consists of the defense evaluation taking also into account the evaluation from the entrance Moodle test.

V. CONCLUSION

In this paper, a straightforward test stand is introduced for non-destructive conductive material defect inspection. The development of this stand was a collaborative effort between Pavol Kababik, a master's level student in electronic engineering, and the author. The test stand is constructed using the educational embedded module myRIO from NI, and it is an open system that can be reprogrammed using LabVIEW by other students who wish to incorporate their own signal processing and presentation techniques. The integration of FPGA, real-time software, and PC software in this system allows students to gain hands-on experience with these components from both hardware and software perspectives. Additionally, students have the option to design alternative or additional hardware components, such as various test probes and amplifiers.

ACKNOWLEDGMENT

The work is a part of the project supported by the Science Grant Agency of the Slovak Republic (No. 1/0413/22).

REFERENCES

[1] M. Willcox, “A brief description of NDT techniques”, NDT Equipment Limited, 2000.

[2] A. L. Ribeiro, H. G. Ramos, J. A Couto, “Liftoff insensitive thickness measurement of aluminum plates using harmonic eddy current excitation and a GMR sensor,” Measurement: Journal of IMEKO, Vol. 45, Issue 9, 2012, pp. 2246 – 2253.

[3] D.J. Pasadas, M. Barzegar, A. L. Ribeiro, H. G. Ramos, “Locating and Imaging Fiber Breaks in CFRP Using Guided Wave Tomography and Eddy Current Testing”, Sensors, Open Access Volume 22, Issue 19, October 2022, Article number 7377.

[4] Reig, C., Cardoso, S., & Mukhopadhyay, S. C. (2013). Giant magnetoresistance (GMR) sensors. Smart Sensors, Measurement, and Instrumentation, 6(1), 1-301.

[5] NVE Corp., AA/AB-Series Analog Magnetic Sensors, July 2019, pp. 1 – 20, [online] https://www.nve.com/Downloads/analog_catalog.pdf

[6] Kathaluwa Liyanage, N. (2016). MyRIO (Doctoral dissertation, Murdoch University).

[7] National Instruments, User guide, and specifications ni myRIO-1900, 2018, [online] https://www.ni.com/myrio.

26th IMEKO TC4 International Symposium
24th International Workshop on ADC and DAC Modelling and Testing
IMEKO TC-4 2023
Pordenone, Italy / September 20-21, 2023

Novel quality assessment protocol based on Kiviat diagram for pulsed wave Doppler diagnostic systems: first results

Giorgia Fiori[1], Gabriele Bocchetta[1], Maurizio Schmid[1], Silvia Conforto[1], Salvatore Andrea Sciuto[1], Andrea Scorza[1]

[1] *Dep. of Industrial, Electronic and Mechanical Engineering, Roma TRE University, Rome, Italy*

***Abstract* – Ultrasound (US) systems are routinely and extensively used in several medical fields despite the lack of an internationally accepted quality standard for their testing. One crucial aspect for Quality Assessment (QA) protocols is the need to summarize the contribution of the large number of existing test parameters in a few meaningful quantities. The study herein proposed fits into this context, focusing on the use of the Kiviat diagram applied to Pulsed Wave Doppler (PWD) equipment QA. Four test parameters, derived from the literature, were objectively assessed through custom-written image analysis-based methods and then scaled for an effective combination. The experimental setup used to collect PWD spectrograms included an intermediate technology level US diagnostic system equipped with a linear array probe and a commercial Doppler flow phantom. Tests were repeated at two Doppler frequencies.**

I. INTRODUCTION

In diagnostic ultrasound (US), Quality Assessment (QA) protocols are deemed necessary in order to monitor the performance level of the imaging equipment over time and detect any non-conformities [1-3]. Progressive worsening of US system performance usually occurs as a slow worsening of the image quality that could impact clinical decision, increasing the risk of misdiagnosis [4-7]. In this regard, many studies in the scientific literature have analysed this process: average annual failure rates of 10% and 14% have been detected for system components and probes, respectively, over a four-year experience [8], and a 40% incidence of defective probes has been found in routine clinical practice [7]. Although several professional organizations attempted to define guidelines for ultrasound QA over the years [9-12], a shared worldwide reference standard has yet to be developed [1,13]. This is associated, among other factors, with the presence of diverse performance parameters, and with the lack of a comprehensive approach to QA [1,3,13]. On this point, Kiviat diagrams have been introduced in [3] to effectively combine experimental test parameters for Color Doppler QA. By calculating the diagram area, it is possible to provide a comprehensive indicator of Color Doppler system performance.

From these considerations, the present study aims at providing the first results of the application of the integrated method proposed in [3] to quantify the overall performance of Pulsed Wave Doppler (PWD) diagnostic systems. Tests were carried out on an intermediate technology level ultrasound system equipped with a linear array probe operating at two Doppler frequencies. PWD performance was assessed in terms of Average Maximum Velocity Sensitivity (AMVS) [14], Velocity Measurements Accuracy (VeMeA), Velocity Profile Discrepancy Index (VPDI) [15,16] and Lowest Detectable Signal (LDS) [17]. Each parameter was estimated from PWD data post-processed through objective image analysis-based methods implemented in MATLAB environment.

II. MATERIALS AND METHODS

A. Experimental setup

The experimental setup consisted of a linear array probe mounted on an intermediate technology level US diagnostic system and a reference test device. The ultrasound probe worked at two operating Doppler

Table 1. Main ultrasound system settings.

Parameter	Setting
B-mode frequency (MHz)	9.0
Doppler frequency (MHz)	$f_1 = 5.0$; $f_2 = 6.3$
Field of view (mm)	70
Wall filter	Minimum
Sample volume length (mm)	1 (AMVS, VeMeA and VPDI) ; 2 (LDS)
Sample volume depth (mm)	40 (AMVS, VeMeA) ; from 35 to 41 (VPDI) ; from 38 to 48 (LDS)
Insonation angle (°)	50
Spectrogram duration (s)	8

frequencies (i.e., the lowest and the central one) by minimizing both pre- and post-processing settings as reported in Table 1.

A commercial flow phantom (Sun Nuclear, Doppler 403TM flow phantom [18]) was included in the setup as reference test device. It consists of a horizontal and a diagonal tube segment (5.0 ± 0.2 mm inner diameter) embedded in a tissue-mimicking material (TMM). A blood-mimicking fluid (BMF) simulating the blood flow is pumped into the circuit in constant or pulsatile mode through an electric flow controller.

PWD spectrograms were collected on a portion of the diagonal segment, by maintaining the ultrasound transducer still in a dedicated holder [18] throughout the acquisitions. The parameters described in the following were tested at constant flows provided by the phantom, as reported in Table 2.

Table 2. Flow rate settings for each test parameter.

Test parameter	Flow mode	Flow rate (ml·s^{-1})
AMVS	constant	5.5 and 7.0
VeMeA	constant	7.0
VPDI	constant	7.0
LDS	constant	2.0

B. Test parameters

The average maximum velocity sensitivity is a sensitivity parameter developed to quantify the US diagnostic system response to flow variations provided by a reference test device [14]. The objective measurement method, proposed and investigated in [14], post-processes PWD spectrograms acquired at two different constant flow rates (Q_1 and Q_2) and allows AMVS calculation as:

$$AMVS = \frac{v_{PW,Q2} - v_{PW,Q1}}{v_{th,Q2} - v_{th,Q1}} \quad (1)$$

where $v_{PW,Q1}$ and $v_{PW,Q2}$ are the mean maximum velocity values retrieved at Q_1 and Q_2, respectively, while $v_{th,Q1}$ and $v_{th,Q2}$ are the corresponding theoretical maximum flow velocities provided by the phantom. In addition, the method estimates the standard deviation of the parameter through the uncertainty propagation law [14].

The velocity measurements accuracy parameter allows the assessment of US system accuracy in the estimation of mean scatterer velocity, as already proposed in [3] for Color Doppler QA. The implemented measurement method assesses the average velocity trend through time as the weighted average of each spectral line [19]. The processing is repeated for three correction angle settings (i.e., insonation angle ± 1°) and the overall mean velocity $\bar{v}_{PW}$ is computed. Finally, the parameter is estimated as follows:

$$VeMeA = \frac{\left|\bar{v}_{PW} - \bar{v}_{th}\right|}{\bar{v}_{th}} \quad (2)$$

where $\bar{v}_{th}$ is the corresponding theoretical mean flow velocity provided by the Doppler phantom. The standard deviation of the parameter is estimated by applying the uncertainty propagation law.

The velocity profile discrepancy index provides an estimation of faults in sample volume length and range gate registration accuracy [15,16], by quantifying the discrepancy between the actual velocities and the theoretical parabolic profile (under laminar flow assumption). As in [15,16], the sample volume (SV) was placed at six depths (from 35 to 37 mm and from 39 to 41 mm with steps of 1 mm) corresponding to six different positions with respect to the radius of the phantom tube. The objective measurement method estimates the mean maximum velocity v_{PW} for each pre-set SV depth, and calculates VPDI [15,16] as in the following:

$$VPDI = \sum_{i=1}^{N} \frac{\left(v_{PW,i} - v_{par,i}\right)^2}{\sigma_{tot,i}^2} \quad (3)$$

where N is the number of collected PWD spectrograms, v_{par} is the velocity value retrieved from the theoretical parabolic profile for a specific position with respect to the tube radius, and σ_{tot} is the total standard deviation estimated by considering the following uncertainty contributions [15,16]: the intrinsic flow dispersion of the maximum velocities, the electronic noise superimposed on the spectrogram and the uncertainty in the sample volume positioning with respect to the radius.

Finally, the Lowest Detectable Signal (LDS) parameter [17], allows quantifying the flow detectability (expressed in dB) in terms of maximum depth of penetration through the following mathematical expression:

$$LDS = \frac{1}{N}\sum_{k=1}^{N}\left(2 f_0 \alpha z_{SV,k} + G_{max,k} - G_{min,k}\right) \quad (4)$$

where f_0 (MHz) is the operating Doppler frequency, α (dB·cm^{-1}·MHz^{-1}) is the (mean) TMM attenuation coefficient, z_{SV} (cm) is the sample volume depth setting, G_{max} (dB) is the maximum Doppler gain value before no negligible noise appears, while G_{min} (dB) is the minimum Doppler gain value at which the Doppler signal can no longer be distinguishable from background noise. The measurement method for G_{min} and G_{max} automatic assessment, investigated in [17], requires data to be collected by varying the Doppler gain from the minimum to the maximum with steps of ΔG for each sample volume depth setting. In this case, steps of 5 dB were applied and repeated for six SV depths (38 to 48 mm) spaced of 2 mm, by adjusting the sample volume in the center of the tube diameter. Specifications of each objective measurement method included in this study are listed in Table 3.

Since the optimal value differs per test parameter, a

Table 3. Variables setting for test parameters assessment.

AMVS [14]	Setting
Adaptive gray level threshold	10% of g_{max}
Number of spectral lines	800
VeMeA	
Number of spectral lines	800
VPDI [15,16]	
Adaptive gray level threshold	10% of g_{max}
Number of spectral lines	800
Minimum SV length increment	1 mm
Profile maximum velocity	v_{PW} at SVD_C
LDS [17]	
Threshold for G_{max} estimation	3
Threshold for G_{min} estimation	2
Regions of interest size	810×144 px
Cells size	6×6 px
Percentage of total cells	1%

g_{max}: maximum gray level value in the spectrogram; SVD_C: sample volume placed in the center of the phantom segment diameter.

parameter-specific mapping equation was applied to express each parameter in the range [0;1] where 1 represents the gold standard, as proposed in [3]. The following equations are used to express the scaled values, denoted with the symbol (*):

$$AMVS^* = 1 - \left(\left|AMVS - 1\right|\right) \tag{5}$$

$$VeMeA^* = \frac{1}{1 + VeMeA} \tag{6}$$

$$VPDI^* = e^{-VPDI/2.2} \tag{7}$$

$$LDS^* = \frac{LDS}{2\alpha f_0 z_{max}} \tag{8}$$

where z_{max} in (8) is the maximum phantom vessel depth. From the scaled values thus obtained, the Kiviat diagram areas were also calculated.

III. MONTE CARLO SIMULATION

The measurement uncertainty associated with the image analysis methods was estimated through a Monte Carlo Simulation (MCS) [20,21] run for 10^4 iterations for each test parameter-Doppler frequency pair. The standard deviations (SDs) of the output distributions retrieved for AMVS and VeMeA were then combined with the corresponding repeatability standard deviations.

Input distributions, expressed as mean ± SD, were assigned to the main quantities influencing each parameter assessment. For both AMVS and VPDI, a uniform distribution (10% ± 1% of the maximum gray level value in the spectrogram g_{max}) was assigned to the threshold for maximum velocities detection and the 800 spectral lines to be processed were randomized, at each cycle without repetition, among all the spectral lines in the image. As regards VeMeA parameter, the spectral lines randomization was applied only. Finally, for LDS assessment, a simulation was carried out for each *k*-th sample volume depth setting [17]: a normal distribution (0.700 ± 0.025 dB·cm^{-1}·MHz^{-1}) was assigned to TMM attenuation, while uniform distributions were chosen for the depth ($z_{SV,k}$ ± 0.3 cm) as well as to the minimum and maximum Doppler gain ($G_{min,k}$ ± 1 dB and $G_{max,k}$ ± 1 dB). The standard deviations of the *N* output distributions were then combined together to estimate the standard uncertainty contribution associated with the parameter.

IV. RESULTS AND DISCUSSION

Results on unscaled and scaled parameters for each test parameter at both operating Doppler frequencies are reported in Table 4. By comparing the outcomes obtained for the same test parameter, compatibility was always guaranteed according to the criterion in [22], however, a

Table 4. Outcomes and scaled outcomes (mean ± SD) for each test parameter according to the Doppler frequency.

Doppler frequency	Test parameter	Outcome	Scaled outcome	Normalized diagram area
Lowest operating frequency f_1	AMVS	0.93 ± 0.27	0.93 ± 0.27	0.45 ± 0.07
	VeMeA	0.96 ± 0.09	0.51 ± 0.02	
	VPDI	0.16 ± 0.07	0.93 ± 0.03	
	LDS	50.1 ± 2.3 dB	0.45 ± 0.02	
Central operating frequency f_2	AMVS	0.94 ± 0.28	0.94 ± 0.28	0.40 ± 0.06
	VeMeA	0.99 ± 0.09	0.50 ± 0.02	
	VPDI	0.25 ± 0.10	0.89 ± 0.04	
	LDS	53.7 ± 2.5 dB	0.38 ± 0.02	

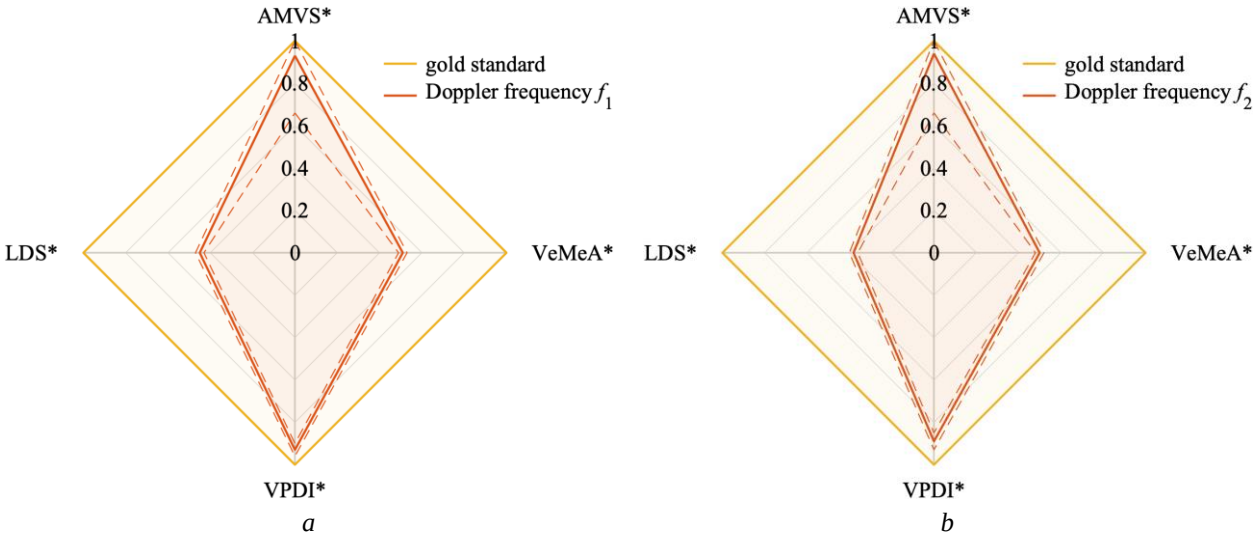

Fig. 1. Scaled outcomes represented on Kiviat diagram for the operating Doppler frequency (a) f_1 and (b) f_2.

proper comparison can be carried out by focusing on the scaled outcomes (Fig. 1). Independently of the operating frequency, the test parameters that significantly deviate from the gold standard were VeMeA and LDS, whilst AMVS parameter showed the highest uncertainty contribution. It is worth noting that, despite a higher LDS (absolute) value was retrieved at frequency f_2 rather than f_1, a better result (i.e., closer to 1) was obtained at the lower Doppler frequency after scaling. This behaviour, which was expected given the higher attenuation that affects high-frequency US waves, was outlined by the adopted scaling. As regards the Kiviat diagram areas, they were normalized with respect to the total area of the polygon (i.e., assuming all test parameters at 1), as in [3]. Therefore, the normalized diagram areas were expected to be as close as possible to 1. As reported in Table 4, they did not show discrepancies [22], suggesting compatible PWD performance between the two operating frequencies of the ultrasound probe.

V. CONCLUSIONS

The study herein proposed would give a contribution in the field of Doppler equipment QA by applying an integrated approach, already investigated in the literature, to PWD. This approach, based on the Kiviat diagram, allows summarizing the contribution of different QA parameters to quantify the overall performance of the US system. In this first study, four test parameters were objectively assessed through the post-processing of PWD spectrograms collected on a commercial reference test device. A linear array probe mounted on an intermediate technology level US diagnostic system was tested at two operating Doppler frequencies. The results obtained suggest that further investigations should be carried out on different phantom and US system settings, as well as on a larger sample of ultrasound diagnostic systems and probes.

ACKNOWLEDGMENT

The Authors wish to thank Jan Galo of the Clinical Engineering Service at I.R.C.C.S. Children Hospital Bambino Gesù for administrative and technical support, and GE Healthcare for hardware supply and technical assistance in data collection.

REFERENCES

[1] J. E. Browne, “A review of Doppler ultrasound quality assurance protocols and test devices”, Phys. Med., vol.30, No.7, November 2014, pp.742-751.

[2] S. Russell, “Ultrasound quality assurance and equipment governance”, Ultrasound, vol.22, No.1, February 2014, pp.66-69.

[3] G. Fiori, A. Pica, S. A. Sciuto, F. Marinozzi, F. Bini, A. Scorza, “A comparative study on a novel quality assessment protocol based on image analysis methods for Color Doppler ultrasound diagnostic systems”, Sensors, vol.22, No.24, December 2022.

[4] J. Vachutka, L. Dolezal, C. Kollmann, J. Klein, “The effect of dead elements on the accuracy of Doppler ultrasound measurements”, Ultrasonic Imaging, vol.36, No.1, January 2014, pp.18-34.

[5] B. Weigang, G. W. Moore, J. Gessert, W. H. Phillips, M. Schafer, “The methods and effects of transducer degradation on image quality and the clinical efficacy of diagnostic sonography”, J. Diagn. Med. Sonog., vol.19, No.1, January/February 2003, pp.3-13.

[6] M. Mårtensson, M. Olsson, L.-Å. Brodin, “Ultrasound transducer function: annual testing is not sufficient”, Eur. J. Echocardiogr., vol.11, No.9, October 2010, pp.801-805.

[7] M. Mårtensson, M. Olsson, B. Segall, A. G. Fraser, R. Winter, L.-A. Brodin, “High incidence of defective ultrasound transducers in use in routine clinical

practice", Eur. J. Echocardiogr., vol.10, No.3, May 2009, pp.389-394.

[8] N. J. Hangiandreou, S. F. Stekel, D. J. Tradup, K. R. Gorny, D. M. King, "Four-year experience with a clinical ultrasound quality control program", Ultrasound Med. Biol., vol.37, No.8, August 2011, pp.1350-1357.

[9] AIUM Technical Standards Committee, "Performance criteria and measurements for Doppler ultrasound devices", 2nd edition, USA, 2002.

[10] IPEM – Institute of Physics and Engineering in Medicine, "Report no. 102: Quality assurance of ultrasound imaging systems," York, UK, 2010.

[11] ACR Guidelines and Standards Committee, "ACR–AAPM Technical standard for diagnostic medical physics performance monitoring of real time ultrasound equipment", revised 2021, https://www.acr.org/-/media/ACR/Files/Practice-Parameters/US-Equip.pdf (accessed June 2023).

[12] EFSUMB, "European course book: technical quality evaluation of diagnostic ultrasound systems - a comprehensive overview of regulations and developments", http://www.kosmos-host.co.uk/efsumb-ecb/coursebook-tqe_ch28.pdf (accessed June 2023).

[13] J. M. Samei, D. E. Pfeiffer, "Clinical Imaging Physics: Current and Emerging Practice", 1st edition, Wiley Blackwell, Hoboken, NJ, USA, 2020.

[14] G. Fiori, F. Fuiano, A. Scorza, M. Schmid, J. Galo, S. Conforto, S. A. Sciuto, "A novel sensitivity index from the flow velocity variation in quality control for PW Doppler: a preliminary study," Proc. of 2021 IEEE International Symposium on Medical Measurements and Applications (MeMeA), 2021.

[15] G. Fiori, G. Bocchetta, S. Conforto, S. A. Sciuto, A. Scorza, "Sample volume length and registration accuracy assessment in quality controls of PW Doppler diagnostic systems: a comparative study", ACTA IMEKO, vol.12, No.2, June 2023, pp.1-7.

[16] G. Fiori, A. Scorza, M. Schmid, J. Galo, S. Conforto, S. A. Sciuto, "A preliminary study on a novel approach to the assessment of the sample volume length and registration accuracy in PW Doppler quality control," Proc. of 2022 IEEE International Symposium MeMeA on Medical Measurements and Applications (MeMeA), 2022.

[17] G. Fiori, F. Fuiano, A. Scorza, J. Galo, S. Conforto, S. A. Sciuto, "A preliminary study on an image analysis based method for lowest detectable signal measurements in pulsed wave Doppler ultrasounds", ACTA IMEKO, vol.10, No.2, June 2021, pp.126-132.

[18] Sun Nuclear Corporation, "Doppler 403™ & mini-Doppler 1430™ flow phantoms", https://www.sunnuclear.com/uploads/documents/datasheets/Diagnostic/DopplerFlow_Phantoms_113020.pdf (accessed June 2023).

[19] F. Marinozzi, F. Bini, A. D'Orazio, A. Scorza, "Performance tests of sonographic instruments for the measure of flow speed," Proc. of 2008 IEEE International Workshop on Imaging Systems and Techniques (IST), 2008.

[20] JCGM 101:2008, "Evaluation of measurement data — Supplement 1 to the Guide to the expression of uncertainty in measurement — Propagation of distributions using a Monte Carlo method", 2008, https://www.bipm.org/documents/20126/2071204/JCGM_101_2008_E.pdf/325dcaad-c15a-407c-1105-8b7f322d651c (accessed June 2023).

[21] G. Bocchetta, G. Fiori, A. Scorza, S. A. Sciuto, "Image quality comparison of two different experimental setups for MEMS actuators functional evaluation: a preliminary study," Proc. of the 25th IMEKO TC4 International Symposium & 23rd International Workshop on ADC and DAC Modelling and Testing, 2022.

[22] J. R. Taylor, "An Introduction to Error Analysis: the Study of Uncertainties in Physical Measurements", 2nd edition, Univ. Science Books, Sausalito, USA, 1996.

26th IMEKO TC4 International Symposium
24th International Workshop on ADC and DAC Modelling and Testing
IMEKO TC-4 2023
Pordenone, Italy / September 20-21, 2023

First experimental results of a novel arterial simulator with PWV adjustment

Federico Filippi[1], Giorgia Fiori[1], Gabriele Bocchetta[1], Salvatore Andrea Sciuto[1], Andrea Scorza[1]

[1] *Dep. of Industrial, Electronic and Mechanical Engineering, Roma TRE University, Rome, Italy*

***Abstract* – Pulse Wave Velocity (PWV) monitoring is a well-established method for both the diagnosis and prevention of cardiovascular diseases. Over the years, many arterial simulators have been made to study PWV dependency on the mechanical and geometrical characteristics of arterial surrogates; in particular, some of them are able to vary the tensional state of vessel walls to cause a change in PWV values. In this paper, a novel arterial simulator is presented, capable of varying the PWV of an arterial surrogate by acting independently on its inner and outer pressures. The simulator under assessment can manage pressures up to three times greater than the atmospheric one. This characteristic provides the possibility to explore many tensional states compared to its predecessors. The experimental outcomes confirm its working principle and an increasing trend in PWV is found. The result uncertainties are up to 10% of the corresponding PWV value.**

I. INTRODUCTION

Since 2000, cardiovascular diseases (CVDs) represent the leading cause of death worldwide [1]; only in 2019, about 15 million people died from heart attack and stroke [2]. In this regard, it is justified the importance to detect CVDs in order to properly diagnose and treat them. A clinical parameter that reflects the health status of the cardiovascular system is arterial stiffness: it's known that the elastic properties of large arteries change because of aging or diseases, e.g., atherosclerosis, hypertension, diabetes mellitus and others [3-5]. A parameter used since the early 20th century to measure and estimate arterial stiffness is the Pulse Wave Velocity (PWV) [6,7], i.e., propagation velocity through vessels of the pulse wave given by heartbeat. Today, the PWV measurement represents a standard method used to assess the health of blood vessels and, consequently, a possible cardiovascular risk for patients [8-10].

Over the decades, many arterial simulators have been developed in order to investigate *in vitro* the correlation between hemodynamic quantities. In this way, it is possible to isolate the phenomenon of interest to perform repeatable measurements without the influence of its variability due to human factor [11]. Recently, an arterial simulator was proposed to simulate variations of arterial stiffness by pre-tensioning the rubber hose which constituted the Arterial Surrogate (AS) [12]. In [13], another experimental setup was implemented with the same purpose. In this case, the arterial stiffness change was simulated by acting on the AS tensioning state by varying its transmural pressure, i.e., the difference between the pressure inside and outside the vessel. The outcomes in [13] are affected by the limited variation in external pressure taking off the possibility of analyzing the effect of various stress-strain conditions.

In this context, the present study focuses on a novel arterial simulator where the PWV of a vessel can be adjusted by operating with transmural pressures with mean pressure up to three times greater than the atmospheric one. This apparatus provides an experimental tool that will be used for a deeper understanding of how the tensional state of the AS, due to transmural pressure, affects its ability to transmit the pressure wave.

The next sections will explain the operating principle of the simulator, its main components, the acquisition protocol, and the main data processing steps. Finally, the first experimental results and their discussion will be reported.

II. MATERIALS AND METHODS

In the scientific literature it is known that the PWV in a vessel depends on its capability to strain upon the passage of a pressure wave, e.g., given by heartbeat [14]; in clinical environment, the Bramwell-Hill equation is commonly used to estimate the PWV in a vessel [6,7]:

$$PWV = \sqrt{\frac{A}{\rho} \cdot \frac{dp}{dA}} \tag{1}$$

where A is the cross-sectional area of the hose, while ρ and p are the density and the inner fluid pressure, respectively. The term:

$$\chi = \frac{1}{A} \cdot \frac{dA}{dp} \tag{2}$$

is called distensibility, i.e., the ability of the vessel to vary its area (dA) in relation to the hose internal pressure variations (dp) given by the heartbeat [7]. It is worth noting that Eq. (1) is valid under the assumption of small deformations only.

The operating principle of the simulator is based on varying the stress-strain state of the vessel by acting on its transmural pressure (ΔP):

$$\Delta P = p_{in} - p_{out} \quad (3)$$

where p_{in} and p_{out} are the inner and outer pressures of vessel walls, respectively. In fact, a change in ΔP induces a non-null stress-strain condition on the vessel constitutive material, that varies the capability of the hose to deform during pulse wave transit, therefore, the value of χ changes in Eq. (2) while keeping *dp* constant. To allow this, a silicon rubber hose, that constitutes the AS (Table 1), is put into a cylindrical polymethyl methacrylate (PMMA) case capable of withstanding pressures greater than the atmospheric pressure (until three times). The system is filled with distilled water as a working fluid. The transmural pressure (ΔP) can be adjusted through two hydraulic circuits connected to the inner and outer environments (Fig. 1).

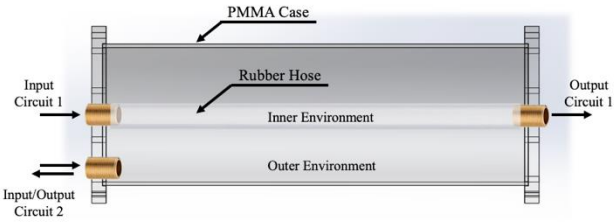

Fig. 1. Principal components of the pressurization case. "Circuit 1" and "Circuit 2" are the hydraulic sections connected to the inner and outer environments, respectively.

Firstly, a centrifugal pump was used to set both p_{in} and p_{out} pressures to the same value which represents the minimum ΔP of the system; then, closing a valve, p_{in} value was changed via air infills inside a hydropneumatic accumulator. Both pressures were continuously monitored with two digital manometers (Keller 23SY). A piston connected to the inner environment generated a pressure perturbation propagating through the whole AS (Fig. 2).

Two strain gauges were attached to the hose at a known distance ($\Delta L = 25.0 \pm 0.1$ cm), in order to detect the transit of the pulse wave: the transit time (Δt) is intended as the difference between the time instants in which the pulse passes through the first and second strain gauge.

Table 1. Main characteristics of the silicon rubber hose used as Arterial Surrogate; values expressed as mean ± standard deviation (STD).

Characteristic	Value
Length	42.0 ± 0.1 cm
Inner diameter	16.0 ± 0.4 mm
Thickness	2.0 ± 0.1 mm

An *ad hoc* electronic circuit was developed for amplification and impedance matching of the strain gauge resistance variations, with the aim to make signals readable for a Data Acquisition System (DAQ).

The PWV in every condition of transmural pressure was then derived by calculating:

$$PWV = \frac{\Delta L}{\Delta t} \quad (4)$$

Therefore, a measurement campaign was carried out to provide a preliminary validation of the working principle of the simulator (Table 2). The pressure of the outer environment was set to a fixed value, whereas the inner pressure was adjusted by steps, in order to change the value of ΔP; this pressure regulation is similar to the human body, where the pressure outside arteries remains approximately constant, instead of the inner one.

The temperature of the system (*T*) was kept constant.

Table 2. Characteristics of the measurement campaign; values expressed as mean ± standard deviation (STD).

Characteristic	Value
System temperature [°C]	20.0 ± 0.5
Outer pressure [kPa]	50.0 ± 2.5
Inner pressure [kPa]	80.0 to 150.0 ± 2.5
Inner pressure steps [kPa]	10.0 ± 2.5

Tests were repeated for 8 values of ΔP and, for each of them, 16 acquisitions were carried out.

With the aim to acquire values from strain-gauge sensors, a DAQ (NI USB-6251) with a software

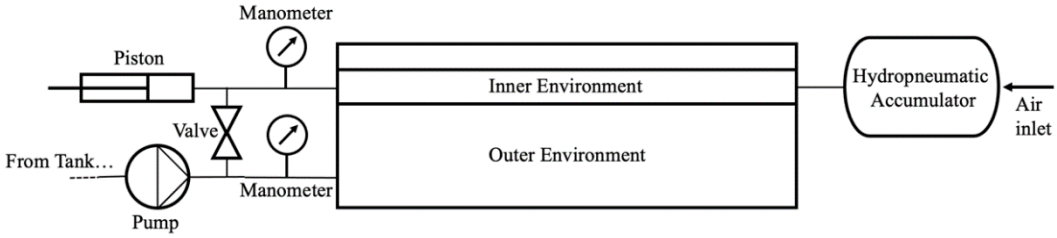

Fig. 2. Scheme of the main components of hydraulic circuit.

(LabView) was used. The main DAQ settings for data acquisition are listed in Table 3.

Table 3. Main settings of DAQ.

Characteristic	Value
Channel sample rate [kS/s]	500
Number of channels	2
Voltage range	± 1 V

To estimate the transit time (Δt) from the data acquired, the following post-processing operations were implemented in MatLab. A low-pass filter was used to remove frequencies above 200 Hz: from the spectral analysis of raw signals, contributions beyond the adopted cutoff frequency were less than 1% with respect to the fundamental frequency amplitude. Then, a cross-correlation was applied to the two filtered strain gauge signals for the estimation of the transit time.

III. RESULTS AND DISCUSSIONS

The PWV results obtained for increasing transmural pressure values are shown in Fig. 3.

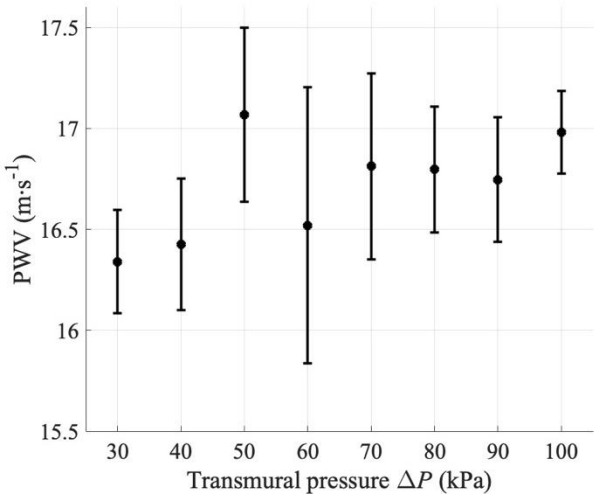

Fig. 3. Relationship between PWV outcomes and transmural pressure applied on AS. Results are represented with error bars, expressed in terms of standard deviation.

The plot shows that mean PWV values have a growing trend as ΔP increases. This behavior is in agreement with [6]: in fact, as p_{in} increases, PWV value raises. This behavior can be explained by making the following considerations: (a) the greater the internal pressure, the greater the volume of water contained in the AS, consequently the greater the value of the cross-sectional area A in Eq. (1); (b) according to [15], the increase of silicon rubber stiffness is related to the increase of its deformation, that implies a reduction of χ, thus an increase of PWV.

On the other hand, the measurement uncertainty was estimated by applying the propagation of the relative standard deviations of the quantities in Eq. (4). The uncertainty of ΔP was considered negligible.

About the standard deviation of PWV results, Fig. 3 shows that (a) error bar sizes are between 2% and 10% with respect to the relative PWV mean value, (b) some error bars are wider than others, e.g., the STD relative to ΔP = 60 kPa is higher about three times with respect to the relative to ΔP = 100 kPa one. This uncertainty values heterogeneity can be attributed to the manual actuation of the piston: pulse duration depends on the actuation force given to the piston. According to [16], strain rate affects the mechanical behavior of the vessel since its constituent material (silicon rubber) has viscoelastic characteristics. In this context, if the pulse is fast, the deformation of vessel walls is less than if the pulse is slower, keeping dp constant. In relation to Eq. 1, a faster pulse causes a decrease in χ (so, an increase in PWV), a slower one causes an increase in χ (then, a decrease in PWV), in the same condition of ΔP. Also, when a high actuation force is provided, the small deformations assumption does not hold and nonlinear behaviors occurred. Since the piston is actuated manually, the variability in the pulse wave magnitude and duration causes unpredictable error bar sizes.

IV. CONCLUSIONS

This paper focuses on a new arterial simulator able to vary the PWV of an arterial surrogate by changing the tensional state of its walls, thus, reproducing the variation of arterial stiffness in the human body. The stress-strain condition can change by varying, independently, inner and outer pressures of the AS, which is embedded in a sealed case and filled with water. A hydraulic circuit, connected to inner and outer environments allows changing liquid pressure. A piston, manually actuated, generates the pulse wave. Two strain gauges were glued at a known distance on the AS, in order to measure the transit time of the perturbation running through the vessel by deformation of its walls during pulse transit. The simulator working principle has been confirmed by first experimental results from a measurement campaign. In particular, the trend of results is in agreement with the reference mathematical model. The non-repeatability of measurements due to manual generation of pulse causes error bars up to 10% of PWV value. More acquisitions are required with a controlled pulse generator to properly characterize the system.

REFERENCES

[1] World Health Organization, “The top 10 causes of death”, https://www.who.int/en/news-room/fact-sheets/detail/the-top-10-causes-of-death (accessed

June 2023).

[2] World Health Organization, "Cardiovascular diseases (CVDs)", https://www.who.int/news-room/fact-sheets/detail/cardiovascular-diseases-(cvds) (accessed June 2023).

[3] I. S. Mackenzie, I. B. Wilkinson, J. R. Cockcroft, "Assessment of arterial stiffness in clinical practice," QJM, vol.95, No.2, February 2002, pp.67-74.

[4] B. Williams, G. Mancia, W. Spiering, E. A. Rosei, M. Azizi, M. Burnier, et al., "2018 ESC/ESH guidelines for the management of arterial hypertension: the task force for the management of arterial hypertension of the European society of cardiology and the European society of hypertension," J. Hypertens., vol.36, No.10, October 2018, pp.1953-2041.

[5] S. P. Glasser, D. K. Arnett, G. E. McVeigh, S. M. Finkelstein, A. J. Bank, D. J. Morgan, J. N. Cohn, "Vascular compliance and cardiovascular disease: a risk factor or a marker?," Am. J. Hypertens., vol.10, No.10, October 1997, pp.1175-1189.

[6] J. C. Bramwell, A. V. Hill, "The velocity of pulse wave in man" Proc. R. Soc. Lond. B., vol.93, No.652, April 1922, pp.298-306.

[7] G. Fiori, F. Fuiano, A. Scorza, S. Conforto, S. A. Sciuto, "Non-invasive methods for PWV measurement in blood vessel stiffness assessment", IEEE Rev. Biomed. Eng., vol.15, January 2022, pp.169–183.

[8] S. Laurent, J. Cockcroft, L. Van Bortel, P. Boutouyrie, C. Giannattasio, D. Hayoz, B. Pannier, C. Vlachopoulos, I. Wilkinson, H. Struijker-Boudier, European Network for Non-invasive Investigation of Large Arteries, "Expert consensus document on arterial stiffness: methodological issues and clinical applications. European Network for Non-invasive Investigation of Large Arteries," Eur. Heart J., vol.27, No. 21, November 2006, pp.2588-2605.

[9] A. Milan, G. Zocaro, D. Leone, F. Tosello, I. Buraioli, D. Schiavone, F. Veglio, "Current assessment of pulse wave velocity: comprehensive review of validation studies," J. Hypertens., vol.37, No.8, August 2019, pp.1547-1557.

[10] H.-L. Kim, S.-H. Kim, "Pulse wave velocity in atherosclerosis," Front. Cardiovasc. Med., vol.6, No.41, April 2019.

[11] F. Fuiano, A. Scorza, S. A. Sciuto, "Functional and metrological issues in arterial simulators for biomedical testing applications: a review," Metrology, vol.2, No.3, August 2022, pp.360-386.

[12] F. Fuiano, G. Fiori, A. Scorza, S. A. Sciuto, "A novel experimental set-up for Young modulus assessment through transit time measurements in biomedical applications," Proc. of the 2021 IEEE International Workshop on Metrology for Industry 4.0 & IoT (MetroInd4.0&IoT), 2021.

[13] F. Fuiano, G. Fiori, F. Vurchio, A. Scorza, S. A. Sciuto, "Transit time measurement of a pressure wave through an elastic tube based on LVDT sensors," Proc. of the 24th IMEKO TC4 International Symposium & 22nd International Workshop on ADC Modelling and Testing, 2020.

[14] Y. C. Fung, "Biomechanics: mechanical properties of living tissues", 2nd edition, Springer, 1993.

[15] C. Kurniawan, A. S. Eko, Y. S. Ayu, P. T. A. Sihite, M. Ginting, P. Simamora, P. Sebayang, "Synthesis and characterization of magnetic elastomer based PEG-Coated Fe_3 O_4 from natural iron sand," IOP Conf. Ser.: Mater. Sci. Eng., vol.202, 2017.

[16] W.D. Callister, D. G. Rethwisch, "Materials Science and Engineering", 8th edition, John Wiley & Sons, 2011.

26th IMEKO TC4 International Symposium
24th International Workshop on ADC and DAC Modelling and Testing
IMEKO TC-4 2023
Pordenone, Italy / September 20-21, 2023

The AMPWISE Project

M. Blagojevic [1], A. Dieudonne[2], L. Kamecki[3], M. E. Kiziroglou[4], K. Krastev[2], D. Marty[3], D. Piguet[5], S. Spasic[1], S. W. Wright[4] and E. M. Yeatman[4]

[1] *Senis AG, 6340, Baar, Switzerland*
[2] *Safran Electrical & Power, 31700, Blagnac, France*
[3] *Serma Ingenierie, 31700, Cornebarrieu, France*
[4] *Imperial College London, SW7 2AZ, U.K*
[5] *CSEM, Neuchatel, 2002, Switzerland*

***Abstract* – This paper presents an energy autonomous Wireless Sensor Network (WSN) for monitoring the structural current in aircraft structures. A hybrid inductive/hall sensing concept is introduced demonstrating 0.5 A resolution, < 2% accuracy and frequency independence, for a 5 A – 100 A Root-Mean-Square (RMS), DC-800 Hz current and frequency range, with 35 mW active power consumption. An inductive energy harvesting power supply with magnetic flux funneling, reactance compensation and supercapacitor storage is demonstrated to provide 0.16 mW of continuous power from the 65 μT RMS field of a 20 A RMS, 360 Hz structural current. A low-power sensor node platform with a custom multi-mode duty cycling network protocol is developed, offering cold starting network association and data acquisition/transmission functionality at 50 μW and 70 μW average power respectively. WSN level operation for 1 minute for every 8 minutes of energy harvesting is demonstrated.**

I. INTRODUCTION

The advancement of aircraft in terms of safety, efficiency, reliability, cost-effective maintenance and passenger comfort is expected to rely largely on sensing technology.

In this paper, an energy autonomous aircraft current monitoring system is introduced, designed for measuring the current flow through the aircraft structural beams, which are used as the return current path of its main electrical power installation. It comprises a differential hall sensor system, an inductive power supply developed for coupling to structural currents, a low power microcontroller and RF communication unit, and a low power protocol developed for enabling sub – mW average power operation while addressing certain aircraft and sensing scenario specifications. The overall system design is confined to industrial aircraft specifications and a certain sensing use case. Its performance is evaluated on a full-size industrial aircraft beam setup, including qualification evaluation for flight testing.

The rest of this paper is organised as follows: The aircraft sensing use case is described in Section II. In Section III, the sensor node architecture including control and communication, sensor and front-end electronics, power supply and packaging are presented. An evaluation summary of the system as a whole is given in Section IV. A conclusion and an outlook for further use and development are presented in Section V.

II. SENSING REQUIREMENTS

In aircraft made of composite, non-conductive materials, the return current of the electrical networks passes through the aluminum alloy structural beams of the airframe. As the role of electricity in aviation is extended to new functionalities, the effect of increased current flow to the electrical infrastructure needs to be evaluated. More specifically, the distribution of the return current path to the structural beam network is of key interest, as beam-to-beam junctions may be affected, resulting in heating, contact degradation (potentially including electromigration effects) and high contact resistance which can increase the risk of hazard. The objective of the sensing use case is to provide a dynamic mapping of current distribution through the aircraft airframe during flight.

A priority for aircraft sensor networks is wireless functionality and energy autonomy, due to the increased significance of weight reduction and infrastructure simplicity in aircraft installations. Therefore, a wireless, energy autonomous and non-invasive monitoring system for aircraft structural currents is targeted.

The current measurement range and resolution is set to 5 A – 100 A and 0.5 A respectively, for direct current (DC) as well as for alternating current (AC), in root-mean-square (RMS) values, with a frequency range between 360 Hz and 800 Hz. The expected minimum average AC current availability is set to 20 A RMS. This value was defined by an internal study in which the aircraft structural current distribution of over 700 electrical loads, supplied using 28V, 115 V or 230 V was analyzed.

Power autonomy adequate for system cold starting and data acquisition once every 8 minutes is required. A total mass for each sensor node in the 50 g range is desirable for

practical installation. Synchronization among SN in the 1 ms range is also desirable.

III. SENSOR NODE DESIGN

A. Overview

The sensor node architecture (Fig. 1) is based on the Nordic Semiconductor NRF52840 SoC, which combines an ARM Cortex M4 microcontroller with a 2.4 GHz low power communication transceiver. The structural current is measured by a differential pair of combined hall-effect and inductive sensors, driven and read by an advanced low-power front end circuit. Both systems are powered by an inductive energy harvesting power supply that collects energy from the AC magnetic flux around the current carrying structure. The power supply includes a power management system based on the Texas Instruments BQ25570 microchip, dual voltage regulation and super-capacitor energy buffering. All systems are integrated into a package suitable for installation on the aircraft structural beams described in Section II.

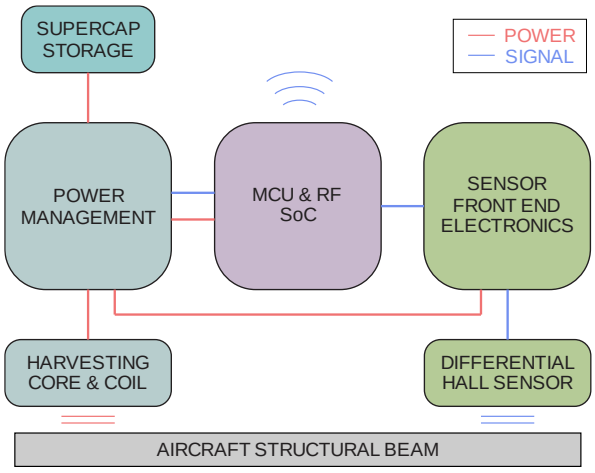

Fig. 1. Block diagram of the Sensor Node.

The overall design is focused on achieving energy autonomy, within the functional specifications required for the use case of Section II. The power consumption measured on each submodule is summarized in Table 1. Each module can be controlled to operate in one of several duty cycle regimes among shut down, sleep and one or more active modes. The sensor node may operate in three different functionality modes: network association, data acquisition/transmission and sleep. Each operating mode uses different duty cycling scenarios, resulting in different average power requirements. The overall average power consumption must be covered by the average harvested incoming power, and higher power modes can be accommodated by the supercapacitor energy buffer for short operating durations. Therefore, power autonomy performance depends not only on energy harvesting provision and electronic component consumption but also on sensor node operation scheduling and on the network protocol.

Table 1. measured consumption of the sensor node.

Module	Mode	Current mA	Power mW
NRF52840 SoC	Active, Acquisition	3.6	6.48
	Active, TDMA TX	25.2	45.4
	Active, TDMA RX	14.5	26.1
	Sleep	0.002	0.0036
Senis AG Structural Current Sensor	Acquisition	7	35 (5V)
	Sleep	< 0.001	< 0.005
Total Sensor Node	Max	32.2	80.4
	Sleep	< 0.003	< 0.0086

B. Communication Module

The communication module is implemented in the 25 mm by 25 mm PCB shown in Fig. 2. The central element is a Nordic Semiconductor nRF52840 communications and micro-controller unit (MCU) system-on-chip (SoC), The nF52840 provides 2.4 GHz low power proprietary communication modes. The MCU is a powerful, yet low power consumption, 64 MHz Arm Cortex M4 with 1 MB program memory and 256 KB RAM.

An external real time clock provides the system alarm clock and metronome. The ability to program a wake-up interrupt enables the nRF52840 to be completely shut down and awaken the next time it is needed. The low deviation of the real time clock, compared to a quartz clock, allows ultra-optimized implementation of the time division multiple access protocol (TDMA), with minimal guard times to compensate deviations, even with large intervals between communication events.

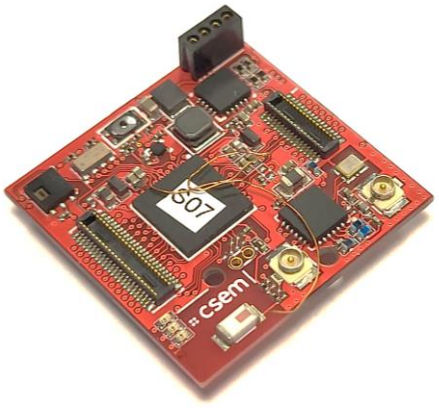

Fig. 2. The communication PCB (25 x25 mm)

C. Structural Current Sensor

The current flow through the structural beam is measured indirectly, through the magnetic field around the beam. Although the current frequency is relatively low (< 1 kHz), the skin effect is significant, due to the large size of the beam cross-section [1]. Indicatively, at 300 Hz the

skin effect depth is below 5 mm for an aluminium conductor, which is smaller than the beam cross section dimensions. The AC current is thereby pushed to the beam edges. The current distribution is non-uniform and frequency dependent. The implemented current sensor combines a Hall sensor and a pick-up coil oriented as shown in Fig. 3. The Hall based sensor was selected due to its DC and AC magnetic field measurement accuracy and its small dimensions and weight.

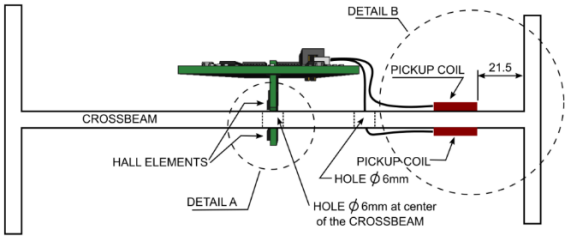

Fig. 3. Current sensor design comprising a couple of Hall sensor and pick-up coil positioned asymmetrically in an antiparallel configuration.

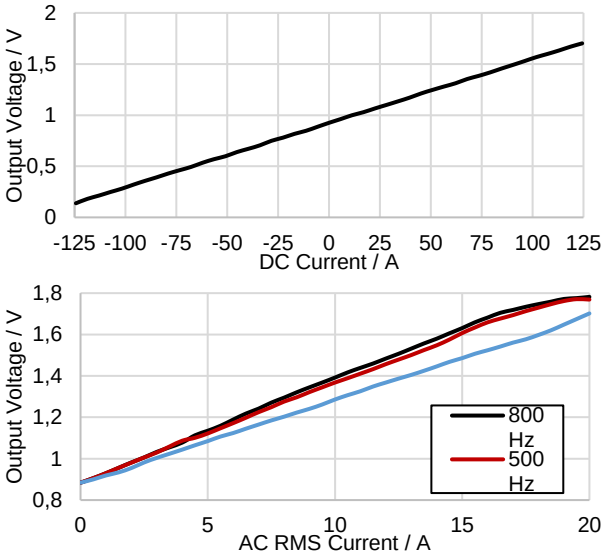

Fig. 4. Up: Voltage output vs DC current. Down: Voltage output vs AC current

Indicative performance results of this sensor system are presented in Fig. 4. A linear relationship between the structural current amplitude and voltage output is observed both for DC and AC measurements, with a distortion for currents over 15 A RMS at 500 Hz and 800 Hz. While the hall/inductive sensor combination demonstrate remarkable frequency invariance between 500 Hz and 800 Hz, the 360 Hz shows a significant deviation. This deviation could be compensated by hardware or data analysis calibration. The output voltage to structural current correlation shown in Fig. 4 demonstrate a worst-case resolution and analysis of 1% and 2% respectively, limited by the signal-to-noise ratio of the voltage output of the hall and inductive transducers.

Table 2. Structural current sensor performance

Feature	Value
Current / magnetic sensitivity	5 mV/A, 2.5 V/mT
Measurement range	5A – 100A
Frequency range	DC – 800 Hz
Resolution	<1% (0.5A)
Accuracy	<2% (1 A) @ 50 A
Current consumption:	7 mA at 5 V DC
Total dimensions and weight	75 mm × 37 mm, 17g

D. Power supply

The power supply module comprises an inductive energy harvester suitable for collecting power from structural currents and a power management system. The energy harvesting concept is illustrated in Fig. 5. A coil with a soft magnetic core is coupled to the magnetic field around the structure, by installation at an edge location where a higher magnetic field is available due to the skin effect, as illustrated in the inset. A funnel core shape is employed to guide flux from a given area through a smaller cross-section, thereby amplifying flux density, and increasing the voltage and power output. A transducer design with optimal coil/core mass ratio is used for maximum transducer power density. These two methods have been introduced in [2] and can provide combined power density increase of as high as two orders of magnitude.

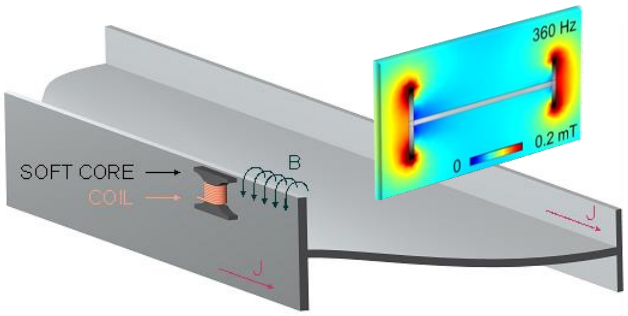

Fig. 5. The concept of inductive energy harvesting from structural current running through an aircraft beam. Inset: indicative simulated magnetic flux density distribution of a 25 A RMS, 360 Hz current illustrating the skin effect.

A photograph of the energy harvester is shown in Fig. 6. It is based on a 10,000 turn, 60 µm Cu wire coil of 6.7 g mass which forms a 20 mm long hollow cylinder with 5 mm and 11 mm inside and outside diameter respectively.

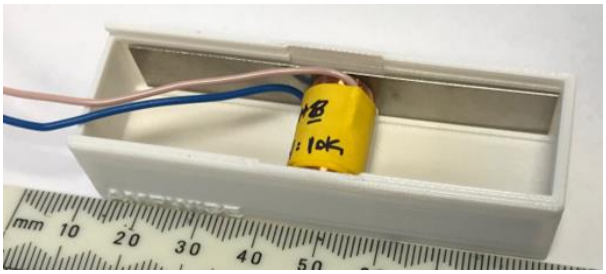

Fig. 6. The inductive energy harvesting transducer (sliding lid not shown).

The power management architecture of the power supply is based on a voltage doubler rectifier in combination with boost and buck converters for supercapacitor energy storage and regulated voltage provision. The rectified output is boosted to a higher voltage level (up to 5.5 V) to allow efficient storage on a supercapacitor. For this purpose, the Texas Instruments BQ25570 is employed [3], which also includes a cold starting booster, maximum power point tracking, secondary storage capability and a buck converter for selectable regulated output.

The power supply has been tested both under emulated magnetic fields and on a full-scale industrial aircraft beam rig, in integration with all sensor node electronics. The harvester output power measured on an ohmic load as a function of structural current amplitude is shown in Fig. 7.

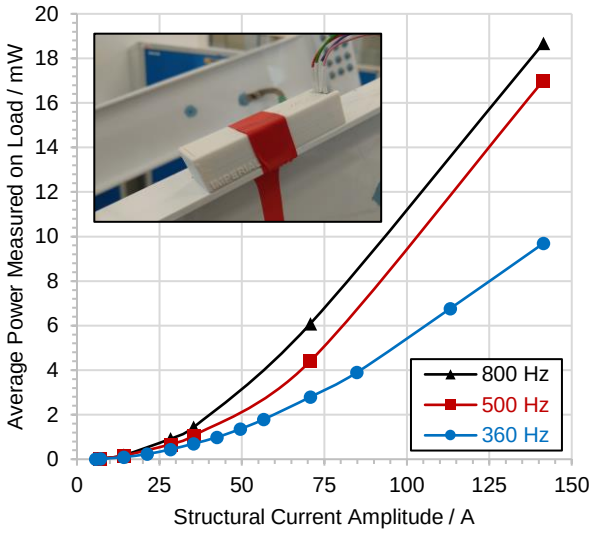

Fig. 7. Harvester output power measured on an ohmic load at half-open-circuit voltage conditions. Inset: The device installed on the industrial test rig.

IV. INTEGRATED SYSTEM TESTS

Flight qualification tests of the complete WSN were performed at an industrial avionics qualifications facility. Wireless communications including multi sensor node pairing and scheduled measurement packet delivery were demonstrated, using two inductive energy harvesting powered sensor nodes. The total power requirements of each sensor node during network association and data acquisition were measured to be 1.1 mW and 0.96 mW respectively. These measurements agree well with the 1.1 mW power consumption observed in the harvesting power supply tests.

Table 3 summarises the overall system performance compared to the specified use case.

Table 3. Demonstrated performance vs use case

Use Case Specification	Demonstrated Performance
Measurement range 5 A -100 A, DC–800 Hz	5 A -100 A, DC–800 Hz
Measurement resolution 0.5 A	< 0.5 A
Measurement accuracy 1%	< 2%
Up to 300 nodes, 30 m range	Supported by RF platform
One measurement / 8 minutes	One measurement / 8 min
Power Autonomy	1 min every 8 mins at 20 A
Measurement synchronization 1 ms	12 µs

V. CONCLUSION

An energy autonomous WSN for monitoring the structural return current path on aircraft during flight was demonstrated. This was enabled by the introduction of a hybrid inductive and hall effect differential sensor for structural currents in combination with hardware filtering for a flat frequency response, and a sensing power consumption of 35 mW. In addition, a low-power sensor node platform with a custom networking protocol that enables duty cycling during both network association and acquisition/transmission. The average power requirement is as low as 70 µW for network association and 50 µW for acquisition/transmission, comparable to the 37 µW of sleep mode consumption.

An inductive energy harvesting approach based on magnetic flux funnelling was adopted and a cold-starting bipolar power management circuit was introduced. The harvesting system was demonstrated to provide energy for a measurement rate of at least one sample every 8 minutes as required by the use case specifications.

REFERENCES

[1] M. E. Kiziroglou, S. W. Wright, and E. M. Yeatman, "Power Supply Based on Inductive Harvesting From Structural Currents," IEEE Internet of Things Journal, vol. 9, no. 10, pp. 7166-7177, 2022.

[2] M. E. Kiziroglou, S. W. Wright, and E. M. Yeatman, "Coil and core design for inductive energy receivers," Sensors and Actuators A: Physical, vol. 313, p. 112206, 2020/10/01/ 2020.

[3] "Texas Instruments BQ25570 nano power boost charger and buck converter for energy harvester powered applications," 2019, Available: www.ti.com/product/BQ25570.

26th IMEKO TC4 International Symposium
24th International Workshop on ADC and DAC Modelling and Testing
IMEKO TC-4 2023
Pordenone, Italy / September 20-21, 2023

Teamwork of Simulations and Hall Sensor Measurements for the Design of Magnetic Sensor Systems

Thomas Schliesch[1], Thomas Lindner[2]

[1] *Max Baermann GmbH, Germany, t.schliesch@max-baermann.de*
[2] *Max Baermann GmbH, Germany, t.lindner@max-baermann.de*

Abstract – **New magnetic sensor systems like stray field compensating specimen demand new challenges for the design of respective permanent magnets and sensors themselves. The collaboration of FEM simulations with 3D-Hall sensor measurements provides new insights how to build and optimize such systems. The paper shows this by the example of two stray field compensating sensors for position detection of rotating systems. The first example provides different stages of the development of a new sensor. The second one shows steps during the improvement of permanent magnets for a commercially available sensor system. Both parts also supply results about the insensitivity of those sensors against external fields up to 20mT.**

I. INTRODUCTION

Magnetic sensors have become more and more complicated during the last decades. Since a few years sensors with compensation of external stray fields became of increased familiarity. Hall sensors doing this are mainly based on the gradient principle where pairs of Hall sensor signals are evaluated and often these sensors consist of arrays of those units. The design of adequate magnets and their impact on those sensors on one hand can be done with numerical simulations of respective magnets. The input to the single sensor elements can be taken from the simulation results. On the other hand, the viability of a combination of single sensor signals for an adequate output of the whole sensor, like e.g. an angle of rotation, should be proved by measurements before investing into hardware. This can be done with devices for 3D Hall sensor measurements and there by combining the single signals to an output similar to that of the aimed final sensor.

The paper will show one example how the combination of simulations, Hall sensor measurements as well the final hardware realization had been done for an external field compensating sensor. This sensor can be used for on-axis as well as for off-axis rotating systems.

Another example refers to a commercially available sensor system where a magnet had to be optimized to provide position information of high accuracy and low noise to signal ratio. The magnet had to be improved with respect to the magnetization pattern as well as with respect to its final shape. Simulation results had to be surveyed by surface mapping of fastidious combinations of field gradients. Further the stray field stability of the final sensor system had to be checked.

II. GRADIENT SENSOR FOR CYLINDRIC MAGNETS WITH AXIAL POLARIZATION

The idea of this sensor was to harvest the radial field components of axially magnetized cylinder magnets at locations, where a mutual movement of magnet and sensor would not alter the field gradient. Fig. 1 shows the simulated distribution of the axial component of remanence of a bow shaped magnetized ring magnet with outer diameter 30mm, inner diameter 16mm, axial length 5mm and with four poles. Magnet material is injection molded isotropic NdFeB here. Magnets like this can provide nearly constancy and large steepness of the radial field component above the magnet's head face. For the one of Fig. 1 the radial field gradient is higher than 30mT/mm at 1.5mm axial distance.

The constant field gradient and the sinusoidal field dependence in angular direction led to the idea to design a sine-cosine sensor by using sensor pairs with adequate phase distance here of $\pi/4$ for the four-pole magnet, which can be generalized to other pole numbers, [1]. Fig. 2 displays the backside of an experimental sensor board, which was finally assembled in a research project with the INNOVENT institute, [2]. The single sensors within one pair had a radial distance of 2.5mm each.

The experimental prove of concept was made with a 3D-Hall measurement device according to Fig. 3 on various magnetic and non-magnetic shafts. Prior to that the same was performed with FEM simulations by combination of single signals on different paths along the magnet.

External fields to proof the stability against external stray fields were applied by permanent magnets as can also be seen in Fig. 3 on the right side.

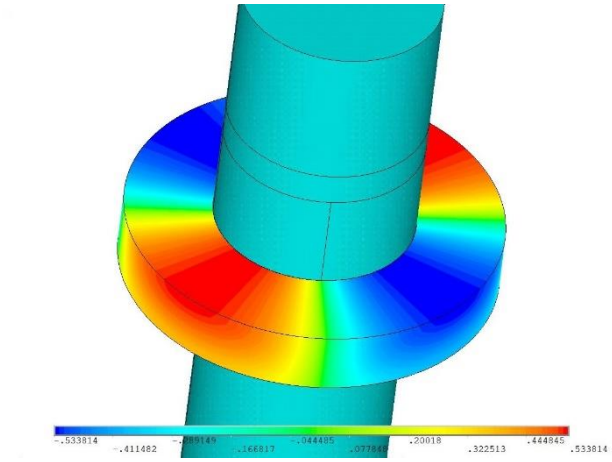

Fig. 1: FEM model of an injection molded NdFeB magnet with axially bow shaped polarization.

Fig. 2: Backside of circuit board of the sensor with two radial Hall-sensor pairs assembled by INNOVENT, [2].

Table 1: Average angular error amplitudes simulated by Hall probe measurements according to Fig. 3

Material	0mT	9mT	0mT	9mT
	non-magnetic shaft		soft magnetic shaft	
Ferrite	5.1	5.7	4.4	5.4
NdFeB	3.1	3.3	2.9	3.5

In Table 1 the simulated results by Hall probe measurements according to Fig. 3 are summarized for two materials. Beside the mentioned isotropic NdFeB magnets with bow shaped polarization in addition anisotropic Ferrite magnets with rigid four pole magnetization were investigated. Measurements were done with non-magnetic as well as with soft magnetic shafts.

Fig.4 provides results for a Ferrite magnet investigated with the real sensor according to Fig. 2. Here stray fields up to 20mT were applied by using respective Helmholtz-coils. As can be seen from Table 1 and from Fig. 4 the stray field resistance could be proven. What was less satisfying are the relatively large angular errors. Those originated mainly from the field shapes of the magnets.

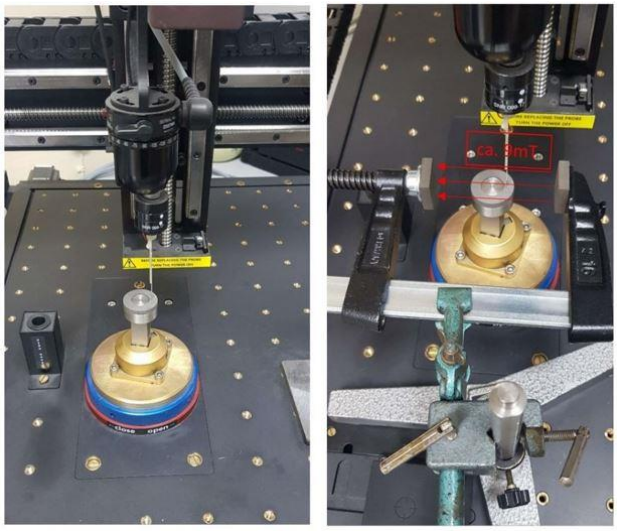

Fig. 3: 3D Hall-measurements and the application of external fields by permanent magnets, [3].

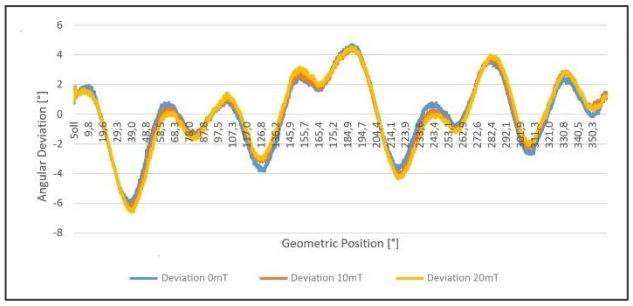

Fig. 4: Angular errors of the final sensor system for a Ferrite magnet at different external fields. Investigations on non-magnetic shaft.

The deviation from a sinus shape of the Ferrite magnet was obvious by the rigid pole pattern with homogeneous magnetization within each pole. But deviations from a sinus magnetization also occurred at the NdFeB magnets due to a non-adequate magnetizing coil. This led to an idea to develop a concept for a sensor to compensate at least partially the higher harmonics in the magnets' signals. The scheme for this, again for a gradient sensor similar to the one above, is provided by Fig.5. Here a combination of different field components as well as again the calculation of differences within the sensor pairs have to be performed.

For the same magnets as discussed above now axial and tangential field components are harvested. The evaluation of the signals of the two new field components were done now at radii more closely to the outer radius of the magnet. Further the axial distance to the head face was raised.

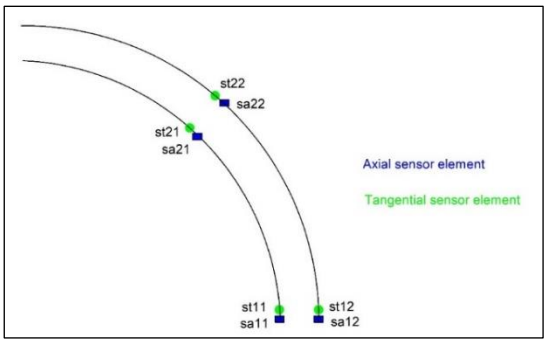

Fig. 5: Sensor concept with partial compensation of higher harmonics as well as of external fields.

Eq. (1)-(3) provide the related scheme of the functionality of the new concept:

$$\begin{aligned} \Delta a_1 &= sa_{12} - sa_{11} \\ \Delta a_2 &= sa_{22} - sa_{21} \\ \Delta t_1 &= st_{12} - st_{11} \\ \Delta t_2 &= st_{22} - st_{21} \end{aligned} \quad (1)$$

After calculating difference signals sine and cosine parts are calculated in the way according to eq. (2). The scheme can be understood by the fact, that in most cases both field components have similar higher harmonics by strength but with opposite sign:

$$\begin{aligned} B_{sin} &= \Delta a_1 + \Delta t_2 \\ B_{cos} &= \Delta a_2 - \Delta t_1 \end{aligned} \quad (2)$$

Finally, we get for the angle of rotation α where n_p is the number of poles:

$$\alpha = \frac{2}{np} \arctan\left(\frac{B_{sin}}{B_{cos}}\right) + \alpha_0 \quad (3)$$

In Fig. 6 the sensor simulation by the 3D-Hall measurement is displayed for a sintered Ferrite magnet. At the top left the single fields are shown at both angular positions, but for clarity only at one radius. One can see clearly that there are large deviations from a sinusoidal shape. The top right picture provides the differences according to eq. (1). The bottom left reveals, that by the concept of eq. (2) a much more viable shape exists, and the bottom right provides the angular error. Here with a non-magnetic shaft the average error amplitude of the Ferrite magnet is much smaller compared to that of the first other sensor, compare to table 1. Similar results exist for the NdFeb-magnets, where the angular errors were reduced by more than 50%.

The sensor principle of Fig. 5 can be used for on-axis and an off-axis systems and can also be used for systems harvesting a radial instead of an axial field component. A respective hardware version of this system has not been built yet, [4].

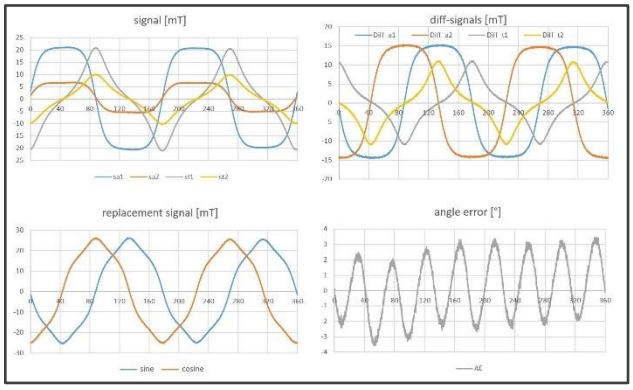

Fig. 6: Simulation of a new sensor concept according to Fig. 5 with 3D-Hall measurements for an anisotropic Ferrite magnet.

III. IMPROVED MAGNETS FOR AN ON-AXIS STRAY FILD IMMUNE SENOR

A sensor which harvests mainly the in-plane components of fields perpendicularly to the axis of a rotating shaft is described in [5] and [6]. Here an array of sensor pairs grouped circularly around the sensor center builds up a final sine-cosine system. The task related to this was to develop and optimize adequate magnets, to prove stray field immunity and to devise a practical system for quality control.

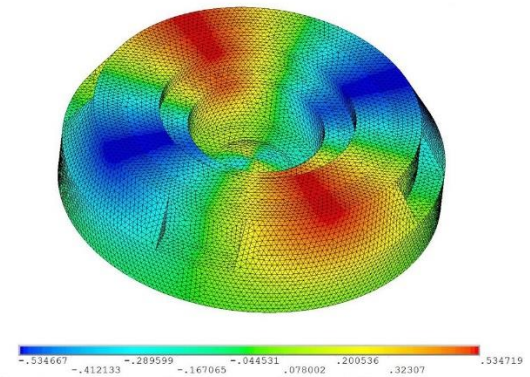

Fig. 7: FEM Analysis results for an on-axis sensor magnet for a stray field immune sensor system, axial component of remanence. Magnet diameter 14mm.

Fig. 7 displays the results of an FEM simulation of a respective magnet. The specimen shown here is made up of injection molded NdFeB with four poles on its head face. The sensor is mainly located at the center of rotation, but there can be eccentricities by mechanical tolerance up to 1.5mm. The bulge in the magnet's

center was devised to increase the space for the melt flow during the injection molding process.

Fig. 8 provides FEM-calculated results by adapting the receipt being described [6] to calculate the angular deviations at 1.5mm radius for two sorts of magnets. Axial distances to the magnet were 1.5 and 2.9mm. According to [6] sensor angles can be calculated by partial derivatives of in-plane field components. The rippled curves belong to full inherent analyses of the sensor.

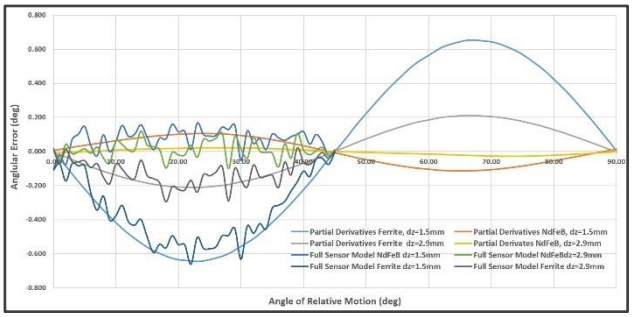

Fig. 8: FEM-calculated angular errors for a quarter of a full sensor path, magnets with geometry as in Fig. 7.

The curves with larger angular errors belong to injection molded Ferrite magnets with uniform direction of polarization within each pole. Fig. 9 displays stray field immunity investigations for such a magnet at radial positions 0mm and 1.3mm and at 1.5mm axial distance, using the real sensor. One can see that the results at the eccentricity position are in approximate agreement with the FEM predictions. On the other hand, a stray field immunity up to 10mT was proven.

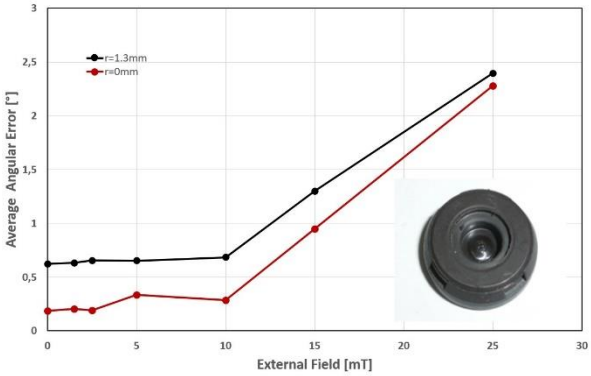

Fig. 9: Stray field immunity of real sensor with injection molded Ferrite with rigid magnetization.

The curves with the much lower angular errors in Fig.8 belong to NdFeB magnets with bow shaped magnetization. According to that, also injection molded, cost effective Ferrite magnets with bow shaped in mold-magnetization were manufactured. Their reduction of angular error could also be verified by real sensor measurements.

According to [6] for a reasonably low noise to signal ratio the parameter dB_{xy}/dxy as being defined in eq. (4) must be larger than 8mT/mm. For the Ferrite specimen it could be reached well by mainly keeping the bore radius inside the specimen as low as possible.

$$\frac{dB_{xy}}{dxy} = \frac{1}{2} \cdot \sqrt{\left(\frac{\partial B_y}{\partial x} + \frac{\partial B_x}{\partial y}\right)^2 + \left(\frac{\partial B_y}{\partial y} - \frac{\partial B_x}{\partial x}\right)^2} \qquad (4)$$

Fig. 10 displays the results of dB_{xy}/dxy above a Ferrite magnet with decreased inner diameter at dz=1.5mm. They were measured by a device according to Fig. 3, utilizing again a 3D Hall sensor. The limit of 8mT/mm is surpassed by far. The results are in excellent agreement with FEM simulations.

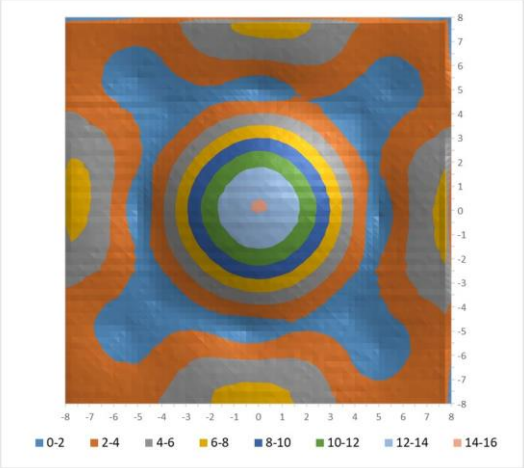

Fig. 10: dB_{xy}/dxy for a Ferrite magnet with decreased bore radius and bow-shaped polarization.

REFERENCES

[1] T.Schliesch, Hall Sensor, WO 2016/166265 A1, Max Baermann GmbH.

[2] Magnetic Off-Axis Sensor System for Control of Rotating Movements – RoCo, AIF Research Project, Germany 2021, Grant KK5209101DH1.

[3] Senis AG, Magnetic Field Mapper MMS-1A-RS.

[4] T.Schliesch, Method to Detect a Relative Angular Position and Magnetic Encoder Device, Patent Pending, 2022.

[5] C.Schott, S.Huber, Arrangement, Method and Sensor for Measuring an Absolute Angular Position Using a Multipole Magnet, WO 2014/029885 A1, Melexis Technologies NV.

[6] Magnet Selection for MLX9037X-Rotary Stray-Field Immune Mode, Application Note, Melexis Technologies NV, 2017.

26th IMEKO TC4 International Symposium
24th International Workshop on ADC and DAC Modelling and Testing
IMEKO TC-4 2023
Pordenone, Italy / September 20-21, 2023

First results on torque estimation by FEA and experimental analysis in a novel CSFH-based microgripper

Gabriele Bocchetta[1], Giorgia Fiori[1], Federico Filippi[1], Pietro Ursi[2], Salvatore Andrea Sciuto[1], Andrea Scorza[1]

[1] *Dep. of Industrial, Electronic and Mechanical Engineering, Roma TRE University, Rome, Italy*
[2] *Dep. of General Surgery and Surgical Specialties "Paride Stefanini", Sapienza University of Rome, Rome, Italy*

***Abstract* – Microgrippers (MGs) are MEMS devices that can manipulate cells and microscopic objects. In this work an approach based on both experimental and a finite element analysis is proposed with the aim of evaluating the torque exerted by the micro-actuator of a novel prototype of MG equipped with electrostatic rotary comb-drives and Conjugate Surface Flexure Hinges (CSFHs) when powered by a 0-20 V peak-to-peak supply voltage. The angular displacement of the micro-actuator has been measured using an image analysis method implemented by the Authors from videos acquired by a camera on a trinocular optical microscope, while the hinge stiffness has been estimated using numerical simulations: the obtained results show that the comb-drive can apply a maximum torque of 1.4 ± 0.2 nNm.**

I. INTRODUCTION

Nowadays, the development of MEMS (Micro Electro-Mechanical Systems) devices is becoming increasingly widespread. Microgrippers (MGs) are devices that have been extensively investigated during the last two decades as potential tools for a wide range of possible applications [1-3], especially in the biomedical field [4-5]. Microgrippers' versatility has lately been demonstrated in operations such as versatile grasping and autonomous pick-and-place [6-7]. MG prototypes embedded with Conjugate Surface Flexure Hinges (CSFHs) [8,9] performed successfully in grasping and releasing agarose microspheres in waterdrops [10]. The CSFH is depicted in detail in Fig. 1. Recent studies have shown that the total number of CSFHs is proportional to the energy necessary to deform the MG structure. As a result, MGs with only one CSFH pair and one pair of electrostatic rotary-comb drives [11-12] demonstrated a wider range of displacement considering the same applied voltage than MGs composed of a double four-bar linkage with multiple CSFHs [13-14].

The present work focuses for the first time on a novel CSFH-based MG equipped with only one CSFH pair, with the aim of investigating the mechanical behavior of the

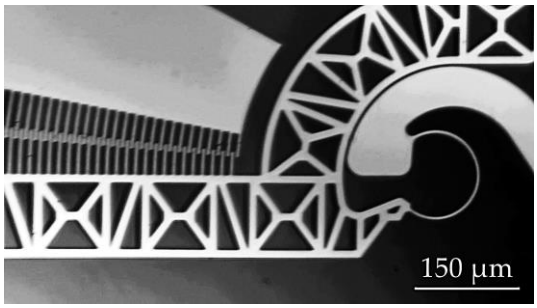

Fig. 1. CSFH and portion of the electrostatic comb-drive.

hinges by means of experimental analysis, based on image analysis method [15], and Finite Element Analysis (FEA), evaluating the torque exerted by electrostatic micro-actuators. A supply voltage in the 0-20 V range has been considered for the Device Under Test (DUT), whose main parameters are listed in Table 1. Since the DUT is free to move, i.e., it does not carry out a manipulation operation, each position assumed during movement has been assessed as an equilibrium condition between the torque exerted by the electrostatic actuator and the resistant torque due to the elastic behavior of the CSFH, which allows the actuation torque estimation as:

$$\tau = k\vartheta \tag{1}$$

where τ stands for the comb-drive's torque, while k and ϑ indicate the CSFH stiffness coefficient and the micro-actuator's angular displacement, respectively. As a first approximation, by considering CSFHs homogeneous, linear elastic beams with uniform, rectangular cross sections and assuming the bending moment as constant, it is possible to estimate the stiffness coefficient k [16-17]:

$$k \cong \frac{1}{12}\frac{Ebh^3}{r_n\alpha} \tag{2}$$

where E indicates the Young's modulus, b is the device thickness, h is the curved beam width, r_n is the neutral axis curvature radius, and α is the subtended angle by the latter. In particular, the experimental analysis aims to measure

Table 1. Microgripper main specifications

Component		Symbol	Value
SOI Wafer	Device layer thickness	b	40 μm
CSFH	Curved beam width	h	5 μm
	Neutral axis curvature radius	r_n	62.5 μm
	Curved beam subtended angle	α	240.9°
Fingers	Number per comb-drive	n	64
	Width	d	4 μm
	Rotor-stator distance	g	3 μm

the actual angular displacement of the micro-actuator, while through FEA the stiffness coefficient of the curved beam can be estimated.

II. MATERIALS AND METHODS

The DUT shown in the 3D rendering in Fig. 2 is a newly developed MG prototype fabricated monolithically by the DRIE (Deep Reactive Ion Etching) process on a SOI (Silicon-on-Insulator) wafer with an aluminum hard mask [18]. Several experimental tests have been carried out to measure the comb-drive angular displacement. In particular, many videos have been recorded using a trinocular optical microscope equipped with a video camera at different magnification levels to capture video of the entire micro-actuator and the CSFH. The acquired videos have been analyzed through a measurement procedure developed in MATLAB. Finally, in order to evaluate the stiffness coefficient, a finite element model (in COMSOL Multiphysics environment), has been implemented by numerically simulating the angular displacement of the micro-actuator as a function of electric potential. The numerical simulations that have been carried out, have as a base the results obtained during the experimental phase. In this way it has been possible to evaluate the stiffeness of the CSFH considering the same comb-drive rotation and the supply voltage used for the actuation of the DUT.

A. Experimental Analysis

The experimental setup implemented to conduct the experimental testing on the DUT consists of the power supply instrumentation, which includes a function generator, a power amplifier, and micropositioners for positioning tungsten needles that power the MG via contact, as well as the image acquisition instrumentation [19], including a trinocular optical microscope with a video camera. The specifications of the main components are listed in Table 2.

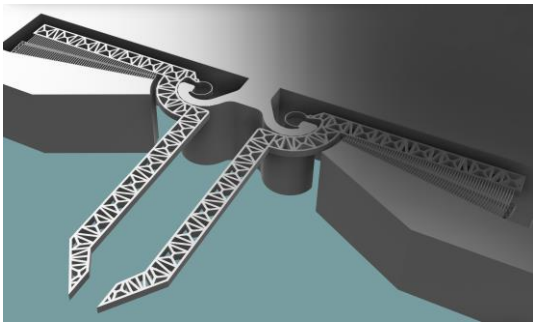

Fig. 2. 3D rendering of the microgripper prototype.

Table 2. Experimental setup main components

Device	Characteristics
Function Generator	Amplitude: 0 to ± 10 V peak-to-peak, Frequency: 0.01 μHz to 5 MHz
Power Amplifier	Amplitude: 0 to ± 20 V
Light Microscope	Zoom: 16×, 20×, 40×, 60×, 80×, 100×
Video camera	23.3 MP, sensor size ½.3 in, maximum video resolution 4K (3840×2160 pixel)
Video Processing Software	In-house algorithm implemented in MATLAB (2022b, MathWorks)
PC	Intel® Core i7-11370H, 32 GB RAM, NVIDIA® RTX™ 3050 Ti

The power supply instrumentation has been configured to generate a trapezoidal ramp signal in the range 0-20 V, and several videos of the DUT have been acquired considering a duration of least thirty periods of the supply signal. In particular, videos of the comb-drive at 40× magnification and videos of the CSFH and of the comb-drive's free end at 80× magnification have been acquired for evaluating the angular displacement. The acquired videos have been processed in MATLAB environment, and the comb-drive angular displacement has been measured by image tracking of many virtual markers positioned within predetermined regions of interest frame by frame.

B. Finite Element Analysis

Numerical simulations have been carried out using the commercial software COMSOL Multiphysics. In order to reduce computational costs, FEA simulations have been performed using the 2D model of the MG, to which was added an out-of-plane thickness of 40 μm. In particular, the 2D model was implemented from the CAD drawing used to create the aluminum hard mask of the fabrication process. To accurately replicate the electrostatic actuation of the comb-drive, the numerical model included the air surrounding the DUT as a free deforming domain. The mesh has been particularly optimized for the thinnest elements of the MG and in the air domain, thus obtaining about 71,000 triangular elements constituting the entire mesh. Non-linearities caused by large deflections have also been considered. The material utilized in the numerical simulations of the MG is Silicon <100>, which is also the material used in the manufacturing of the DUT. The material's Young's modulus is in accordance with [20].

III. UNCERTAINTY ANALYSIS

In order to discuss the outcomes of the study, an uncertainty analysis has been carried out, taking into

Table 3. Uncertainty sources in the experimental tests

Source of uncertainty	Value
Function generator amplitude	1% of $V_{peak\text{-}to\text{-}peak}$ + 2 mV
Power amplifier amplitude	2 mV
Optical system	1 µm
Video tracking algorithm	0.05°

account the main sources of error in the experimental analysis. Uncertainties have been expressed as standard deviations and the total uncertainty (σ_T) has been determined by combining Type A (σ_A) and Type B (σ_B) uncertainties as the root sum of squares as described in [21]. Type A uncertainties can be determined directly from the standard deviation of the obtained results, while Type B uncertainties have been computed using the error sources retrieved from the datasheets of the devices (Table 3). The optical system's uncertainty has been overall estimated to be 1 µm because of the lateral resolution, which is dependent on the incident light diffraction and wavelength, and the pixel resolution [22], as well as the uncertainty of the measurement procedure, which has been evaluated using a Monte Carlo Simulation (MCS) with 10^4 iterations. The total number of virtual markers inserted in the ROIs has been made to vary randomly, together with their relative coordinates, at each MCS iteration, which results in a variation of the x- and y-coordinates of the markers' centroid. As regards the uncertainty of the results obtained with the FEA, the geometric dimensions of the MG have been made to vary with an MCS with 10^4 iterations, considering the uncertainty caused by the DRIE process [8]. Finally, the uncertainty associated with the micro actuator's torque evaluation has been estimated by propagating the uncertainties of both the stiffness coefficient in (2) and the comb-drive's rotation [23].

IV. RESULTS AND DISCUSSION

Fig. 3 depicts the comb-drive displacement as

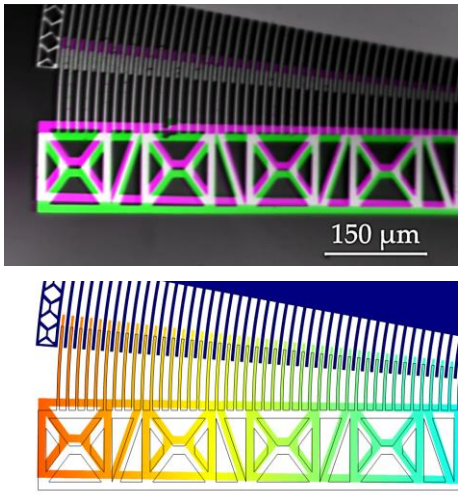

(a)

(b)

Fig. 3. Maximum displacement of the comb-drive evaluated by (a) experimental analysis and (b) FEA.

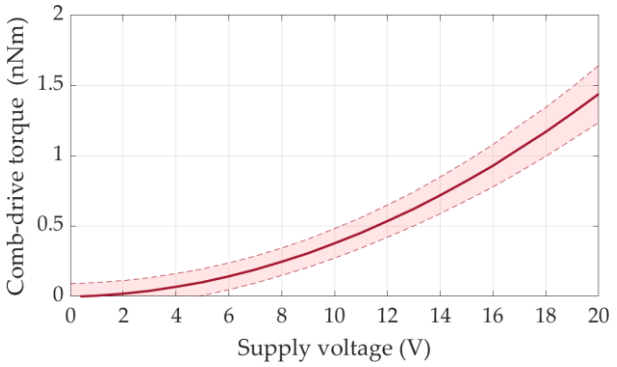

Fig. 4. Torque applied by the micro-actuator as a function of the supply voltage.

determined by means of both experimental and finite element analyses, applying to the MG a power supply in the range of 0-20 V peak-to-peak. According to the obtained results, the maximum displacement is 17.1 ± 1.1 µm, which corresponds to a rotation of 0.79° ± 0.05°. The curved beam stiffness coefficient has been evaluated at 0.10 ± 0.01 µNm/rad. This means that the comb-drive applies a torque of 1.4 ± 0.2 nNm in order to deform the CSFH of the collected angular displacement. Fig. 4 shows the evolution of the torque applied by the micro-actuator as a function of the supply voltage. In particular, torque is a function of the square of the supply voltage, which is consistent with the literature [10,24], both as trend and as order of magnitude.

V. CONCLUSIONS

The present study focused on a preliminary evaluation of the torque applied by the micro-actuator of a MG prototype equipped with a pair of CSFHs and electrostatic rotary comb-drives. Experimental and finite element analyses have been used in order to estimate the dynamic characteristics of the prototype. Videos of the DUT have been acquired using a trinocular optical microscope equipped with a video camera, which have been subsequently elaborated with an in-house algorithm implemented in MATLAB, and numerical simulations have been performed in COMSOL Multiphysics. Moreover, an uncertainty analysis has been carried out to assess the quality of the obtained results, which revealed that the micro-actuator under test is able to apply a maximum torque of 1.4 ± 0.2 nNm. In the near future, it will be important to improve the experimental setup as well as the numerical model used during the FEA and to carry out experimental tests to evaluate the torque applied by the micro-actuators when the MG performs a grasping and manipulation operation.

REFERENCES

[1] Z. Lyu, Q. Xu, "Recent design and development of piezoelectric-actuated compliant microgrippers: A review", Sensors and Actuators A: Physical, vol.331, November 2021, 113002.

[2] S. Gunasekaran, S. Periyagounder, S. Annamalai, A. Balaji, "Design and analysis of compliant micrograpper - A review," AIP Conference Proceedings, 2020, vol.2283, No.1.

[3] S. Yang, Q. Xu, "A review on actuation and sensing techniques for MEMS-based microgrippers", Journal of Micro-Bio Robotics, vol.13, No.1–4, October 2017, pp. 1–14.

[4] D. O. Otuya, Y. Verma, H. Farrokhi, L. Higgins, M. Rosenberg, C. Damman, et al., "Non-endoscopic biopsy techniques: a review", Expert Rev Gastroenterol Hepatol, vol.12, No.2, February 2018, pp. 109–117.

[5] K. R. Oldham, "Applications of MEMS technologies for minimally invasive medical procedures", in "MEMS for Biomedical Applications", Woodhead Publishing, 2012, pp. 269–290.

[6] T. Nishimura, Y. Fujihira, T. Watanabe, "Micrograpper-Embedded Fluid Fingertip-Enhancing Positioning and Holding Abilities for Versatile Grasping", J. Mechanisms Robotics, vol.9, No.6, October 2017, 061017.

[7] J. Zhang, O. Onaizah, K. Middleton, L. You, E. Diller, "Reliable Grasping of Three-Dimensional Untethered Mobile Magnetic Micrograpper for Autonomous Pick-and-Place", IEEE Robotics and Automation Letters, vol.2, No.2, April 2017, pp. 835–840.

[8] N. P. Belfiore, G. B. Broggiato, M. Verotti, R. Crescenzi, M. Balucani, A. Bagolini, et al., "Development of a MEMS technology CSFH based micrograpper," Proc. of 23rd International Conference on Robotics in Alpe-Adria-Danube Region (RAAD), 2014, pp. 1–8.

[9] N. P. Belfiore, G. B. Broggiato, M. Verotti, M. Balucani, R. Crescenzi, A. Bagolini, et al., "Simulation and construction of a mems CSFH based micrograpper", International Journal of Mechanics and Control, vol.16, No. 1, January 2015, pp. 21–30.

[10] F. Vurchio, P. Ursi, A. Buzzin, A. Veroli, A. Scorza, M. Verotti, et al., "Grasping and releasing agarose micro beads in water drops", Micromachines, vol.10, No.7, June 2019, pp. 1–15.

[11] F. Vurchio, F. Orsini, A. Scorza, S.A. Sciuto, "Functional characterization of MEMS Micrograpper prototype for biomedical application: Preliminary results," Proc. of 2019 IEEE International Symposium on Medical Measurements and Applications (MeMeA), 2019.

[12] R. Cecchi, M. Verotti, R. Capata, A. Dochshanov, G. B. Broggiato, R. Crescenzi, et al., "Development of micro-grippers for tissue and cell manipulation with direct morphological comparison", Micromachines, vol.6, No.11, November 2015, pp. 1710–1728.

[13] G. Bocchetta, G. Fiori, A. Scorza, N. P. Belfiore, S. A. Sciuto, "First results on the functional characterization of two rotary comb-drive actuated MEMS micrograpper with different geometry," Proc. of 25th IMEKO TC4 International Symposium and 23rd International Workshop on ADC and DAC Modelling and Testing, 2022, pp. 151–155.

[14] N. P. Belfiore, A. Bagolini, A. Rossi, G. Bocchetta, F. Vurchio, R. Crescenzi, et al., "Design, fabrication, testing and simulation of a rotary double comb drives actuated micrograpper", Micromachines, vol.12, No.10, October 2021, pp. 1–21.

[15] F. Vurchio, G. Fiori, A. Scorza, S. A. Sciuto, S. A. "A comparison among three different image analysis methods for the displacement measurement in a novel MEMS device," Proc. of. 24th IMEKO TC4 International Symposium and 22nd International Workshop on ADC and DAC Modelling and Testing, 2020, pp. 327–331.

[16] P. Ursi, A. Rossi, F. Botta, N. P. Belfiore, "Analytical Modeling of a New Compliant Microsystem for Atherectomy Operations", Micromachines, vol.13, No.7, July 2022, pp. 1094–1123.

[17] J. Liu, N. A. Abu Osman, M. Al Kouzbary, H. Al Kouzbary, N. A. Abd Razak, H. N. Shasmin, et al., "Stiffness estimation of planar spiral spring based on Gaussian process regression", Scientific Reports, vol.12, No.1, July 2022, pp. 1–15.

[18] A. Bagolini, S. Ronchin, P. Bellutti, M. Chistè, M. Verotti, N. P. Belfiore, "Fabrication of Novel MEMS Micrograpers by Deep Reactive Ion Etching with Metal Hard Mask", J. Microelectromechanical Syst., vol.26, No.4, May 2017, pp. 926–934.

[19] G. Bocchetta, G. Fiori, A. Scorza, S. A. Sciuto, "Image quality comparison of two different experimental setups for MEMS actuators functional evaluation: a preliminary study," Proc. of 25th IMEKO TC4 International Symposium and 23rd International Workshop on ADC and DAC Modelling and Testing, 2022, pp. 320–324.

[20] B. Bhushan, X. Li, "Micromechanical and tribological characterization of doped single-crystal silicon and polysilicon films for microelectromechanical systems devices", J. Mater. Res., vol.12, No.1, January 1997, pp. 54–63.

[21] J. R. Taylor, "An introduction to Error Analysis: The study of Uncertainties in Physical Measurements", 2nd edition, University Science Books, New York, USA, 1997.

[22] P.Prasad, "Introduction to Biophotonics", John Wiley and Sons, Inc, 2003.

[23] C. E. Papadopoulos, H. Yeung, "Uncertainty estimation and Monte Carlo simulation method", Flow Measurement and Instrumentation, vol.12, No.4, August 2001, pp. 291–298.

[24] C.-C. Tu, K. Fanchiang, C.-H. Liu, "1xN rotary vertical micromirror for optical switching applications," Proc. SPIE 5719, MOEMS and Miniaturized Systems V, 2005, pp. 14–22.

26th IMEKO TC4 International Symposium
24th International Workshop on ADC and DAC Modelling and Testing
IMEKO TC-4 2023
Pordenone, Italy / September 20-21, 2023

A Preliminary Comparison of Three Methods for the Assessment of Pulse Wave Transit Time in an Arterial Simulator

Federico Filippi[1], Giorgia Fiori[1], Gabriele Bocchetta[1], Salvatore Andrea Sciuto[1], Andrea Scorza[1]

[1] *Dep. of Industrial, Electronic and Mechanical Engineering, Roma TRE University, Rome, Italy*

***Abstract* – Arterial simulators are useful tools to reproduce the Pulse Wave Velocity (PWV) behavior depending on vessel characteristics. This quantity is related to the Pulse Transit Time (PTT), i.e., the time interval required for the pulse wave to travel between two sites in a vessel. In the literature, there is a lack of comparison of PTT evaluation methods from signals acquired through arterial simulators. In the present study, three PTT estimation methods (peak-to-peak, tangent-secant and cross-correlation) have been applied to two signals simulating the pressure wave traveling in an Arterial Surrogate (AS) over time. Tests have been repeated for different imposed delays between the generated waveforms. From the obtained results, the cross-correlation method showed the lowest discrepancy values between estimated and imposed time delay.**

I. INTRODUCTION

Pulse Wave Velocity (PWV) measurement in human body vessels represents a well-known technique for preventing and detecting many cardiovascular diseases [1-3]. In the clinical environment, many devices can measure PWV by estimating the time required for the pulse wave to travel a known distance within a vessel [4]: this time interval is known in the literature as Pulse Transit Time (PTT). From the last decades of the XX century, many procedures have been implemented through signal analysis to estimate PTT from waveforms acquired by transducers on human bodies [5,6]: some of them resulted more reliable than others depending on the application and setup conditions. Over the years, a few arterial simulators have been developed to study *in vitro* the characteristics of vessels through PWV assessments [7]. Although these simulators have different configurations based on the phenomenon to be reproduced, they are usually based on the same main components: (a) a real vessel or an Arterial Surrogate (AS) connected to a hydraulic circuit, (b) a pumping system able to generate pulse waves and (c) a sensing system for the detection of the pulse wave transit inside the vessel [7]. However, there is a lack in the literature about the reliability of measurement methods to evaluate PTT on arterial simulators.

This work aims to test some of the well-known methods for PTT estimation on waveforms similar to that provided from a novel AS [8]. The use of simulated signals has the advantage of isolating the phenomenon of pressure wave propagation, depending on the characteristics of the system [9], from other phenomena that overlap, such as turbulence effects of the flow [10]: in this way, it is possible to evaluate the performance of methods applied only to PTT estimation. For this purpose, some numerical simulations have been implemented in MATLAB environment: two waveforms, such as those in Fig.1, have been generated, in order to reproduce the pressure pattern at two different sites on the AS during pressure pulse transit; these waveforms, have noise components and amplitude attenuation depending on the path traveled within the AS and its characteristics. Therefore, different delay values τ have been imposed between the two waveforms, which represent the PTT to be determined at the end of the simulation. Then, the waveforms are sampled and filtered to simulate the acquisition process. Finally, three methods for evaluating the PTT are applied.

In the next sections, the waveform characteristics and their processing have been described as well as the methods considered to evaluate the PTT; finally, the test results have been proposed and discussed.

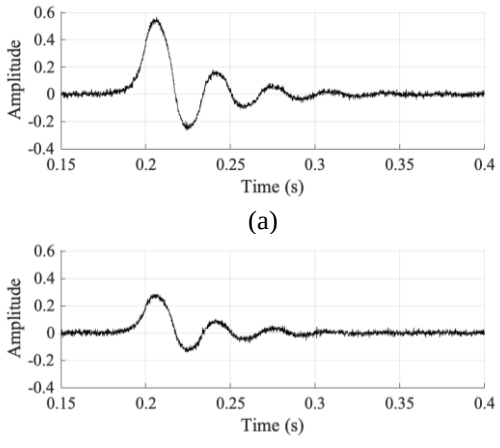

Fig. 1. Pressure waveforms over time: (a) in the first site and (b) the second one of the arterial surrogate.

II. WAVEFORMS GENERATION

In an arterial simulator, ASs response can be modeled based on a second-order system behavior in which the mass of the system is constituted by the fluid inside the vessel, while the elastic and the damper elements are related to viscoelastic properties of the hose [11]. When a perturbation, e.g., a pressure pulse occurs, the pressure trend in two different sites of the vessel can be described by waveforms like the example shown in Fig. 1: curves are characterized by a maximum amplitude A_{max}, an oscillatory movement component, that depends on the system's fundamental frequency f_n, and a damping component due to pressure losses along the vessel and the viscoelastic properties [9].

In this work, to simulate the transit of a pulse wave through two different sites on an AS, a couple of waveforms ($y_{1,o}$ and $y_{2,o}$) have been independently generated in a MATLAB environment, considering that the maximum amplitude of the second one has been reduced by 50% compared to the first one to take into account the losses along the vessel. In this study, it is assumed that there is no significant change in the frequency content between the two waveforms: in fact, the two measurement sites are considered to be close to each other, e.g., tens of centimeters [12]. The main specifications of both generated waveforms are listed in Table 1.

Table 1. Characteristics of the simulated waveforms.

Characteristic	Value
Sample number	10^5
Duration	1 s
Fundamental frequency f_n	30 Hz
Maximum amplitude of $y_{1,o}$	$A_1 = 0.55$
Maximum amplitude of $y_{2,o}$	$A_2 = 50\%$ of A_1

In order to simulate a real data acquisition process, the following components of noise have been added to the generated signals:

- gaussian noise, whose amplitude has been obtained by setting a fixed Signal-to-Noise Ratio (SNR);

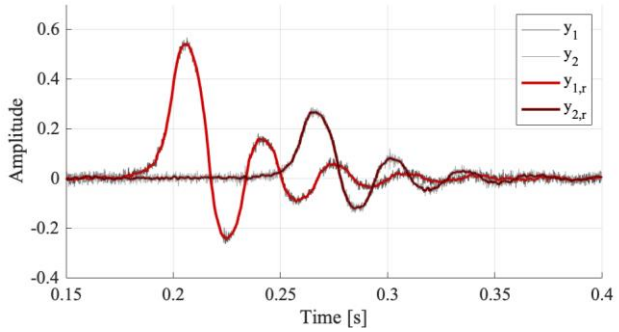

Fig. 2. Waveforms with noise components ($y_{1,r}$ and $y_{2,r}$) and filtered waveforms (y_1 and y_2).

Table 2. Characteristics of noise components and of low-pass filter.

Component		Characteristic	Value
Noise	Gaussian	SNR	15
	Power grid	Amplitude A_{np}	0.002
		Frequency f_{np}	50 Hz
	Bending vibrations	Amplitude A_{nb}	0.01
		Frequency f_{nb}	5 Hz
Low-pass filter		Cut-off frequency f_C	1 kHz

- a 50 Hz interference (n_P) from the power grid;
- a 5 Hz bending vibration (n_B) of the AS.

The resulting signals ($y_{1,r}$ and $y_{2,r}$) have been collected at a sampling rate of 10^4 S/s.

Finally, the two waveforms have been filtered before being processed by the PTT measurement methods. In Fig. 2 the two signals are shown before and after the filtering process. In particular, a low-pass filter has been applied based on a zero-phase filtering technique by processing data first forward and then backward. This allowed preserving the two waveforms in the time domain [13]. In Table 2 the characteristics of noise components and low-pass filter are reported.

III. TRANSIT-TIME ESTIMATION METHODS

In this section the three methods applied for the PTT evaluation are outlined: they are the Peak-to-Peak (PP), the Tangent-Secant (TS) and the Cross Correlation (CC) method, respectively.

A. Peak-to-Peak method

In the peak-to-peak method, the PTT estimation is carried out by assessing the time distance between the main peaks of the waveforms, as shown in Fig. 3.

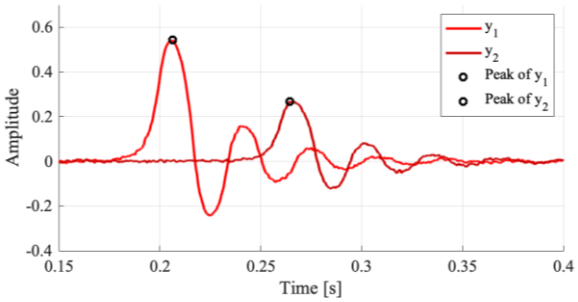

Fig. 3. Example of individuation of waveforms peaks with peak-to-peak method.

B. Tangent-Secant method

In the tangent-secant method, the PTT is estimated by calculating the time distance between the waveforms' feet [5]. In particular, the maximum point of the first derivative over time of each signal has been first evaluated, then the

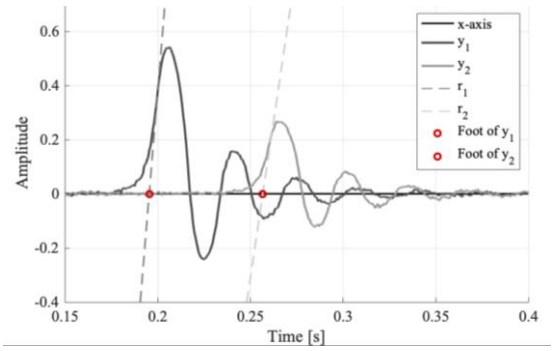

Fig. 4. Individuation of waveforms foot with tangent-secant method.

tangent line has been drawn on each waveform at that point. The foot of the waveform has been identified by the intersection between the tangent line and the *x*-axis (Fig. 4). A 35% threshold of the maximum amplitude of the signal has been set to ensure that the forefront of the waveform is considered.

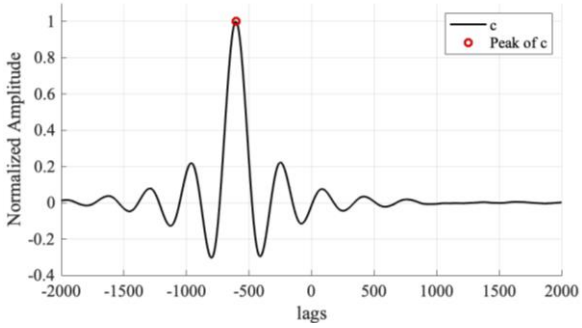

Fig. 5. Example of peak individuation of cross-correlation function.

Table 3. Distribution assigned to variables in MCSs.

Variable	Distribution	Variability
Imposed delay	Uniform	$\tau \pm 1\%$
Cut-off frequency	Uniform	$f_C \pm 1\%$
Amplitude of n_P	Uniform	$A_{np} \pm 1\%$
Amplitude of n_B	Uniform	$A_{nb} \pm 1\%$

C. Cross-Correlation method

The cross-correlation method is usually used to evaluate the similarity degree of two waveforms [14]. By applying this method to the waveforms, the second (y_2) is shifted along the *x*-axis step by step (one step is called lag – one lag corresponds to one sampling period), then, the integral of the product between y_1 and y_2 is calculated for each position: in the cross-correlation function (Fig. 5) the distance of the peak from zero multiplied by the sampling period is representative of the time distance between the two waveforms, that is the PTT.

IV. MONTE CARLO SIMULATION

To test the repeatability of the three methods applied to the AS, eleven Monte Carlo simulations (MCSs) have been carried out, one for each value of imposed delay τ, with 10^4 iterations each. Values of τ have been selected considering reasonable values of PTT measured locally in vessels, e.g., tens of centimeters, in which the PWV varies from physiological to pathological conditions, i.e., in the range 5-15 m·s^{-1} [4,15]. A distribution has been assigned to each value τ to consider the uncertainty given by the digital computational process. Noise contributions, added to waveforms, have been generated at each iteration. In addition, a distribution has been assigned to the cut frequency of the low-pass filter to evaluate the

Table 4. Results of the three methods with respect to imposed delay values.

	Peak-to-Peak		Tangent-Secant		Cross-Correlation	
Imposed delay τ (ms)	**Estimated delay** (ms)	**Discrepancy** (ms)	**Estimated delay** (ms)	**Discrepancy** (ms)	**Estimated delay** (ms)	**Discrepancy** (ms)
10.4 ± 0.1	10.6 ± 0.9	0.2 ± 0.9	11.1± 0.7	0.7 ± 0.7	10.4 ± 0.1	0.0 ± 0.1
15.7 ± 0.1	15.8 ± 0.9	0.1 ± 0.9	16.5 ± 0.7	0.8 ± 0.7	15.7 ± 0.1	0.0 ± 0.1
20.1 ± 0.1	20.0 ± 0.9	0.1 ± 0.9	20.8 ± 0.7	0.7 ± 0.7	20.1 ± 0.1	0.0 ± 0.1
25.3 ± 0.1	25.3 ± 0.9	0.0 ± 0.9	25.9 ± 0.7	0.6 ± 0.7	25.3 ± 0.1	0.0 ± 0.1
30.9 ± 0.1	31.1 ± 0.9	0.2 ± 0.9	31.6 ± 0.7	0.7 ± 0.7	30.9 ± 0.1	0.0 ± 0.1
35.3 ± 0.1	35.4 ± 0.9	0.1 ± 0.9	36.0 ± 0.7	0.7 ± 0.7	35.3 ± 0.1	0.0 ± 0.1
40.1 ± 0.1	40.0 ± 0.9	0.1 ± 0.9	40.8 ± 0.7	0.7 ± 0.7	40.1 ± 0.1	0.0 ± 0.1
45.6 ± 0.1	45.6 ± 0.9	0.0 ± 0.9	46.2 ± 0.7	0.6 ± 0.7	45.6 ± 0.1	0.0 ± 0.1
50.2 ± 0.1	50.3 ± 0.9	0.1 ± 0.9	50.9 ± 0.7	0.7 ± 0.7	50.2 ± 0.1	0.0 ± 0.1
55.9 ± 0.1	56.0 ± 0.9	0.1 ± 0.9	56.7 ± 0.7	0.8 ± 0.7	55.9 ± 0.1	0.0 ± 0.1
60.5 ± 0.1	60.4 ± 0.9	0.1 ± 0.9	61.2 ± 0.7	0.7 ± 0.7	60.5 ± 0.1	0.0 ± 0.1

Outcomes are expressed as mean ± Standard Deviation (SD).

contribution of filtering. In Table 3, the specifications of all variables considered in the MCSs are listed.

V. RESULTS AND DISCUSSIONS

Results of the simulations are listed in Table 4. Considering the discrepancy between attended and measured values, the TS method shows a higher gap, with a maximum discrepancy of 0.8 ms, whereas PP and CC methods are comparable with maximum discrepancies of 0.1 ms and 0.0 ms, respectively. The restrained discrepancies are likely due to the fact that the generated waveforms do not include all the frequency contents characterizing actual waveforms acquired from the arterial simulator. As regards the standard deviation (SD) values, PP and TS methods are 0.9 ms and 0.7 ms, respectively, and they keep constant for increasing time delays. On the other hand, SD values for the CC method are smaller than the others (i.e., ± 0.1 ms) since the temporal resolution, determined by the sampling frequency setting, in this case, represents the main uncertainty contribution.

VI. CONCLUSIONS

In this work, through Monte Carlo simulations, in MatLab environment, three computational methods for the PTT estimation have been compared: peak-to-peak, tangent-secant and cross-correlation. The methods have been applied to simulated signals from an arterial simulator. In particular, two waveforms have been generated with different amplitudes at which low-frequency noise and Gaussian noise components have been appended. The two signals have been shifted by different delay values to simulate changing in PTT. Results highlight the cross-correlation method is characterized by the lowest discrepancy value (0.0 ± 0.1 ms), while peak-to-peak and tangent-secant methods are characterized by maximum discrepancies of 0.2 ± 0.9 ms and 0.8 ± 0.7 ms, respectively. In the near future, it will be important to improve the PTT measurement procedure in order to apply the methods on experimentally acquired signals.

REFERENCES

[1] I. S. Mackenzie, I. B. Wilkinson, J. R. Cockcroft, “Assessment of arterial stiffness in clinical practice,” QJM, vol.95, No.2, February 2002, pp.67–74.

[2] B. Williams, G. Mancia, W. Spiering, E. A. Rosei, M. Azizi, M. Burnier, et al., “2018 ESC/ESH guidelines for the management of arterial hypertension: the task force for the management of arterial hypertension of the European society of cardiology and the European society of hypertension,” J. Hypertens., vol.36, No.10, October 2018, pp.1953–2041.

[3] S. P. Glasser, D. K. Arnett, G. E. McVeigh, S. M. Finkelstein, A. J. Bank, D. J. Morgan, J. N. Cohn, “Vascular compliance and cardiovascular disease: a risk factor or a marker?”, Am. J. Hypertens., vol.10, No.10, October 1997, pp.1175–1189.

[4] G. Fiori, F. Fuiano, A. Scorza, S. Conforto, S. A. Sciuto, “Non-invasive methods for PWV measurement in blood vessel stiffness assessment”, IEEE Rev. Biomed. Eng., vol.15, January 2022, pp.169–183.

[5] Y. C. Chiu, P. W. Arand, S. G. Shroff, T. Feldman, J. D. Carroll, “Determination of pulse wave velocities with computerized algorithms”, American Heart Journal, vol.121, No.5, May 1991, pp. 1460–1470.

[6] S. C. Millasseau, A. D. Stewart, S. J. Patel, S. R. Redwood, P. J. Chowienczyk, “Evaluation of carotid-femoral pulse wave velocity: Influence of timing algorithm and heart rate”, Hypertension, vol.45, No.2, January 2005, pp. 222–226.

[7] F. Fuiano, A. Scorza, S. A. Sciuto, “Functional and Metrological Issues in Arterial Simulators for Biomedical Testing Applications: A Review”, Metrology, vol.2, No.3, pp. 360–386.

[8] F. Fuiano, G. Fiori, A. Scorza, S. A. Sciuto, “A novel experimental set-up for Young Modulus Assessment through Transit Time measurements in Biomedical applications,” Proc. of 2021 IEEE MetroInd4.0&IoT, 2021, pp. 117–121.

[9] M. S. Ghidaoui, M. Zhao, D. A. McInnis, D. H. Axworthy, “A Review of Water Hammer Theory and Practice”, ASME. Appl. Mech. Rev., vol.58, No.1, January 2005, pp. 49–76.

[10] Y. C. Fung, “Biodynamics: circulation”, 1st edition, Springer, 1984.

[11] Y. C. Fung, “Biomechanics: mechanical properties of living tissues”, 2nd edition, Springer, 1993.

[12] F. Fuiano, G. Fiori, F. Vurchio, A. Scorza, S. A. Sciuto, “Transit Time Measurement of a Pressure Wave through an elastic tube based on LVDT sensors,” Proc. of. 24th IMEKO TC4 International Symposium, 2020, pp. 321–326.

[13] S. K. Mitra, “Digital Signal Processing”, 2nd ed, McGraw-Hill, New York, USA, 2001.

[14] M. Benthin, P. Dahl, R. Ruzicka, K. Lindström, “Calculation of pulse-wave velocity using cross correlation—Effects of reflexes in the arterial tree”, Ultrasound in Medicine & Biology”, vol.17, No.5, 1991, pp. 461–469.

[15] T. Pereira, C. Correia, J. Cardoso, “Novel Methods for Pulse Wave Velocity Measurement”, J Med Biol Eng, vol.35, No.5, October 2015, pp. 555–565.

26th IMEKO TC4 International Symposium
24th International Workshop on ADC and DAC Modelling and Testing
IMEKO TC-4 2023
Pordenone, Italy / September 20-21, 2023

Magnetic stray field analysis over large areas using Hall- and magneto-optical sensors

Benjamin Wenzel[1], Matthias Schmidt[1]

[1] *Matesy GmbH*, Löbstedter Straße 101-103, 07749, Jena*
b.wenzel@matesy.de

***Abstract* – In this paper, fast and large-area measurements using Hall sensors and magneto-optical sensors are presented, which are suitable for 100% in-line testing of magnetic assemblies in industry. The advantages of the two methods are explained and illustrated using real measurement examples. We show how identically designed magnetic components can be compared easily and quickly based on their stray fields. High-resolution measurements of miniaturized magnetic structures are carried out using magneto-optical measurement technology and the results are presented.**

I. INTRODUCTION

Permanent magnets and magnetic assemblies are used today in many areas of industry, aerospace, and medical technology. A strong increase in the use of permanent magnets is currently due to the rapidly increasing demand for electromobility [1]. The quality of the magnets used is becoming increasingly important to produce efficient products that save natural and energy resources. The quality check is often determined based on the stray field distribution of the permanent magnets. Some mapping methods are already very well-known and described [2], [3], [4]. Most of these methods work with single magnetic field sensors that are scanning over the surface. Hall-, XMR-, NV center-, magneto-optical sensors and sensor coils are typically used. In the laboratory use, this enables a very high geometric resolution to analyze the stray fields precisely. Unfortunately, the scan times for these methods are in the minutes, or even hours, timeframe. This paper describes a method that significantly accelerates the scanning process and thus enables 100% in-line testing of all components produced. Matesy uses a Hall sensor array that can simultaneously analyze a measuring length of up to 317.5 mm with one movement. For area scans with high resolution, Matesy uses so-called magneto-optical sensors with which lateral resolutions of up to 25 µm can be achieved.

II. HALL SENSOR MEASUREMENTS

A Hall sensor line called MHLS (Matesy Hall Line Sensor) was developed in order to be able to quickly and extensively examine stray fields from magnetic assemblies. This combines a compact and robust design with sensitive 3-axis Hall sensors that are arranged in the longitudinal direction of the measuring line with a pitch of 2.5 mm. The calibrated measuring standard range is ± 800 mT for each direction and it is temperature-compensated for use in industrial environments. The MHLS can be built up modularly, up to a measuring length of 317.5 mm. The maximum measuring rate is 200 S/s. The sensor line is calibrated in the homogeneous magnetic field volume of an electromagnet. The figure below shows an MHLS with the sensor ICs arranged:

Fig. 1: MHLS 320 measurement line with arrangement of the sensor ICs on the PCB

In principle, planar and rotary measurements can be carried out with the sensor line, depending on which positioning system is used [5].

A. Planar measurements

For the planar measurements, the MHLS was equipped to a PT15B_V3-120-500 gantry from iTK Dr. Kassen GmbH. This achieves a measuring area of 500 mm x 500 mm and a z-stroke of 100 mm in the current setup. The assembled magnetic field mapper and a measurement result are shown in the following figures:

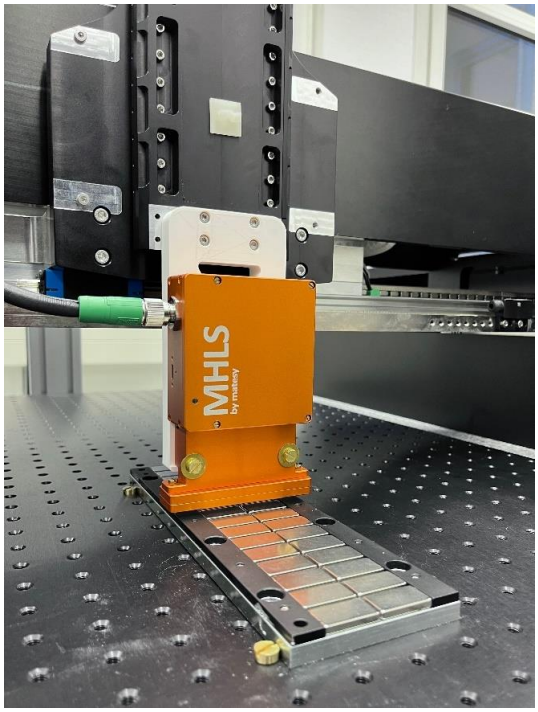

Fig. 2: Measurement setup for linear motor modules

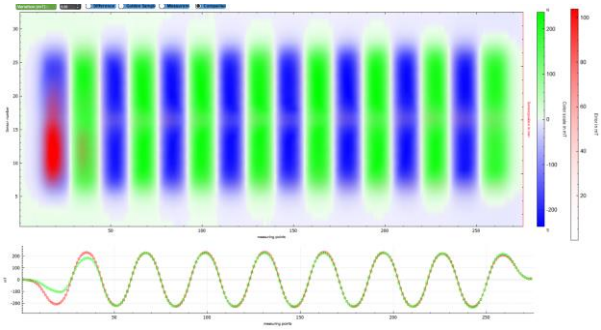

Fig. 3: Compared measurement results of two linear motor magnet modules, with red marking of error areas (top) and line diagram for both magnet modules in the region of the highest error (bottom)

For the stray field analysis, in 5 mm distance to the magnet surface, 2 magnet modules of linear motors were measured. The magnetic field image in Fig. 3 shows a comparison of the two magnet modules using the Golden Sample method. The deviations in the stray field of both modules are shown in red. It is very easy to see that the last two magnets compared of the magnet module deviate from the Golden Sample by up to 110 mT and are therefore significantly weaker. The scan was recorded with a resolution of 1 mm in the scanning direction, a speed of 100 mm/s and lasts 2.75 s for the whole magnet module shown. The recording of measured values is released by a trigger signal that is generated by the iTK gantry control. This means that each measured magnetic field value can be assigned an exact position on the scan area. Using the golden sample method, faulty magnet modules can be quickly found and sorted out, as shown here.

B. Measurements of rotating parts

To check the quality of the stray field of permanent magnet rotors, the MHLS was built into the RMP (Matesy Rotor Mapper) for these measurements and triggered using a high-resolution encoder on the axis of rotation. This results in an angular resolution of the measurement of 0.09°. The entire measurement took 20 seconds per rotor. It will take just 2 seconds if we change the angular resolution to 0.9°. An image of the measured rotor type in the measurement setup is shown in the following figure:

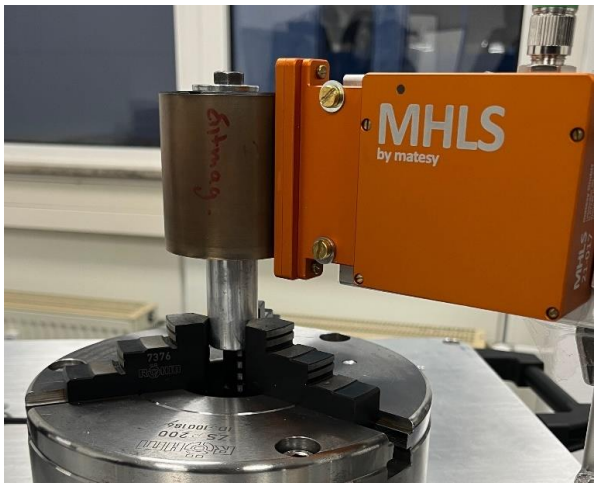

Fig. 4: Measurement setup for permanent magnet rotors

The measurement of 2 rotors was also evaluated here using the Golden Sample method and is shown in Fig. 5. It is again very easy to identify how the compared rotor deviates from the Golden Sample in the stray field. A field-weakening of up to 22 mT could be determined in the red marked areas. This process enables faulty rotors to be sorted out before they are assembled with the stator and thus also helps with quality testing in rotor production.

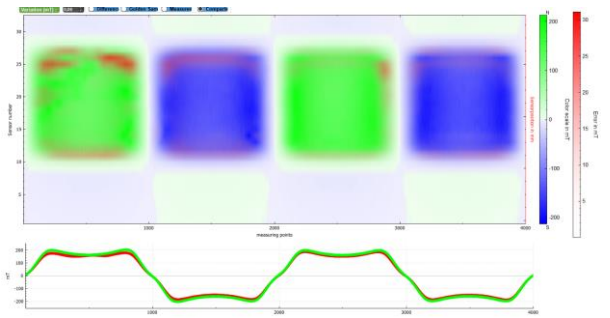

Fig. 5: Compared measurement results of two permanent magnet rotors with red marking of error areas (top) and line diagram from both rotors in the region of the highest error (bottom)

III. MAGNETO-OPTICAL MEASUREMENTS

The now shown results are made by magneto-optical principle which is based on the Faraday effect [6]. It describes the rotation of the polarization plane of linearly polarized light that passes through the magneto-optical sensor. The plane rotation is due to different refractive indices of the magneto-optical sensor for left- and right-circularly polarized wave parts of the polarized light. Viewed with help of another polarizer (analyzer) in nearly crossed orientation, one gets a highly resolved magneto-optical image of the different locally rotated light, which is a result of the applied or present magnetic stray fields. The following figure shows the Faraday effect in reflection mode which is used in cmos-magview technology by Matesy.

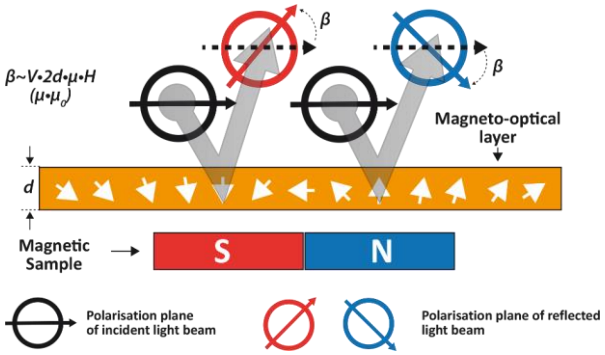

Fig. 1: Magneto-optical setup in reflection mode

A. Magnetic encoder testing

A magnetic scale with a diameter of 36 mm was investigated to determine zero crossings of the magnetic poles. The samples were positioned by hand directly on the magneto-optical sensor and different alignments were tested. Therefore, the measurement results show the real magnetic near field because the distance between the sample surface and the sensor plane is just a few microns. For the measurements, a cmos-magview XL with a calibrated measurement range of ± 125 mT and 60 µm lateral resolution was used. Additionally, a costumer specific software for automated detection of magnetic pole widths was developed. The repeatability of angular measurements was 0.02°. Due to the zero-crossing and circumference line detection the positioning between the outer and inner pole ring could be detected as well.

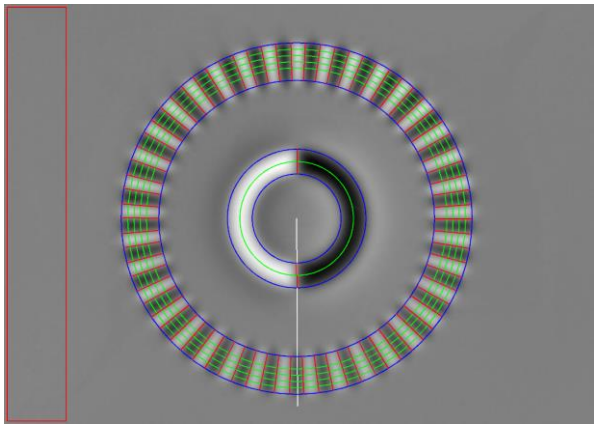

Fig. 7: Magneto-optical measurement result of a rotary encoder with 36 mm diameter

B. Electrical steel sheet testing

The quality control requirements for electrical steel are constantly increasing. Domain structures can be made visible by means of magneto-optical investigations on electrical steel, which allow conclusions to be drawn about the material properties [7]. In the magneto-optical image shown here in Fig. 8, the domains of a grain-oriented laser-treated (LMDR) electrical steel sheet are shown. It is a stitched image of 6 x 6 mm individual exposures. The overall size of the recording is approx. 100 mm x 65 mm. The lateral resolution of the image is 25 µm. Up until now, it has not been possible to characterize electrical steel sheets with this resolution and image size. It is very easy to see how the domains of the electrical sheet are interrupted by the introduced laser lines. This leads to domain refinement in the vertical direction of the image. The zoom section (framed in blue) shows a more misaligned area of the electrical sheet, which can be recognized by the higher domain contrast.

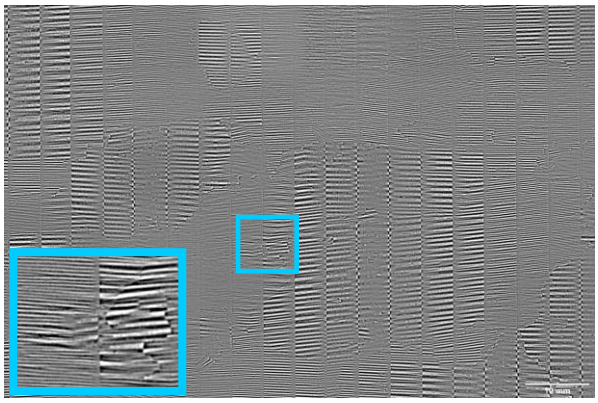

Fig. 8: Stitched magneto-optical domain image of a laser-treated, grain-oriented electrical steel sheet

IV. CONCLUSIONS AND ACKNOWLEDGMENT

Both hall scans with MHLS and large-area magneto-optical recordings using cmos-magview are efficient tools for 100% end-of-line control. In combination with the right evaluations in the software, the properties of the magnetic assemblies and test objects can be determined effectively, and defective parts can be sorted out quickly. As a further development, it is planned to combine the MHLS with a laser distance sensor to obtain a magneto-mechanical reference for the measurement. We thank the colleagues from INNOVENT e.V. for providing the magneto-optical recording and the Federal Ministry of Economics and Climate Protection, who supported the development of the MHLS as part of the ZIM program.

REFERENCES

[1] EV-Volumes - The Electric Vehicle World Sales Database.(o. D.). https://www.ev-volumes.com/evphev-forecast-example.png, 06-22-2023

[2] H. Husstedt, “Measurement of Magnetic Fields for the Testing of Automotive Sensors”, Dissertation March, 2014, AlpsAdriatic University Klagenfurt, Austria

[3] H. Husstedt, U. Ausserlechner, M. Kaltenbacher.: Accurate Scanning of Magnetic Fields. In book: Smart Sensors for Industrial Applications (Devices, Circuits, and Systems), pages 273-288, Chapter: 17, 2013.

[4] D. Popovic Renella, and S. Spasic. "Quality Control of Permanent Magnets for Industrial Applications: Integrating Magnetic Field Mapping and Crack Detection." 21st IMEKO TC-4 International Symposium on Understanding the World through Electrical and Electronic Measurement/19th International Workshop on ADC Modelling and Testing Conference Location Budapest, HUNGARY. IMEKO Location BUDAPEST, 2016.

[5] M. Schmidt, “100% Quality Control of Permanent Magnets for Industrial Applications”, Magnetics Conference 2022, Orlando FL.

[6] T. Hibiya, P. Görnert, in Liquid Phase Epitaxy of Electronic, Optical and Optoelectronic Materials (Eds: P. Capper, M. Mauk), John Wiley & Sons Ltd., pages 305 - 339, Chichester 2007.

[7] H. Richert, H. Schmidt, S. Lindner, M. Lindner, B. Wenzel, R. Holzhey, R. Schäfer.: “Dynamic Magneto-Optical Imaging of Domains in Grain-Oriented Electrical Steel”. In steel research international, Volume 87, Issue 2, pages 232-240, 2015.

26th IMEKO TC4 International Symposium
24th International Workshop on ADC and DAC Modelling and Testing
IMEKO TC-4 2023
Pordenone, Italy / September 20-21, 2023

Current Measurements for Fault Diagnosis in Induction Motors

Simone Mari, Andrea Credo, Giovanni Bucci, Fabrizio Ciancetta, Edoardo Fiorucci, Andrea Fioravanti

University of L'Aquila, Dept. of Industrial and Information Engineering and Economics, Monteluco di Roio, 67100, L'Aquila (AQ), Italy
Correspondence: simone.mari@graduate.univaq.it

Abstract **– Predictive maintenance has become increasingly important in modern industry as it can prevent unplanned production interruptions and reduce maintenance costs. This is especially important for companies working with expensive and complex machinery, such as those used in manufacturing, transportation, and energy. Predictive maintenance uses sensors and data analytics to monitor equipment performance and predict when a failure or breakdown might occur. This paper presents a preliminary study on the use of absorbed currents measurement of a three-phase induction motor aimed at electrical fault diagnostics. In detail, a 4-pole high efficiency induction motor with 3kW of rated power was simulated in the Ansys Electronic Desktop environment. The simulated operation is with direct mains power supply. The motor was simulated initially at no load, then load torque values of 20%, 40%, 60%, 80% and 100% of rated value were evaluated. The currents drawn on the three phases were evaluated with a computational step of 500 µs, corresponding to a sampling rate of 2 kHz. The same simulations were subsequently repeated by reproducing five different fault conditions in the motor. Therefore, an analysis of the waveforms of the absorbed currents is provided and a diagnostic system based on their analysis is proposed.**

I. INTRODUCTION

With the development of Industry 4.0, there has been a significant increase in the complexity and efficiency of systems in the industrial sector. Electric motors provide the main source of energy for machinery and must be in excellent condition over time to maintain high levels of productivity. The various components in the motor may be subject to both electrical and mechanical failures, causing slowdowns in the company's production process and significant economic losses. To verify the correct functioning of the motor and the condition of the components, various maintenance strategies are implemented, which differ in machine downtime and cost [1],[2]. By using the correct maintenance strategy and intervening only when necessary, machine productivity time can be optimized, costs can be reduced for the company, and operational safety can also be improved [3],[4].

The literature proposes numerous systems for fault detection on induction motors, utilizing measurements of both current and vibration and acoustic emission. However, these methods primarily focus on detecting mechanical faults such as damaged bearings or misalignment. The potential of using current measurement as a diagnostic system for electrical faults has not been extensively explored, leaving a gap in the literature. To address this, this paper presents a novel approach for diagnosing electrical faults by measuring phase currents. A 4-pole high efficiency induction motor with 3kW of rated power was simulated under varying load conditions, and different electrical fault conditions on both the stator and rotor were analyzed in the simulations. The waveforms of the absorbed currents were thoroughly examined and compared across all conditions. This enabled the creation of a diagnostic system that can effectively indicate the presence of faults. The proposed method has the potential to provide valuable insights into the detection and diagnosis of electrical faults in induction motors, which can improve the overall efficiency and reliability of the system. By identifying faults early on, necessary repairs can be made before they escalate, reducing downtime and maintenance costs. Overall, this research contributes to the development of more comprehensive and effective fault detection systems for induction motors.

II. ELECTROMAGNETIC SIMULATION

The validation of the proposed method is based on Finite Element Analysis (FEA) which simulates an electromechanical transient of the induction motor.

The electromechanical transient simulation considers the computation of the torque with FEA and the speed is computed considering the differential equation of the mechanical rotational speed considering the rotor and possible load inertia, the initial speed, and the damping coefficient. The considered motor is a 4-pole high-efficiency induction motor with 3kW of rated power. The main parameters of the motor are reported in Table I.

The adopted mesh and the geometry of the motor are shown in Fig. 1. The element size has been selected in order to speed up the burden of computational time maintaining a good approximation in the results. This is necessary because, in order to evaluate all phenomena correctly, it is necessary to have a big simulation time with a reduced time step.

Table 1. Main Induction Motor Parameters.

Parameters	**Unit**	**Value**
Phase voltage (rms)	*Vrms*	240
Phase Current	*Irms*	7.7
Number of poles		4
Stack length	*mm*	130
Outer Stator Diameter	*mm*	240
Inner Stator Diameter	*mm*	7.7
Wire Size	mm^2	240
Number of turns per phase		198
Number of Stator Slots		36
Number of Rotor Slots		28

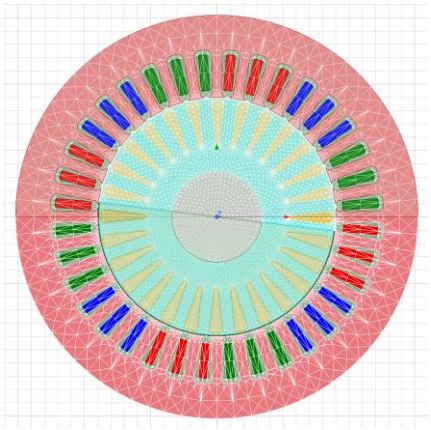

Fig. 1. Model and mesh of the simulated Induction Motor

The simulations include a first period in which the motor reaches its steady state at no load conditions; after that, it has been introduced a first torque step of 20% of rated torque (4 Nm). This torque value is maintained for 4s in order to reach the steady state; therefore, further torque steps with the needed time for obtaining the steady state. The values for the torque steps are 40% (8 Nm), 60% (12 Nm), 80% (16 Nm), and 100% (20 Nm) and the time steps are 2s for the 40% of torque step and 1s for the others. In the final version this time step will be increased to better evaluate the results in steady state operation.

In Figure 2 it is reported the speed, the load and the electromagnetic torque of the simulated motor without faults.

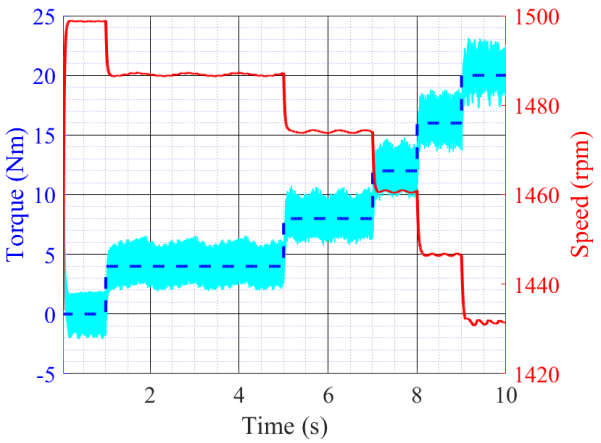

Fig. 2. Speed, load and torque without faults

From the simulation results it is possible to see a high-frequency torque oscillation and a little low-frequency speed oscillation, mainly due to the normal operation of the induction motor supplied with a constant frequency by the grid. With the FEA also some of the typical faults in the electrical machines have been simulated:

1) A short coil in the phase
2) Two short coils in two different phases
3) A no-filled rotor slot
4) A short coil in the phase with a no-filled rotor slot
5) Two short coils in two different phases with a no-filled rotor slot

In Figure 3 it is reported, as an example, the speed, the load and the electromagnetic torque of the simulated motor with one of the presented faults, in particular a no-filled rotor slot.

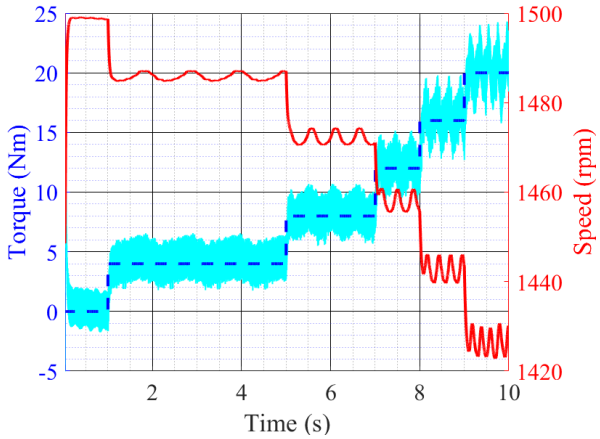

Fig. 3. Speed, load and torque with faults

It is clear from the figure that the fault introduces a higher distortion in the torque (in the high and low frequencies) and speed (in the low frequencies). To this further oscillations has to be associated with phase current oscillations which can be measured during the machine operation. The idea at the basis of this paper is to evaluate how much the faults impact the high and low frequencies

oscillation in the phase currents and associate to these values the associated fault.

III. DATA ANALYSIS

To evaluate the results of the simulation described above in the first instance, transient states are filtered out and steady-state conditions are analyzed independently. The signals of the absorbed currents on the three phases were processed by Fast Fourier Transform (FFT) in order to evaluate their harmonic content. As shown in Fig. 4, the current drawn by the motor is predominantly a sine wave at 50 Hz, the harmonic content is definitely paltry to be appreciated for diagnostic purposes. The only effects reflected by faults on the spectrum of the absorbed current can be found in a harmonic cluster around the fundamental frequency at 50 Hz, in the case of a no-filled rotor slot, and an amplitude variation of the same 50 Hz, in the case of a short coil in the phase. In particular, note that the harmonic cluster present in the case of a no-filled rotor slot is due to an amplitude modulation of the current introduced by the fault. Fig. 5 shows the current drawn by Phase 1 of the motor when simulated with a no-filled rotor slot and load torque of 80 Nm. As a result of these evaluations, it was decided to implement a diagnostic system to detect faults and anomalies on induction motors by evaluating the relationship between the rms values of the different phases and the presence of a low-frequency modulating signal. In order to evaluate the modulating signal, the simulation was repeated to obtain steady states of 4 s each, which for a computational step of 500 µs corresponds to 8000 points. The simplest way to demodulate a signal is to obtain through a diode the absolute value of the received signal and then low-pass filter it, removing the high-frequency component. First, the diode is simulated by obtaining the absolute value of the current signal. Then, the output of the diode is filtered. For this purpose, a Butterworth filter is designed using Python's SciPy library. Finally, the signal mean is removed. Table 2 shows the frequency and amplitude values of the modulating signals obtained by demodulation of the absorbed current. Only the values for fault conditions 3), 4), 5) are reported since fault conditions 1) and 2) do not report any amplitude modulation. Fig. 6, on the other hand, shows a graphical indication of the phase-to-phase ratios of the rms values of the currents. it is evident that fault condition 3) has no discriminating factor compared with healthy motor conditions, while in all other cases the fault condition can be detected by imposing appropriate upper and lower limit values.

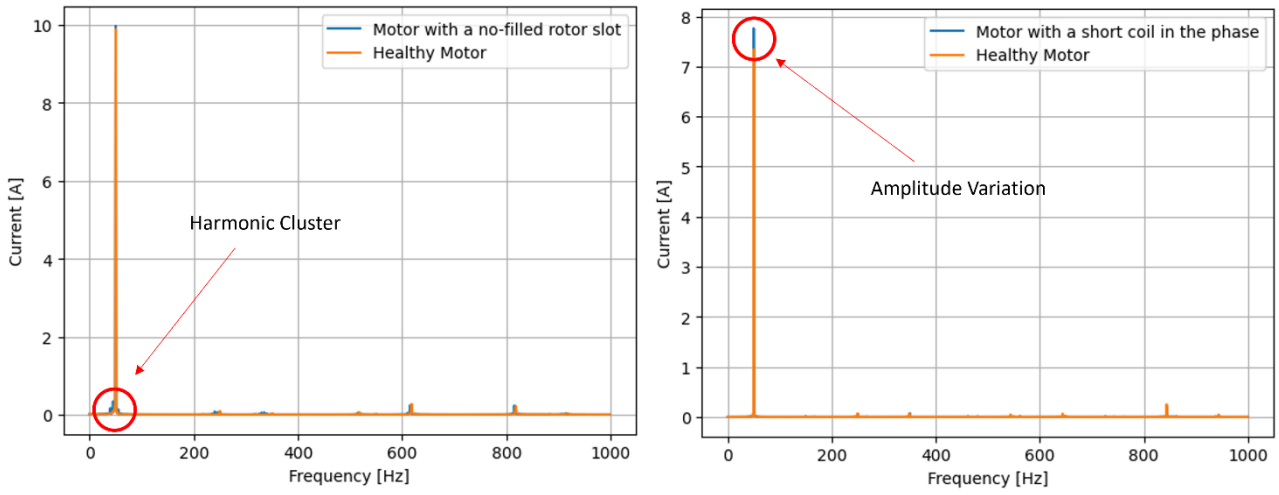

Fig. 4. Comparison of the harmonic contents of the absorbed current of the healthy motor compared with motors in which fault conditions were simulated.

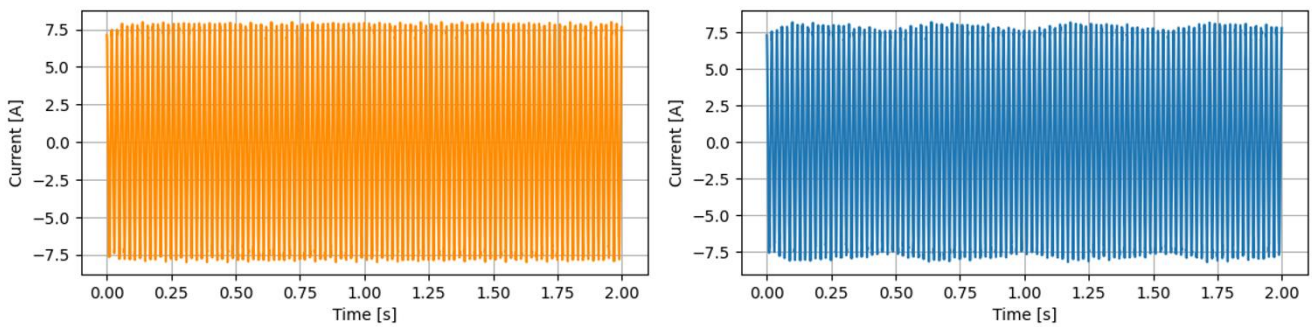

Fig. 5. Currents absorbed by the Phase 1 of the healthy motor (left) and the motor with a no-filled rotor slot (right).

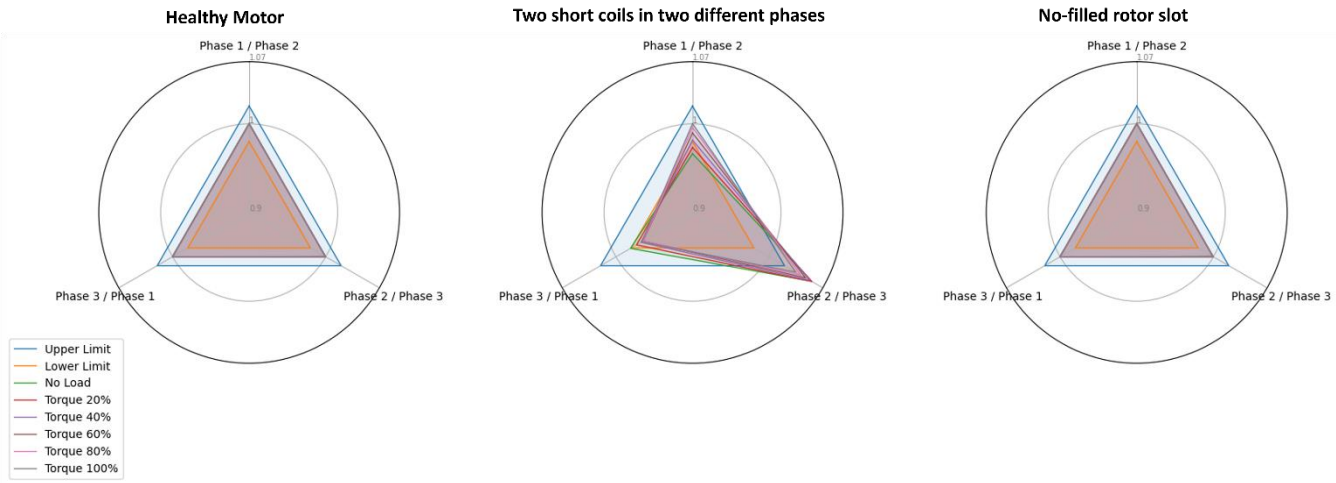

Fig. 6. Relationship between rms values of currents on different phases for healthy motor (left), motor with two short coils in two different phases (middle) and motor with no-filled rotor slot (right).

Table 2. Frequency and amplitude of the modulating signal extracted from the absorbed current.

Torque	Fault Condition 3		Fault Condition 4		Fault Condition 5	
	f [Hz]	Amp. [A]	f [Hz]	Amp. [A]	f [Hz]	Amp. [A]
20%	0.93	1.20	0.93	1.20	0.93	1.20
40%	1.95	0.79	1.95	0.76	2.00	0.73
60%	2.98	1.01	2.98	0.95	2.98	0.86
80%	3.61	0.64	3.61	0.63	3.61	0.62
100%	5.19	1.15	5.19	1.28	5.19	1.19

IV. CONCLUSIONS AND FUTURE DEVELOPMENTS

In this paper, a preliminary study was conducted to explore the potential of using the measurement of absorbed currents of a 3-phase induction motor for electrical fault diagnosis. The study involved simulating a high-efficiency 4-pole induction motor with a power rating of 3 kW in the Ansys Electronic Desktop environment. The motor was simulated under different load conditions, and the currents drawn on the three phases were evaluated with a high sampling rate of 2 kHz. The study also simulated five different fault conditions in the motor and analyzed the waveforms of the absorbed currents. The results showed that the rotor and stator faults are reflected differently on the current absorptions, and the relationship between the rms values of the different phases and the presence of a low-frequency modulating signal was evaluated. The study successfully developed a system that allowed all five simulated fault situations to be discriminated. Future research will involve measuring currents on real induction motors and reproducing fault conditions to validate the proposed diagnostic system in real-world situations. The study has promising implications for the development of efficient and accurate electrical fault diagnosis systems for induction motors, which could improve maintenance practices and reduce downtime in various industries.

REFERENCES

[1] H. Henao et al., "Trends in fault diagnosis for electrical machines: A review of diagnostic techniques," IEEE Ind. Electron. Mag., vol. 8, no. 2, pp. 31–42, Jun. 2014.

[2] F. C. Trutt, J. Sottile, and J. L. Kohler, "Detection of AC machine winding deterioration using electrically excited vibrations," IEEE Trans. Ind. Appl., vol. 37, no. 1, pp. 10–14, Jan. 2001.

[3] G. Bucci, F. Ciancetta, A. Fioravanti, E. Fiorucci, S Mari, A. Silvestri, “Online SFRA for Reliability of Power Systems: Characterization of a Batch of Healthy and Damaged Induction Motors for Predictive Maintenance”. Sensors 2023, 23, 2583,

[4] D. Siyambalapitiya, P. McLaren, “Reliability improvement and economic benefits of online monitoring system for large induction machines”. IEEE Trans. Ind. Applicat. 1990, 26, 1018–1025.

26th IMEKO TC4 International Symposium
24th International Workshop on ADC and DAC Modelling and Testing
IMEKO TC-4 2023
Pordenone, Italy / September 20-21, 2023

Phase Noise Measurement of ASIC Voltage Controlled Oscillator and PLL Circuit ADF4002

Patrik Jurík[1], Miroslav Sokol[1], Pavol Galajda[1]

[1] *1st, Department of Electronics and Multimedia Telecommunications, Technical University of Kosice, Nemcovej 32, 041 20 Kosice, Slovakia, patrik.jurik@tuke.sk, miroslav.sokol@tuke.sk, pavol.galajda@tuke.sk*

* ***Abstract –*** **This article describes phase noise measurement of a designed ASIC voltage-controlled oscillator in 0.25 µm SiGe BiCMOS technology, with frequency synthesizer ADF4002 from Analog Devices. The oscillator topology utilized in this design is based on a crosscoupled-transistor configuration, and it incorporates two options for frequency control: varicap and capacitor bank. The oscillator frequency is 11.13 GHz with an adjustment frequency range around ±250 MHz. Phase noise measurements were performed on a custom evaluation board. Oscillator with PLL achieves phase noise λ(100 kHz)= -70 dBc at f_c = 11.1353 GHz. The article contains phase noise measurement of ASIC comparisons based on selected parameters, dividers and ADF4002 settings. Comparison with the commercial oscillator TGV2566SM and PLL ADF4002 is introduces as well. Details of the measurement setup and different filter parameters are discussed.**

I. INTRODUCTION

Phase noise measurement is a critical aspect in the characterization and evaluation of voltage-controlled oscillators (VCOs) used in modern communication systems. VCOs are essential components in frequency synthesizers, which are widely used in various applications such as wireless communication, radar systems and satellite communication. The accurate measurement of phase noise helps determine the stability and spectral purity of VCOs, thereby influencing the overall performance of these systems.

We are currently concentrating our research efforts on the creation of a sensor system using Ultra-Wideband (UWB) M-sequence technology. This UWB system has various applications such [1],[2],[3]. Throughout our work, we have successfully designed several specialized rf circuits including a mixer [4], Ultra-wideband amplifier [5], divider [6], and UWB transceiver [7].

In this article, we delve into the phase noise measurement of a designed ASIC VCO implemented in a 0.25 μm SiGe BiCMOS technology by IHP. The VCO is assembled on an evaluation board with the Phase locked loop circuit(PLL) ADF4002 from Analog Devices, which offers enhanced frequency control capabilities. The oscillator topology utilized in this design is based on a crosscoupled-transistor configuration, and it incorporates two options for frequency control: varicap and capacitor bank. This dual control mechanism allows for precise adjustment of the VCO frequency within a range of ±250 MHz around the central frequency of 11.13 GHz.

To evaluate the characteristics of the designed VCO, we performed phase noise measurements on a custom evaluation board. When coupled the VCO with a phase-locked loop (PLL), phase noise level of λ(100 kHz) = -70 dBc/Hz at a carrier frequency of 11.1353 GHz was achieved. The article presents a comprehensive analysis of the phase noise measurements, focusing on various parameters such as dividers and ADF4002 settings [8]. By comparing the phase noise performance under different configurations, we gain insights into the effects of these parameters on the spectral purity of the VCO. Throughout the article, we

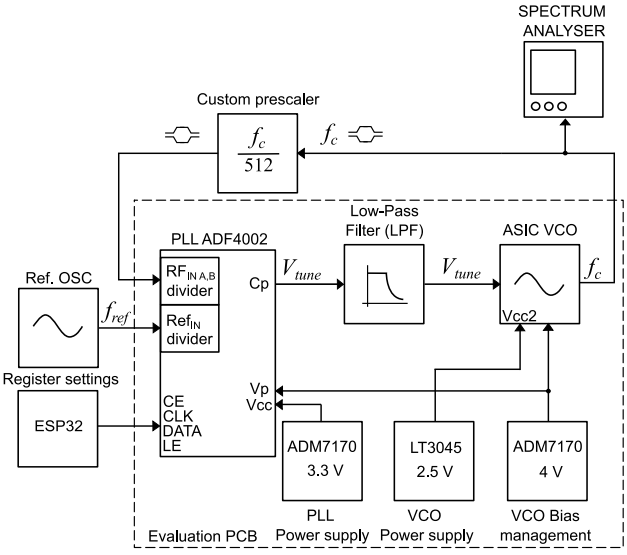

Fig. 1. Block diagram of single channel phase noise test set.

provide detailed information about the experimental setup used for the phase noise measurements. By elucidating the methodology used in this study, we aim to facilitate a thorough understanding of the phase noise measurement process for VCOs. The results and findings presented in

this article contribute to the advancement of VCO design and optimization, particularly in the context of frequency synthesizers for ultrawideband radar systems.

In section II. equipment setup and evaluation of printed circuit board will be discussed, in section III. voltage-controlled oscillator is discussed. Section IV. consist of measurement PLL+VCO configuration with filter variations and divider options. In summary, this article focuses on the phase noise measurement of an ASIC VCO implemented in a SiGE BiCMOS technology, utilizing the ADF4002 frequency synthesizer from Analog Devices. Through detailed experimental analysis, we examine the impact of various parameters on the phase noise performance, offering valuable insights for the design and evaluation of VCOs in modern communication systems.

II. EQUIPMENT SETUP AND EVALUATION BOARD

In Fig. 1 is a block diagram of the measurement setup and evaluation board. For measurement of phase noise was used an Agilent N9020A spectrum analyzer with a frequency range of up to 26.5 GHz. A Keysight N5183B signal generator with frequency range from 9 kHz up to 32 GHz was used as a reference oscillator (in Fig. 1 Ref. OSC). The evaluation board (Fig. 2) consist of Phase locked loop circuit ADF4002 with low noise power supply ADM7170 set to 3.3 V. The ADF4002 supports the ability to set internal circuit parameters using an SPI compatible bus [8]. We used the ESP32 development board to set the parameters of the reference oscillator divider(Ref_{IN}), RF signal divider(RF_{IN}), and other settings. The f_c signal fed to the ADF4002 is divided by 512 in the external divider since the ADF4002 operates in the range of 5 MHz to 400 MHz. The *Cp* output of the ADF4002 represents the V_{tune} voltage which passes through the low-pass filter block and is then fed to the varicap in the voltage-controlled oscillator. The oscillator is powered with ultra low noise linear regulator LT3045 with output set to 2.5 V. Designed ASIC VCO is possible to connect to external bias voltages to change DC operating point of internal circuits. For easier adjustment of these voltages, there are adjustment trimmers on the printed circuit board. As printed circuit board (PCB), the Rogers RO4360G2 material, with 0.508 mm thickness and $\varepsilon_r = 6.15$ was used. The whole evaluation board is powered by 5 V with 80 mA consumption. Our spectral analyzer does not contain an application for measuring the phase noise, based on that phase noise measurement where performed on a spectral analyzer with direct spectrum technique [9].

III. VOLTAGE-CONTROLLED OSCILLATOR DESIGN

Designed voltage-controlled oscillator is a differential oscillator based on BJT NPN transistors in crosscoupled

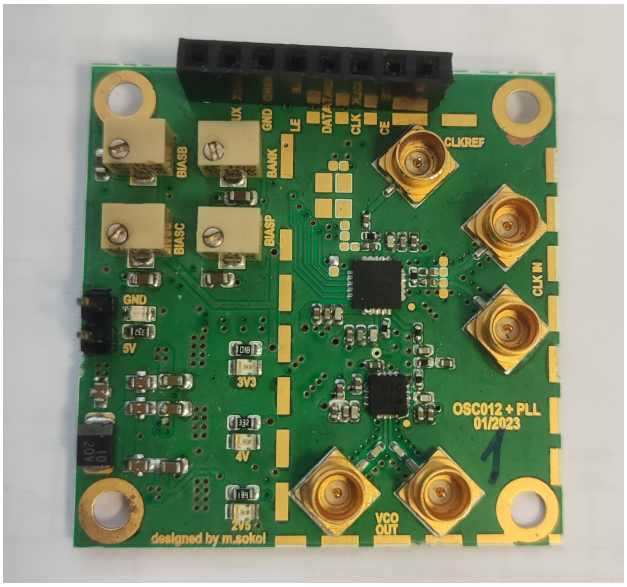

Fig. 2. Evaluation printed circuit board, substrate RO4360G2.

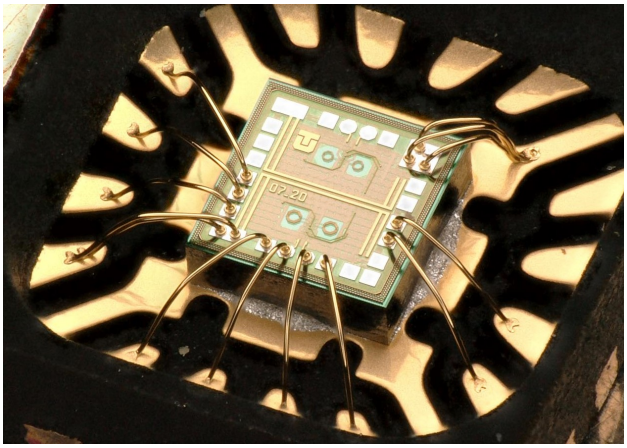

Fig. 3. Naked die of ASIC voltage controlled oscillator in QFN 3x3 mm package.

configuration topology, realized as an application-specific integrated circuit (ASIC)[10],[11],[12]. Fig. 3 shows a naked die, wire bonded in QFN package. The oscillator was primarily designed for the UWB sensor system operating in baseband, with master clock 11 GHz, and useful bandwidth up to 5.5 GHz. As mentioned the oscillator can be adjusted using 5 different bias voltages, three voltages are used to set the operating points of the transistors, and the remaining two are used for frequency control. Frequency of the oscillator can be controlled in two ways, by connecting the voltage to the varicap or by switching on the capacitive bank. For measurement described in this article the voltage on the varicap was regulated and voltage of the capacitive bank was set to a 0 V. The main advantage

of our custom oscillator is its low power consumption, the oscillator consumes only 40 mA at 2.5 V supply voltage. The oscillator itself is an unlocked free-running oscillator and does not achieve the required frequency stability, when locked to a PLL ADF4002 achieves better characteristics.

Component	Filter 1	Filter 2	Filter 3
C1	22 nF	100 pF	1 nF
C2	47 nF	4.7 nF	10 nF
C3	1.5 nF	100 pF	1 nF
R1	220Ω	1 kΩ	1 kΩ
R2	1 kΩ	1 kΩ	1 kΩ
Loop BW [kHz]	82 $\phi 30°$	456 $\phi 46°$	176 $\phi 350°$

Table 1. Filter component configuration.

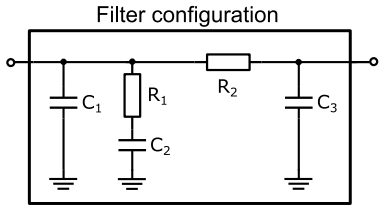

Fig. 4. Schematic of filter configuration.

IV. MEASUREMENT OF PLL+VCO

One of the key parts of the PLL and oscillator connection is the low pass filter applied to the V_{tune} voltage that drives the varicap. Analog devices provide a tool to simulate the effect of the filter ADIsimPLL [13].The low pass filter schematic is shown in Fig. 4. In article three filter configurations were tested with different component values shown in Table 1. The goal was to stabilise the oscillator frequency and suppress spurs around the oscillating frequency, and test the ADF4002 settings and compatibility with our ASIC. The reference clock(RF_{IN}) from external signal generator for ADF4002 was 42.540 MHz.

A. *Filter comparison with Divider Ref_{IN}/4 and RF_{IN}/2*

Fig. 5 shows a comparison of 3 filters, it is possible to see spurs around oscillating frequency. 3rd filter has a higher phase noise around 100 kHz from oscillating frequency, it is also possible to see higher spurs than filter options 1 and 2. Filters 2 and 3 exhibit better phase noise characteristics, and lower spurs. The divider in ADF4002 was set to divide reference frequency(Ref_{IN}) by 4. Divider for f_c frequency (RF_{IN}) was set to 2 for signal dividing. The max amplitude of all 3 configurations were -6.65 [dBm], and phase noise amplitude from oscillator frequency at 100 kHz was -70 dBc/Hz.

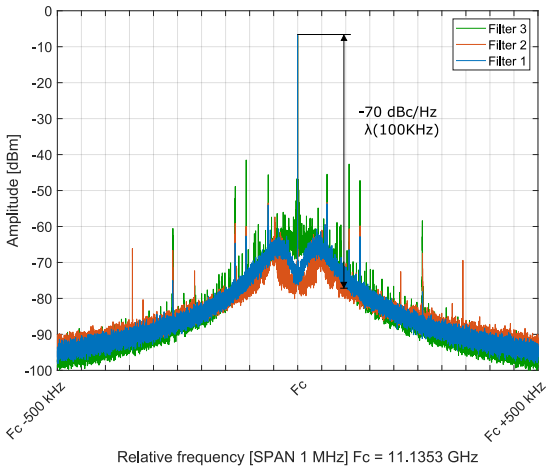

Fig. 5. Phase noise comparison based on used filters and set dividers of reference Clock (Ref_{IN}/4), and divider of oscillator signal (RF_{IN}/2), SPAN 1 MHz.

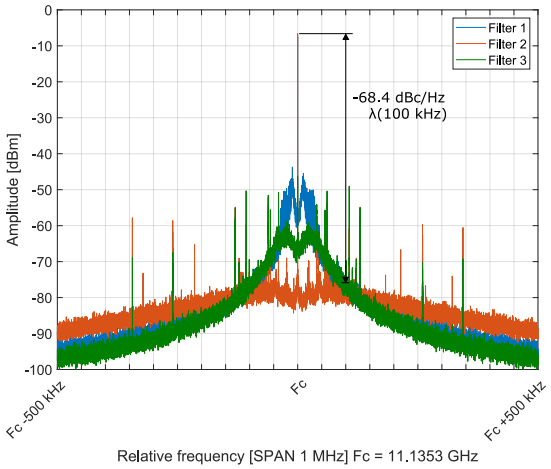

Fig. 6. Phase noise comparison based on used filters and set dividers of reference Clock (Ref_{IN}/2), and divider of oscillator signal (RF_{IN}/1), SPAN 1 MHz.

B. *Filter comparison with Divider Ref_{IN}/2 and RF_{IN}/1*

Different settings of ADF4002 were used in the second measurement, the reference clock divider was set to divide by 2 and divider of oscillator frequency f_c was set to divide by 1. This settings occurs on some occasion better performance. For a filter, configuration is possible to see from Fig. 6, the 2nd filter has the best phase noise characteristic -68 dBc/Hz at 100 kHz, but higher spurs occur around f_c. Filter 1 have the worst phase noise around oscillating frequency -45 dBc/Hz at 10 kHz but has a better tendency to decrease than filter 2.

C. Comparison of designed VCO+PLL and commercial VCO+PLL

We had a commercial voltage-controlled oscillator TGV2566SM [14] in connection with phase-locked loop circuit ADF4002 from Analog devices. This configuration is used in the UWB sensor node. To compare the phase noise envelope, we created a plot with the relative X-axis (see Fig. 7), the commercial oscillator operates at a different frequency (13.3119 GHz) than our oscillator (11.1353 GHz). From the graph, we can see the overall lower phase noise, In the vicinity of f_c is about -10 dBc/Hz and at the level of $\pm$ 500 kHz is about -15 dBc/Hz. Additionally, the graph also reveals the presence of lateral spurs at a level of around +-480 kHz.

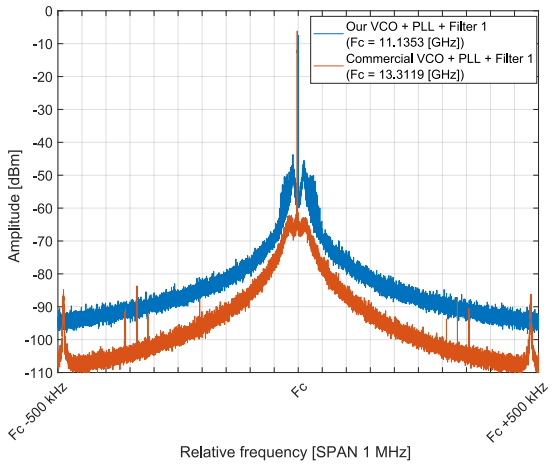

Fig. 7. Phase noise comparison of our solution and commercial solution, both solutions had filter configuration 1, $Ref_{IN}/2$ and $RF_{IN}/1$. Commercial VCO has different oscillator frequency (13.3199 GHz), because of that x-axis is relative for comparison.

V. CONCLUSION

This article presents an assessment board for an ASIC voltage-controlled oscillator that was designed in connection with the phase-locked loop (PLL) circuit ADF4002 from analog devices. The entire power consumption of the PCB was 400 mW, powered by a 5 V supply. The characteristics of the oscillator, in conjunction with the PLL circuit, were notably enhanced, particularly in terms of the stability of the output frequency at 11.1353 GHz and the overall phase noise. Among the three available filter configurations, configurations 1 and 2 are suitable depending on the divider setting of ADF4002. The oscillator achieved a phase noise level of -70 dBc/Hz at 100 kHz, with an output power of -6.65 dBm. Note that it is also important to take into account the losses that occur in the coaxial cables.

VI. ACKNOWLEDGMENT

This work was supported by the Slovak Research and Development Agency under the Contract No. APVV-22-0400 and Scientific Grant Agency (VEGA) under the Contract No. 1/0584/20. We would like to acknowledge the research team at Ilmsens, GmbH. in Ilmenau, Germany for participating and supporting this research.

REFERENCES

[1] D. Kocur, P. Kazimir, J. Fortes, D. Novak, M. Drutarovsky, P. Galajda and R. Zetik, "Short-Range UWB Radar: Surveillance Robot Equipment of the Future," IEEE International Conference on Systems, Man, and Cybernetics (SMC), San Diego, 2014, pp.3767-3772 .

[2] P. Galajda, M. Pecovsky, J. Gazda and M. Drutarovsky, Novel MSequence UWB Sensor for Ground Penetrating Radar Application," 7th IEEE Asia-Pacific Conference on Antennas and Propagation (APCAP), Auckland, NEW ZEALAND, 2018, pp. 110-111

[3] M. Ziga, P. Galajda, S. Slovak, and M. Kmec, "Determination of the quality of frying oil based on UWB impedance spectrometer." IEEE, 16th International Radar Symposium (IRS), Dresden, GERMANY, 2015,pp. 955-960.

[4] Sokol, Miroslav, and Pavol Galajda. "Integrated up-down converter for multi-band uwb m-sequence based radar." 2021 21st International Radar Symposium (IRS). IEEE, 2021.

[5] M. Sokol, et al. "Differential Amplifier Based on Cherry-Hooper Topology for UWB M-sequence Radars." 2019 IEEE Radar Conference (RadarConf). IEEE, 2019.

[6] SOKOL, Miroslav; GALAJDA, Pavol; JURIK, Patrik. "A High-Speed Differential Frequency Divider-by-7 With a 50% Output Duty Cycle." In: 2022 32nd International Conference Radioelektronika (RADIOELEKTRONIKA). IEEE, 2022. p. 1-5.

[7] P. Galajda, S. Slovak, M. Sokol, M. Pecovsky, and M. Kmec, "Integrated M-Sequence Based Transceiver for UWB Sensor Networks," RADIOENGINEERING, vol. 28, no. 1, 2019, pp.175-182.

[8] Phase detector/frequency synthesizer data sheet ADF4002 - Analog Devices. [Online]. Available: https://www.analog.com/media/en/technical-documentation/data-sheets/ADF4002.pdf. [Accessed: 06-Jun-2023]

[9] ROHDE, Ulrich L.; PODDAR, Ajay K.; APTE, Anisha M. Getting its measure: Oscillator phase noise measurement techniques and limitations. IEEE Microwave Magazine, 2013, 14.6: 73-86.

[10] JURIK, Patrik; SOKOL, Miroslav; GALAJDA, Pavol. Design of High Frequency Oscillators for Ultra-Wideband Systems. In: 2021 31st International Con-

ference Radioelektronika (RADIOELEKTRONIKA). IEEE, 2021. p. 1-5.

[11] JIA, Lin, et al. 9.3-10.4-GHz-band cross-coupled complementary oscillator with low phase-noise performance. IEEE transactions on microwave theory and techniques, 2004, 52.4: 1273-1278.

[12] ULLAH, Farman, et al. A bandwidth-enhanced differential LC-voltage controlled oscillator (LC-VCO) and superharmonic coupled quadrature VCO for K-band applications. Electronics, 2018, 7.8: 127.

[13] ADIsimPLL | Design Center | Analog Devices. [Online]. Available: https://www.analog.com/en/design-center/adisimpll.html. [Accessed: 03-Jun-2023]

[14] "TGV2566-SM," RFMW. [Online]. Available: https://www.rfmw.com/products/detail/tgv2566sm-qorvo/496270/. [Accessed: 03-Jun-2023]

ACADEMIA meets INDUSTRY
2023 IMEKO TC-4 International Symposium
Proceedings

Editors

Dr. Dragana Popovic Renella, SENIS Switzerland (*dragana@senis.swiss*)

Dr. Jakub Svatos, Czech Technical University, Czech Republic (*svatoja1@fel.cvut.cz*)

Prof. Platon Sovilj, University of Novi Sad, Serbia (*platon@uns.ac.rs*)

IMEKO
Lajos utca 74-76 Budapest
H-1036 HUNGARY

© 2023 IMEKO

ISBN: 978-3-033-09885-5

All rights reserved. No part of this publication may be reproduced in any form, nor may it be stored in a retrieval system or transmitted in any form, without written permission from the copyright holders.